uOttawa

L'Université canadienne
Canada's university

**FACULTÉ DES ÉTUDES SUPÉRIEURES ET POSTOCTORALES**

uOttawa

L'Université canadienne
Canada's university

**FACULTY OF GRADUATE AND POSDOCTORAL STUDIES**

Alan Lloyd

AUTEUR DE LA THÈSE / AUTHOR OF THESIS

M.A.Sc. (Civil Engineering)

GRADE / DEGREE

Department of Civil Engineering

FACULTÉ, ÉCOLE, DÉPARTEMENT / FACULTY, SCHOOL, DEPARTMENT

Performance of Reinforced Concrete Columns Under Shock Tube Induced Shock Wave Loading

TITRE DE LA THÈSE / TITLE OF THESIS

Murat Saatcioglu

DIRECTEUR (DIRECTRICE) DE LA THÈSE / THESIS SUPERVISOR

Timo Tikka

CO-DIRECTEUR (CO-DIRECTRICE) DE LA THÈSE / THESIS CO-SUPERVISOR

Nova Naumoski

Abass Braimah

Gary W. Slater

Le Doyen de la Faculté des études supérieures et postdoctorales / Dean of the Faculty of Graduate and Postdoctoral Studies

# PERFORMANCE OF REINFORCED CONCRETE COLUMNS UNDER SHOCK TUBE INDUCED SHOCK WAVE LOADING

by

Alan Lloyd

A thesis submitted to
the Faculty of Graduate Studies and Research
in partial fulfillment of the requirements
for the degree of
**Master of Applied Sciences**
in Civil Engineering

Department of Civil Engineering
Faculty of Engineering
University of Ottawa
February 2010

*The M.A.Sc. in Civil Engineering Program
is a joint program with Carleton University
administered by the Ottawa-Carleton
Institute for Civil Engineering

*Your file Votre référence*
*ISBN:* 978-0-494-65532-0
*Our file Notre référence*
*ISBN:* 978-0-494-65532-0

# Abstract

Recent events including deliberate attacks and accidental explosions have highlighted the need for greater research in structural response to blast loading. One of the primary research focuses has been on the prevention of progressive collapse of structures. The response of vertical load transferring members, such as columns, is of particular importance to progressive collapse prevention. In order to understand and predict the behaviour of the global structure during and after a blast loading event, a greater understanding of column behaviour must be developed. Currently there is a limited amount of experimental test data available on the response of reinforced concrete columns exposed to blast loads. This thesis presents the results of experimental research involving tests of scaled reinforced concrete columns exposed to shock wave induced impulsive loads using the University of Ottawa Shock Tube.

A total of 14 half scale reinforced concrete columns were constructed and tested under blast pressures. The columns were designed according to Canadian Standard Association (CSA) Standard A23.3 for the "Design of Concrete Structures" (2006) standard as first story columns for both seismic and non-seismic regions. Axial load was applied to levels similar to what can be expected in actual structures. The columns were exposed to various pressure–impulse combinations which resulted in a range of column response. Comparisons are made between seismically designed and detailed columns and those that represent non-seismic gravity load columns in terms of displacement under similar shockwave loading.

In addition, numerical analyses were conducted using single degree of freedom dynamic analysis. The numerical analysis accounts for the loss of axial load observed with horizontal displacement, strain rate effects on material strengths, the formation of plastic hinges in the column near the supports and at mid-height and the corresponding change in resistance and the response mode shape. The numerical analysis is validated with the experimental results and proven to accurately predict displacement of reinforced concrete columns under shock wave loading. The results indicate that an equivalent single degree

of freedom model may be used to determine the response of a column under air blast induced shock loading if proper displacement-resistance models that account for material strength increase factors and change in axial load are used.

# Acknowledgements

I would like to thank my two supervisors, Dr. Murat Saatcioglu and Dr. Timo Tikka, for their guidance and support on this project. I have also been fortunate to have been assisted by a fellow graduate student, Mr. Eric Jacques, with building and testing specimens in the laboratory.

The support of my wife, René Beaubien, has been critical to my success as a student through many years of study. Without her understanding and willingness to commit to this endeavour, I would not be at this point today.

Finally, I would like to acknowledge the financial support from NSERC, OGS, and the University of Ottawa that allowed me to focus my time on this research.

# Table of Contents

# List of Tables

# List of Figures

# Notations

| | | |
|---|---|---|
| $A_g$ | = | gross cross-sectional area of column |
| $a_o$ | = | speed of sound in ambient atmosphere |
| $A_s$ | = | area of longitudinal reinforcing steel |
| $A_T$ | = | transformed cross-sectional area of column |
| $b$ | = | Friedlander equation decay constant |
| $c$ | = | damping coefficient in dynamic equation of motion |
| $C_p$ | = | specific heat capacity at constant pressure |
| $C_r$ | = | mach reflection coefficient |
| $C_v$ | = | specific heat capacity at constant volume |
| $d$ | = | diameter of an explosive charge |
| $d_{EXP}$ | = | maximum mid-height displacement recorded experimentally |
| $DIF$ | = | dynamic increase factor accounting for material strength increase under high strain rates |
| $DLF$ | = | dynamic load factor determined as the ratio of dynamic and static maximum displacement |
| $d_{max}$ | = | maximum mid-height displacement |
| $d_{SDOF}$ | = | maximum mid-height displacement predicted by single degree of freedom model |
| $E_c$ | = | modulus of elasticity of concrete |
| $E_s$ | = | elastic modulus of steel |
| $F$ | = | equivalent single degree of freedom external force |
| $f(t)$ | = | external forcing function in dynamic equation of motion |
| $f'_c$ | = | static strength of concrete |
| $f'_{dc}$ | = | dynamic strength of concrete |
| $f_{du}$ | = | dynamic ultimate stress of reinforcing steel |
| $f_{dy}$ | = | dynamic yield stress for reinforcing steel |
| $f_u$ | = | static ultimate stress of reinforcing steel |

$f_y$ = static yield stress of reinforcing steel

$h$ = height of column cross section

$I$ = incident impulse over the negative phase

$I_r$ = reflected impulse over the positive phase

$I_s$ = incident impulse over the positive phase

$k$ = stiffness in dynamic equation of motion

$K$ = equivalent single degree of freedom stiffness

$K_L$ = load factor for single degree of freedom conversion

$K_m$ = mass factor for single degree of freedom conversion

$L$ = length of the column

$L_D$ = shock tube driver length

$m$ = mass in dynamic equation of motion

$M$ = equivalent single degree of freedom mass

$n$ = ratio of steel modulus of elasticity to concrete modulus of elasticity

$P$ = axial load applied to column

$p(t)$ = incident overpressure at a time within the positive phase

$P_D$ = shock tube driver pressure

$p_o$ = ambient atmospheric pressure

$P_o$ = concentric axial load capacity of column

$p_r$ = reflected overpressure

$p_s$ = incident overpressure

$q_s$ = maximum dynamic pressure of shock wave front

$R$ = standoff distance from explosive charge

$s$ = spacing of transverse steel

$t_a$ = arrival time of shock wave

$T_d$ = effective positive phase duration for linear pressure-time history

$t_d$ = positive phase duration of shock wave

$t_{EXP}$ = time to reach maximum mid-height displacement after the start of shock wave loading recorded experimentally

$t_{max}$ = time to reach maximum mid-height displacement after the start of shock wave loading

$T_N$ = Natural period of vibration

$T_s$ = positive phase duration

$t_{SDOF}$ = time to reach maximum mid-height displacement after the start of shock wave loading predicted by single degree of freedom model

$u$ = displacement in dynamic equation of motion

$\dot{u}$ = velocity in dynamic equation of motion

$u_{dyn}$ = maximum displacement under dynamic loading

$\ddot{u}$ = acceleration in dynamic equation of motion

$U_s$ = wave front velocity of shock wave

$u_s$ = velocity of air particles in shock wave

$u_{st}$ = maximum displacement under static loading

$W$ = mass (weight) of an explosive charge

$y_c$ = iso-displacement value for pressure-impulse curves

$Z$ = scaled distance determined as the standoff distance divided by the cube root of charge mass

$\alpha_1$ = angle of reflecting plane parallel to direction of shock wave

$\gamma$ = specific heat capacity ratio

$\Delta G$ = Gibbs free energy change of energy dissipated in an explosion

$\Delta H$ = enthalpy change in an explosion

$\Delta p_{min}$ = peak negative pressure

$\Delta S$ = entropy change in an explosion

$\varepsilon'_c$ = average strain rate for concrete

$\varepsilon'_s$ = average strain rate for steel

$\varepsilon_{axial}$ = initial axial strain in column due to axial load

$\varepsilon_{max}$ = total maximum strain in tension steel

$\varepsilon_{max+tot\ res}$ = total maximum strain in tension steel plus cumulative residual strain from previous tests

$\varepsilon_{max\text{-}axial}$ = maximum recorded strain in tension steel not including initial axial strain

$\varepsilon_{residual}$ = relative residual strain in tension steel after test

$\varepsilon_{tot\ res}$ = cumulative residual strain in tension steel

$\theta$ = support rotation

$\rho_o$ = density of ambient atmosphere

$\rho_{rs}$ = longitudinal reinforcement ratio

$\rho_s$ = density of shock wave front

$\rho_t$ = volumetric ratio of transverse steel volume to volume of concrete

$\sigma_{dyn}$ = material strength under high strain rate dynamic loading

$\sigma_{st}$ = material strength under static loading

$\varphi$ = non-dimensional mode shape

$\omega$ = natural frequency of vibration

# 1 CHAPTER 1

# Introduction

## *1.1 General*

Recent events including deliberate attacks and accidental explosions have highlighted the need for greater research in structural response to blast loading. Currently, within Canada and abroad, there is a significant demand for engineering guidelines for mitigation of blast loads effects on structures with very little experimental research completed to provide this guidance. Blast induced shock wave loading on structures shares many parallels with other extreme loading including wind and earthquake amongst others. The primary similarity is that under all of these scenarios, a dynamic load is applied to the structure in a different direction than typical gravity load cases. These loads require a designer to account for lateral loads on axial members such as columns and walls, out of plane loading on planar member such as beams, and inelastic demands on structural members that result in changes in local and global structural behaviour. The primary difference between blast loading and other examples of non gravity loading is the time scale involved. Depending on many factors, such as explosive size, distance from the structure, geometry of the structure and the nature of the surrounding environment, the duration of blast loading will differ. However, for general high explosives, the typical load duration will last for a fraction of a second rather than many seconds or minutes for earthquake and wind loading. Peak pressure of blast loads also have the potential to be significantly larger than those associated with wind and earthquakes.

Currently there is little information available on design and performance of reinforced concrete elements under blast-induced shock waves. Some of the limited research in the area is classified, providing challenges for structural engineers who are faced with the intricacies of design under blast loads. Experimental research is especially lacking in the field because of the difficulties and prohibitive costs associated with field testing for research purposes. The current research project

is aimed towards filling this research gap, while generating experimental and analytical design information for reinforced concrete columns.

This chapter will present the objective and scope of current research while introducing the nature of blast loading and the response of structures to impulsive shock wave loading. The particular focus will be on reinforced concrete members and specifically reinforced concrete columns. A historical overview of a real structure's response to blast loads along with a summary of the experimental work on reinforced concrete columns available in the literature is provided.

## *1.2 Objective*

The objective of the current research project is to investigate performance of reinforced concrete columns subjected to blast loads. The objective includes combined experimental and analytical characteristics of reinforced concrete columns under blast loads with a view of providing design information. Also included in the objective is to contribute towards the operation and calibration of the newly installed Shock Tube of the University of Ottawa for simulation of blast-induced shock waves.

## *1.3 Scope*

The following forms the scope of the current investigation:

- Literature review on the characteristics of blast phenomenon and structural response to blast shock waves.
- Literature review of previous research.
- Calibration and operation of the newly acquired Shock Tube for blast load simulation for use in experimental column research.
- Design, construction and instrumentation of 14 large-scale square and rectangular columns for shock testing.
- Conducting tests of column specimens under different impulsive loads corresponding to different charge-distance combinations by means of a shock tube.

- Evaluation of test data and presentation of test results.
- Development of force-displacement relationships for reinforced concrete columns subjected to transverse loading.
- Application of force-displacement relationships as stiffness models in equivalent single degree of freedom numerical integration dynamic analysis techniques
- Comparison of analytically predicted displacements with experimentally recorded displacements

## *1.4 Explosive Classification*

Explosions are typically grouped in three categories based on the nature of the energy release mechanism. These categories are physical, nuclear and chemical. Smith and Hetherington (1994) give examples of these three explosion events as the following:

Physical: a catastrophic failure of a pressure vessel resulting in a shock wave and possible high velocity projectiles.

Nuclear: the energy released due to the redistribution of protons and neutrons in the formation of different atomic nuclei.

Chemical: an exothermic reaction that occurs with the rapid oxidation of fuel elements such as carbon and hydrogen. This reaction will produce enormous heat energy and rapidly expanding gases resulting in a shock wave.

In conventional explosives (non nuclear) there are two main classification levels; high explosives and low explosives. Low explosives are those that burn to create heat, smoke, gases, fire and noise such as propellants and pyrotechnics (Bulson 1997). High explosives rapidly detonate releasing significant amounts of energy in the form of heat and pressure. These explosives form shock waves that will propagate through the surrounding atmosphere and interact with nearby

objects. The most common benchmark for comparison of different high explosive types is Trinitrotoluene (TNT). Other examples include military grade explosives such as Composition B and C-4, and improvised explosives such as ammonium nitrate and fuel oil (ANFO).

## *1.5 Energy of Explosions*

Smith and Hetherington (1994) define the chemical reaction that occurs in the detonation of high explosives as exothermic, one where energy is released. This reaction may occur due to a number of reasons depending on the nature of the initially stable compounds forming the explosive materials. All, however, involve an initial addition of energy into a system to drive the reaction such as an increase in heat or pressure or the addition of a catalyst material. The reaction process is complicated and differs depending on the materials involved; however, very definite generalizations of energy changes can be easily described.

The resultant energy dissipated in an explosion, a measure of the work capacity of the chemical reaction, is a quantity called the Gibbs Free Energy change. This quantity is the combination of the change in entropy and enthalpy of the reactants and products involved in the explosion and is shown in Equation 1.1. In Equation 1.1, the Gibbs Free Energy change is represented by $\Delta G$ and is a negative value meaning that energy is being released from the system. The change in enthalpy of the reactants and products is shown as $\Delta H$. The entropy change is shown as $\Delta S$ and the temperature of the products of the reaction is $T$.

[1.1] $$\Delta G = \Delta H - T\Delta S$$

Since the reaction is exothermic, meaning energy is released from the reactants while forming the products of the reaction, the change in enthalpy is negative. In high explosives this change in energy as described in Equation 1.2, is a very large negative term that is commonly known as the heat of explosion. In this equation the heat of the explosion is the total change in enthalpy which is taken as the difference in the enthalpy change of the products and that of the reactants.

[1.2] $\Delta H = \sum(\Delta H(products) - \Delta H(reactants))$

The change in entropy of the system, $\Delta S$, is a large positive value that reflects the formation of the gaseous products of the reaction. The sum of the multiplication of temperature ($T$) and entropy change ($\Delta H$) for all the products of the reaction give a large positive energy change that represents the expansion of gases which will form a shock wave in the explosion.

## *1.6 High Explosive Equivalencies*

When detonated, high explosives will produce a shock wave with a pressure distribution that is dependent on the energy potential of the explosive material. It is common procedure to normalize the mass of any high explosive material into an equivalent mass of TNT using a conversion factor based on the energy potential of the two high explosives. This equivalent mass of TNT is then used to generate the pressure distribution of the explosive in question. Conversion factors for various explosives are available in the literature for both the equivalent TNT pressure factor and the equivalent TNT impulse factor. Some of these conversion factors for various explosives are listed in Table 1.1 (Hyde 1992). All further references to explosive mass in this work are to TNT or TNT equivalent explosives.

## *1.7 Shock Wave Pressures*

The detonation of high explosives in air will produce a number of effects that may influence a structure. These effects are a shock wave, a fire ball, a high velocity wind, and possible projectile debris. Depending on the size of the explosion, its proximity to the structure, and the nature of the structure, each effect of the blast will have differing degrees of influence on the structural response. For explosions that occur outside of the structure, the primary focus of this research, the shock wave itself generally has the most significant impact on the structure.

A shock wave in air is a zone of compressed atmosphere that is moving at a velocity greater that the speed of sound in normal atmospheric conditions. As the shock wave progresses, it

compresses the surrounding atmosphere. This compression increases the pressure within the atmosphere creating what is referred to as incident pressure which is independent of the velocity of the air particles within the shock wave itself. If the shock wave interacts with an object, the velocity change in the air particles will cause further compression and create what is known as dynamic pressure. The following sections will further explain and quantify the pressure-time relationship in a shock wave prior to and during the interaction with surrounding objects.

## *1.8 Scaling Laws*

Hopkinson in 1915 and Cranz in 1926 describe a relationship for pressures proportional to the cube root of charge mass and standoff distances for atmospheric explosions (Baker 1983). This relationship, known as the Hopkinson-Cranz Scaling Law, is used to normalise explosions to generalize pressure and impulse relationships. The Hopkinson-Cranz scaling law states that: "Self-similar blast waves are produced at identical scaled distances when two explosive charges of similar geometry and of the same explosive, but of different sizes, are detonated in the same atmosphere" (Baker 1983). The Hopkinson-Cranz scaling law assumes that charge weight or mass is proportional to the cube root of the diameter of the charge as shown in Equation 1.3 where $W_i$ is the mass of the explosive charge and $d_i$ is the diameter of the charge.

$$W_1 \propto d_1^{\,3}$$

*and*

$$W_2 \propto d_2^{\,3} \qquad [1.3]$$

$$\therefore \frac{W_1}{W_2} = \left(\frac{d_1}{d_2}\right)^3$$

From this relationship, if a charge mass $W_1$ results in an incident pressure at standoff distance $R_1$, then a charge of mass $W_2$ will result in the same incident pressure at a standoff distance of $R_2$ where the relationship between $R_1$ and $R_2$ is described in Equation 1.4 and shown graphically in Figure 1.1.

$$[1.4] \quad \frac{R_1}{R_2} = \left(\frac{W_1}{W_2}\right)^{\frac{1}{3}}$$

To simplify this relationship, the term scaled distance, $Z$ in units *distance per mass*$^{1/3}$, is introduced where the scaled distance is the constant of proportionality between standoff distances and charge weights that result in the same incident pressures $p_s$. The formula for scaled distance is shown in Equation 1.5, where a smaller scaled distance results in a larger incident pressure.

$$[1.5] \quad Z = \frac{R}{W^{\frac{1}{3}}}$$

The use of scaling laws directly relate incident pressures of different explosions, however in the simple format described by Hopkinson and Cranz other properties such as impulse, wave front velocity, arrival time, particle velocity, and dynamic pressure are not linearly proportional to scaled distance. Various relationships have been developed to describe these wave front properties as functions of charge weight and standoff distance or scaled distance.

## *1.9 Shock Wave front Parameters*

Prior to the interaction of a shock wave with any surrounding objects, the blast wave can for a free air blast can be considered as having spherical symmetry in all properties radiating out from the center of the explosion. At any given standoff distance, there are several important properties of the shock wave at the wave front which is the point of interaction between the shock wave and the surrounding atmosphere. Three of these properties are of primary interest: shock wave front velocity, shock wave density, and dynamic pressure. With the knowledge of these three properties, along with standoff distance and charge weight, the shock wave interaction on surrounding objects of known geometry can be fully described. Rankine and Hugoniot first presented these relationships in 1870 (Smith 1994), shown in Equations 1.6 through 1.8, which were further developed by Lipmann and Roshko in 1957.

[1.6] $$U_s = \sqrt{\frac{6p_s + 7p_o}{7p_o}} \cdot a_o$$

[1.7] $$\rho_s = \frac{6p_s + 7p_o}{p_s + 7p_o} \cdot \rho_o$$

[1.8] $$q_s = \frac{5p_s^{\,2}}{2(p_s + 7p_o)}$$

Where $U_s$ is wave front velocity, $p_s$ is incident pressure, $p_o$ is ambient atmosphere pressure ahead of the shock wave, $a_o$ is the speed of sound in ambient atmosphere conditions, $\rho_o$ is the ambient atmosphere density ahead of the shock wave, $\rho_s$ is the density at the shock wave front, and $q_s$ is the maximum dynamic pressure of the wave front (Smith and Hetherington 1994).

Brode (1955) found the relationship between peak incident overpressure, $p_s$ (kPa), and scaled distance, $Z$ $(m/kg^{1/3})$, for spherical explosions in air as two cubic functions valid over different domains as shown in Equation 1.9.

[1.9] $$p_s = \frac{670}{Z^3} + 100 \qquad (p_s > 10{,}000\ kPa)$$

$$p_s = \frac{97.5}{Z} + \frac{145.5}{Z^2} + \frac{585}{Z^3} - 1.9 \qquad (10 < p_s < 10{,}000\ kPa)$$

Henrych (1979) expanded on the work of Brode to find improved equations for peak incident pressure at the wave front using experimental and numerical data. The Henrych relationship for incident pressure *(kPa)*, Equation 1.10, along with the one proposed by Brode are shown in Figure 1.2.

[1.10] $$p_s = \frac{14.072}{Z} + \frac{554}{Z^2} - \frac{35.7}{Z^3} + \frac{0.625}{Z^4} \qquad (0.05 \le Z < 0.3)$$

$$p_s = \frac{619.4}{Z} - \frac{32.6}{Z^2} + \frac{213.2}{Z^3} \qquad (0.3 \le Z < 1.0)$$

$$p_s = \frac{662}{Z} - \frac{405}{Z^2} + \frac{328.8}{Z^3} \qquad (1.0 \leq Z < 10)$$

Both the Brode and Henrych relationships for peak incident pressure are significantly more accurate for larger scaled distances or far field explosions, than for near field explosions (Smith and Hetherington 1994).

## *1.10 Shock Wave Parameters*

Relative to a fixed position, a shock wave will have a distinct variation with time. This pressure time relationship can be quantified by peak incident pressure, positive phase duration ($T_s$), positive phase impulse ($I_s$), peak negative pressure ($\Delta p_{min}$), negative phase duration ($T^-$), and negative phase impulse ($I^-$) (Smith and Hetherington 1994). These parameters are shown in Figure 1.3 as values normalized by the cube root of the mass of the explosive. The positive phase impulse of the shock wave is the area under the pressure time curve for the positive phase of the shock wave as described by Equation 1.11. For scaled distances larger than $Z=1.6$, Brode empirically found that the peak negative pressure was proportional to the inverse of scaled distance (Equation 1.12). The negative phase duration and negative phase impulse are shown in Equations 1.13 and 1.14 (Smith and Hetherington 1994).

[1.11] $$I_s = \int_a^{a+T_s} p(t)dt$$

[1.12] $$\Delta p_{\min} = -\frac{0.35}{Z} \qquad (Z > 1.6)$$

[1.13] $$T^- = 1.25W^{1/3}$$

[1.14] $$I^- \approx I_s\left[1 - \frac{1}{2Z}\right]$$

The positive phase incident pressure-time history is commonly described by the Friedlander equation, Equation 1.15, as an exponential decay curve with a decay constant (Table 1.2) that is an empirical function of scaled distance (Smith and Hetherington 1994).

$$[1.15] \quad p(t) = p_s\left[1-\frac{t}{T_s}\right]e^{-\frac{bt}{T_s}}$$

## *1.11 Shock Wave Reflections*

When a shock wave interacts with an object, including the ground, it loses spherical symmetry. The pressures that the object experiences become a combination of the pressure due to the compressed atmosphere, stagnation pressure, and the dynamic pressure due to the moving air particles. The geometry of the object itself will change the properties of the shock wave as pressures will be reflected and air particles will be forced to change direction of flow. This section will introduce some of the concepts of shock wave reflections which occur during interaction with surrounding objects.

### 1.11.1 Hemispherical Shock Waves

If an explosive charge is detonated directly on a perfectly smooth rigid surface, the corresponding shock wave has hemispherical symmetry. The parameters of the shock wave, including the pressure-time history described in Equation 1.15, can simply be modified by recognizing the equivalence between the spherical symmetry lines radiating from the centre of a spherical shock wave and the complete reflection of the rigid surface. This is illustrated in Figure 1.4 where the change in a parameter with respect to distance perpendicular to the radial line of symmetry is zero for any of the blast wave parameters including pressure, wave velocity, and particle velocity. In other words, the flux of any parameter is zero perpendicular to the blast radius. This zero flux perpendicular to the line of symmetry is also true for all points in the hemispherical shock wave, also shown in Figure 1.4, including at the rigid surface. From this understanding, it is evident that the mass of the hemispherical explosion produces a shock wave with all parameters equivalent to that of a spherical explosion of twice the explosive mass.

This principle is commonly applied to quantify shock waves for explosives on ground surfaces. Real ground surfaces are not perfectly smooth and rigid. Since they are not rigid, a surface explosion will not have complete reflection, and a crater will be produced. Since they are not perfectly smooth, there will be drag forces associated with the movement of air particles that will disrupt the hemispherical symmetry. Both of these effects reduce the magnitude of the surface explosion to less than the equivalent double mass spherical explosion. It has been found that a good approximation for the equivalent explosive mass magnification factor to equate spherical to hemispherical blasts while accounting for energy absorption in the ground is *1.8* (Smith and Hetherington 1994).

### 1.11.2 Normal Reflections

If a planar shock wave were to interact with a rigid wall that is infinite in width and height and perpendicular to the direction of the shock wave motion, the pressures would be amplified. When the shock wave meets the rigid wall, the air particles will be forced to an abrupt stop. These air particles will be further compressed by the incoming shock wave creating a reflected pressure at the wall that is greater than the incident pressure. Rankine and Hugoniot found an equation for the reflected pressure using conservation of energy and momentum (Smith and Hetherington 1994). In Equation 1.16, the dynamic pressure, $q_s$, is multiplied by a factor of the specific heat ratio for air, $C_p/C_v=\gamma$, where $\gamma=1.4$.

[1.16] $$p_r = 2p_s + (1+\gamma)q_s$$

Using the previous equation, the equation for dynamic pressure, Equation 1.17, and an ideal gas assumption for air, the reflected pressure may be calculated as only a function of ambient atmosphere pressure, $p_o$, and incident pressure as found in Equation 1.18. In Equation 1.17, $\rho_s$, is the density of air in the ambient atmosphere and $u_s$ is the velocity of the air particles in the shock wave.

[1.17] $q_s = \frac{1}{2}\rho_s u_s^2$

[1.18] $p_r = 2p_s\left[\frac{7p_o + 4p_s}{7p_o + p_s}\right]$

### 1.11.3 Oblique Reflections

The angle of incidence is the angle between the tangent to the shock front isobar and the plane of the surface with which it is interacting. The reflection of the shock wave becomes more complex as the angle of incidence, $\alpha_I$, deviates from $0$ °. In general, the reflected pressure is proportionally smaller as the angle of the reflecting plane decreases. When the reflecting plane is parallel to the direction of the shock wave, there is no reflection and the pressure is equal to the incident pressure. An exception occurs at an angle of around $\alpha_I = 40°$ where the wave reflecting off the reflecting plane interacts with the incident shock wave and creates a third shock wave, called Mach reflection and is shown as the creation of a triple point between the incident wave, reflected wave, and Mach wave in Figure 1.5. This Mach reflection creates a shock wave called the Mach stem which moves along the reflecting plane. The pressures in the Mach stem may be significantly higher than the incident pressures. Pressures within the Mach stem are found as a function of the incident pressure and reflecting angle which give a reflection coefficient, $C_r$, which is multiplied with the incident pressure as shown in Equation 1.19 (TM 5-1300 1990). Mach reflection coefficients are shown in Figure 1.6 for various incident pressures and reflecting angles.

[1.19] $p_r = C_r p_s$

### 1.11.4 Interaction with Real Structures

As a shock wave interacts with a real structure of finite dimensions, the forces on the structure change with time and location on the structure. As the wave passes over the structure, there are

drag forces due to the dynamic pressure and the movement of air particles. This research is focused on structural response to reflected pressure therefore the complex shock wave interaction with finite structures beyond pure reflection will not be presented in this study.

## *1.12 Structural Response to Shock Waves*

Structural response to shock wave loading is a transient dynamic problem. The combination of external loading and inertia forces are resisted by internal elastic and damping forces within the structure and structural members. The relationship between natural period of the global structure, natural period of structural members, duration of the shock wave loading, geometry of the structure, and location of the loading are significant in determining how the structure will respond. Due to the relatively small mass and large stiffness of individual structural members, natural periods of the members tend to be significantly smaller than those of the entire structure. Since shock wave durations are short, in the order of milliseconds for conventional high explosives, the ratio of shock wave duration to natural period of structural member is far closer to unity than that of the duration to the global natural period. As a result, the total forces on a member can be amplified significantly due to dynamic forces, specifically inertia forces and the response of local members to shock wave loading. This section will outline some of the principles of transient dynamic response of structures under shock wave loading. The dynamic equilibrium equation will be presented and an equivalent single degree of freedom analysis (SDOF) method will be discussed. An equivalent static analysis procedure that accounts for the dynamic loading will also be presented along with a brief overview of the application of the analysis procedures for reinforced concrete members.

### 1.12.1 Equation of Motion

An object of mass $m$ and stiffness $k$ with a damping coefficient $c$ that is subjected to an external loading equal to $f(t)$ will be in dynamic equilibrium at any time. This dynamic equilibrium is expressed in Equation 1.20 (Biggs 1964) where $\ddot{u}$ is acceleration, $\dot{u}$ is velocity, and $u$ is displacement of the object.

[1.20] $m\ddot{u} + c\dot{u} + ku = f(t)$

In the dynamic equation of motion, the inertia force is the product of mass and acceleration, the damping force is the product of the damping coefficient and velocity. The elastic force is the product of the stiffness and displacement.

### 1.12.2 Equivalent Single Degree of Freedom Approach

A common method of member analysis under shock wave loading is the equivalent SDOF approach. In this method, member properties mass and stiffness and the external loading are converted into an equivalent single degree of freedom by using deformed shape factors (Biggs 1964) that relate to the motion of a single point of interest in a single direction of motion. The damping coefficient is generally ignored as it has negligible contribution to the equation of motion during the first cycle up to maximum displacement (TM 5-1300 1990). In order to idealize the system into an equivalent SDOF, the displaced shape function, $\varphi$, must be known where $\varphi$ is a non dimensional mode shape shown in Figure 1.8. Once the shape function is known, mass factors ($K_m$) and load factors ($K_L$) may be found according to Equations 1.21 and 1.22 respectively (Biggs 1964). The load and mass factors described in Equations 1.21 and 1.22 are only valid when the mass and load are not variable along the member length.

[1.21] $K_m = \int \varphi^2(x)dx$

[1.22] $K_L = \int \varphi(x)dx$

The stiffness of the structural component is determined with respect to a unit displacement in the direction of the chosen degree of freedom due to the actual applied load. The mass is the total mass of the structural element. Conversion to an equivalent SDOF system is simply the product of the load factors and the stiffness, the load factors and the total load and the mass factors and the total mass. If the structure remains elastic, it will have only one set of conversion factors. If the structure undergoes inelastic deformation, multiple mode shapes must be used to obtain

multiple conversion factors. Equation 1.23 shows the equivalent SDOF equation of motion for the structural element which is shown graphically in Figure 1.7.

[1.23] $K_m m\ddot{u} + K_L k u = K_L f(t)$

This equation of dynamic equilibrium may be solved in multiple ways. If the forcing function is easily defined and the system remains linear in both geometry and material properties, it is possible to find a closed form solution. If the system is more complicated, a numerical integration solution may be necessary. The US Departments of the Army, the Navy, and the Air Force Structures to Resist the Effects of Accidental Explosions (TM 5-1300 1990) recommends the use of the average acceleration method for numerical integration. In this method, the response is divided into a series of finite time steps and the displacement and velocity of the SDOF system are related to the average acceleration at each time step. In each time step the mass, stiffness and force in the SDOF system are updated based on resistance curves and the pressure history of the blast.

#### *1.12.2.1* ***Resistance-Displacement Curves***

Prior to any dynamic analysis, and as part of determining conversion factors and mode shapes, a force resistance curve for the structural element must be developed. This curve, shown by example of a fixed ended beam in Figure 1.8, accounts for changes in stiffness due to inelastic behaviour such as plastic hinge formation. The stiffness of the member at any deformation point is taken as the slope of the resistance-displacement curve.

### 1.12.3 Equivalent Static Procedure

It is common to represent the pressure-time history as a linear relationship for the equivalent SDOF procedure (Smith and Hetherington 1994). This is done by ensuring that peak pressure and total positive phase impulse are unchanged. The effective duration of the shock wave, $T_d$, is defined in Equation 1.24 and the pressure time history, $P(t)$, is defined in Equation 1.25 and shown graphically in Figure 1.9.

[1.24] $T_d = 2\frac{I_r}{p_r}$

[1.25] $P(t) = p_r\left(1-\frac{t}{T_d}\right)$

Using the above pressure-time history and the dynamic equation of motion, it can be shown that the displacement at the degree of freedom at any time, $u$, has a closed form solution for an elastic member (Equation 1.26). In this equation, the natural frequency of the equivalent SDOF system is $\omega$, $F$ is the peak reflected pressure multiplied by its tributary area and the load factor $K_L$ and $K$ is the stiffness of the total system multiplied by the load factor $K_L$ (Smith and Hetherington 1994).

[1.26] $u(t) = \frac{F}{K\omega t_d}[\sin \omega t_d - \sin \omega(t - T_d)] - \frac{F}{K}\cos \omega t$

To equate the dynamic system into an equivalent static system, a dynamic load factor (*DLF*) is introduced to account for the inertia forces. This dynamic load factor is the ratio of the displacement under dynamic loading divided by the displacement under pure static loading equal at the magnitude of the peak force, $F$. This ratio is shown in Equation 1.27 where $u_{dyn}$ is the maximum displacement under dynamic loading and $u_{st}$ is the displacement under static loading. Using Equation 1.26 and the calculated static displacement in Equation 1.28, the dynamic load factor for an equivalent SDOF system with a triangular force-time relationship is described by Equation 1.29 and shown in Figure 1.10. Once the dynamic load factor is known, the equivalent static analysis procedure to find maximum deflection is done simply by multiplying the static deflection by the dynamic load factor.

[1.27] $DLF = \frac{u_{dyn}}{u_{st}}$

[1.28] $u_{st} = \frac{F}{K}$

[1.29] $$DLF = \frac{1}{\omega t_d}[\sin \omega t_d - \sin \omega(t - t_d)] - \cos \omega t$$

Since more complicated loading patterns and inelastic response curves yield no closed form solutions similar to Equation 1.29, Graphical curves for the dynamic load factor of various loading types and force resistance curves are available in the US Department of the Army, the Navy, and the Air Force Structures to Resist the Effects of Accidental Explosions (1990). These curves were developed based on numerical integration techniques on equivalent SDOF models.

### 1.12.4 Material Increase Factors

Both reinforcing steel and concrete experience a change in material properties under the high strain rates associated with shock wave loading. In concrete, the high rate of strain will cause an increase in the initial elastic modulus and an increase in the crushing strain. In steel, there will be an increase in yield stress and an increase in ultimate stress. Figures 1.11 and 1.12, reproduced from TM 5-1300 (1990), show the general shape of the stress-strain curves for concrete and steel under high strain rates respectively. In order to account for the increase in strengths under high strain rates, a coefficient called the dynamic increase factor (*DIF*) is introduced. The dynamic increase factor is the ratio of the strength at a point of interest on the stress strain curve under high strain rate dynamic loading, $\sigma_{dyn}$, divided by the strength at the corresponding strain under static loading, $\sigma_{st}$ (Equation 1.30). Numerous studies have been undertaken to try to accurately determine dynamic increase factors for concrete and steel, the results from some of these studies are shown in Figures 1.13 and 1.14 for concrete in compression and tension respectively (Lu and Xu, 2004).

[1.30] $$DIF = \frac{\sigma_{dyn}}{\sigma_{st}}$$

TM 5-1300 (1990) accounts for dynamic increase factors in an iterative manner for both the equivalent SDOF procedure and the equivalent static procedure by first providing an initial

dynamic increase factor based on material, element type and explosion type (Table 1.3). Using these increase factors, the time to maximum displacement is determined and an average strain rate is calculated from Equations 1.31 for concrete and 1.32 for steel.

$$[1.31] \quad \varepsilon'_c = \frac{0.002}{t_E}$$

$$[1.32] \quad \varepsilon'_s = \frac{f_{dy}}{E_s t_E}$$

Where $\varepsilon'_c$ is the average strain rate for concrete, $\varepsilon'_s$ is the average strain rate for steel, $t_E$ is the time to reach yield in reinforcement based on the resistance-displacement curve and the dynamic response, $f_{dy}$ is the dynamic yield stress for reinforcing steel from the previous iteration, and $E_s$ is the elastic modulus of the steel. These new strain rates are used to update the dynamic increase factor based on design charts shown in Figure 1.15 for concrete and Figure 1.16 for steel and the analysis is repeated until convergence is achieved.

### 1.12.5 Pressure – Impulse Diagrams

The two forces acting on a structure or structural member subjected to blast loads are the applied shock wave loading and the inertia force that occurs during dynamic response. How the element will respond depends on the mass, the stiffness, the maximum pressure and the shape and duration of the blast load. If the mass and stiffness, properties of the element itself, are held constant, the primary variables for structural response are the maximum pressure and the shape and duration of the blast load, which may be quantified as the impulse. For any given response parameter, be it maximum displacement or some quantitative damage level, there is an infinite combination of pressures and impulses that will cause this response. A graphical technique, pressure-impulse diagrams (*p-I* diagrams), has been developed using this concept to normalize structural response to any blast load (Li and Meng 2002).

Pressure-impulse diagrams are created by setting the maximum displacement equal to a predetermined value, $y_c$, and solving for different combinations of pressure and impulse that will cause this displacement. By plotting an iso-displacement curve on the pressure-impulse coordinate system, three distinct regions are evident. Figure 1.17 shows these regions as the quasi-static region where the duration of the pulse loading is much larger than the period of the structure, the dynamic region where the load duration is similar to the structural period, and the impulsive region where the duration is much smaller than the period. For an elastic structure, it is possible to define the asymptotes of the quasi-static region (Equation 1.33) and the impulsive region (Equation 1.34) in a closed form solution using the known structural stiffness, $K$, and mass, $M$, along with the extreme cases of a finite load suddenly applied for an infinite duration (quasi-static) and an infinite load suddenly applied for a duration approaching zero (impulsive) (Li and Meng 2002). In these equations, the pressure and impulse values are defined per unit area. Similar asymptotes may be defined for inelastic structures; however these do not have a closed form solution and must be solved iteratively.

[1.33] $$p = \frac{Ky_c}{2}$$

[1.34] $$I = \sqrt{KM}\, y_c$$

The quasi-static and impulsive asymptotes may be used as a preliminary analysis tool to give the limits of structural response. Depending on the duration of the blast load and the natural frequency of the structure, $\omega$, these limits may be close to the actual response of the structure. For a majority of structural components exposed to blast induced shock waves, the response is somewhere between these limits, in the dynamic region. Smith and Hetherington (1994) have found a proportional relationship between the duration of the pulse loading and the period of the structure to predict in which region the structural response will be determined by equating the non dimensional value of natural frequency multiplied by the duration of the blast load to predetermined constants. This relationship is shown in Equation 1.35 where $\omega$ is the natural frequency of the structure.

[1.35] $0.4 > \omega t_d$ *(Impulsive)*

$0.4 < \omega t_d < 40$ *(Dynamic)*

$40 < \omega t_d$ *(Quasi-static)*

## *1.13 History of Accidential and Malicious Explosions*

Bangash and Bangash (2006) present a case study of recent buildings exposed to explosive attacks. In this section, seven of these cases are summarized.

### 1.13.1 The Alfred P. Murrah Federal Building - 1995

The Alfred P. Murrah Federal Building, located in Oklahoma City, Oklahoma, USA was the target of an explosive attack in April 1995. It is estimated that *1800 kg* of ANFO high explosives was detonated in the form of a car bomb located between three and five meters away from the structure. The TNT equivalent of this explosive was approximately *1476 kg* which would produce peak incident pressures of *13,550 kPa (3 m)* and *6747 kPa (5 m)* and positive phase incident impulses between *3440 kPa-ms (3m)* and *2162 kPa-ms (5m)* when detonated as a hemispherical explosion (Hyde 1992).

The nine-storey reinforced concrete structure lost a total of four main storey columns due to the blast loading which lead to the progressive collapse of a significant amount of the structure. A total of *168* fatalities and numerous injuries were caused by the combination of the explosion and progressive collapse of the structure.

### 1.13.2 The World Trade Center - 1992

On 26 February 1992, the north tower of the World Trade Center located in New York City, New York, USA was attacked with approximately *816 kg* of high explosive ANFO in the form of a vehicle bomb located in an underground parking facility two levels below the ground floor. The explosion caused two storeys of reinforced concrete slabs to be blown out and extensive

damage to the underground parking facility. The TNT equivalent of the ANFO explosive was *572.6 kg*.

### 1.13.3 Jewish Community Centre, Buenos Aires - 1994

On 18 July 1994 approximately *275 kg* of high explosives was detonated between three and five meters away from the Jewish Community Centre in Buenos Aires, Argentina. The explosion caused the failure of exterior brick masonry load bearing walls which supported floor slabs.

### 1.13.4 St. Mary Axe, London - 1992

On 11 April 1992 a vehicle bomb containing *350 kg* of TNT exploded in the neighbourhood of St. Mary Axe, London, England. This explosion caused significant damage to many buildings including the ten-storey reinforced concrete with masonry walls European Development Bank.

### 1.13.5 Bishopgate, London - 1992

The neighbourhood of Bishopgate, London, England experienced a high explosive vehicle bomb blast on 23 April 1992. This blast destroyed several buildings and caused over forty casualties.

### 1.13.6 Docklands, London - 1996

On 9 February 1996 a vehicle bomb carrying the approximate equivalent of *500 kg* TNT in the form of a homemade high explosive detonated in the Docklands neighbourhood, London, England. This blast caused extensive damage to non structural elements in several buildings.

### 1.13.7 Al-Khobar, Saudi Arabia - 1996

The Al-Khobar Towers in Saudi Arabia was subjected to a blast equivalent to approximately *2270 kg* of TNT on 26 June 1996 in the form of a vehicle bomb. The blast caused severe damage to the façade of the structure along with many of the horizontal structural elements.

## *1.14 Experimental Case Studies of Explosions on Reinforced Concrete Columns*

### 1.14.1 S.C. Woodson and J.T. Baylot, 1999

In an effort to better understand the response of reinforced concrete columns to blast effects, the authors built two quarter-scaled reinforced concrete models and subjected them to explosive loading. The models were two storeys tall, two bays wide and one bay deep with reinforced concrete construction for the columns, beams, and slabs and various masonry infill wall designs for cladding. Additional mass was added to the top of the structure to represent a four storey structure. The columns were designed for a low seismic region. The scale models were subjected to multiple explosions leading to various failure mechanisms.

The four corner columns of the models were over designed to withstand the expected blast loads while the exterior columns in the centre of two bays were designed as test columns. The test columns were *910 mm* in length cast integrally with the beam and slab connections at the floor levels. Two of each square cross section measuring *89 mm* and *76 mm* were used with one of each cross section in each scale model. Columns were reinforced with *400 MPa 6.45 $mm^2$* and *450 MPa 32.3 $mm^2$* deformed wire, and *440 MPa 3.23 $mm^2$* smooth wire lateral ties were used. Concrete strength with an average strength of *44.8 MPa* at the time of testing and a maximum aggregate size of *10 mm* was used in the construction.

The authors carried out five tests that represented different placement of explosives and different cladding designs. The results of these tests are as follows:

Open Frame – Large Standoff

> In this model there was no masonry cladding used so all bays were open. *7.10 kg* of Composition C-4 (TNT equivalent of *9.73 kg* for pressure and *8.45 kg* for impulse) were placed on a light plywood platform located *228 mm* from the ground surface. The explosives were located *1524 mm* away from the centre of the test column and were

aligned to be perpendicular to the face of the column. The resulting explosion caused little damage to the column aside from hairline cracks. No residual displacement was evident.

Open Frame – Small Standoff

The first test was repeated with exactly the same explosive mass located perpendicular to the column in an open frame at *1067 mm* standoff distance. This explosion caused some damage to the column including approximately *6.4 mm* residual displacement and larger cracks. The column was still able to support the mass of the structure and applied mass at the top of the structure.

Fully Clad

In this test, the same explosive properties of mass and location as in test two were used. The bays of the frames were fully clad with quarter scale masonry blocks. The column suffered considerable damage in the lower storey with approximately *114 mm* residual displacement and some damage in the upper storey with approximately *25 mm* residual displacement. The authors judged that the column was structurally deficient and not able to withstand the mass of the structure and the applied mass and that the load transfer to a spandrel beam was all that prevented collapse.

Partially Clad

This test used the same mass and location of explosive as tests 2 and 3 however the masonry cladding differed from test three. In this test, openings were left in the masonry that were equivalent to *33 %* of the bay area and represented windows in the structure. The lower storey column had a residual displacement of *76 mm* and the upper storey column had a residual displacement of *14 mm.* A similar load transfer to the spandrel beam as in test 3 was observed and the structure remained standing.

Parking Garage

Once again, the same mass and location of explosive as in tests 2 through 4 was used for this test. There was no masonry cladding used on the lower storey and complete infill

masonry on the upper storey. This test setup was intended to represent a building with a main storey parking facility with open bays. The lower storey column did not see significant damage due to the lack of any cladding. The upper storey column had approximately *76 mm* residual displacement and the upper storey edge beam was needed to sustain the load transferred from the damaged column.

The conclusions of the experimental tests were that reinforced concrete frames responded better to explosive loading if there was little area to reflect the shock wave pressure, such as infill walls. Aside from columns, the authors also were concerned with the slabs and beams in the structure and found that the structures with openings had significantly more damage to the slabs that the fully clad structures. It was also concluded that the spandrel beam needs to be of sufficient strength to accommodate the force transfer due to the loss of one or more columns.

### 1.14.2 J. Magnusson, 2007

Magnusson tested a total of *89* reinforced concrete beams under both static and air blast loading. *49* of beams were reinforced with *500 MPa* steel and *40* were reinforced solely with steel fibres that comprised *1 %* of the volume of the beams. The blast tests were simulated with an explosive driven shock tube.

In all of the static tests, the mode of failure was pure flexure for the beams. However, Magnusson found that in some cases under the blast loading the mode of failure would be shear failure. This shear dominant behaviour was likely due to the limited shear material strength increase that concrete develops. For the beams reinforced with steel fibres rather than traditional longitudinal bars, the shear mode of failure was prevented under blast loading. By comparing the support reactions of beams under static loading to those under dynamic blast loading, it was found that the beams could withstand larger forces under dynamic loading with the same degree of damage as static loading. Based on the displacement time histories recorded during the blast load tests, Magnusson observed that less stiff elements will deflect readily and gain high kinetic energy while more stiff elements will deflect less and attain high internal strain energy. The

stiffer elements were more likely to fail in shear rather than flexure under the dynamic loads. Less stiff elements eventually failed in flexure.

### 1.14.3 L.C Muszynski and M.R. Purcell, 2003

The authors performed tests on both normal construction reinforced concrete beam, wall and column structures as well as the same structures fitted with externally applied carbon fibre sheets and glass fibre sheets exposed to explosive loading. The columns were cast integrally with the walls. Two structures were tested, one with carbon and glass external reinforcement and one normal construction. A series of explosive tests were undertaken to evaluate the effectiveness of the externally applied reinforcement.

Window Testing

The first two tests were designed to test windows, not structural components. Large standoff distances, ranging from *31.5 m* to *65.1 m* were used with *806 kg* of TNT. These tests caused minimal damage to no damage in both structures.

Structure Testing

Two further explosive detonations were triggered, both using *806 kg* of TNT. The standoff distance was *14 m* and *13.5* meters for the structure with external carbon and glass reinforcement and *15.9 m* for both tests on the structure with normal construction. The maximum reflected pressures on the structures ranged from *1786 kPa* to *2930 kPa* and reflected impulses ranged from *4262 kPa-ms* to *5241 kPa-ms*. Under the first large explosive test, the normal construction structure saw significant damage including the failure of columns in flexure and stress fractures between the columns and the walls. The structure with externally applied reinforcement saw less damage with some spalling of concrete on the columns and some stress fractures at the joints between the columns and

walls. The second large explosive test caused complete collapse of the already damaged normal construction structure. The structure with external reinforcement remained intact while some of the carbon and fibre laminate ruptured. There was no spalling in the walls that were reinforced with either external carbon fibre or glass fibre.

The authors concluded that the use of carbon and glass fibre laminates increased the capacity of the structures to withstand air blast loads.

### 1.14.4 A. Schenker et al., 2007

The authors carried out two full scale high explosive tests on reinforced concrete slabs fitted with sacrificial aluminium foam protection layers. The one way slabs spanned *3 m* and were exposed to air blasts resulting from *1000 kg* of TNT detonated as hemispherical explosions located at a standoff distance of *20 m*. A total of four slabs were tested, two of which were high strength concrete slabs with *100 MPa* compressive strength concrete and two were normal strength concrete slabs with *30 MPa* compressive strength concrete. One slab in each strength group had a protective layer of aluminium foam designed to dissipate blast energy by plastic deformation and one control slab that was normal construction.

The authors recorded a reduction in acceleration, velocity and displacement in the slabs protected with the sacrificial aluminium foam layer in comparison with the normal construction slabs. There was a corresponding reduction in the strain at the center of the slabs for the protected slabs compared with the normal construction slabs. The authors concluded that the aluminium foam protective layer clearly modified the response of the slabs, however they were unable to draw conclusions on the efficiency of the foam for practical use.

### 1.14.5 F. Toutlemonde et al., 1995

The authors of this study set out to explore the change in behaviour of concrete under high strain rates, specifically the apparent increase in compressive and tensile strength. Parameters including free water content and pore size of concrete matrix were explored by testing non reinforced concrete slabs in a shock tube. Concrete strengths varied from *35 MPa* to *115 MPa* for the tests and free water content was held constant at saturated (*100 %*) or dry (*0%*). It was concluded that the free water within the pores of the concrete has a significant influence on the apparent strength increase in concrete under high strain rates. This strength increase is not apparent in shear and may cause a shear failure mechanism in a concrete member that would otherwise be flexural dominate under static loading.

### 1.14.6 A.G. Razaqpur, A. Tolba and E. Contestabile, 2007

Field tests using high explosives on *8* reinforced concrete slabs retrofitted with glass fibre reinforced polymers (GFRP) were undertaken. The slabs measured *1000 mm* by *1000 mm* and *70 mm* thick and were made of *40 MPa* concrete with top and bottom steel mesh. Of the eight slabs, five were normal construction and three were retrofitted with the externally applied glass fibre laminates. The slabs were exposed to ANFO high explosive detonations at *3.1 m* standoff distances. Charge weights were *22.4 kg* (*18.37 kg* TNT equivalent for pressure and impulse) and *33.4 kg* (*27.39 kg* TNT equivalent).

The authors observed a significant improvement in performance for the slabs retrofitted with GFRP laminate compared with the normal construction slabs in terms of deflection, damage level, and residual strength for the *22.4 kg* explosions. There was no apparent improvement in performance of the retrofitted slabs under the *33.4 kg* explosion when compared with the normal construction slabs.

*TABLE 1.1 - TNT Mass Equivalent Factors (Hyde 1992)*

| Explosive Type | Equivalent TNT Mass Factor | |
|---|---|---|
| | Pressure | Impulse |
| ANFO | 0.82 | 0.82 |
| Composition A-3 | 1.09 | 1.07 |
| Composition B | 1.11 | 0.98 |
| Composition C-4 | 1.37 | 1.19 |
| H-6 | 1.38 | 1.15 |
| HBX-1 | 1.17 | 1.16 |
| Octal (75/25) | 1.06 | 1.06 |
| Pentolite | 1.42 | 1.00 |
| RDX | 1.14 | 1.09 |
| TNT | 1.00 | 1.00 |
| Tritonal | 1.07 | 0.96 |

*TABLE 1.2 - Decay Constants Reproduced from Smith and Hetherington (1994)*

| Scaled Distance Z ($m/kg^{1/3}$) | Decay Constant b |
|---|---|
| 0.4 | 8.50 |
| 0.6 | 8.60 |
| 0.8 | 10.00 |
| 1.0 | 9.00 |
| 1.5 | 3.50 |
| 2.0 | 1.90 |
| 5.0 | 0.65 |
| 10.0 | 0.20 |
| 20.0 | 0.12 |
| 50.0 | 0.24 |
| 100.0 | 0.50 |

*TABLE 1.3 - Initial Design Dynamic Increase Factors Reproduced from the US Department of the Army, the Navy, and the Air Force Structures to Resist the Effects of Accidental Explosions (TM 5-1300 1990)*

| Type of Stress | Far Design Range | | | Close-In Design Range | | |
|---|---|---|---|---|---|---|
| | Reinforcing Bars | | Concrete | Reinforcing Bars | | Concrete |
| | $f_{dy}/f_y$ | $f_{du}/f_u$ | $f'_{dc}/f'_c$ | $f_{dy}/f_y$ | $f_{du}/f_u$ | $f'_{dc}/f'_c$ |
| Bending | 1.17 | 1.05 | 1.19 | 1.23 | 1.05 | 1.25 |
| Diagonal Tension | 1.00 | | 1.00 | 1.10 | 1.00 | 1.00 |
| Direct Shear | 1.10 | 1.00 | 1.10 | 1.10 | 1.00 | 1.10 |
| Bond | 1.17 | 1.05 | 1.00 | 1.23 | 1.05 | 1.00 |
| Compression | 1.10 | | 1.12 | 1.13 | | 1.16 |

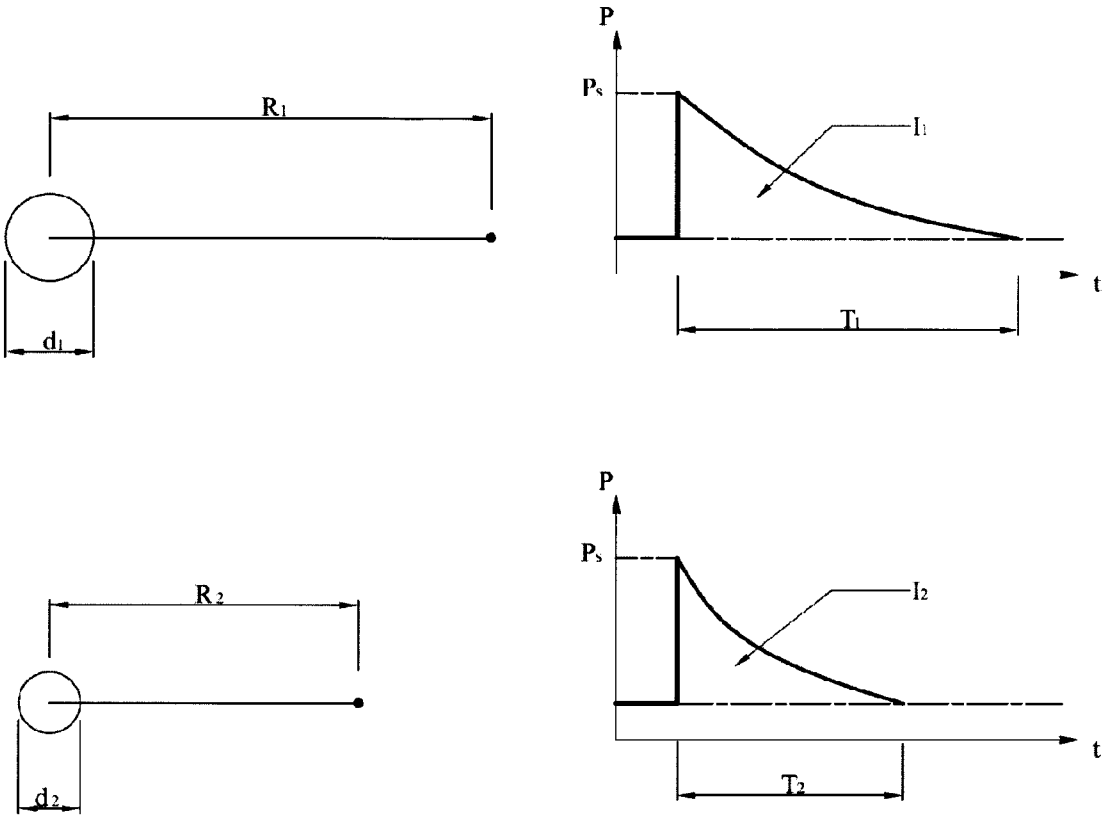


*Figure 1-1: Equivalent Scaled Distance Explosions*

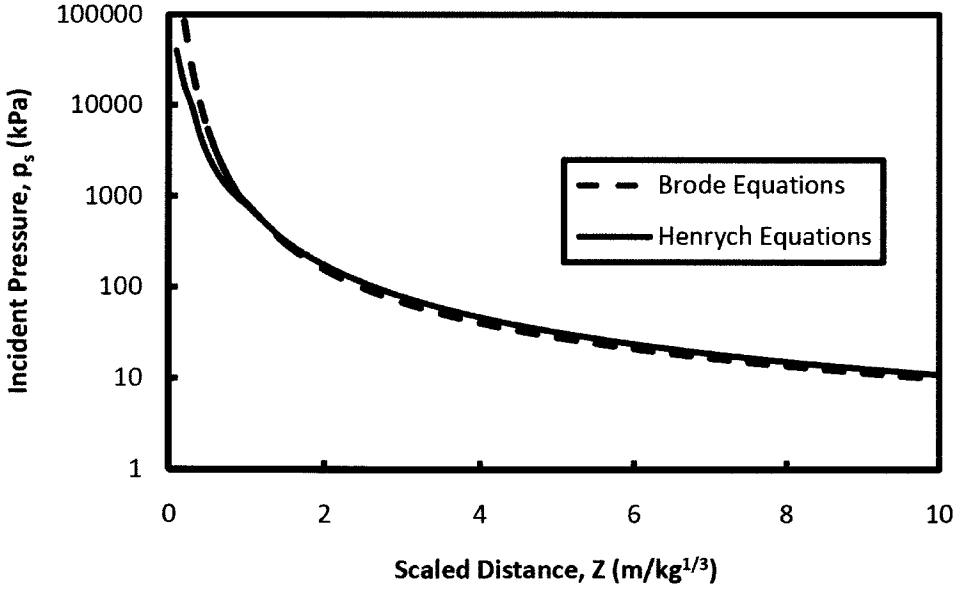


*Figure 1-2: Peak Incident Pressure vs Scaled Distance as Described by Brode and Henrych*

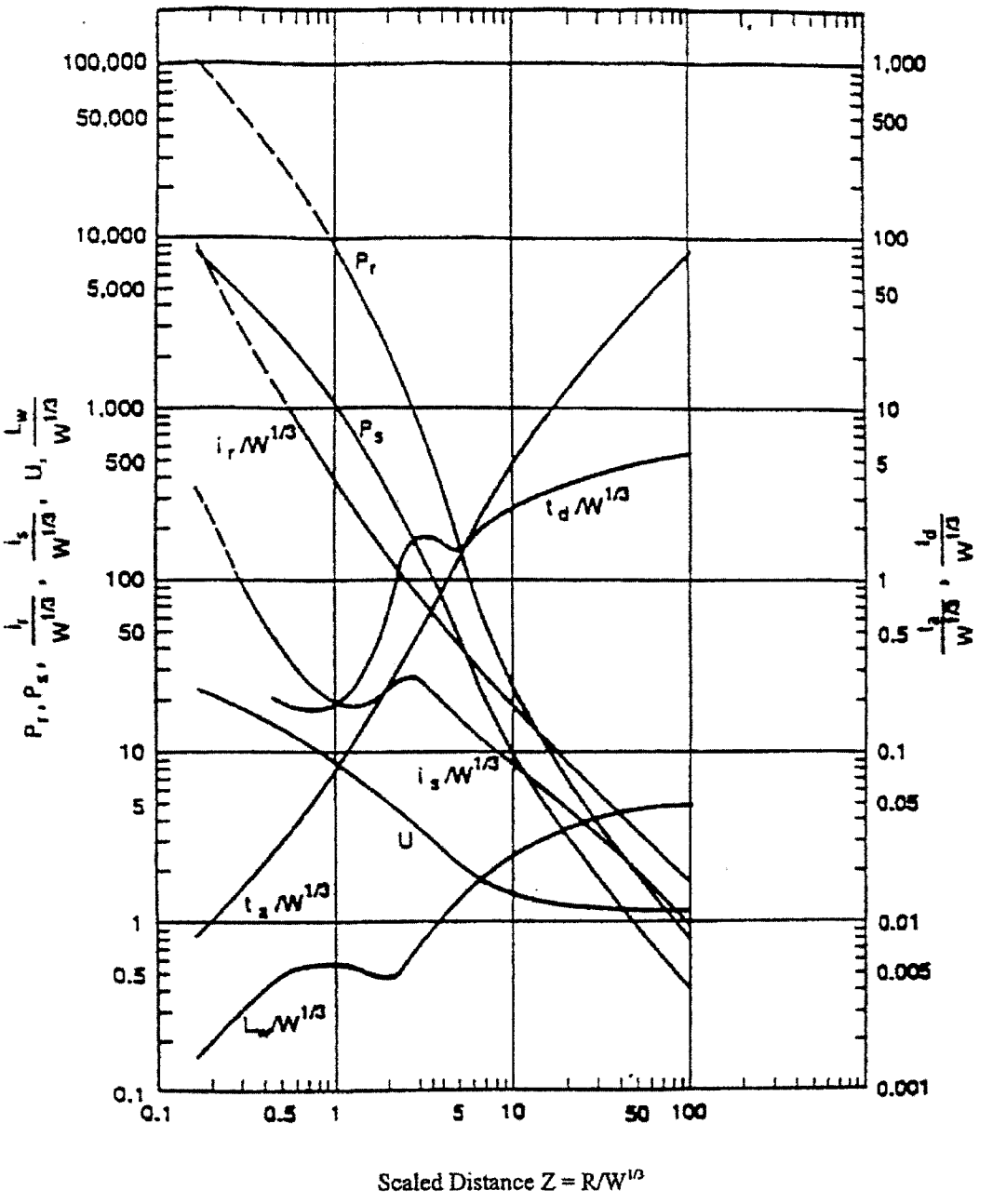


*Figure 1-3: Noramilzed Shock Wave Parameters for Spherical Explosion Reproduced from the US Department of the Army, the Navy, and the Air Force Structures to Resist the Effects of Accidental Explosions (TM 5-1300 1990)*

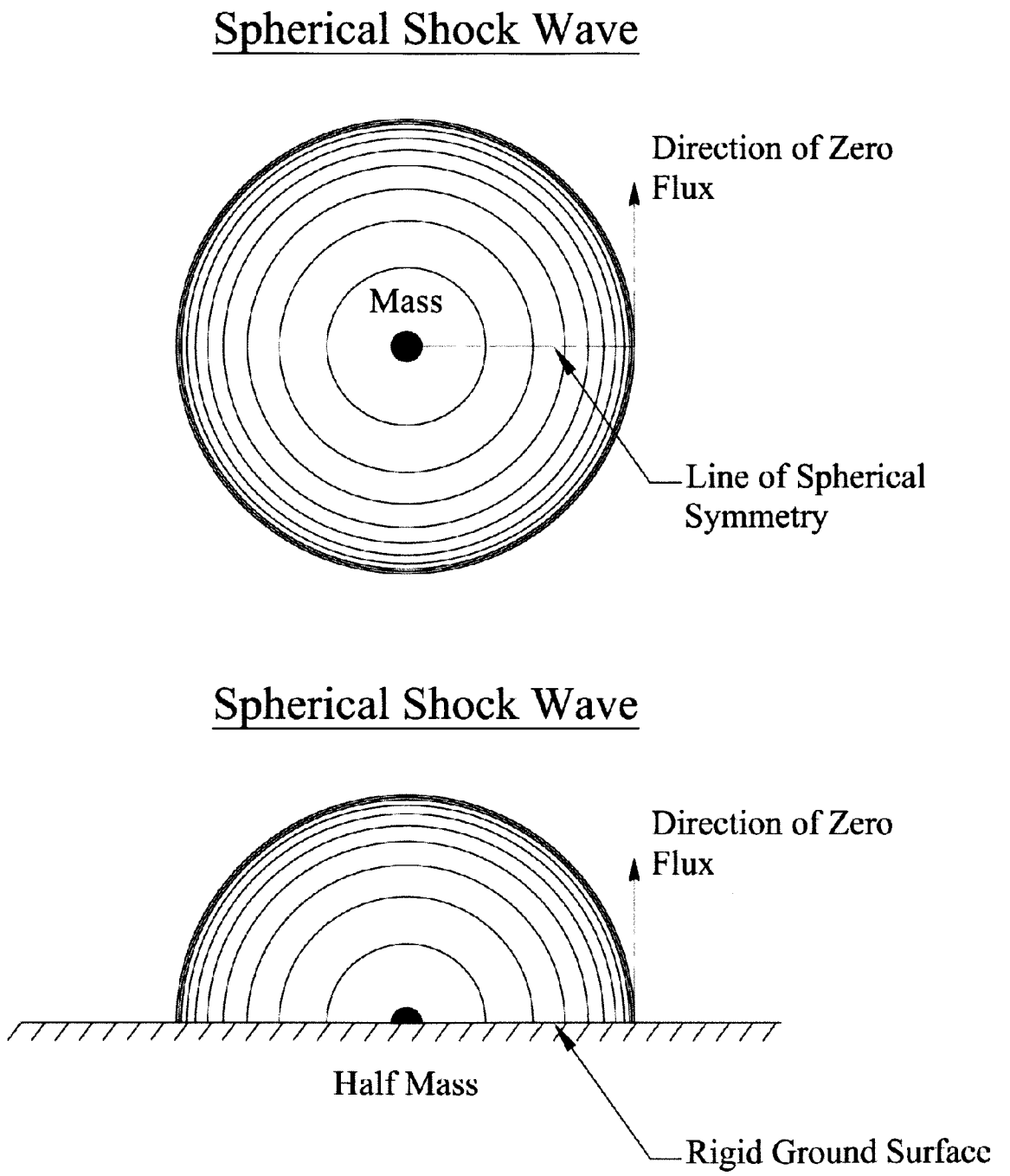


*Figure 1-4: Spherical and Hemispherical Symmetry in Shock Waves*

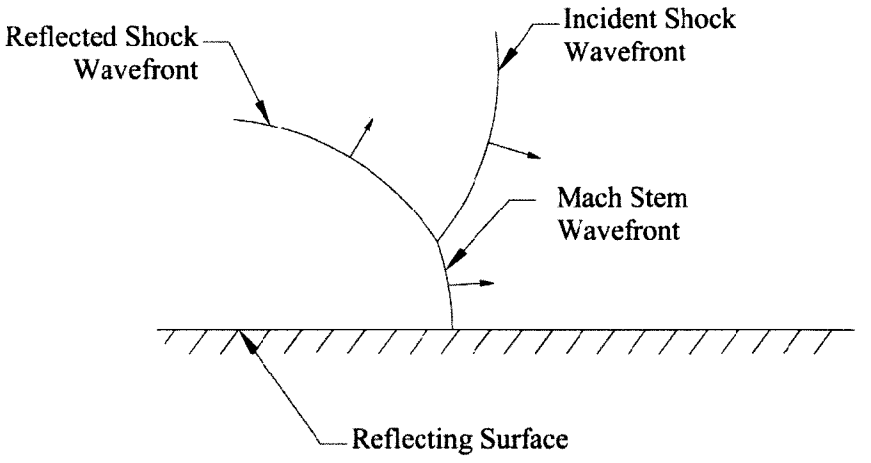


*Figure 1-5: Triple Point at the Creation of Mach Stem Reflection*

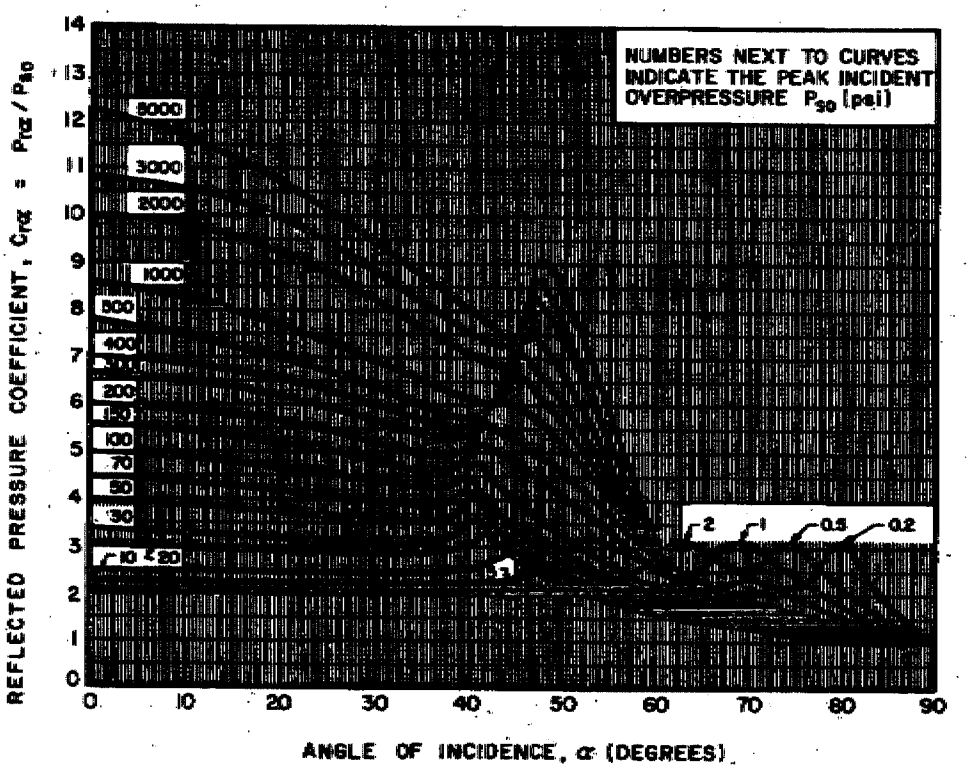


*Figure 1-6: Reflected Pressure Coefficients vs Angle of Incidence for Various Incident Pressures Reproduced from the US Department of the Army, the Navy, and the Air Force Structures to Resist the Effects of Accidental Explosions (TM 5-1300 1990)*

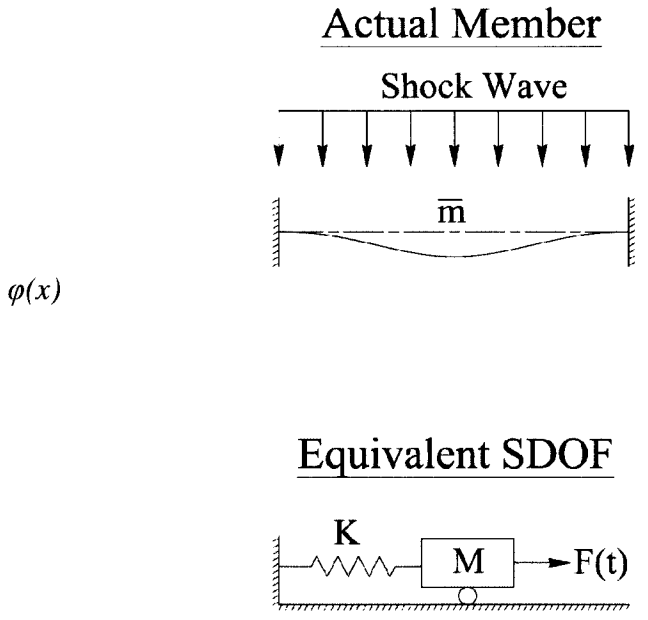


*Figure 1-7: Equivalent Single Degree of Freedom System*

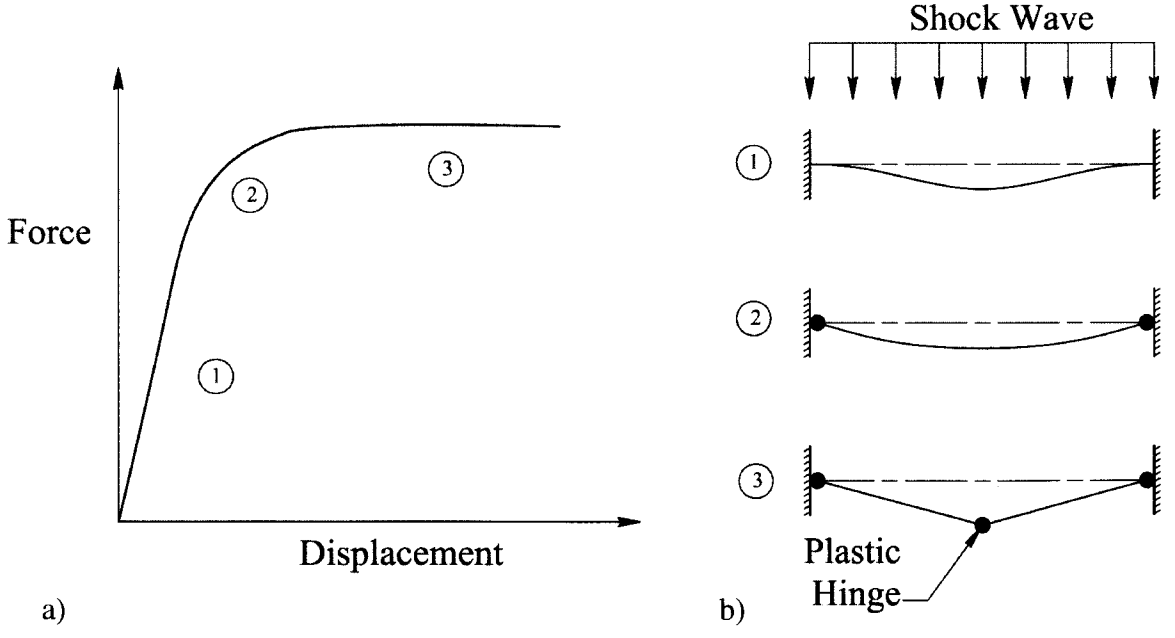


*Figure 1-8: a) Force Displacement Curve for Inelastic Element; b) Progression of Damage through Three Mode Shapes*

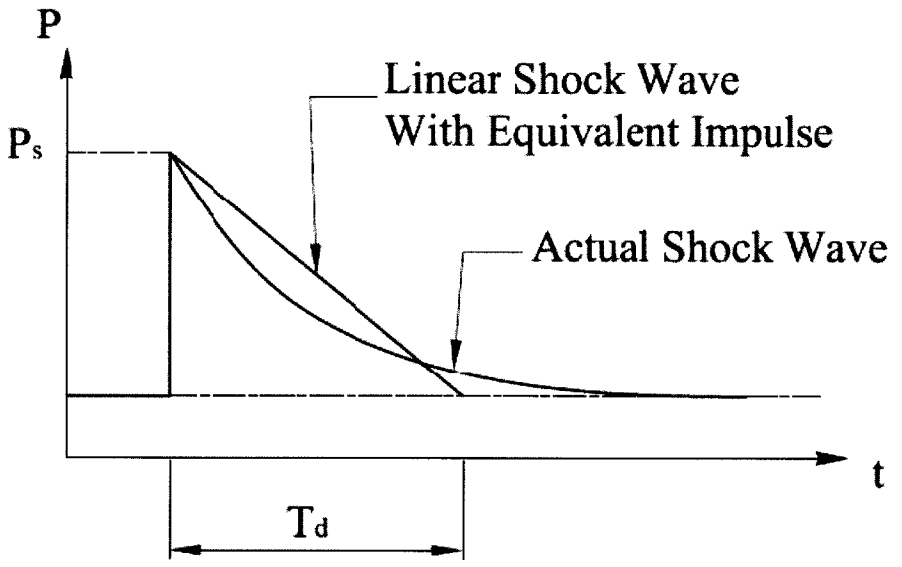


*Figure 1-9: Equivalent Impulse Simplified Shock Wave*

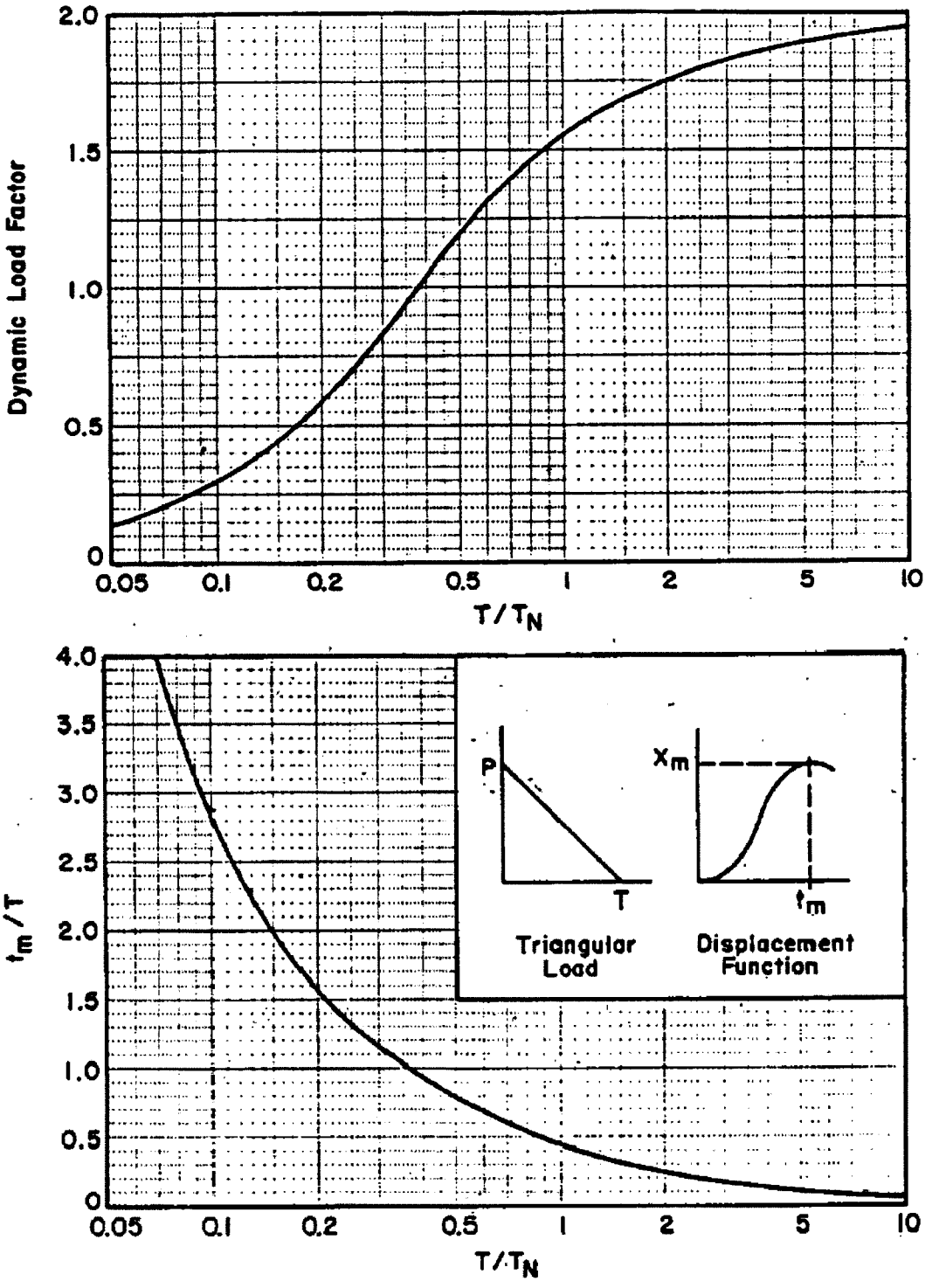


*Figure 1-10: Dynamic Load Factor and Time to Maximum Displacement for Elastic SDOF System Under Triangular Force-Time Distributions Reproduced from the US Department of the Army, the Navy, and the Air Force Structures to Resist the Effects of Accidental Explosions*

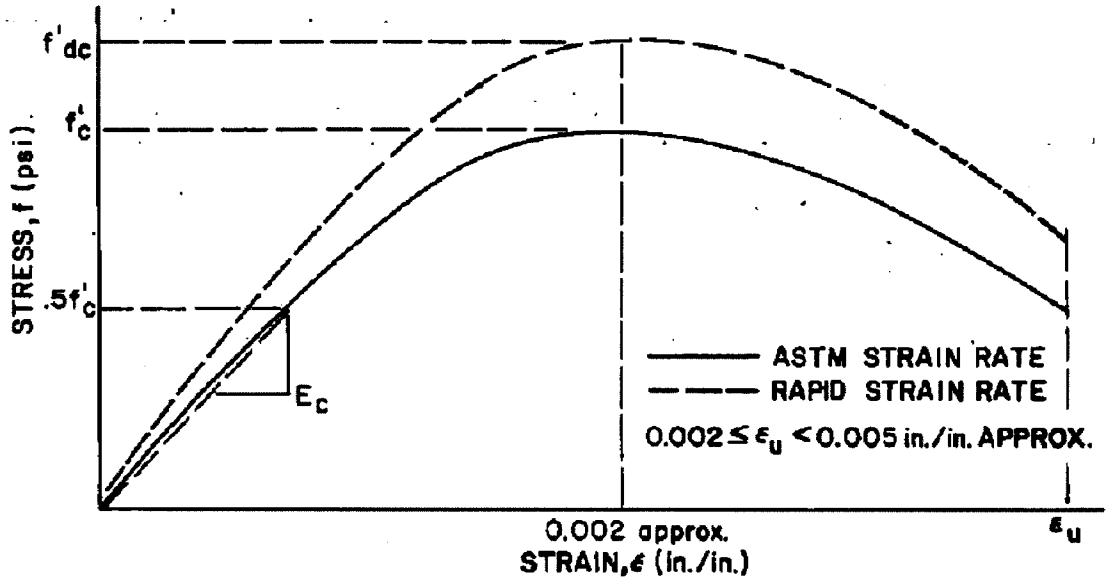


*Figure 1-11: Concrete Stress vs Strain Curve Under High Strain Rates as Reproduced from the US Department of the Army, the Navy, and the Air Force Structures to Resist the Effects of Accidental Explosions (TM 5-1300 1990)*

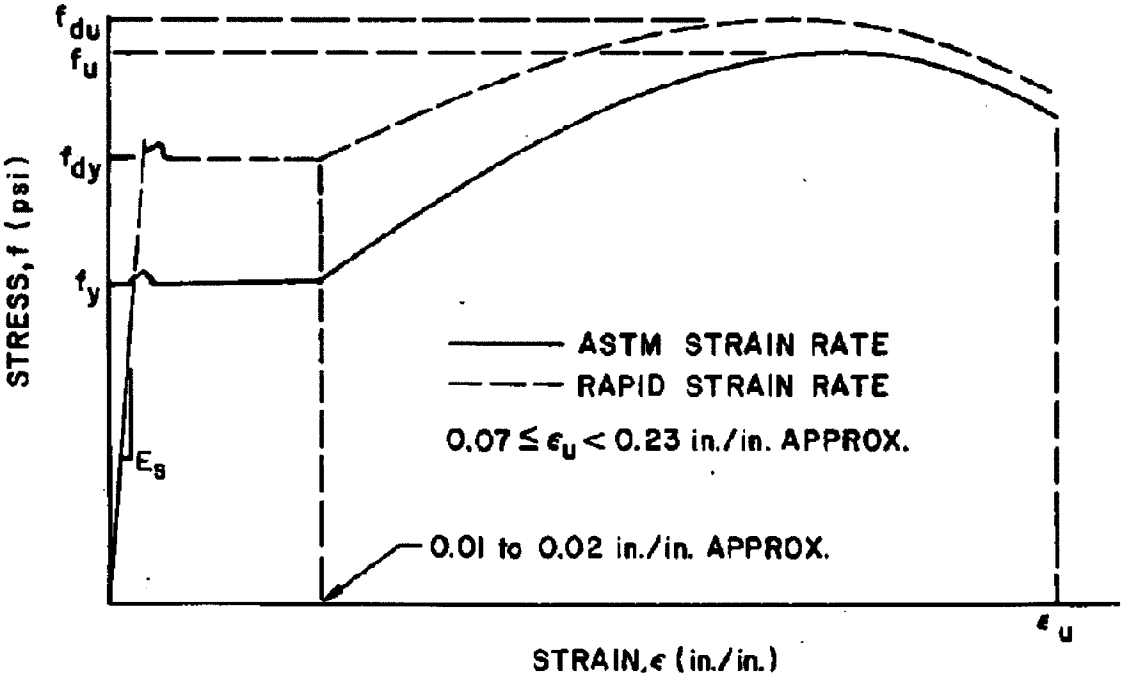


*Figure 1-12: Steel Stress vs Strain Curve Under High Strain Rates as Reproduced from the US Department of the Army, the Navy, and the Air Force Structures to Resist the Effects of Accidental Explosions (TM 5-1300 1990)*

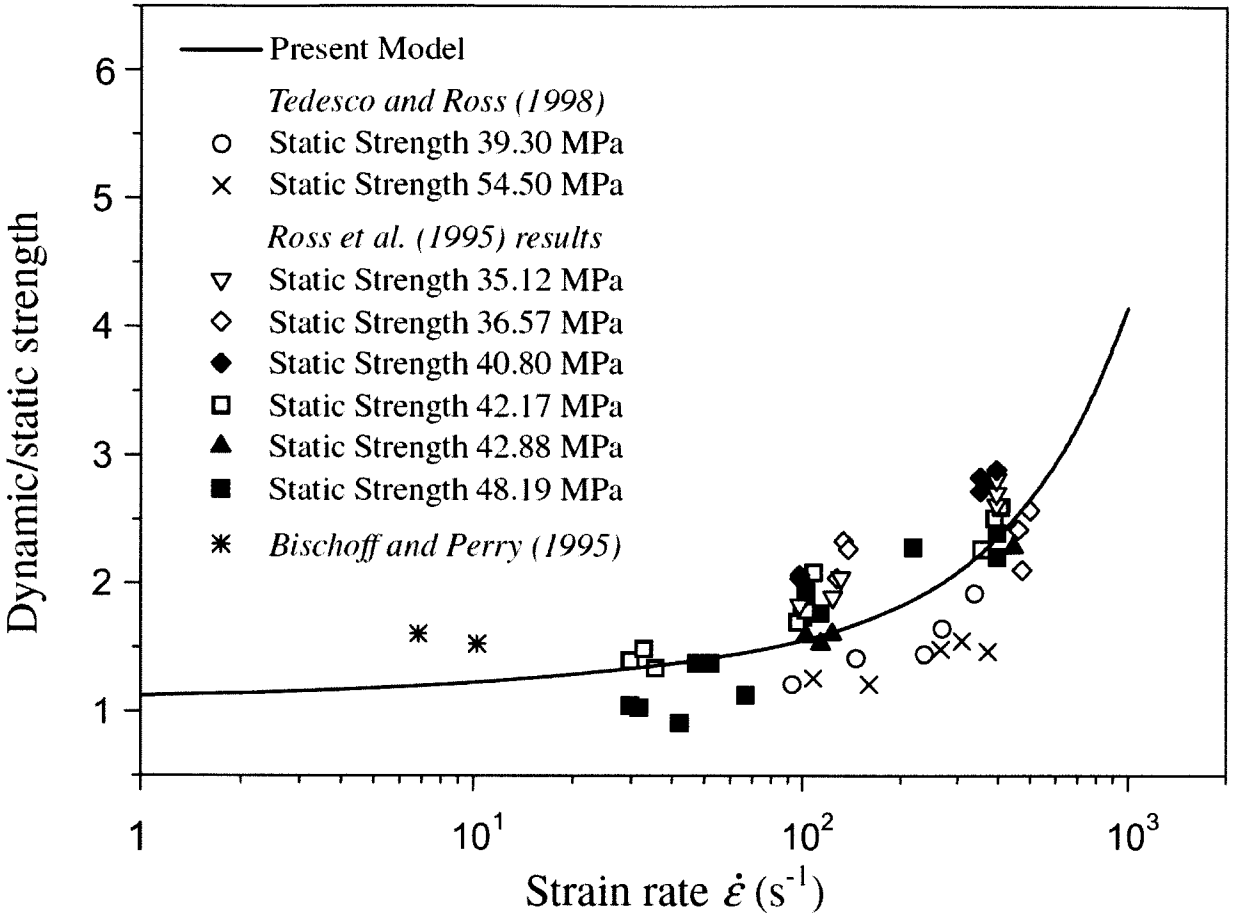


***Figure 1-13: Dynamic Increase Factor for Concrete in Compression as Reproduced from Lu and Xu, 2004***

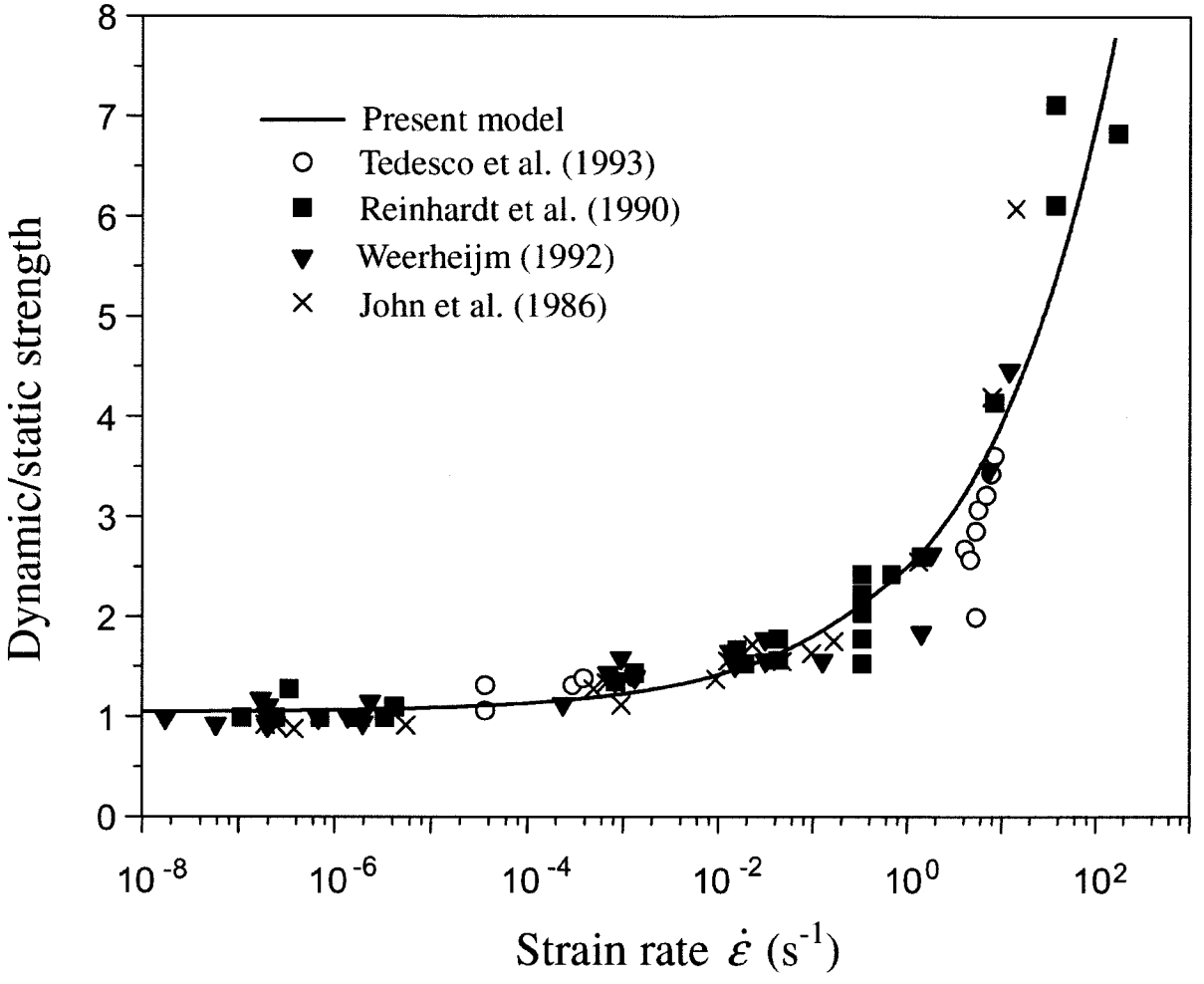


***Figure 1-14: Dynamic Increase Factor for Concrete in Tension as Reproduced from Lu and Xu 2004***

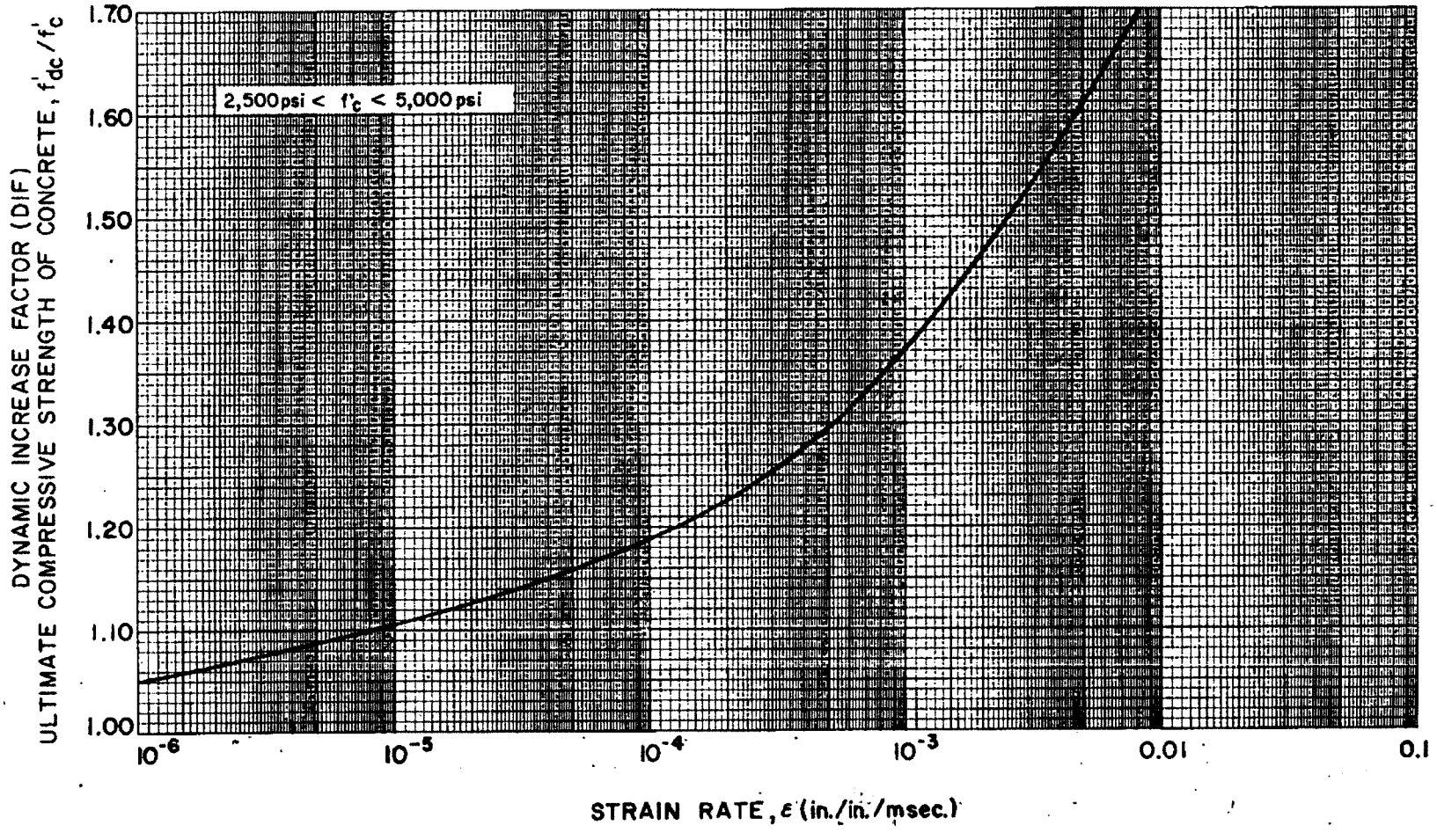


*Figure 1-15: Dynamic Increase Factor for Concrete Reproduced from the US Department of the Army, the Navy, and the Air Force Structures to Resist the Effects of Accidental Explosions (TM 5-1300 1990)*

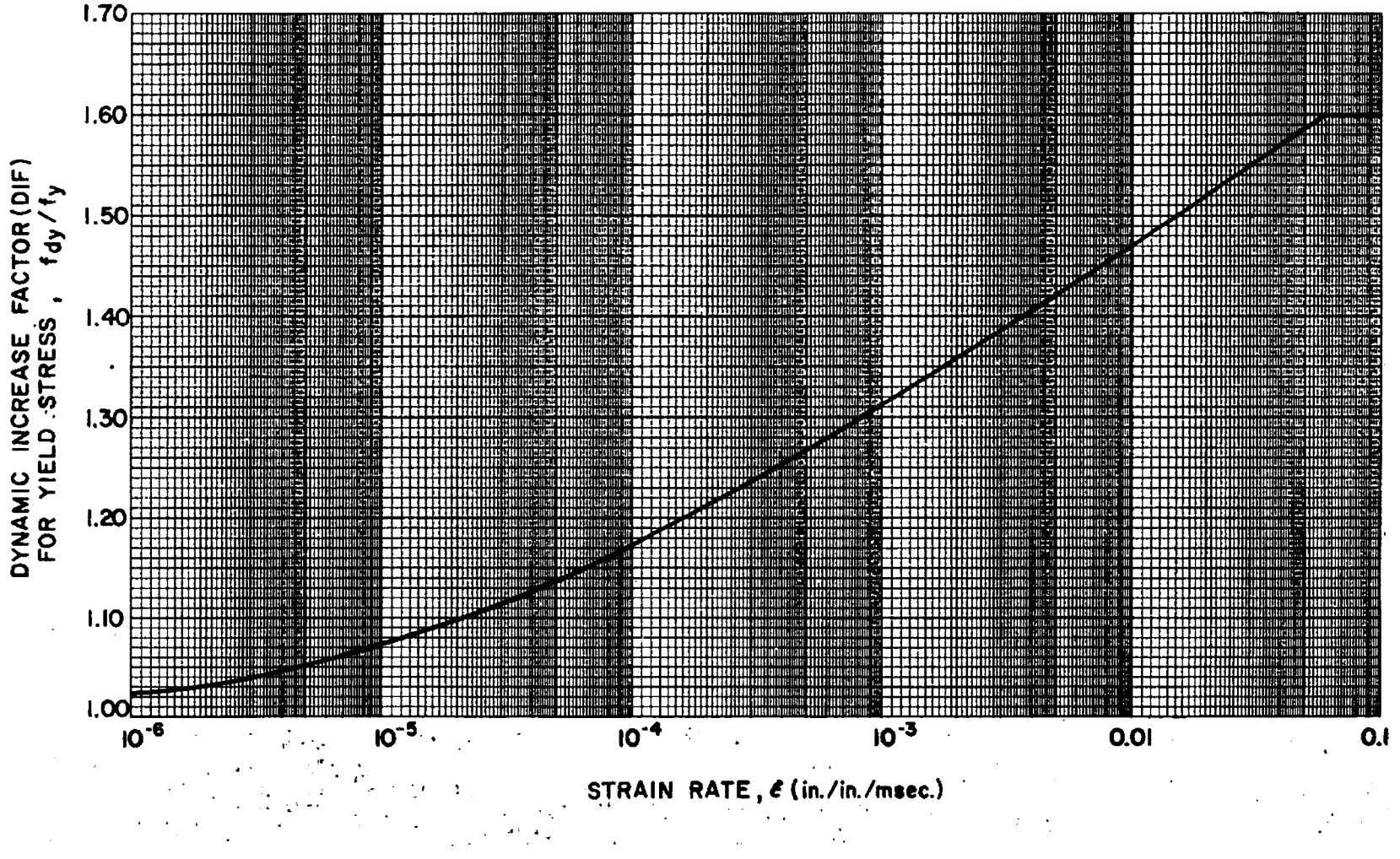


*Figure 1-16: Dynamic Increase Factor for Steel Reproduced from the US Department of the Army, the Navy, and the Air Force Structures to Resist the Effects of Accidental Explosions (TM 5-1300 1990)*

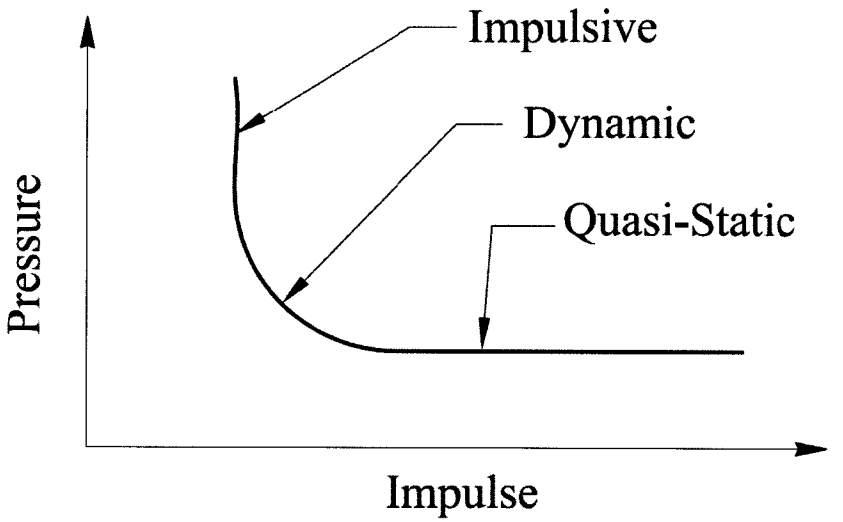


*Figure 1-17: Pressure-Impulse Diagram for Iso-Damage Level*

# 2 CHAPTER 2

# Shock Tube

## *2.1 General*

The experimental component of current research on reinforced concrete columns was conducted using the newly installed Shock Tube at the University of Ottawa. The column research was the first research program conducted using the shock tube, and hence some preliminary work was necessary before the column tests could be conducted. This work involved the calibration and verification of the shock tube in terms of the characteristics of impulsive pressures that could be attained, and distribution of reflected pressure near the test area. A significant number of calibration tests were conducted on a well-instrumented rigid steel plate. For each shock wave generated, piezoelectric dynamic pressure sensors were used to measure the reflected pressure-time history at the end of the shock tube. More gauges were installed along the walls of the shock tube expansion section to measure the incident pressure of the shock wave prior to interaction with the reflecting surface and to measure the shock front velocity. The pressure-time history data from these gauges was used to examine the properties of the shock waves that can be generated with the shock tube. These observations on shock wave properties, as well as the characteristics and specifications of the shock tube are discussed within the following sections.

## *2.2 Generation of Shock Wave with Shock Tube*

The shock tube used to apply shock wave loading can simulate a wide range of explosions with varying pressures and impulses. The shock tube is comprised of a variable length driver section, a double diaphragm firing control section with a spool section located between the diaphragms, an expansion section and a rigid end frame as shown in Figures 2.1 and 2.2. The driver section is a series of *597 mm* inside diameter pipes with *19 mm* wall thickness. The length of the driver

section is variable between *305 mm* and *5185 mm* in *305 mm* increments. Depending on the desired shock wave parameters, including peak pressure and total impulse, a driver length is selected. The spool section is a *90 mm* long FIKE Combination Disk Holder (Fike 2005). The flanges on the spool section are designed to mate with the flanges on the driver and the flange located between the spool and the beginning of the expansion section. The flanges have *30* ° inlets that mate with protrusions on the coupling flanges of the driver and expansion section (Figure 2.3). When held together with 20 Grade 8 high-strength threaded rods *31.75 mm* in diameter, the driver-spool-expansion section flanges clamp the diaphragms in place. There are two diaphragms employed in the operation of the shock tube. Each diaphragm is comprised of up to three sheets of *813 mm* by *813 mm* grade 1100 aluminium foil of varying thickness. The foils have twenty *38 mm* holes in a circular pattern centered on a radius of *374.65 mm* with an angle of *18* ° between holes (Figure 2.3). These holes are provided to accommodate the twenty threaded rods that clamp the driver and spool to the expansion section. The expansion section connects to the driver-spool combination and to the rigid end frame. It begins with a *1920 mm* pipe splay as a transition from the circular driver cross section to the square expansion section cross section. Over a length of *6096 mm* the cross section of the expansion section increases from 597 mm diameter circular to a *2032 mm* by *2032 mm* square opening at the rigid end frame. The entire length of the square expansion section is comprised of *12.7 mm* thick stiffened steel plates. The end frame is square with a *2032 mm* by *2032 mm* opening and a *203.2 mm* wide, *12.7 mm* thick stiffened steel plate surrounding the opening. There are a total of twenty *19 mm* holes located in the end frame for connecting samples to the shock tube.

The operation of the shock tube involves charging the driver and spool simultaneously to desired pressures and then triggering firing by draining pressure from the spool section which causes rupture of the diaphragms. Diaphragm combinations are chosen based on rupture pressures of the diaphragms and desired pressures in the driver.

## 2.3 *Planarity of Reflected Shock Wave*

Three test shots were done using a rigid steel reflecting plate mounted to the testing frame in order to investigate the planarity of the shock waves. The reflecting plate was instrumented with twelve piezoelectric dynamic pressure gauges mounted at twelve locations across its face, as illustrated in Figure 2.4. These gauges were used to record reflected pressure time histories and differential arrival times. The time histories were integrated to form reflected impulse time histories. The maximum reflected pressures, reflected impulse, relative arrival times, and positive phase durations were then compared at these points along the face of the reflecting surface to determine the shape of the shock wave in the plane of the testing frame at specific times.

The first test was completed using an *1830 mm* driver length with *276 kPa* driver pressure. Table 2.1 shows the results of this test at the twelve gauges, located in horizontal ($x$) and vertical ($y$) coordinates ($mm$) from the centre of the reflecting plate. The maximum reflected pressure ($P_r$) varied between *52.5 kPa* and *59.5 kPa*. The reflected impulse ($I_r$) over the positive phase varied between *399.9 kPa-ms* and *445.3 kPa-ms*. The positive phase duration ($t_d$) varied between *16.89 ms* and *18.32 ms* while the relative time of arrival ($t_a$), the difference between the arrival time at any point and the first recorded arrival time, was a maximum of *0.26 ms*. Table 2.1 lists the ratios of the: positive phase duration at any point to the maximum positive phase duration recorded ($t_d/t_{d,max}$); reflected pressure at any point to maximum reflected pressure recorded ($P_r/P_{r,max}$); and reflected impulse at any point to maximum reflected impulse recorded ($I_r/I_{r,max}$). Table 2.1 shows an average positive phase duration ratio of *0.96* with a corresponding standard deviation and coefficient of variation are *0.0249* and *2.59 %*, respectively. For the reflected pressure ratio, an average of *0.94* was obtained with a standard deviation and coefficient of variation of *0.0404* and *4.28 %*, respectively. The average reflected impulse ratio was computed as *0.93* while the standard deviation and coefficient of variation were *0.0357* and *3.82 %*, respectively.

The second test used the same *1830 mm* driver length as the first test, however, the driver pressure was significantly larger at *518 kPa*. The results for the second test at the twelve gauge locations across the reflecting plane are listed in Table 2.2. For this test, the reflected pressure varied between a minimum of *90.8 kPa* and a maximum of *104.4 kPa*, the reflected impulse over the positive phase varied between *671.2 kPa-ms* and *740.8 kPa-ms*, the positive phase duration varied between *20.72 ms* and *24.17 ms*, and the maximum relative time of arrival was *0.26 ms*. Table 2.2 shows an average positive phase duration ratio of *0.96* with a standard deviation of *0.0391* and a coefficient of variation of *4.05 %*. An average reflected pressure ratio of 0.91 with a standard deviation of *0.0455* and a coefficient of variation of *5.01 %* was obtained. The reflected impulse ratio was calculated to have an average of *0.92*, a standard deviation of *0.0444* and a coefficient of variation of *4.84 %*.

The third test for shock wave planarity used a driver length of *4880 mm* and a driver pressure of *518 kPa*. The results of this test, presented in Table 2.3, shows the reflected pressures varying between *87.2 kPa* and *97.5 kPa*, reflected impulses varying from *2167.5 kPa-ms* to *2426.9 kPa-ms*, positive phase durations ranging from *67.20 ms* to *71.44 ms*, and a maximum relative arrival time of *0.29 ms*. This test resulted in an average positive phase duration ratio of *0.97* with a standard deviation of *0.0348* and a coefficient of variation of *3.60 %*. An average reflected pressure ratio of average of *0.95* with a standard deviation of *0.0340* and a coefficient of variation of *3.57 %* was recorded. The reflected impulse ratios were computed as having an average of *0.93*, a standard deviation of *0.0335* and a coefficient of variation of *3.62 %*.

Based on the relatively small difference in maximum relative time of arrivals in these three tests, it can be concluded that the shock wave arrives at all points along the plane of reflecting at approximately the same time. The average values for the ratios of reflected pressure, reflected impulse, and positive phase duration are all close to unity (*1.0*) with low standard deviations (*0.034* to *0.0404*) and coefficients of variation (*3.57 %* to *5.09 %*) indicates that the shock waves generated in the shock tube appear to be essentially planar (i.e. uniform) in pressure, impulse, arrival time, and positive phase duration across the face of the reflecting surface.

## *2.4 Driver Length and Driver Pressure Influence on Reflected Pressure, Reflected Impulse and Positive Phase Duration*

The length of the driver section combined with the driver pressure control the wave shape at the reflecting surface. In general, longer driver lengths lead to shock waves with longer positive phase durations and higher driver pressures causes the shock waves to have higher maximum reflected pressures. Sixty different test shots have been undertaken with the shock tube and the pressure time history data from those shots has been sorted according to driver lengths and driver pressure combinations. The results of these tests are summarized in this section along with a discussion regarding prediction of shock wave parameters.

### 2.4.1 Reflected Pressure

Figure 2.5 shows a scatter plot of maximum recorded reflected pressures versus driver pressure for different driver lengths. Reflected pressures were recorded on one pressure gauge located *50 mm* from the face of the reflecting plane. As expected, it can be observed that a larger driver pressure will result in a larger reflected pressure, where the maximum reflected pressure value achievable is approximately *100 kPa*. It can also be seen, that in the majority of cases, driver length has only a minor influence on reflected pressure. The only exception to this occurs at the smallest driver length of *305 mm* where the reflected pressures are significantly lower than the trend from all other driver lengths. A best fit curve has been added to the scatter plot for the *305 mm* driver length values to help differentiate them from those of the other driver lengths. This deviation is primarily due to the relatively small volume of compressed air for a *305 mm* driver expanding through the spool section into the large expansion section when compared with the larger volumes associated with longer driver lengths.

Some of the deviation from the trend in the driver pressure versus reflected pressure relationship may be attributed to errors in accurately recording the driver pressure. The firing of the shock tube is a manual operation that involves incrementally increasing the driver pressure and spool pressure to desired levels and then draining spool section to cause aluminium foil diaphragms to

rupture. This process is described further in Chapter 3. During this process, the pressures in the driver and spool section are monitored from a digital readout on the control panel of two static pressure gauges, one in the driver section and one in the spool section. Once firing is triggered by draining the spool section, there is a slight delay before rupture of the diaphragms. During this time, the diaphragms will deform, forming a convex surface at the end of the driver section. This slightly increases the driver section volume and reduces the driver section pressure. For all tests, an attempt was made to record the actual driver pressure at the instant of diaphragm rupture, however, this proved to be difficult in some cases. This inaccuracy is more significant for the shorter driver lengths, as any deformation in the diaphragms will cause a relatively larger increase in driver section volume and a corresponding decrease in driver pressure.

A further source of inaccuracy in recording the actual driver pressure is associated with the double driver firing mechanism. The *76 mm* long spool section has two diaphragms: one located between the driver section and the spool section; and the other located between the spool section and the expansion section. During firing, the spool section is brought to atmospheric pressure causing the pressure differential between the spool section and the driver section to be high enough to rupture the first diaphragm. Once this diaphragm ruptures, the compressed air from the driver section expands into the spool section and interacts with the second diaphragm causing it to rupture and allowing the shock wave to move through the expansion section. For the larger driver lengths, this *76 mm* expansion into the spool section has a negligible effect on the driver pressure, however, for very short driver sections, this *76 mm* expansion prior to the rupture of the second diaphragm leads to a decrease in the effective driver pressure. The effect of this is likely of less significance than the previously mentioned cause of deviation in reflected pressure-time histories.

Both of these inaccuracies may be attributed as sources of error when considering the influence of driver pressure and driver length on other parameters of the shock wave and when considering the predictability of shock wave parameters.

### 2.4.2 Reflected Impulse

Figure 2.6 shows the reflected impulse over the positive phase plotted against driver pressure for various driver lengths with a logarithmic scale for the reflected impulse axis and a linear scale for the driver pressure axis. Best fit lines have been added to the scatter plot to better show the different driver lengths. A longer driver length will cause the shock wave to have a longer positive phase duration since there is more volume of compressed air creating the shock wave. As with reflected pressure, the same inaccuracies with the recorded driver pressure must be considered for the impulse versus driver pressure relationship. The maximum reflected impulse for the positive phase that can be achieved in the shock tube is approximately *2200 kPa-ms*.

One further effect that, in some cases, can influence the positive phase reflected impulse values is tertiary reflections. This effect is discussed in the positive phase duration section below.

### 2.4.3 Positive Phase Duration

Figure 2.7 shows the positive phase duration verses the driver pressure for varying driver lengths. Best fit lines have been added to differentiate the different driver lengths. For driver lengths below *3355 mm*, the positive phase duration is relatively independent of driver pressure, however, for longer driver lengths, both driver pressure and driver length have a significant influence on positive phase duration. Significant scatter is evident in the plot of positive phase duration versus driver pressure, this is largely due to two factors: inaccuracy due to signal noise; and tertiary reflections.

Figure 2.8 shows an example reflected pressure-time and reflected impulse-time history generated using a *2745 mm* long driver with a driver pressure of *497 kPa*. This figure shows that the exact positive phase duration may be difficult to determine due to the amount of signal noise and the gradual slope of the pressure versus time relationship at the end of the positive phase. In the integration of the pressure-time relationship to determine impulse, unbiased signal noise (that is equally distributed above and below the real pressure values) is eliminated. To overcome the

difficulties in directly determining the positive phase duration from the pressure time history, the positive phase duration was taken at the local maximum of the impulse-time relationship.

Tertiary reflections are the internal reflections within the shock tube as the wave interacts with the end of the driver section. These reflections generally occur after the end of the positive phase duration as shown in Figure 2.9 by example of a pressure and impulse-time history for a shock wave generated using a driver length of *2745 mm* and a driver pressure of *69.0 kPa*. Since the tertiary reflections occur as shock fronts rather than more gradual deflagration waves, they have no influence on the positive phase duration if the maximum tertiary pressure occurs after the initial shock wave has passed through its positive phase. In some cases, depending on driver length and driver pressure, the tertiary shock waves can occur during the initial positive phase. In these cases, the positive phase can be significantly extended. This also leads to an increase in impulse over the positive phase as higher pressures are introduced during the initial shock wave decay period and the positive phase is extended. Tertiary shock waves are discussed in more detail in following sections.

## *2.5 Driver Length and Driver Pressure Influence on Shock Front Velocity*

The shock front velocity of the shock waves generated in the shock tube was measured using two pressure gauges located on the walls of the expansion section located *50 mm* and *1067 mm* away from the reflecting surface on the test frame. The distance between theses gauge locations was divided by the difference in arrival time at these two locations to compute wave front velocity. Wave front velocities are plotted versus reflected pressures for six different driver lengths shown in Figures 2.10 a) through f) and in Figure 2.11 for all driver lengths in one figure. In general, the wave front velocities are greater than sound speed (the speed of sound in specified medium of known density and temperature), *0.34029 m/ms*, at standard temperature and pressure (*20 °C*, seal level atmosphere). The wave front velocities have a slight positive trend, increasing with reflected pressures.

According to the Rankine and Hugoniot equation (Equation 1.6) for shock wave velocity, the wave velocity is only a function of the sound speed in ambient atmosphere, the ambient atmospheric pressure and the incident overpressure of the shock wave. Since there were no measurements for incident pressures at the reflecting plane, reflected pressures have been compared with the wave front velocity. Equation 1.6 describes a wave front velocity that increases by the square root of the sum of the incident overpressure and the atmospheric pressure divided by the atmospheric pressure and all multiplied by the ambient atmospheric sound speed. In Equation 1.16, Rankine and Hugoniot describe the relationship between reflected pressure, incident pressure and dynamic pressure for normal reflecting planes. Smith and Hetherington (1994) state that for far range explosions, or those that create a shock wave with a large positive phase duration and small overpressure, similar to what is generated with the shock tube, this relationship is simplified to the reflected pressure being approximately two times the incident overpressure. Using this rational, Figure 2.11 also shows the Rankine Hugoniot predicted wave front velocities for the case of reflected pressure being twice the incident over pressure. Although there is some scatter in the experimental results, there does appear to be some agreement with between experimental and predicted results.

The low wave front velocities and corresponding low particle velocities would result in small diffraction forces if the shock wave was allowed to transverse the test specimen. Use of the shock tube for diffraction tests is not recommended.

## *2.6 Tertiary Reflections within the Shock Tube*

Over the duration of each test, there are three noticeable behaviours in the pressure-time history. The first is the initial shock front followed by a decay, or rarefaction (the expansion wave of a compressed of a compressed medium), into the negative phase. After this, there tends to be a deflagration pressure wave; a compression wave traveling below the sound speed that does not form a shock front. This second increase in pressure tends to be a substantial fraction of the original reflected pressure. Following this deflagration wave, there are tertiary reflected pressure peaks that occur as a result of the internal reflections within the shock tube. These internal

reflections occur as the shock wave reflects off the end of the driver section. As time progresses, the tertiary shock waves and any corresponding deflagration waves become damped out and the pressures return to atmospheric conditions. Figure 2.12 shows these different features for a shock wave generated using *518 kPa* driver pressure and *1830 mm* driver length. In this figure the deflagration wave begins to occur at around *30 ms* and continues until it reaches its maximum pressure of around *28 kPa* at *40 ms* when it enters a decay curve. Shortly after the deflagration wave there is a tertiary shock wave that occurs at *52 ms* and again at *88 ms, 98 ms* and *137 ms*. These secondary reflections decrease in magnitude with time and eventually pressure returns to atmospheric conditions. This section discusses these secondary pressure waves as they relate to different driver lengths and driver pressures.

### 2.6.1 Initial Reflected Pressures and Deflagration Pressures

Following the initial shock and the rarefaction into below atmospheric pressures, a deflagration wave will occur and attempt to return the low density air to normal pressures. This wave will initially return the atmosphere into a compressed state and then decay in a second rarefaction wave and continue this process until the non-ambient pressures are damped out of the system. For shock waves within the shock tube generally only the initial rarefaction wave is easily observed as tertiary shock fronts begin to occur and disrupt the rarefaction-deflagration behaviour. The magnitude of the reflected pressure, reflected impulse and duration of the deflagration wave is dependent on the properties of the initial shock wave. Of these properties, only the maximum deflagration pressure is quantifiable from the pressure-time histories generated using the shock tube. The other properties of the deflagration wave are not known since the deflagration waves are disrupted by tertiary shock waves. Figure 2.13 shows the relationship between the maximum deflagration pressure and the maximum reflected pressure of the initial shock wave. There is a general positive trend in this relationship.

### 2.6.2 Initial Reflected Pressures and Tertiary Reflected Pressures

After the initial reflection at the load frame, there are several tertiary reflections that occur within the shock tube itself. These reflections interact with reflecting plane mounted on the load frame

and appear as distinct shock waves. The arrival time, magnitude of pressure and duration of these secondary reflections is a function of the pressure within the shock tube and the length of the shock tube.

Figure 2.14 shows the maximum tertiary reflected pressure for the first tertiary shock wave plotted against the initial maximum reflected pressure. There is a general trend where the larger the initial reflected pressure, the larger the tertiary reflected pressure. This trend does not seem to have any direct relationship to driver length.

The arrival time of the tertiary shock wave is plotted against the reflected pressure of the initial shock wave for various driver lengths in Figure 2.15. This figure shows that the arrival time of the tertiary shock wave appears to be primarily dependent on the length of the driver section and relatively independent of the reflected pressure. In general, the longer the shock tube driver section is, the later the tertiary shock wave will arrive.

The positive phase duration of the tertiary shock wave is shown plotted against the positive phase duration of the initial shock wave in Figure 2.16. From this figure, there is a general trend of an increase in tertiary positive phase duration with an increase in initial positive phase duration. Figure 2.17 shows the same relationship, however, the ratio of the initial positive phase duration to the tertiary positive phase duration has been plotted and organized by driver lengths. This relationship shows that generally the initial positive phase duration is larger than the tertiary positive phase duration, with the ratio ranging from slightly below unity, *0.95*, to well above unity at *3.87*. There is no apparent trend of positive phase duration ratio based on driver length.

*TABLE 2.1 - Shock Wave Properties at Various Locations on Reflecting Plane for Shock Wave Generated with 1830mm Driver Length and 276kPa Driver Pressure*

| Driver Pressure | Driver Length | Gauge Number | Gauge Location | | Reflected Pressure | Reflected Impulse | Positive Phase Duration | Relative Time of Arrival | Positive Phase Duration Ratio | Reflected Pressure Ratio | Reflected Impulse Ratio |
|---|---|---|---|---|---|---|---|---|---|---|---|
| $P_D$ (kPa) | $L_D$ (mm) | | $x$ (mm) | $y$ (mm) | $P_r$ (kPa) | $I_r$ (kPa-ms) | $t_d$ (ms) | $t_a$ (ms) | $t_d/t_{d,max}$ | $P_r/P_{r,max}$ | $I_r/I_{r,max}$ |
| 276 | 1830 | 1 | 864 | -864 | 57.9 | 414.3 | 17.28 | 0.00 | 0.94 | 0.97 | 0.93 |
| | | 2 | 457 | -864 | 53.5 | 417.1 | 16.89 | 0.10 | 0.92 | 0.90 | 0.94 |
| | | 3 | 50 | -864 | 55.5 | 446.3 | 17.46 | 0.13 | 0.95 | 0.93 | 1.00 |
| | | 4 | -864 | -864 | 59.5 | 413.9 | 18.07 | 0.00 | 0.99 | 1.00 | 0.93 |
| | | 5 | 864 | 50 | 53.3 | 404.2 | 18.13 | 0.15 | 0.99 | 0.90 | 0.91 |
| | | 6 | 457 | 50 | 52.5 | 399.9 | 17.35 | 0.23 | 0.95 | 0.88 | 0.90 |
| | | 7 | 50 | 50 | 57.8 | 445.3 | 17.69 | 0.26 | 0.97 | 0.97 | 1.00 |
| | | 8 | -864 | 50 | 56.2 | 403.8 | 18.32 | 0.14 | 1.00 | 0.94 | 0.91 |
| | | 9 | 864 | 864 | 59.5 | 406.0 | 17.99 | 0.01 | 0.98 | 1.00 | 0.91 |
| | | 10 | 457 | 864 | No Data | | | | | | |
| | | 11 | 50 | 864 | 55.5 | 410.4 | 17.31 | 0.14 | 0.94 | 0.93 | 0.92 |
| | | 12 | -864 | 864 | 56.7 | 425.4 | 17.22 | 0.01 | 0.94 | 0.95 | 0.96 |
| | | | | | | Average | | | 0.96 | 0.94 | 0.94 |
| | | | | | | Standard Deviation | | | 0.0249 | 0.0404 | 0.0358 |
| | | | | | | Coefficient of Variation (%) | | | 2.59 | 4.28 | 3.82 |
| | | | | | | min | | | 0.92 | 0.88 | 0.90 |
| | | | | | | max | | | 1.00 | 1.00 | 1.00 |

*TABLE 2.2 - Shock Wave Properties at Various Locations on Reflecting Plane for Shock Wave Generated with 1830mm Driver Length and 518kPa Driver Pressure*

| Driver Pressure | Driver Length | Gauge Number | Gauge Location | | Reflected Pressure | Reflected Impulse | Positive Phase Duration | Relative Time of Arrival | Positive Phase Duration Ratio | Reflected Pressure Ratio | Reflected Impulse Ratio |
|---|---|---|---|---|---|---|---|---|---|---|---|
| $P_D$ (kPa) | $L_D$ (mm) | | $x$ (mm) | $y$ (mm) | $P_r$ (kPa) | $I_r$ (kPa-ms) | $t_d$ (ms) | $t_a$ (ms) | $t_d/t_{d,max}$ | $P_r/P_{r,max}$ | $I_r/I_{r,max}$ |
| 518 | 1830 | 1 | 864 | -864 | 96.3 | 691.9 | 23.81 | 0.00 | 0.99 | 0.92 | 0.92 |
| | | 2 | 457 | -864 | 98.2 | 694.3 | 23.25 | 0.09 | 0.96 | 0.94 | 0.92 |
| | | 3 | 50 | -864 | 96.5 | 740.8 | 20.72 | 0.13 | 0.86 | 0.92 | 0.98 |
| | | 4 | -864 | -864 | 90.8 | 688.8 | 22.71 | 0.02 | 0.94 | 0.87 | 0.91 |
| | | 5 | 864 | 50 | 91.9 | 683.3 | 23.36 | 0.12 | 0.97 | 0.88 | 0.91 |
| | | 6 | 457 | 50 | 87.6 | 671.2 | 24.17 | 0.21 | 1.00 | 0.84 | 0.89 |
| | | 7 | 50 | 50 | 94.1 | 754.6 | 24.07 | 0.26 | 1.00 | 0.90 | 1.00 |
| | | 8 | -864 | 50 | 93.5 | 679.3 | 24.06 | 0.14 | 1.00 | 0.90 | 0.90 |
| | | 9 | 864 | 864 | 101.0 | 688.7 | 22.88 | 0.02 | 0.95 | 0.97 | 0.91 |
| | | 10 | 457 | 864 | 90.7 | 677.0 | 23.78 | 0.11 | 0.98 | 0.87 | 0.90 |
| | | 11 | 50 | 864 | 92.5 | 623.4 | 23.73 | 0.14 | 0.98 | 0.89 | 0.83 |
| | | 12 | -864 | 864 | 104.4 | 711.9 | 23.15 | 0.01 | 0.96 | 1.00 | 0.94 |
| | | | | | | Average | | | 0.96 | 0.91 | 0.92 |
| | | | | | | Standard Deviation | | | 0.0391 | 0.0455 | 0.0444 |
| | | | | | | Coefficient of Variation (%) | | | 4.05 | 5.01 | 4.84 |
| | | | | | | min | | | 0.86 | 0.84 | 0.83 |
| | | | | | | max | | | 1.00 | 1.00 | 1.00 |

*TABLE 2.3 - Shock Wave Properties at Various Locations on Reflecting Plane for Shock Wave Generated with 4880mm Driver Length and 518kPa Driver Pressure*

| Driver Pressure | Driver Length | Gauge Number | Gauge Location | | Reflected Pressure | Reflected Impulse | Positive Phase Duration | Relative Time of Arrival | Positive Phase Duration Ratio | Reflected Pressure Ratio | Reflected Impulse Ratio |
|---|---|---|---|---|---|---|---|---|---|---|---|
| $P_D$ (kPa) | $L_D$ (mm) | | x (mm) | y (mm) | $P_r$ (kPa) | $I_r$ (kPa-ms) | $t_d$ (ms) | $t_a$ (ms) | $t_d/t_{d,max}$ | $P_r/P_{r,max}$ | $I_r/I_{r,max}$ |
| 518 | 4880 | 1 | 864 | -864 | 97.5 | 2241.2 | 67.72 | 0.00 | 0.95 | 1.00 | 0.92 |
| | | 2 | 457 | -864 | 90.8 | 2244.9 | 69.35 | 0.07 | 0.97 | 0.93 | 0.93 |
| | | 3 | 50 | -864 | 95.7 | 2426.9 | 67.20 | 0.12 | 0.94 | 0.98 | 1.00 |
| | | 4 | -864 | -864 | 97.5 | 2244.2 | 69.89 | 0.02 | 0.98 | 1.00 | 0.92 |
| | | 5 | 864 | 50 | 87.2 | 2207.1 | 69.75 | 0.16 | 0.98 | 0.89 | 0.91 |
| | | 6 | 457 | 50 | 90.1 | 2179.9 | 70.09 | 0.24 | 0.98 | 0.92 | 0.90 |
| | | 7 | 50 | 50 | 93.6 | 2349.9 | 63.00 | 0.29 | 0.88 | 0.96 | 0.97 |
| | | 8 | -864 | 50 | 92.7 | 2200.5 | 70.67 | 0.18 | 0.99 | 0.95 | 0.91 |
| | | 9 | 864 | 864 | 91.0 | 2167.5 | 71.44 | 0.14 | 1.00 | 0.93 | 0.89 |
| | | 10 | 457 | 864 | 93.2 | 2203.4 | 70.81 | 0.06 | 0.99 | 0.96 | 0.91 |
| | | 11 | 50 | 864 | No Data | | | | | | |
| | | 12 | -864 | 864 | No Data | | | | | | |
| | | | | | Average | | | | 0.97 | 0.95 | 0.93 |
| | | | | | Standard Deviation | | | | 0.0348 | 0.0340 | 0.0335 |
| | | | | | Coefficient of Variation (%) | | | | 3.60 | 3.57 | 3.62 |
| | | | | | min | | | | 0.88 | 0.89 | 0.89 |
| | | | | | max | | | | 1.00 | 1.00 | 1.00 |

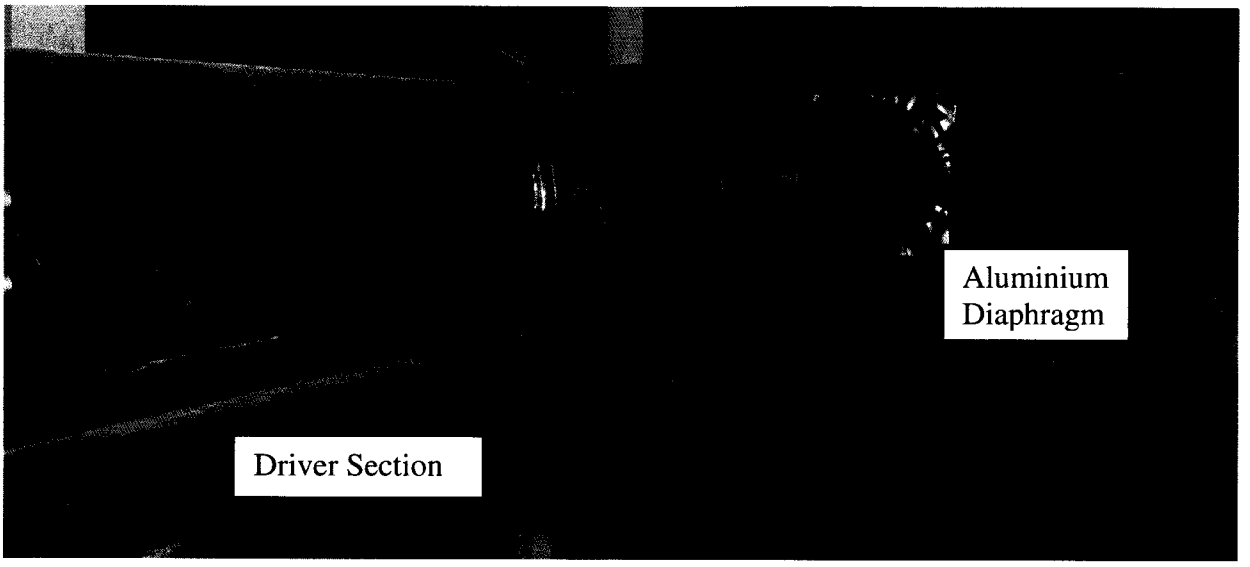


a)

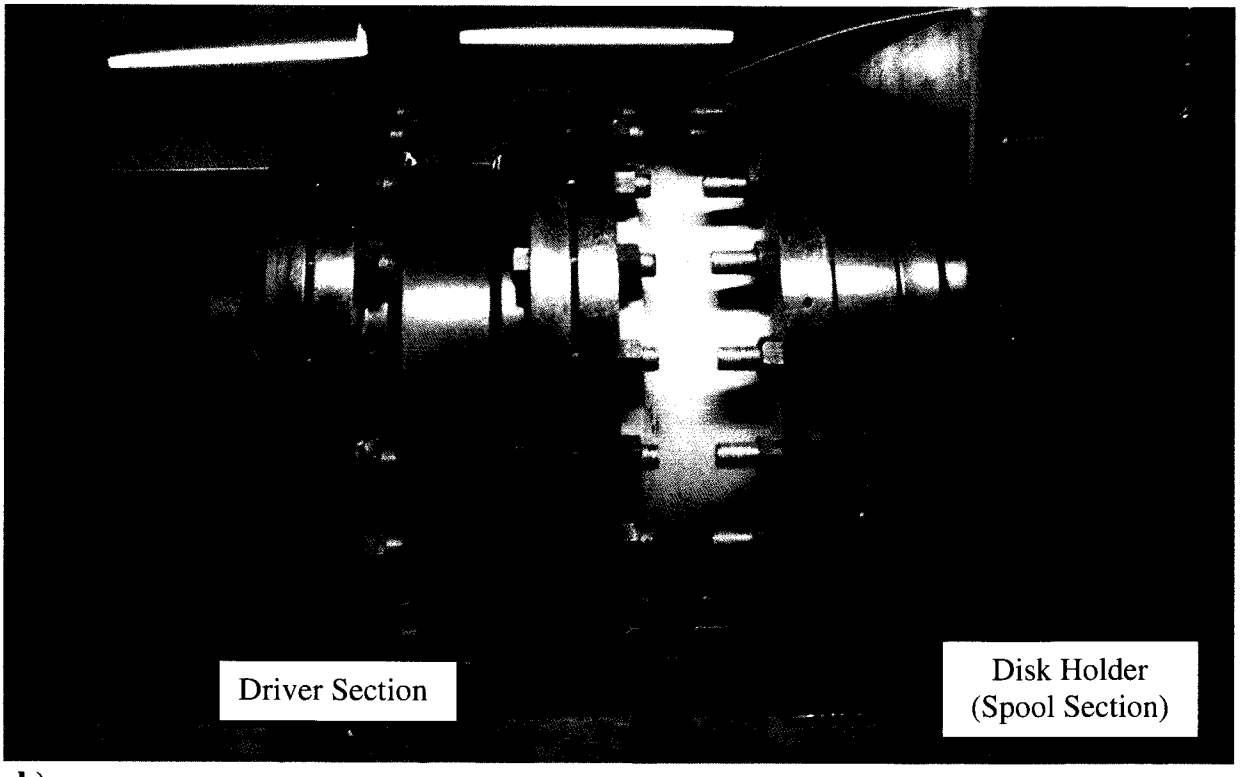


b)

*Figure 2-1: Shock Tube: a) Driver Section; b) Disk Holder (Spool) Section*

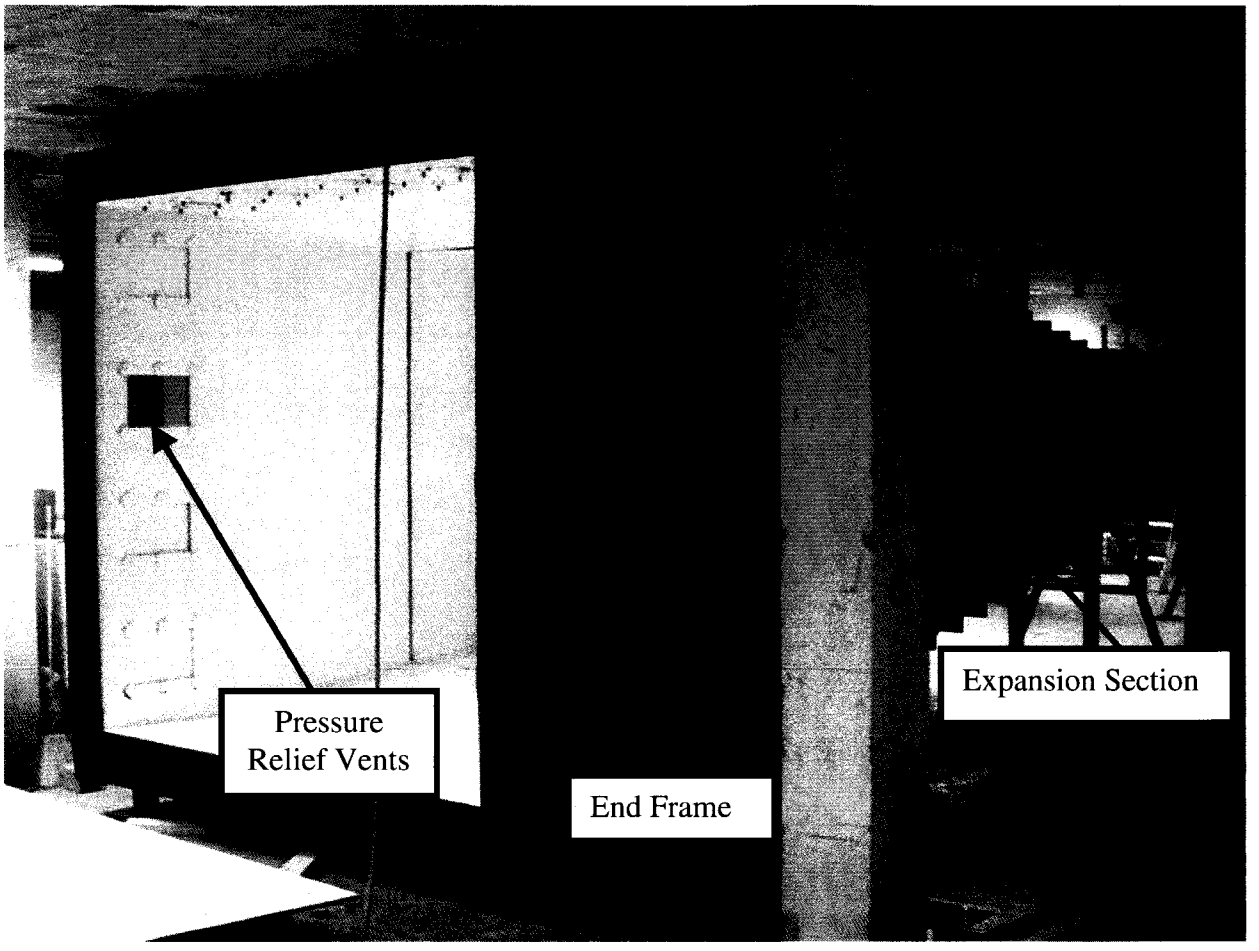


*Figure 2-2: Shock Tube Expansion Section and End Frame*

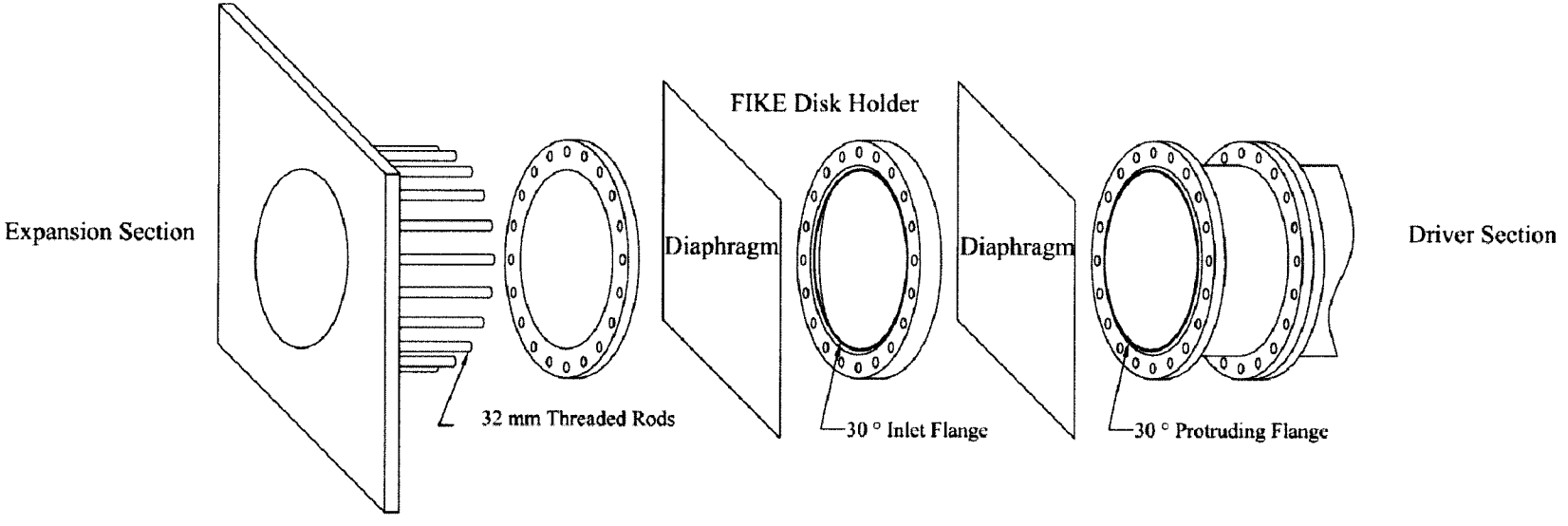


***Figure 2-3: Detailing of Disk Holder (Spool Section) and Diaphragm Sections of Shock Tube***

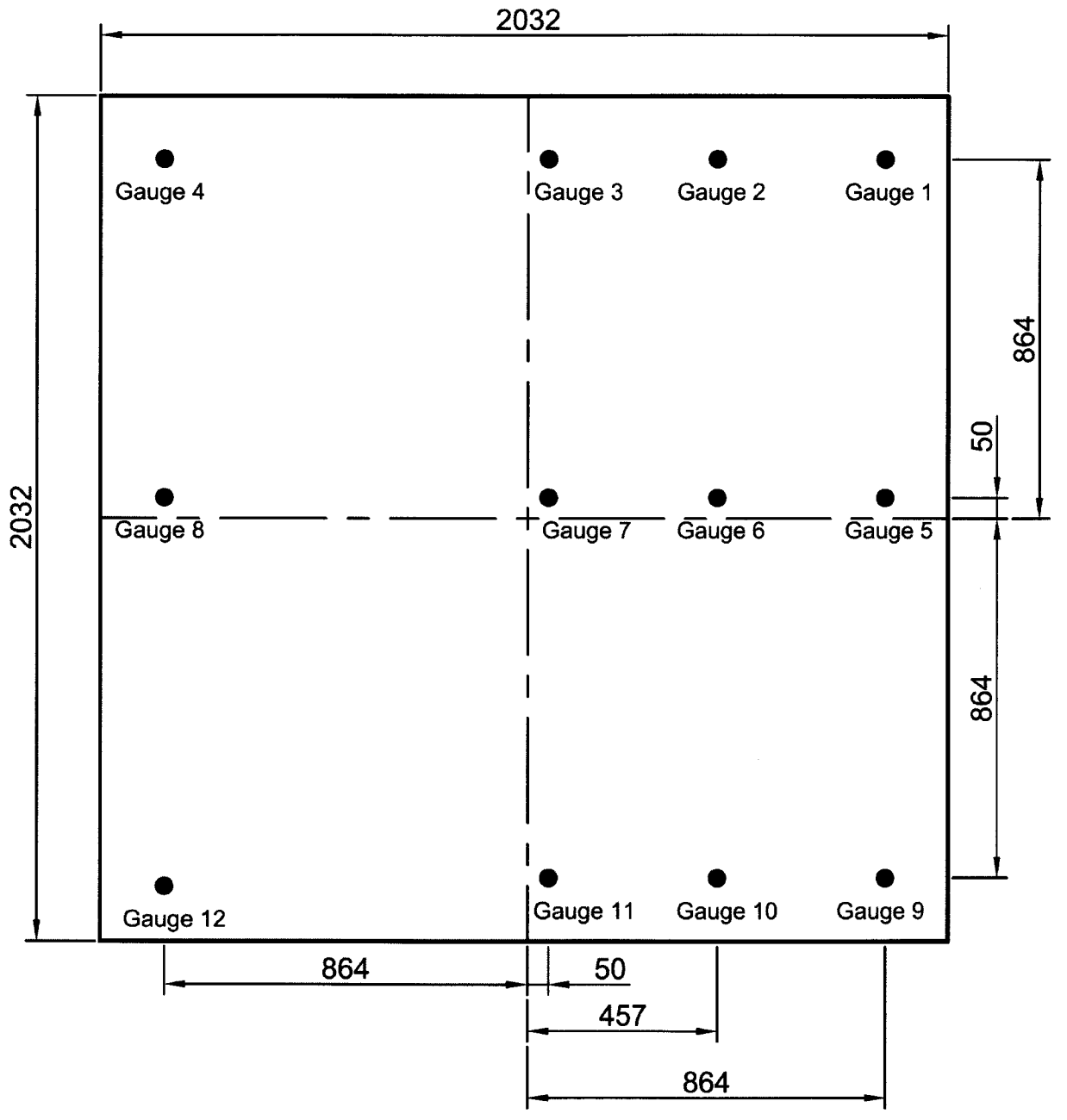


*Figure 2-4: Locations of Pressure Gauges in Reflecting Plate Mounted on Test Frame*

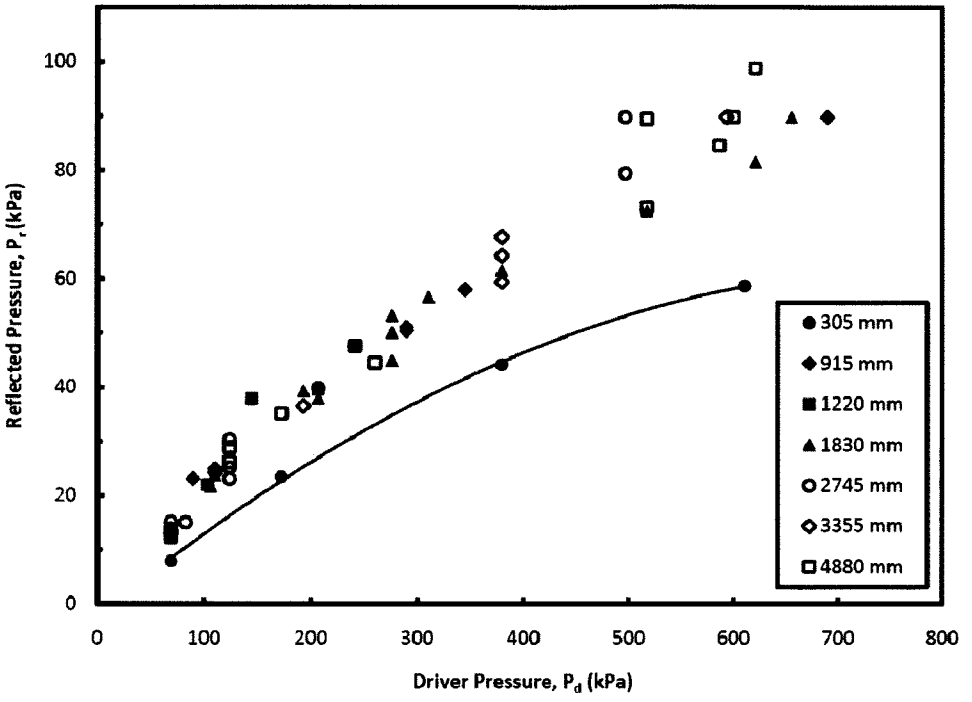


*Figure 2-5: Reflected Pressure versus Driver Pressure for Different Driver Lengths*

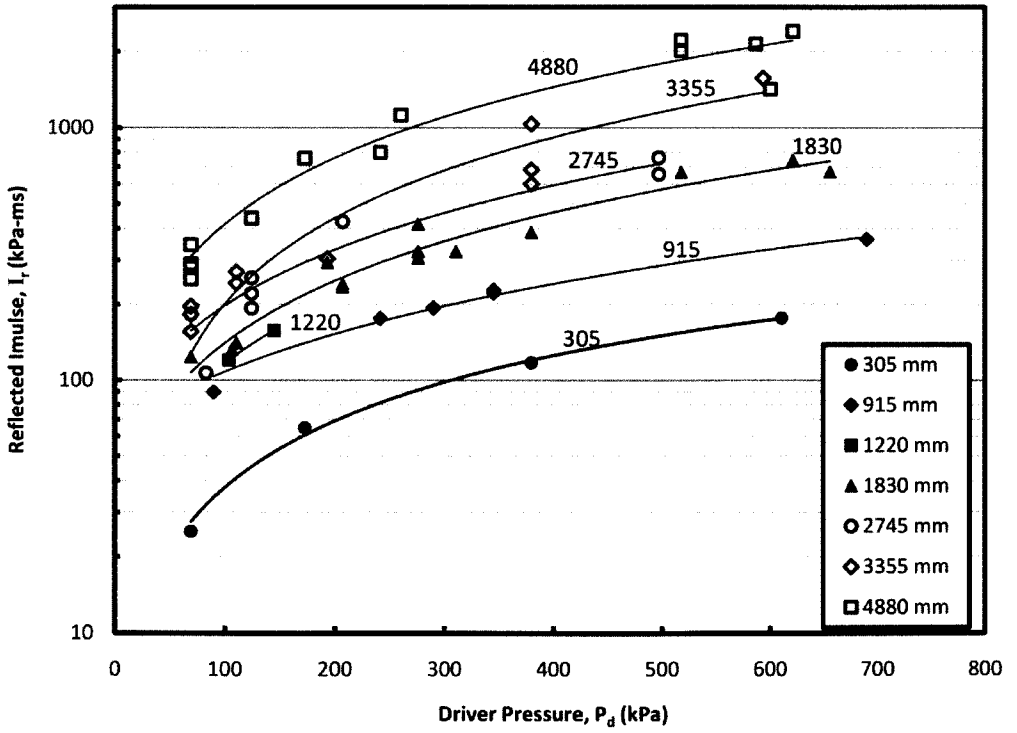


*Figure 2-6: Reflected Impulse versus Driver Pressure for Different Driver Lengths*

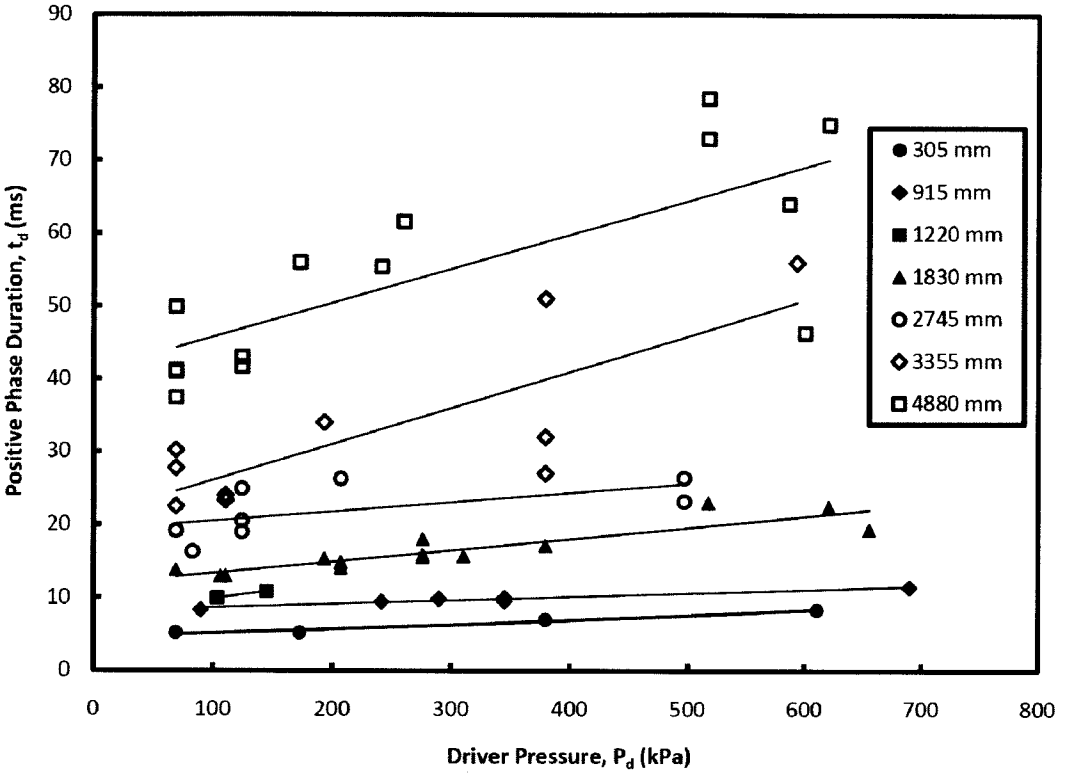


*Figure 2-7: Positive Phase Duration versus Driver Pressure for Different Driver Lengths*

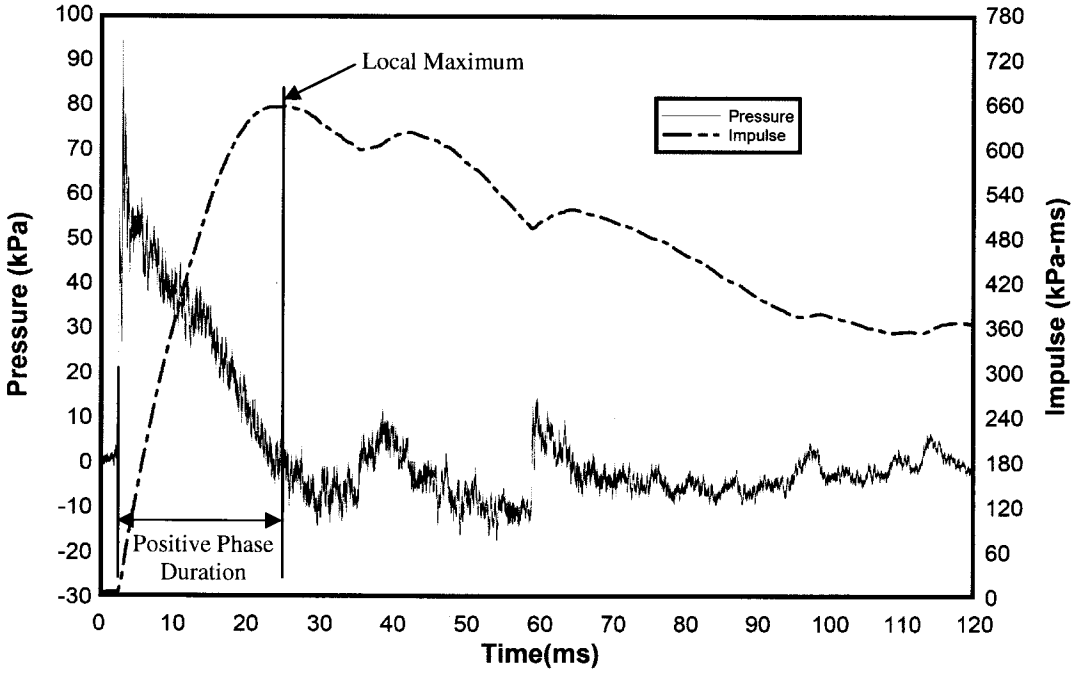


Figure 2-8: Positive Phase Reflected Pressure and Reflected Impulse Time History for Shock Wave Generated Using 2745 mm Driver Length and 497 kPa Driver Pressure

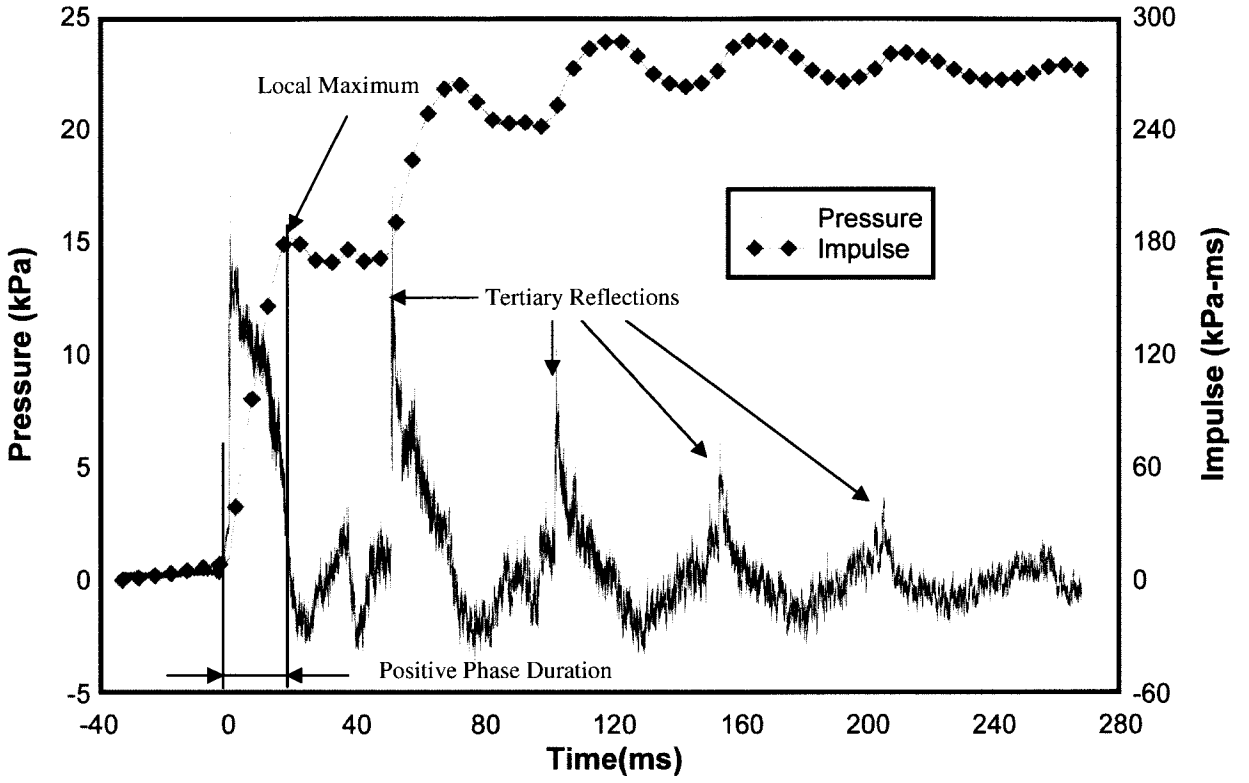


*Figure 2-9: Reflected Pressure and Reflected Impulse Time History for Shock Wave Generated Using 2745 mm Driver Length and 69.0 kPa Driver Pressure*

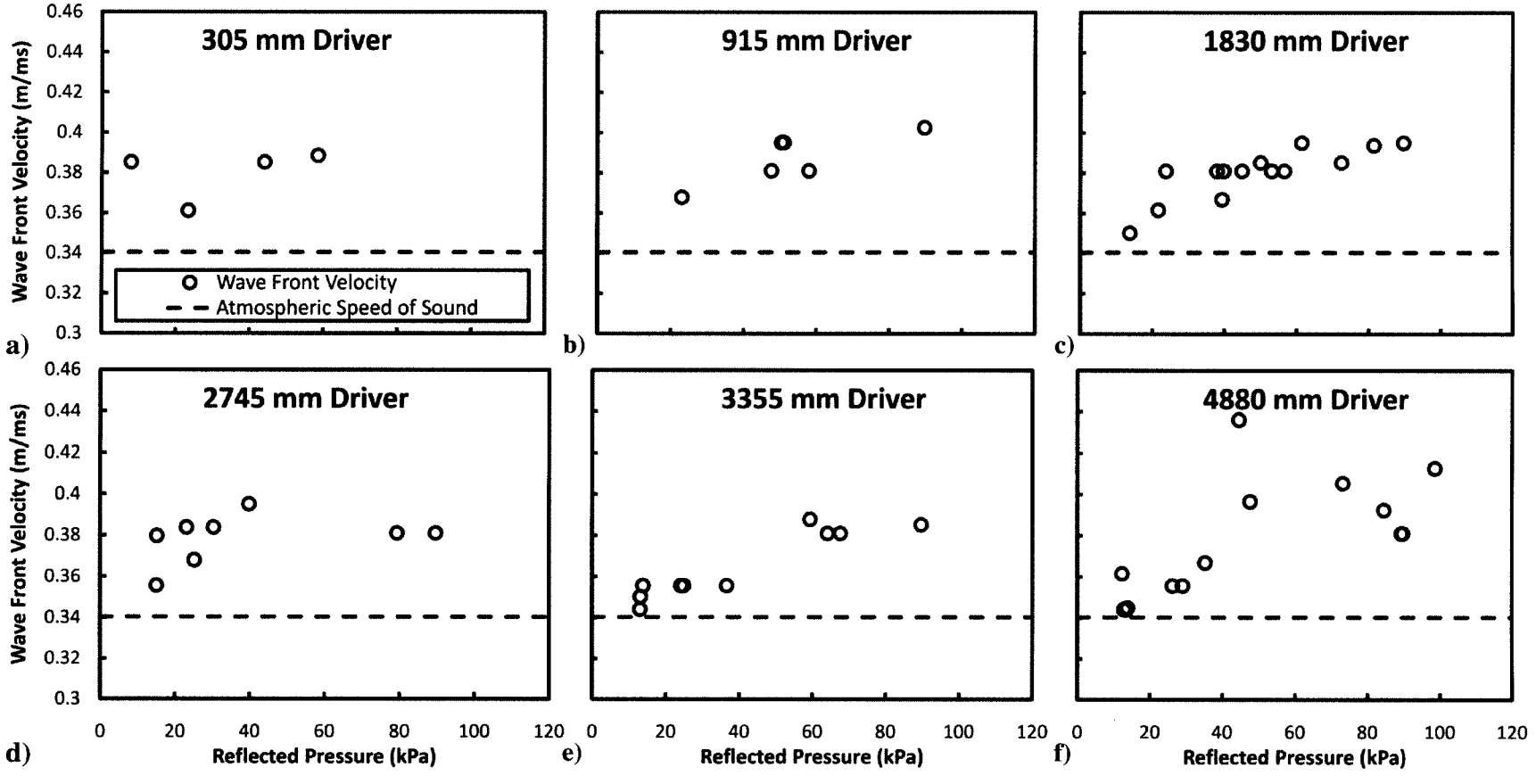


*Figure 2-10: Wave Front Velocity versus Reflected Pressure for: a) 305 mm Driver Length; b) 915 mm Driver Length; c) 1830 mm Driver Length; d) 2745 mm Driver Length; e) 3355 mm Driver Length; f) 4880 mm Driver Length*

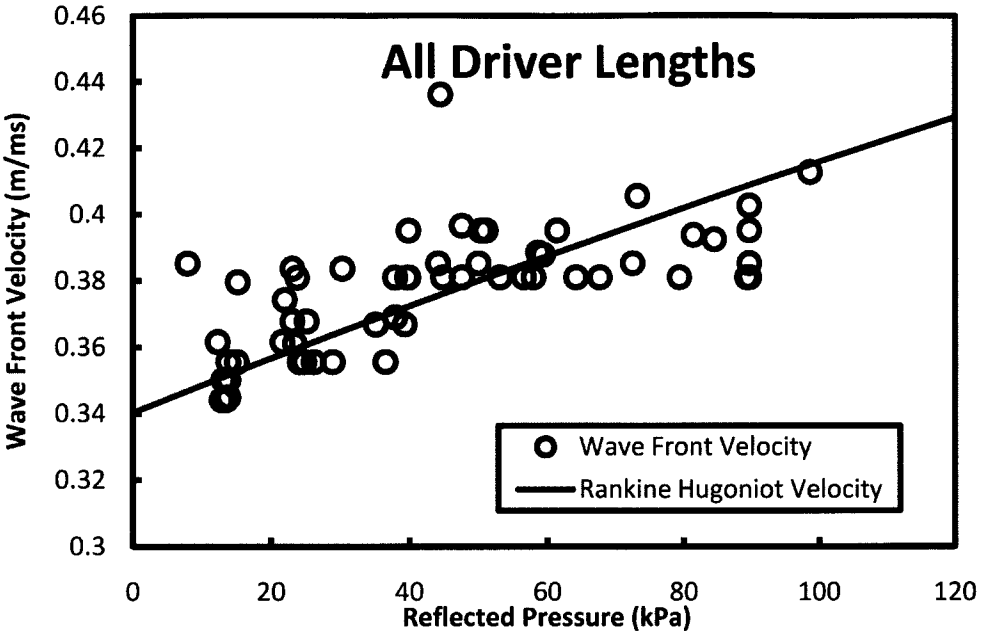


*Figure 2-11: Wave Front Velocity versus Reflected Pressure for All Driver Lengths*

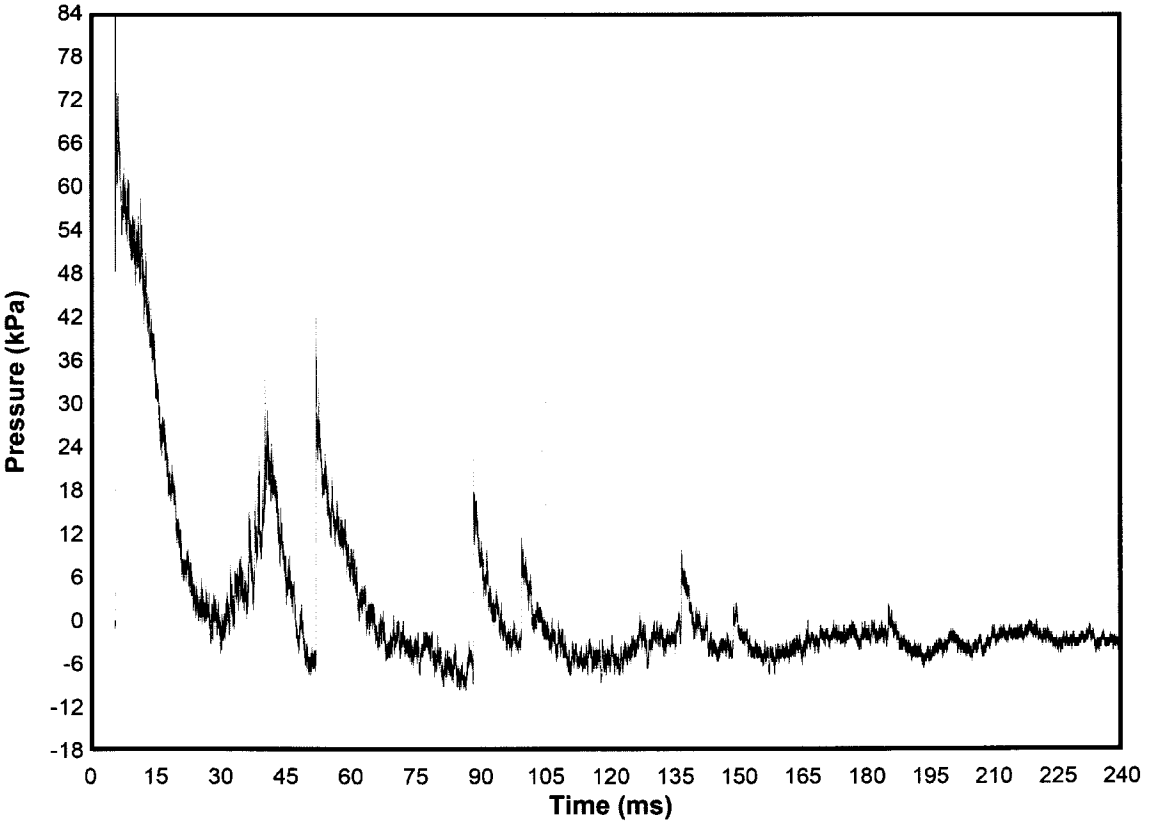


*Figure 2-12: Pressure-Time History for a Shock Wave Generated with 518 kPa Driver Pressure and 1830 mm Driver Length*

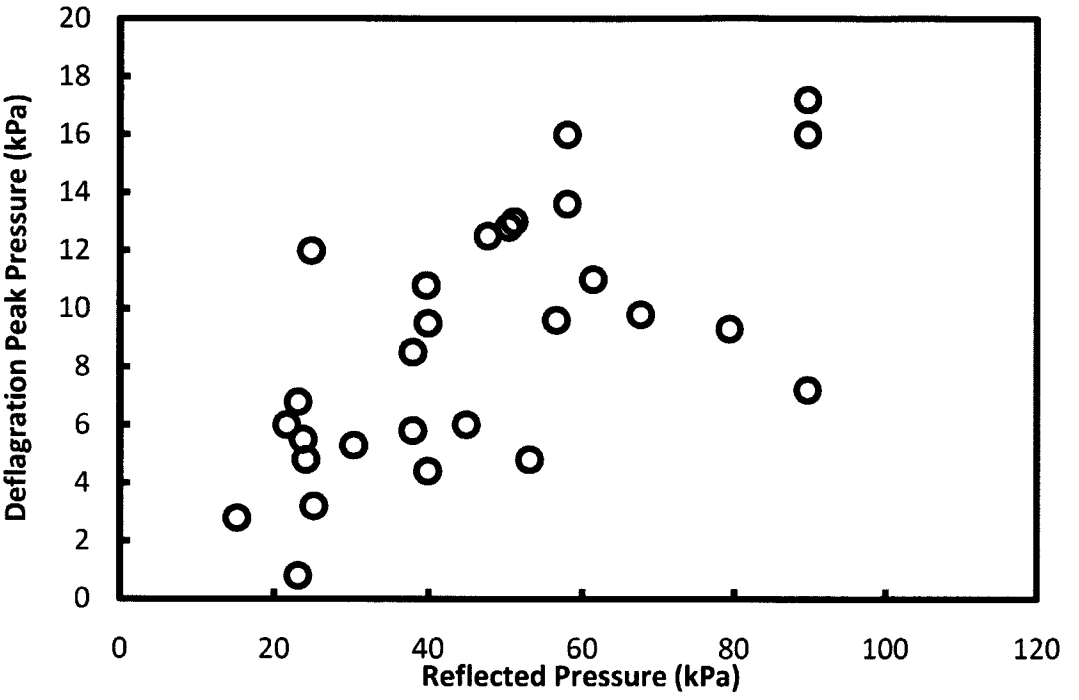


*Figure 2-13: Peak Deflagration Pressure versus Maximum Initial Reflected Pressure*

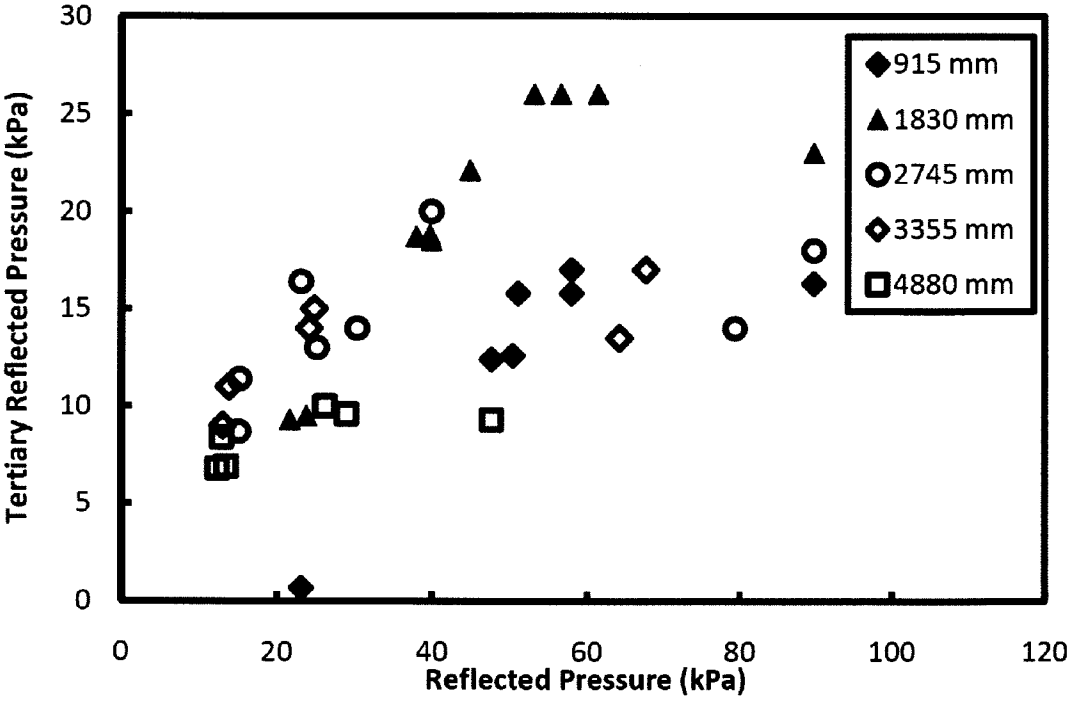


*Figure 2-14: Maximum Tertiary Reflected Pressure versus Maximum Initial Reflected Pressure*

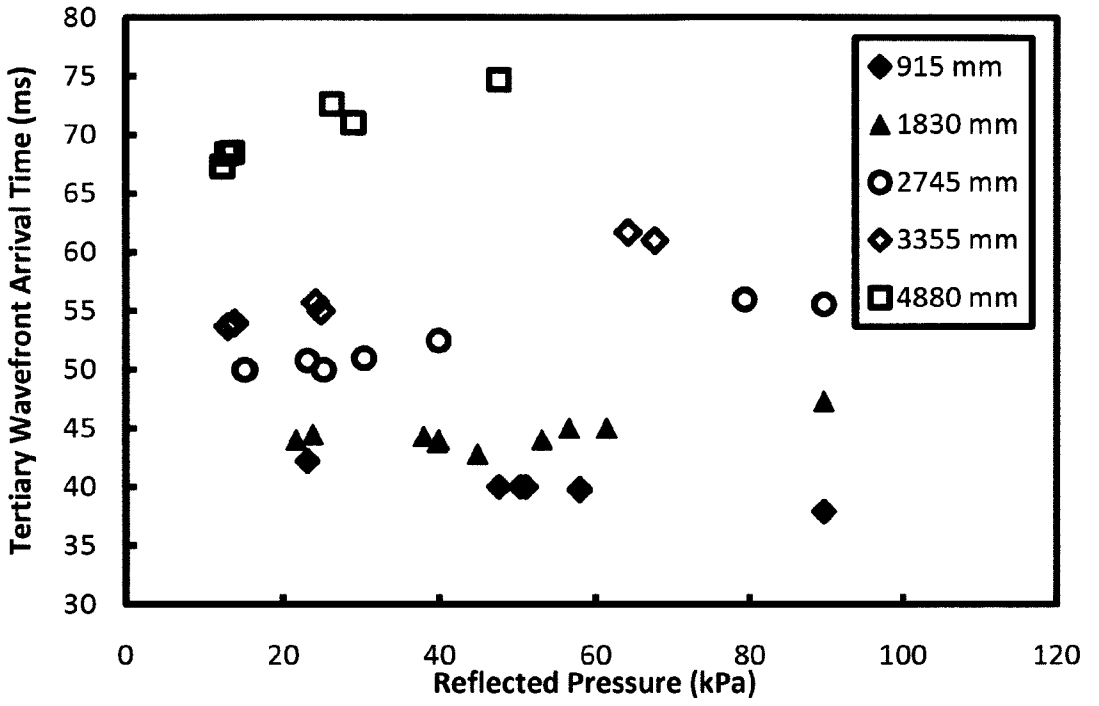


*Figure 2-15: Arrival Time of Tertiary Shock Wave front versus Maximum Initial Reflected Pressure for Different Driver Lengths*

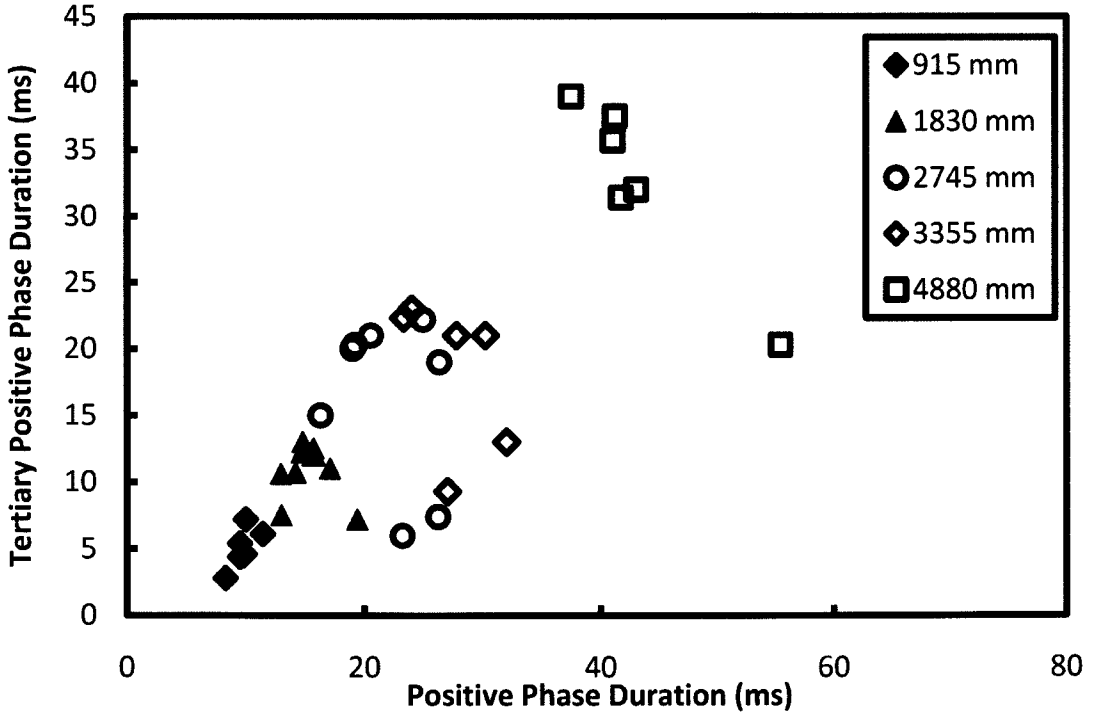


*Figure 2-16: Tertiary Positive Phase Duration versus Initial Positive Phase Duration for Different Driver Lengths*

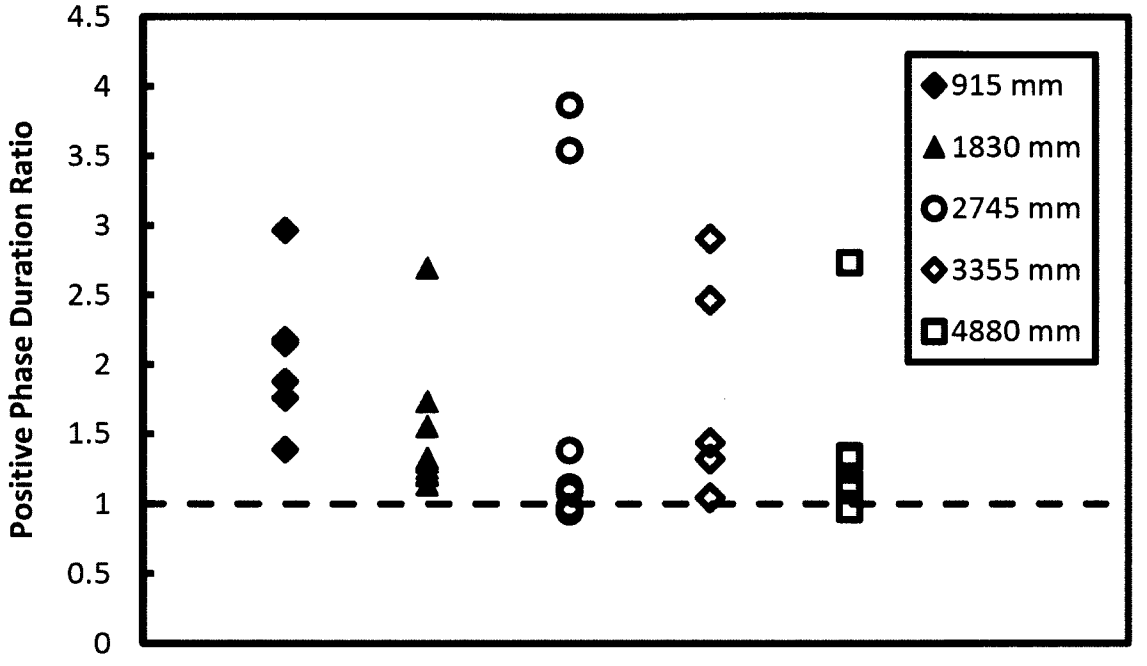


*Figure 2-17: Ratio of Initial Positive Phase Duration to Tertiary Positive Phase Duration for Different Driver Lengths*

# 3 CHAPTER 3

# Experimental Program

## *3.1 General*

The experimental program was designed to test the response of reinforced concrete columns to shock waves. A total of fourteen columns were tested under various combinations of pressure and impulse. Columns were designed to be representative of seismic and non seismic main storey construction. Axial load was applied to levels consistent with construction service loads. The primary parameters being explored were volumetric ratio and spacing of transverse steel and variation of pressure and impulse combinations. This chapter describes the construction and testing program carried out in this research.

## *3.2 Description of Test Specimens*

Fourteen half scale reinforced concrete columns, designed according to CSA A23.3-04 standards, were built and tested for this program. The columns were designed to represent first storey exterior columns. Seven columns were designed for non seismic zones and five for seismic zones where the different designs were provided with different confinement hoop spacing. Each column was rectangular in cross section and had a height of *1980 mm* between supports and a total height of *2438 mm*. Two different cross sections were used: Twelve columns were *100 mm by 150* mm tested in bending about the weak axis and two were *150 mm by 150 mm*. The detailing of the columns, labelled RC-1 through RC-14, is shown in Figures 3.1 through 3.3.

Two different concrete mixes were used in constructing the columns. Both of the mixes had maximum aggregate sizes of *10 mm* and used Type 30 High-Early Cement to ensure the concrete was fully cured at the time of testing. Columns RC-1 and RC-2 had cylinder strengths of *46*

*MPa* at the date of testing and columns RC-3 through RC-14 had strengths of *58 MPa* at the date of testing. Each of the columns was reinforced with a total of four *483 MPa 10M* deformed longitudinal reinforcing steel bars located one in each corner of the column. The longitudinal steel bars were *2400 mm* in length with *90* ° hooks extending *75 mm* into the core of the columns. The longitudinal reinforcing ratio was *2.67 %* for columns RC-1 through RC-12 and *1.79 %* for columns RC-13 and RC-14. The cover to the longitudinal bars was *20 mm* for all columns. Shear ties were provided in the form of rectangular closed ties with *135* ° hooks extending approximately *40 mm* into the core of the column. In all cases, the shear ties were *580 MPa* non deformed steel wire with a diameter of *6.3 mm* and a cross sectional area of *31.2* $mm^2$. The volumetric ratio for the shear steel varied between *0.86 %* for columns RC-13 and RC-14, *1.52%* for columns RC-1, 2, 3, 5, 7, 9, 11, and *3.04%* for columns RC-4, 6, 8, 10, 12. Shear ties were spaced at *h/2* for ordinary construction columns (columns RC-1, 2, 3, 5, 7, 9, 11, 13, 14) and *h/4* for seismically detailed columns (columns RC-4, 6, 8, 10, 12) and was constant for the entire height of all columns. A summary of the column properties and detailing can be found in Table 3.1.

## *3.3 Description of Test Setup*

Columns RC-2 through RC-14 were tested under combined axial loading and transverse loading simulating a blast induced shock wave. Column RC-1 was tested under only transverse loading. The axial loading was applied with hydraulic jacks and the transverse loading was applied using a high pressure air shock wave induced with a shock tube.

### 3.3.1 Axial Loading Mechanism

Axial load was applied to the columns using a hydraulic jack located between the bottom of the column and the floor of the laboratory. A steel block was placed between the top of the column and the *914 mm* thick concrete strong floor of the Structures Laboratory which happened to form the ceiling of the test area. The axial load level applied was *350 kN* for columns RC-2 through RC-12 and *400 kN* for columns RC-13 and RC-14. No axial load was applied to column RC-1.

Once the axial load was applied, the hydraulic jack was locked and the column was fixed to the end frame of the shock tube.

### 3.3.2 Lateral Load Transferring Mechanism

A composite steel beam and steel membrane system was designed to collect the pressure generated by the shock wave and act as the lateral load transfer mechanism by applying a series of point loads along the length of the column as shown in Figure 3.4. The composite steel beam and steel membrane system was fabricated using fifteen *76.2 mm by 76.2 mm by 6.35 mm* thick hollow square structural steel transfer beams which were attached to a *0.71 mm* thick steel sheet at *127 mm* on centre. These transfer beams were placed perpendicular to the column height and were *2438 mm* long. The steel sheet covered the entire area of the end frame, *2438 mm* by *2438 mm*. Neither the sheet nor the steel beams were attached to the end frame during testing and therefore were free to move and distribute the load entirely to the column being tested.

### 3.3.3 Lateral Restraints

For all of the tests the columns were restrained at both ends from lateral movement and partially restrained against rotation. The supports were intended to provide full rotational restraint, however this proved difficult to provide in practice. Lateral and rotational restraints were provided using steel plates welded onto steel channels and hollow structural sections. The column was clamped between two of the steel plates at the top and bottom using *15.9 mm* bolts and the plates were affixed to the end frame of the shock tube. The end supports system is shown in Figures 3.4 and 3.5.

## *3.4 Material Properties*

### 3.4.1 Concrete

Two concrete mixes were used for the columns. Mix one for columns RC-1 and RC-2 had cylinder strengths of *46.5 MPa* at the date of testing and mix two for columns RC-3 through RC-

14 had cylinder strengths of *58 MPa* at the testing dates. Both concrete batches used Type 30 High-Early Cement with a 10 mm maximum size crushed siliceous aggregate. Cylinder strengths were measured using a Forney testing machine with a *2200 kN* maximum capacity. Sets of three cylinders were tested at different dates leading up to the testing program. Prior to testing, each cylinder was ground smooth on both ends to ensure a uniform pressure distribution during testing.

### 3.4.2 Steel

Longitudinal steel reinforcement for all of the columns consisted of four 10M (*11.3 mm* diameter) deformed reinforcing bars with a yield strength of *483 MPa* at a yield strain of *0.24 %*. Transverse steel ties were fabricated from *6.3 mm* diameter non deformed steel wire with a yield strength of *580 MPa* at a yield strain of *0.22 %*. Coupon tests were performed on sections of the steel bars to determine actual yield strength, ultimate strength, and strain at ultimate strength. The stress strain curves for both steel types are shown in Figure 3.6.

## *3.5 Construction of Test Specimens*

The construction of the test specimens was completed in five stages at the University of Ottawa Structures Laboratory. These stages included bending of steel ties, assembly of steel reinforcement cages, application of electrical resistance strain gauges on the steel cages, construction of form work, and casting of concrete. The reinforcing steel and the concrete were both provided by local companies.

Bending of the steel ties was done with a hand bending jig designed to provide exact dimensions of the steel ties. The *6.3 mm* wire was first cut to the length needed for each size ties. Three *90* ° bends and two *135* ° bends were provided for each tie. Assembly of the steel cages was done by first marking out tie spacing on each of the four longitudinal reinforcing bars per column. The transverse reinforcement was then placed on the steel bars and tied in place using quick tie wires. Strain gauges were applied to the longitudinal steel and to select transverse ties in prescribed

locations. Prior to application of strain gauges, the deformed longitudinal bars were smoothed using an angle grinder and cleaned with a weak acid and a weak base. The strain gauge locations were marked on the bars and strain gauges were glued to the bars. Once the strain gauge glue had set, the lead wires were insulated from the reinforcing steel using electrical tape. Two wire lead wires were then soldered to the strain gauge leads and insulated from each other using electrical tape. The final step was to protect the strain gauges and leads by wrapping them with a layer of electrical tape and applying a layer of silicone. Formwork was constructed using *19 mm* thick plywood and assembled in a manner such that the columns could be case horizontally. During casting, a concrete vibrator was used to ensure uniform concrete distribution. The columns were watered once daily for fourteen days and covered with wet burlap to control heat during curing. Figures 3.7 and 3.8 show the construction of a steel cage and the steel cages placed in formwork prior to casting, respectively.

### 3.5.1 Instrumentation

Each column was instrumented with electric resistance strain gauges located on the longitudinal reinforcing bars and on select transverse ties. The strain gauges were *350 ohm* linear strain gauges *6 mm* in length. Ten strain gauges were placed on two of the longitudinal reinforcing bars in each column at various locations along the length. One set of gauges was located on one of the bars closest to the transverse loading (shock wave) side and one set on a bar on the opposite side. Strain gauges were also located on the shear ties near the support region. The top half of the column shown in Figure 3.9 gives the locations of six of the strain gauges placed on the longitudinal reinforcing bars for each column. An additional four strain gauges were located in the lower half of the column and were placed symmetrically about mid height of the column.

During testing, one linear variable differential transducer (LVDT) with a *300 mm* stroke was placed at mid height of the column to measure mid height deflection. The LVDT was connected to both the column and a support stand in a manner that allowed rotation at both ends of the LVDT. Figure 3.10 shows the LVDT attached to a column mounted on the test frame.

A high speed camera was placed at the side of the column during testing, shown in Figure 3.11, and recorded the column response at a frame rate of *1000 frames per second.* The camera was located *2500 mm* from the edge of the column in each test.

Pressure measurements along the length of the shock tube and near the load transfer mechanism were taken to record the incident and reflected pressure time history for each test. These readings were measured using voltage differential high resolution ICP pressure probes with *14.5 mV/kPa* sensitivity capable of reading a maximum pressure of *345 kPa (5000 mV).*

## *3.6 Test Procedure and Loading Program*

Prior to testing, the load transfer mechanism was installed on the end of the shock tube. The bottom of each column was then placed on the hydraulic jack used to apply the axial load and the supports at the top and bottom of the column were installed. The axial load was applied prior to tightening the supports with eight *16 mm* diameter bolts each. The strain gauge leads were then connected to the data acquisition unit and an LVDT was placed at mid height of the column.

The length of the driver section was constant for any particular column. Each column was exposed to multiple shots in order to explore the column response in both the elastic and inelastic regions. The driver pressure and driver length were selected to produce the desired reflected pressure and reflected impulse at the location of the test specimen.

### 3.6.1 Data Acquisition

Two digital oscilloscopes reading at *100,000 Hz (samples per second)* were used as the Data acquisition (DAC) during testing. Nine channels recorded strain readings, four channels recorded pressure readings and one channel recorded displacement. The DAC system was set to continuously measure and record strain, displacement, and pressure in an overwriting loop until a trigger signal was received on one of the pressure channels. When the pressure at the face of the load transferring system reached a certain preset level, the DAC would begin writing data to the hard disk for a duration of *300 ms* with *10 ms* of pre trigger values recorded for baseline

readings. The same trigger signal was sent to the high speed camera through a fibre optic cable so that the camera would begin recording at the same time as the DAC system. The high speed camera recorded on a continuous loop until a trigger signal was received, at which point *100* ms of pre-trigger recorded frames were saved and a further *2.1* seconds of post-trigger frames were recorded.

*TABLE 3.1 - Properties of Test Specimens*

| Column | Compressive Strength of Concrete | Cross Section Width | Cross Section Thickness | Longitutional Reinforcing Ratio | Spacing of Transverse Steel | Volumetric Ratio of Transverse Steel | Axial Load Level | |
|---|---|---|---|---|---|---|---|---|
| | $f'_c$ (MPa) | (mm) | (mm) | $\rho_{rs}$ (%) | s (mm) | $\rho_t$ (%) | (kN) | $P/P_o$ |
| RC-1 | 46.5 | 150 | 100 | 2.67 | 50 | 1.52 | 0 | 0.00 |
| RC-2 | 46.5 | 150 | 100 | 2.67 | 50 | 1.52 | 350 | 0.42 |
| RC-3 | 58 | 150 | 100 | 2.67 | 50 | 1.52 | 350 | 0.35 |
| RC-4 | 58 | 150 | 100 | 2.67 | 25 | 3.04 | 350 | 0.35 |
| RC-5 | 58 | 150 | 100 | 2.67 | 50 | 1.52 | 350 | 0.35 |
| RC-6 | 58 | 150 | 100 | 2.67 | 25 | 3.04 | 350 | 0.35 |
| RC-7 | 58 | 150 | 100 | 2.67 | 50 | 1.52 | 350 | 0.35 |
| RC-8 | 58 | 150 | 100 | 2.67 | 25 | 3.04 | 350 | 0.35 |
| RC-9 | 58 | 150 | 100 | 2.67 | 50 | 1.52 | 350 | 0.35 |
| RC-10 | 58 | 150 | 100 | 2.67 | 25 | 3.04 | 350 | 0.35 |
| RC-11 | 58 | 150 | 100 | 2.67 | 50 | 1.52 | 350 | 0.35 |
| RC-12 | 58 | 150 | 100 | 2.67 | 25 | 3.04 | 350 | 0.35 |
| RC-13 | 58 | 150 | 150 | 1.78 | 75 | 0.86 | 400 | 0.28 |
| RC-14 | 58 | 150 | 150 | 1.78 | 75 | 0.86 | 400 | 0.28 |

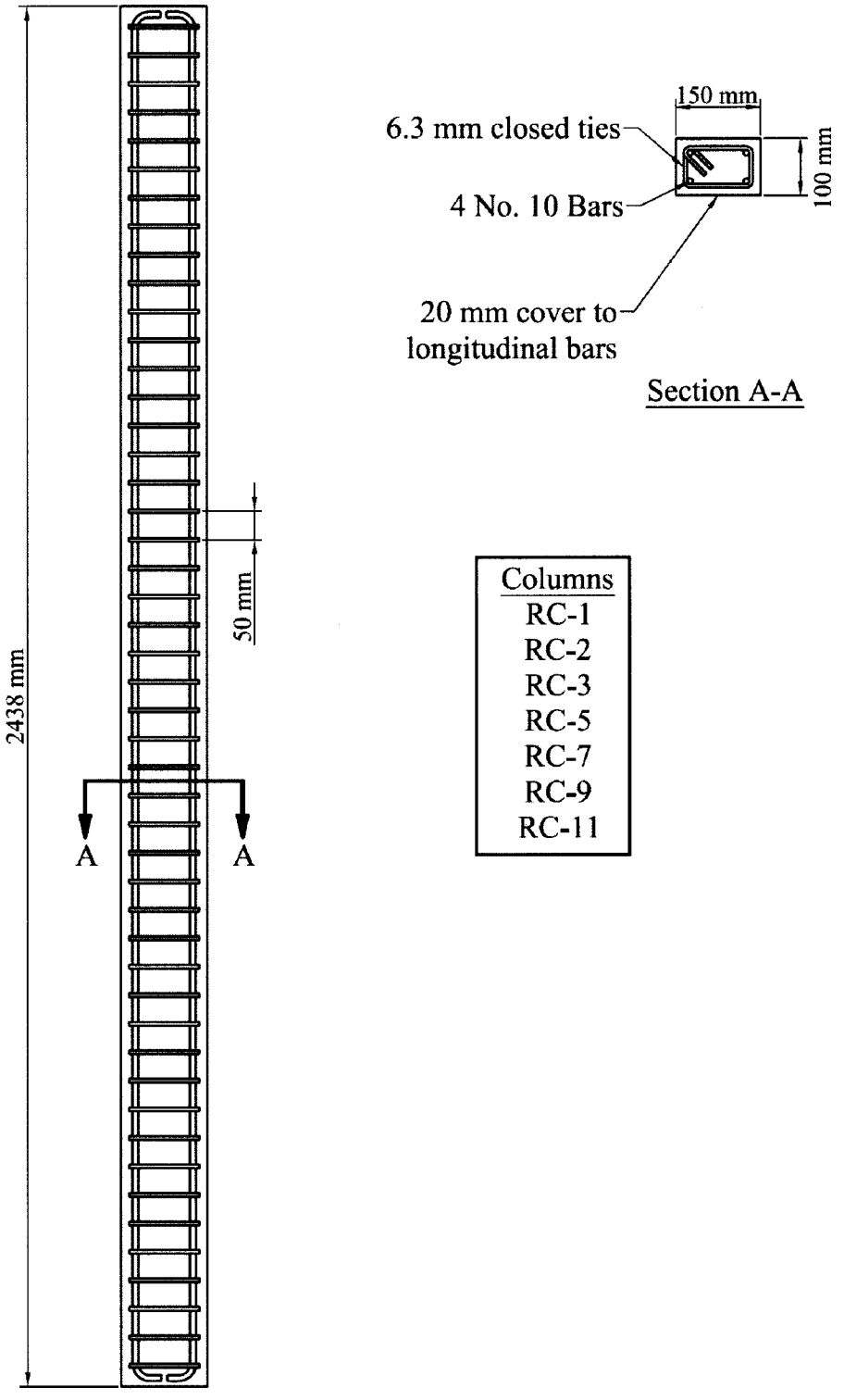


*Figure 3-1: Reinforcement Details of 100x150 mm Non-Seismic Columns*

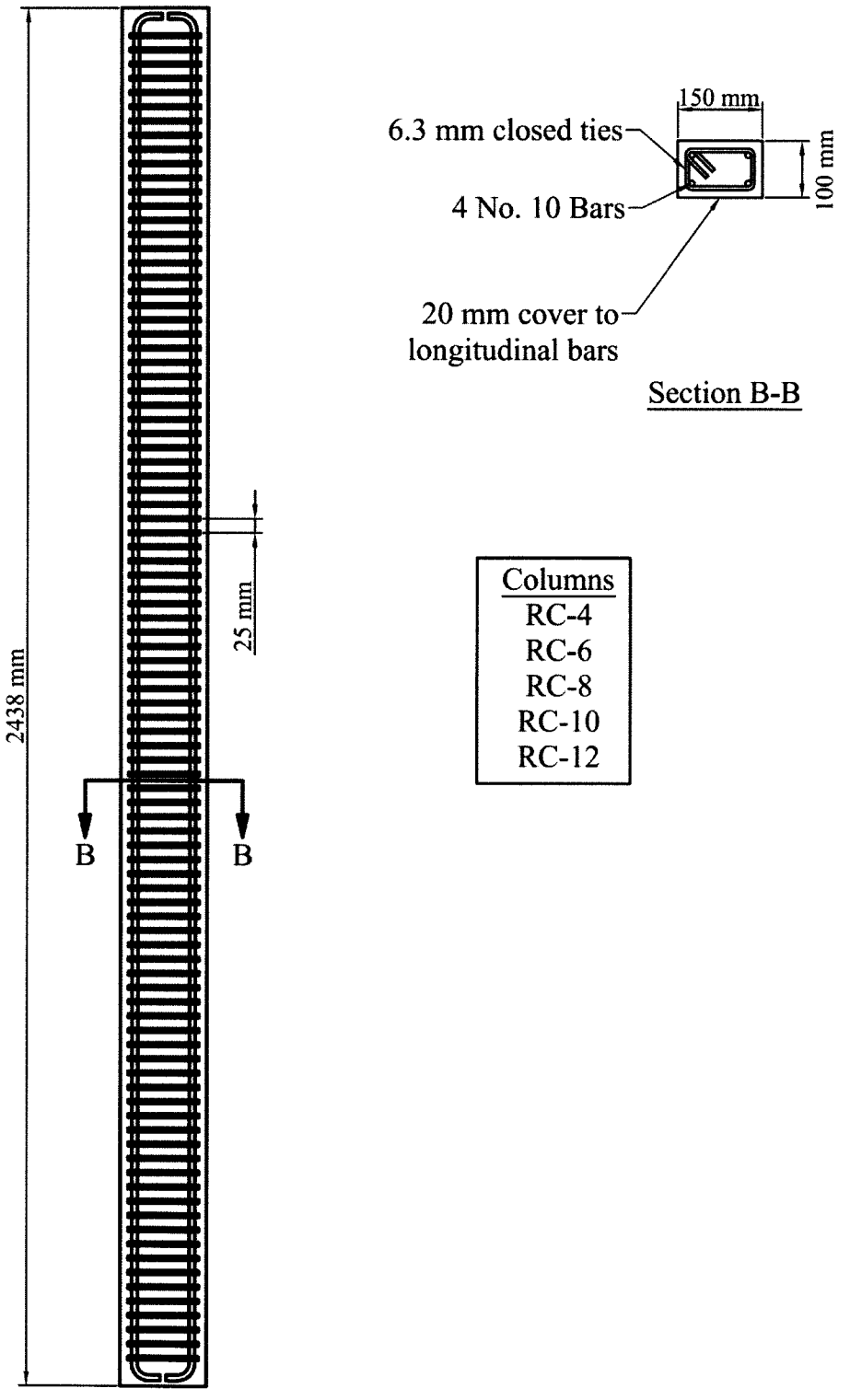


*Figure 3-2: Reinforcement Details of 100x150 mm Seismic Columns*

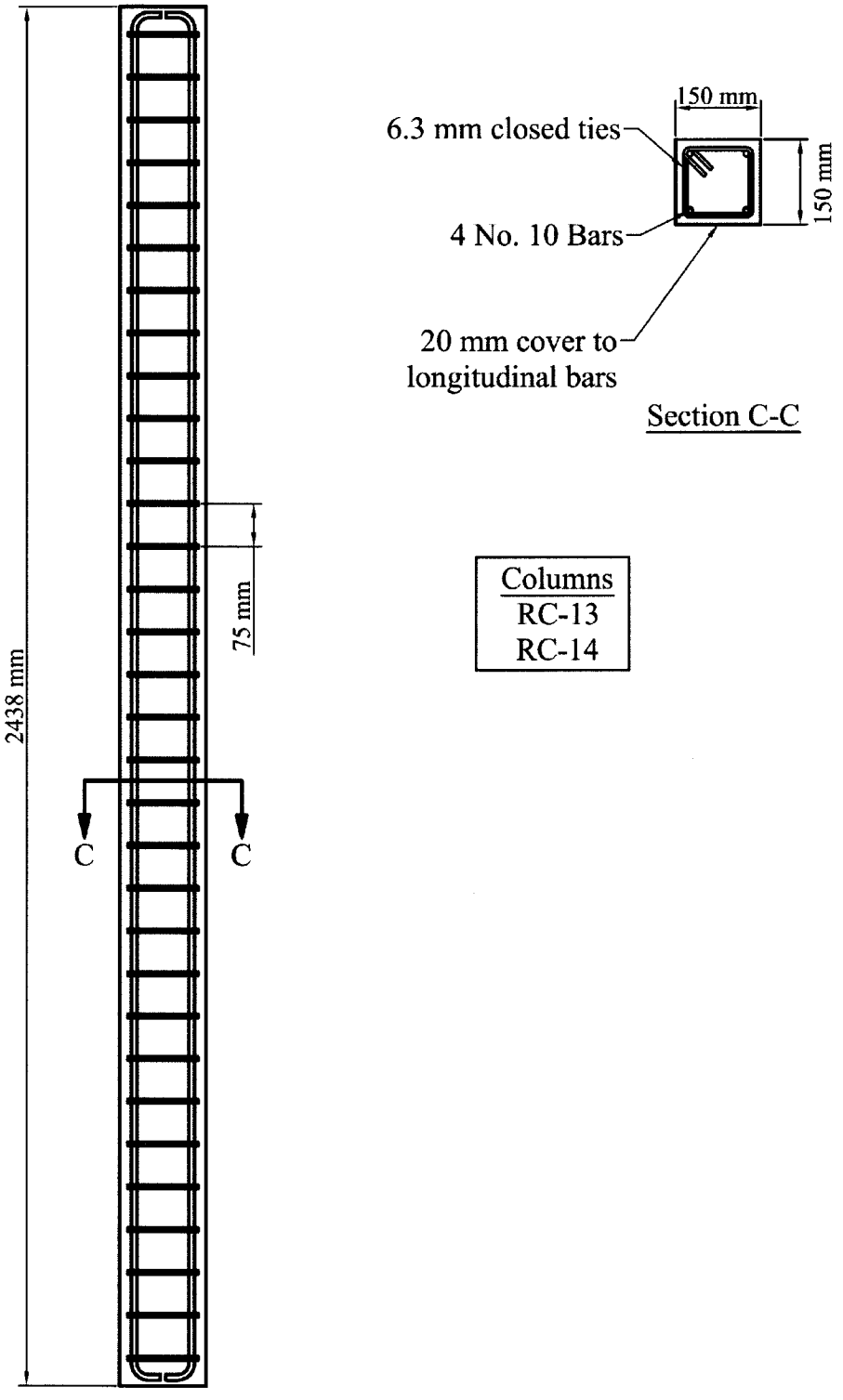


*Figure 3-3: Reinforcement Details of 150x150 mm Non-Seismic Columns*

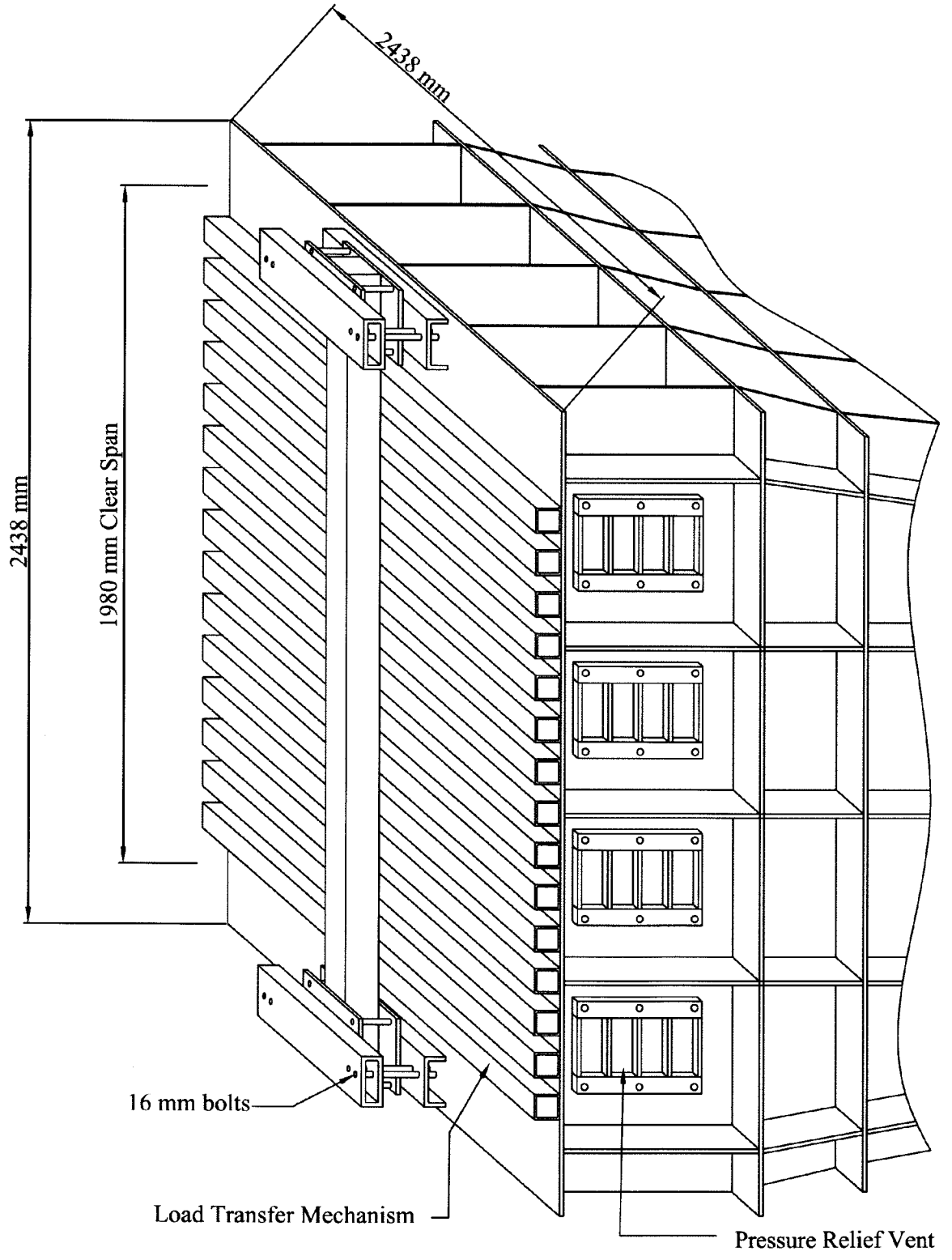


*Figure 3-4: Detailing of Load Column Test Setup and Load Transfer Mechanism*

*Figure 3-5: Column End Supports*

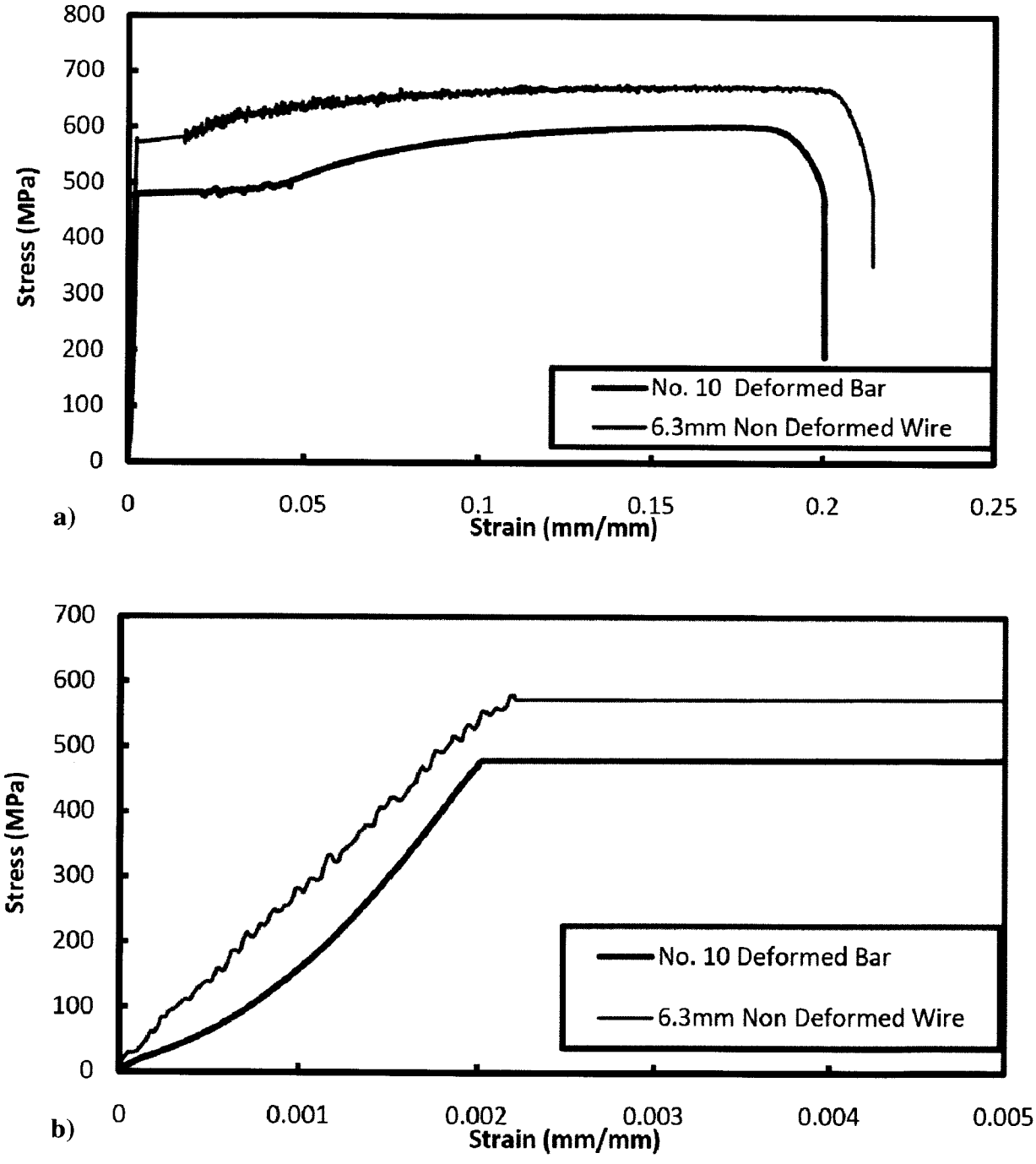


*Figure 3-6: Stress-Strain Relationships for Longitudinal Steel, No. 10, and Transverse Steel, 6.3 mm: a) Elastic and Plastic Region; b) Elastic Region*

*Figure 3-7: Construction of Reinforcing Steel Cages*

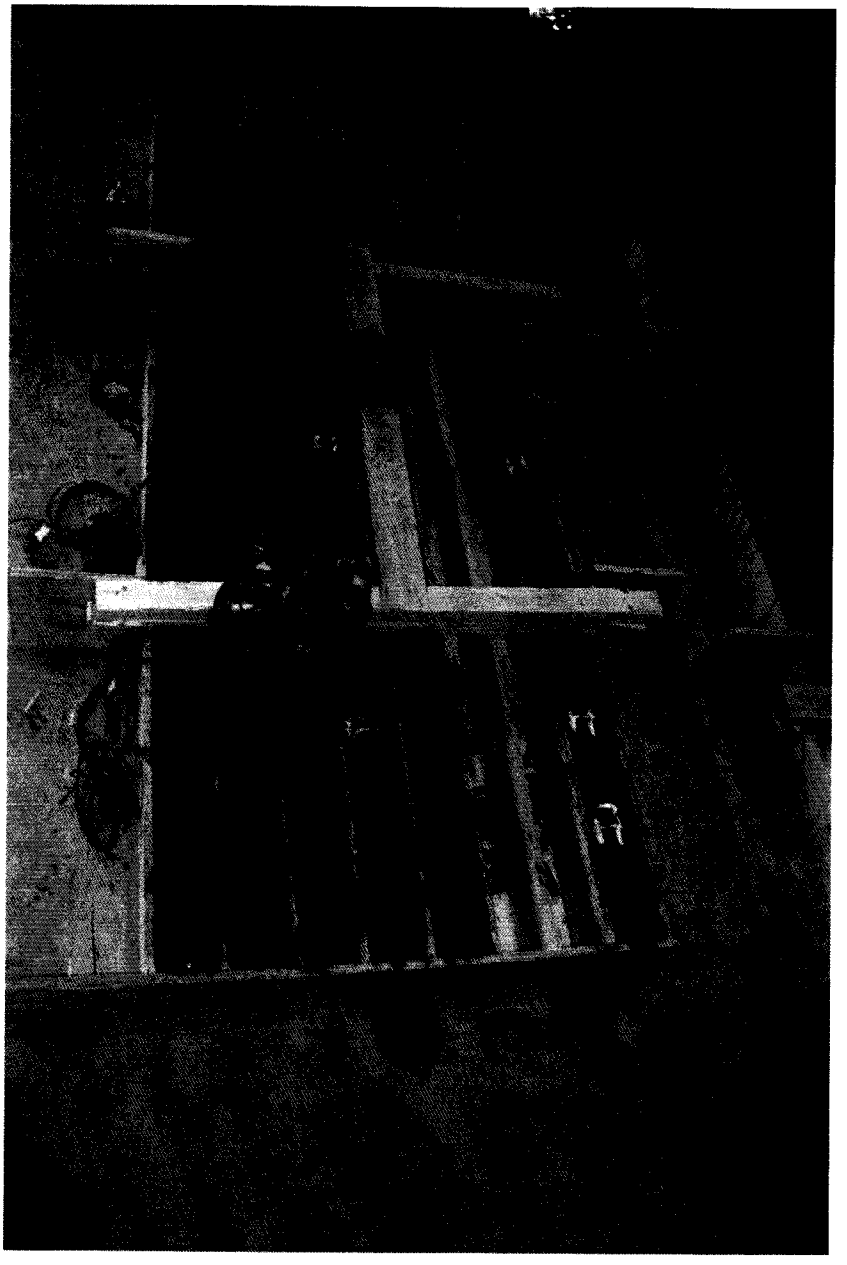

*Figure 3-8: Reinforcing Steel Cages in Formwork Prior to Casting*

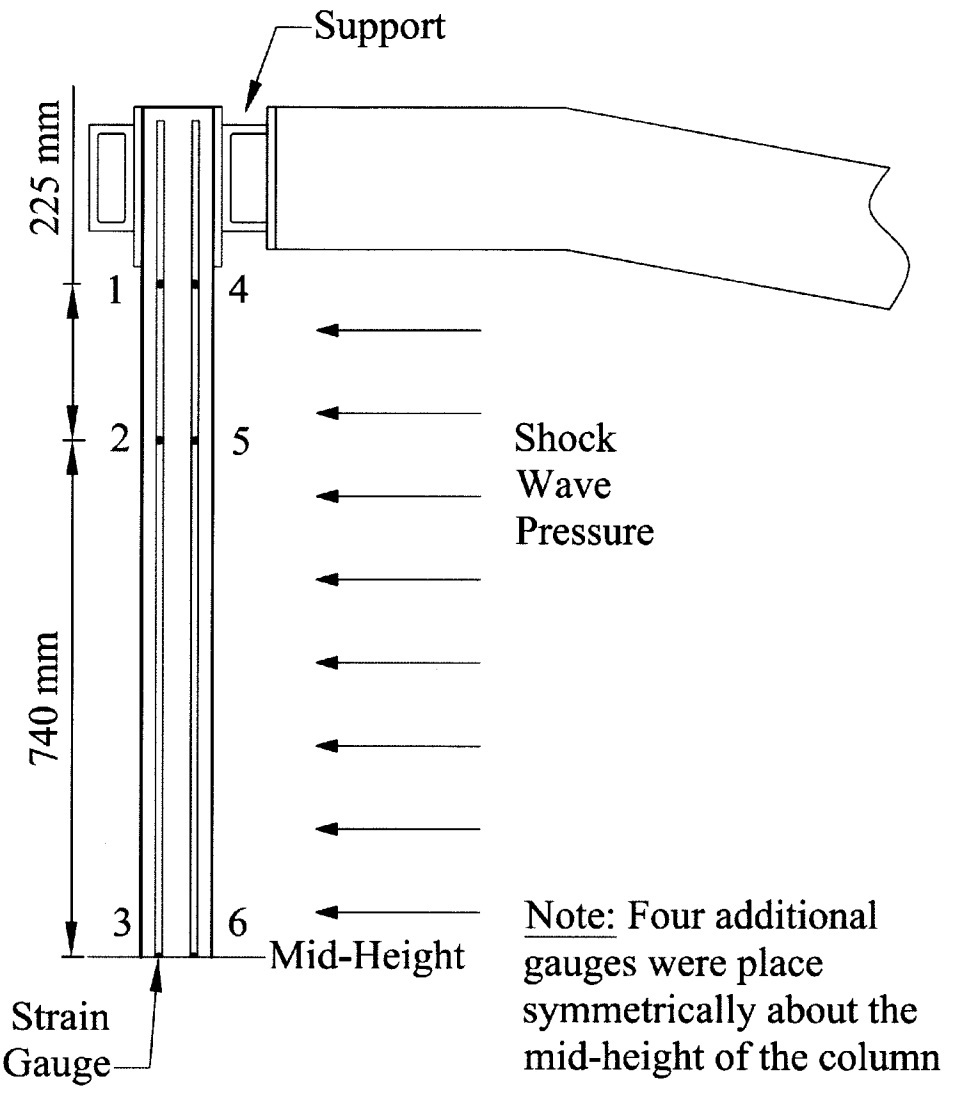


*Figure 3-9: Strain Gauge Locations*

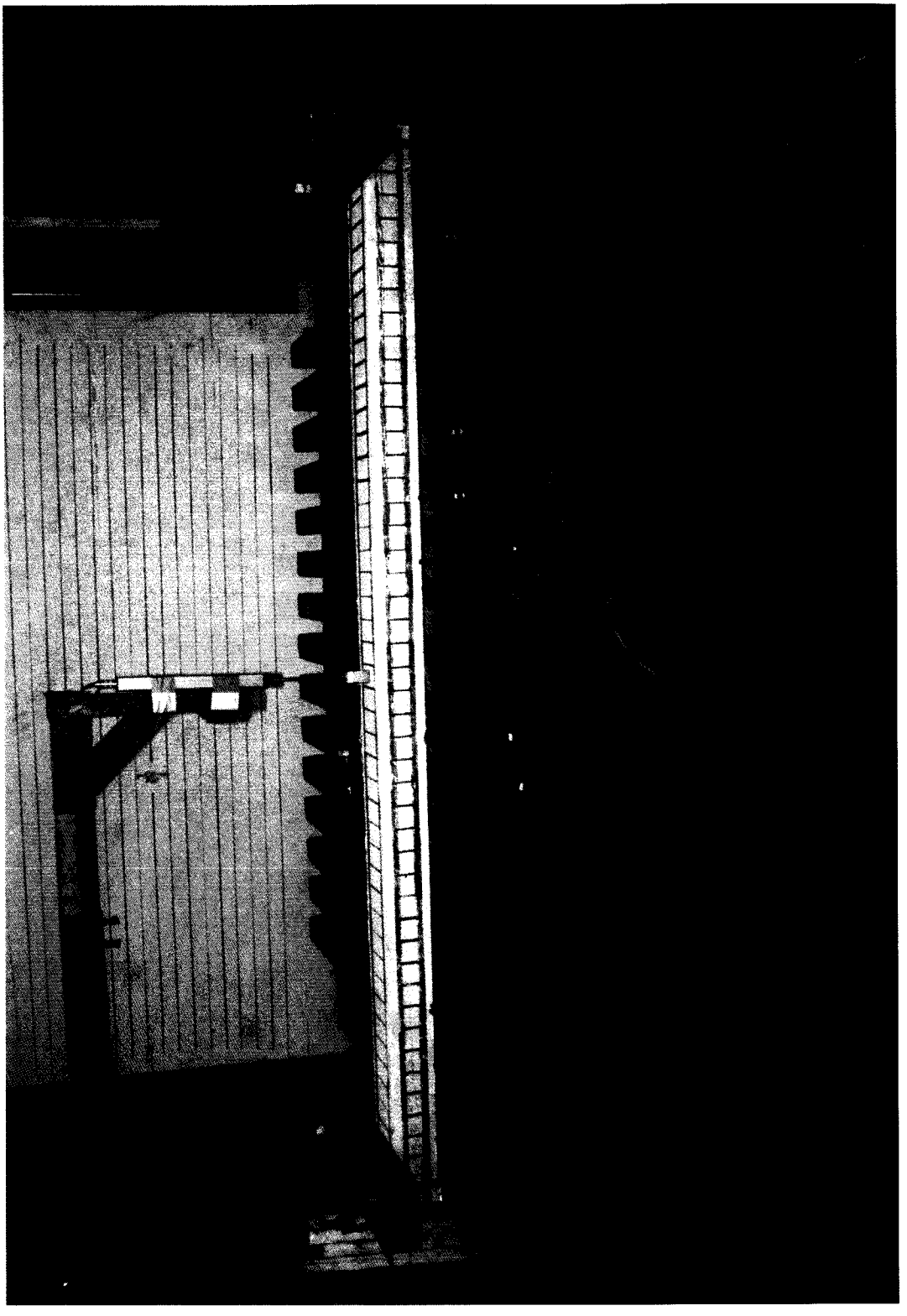

*Figure 3-10: Column on Test Frame with LVDT attached at Mid Height*

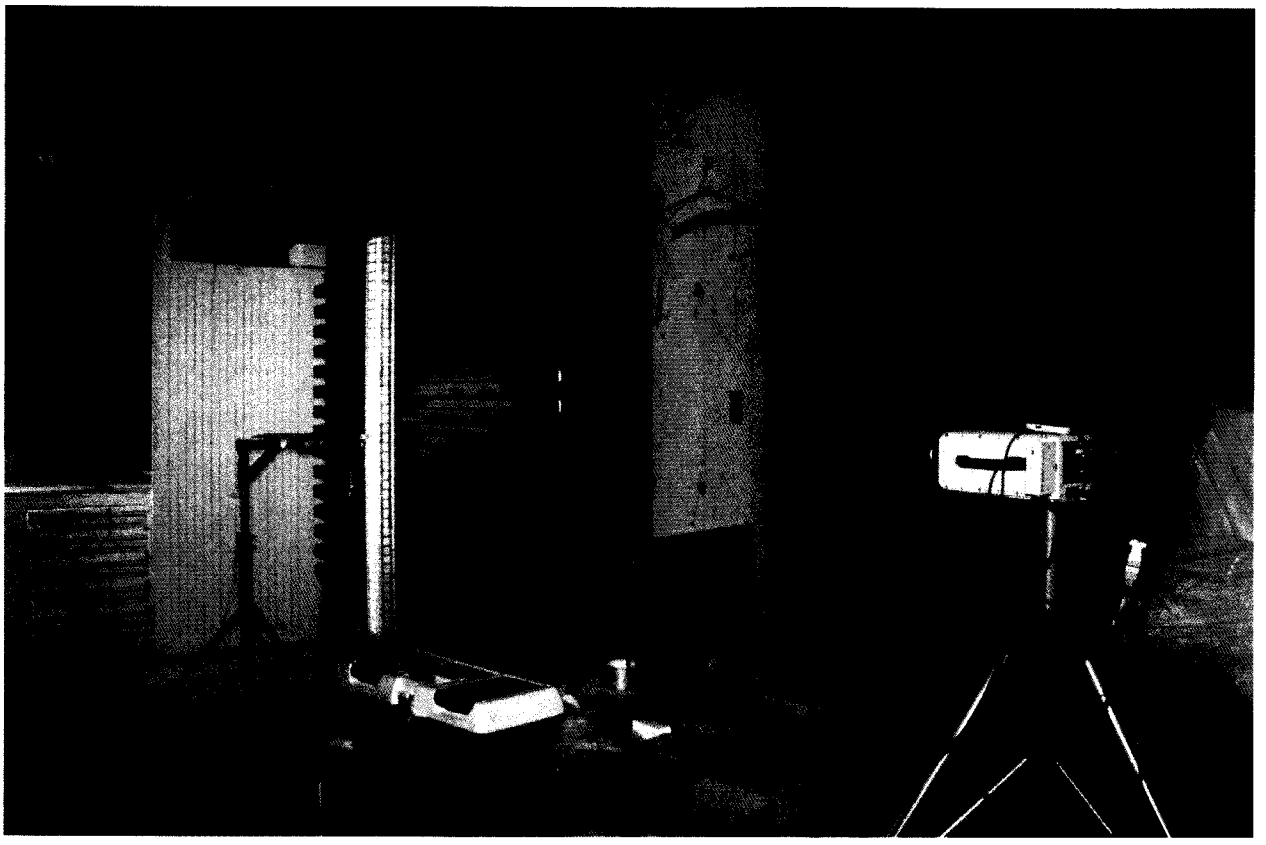

*Figure 3-11: High Speed Camera Monitoring Column on Test Frame*

# 4 CHAPTER 4

# Experimental Results

## *4.1 General*

The observed results of the experimental tests on *14* reinforced concrete columns are presented in this chapter. Each of the columns was tested with a series of shock waves increasing in magnitude until significant damage was observed in the column. The measured mid-height displacement, strain in the longitudinal reinforcing steel at the mid-height and support regions, and pressure time histories are discussed for each test. Plots of the applied reflected pressure and impulse time histories are shown for each test along with the resulting mid-height displacement. In this section, each column is designated sequentially with the test number augmenting the column designation. For example, RC-3-2 designates the second test on column number 3.

Plots of strain time histories for each test may be found in Appendix A.

### 4.1.1 Load Transferring Device on Pressure and Impulse Values

All of the given pressure and impulse values are those that were recorded acting on the load transferring device located at the end of the shock tube. This device was employed to transfer all of the pressure over the face of the shock tube opening onto the column as a uniformly distributed load. It is important to note that a column without a similar load transferring device to increase tributary area would not respond as significantly to the same applied pressure.

### 4.1.2 Supports

The supports, intended to fully prevent rotation at the ends of the columns, did not provide fully fixed conditions. It is evident from the strains at the support region and the mid-height of the

column as well as the recorded video and the observed damage levels that the most significant response of the columns occurred at mid-height. In cases where only one plastic hinge would begin to occur, it would inevitably form at the mid height. In all cases, larger maximum strain and residual strain on the reinforcing steel were measured at mid-height of the columns when compared with the strains near the support region.

### 4.1.3 Seismic and Non-Seismic Columns

Two sets of 5 columns were exposed to similar testing regimens. These columns were designed as columns for seismic regions and columns for non-seismic regions. The only difference between the two sets was the spacing of transverse reinforcement. It was observed that there was no significant difference in response between similarly loaded columns designed for the two types of regions. The final section of this chapter explores the response of the two sets of columns.

## *4.2 Experimental Results*

A summary of the testing regimen for each column are listed in Table 4.1. This table includes the driver length ($L_D$) and driver pressure ($P_D$) used in each test along with the recorded maximum reflected pressure ($P_r$), total reflected impulse over the positive phase duration ($I_r$), positive phase duration ($t_d$), maximum mid-height displacement ($d_{max}$), and the time to reach maximum mid-height displacement ($t_{max}$). Table 4.1 also reports the maximum support rotation ($\theta_{max}$) for each test where the support rotation is calculated as the mid-height displacement divided by half the column length and converted to degrees. Table 4.2 gives a summary of the tension strain in the longitudinal reinforcing steel located at mid-height of the column and at the column support level. The strain in the column due to the applied axial load, $\varepsilon_{axial}$ in Equation 4.1, is calculated using the suggested value for the elastic modulus of concrete ($E_c$) given Canadian Standard Association (CSA) Standard A23.3 for the "Design of Concrete Structures" (2006) shown in Equation 4.2. In Equation 4.1, $P$ is the axial load, $L$ is the length of the column, and $A_T$ is the transformed area of the column given in Equation 4.3. In Equation 4.3, $A_g$ is the gross column cross-section area, $n$ is the ratio of the elastic modulus for steel, $E_s$ ($200{,}000\ MPa$), and the

elastic modulus for concrete, $E_c$, given in Equation 4.4, and $A_s$ is the area of the longitudinal reinforcing steel in the column.

[4.1] $$\varepsilon_{axial} = \frac{PL}{A_T E_c}$$

[4.2] $$E_c = 4500\sqrt{f'_c} \quad (MPa)$$

[4.3] $$A_T = A_g + (n-1)A_s$$

[4.4] $$n = \frac{E_s}{E_c}$$

Prior to each test and after the application of axial load, all strain gauges were set to record zero initial strain providing a relative strain-time history for each test. The axial strain, $\varepsilon_{axial}$, is added to the maximum recorded strain, $\varepsilon_{max\text{-}axial}$, to give the total maximum strain value, $\varepsilon_{max}$, in the tension reinforcing steel that occurred during each test. As each column was subjected to multiple tests, the cumulative maximum strain value, $\varepsilon_{max+tot\ res}$, is calculated as the sum of $\varepsilon_{max}$ and the cumulative residual strain in the reinforcing steel, $\varepsilon_{tot\ res}$, prior to the test in question. The residual strain in the reinforcing steel, $\varepsilon_{residual}$, is the recorded strain value at the completion of each test. Finally, a value of the time to reach maximum strain, $t_{max}$, is given for each test in Table 4.2. The values for strain in compression steel at the supports and column mid-height reported in Table 4.2 are taken at the same time as those for tension steel.

### 4.2.1 Column RC-1

Column RC-1 had a cross section measuring *100 mm by 150 mm* with *46.5 MPa* concrete strength. The column was reinforced with *6.35 mm* closed hoops spaced at *50 mm* and four *10M* longitudinal reinforcing steel bars. There was no applied axial load for this specimen. The support system for this column allowed for significant rotation and was modified for all subsequent specimen tests.

#### *4.2.1.1 RC-1-1*

Test RC-1-1 used a *1219.2 mm* driver length with *103.5 kPa* driver pressure resulting in a reflected pressure of *22.0 kPa*, a reflected impulse over the positive phase of *120.1 kPa.ms*, and a positive phase duration of *10.0 ms* as shown in Figure 4.1 and listed in Table 4.1. Maximum mid-height displacement, shown as a time-history in Figure 4.2, of the column was measured to *13.9 mm* (*0.80* ° Support rotation) at *28.4 ms* after the start of the shock wave loading.

The resulting strains on the tension longitudinal reinforcing steel (loaded side at supports and opposite to loaded side at mid-height) were less than yield strain in all instances. Maximum total strain, $\varepsilon_{max}$ in Table 4.2, was *0.157 % and 0.019 %* occurring at *27.1 ms* and *25.6 ms* after the start of the shock wave loading at the mid-height and supports, respectively. The recorded residual strains, $\varepsilon_{residual}$ in Table 4.2, were *0.004 %* and *-0.006 %* for the mid-height and support steel respectively.

There was no visible damage, no cracking or concrete crushing, resulting from this test.

#### *4.2.1.2 RC-1-2*

Test RC-1-2 used a *1219.2 mm* driver length with *144.9 kPa* driver pressure resulting in a reflected pressure of *38.0 kPa*, a reflected impulse of *157.7 kPa-ms* over the positive phase, and a positive phase duration of *10.4 ms*. The pressure and impulse time histories are plotted in Figure 4.3 and maximum values are listed in Table 4.1. The maximum measured mid-height displacement was *20.8 mm* (*1.20* °) occurring at *28.9 ms* after the start of the shock wave loading. The displacement time history is shown in Figure 4.4 and maximum values are listed in Table 4.1.

The maximum recorded strain, $\varepsilon_{max}$, during the column response was *0.226 %* and *0.019 %* for the tension steel located at mid-height and the support region, respectively. These strains occurred at *27.6 ms* and *26.2 ms* after the start of the shock wave loading. Total maximum strains ($\varepsilon_{max+tot\ res}$), the sum of the residual strain from previous tests ($\varepsilon_{tot\ res}$) and the maximum recorded strain for the test in question ($\varepsilon_{max}$), were *0.230 %* and *0.013 %* for mid-height and support

regions, respectively. The mid-height tension steel had a recorded residual strain, $\varepsilon_{residual}$, of *0.001 %* and a cumulative residual strain, $\varepsilon_{tot\ res}$, of *0.005 %* after the test. The support region tension steel had *0.000 %* recorded residual strain and *-0.006 %* cumulative residual strain after the test. Summary values for strain are listed in Table 4.2.

Small flexural cracks were observed at the mid-height location after the test. There was no evidence of further damage such as concrete crushing or residual displacement. Figure 4.5 a) shows the side view of column RC-1 after test 2.

#### *4.2.1.3 RC-1-3*

Test RC-1-3 used a *1219.2 mm* driver length with *289.8 kPa* driver pressure (Table 4.1). Due to an error in the triggering of the data acquisition system and the camera, there were no recorded reflected pressures, displacements, or video for this test. Strain data was successfully recorded on a second data acquisition system using a different trigger.

The maximum recorded strain, $\varepsilon_{max}$, during the column response was *0.605 %* and *0.092 %* for the tension steel located at mid-height and the support region respectively. These strains occurred at *29.9 ms* and *34.5 ms* after the start of the shock wave loading. Total maximum strains ($\varepsilon_{max+tot\ res}$), the sum of the residual strain from previous tests ($\varepsilon_{tot\ res}$) and the maximum recorded strain for the test in question ($\varepsilon_{max}$), were *0.610 %* and *0.086 %* for mid-height and support regions respectively. The mid-height tension steel had a recorded residual strain, $\varepsilon_{residual}$, of *0.074 %* and a cumulative residual strain, $\varepsilon_{tot\ res}$, of *0.078 %* after completing the test. The support region tension steel had *0.003 %* recorded residual strain and *-0.003 %* cumulative residual strain after the test. Summary values for strain are listed in Table 4.2.

Figure 4.5 b) shows column RC-1 after test 3. There was approximately 25 *mm* residual mid-height displacement measured after test 3. Mid-height tension cracks, shown in Figure 4.5 c), were observed. There was no significant damage at the support region after test 3 as shown in Figure 4.5 d). In general, damage was limited to small visible tension cracks in the concrete at mid-height and the residual displacement.

### 4.2.2 Column RC-2

Column RC-2 had a cross section measuring *100 mm by 150 mm* with *46.5 MPa* concrete strength. The column was reinforced with *6.35 mm* hoops spaced at *50 mm* and four *10M* longitudinal reinforcing steel bars. The column was subjected to an axial load of *350 kN* applied prior to each shock wave test: RC-2-1 and RC-2-2. The axial load resulted in an initial axial strain, $\varepsilon_{axial}$, of *-0.066 %* as calculated using Equations 4.1 through 4.4. This initial axial strain, a constant compression strain throughout the column, is added to recorded values to give total strain in the longitudinal tension reinforcing steel located on the loaded side of the columns at the support region and the opposite to loaded side at mid-height.

#### *4.2.2.1 RC-2-1*

Test RC-2-1 used a *2743.2 mm* driver length with *124.2 kPa* driver pressure resulting in a reflected pressure of *23.1 kPa*, a reflected impulse over the positive phase of *193.2 kPa.ms*, and a positive phase duration of *24.9 ms* as shown in Figure 4.6 and listed in Table 4.1. Maximum mid-height displacement of the column, shown as a time-history in Figure 4.7, was measured as *24.2 mm* (*1.40* °) at *28.8 ms* after the start of the shock wave loading.

The resulting strains on the tension longitudinal reinforcing steel (loaded side at supports and opposite to loaded side at mid-height) were recorded with a baseline (zero strain value) set as the strain in the reinforcing steel prior to each test. Therefore, the maximum and residual strain records summarized in Table 4.2 are added to initial strains present in the reinforcing steel to produce the total strain values. The initial axial strain, constant through the column, was *-0.066 %*. The maximum total strain (accounting for the initial axial strain), $\varepsilon_{max}$ in Table 4.2, was *0.159 % and 0.042 %* occurring at *26.6 ms* and *23.0 ms* after the start of the shock wave loading for mid-height and support steel respectively. The recorded residual strains, $\varepsilon_{residual}$ in Table 4.2, were *0.062 %* and *0.000 %* for the mid-height and support steel, respectively, and there was *7 mm* residual displacement at mi-height of the column.

After test 1 on RC-2, small visible tension cracks in the concrete were observed at mid-height. Figure 4.10 a) shows column RC-2 after test 1.

#### *4.2.2.2 RC-2-2*

Test RC-2-2 used a *2743.2 mm* driver length with *207.0 kPa* driver pressure resulting in a reflected pressure of *39.9 kPa*, a reflected impulse over the positive phase of *425.7 kPa.ms*, and a positive phase duration of *26.3 ms* as shown in Figure 4.8 and listed in Table 4.1. Maximum mid-height displacement was recorded as 66.4 *mm* (*3.84* °) at 46.3 *ms* after the start of the shock wave loading. The displacement time-history for this test is shown in Figure 4.9.

All strain gauges located at mid-height and at the support regions were lost during or prior to this test. Therefore, there is no record of strain for this test.

Figure 4.10 b) shows the displaced shape of the damaged column after test 2 including the *7 mm* residual displacement from test 1 and *45 mm* residual displacement from test 2 (*52 mm* total cumulative residual displacement). There was significant tension cracking of the concrete at mid-height and loss of concrete cover on the loaded (compression) side at mid-height as shown in Figure 4.10 c). Tension cracks were clearly visible in the concrete on the loaded side of the column in the support regions. Figure 4.10 d) shows the support region on the column after test 2.

### 4.2.3 Column RC-3

Column RC-3 had a cross section measuring *100 mm by 150 mm* with *58 MPa* concrete strength. The column was reinforced with *6.35 mm* closed steel hoops spaced at *50 mm* and four *10M* longitudinal reinforcing steel bars. The column was subjected to an axial load of *350 kN*, applied prior to each test. This axial load resulted in an initial axial strain, $\varepsilon_{axial}$, of *-0.060 %* calculated using Equations 4.1 through 4.4, which was added to recorded values to compute the total strain

in the longitudinal tension reinforcing steel located on the loaded side of the columns at the support region and the opposite to loaded side at mid-height.

Column RC-3 was loaded with three shock waves: RC-3-1; RC-3-2; and RC-3-3. A summary of the results of these tests is provided below.

#### *4.2.3.1 RC-3-1*

A driver length of *914.4 mm* and driver pressure of *289.8 kPa*, for test RC-3-1 created a shock wave with *51.1 kPa* reflected pressure, *193.2 kPa.ms* reflected impulse over the positive phase, and *9.9 ms* positive phase duration (Table 4.1). The maximum recorded mid-height displacement of *15.0 mm* (*0.87* °) occurring *18.3 ms* after the start of the shock wave. The pressure and impulse-time histories are shown in Figure 4.11 and the mid-height displacement-time history is shown in Figure 4.12.

The total maximum strain in the reinforcing steel in tension at mid-height of *0.121* % and *0.017%* on the tension reinforcing steel at the support region occurred at *21.8 ms* and *18.1 ms*, respectively. Residual strains of *0.005* % at mid-height and *-0.009* at the supports were recorded for the end of the test. A summary of strain values for this test are listed in Table 4.2.

There was *4.5 mm* residual mid-height displacement after test RC-3-1. Some small cracks were visible in the tension concrete at mid-height after this test. No other damage was visible.

#### *4.2.3.2 RC-3-2*

Test RC-3-2 used a driver length of *914.4 mm* and a driver pressure of *345 kPa* to create a shock wave with *58.0 kPa* reflected pressure, *222.2 kPa.ms* reflected impulse over the positive phase, and *10.0 ms* positive phase duration (Table 4.1). This shock wave resulted in a maximum displacement of *19.2 mm* (*1.11* °) at mid-height that occurred *22.6 ms* after the start of the shock wave loading. The reflected pressure and reflected impulse-time histories are shown in Figure 4.13 and the mid-height displacement-time history is shown in Figure 4.14.

The total maximum mid-height strain for tension steel in column RC-3-2 was *0.140 %* while the total maximum strain for the tension steel at the supports was *0.035 %*. These strains occurred at *22.5 ms* and *18.5 ms* for the mid-height and support locations respectively after the start of the shock wave loading. The mid-height tension steel had a *0.000 %* residual strain after test 2 and, when added to the residual strain from test 1, a cumulative residual strain of *0.005 %*. The tension steel near the support had a residual strain of *-0.007 %* after test 2 for a cumulative residual strain of *-0.016 %*.

After test RC-3-2 there was an additional *3.3 mm* residual displacement recorded for a *7.8 mm* cumulative residual displacement for all tests on column RC3. There was no change noticed in the tension cracks at mid-height between test RC-3-1 and RC-3-2. There were no other visible signs of damage to the specimen. Figure 4.17 a) shows column RC-3 after test 2.

#### *4.2.3.3 RC-3-3*

Test RC-3-3 used a *914.4 mm* driver length with *690.0 kPa* driver pressure resulting in a reflected pressure of *89.7 kPa*, a reflected impulse over the positive phase of *362.3 kPa.ms*, and a positive phase duration of *11.5 ms* as shown in Figure 4.15 and listed in Table 4.1. Maximum mid-height displacement recorded in the time-history (Figure 4.16) for the column was *76.4 mm* (*4.42 °*) at *52.0 ms* after the start of the shock wave loading.

All strain gauges were damaged during the tests on column RC-3, therefore, there was no useable strain data at the end of test RC-3-3.

After test 3 on specimen RC-3, there was an additional *51 mm* residual mid-height displacement (*58.8 mm* cumulative). Significant cracking in tension concrete was evident at both the support and mid-height regions as shown in Figure 4.17 b). There was also a loss of cover concrete on the compression side at both the support and mid-height of the column. Figure 4.17 c) shows the damaged mid-height of the column and Figure 4.17 d) shows the damaged support region of the column.

### 4.2.4 Column RC-4

Column RC-4 had a cross section measuring *100 mm by 150 mm* with *58 MPa* concrete strength. The column was reinforced with *6.35 mm* closed steel hoops spaced at *25 mm* and four *10M* longitudinal reinforcing steel bars. The column was subjected to an axial load of *350 kN*, applied prior to each shock wave test. This axial load resulted in an initial axial strain, $\varepsilon_{axial}$, of *-0.060 %* as calculated using Equations 4.1 through 4.4.

Column RC-4 was loaded with five shock waves: RC-4-1; RC-4-2; RC-4-3; RC-4-4; and RC-4-5. A summary of the results of these tests is provided below.

#### *4.2.4.1 RC-4-1*

The driver length and pressure for test RC-4-1 was *914.4 mm* and *124.2 kPa*, respectively, combined to create a shock wave with *2.90 kPa* reflected pressure, *12.80 kPa.ms* reflected impulse over the positive phase, and *8.3 ms* positive phase duration (Table 4.1). The pressure and impulse-time histories are shown in Figure 4.18.

There was no displacement data or strain recorded at mid-height on the tension reinforcing steel for this test due to a problem with the displacement gauge strain gauge connections to the data acquisition system.

For the longitudinal tension reinforcing steel located near the supports, the total maximum strain was *-0.044 %* occurring at *13.0 ms* after the start of the shock wave loading. There was no recorded residual strain.

There was no visible sign of damage to the specimen after test *RC-4-1*.

#### *4.2.4.2 RC-4-2*

Test RC-4-2 used a driver length of *914.4 mm* and a driver pressure of *241.5 kPa* to create a shock wave with *47.6 kPa* reflected pressure, *176.0 kPa.ms* reflected impulse over the positive phase, and 9.5 *ms* positive phase duration (Table 4.1). This shock wave caused a maximum displacement of *7.5 mm* (*0.43* °) at mid-height that occurred *21.3 ms* after the start of the shock wave loading. The reflected pressure and reflected impulse-time histories are shown in Figure 4.19 and the mid-height displacement-time history is shown in Figure 4.20.

The total maximum strains at mid-height and support regions for the tension steel were *0.182 %* and *-0.003 %*, respectively, occurring at *17.8 ms* and *16.5 ms* after the start of the shock wave loading. Residual strains due to this loading at the same locations were *0.012 % and 0.000 %*.

There was no visible damage to column RC-4 after test 2. No residual displacement was recorded at the mid-height of the column.

#### *4.2.4.3 RC-4-3*

The driver length for test RC-4-3 was *914.4 mm* and the driver pressure was *289.8 kPa*, resulting in a shock wave with a *50.4 kPa* reflected pressure, a *193.9 kPa.ms* reflected impulse over the positive phase, and a *9.8 ms* positive phase duration (Table 4.1). The maximum recorded mid-height displacement was *13.5 mm* (*0.78* °) at *20.6 ms* after the start of the shock wave. The pressure and impulse-time histories are shown in Figure 4.21 and the mid-height displacement-time history is shown in Figure 4.22.

The total maximum strain on the reinforcing steel in tension at mid-height was *0.182 %* while the maximum was *-0.008 %* on the tension reinforcing steel at the support region. These values occurred at *22.9 ms* and *16.9 ms* respectively. Residual strains of *0.000 %* at mid-height (*0.012 %* cumulative) and *0.000* at the supports (*0.000 %* cumulative) were recorded for this test. A summary of strain values for this test is listed in Table 4.2.

At the end of test RC-4-3 there was *0.8 mm* of residual mid-height displacement with some small visible cracks in the tension concrete at mid-height. No other damage was visible.

#### *4.2.4.4 RC-4-4*

Test RC-4-4 used a driver length of *914.4 mm* and a driver pressure of *345 kPa* to create a shock wave with *58.0 kPa* reflected pressure, *227.7 kPa.ms* reflected impulse over the positive phase, and *9.5 ms* positive phase duration (Table 4.1). This shock wave resulted in a maximum displacement of *18.2 mm* (*1.05* °) at mid-height that occurred *24.0 ms* after the start of the shock wave loading. The reflected pressure and reflected impulse-time histories are shown in Figure 4.23 and the mid-height displacement-time history is shown in Figure 4.24.

The total maximum mid-height strain for tension steel in column RC-4-4 was *0.182 %* while the total maximum for tension steel at the supports was *-0.003 %*. These strains occurred at *24.6 ms* and *16.0 ms* for the mid-height and support locations respectively after the start of the shock wave loading. The mid-height tension steel was measured to have *0.003 %* residual strain due to test 4 for a cumulative residual strain of *0.012 %*. The tension steel near the support had a residual strain of *0.000 %* for test 4 and a cumulative residual strain of *0.000 %*.

After test RC-4-4 there was *2.0 mm* residual displacement recorded (*2.8 mm* cumulative). Additional tension cracks in the concrete at mid-height were noticed. There were no other signs of damage to the specimen. Figure 4.25 a) shows column RC-4 after test 4.

#### *4.2.4.5 RC-4-5*

Test RC-4-5 used a *914.4 mm* driver length with *690.0 kPa* driver pressure. Due to an error with the trigger signal, the data acquisition system did not record and pressure, displacement or strain data for this test.

After test 5 on specimen RC-4, there was significant damage in both the mid-height and support regions of the column. Figure 4.25 b) shows the damaged shape of the column after test 5, with clearly visible residual displacement of approximately *80 mm* at mid-height. Figure 4.25 c)

shows the tension cracks at mid-height of the column. There was a loss of cover concrete in the compression regions at mid-height and the supports. The tension cracks at the support region are shown in Figure 4.25 c).

### 4.2.5 Column RC-5

Column RC-5 had a cross section measuring *100 mm* by *150 mm* and was bent about the weak axis. Concrete strength was measured as *58 MPa* at the time of testing. Closed steel hoops were spaced at *50 mm* along the length of the column and there were four 10M longitudinal reinforcing steel bars. A *350 kN* axial load was applied to the column prior to each shock wave test.

Column RC-5 was loaded with three shock waves: RC-5-1; RC-5-2; and RC-5-3. A summary of the results of these tests is provided below.

#### *4.2.5.1 RC-5-1*

Test RC-5-1 used a driver length of *1828.8 mm* and a driver pressure of *110.4 kPa.* This combination caused a shock wave with *23.8 kPa* reflected pressures, *140.8 kPa.ms* reflected impulse over the positive phase, and a positive phase duration of *13.0 ms* (Table 4.1). This shock wave loading caused a maximum mid-height displacement of *3.5 mm* (*0.20* °) at *23.0 ms.* Reflected pressure and reflected impulse-time histories are given in Figure 4.26 while the mid-height displacement-time history is shown in Figure 4.27.

The total maximum mid-height strain for tension steel in column RC-5-1 was *0.043* % while the total maximum for tension steel at the supports was -0.033 %. These strains occurred at *21.6 ms* and *20.0 ms* for the mid-height and support locations respectively after the start of the shock wave loading. After completion of the tests the mid-height tension steel had a *0.015* % residual strain and the tension steel near the support had a residual strain of *-0.004* %.

There was no measurable residual displacement after test RC-5-1 and there was no visible sign of damage to the specimen.

#### *4.2.5.2 RC-5-2*

Test RC-5-2 used a driver length of *1828.8 mm* and a driver pressure of *207.0 kPa* to create a shock wave with *39.9 kPa* reflected pressure, *241.5 kPa.ms* reflected impulse over the positive phase, and *14.8 ms* positive phase duration (Table 4.1). This shock wave resulted in a maximum displacement of *19.4 mm* (*1.12* °) at mid-height that occurred *26.0 ms* after the start of the shock wave loading. The reflected pressure and reflected impulse-time histories are shown in Figure 4.28 and the mid-height displacement-time history is shown in Figure 4.29.

The total maximum mid-height strain for tension steel in column RC-5-2 was *0.256* % while the total maximum for tension steel at the supports was 0.054 %. These strains occurred at *26.7 ms* and *22.5 ms* for the mid-height and support locations respectively after the start of the shock wave loading. The mid-height tension steel had a *0.016* % residual strain after test 2 for a cumulative residual strain of *0.031%*. The tension steel near the support had a residual strain of *0.000* % after test 2 for a cumulative residual strain of *-0.004* %.

For test RC-5-2 there was *2.3 mm* recorded residual displacement recorded (*2.3 mm* cumulative). Some tension cracks in the concrete at mid-height were noticed. There were no other visible signs of damage to the specimen. Figure 4.32 a) shows column RC-5 after test 2.

#### *4.2.5.3 RC-5-3*

Test RC-5-3 used a driver length of *1828.8 mm* and a driver pressure of *276.0 kPa.* This combination caused a shock wave with *53.1 kPa* reflected pressures, *324.3 kPa.ms* reflected impulse over the positive phase, and a positive phase duration of *15.8 ms* (Table 4.1). This shock wave loading caused a maximum mid-height displacement of *45.5 mm* (*2.63* °) at *37.0 ms.* Reflected pressure and reflected impulse-time histories are given in Figure 4.30 while the mid-height displacement-time history is shown in Figure 4.31.

There was no usable strain data for the tension steel at the mid-height of column RC-5-3.
The total maximum for tension steel at the supports was 0.187 %, which occurred *28.7 ms* after the start of the shock wave loading. The tension steel near the support had a residual strain of 0.112 % after test 3 for a cumulative residual strain of *0.108* % (Table 4.2).

Specimen RC-5 had a residual displacement of *19.1 mm* at mid-height after test 3 (*21.4 mm* cumulative). Figure 4.32 b) shows the displaced shape of the damaged column after test 3. Tension cracks and the spalling of cover concrete on the compression (loaded) side at mid-height are clearly shown in Figure 4.32 c). The tension cracks in the support region are shown in Figure 4.32 d).

### 4.2.6 Column RC-6

Column RC-6 had a cross section measuring *100 mm* by *150 mm* and was bent about the weak axis. Concrete strength was measured as *58 MPa* at the time of testing. Closed steel hoops were spaced at *25 mm* along the length of the column and there were four 10M longitudinal reinforcing steel bars. A *350 kN* axial load was applied to the column prior to each shock wave test.

Column RC-6 was loaded with three shock waves: RC-6-1; RC-6-2; and RC-6-3. The test results are summarized in the following sections.

#### *4.2.6.1 RC-6-1*

Test RC-6-1 used a driver length of *1828.8 mm* and a driver pressure of *106.3 kPa.* This combination caused a shock wave with *21.7 kPa* reflected pressures, *132.5 kPa.ms* reflected impulse over the positive phase, with a positive phase duration of *13.0 ms* (Table 4.1). This shock wave loading caused a maximum mid-height displacement of *5.1 mm* (*0.29* °) at *22.0 ms.*

Reflected pressure and reflected impulse-time histories are given in Figure 4.33 while the mid-height displacement-time history is shown in Figure 4.34.

The total maximum mid-height strain for tension steel in column RC-6-1 was *0.013 %* while the total maximum for tension steel at the supports was *-0.014 %*. These strains occurred at *21.4 ms* and *20.3 ms* for the mid-height and support locations, respectively, after the start of the shock wave loading. The mid-height tension steel had a *0.004 %* residual strain. The tension steel near the support had a residual strain of *0.000 %*.

There was no residual displacement recorded for test RC-6-1 and there was no visible sign of damage to the specimen.

#### *4.2.6.2 RC-6-2*

Test RC-6-2 used a driver length of *1828.8 mm* and a driver pressure of *207.0 kPa* to create a shock wave with *38.0 kPa* reflected pressure, *234.6 kPa.ms* reflected impulse over the positive phase, with a *14.2 ms* positive phase duration (Table 4.1). This shock wave resulted in a maximum displacement of *22.0 mm* (*1.27 °*) at mid-height that occurred *28.0 ms* after the start of the shock wave loading. Figure 4.35 shows reflected pressure and reflected impulse-time histories and the mid-height displacement-time history is shown in Figure 4.36.

The total maximum tension steel strain in column RC-6-2 at the mid-height of *0.260 %* and at the supports of *0.075 %* occurred at *27.2 ms* and *18.8 ms*, respectively, after the start of the shock wave loading. The mid-height tension steel had a *0.060 %* residual strain due to test 2 for a cumulative residual strain of *0.064%*. The tension steel near the support had a residual strain of *0.000 %* after test 2 for a cumulative residual strain of *0.000 %*.

After test RC-6-2 there was *6.0 mm* residual displacement recorded (*6.0 mm* cumulative). Some tension cracks in the concrete at mid-height were visible. There were no other signs of damage to the specimen. Figure 4.39 a) shows column RC-6 after test 2.

#### *4.2.6.3 RC-6-3*

Test RC-6-3 used a driver length of *1828.8 mm* and a driver pressure of *276.0 kPa.* This combination caused a shock wave with *44.9 kPa* reflected pressures, *305 kPa.ms* reflected impulse over the positive phase, and a positive phase duration of *15.7 ms* (Table 4.1). This shock wave loading caused a maximum mid-height displacement of *52.0 mm* (*3.01* °) at *49.0 ms.* Reflected pressure and reflected impulse-time histories are given in Figure 4.37 while the mid-height displacement-time history is shown in Figure 4.38.

The strain gauges on the tension steel at both the mid-height and close to the support region of column were damaged during test RC-6-3 resulting in no usable strain data.

Specimen RC-6 had a residual displacement of *35.8 mm* at mid-height at the end of test 3 for a *41.8 mm* cumulative residual displacement. Figure 4.39 b) shows the displaced shape of the damaged column after test 3. Tension cracks and the loss of cover concrete on the compression (loaded) side at mid-height are clearly visible in Figure 4.39 c). The locations of tension cracks in the support region are shown in Figure 4.39 d).

### 4.2.7 Column RC-7

Column RC-7 had a cross section measuring *100 mm* by *150 mm* and was bent about the weak axis. Concrete strength was measured as *58 MPa* at the time of testing. Closed steel hoops were spaced at *50 mm* along the length of the column and there were four 10M longitudinal reinforcing steel bars. A *350 kN* axial load was applied to the column prior to each shock wave test.

Column RC-7 was loaded with three shock waves: RC-7-1; RC-7-2; and RC-7-3. A summary of the results of these tests is provided below.

#### *4.2.7.1 RC-7-1*

The driver length for test RC-7-1 was *2473.2 mm* and the driver pressure was *69.0 kPa.* This combination of driver length and driver pressure created a shock wave with *15.2 kPa* reflected pressure, *182.9 kPa.ms* reflected impulse over the positive phase, and *19.2 ms* positive phase duration (Table 4.1). The maximum mid-height displacement was *15.0 mm* (*0.87* °) occurring *25.0 ms* after the start of the shock wave. The pressure and impulse-time histories are shown in Figure 4.40 and the mid-height displacement-time history is shown in Figure 4.41.

The total maximum strain on the reinforcing steel in tension at mid-height of *0.099* % and *-0.001* % on the tension reinforcing steel at the support region occurred at *23.9 ms* and *23.2 ms*, respectively, after the start of the shock wave loading. There was a recorded residual strain of *0.011* % at mid-height and *0.006* % at the supports. A summary of strain values for this test is listed in Table 4.2.

There was *2.8 mm* residual mid-height displacement after test RC-7-1. Some small cracks were visible in the tension concrete at mid-height after this test. No other damage was visible.

#### *4.2.7.2 RC-7-2*

Test RC-7-2 used a driver length of *2743.2 mm* and a driver pressure of *124.2 kPa* to create a shock wave with *30.4 kPa* reflected pressure, *254.6 kPa.ms* reflected impulse over the positive phase, and *20.5 ms* positive phase duration (Table 4.1). This shock wave resulted in a maximum displacement of *24.0 mm* (*1.39* °) at mid-height that occurred *27.0 ms* after the start of the shock wave loading. The reflected pressure and reflected impulse-time histories are shown in Figure 4.42 and the mid-height displacement-time history is shown in Figure 4.43.

The total maximum mid-height strain for tension steel in column RC-7-2 was *0.180* % while the total maximum for tension steel at the supports was *0.031* %. These strains occurred at *25.5 ms* and *24.4 ms* for the mid-height and support locations respectively after the start of the shock wave loading. The mid-height tension steel had a *0.003* % residual strain after test 2 for a

cumulative residual strain of *0.014 %*. The tension steel near the support had a residual strain of *0.009 %* after test 2 for a cumulative residual strain of *0.015 %*.

After test RC-7-2 there was *4.8 mm* residual displacement recorded (*7.6 mm* cumulative). There were no further signs of damage beyond the tension cracks in the concrete at mid-height that developed after test RC-7-1. Figure 4.46 a) shows column RC-7 after test 2.

#### *4.2.7.3 RC-7-3*

Test RC-7-3 used a *2743.2 mm* driver length with *496.8 kPa* driver pressure resulting in a reflected pressure of *89.7 kPa*, a reflected impulse over the positive phase of *762.5 kPa.ms*, and a positive phase duration of *26.2 ms* as shown in Figure 4.44 and listed in Table 4.1. Maximum mid-height displacement, shown as a time-history in Figure 4.45, of the column was *208 mm* (*12.03 °*) at *55.0 ms* after the start of the shock wave loading.

The strain gauges on the tension steel at both the mid-height and close to the support region of column were damaged during test RC-7-3 resulting in no usable strain data.

After test RC-7-3, there was *163 mm* residual mid-height displacement for a cumulative residual displacement of *170.6 mm*. Wide cracks in tension concrete were evident at both the support and mid-height regions as shown in Figure 4.46 b). There was loss of cover concrete on the compression side at both the support and mid-height of the column. Figure 4.46 c) shows the damaged mid-height of the column and Figure 4.36 d) shows the damaged support region of the column.

### 4.2.8 Column RC-8

Column RC-8 had a cross section measuring *100 mm* by *150 mm* and was bent about the weak axis. Concrete strength was measured as *58 MPa* at the time of testing. Closed steel hoops were spaced at 25 *mm* along the length of the column and there were four 10M longitudinal

reinforcing steel bars. A *350 kN* axial load was applied to the column prior to each shock wave test.

Column RC-8 was loaded with three shock waves: RC-8-1; RC-8-2; and RC-8-3. A summary of the results of these tests is provided below.

#### *4.2.8.1 RC-8-1*

Test RC-8-1 used a driver length of *2473.2 mm* and a driver pressure of *82.8 kPa* that created a shock wave with a *15.0 kPa* reflected pressure, a *107.0 kPa.ms* reflected impulse over the positive phase, and a *16.3 ms* positive phase duration (Table 4.1). Maximum mid-height displacement was measured as *2.2 mm* (*0.13* °) occurring *20.0 ms* after the start of the shock wave. The pressure and impulse-time histories are shown in Figure 4.47 and the mid-height displacement-time history is shown in Figure 4.48.

Total maximum strain on the reinforcing steel in tension at mid-height was *-0.031* % while the maximum was *-0.044* % on the tension reinforcing steel at the support region occurring at *17.3 ms* and *16.3 ms* respectively. There was a recorded residual strain of *0.001* % at mid-height and *-0.002* at the supports. A summary of strain values for this test is listed in Table 4.2.

There was no residual displacement after test RC-8-1 and there were no visible signs of damage to the specimen.

#### *4.2.8.2 RC-8-2*

Test RC-8-2 used a driver length of *2743.2 mm* and a driver pressure of *124.2 kPa* creating a shock wave with a *25.2 kPa* reflected pressure, a *220.8 kPa.ms* reflected impulse over the positive phase, and a *19.0 ms* positive phase duration (Table 4.1). This shock wave resulted in a maximum displacement of *16.8 mm* (*0.97* °) at mid-height that occurred *28.0 ms* after the start of the shock wave loading. The reflected pressure and reflected impulse-time histories are shown in Figure 4.49 and the mid-height displacement-time history is shown in Figure 4.50.

Total maximum mid-height strain for tension steel in column RC-8-2 was *0.166 %* while the total maximum for tension steel at the supports was *0.013 %* occurring at *26.8 ms* and *26.4 ms*, respectively, after the start of the shock wave loading. The mid-height tension steel had a *0.019 %* residual strain after test 2 for a cumulative residual strain of *0.020 %*. The tension steel near the support had a residual strain of *0.006 %* after test 2 for a cumulative residual strain of *0.005 %*.

After test RC-8-2 there was *1.9 mm* residual displacement recorded (*1.9 mm* cumulative). Small tension cracks were visible in the concrete at mid-height and there were no other signs of damage. Figure 4.52 a) shows column RC-8 after test 2.

#### *4.2.8.3 RC-8-3*

Test RC-8-3 used a *2743.2 mm* driver length with *496.8 kPa* driver pressure resulting in a reflected pressure of *79.4 kPa*, a reflected impulse over the positive phase of *655.5 kPa.ms*, and a positive phase duration of *23.2 ms* as shown in Figure 4.51 and listed in Table 4.1. Maximum mid-height displacement, shown as a time-history in Figure 4.52, of the column was *264.0 mm* (*15.27 °*) at *127.0 ms* after the start of the shock wave loading.

The strain gauges on the tension steel at both the mid-height and close to the support region of column were damaged during test RC-8-3 resulting in no usable strain data.

After test 3 on specimen RC-8, there was *148 mm* residual mid-height displacement for a cumulative total of *249.9 mm*. Large and prevalent cracks in tension concrete were visible at both the support and mid-height regions as shown in Figure 4.53 b). There was significant loss of cover concrete on the compression side at both the support and mid-height of the column. Figure 4.53 c) shows the damaged mid-height of the column and Figure 4.53 d) shows the damaged support region of the column.

### 4.2.9 Column RC-9

Column RC-9 had a cross section measuring *100 mm* by *150 mm* and was bent about the weak axis. Concrete strength was measured as *58 MPa* at the time of testing. Closed steel hoops were spaced at 50 *mm* along the length of the column and there were four 10M longitudinal reinforcing steel bars. A *350 kN* axial load was applied to the column prior to each shock wave test.

Column RC-9 was loaded with three shock waves: RC-9-1; RC-9-2; and RC-9-3. A summary of the results of these tests is provided below.

#### *4.2.9.1 RC-9-1*

Test RC-9-1 used a *3352.8 mm* driver length a *69kPa* driver pressure to create a shock wave with a *13.8 kPa* reflected pressure, a *182.2 kPa.ms* reflected impulse over the positive phase, and a *27.8 ms* positive phase duration (Table 4.1). A maximum measured mid-height displacement of *14.4 mm* (*0.83* °) occurred *29 ms* after the start of the shock wave. The pressure and impulse-time histories are shown in Figure 4.54 and the mid-height displacement-time history is shown in Figure 4.55.

Total maximum strain on the reinforcing steel in tension at mid-height was *0.085* % and *-0.009* % on the tension reinforcing steel at the support region occurred at *29.5 ms* and *27.1 ms* respectively. There was a recorded residual strain of *0.022* % at mid-height and *-0.0025* % at the supports. A summary of strain values for this test is listed in Table 4.2.

*5.4 mm* residual displacement was recorded at mid-height of column RC-9 after test 1. Some cracking in the tension concrete at mid-height was visible after test1 and there was no other visible damage.

#### *4.2.9.2 RC-9-2*

Test RC-9-2 used a driver length of *3352.8 mm* and a driver pressure of *110.4 kPa* to create a shock wave with a *24.8 kPa* reflected pressure, a *269.1 kPa.ms* reflected impulse over the positive phase, and a *24.0 ms* positive phase duration (Table 4.1). This shock wave resulted in a maximum displacement of *27.5 mm* (*1.59* °) at mid-height that occurred *32.0 ms* after the start of the shock wave loading. The reflected pressure and reflected impulse-time histories are shown in Figure 4.56 and the mid-height displacement-time history is shown in Figure 4.57.

The total maximum mid-height strain for tension steel in column RC-9-2 was *0.291* % while the total maximum for tension steel at the supports was *.069%*. These strains occurred at *29.8 ms* and *28.1 ms* for the mid-height and support locations respectively after the start of the shock wave loading. The mid-height tension steel had a *0.036* % residual strain after test 2 for a cumulative residual strain of *0.058* %. The tension steel near the support had a residual strain of *0.008* % after test 2 for a cumulative residual strain of *0.003* %.

After test RC-9-2 there was *4.7 mm* residual displacement recorded for a total cumulative residual displacement of *10.1 mm*. There was no further damage visible beyond the tension cracks at mid-height formed after test RC-9-1. Figure 4.60 a) shows column RC-9 after test 2.

#### *4.2.9.3 RC-9-3*

Test RC-9-3 used a *3352.8 mm* driver length and *379.5 kPa* driver pressure to create a shock wave with a reflected pressure of *67.6 kPa*, a reflected impulse over the positive phase of *683.1 kPa.ms*, and a positive phase duration of *32.0 ms* as shown in Figure 4.58 and listed in Table 4.1. Maximum mid-height displacement, shown as a time-history in Figure 4.59, of the column was *171.0 mm* (*9.89* °) at *54.0 ms* after the start of the shock wave loading.

The strain gauges on the tension steel at both the mid-height and close to the support region of column were damaged during test RC-9-3 resulting in no usable strain data.

After test 3 on specimen RC-9, there was *126 mm* residual mid-height displacement for a total cumulative residual displacement of *136.1 mm*. The interior plastic hinge formed approximately *150 mm* above mid-height location where there were large and prevalent cracks in tension concrete visible and a significant amount of cover concrete lost in the compression region as seen in Figure 4.60 c). There was loss of concrete cover in the compression region and visible tension cracks in the concrete at the supports as shown in Figure 4.60 b) and 4.60 d).

### 4.2.10 Column RC-10

Column RC-10 had a cross section measuring *100 mm* by *150 mm* and was bent about the weak axis. Concrete strength was measured as *58 MPa* at the time of testing. Closed steel hoops were spaced at 25 *mm* along the length of the column and there were four 10M longitudinal reinforcing steel bars. A *350 kN* axial load was applied to the column prior to each shock wave test.

Column RC-10 was loaded with three shock waves: RC-10-1; RC-10-2; and RC-10-3. A summary of the results of these tests is provided below.

#### *4.2.10.1 RC-10-1*

Test RC-10-1 used a driver length of *3352.8 mm* and a driver pressure of *69kPa* to create a shock wave with a *13.0 kPa* reflected pressure, a *155.9 kPa.ms* reflected impulse over the positive phase, and a *30.2 ms* positive phase duration (Table 4.1). A maximum mid-height displacement of *10.8 mm* (*0.62* °) occurred *32.0 ms* after the start of the shock wave. The pressure and impulse-time histories are shown in Figure 4.61 and the mid-height displacement-time history is shown in Figure 4.62.

Strain gauges on the tension steel in the support region were damaged during the construction of column RC-10, therefore, there was no strain data for this region. A total maximum strain in the tension steel at mid-height was *0.063 %* occurred *28.1 ms* after the start of the shock wave loading. A residual strain of *0.011 %* was recorded at mid-height.

There was *2.9 mm* residual displacement at mid-height of column RC-10 after test 1. Some cracking in the tension concrete at mid-height was visible after test1.

#### *4.2.10.2* ***RC-10-2***

Test RC-10-2 used a driver length of *3352.8 mm* and a driver pressure of *110.4 kPa* to create a shock wave with a *24.2 kPa* reflected pressure, a *242.9 kPa.ms* reflected impulse over the positive phase, a and *24.0 ms* positive phase duration (Table 4.1). This shock wave resulted in a maximum displacement of *21.7 mm* (*21.4* °) at mid-height that occurred *30.0 ms* after the start of the shock wave loading. The reflected pressure and reflected impulse-time histories are shown in Figure 4.63 and the mid-height displacement-time history is shown in Figure 4.64.

A total maximum strain in the tension steel at mid-height of *0.215 %* occurred *28.4 ms* after the start of the shock wave loading. A residual strain of *0.004 %* was recorded at mid-height for test 2 for a total cumulative residual strain at mid-height of *0.014%*..

After test RC-10-2 there was *2.6 mm* residual mid-height displacement recorded (*5.5 mm* cumulative). There was no further visible damage beyond the tension cracks at mid-height formed after test RC-10-1. Figure 4.67 a) shows column RC-10 after test 2.

#### *4.2.10.3* ***RC-10-3***

Test RC-10-3 used a *3352.8 mm* driver length with *379.5 kPa* driver pressure to create a reflected pressure of *64.2 kPa*, a reflected impulse over the positive phase of *600.3 kPa.ms*, and a positive phase duration of *27.0 ms* as shown in Figure 4.65 and listed in Table 4.1. Maximum mid-height displacement, shown as a time-history in Figure 4.66, of the column was measured at *156.0 mm* (*9.02* °) at *53.0 ms* after the start of the shock wave loading.

The remaining strain gauges on the tension steel were damaged during test RC-10-3 resulting in no usable strain data.

After test RC-10-3, there was *128 mm* residual mid-height displacement measured for a total cumulative of *133.5 mm*. Large and prevalent cracks in tension concrete were visible at both the support and mid-height regions as shown in Figure 4.67 b). There was significant loss of cover concrete on the compression side at both the support and mid-height of the column. Figure 4.67 c) shows the damaged mid-height of the column and Figure 4.57 d) shows the damaged support region of the column.

### 4.2.11 Column RC-11

Column RC-11 had a cross section measuring *100 mm* by *150 mm* and was bent about the weak axis. Concrete strength was measured as *58 MPa* at the time of testing. Closed steel hoops were spaced at 50 *mm* along the length of the column and there were four 10M longitudinal reinforcing steel bars. A *350 kN* axial load was applied to the column prior to each shock wave test.

Column RC-11 was loaded with two shock waves: RC-11-1; and RC-11-2. A summary of the results of these tests is provided below.

#### *4.2.11.1* ***RC-11-1***

Test RC-11-1 used a driver length of *4876.8 mm* and a driver pressure of *69.0 kPa* to create a shock wave with a *12.8 kPa* reflected pressure, a *252.5 kPa.ms* reflected impulse over the positive phase, and a *37.5 ms* positive phase duration (Table 4.1). There was no recorded displacement data for test RC-11-1 due to an instrumentation error. The pressure and impulse-time histories are shown in Figure 4.68.

A total maximum strain of *0.118 %* and *-0.042%* for the mid-height for tension steel and the support region tension steel, respectively, was measured in test RC-11-1. These strains occurred at *33.7 ms* and *32.3 ms* for the mid-height and support locations, respectively, after the start of

the shock wave loading. Residual strain was measured at *-0.008 %* for the mid-height tension steel and *0.002 %* for tension steel at the support region.

There was some visible cracking in the tension concrete at mid-height after test RC-11-1. Figure 4.71 a) shows specimen RC-11 after test 1.

#### *4.2.11.2 RC-11-2*

Test RC-11-2 used a *4876.8 mm* driver length with a *124.2 kPa* driver pressure to create a shock wave with a reflected pressure of *26.2 kPa*, a reflected impulse over the positive phase of *440.2 kPa.ms*, and a positive phase duration of *41.7 ms* as shown in Figure 4.69 and listed in Table 4.1. Maximum mid-height displacement, shown as a time-history in Figure 4.70, of the column was measured at *61.8 mm* (*3.57 °*) at *53.0 ms* after the start of the shock wave loading.

Total maximum mid-height strain for tension steel in column RC-11-2 was *0.242 %* and *0.262%* for tension steel at the supports occurred at *51.1 ms* and *51.5 ms* for the mid-height and support locations, respectively, after the start of the shock wave loading. The residual strain was measured at *0.052 %* and *0.044 %* for the mid-height tension steel and the tension steel near the support, respectively, resulting in *0.144 %* and *0.146 %* total cumulative residual strain.

A residual mid-height displacement of *42 mm* was measured after test RC-11-2. An interior plastic hinge formed approximately *125 mm* below the mid-height of the column. Large and prevalent cracks in tension concrete were visible in the mid-height region as shown in Figure 4.71 b). Smaller cracks were visible in the tension concrete in the support region. There was significant loss of cover concrete on the compression side at the mid-height of the column. Figure 4.71 c) shows the damaged mid-height of the column and Figure 4.71 d) shows the damaged support region of the column.

### 4.2.12 Column RC-12

Column RC-12 had a cross section measuring *100 mm* by *150 mm* and was bent about the weak axis. Concrete strength was measured as *58 MPa* at the time of testing. Closed steel hoops were spaced at *25 mm* along the length of the column and there were four 10M longitudinal reinforcing steel bars. The column was subjected to an axial load of *350 kN* applied prior to each shock wave test.

Column RC-12 was loaded with two shock waves: RC-12-1; and RC-12-2. A summary of the results of these tests is provided below.

#### *4.2.12.1 RC-12-1*

Test RC-12-1 used a driver length of *4876.8 mm* and a driver pressure of *69.0 kPa* to create a shock wave with a *13.5 kPa* reflected pressure, a *280.1 kPa.ms* reflected impulse over the positive phase, and a *41.2 ms* positive phase duration (Table 4.1). Maximum mid-height displacement of the column was measured at *18.4 mm* (*1.06* °) at *37.0 ms* after the start of the shock wave loading. The pressure and impulse-time histories for test RC-12-1 are shown in Figure 4.72 and the displacement-time histories are shown in Figure 4.73

The total maximum mid-height strain for tension steel in column RC-12-1 was *0.176* % while the total maximum for tension steel at the supports was *0.011%*. These strains occurred at *36.2 ms* and *34.0 ms* for the mid-height and support locations, respectively, after the start of the shock wave loading. Residual strain was measured *0.031* % and *0.013* % for the tension steel located at mid-height and near the support, respectively.

After test RC-12-1, the mid-height residual displacement was measured at *3.6 mm*. There was some cracking in the tensile concrete face at mid-height was visible after test RC-12-1. Figure 4.76 a) shows specimen RC-12 after test 1.

#### *4.2.12.2* ***RC-12-2***

Test RC-12-2 used a *4876.8 mm* driver length and a *124.2 kPa* driver pressure to create a shock wave with a reflected pressure of *29.0 kPa*, a reflected impulse over the positive phase of *438.2 kPa.ms*, and a positive phase duration of *43.0 ms* as shown in Figure 4.74 and listed in Table 4.1. Maximum mid-height displacement, shown as a time-history in Figure 4.75, of the column was *58.0 mm* (*3.35* °) at *50.0 ms* after the start of the shock wave loading.

The strain gauges on the tension steel at both the mid-height and close to the support region of column were damaged during test RC-12-2 resulting in no usable strain data.

After test 2 RC-12-2, there *32 mm* residual mid-height displacement was measured. Large cracks in tension concrete were visible in the mid-height region as shown in Figure 4.76 b). Smaller cracks were visible in the tension concrete in the support region shown in Figure 4.76 d). There was significant loss of cover concrete on the compression side at the mid-height of the column. Figure 4.76 c) shows the damaged mid-height of the column.

### 4.2.13 Column RC-13

Column RC-13 had a cross section measuring *150 mm by 150 mm* with *58 MPa* concrete strength. The column was reinforced with *6.35 mm* closed steel hoops spaced at *75 mm* and four *10M* longitudinal reinforcing steel bars. The column was subjected to an axial load of *400 kN* applied prior to each shock wave test.

Column RC-13 was loaded with five shock waves: RC-13-1; RC-13-2; RC-13-3; and RC-3-4. A summary of the results of these tests is provided below.

#### *4.2.13.1* ***RC-13-1***

Test RC-13-1 used a driver length of *1828.8 mm* and a *207.0 kPa* driver pressure to create a shock wave with a *39.7 kPa* reflected pressure, a *241.5 kPa.ms* reflected impulse over the

positive phase, and a *14.7 ms* positive phase duration (Table 4.1). Maximum mid-height displacement was measure at *9.6 mm* (*0.56* °) and occurred *19.4 ms* after the start of the shock wave loading. The reflected pressure and reflected impulse-time histories are shown in Figure 4.77 and the mid-height displacement-time history is shown in Figure 4.78.

The total maximum strains measured at *0.158* % and *-0.026* % occurring *20.7 ms* and *11.2 ms* after the start of the shock wave loading for the tension steel at mid-height and the support regions, respectively. The mid-height tension steel had a *0.006* % residual strain and the tension steel near the support had a residual strain of *0.000* % after test RC-13-1. Summary strain values are shown in Table 4.2.

There was no visible sign of damage to the specimen and no recorded residual displacement after test *RC-13-1*.

#### *4.2.13.2* ***RC-13-2***

Test RC-13-2 used a driver length of *1828.8 mm* and a driver pressure of *310.5 kPa* to create a shock wave with a *56.6 kPa* reflected pressure, a *324.3 kPa.ms* reflected impulse over the positive phase, and a *15.6 ms* positive phase duration (Table 4.1). This shock wave loading resulted in a maximum displacement of *18.8 mm* (*1.09* °) at mid-height that occurred *20.8 ms* after the start of the shock wave loading. The reflected pressure and reflected impulse-time histories are shown in Figure 4.79 and the mid-height displacement-time history is shown in Figure 4.80.

Some of the strain gauges were damaged prior to test RC-13-2 resulting in no usable strain data for tension steel located in the support regions. The total maximum strain at mid-height was *0.305* % occurring *20.1 ms* after the start of the shock wave loading. Residual strain in the same location was *0.033* % for a cumulative residual strain of *0.039* %.

After test RC-13-2, there was some minor visible cracking in the tension concrete at mid-height of the column and *1.8 mm* residual displacement.

#### *4.2.13.3* ***RC-13-3***

Test RC-13-3 used a driver length of *1828.8 mm* and a driver pressure of *379.5 kPa* to create a shock wave with a *61.4 kPa* reflected pressure, a *386.4 kPa.ms* reflected impulse over the positive phase, a and *17.1 ms* positive phase duration (Table 4.1). A maximum mid-height displacement was *30.2 mm* (*1.75* °) occurred *23.6 ms* after the start of the shock wave. The pressure and impulse-time histories are shown in Figure 4.81 and the mid-height displacement-time history is shown in Figure 4.82.

The strain gauges on the tension steel at both the mid-height and close to the support region of column were damaged during tests on column RC-13 resulting in no usable strain data.

There was *9.2 mm* residual mid-height displacement measured after test RC-13-3 for a total cumulative of *11.0 mm*. Some small cracks were visible in the tension concrete at mid-height after this test. No other damage was visible. Figure 4.85 a) shows column RC-13 after test 3.

#### *4.2.13.4* ***RC-13-4***

Test RC-13-4 used a driver length of *1828.8 mm* and a driver pressure of *655.5 kPa* to create a shock wave with an *89.7 kPa* reflected pressure, a *669.3 kPa.ms* reflected impulse over the positive phase, and a *19.4 ms* positive phase duration (Table 4.1). This shock wave resulted in a maximum displacement of *100.4 mm* (*5.81* °) at mid-height that occurred *42.0 ms* after the start of the shock wave loading. The reflected pressure and reflected impulse-time histories are shown in Figure 4.83 and the mid-height displacement-time history is shown in Figure 4.84.

The strain gauges on the tension steel at both the mid-height and close to the support region of column were damaged during previous tests on column RC-13 resulting in no usable strain data.

After test RC-13-4 there was *74.8 mm* residual displacement recorded for a total cumulative of *85.8 mm*. There was significant damage visible in both the mid-height and support regions of the column. Figure 4.85 b) shows the damaged shape of the column after test 4. Figure 4.85 c) shows

the visible tension cracks at mid-height of the column. There was a loss of cover concrete in the compression regions at mid-height and the supports. The tension cracks at the support region are shown in Figure 4.85 c).

### 4.2.14 Column RC-14

Column RC-14 had a cross section measuring *150 mm by 150 mm* with *58 MPa* concrete strength. The column was reinforced with *6.35 mm* closed steel hoops spaced at *75 mm* and four *10M* longitudinal reinforcing steel bars. The column was subjected to an axial load of *400 kN* applied prior to each shock wave test.

Column RC-14 was loaded with five shock waves: RC-14-1; RC-14-2; RC-14-3; and RC-14-4. A summary of the results of these tests is provided below.

#### *4.2.14.1* ***RC-14-1***

Test RC-14-1 used a driver length of *4876.8 mm* and a driver pressure of *69.0 kPa* to create a shock wave with a *12.3 kPa* reflected pressure, a *289.8 kPa.ms* reflected impulse over the positive phase, and a *41.0 ms* positive phase duration (Table 4.1). Maximum mid-height displacement was measure at *5.5 mm* (*0.32* °) and occurred *20.0 ms* after the start of the shock wave loading. The reflected pressure and reflected impulse-time histories are shown in Figure 4.86 and the mid-height displacement-time history is shown in Figure 4.87.

The total maximum mid-height strain for tension steel in column RC-14-1 was *0.024* % while the total maximum for tension steel at the supports was *-0.019* %. These strains occurred at *20.0 ms* and *17.8 ms* for the mid-height and support locations, respectively, after the start of the shock wave loading. Residual strains of *0.010* % and *0.006* % for the mid-height tension steel and the tension steel near the support region, respectively. Summary strain values are shown in Table 4.2.

*2.0 mm* residual displacement measured and no visible signs of damage to the specimen after test RC-14-1.

#### *4.2.14.2* ***RC-14-2***

Test RC-14-2 used a driver length of *4876.8mm* and a driver pressure of *124.2 kPa* (Table 4.1). Due to an instrumentation error, no pressures or displacement values were recorded during this test.

The total maximum mid-height strain for tension steel in column RC-14-2 was *0.094 %* while the total maximum for tension steel at the supports was *-0.002%*. These strains occurred at *20.2 ms* and *19.5 ms* for the mid-height and support locations, respectively, after the start of the shock wave loading. The mid-height tension steel had a *0.013 %* residual strain after test 2 for a cumulative residual strain of *0.023%*. The tension steel near the support had a residual strain of *0.002 %* for a cumulative residual strain of *0.008 %*. Summary strain values are shown in Table 4.2.

After test RC-14-2, there was some minor cracking visible in the tension concrete at mid-height of the column.

#### *4.2.14.3* ***RC-14-3***

Test RC-14-3 used a driver length of *4876.8 mm* and a driver pressure of *241.5 kPa* to create a shock wave with a *47.6 kPa* reflected pressure, a *800.4 kPa.ms* reflected impulse over the positive phase, and a *55.4 ms* positive phase duration (Table 4.1). Maximum mid-height displacement was measured at *20.8 mm* (*1.20* °) and occurred at *27.0 ms* after the start of the shock wave. The pressure and impulse-time histories are shown in Figure 4.88 and the mid-height displacement-time history is shown in Figure 4.89.

The total maximum mid-height strain for tension steel in column RC-14-3 was *0.335 %* while the total maximum for tension steel at the supports was *0.017%*. These strains occurred at *26.6 ms*

and *19.2 ms* for the mid-height and support locations, respectively, after the start of the shock wave loading. The mid-height tension steel had a *0.044 %* residual strain after test 3 for a cumulative residual strain of *0.067%*. The tension steel near the support had a residual strain of *-0.012 %* for a cumulative residual strain of *-0.004 %*. Summary strain values are listed in Table 4.2.

There was *2.7 mm* residual mid-height displacement measured after test RC-14-3. Some small cracks were visible in the tension concrete at mid-height after this test. No other damage was visible. Figure 4.92 a) shows column RC-14 after test 3.

#### *4.2.14.4* ***RC-14-4***

Test RC-14-4 used a driver length of *4876.8mm* and a driver pressure of *600.3 kPa* to create a shock wave with an *89.7 kPa* reflected pressure, a *1421.4 kPa.ms* reflected impulse over the positive phase, and a *46.2 ms* positive phase duration (Table 4.1). This shock wave resulted in a maximum displacement of more than *300 mm* (maximum stroke of displacement gauge) at mid-height that occurred an unknown time after the start of the shock wave loading due to the severe damage caused by the shock wave loading and the limitations of the displacement gauge. The reflected pressure and reflected impulse-time histories are shown in Figure 4.90 and the mid-height displacement-time history is shown in Figure 4.91.

The strain gauges on the tension steel at both the mid-height and close to the support region of column were damaged during test RC-14-4 resulting in no usable strain data.

After test RC-14-4 there was considerable damage to the specimen. Plastic hinges formed at mid-height and at the support regions as shown in Figure 5.92 b). The longitudinal reinforcing steel on the side opposite to the plane of the shock wave loading ruptured at mid-height as shown in Figure 5.92 c). The concrete at the support region was completely destroyed and allowed the longitudinal reinforcing steel to pull out as shown in Figure 5.92 d). Cover concrete was lost in the compression zones at both mid-height and support regions.

## *4.3 Seismic vs Non-Seismic Columns*

An effort was made to compare the response of columns designed for seismic regions with those designed for non-seismic regions. Columns RC-3, 5, 7, 9, and 11 were designed as non-seismic region columns with transverse steel spaced equally along the length of the column at a distance of *50 mm* (half of cross-section height). Columns RC-4, 6, 8, 10, and 12 were designed as seismic region columns with transverse steel spaced equally along the length of the column at *25 mm*. All other details of the two column sets were kept equal. These columns were tested under similar shock wave and axial loading regimens. The maximum displacement levels were recorded along with the applied reflected pressures and applied reflected impulses. A comparison between the ratios of displacement levels is used to draw conclusions towards the response of seismic and non-seismic detailed columns under blast loads.

Figure 4.93 shows the displacement ratio calculated as maximum mid-height displacements for seismic columns divided by maximum displacement of the non-seismic detailed columns tested under similar pressure-impulse combinations. These ratios are plotted against the maximum non-seismic displacement values. In total there were eleven companion tests that were considered to have been tested under similar pressures and impulses where the ratios of reflected pressure and reflected impulse of seismic columns divided by non-seismic columns was within *20 %* of unity (*1.0*). The computed average maximum displacement ratio of 0.9350 indicates a slightly higher maximum displacement for the non-seismic columns when compared to the seismic columns and the standard deviation of the displacement ratios was 0.2872. In Figure 4.94, the ratios of the applied maximum reflected pressures and reflected impulses over the positive phase are shown. These ratios are calculated as the recorded level for the seismic columns divided by the recorded level for the non-seismic companion columns and are plotted against the same axis as Figure 4.93 for ease of comparison. The average pressure and impulse ratio for the seismic over non-seismic columns is 0.9262 and 0.9087, respectively, with corresponding standard deviations of

0.0754 and 0.0476. These ratios show that in general, the non-seismic columns were coincidently tested under slightly higher pressures and impulses than the seismic columns.

Given the slight discrepancy in pressure and impulse levels between the two sets of tests, and the large standard deviation for the displacement ratios it is difficult to conclude if there is significant differences in behaviour between the seismic and non-seismic detailed columns. It is likely that for columns with high slenderness ratios, $L/h=19.8$ in these tests, the confinement of core concrete in seismic detailed columns does not contribute significantly to the response under impulse shock wave loading. Additionally, as the axial load was applied using a non-compressible fluid jack, any shortening of the column's projected length with horizontal displacement will result in a drop in vertical load. It was found that a column will transition into pure beam bending behaviour (no axial load) early in it's response to the shock wave loading with the provided axial load mechanism. It is likely that the loss of axial load negated most of the confinement benefits that may exist in columns designed for seismic regions. This drop in axial load is discussed further in the following chapter.

*TABLE 4.1 - Pressure, Impulse, Maximum Displacement, and Time Maximum Displacement Values*

| | $L_D$ (mm) | $P_D$ (kPa) | $P_r$ (kPa) | $I_r$ (kPa-ms) | $t_d$ (ms) | $d_{max}$ (mm) | $\theta_{max}$ (degrees) | $t_{max}$ (ms) |
|---|---|---|---|---|---|---|---|---|
| RC- 1- 1 | 1219.2 | 103.5 | 22.0 | 120.1 | 10.0 | 13.9 | 0.80 | 28.4 |
| 2 | 1219.2 | 144.9 | 38.0 | 157.7 | 10.4 | 20.8 | 1.20 | 28.9 |
| 3 | 1219.2 | 289.8 | | | No Data | | | |
| RC- 2- 1 | 2743.2 | 124.2 | 23.1 | 193.2 | 24.9 | 24.2 | 1.40 | 28.8 |
| 2 | 2743.2 | 207.0 | 39.9 | 425.7 | 26.3 | 66.4 | 3.84 | 46.3 |
| RC- 3- 1 | 914.4 | 289.8 | 51.1 | 193.2 | 9.9 | 15.0 | 0.87 | 18.3 |
| 2 | 914.4 | 345.0 | 58.0 | 222.2 | 10.0 | 19.2 | 1.11 | 22.6 |
| 3 | 914.4 | 690.0 | 89.7 | 362.3 | 11.5 | 76.4 | 4.42 | 52.0 |
| RC- 4- 1 | 914.4 | 124.2 | 2.9 | 12.8 | 8.3 | | No Data | |
| 2 | 914.4 | 241.5 | 47.6 | 176.0 | 9.5 | 7.5 | 0.43 | 21.3 |
| 3 | 914.4 | 289.8 | 50.4 | 193.9 | 9.8 | 13.5 | 0.78 | 20.6 |
| 4 | 914.4 | 345.0 | 58.0 | 227.7 | 9.5 | 18.2 | 1.05 | 24.0 |
| 5 | 914.4 | 690.0 | | | No Data | | | |
| RC- 5- 1 | 1828.8 | 110.4 | 23.8 | 140.8 | 13.0 | 3.5 | 0.20 | 23.0 |
| 2 | 1828.8 | 207.0 | 39.9 | 241.5 | 14.8 | 19.4 | 1.12 | 26.0 |
| 3 | 1828.8 | 276.0 | 53.1 | 324.3 | 15.8 | 45.5 | 2.63 | 37.0 |
| RC- 6- 1 | 1828.8 | 106.3 | 21.7 | 132.5 | 13.0 | 5.1 | 0.29 | 22.0 |
| 2 | 1828.8 | 207.0 | 38.0 | 234.6 | 14.2 | 22.0 | 1.27 | 28.0 |
| 3 | 1828.8 | 276.0 | 44.9 | 305.0 | 15.7 | 52.0 | 3.01 | 49.0 |
| RC- 7- 1 | 2743.2 | 69.0 | 15.2 | 182.9 | 19.2 | 15.0 | 0.87 | 25.0 |
| 2 | 2743.2 | 124.2 | 30.4 | 254.6 | 20.5 | 24.0 | 1.39 | 27.0 |
| 3 | 2743.2 | 496.8 | 89.7 | 762.5 | 26.2 | 208.0 | 12.03 | 55.0 |

*TABLE 4.1 - Pressure, Impulse, Maximum Displacement, and Time Maximum Displacement Values (Continued)*

| | $L_D$ (mm) | $P_D$ (kPa) | $P_r$ (kPa) | $I_r$ (kPa-ms) | $t_d$ (ms) | $d_{max}$ (mm) | $\theta_{max}$ (degrees) | $t_{max}$ (ms) |
|---|---|---|---|---|---|---|---|---|
| RC- 8- 1 | 2743.2 | 82.8 | 15.0 | 107.0 | 16.3 | 2.2 | 0.13 | 20.0 |
| 2 | 2743.2 | 124.2 | 25.2 | 220.8 | 19.0 | 16.8 | 0.97 | 28.0 |
| 3 | 2743.2 | 496.8 | 79.4 | 655.5 | 23.2 | 264.0 | 15.27 | 127.0 |
| RC- 9- 1 | 3352.8 | 69.0 | 13.8 | 182.2 | 27.8 | 14.4 | 0.83 | 29.0 |
| 2 | 3352.8 | 110.4 | 24.8 | 269.1 | 24.0 | 27.5 | 1.59 | 32.0 |
| 3 | 3352.8 | 379.5 | 67.6 | 683.1 | 32.0 | 171.0 | 9.89 | 54.0 |
| RC- 10- 1 | 3352.8 | 69.0 | 13.0 | 155.9 | 30.2 | 10.8 | 0.62 | 28.3 |
| 2 | 3352.8 | 110.4 | 24.2 | 242.9 | 23.3 | 21.4 | 1.24 | 30.0 |
| 3 | 3352.8 | 379.5 | 64.2 | 600.3 | 27.0 | 156.0 | 9.02 | 53.0 |
| RC- 11- 1 | 4876.8 | 69.0 | 12.8 | 252.5 | 37.5 | | No Data | |
| 2 | 4876.8 | 124.2 | 26.2 | 440.2 | 41.7 | 61.8 | 3.57 | 53.0 |
| RC- 12- 1 | 4876.8 | 69.0 | 13.5 | 280.1 | 41.2 | 18.4 | 1.06 | 37.0 |
| 2 | 4876.8 | 124.2 | 29.0 | 438.2 | 43.0 | 58.0 | 3.35 | 50.0 |
| RC- 13- 1 | 1828.8 | 207.0 | 39.7 | 241.5 | 14.7 | 9.6 | 0.56 | 19.4 |
| 2 | 1828.8 | 310.5 | 56.6 | 324.3 | 15.6 | 18.8 | 1.09 | 20.8 |
| 3 | 1828.8 | 379.5 | 61.4 | 386.4 | 17.1 | 30.2 | 1.75 | 23.6 |
| 4 | 1828.8 | 655.5 | 89.7 | 669.3 | 19.4 | 100.4 | 5.81 | 42.0 |
| RC- 14- 1 | 4876.8 | 69.0 | 12.3 | 289.8 | 41.0 | 5.5 | 0.32 | 20.0 |
| 2 | 4876.8 | 124.2 | | | No Data | | | |
| 3 | 4876.8 | 241.5 | 47.6 | 800.4 | 55.4 | 20.8 | 1.20 | 27.0 |
| 4 | 4876.8 | 600.3 | 89.7 | 1421.4 | 46.2 | 300+ | No Data | |

*TABLE 4.2 - Strain and Time to Maximum Strain*

| | Mid-Height Tension Steel | | | | | | | Support Tension Steel | | | | | | |
|---|---|---|---|---|---|---|---|---|---|---|---|---|---|---|
| | $\varepsilon_{axial}$ (%) | $\varepsilon_{max\text{-}axial}$ (%) | $\varepsilon_{max}$ (%) | $t_{max}$ (ms) | $\varepsilon_{max+tot\ res}$ (%) | $\varepsilon_{residual}$ (%) | $\varepsilon_{tot\ res}$ (%) | $\varepsilon_{axial}$ (%) | $\varepsilon_{max\text{-}axial}$ (%) | $\varepsilon_{max}$ (%) | $t_{max}$ (ms) | $\varepsilon_{max+tot\ res}$ (%) | $\varepsilon_{residual}$ (%) | $\varepsilon_{tot\ res}$ (%) |
| RC- 1- 1 | 0.000 | 0.157 | 0.157 | 27.1 | 0.157 | 0.004 | 0.004 | 0.000 | 0.019 | 0.019 | 25.6 | 0.019 | -0.006 | -0.006 |
| 2 | 0.000 | 0.226 | 0.226 | 27.6 | 0.230 | 0.001 | 0.005 | 0.000 | 0.019 | 0.019 | 26.2 | 0.013 | 0.000 | -0.006 |
| 3 | 0.000 | 0.605 | 0.605 | 29.9 | 0.610 | 0.074 | 0.078 | 0.000 | 0.092 | 0.092 | 34.5 | 0.086 | 0.003 | -0.003 |
| RC- 2- 1 | -0.066 | 0.225 | 0.159 | 26.6 | 0.159 | 0.062 | 0.062 | -0.066 | 0.109 | 0.042 | 23.0 | 0.042 | 0.000 | 0.000 |
| 2 | No Data | | | | | | | | | | No Data | | | |
| RC- 3- 1 | -0.060 | 0.121 | 0.060 | 21.8 | 0.060 | 0.005 | 0.005 | -0.060 | 0.077 | 0.017 | 18.1 | 0.017 | -0.009 | -0.009 |
| 2 | -0.060 | 0.201 | 0.140 | 22.5 | 0.146 | 0.000 | 0.005 | -0.060 | 0.095 | 0.035 | 18.5 | 0.026 | -0.007 | -0.016 |
| 3 | No Data | | | | | | | | | | No Data | | | |
| RC- 4- 1 | No Data | | | | | | | -0.060 | 0.016 | -0.044 | 13.0 | -0.044 | 0.000 | 0.000 |
| 2 | -0.060 | 0.136 | 0.075 | 17.8 | 0.075 | 0.012 | 0.012 | -0.060 | 0.057 | -0.003 | 16.5 | -0.003 | 0.000 | 0.000 |
| 3 | -0.060 | 0.182 | 0.122 | 22.9 | 0.134 | 0.000 | 0.012 | -0.060 | 0.053 | -0.008 | 16.9 | -0.008 | 0.000 | 0.000 |
| 4 | -0.060 | 0.236 | 0.176 | 24.6 | 0.188 | 0.003 | 0.015 | -0.060 | 0.048 | -0.013 | 16.0 | -0.013 | 0.000 | 0.000 |
| 5 | No Data | | | | | | | | | | No Data | | | |
| RC- 5- 1 | -0.060 | 0.104 | 0.043 | 21.6 | 0.043 | 0.015 | 0.015 | -0.060 | 0.027 | -0.033 | 20.0 | -0.033 | -0.004 | -0.004 |
| 2 | -0.060 | 0.317 | 0.256 | 26.7 | 0.271 | 0.016 | 0.031 | -0.060 | 0.114 | 0.054 | 22.5 | 0.050 | 0.000 | -0.004 |
| 3 | No Data | | | | | | | -0.060 | 0.248 | 0.187 | 28.7 | 0.183 | 0.112 | 0.108 |
| RC- 6- 1 | -0.060 | 0.073 | 0.013 | 21.4 | 0.013 | 0.004 | 0.004 | -0.060 | 0.046 | -0.014 | 20.3 | -0.014 | 0.000 | 0.000 |
| 2 | -0.060 | 0.321 | 0.260 | 27.2 | 0.264 | 0.060 | 0.064 | -0.060 | 0.135 | 0.075 | 18.8 | 0.075 | 0.000 | 0.000 |
| 3 | No Data | | | | | | | | | | No Data | | | |
| RC- 7- 1 | -0.060 | 0.159 | 0.099 | 23.9 | 0.099 | 0.011 | 0.011 | -0.060 | 0.059 | -0.001 | 23.2 | -0.001 | 0.006 | 0.006 |
| 2 | -0.060 | 0.240 | 0.180 | 25.5 | 0.191 | 0.003 | 0.014 | -0.060 | 0.091 | 0.031 | 24.4 | 0.037 | 0.009 | 0.015 |
| 3 | No Data | | | | | | | | | | No Data | | | |

*TABLE 4.2 - Strain and Time to Maximum Strain (Continued)*

| | Mid-Height Tension Steel | | | | | | | Support Tension Steel | | | | | | |
|---|---|---|---|---|---|---|---|---|---|---|---|---|---|---|
| | $\varepsilon_{axial}$ (%) | $\varepsilon_{max\text{-}axial}$ (%) | $\varepsilon_{max}$ (%) | $t_{max}$ (ms) | $\varepsilon_{max+tot\ res}$ (%) | $\varepsilon_{residual}$ (%) | $\varepsilon_{tot\ res}$ (%) | $\varepsilon_{axial}$ (%) | $\varepsilon_{max\text{-}axial}$ (%) | $\varepsilon_{max}$ (%) | $t_{max}$ (ms) | $\varepsilon_{max+tot\ res}$ (%) | $\varepsilon_{residual}$ (%) | $\varepsilon_{tot\ res}$ (%) |
| RC- 8- 1 | -0.060 | 0.029 | -0.031 | 17.3 | -0.031 | 0.001 | 0.001 | -0.060 | 0.016 | -0.044 | 16.3 | -0.044 | -0.002 | -0.002 |
| 2 | -0.060 | 0.226 | 0.166 | 26.8 | 0.167 | 0.019 | 0.020 | -0.060 | 0.074 | 0.013 | 26.4 | 0.012 | 0.006 | 0.005 |
| 3 | | | | No Data | | | | | | | No Data | | | |
| RC- 9- 1 | -0.060 | 0.145 | 0.085 | 29.5 | 0.085 | 0.022 | 0.022 | -0.060 | 0.051 | -0.009 | 27.1 | -0.009 | -0.005 | -0.005 |
| 2 | -0.060 | 0.351 | 0.291 | 29.8 | 0.313 | 0.036 | 0.058 | -0.060 | 0.129 | 0.069 | 28.1 | 0.064 | 0.008 | 0.003 |
| 3 | | | | No Data | | | | | | | No Data | | | |
| RC- 10- 1 | -0.060 | 0.123 | 0.063 | 28.1 | 0.063 | 0.011 | 0.011 | | | | No Data | | | |
| 2 | -0.060 | 0.275 | 0.215 | 28.4 | 0.225 | 0.004 | 0.014 | | | | No Data | | | |
| 3 | | | | No Data | | | | | | | No Data | | | |
| RC- 11- 1 | -0.060 | 0.179 | 0.118 | 33.7 | 0.118 | -0.008 | -0.008 | -0.060 | 0.019 | -0.042 | 32.3 | -0.042 | 0.002 | 0.002 |
| 2 | -0.060 | 0.303 | 0.242 | 51.1 | 0.234 | 0.052 | 0.044 | -0.060 | 0.322 | 0.262 | 51.5 | 0.264 | 0.144 | 0.146 |
| RC- 12- 1 | -0.060 | 0.236 | 0.176 | 36.2 | 0.176 | 0.031 | 0.031 | -0.060 | 0.072 | 0.011 | 34.0 | 0.011 | 0.013 | 0.013 |
| 2 | | | | No Data | | | | | | | No Data | | | |
| RC- 13- 1 | -0.048 | 0.206 | 0.158 | 20.7 | 0.158 | 0.006 | 0.006 | -0.048 | 0.022 | -0.026 | 11.2 | -0.026 | 0.000 | 0.000 |
| 2 | -0.048 | 0.352 | 0.305 | 20.1 | 0.311 | 0.033 | 0.039 | | | | No Data | | | |
| 3 | | | | No Data | | | | | | | No Data | | | |
| 4 | | | | No Data | | | | | | | No Data | | | |
| RC- 14- 1 | -0.048 | 0.071 | 0.024 | 20.0 | 0.024 | 0.010 | 0.010 | -0.048 | 0.029 | -0.019 | 17.8 | -0.019 | 0.006 | 0.006 |
| 2 | -0.048 | 0.141 | 0.094 | 20.2 | 0.103 | 0.013 | 0.023 | -0.048 | 0.045 | -0.002 | 19.5 | 0.003 | 0.002 | 0.008 |
| 3 | -0.048 | 0.383 | 0.335 | 26.6 | 0.357 | 0.044 | 0.067 | -0.048 | 0.065 | 0.017 | 19.2 | 0.025 | -0.012 | -0.004 |
| 4 | | | | No Data | | | | | | | No Data | | | |

*TABLE 4.2 - Strain and Time to Maximum Strain (Continued)*

| | Mid-Height Compression Steel | | | | | | | Support Compression Steel | | | | | | |
|---|---|---|---|---|---|---|---|---|---|---|---|---|---|---|
| | $\varepsilon_{axial}$ (%) | $\varepsilon_{max\text{-}axial}$ (%) | $\varepsilon_{max}$ (%) | $t_{max}$ (ms) | $\varepsilon_{max+tot\ res}$ (%) | $\varepsilon_{residual}$ (%) | $\varepsilon_{tot\ res}$ (%) | $\varepsilon_{axial}$ (%) | $\varepsilon_{max\text{-}axial}$ (%) | $\varepsilon_{max}$ (%) | $t_{max}$ (ms) | $\varepsilon_{max+tot\ res}$ (%) | $\varepsilon_{residual}$ (%) | $\varepsilon_{tot\ res}$ (%) |
| RC- 1- 1 | 0.000 | -0.002 | -0.002 | 27.1 | -0.002 | -0.004 | -0.004 | | | | No Data | | | |
| 2 | 0.000 | 0.007 | 0.007 | 27.6 | 0.003 | 0.000 | -0.004 | | | | No Data | | | |
| 3 | 0.000 | 0.179 | 0.179 | 29.9 | 0.174 | 0.115 | 0.110 | | | | No Data | | | |
| RC- 2- 1 | -0.066 | -0.464 | -0.530 | 26.6 | -0.530 | -0.367 | -0.367 | -0.066 | 0.224 | 0.157 | 26.6 | 0.157 | 0.023 | 0.023 |
| 2 | | | | No Data | | | | | | | No Data | | | |
| RC- 3- 1 | -0.060 | -0.088 | -0.148 | 21.8 | -0.148 | -0.038 | -0.038 | -0.060 | -0.038 | -0.098 | 21.8 | -0.098 | 0.000 | 0.000 |
| 2 | -0.060 | -0.074 | -0.135 | 22.5 | -0.173 | -0.034 | -0.072 | -0.060 | -0.041 | -0.101 | 22.5 | -0.101 | 0.000 | 0.000 |
| 3 | | | | No Data | | | | | | | No Data | | | |
| RC- 4- 1 | -0.060 | -0.021 | -0.081 | 21.8 | -0.081 | -0.002 | -0.002 | -0.060 | -0.008 | -0.068 | 21.8 | -0.068 | 0.001 | 0.001 |
| 2 | -0.060 | -0.055 | -0.116 | 17.8 | -0.118 | -0.011 | -0.013 | -0.060 | -0.021 | -0.081 | 17.8 | -0.080 | 0.008 | 0.009 |
| 3 | -0.060 | -0.048 | -0.109 | 22.9 | -0.122 | -0.006 | -0.019 | -0.060 | -0.022 | -0.083 | 22.9 | -0.074 | 0.000 | 0.009 |
| 4 | -0.060 | -0.066 | -0.126 | 24.6 | -0.146 | -0.020 | -0.039 | -0.060 | -0.024 | -0.084 | 24.6 | -0.076 | 0.000 | 0.009 |
| 5 | | | | No Data | | | | | | | No Data | | | |
| RC- 5- 1 | -0.060 | -0.033 | -0.093 | 21.6 | -0.093 | -0.013 | -0.013 | -0.060 | -0.054 | -0.115 | 21.6 | -0.115 | 0.000 | 0.000 |
| 2 | -0.060 | -0.074 | -0.135 | 26.7 | -0.147 | -0.053 | -0.065 | -0.060 | -0.092 | -0.152 | 26.7 | -0.152 | 0.000 | 0.000 |
| 3 | | | | No Data | | | | | | | No Data | | | |
| RC- 6- 1 | -0.060 | -0.016 | -0.076 | 21.4 | -0.076 | -0.009 | -0.009 | -0.060 | -0.013 | -0.074 | 21.4 | -0.074 | 0.000 | 0.000 |
| 2 | | | | No Data | | | | | | | No Data | | | |
| 3 | | | | No Data | | | | | | | No Data | | | |
| RC- 7- 1 | -0.060 | -0.073 | -0.134 | 23.9 | -0.134 | -0.025 | -0.025 | -0.060 | -0.023 | -0.083 | 23.9 | -0.083 | 0.000 | 0.000 |
| 2 | | | | No Data | | | | | | | No Data | | | |
| 3 | | | | No Data | | | | | | | No Data | | | |

*TABLE 4.2 - Strain and Time to Maximum Strain (Continued)*

| | Mid-Height Compression Steel | | | | | | | Support Compression Steel | | | | | | |
|---|---|---|---|---|---|---|---|---|---|---|---|---|---|---|
| | $\varepsilon_{axial}$ (%) | $\varepsilon_{max\text{-}axial}$ (%) | $\varepsilon_{max}$ (%) | $t_{max}$ (ms) | $\varepsilon_{max+tot\ res}$ (%) | $\varepsilon_{residual}$ (%) | $\varepsilon_{tot\ res}$ (%) | $\varepsilon_{axial}$ (%) | $\varepsilon_{max\text{-}axial}$ (%) | $\varepsilon_{max}$ (%) | $t_{max}$ (ms) | $\varepsilon_{max+tot\ res}$ (%) | $\varepsilon_{residual}$ (%) | $\varepsilon_{tot\ res}$ (%) |
| RC- 8- 1 | -0.060 | -0.028 | -0.088 | 17.3 | -0.088 | -0.005 | -0.005 | | | | No Data | | | |
| 2 | -0.060 | -0.096 | -0.156 | 26.8 | -0.161 | -0.034 | -0.039 | | | | No Data | | | |
| 3 | | | | No Data | | | | | | | No Data | | | |
| RC- 9- 1 | -0.060 | -0.047 | -0.108 | 29.5 | -0.108 | -0.018 | -0.018 | -0.060 | -0.043 | -0.103 | 27.1 | -0.103 | 0.000 | 0.000 |
| 2 | -0.060 | -0.064 | -0.124 | 29.8 | -0.142 | -0.023 | -0.041 | -0.060 | -0.068 | -0.128 | 28.1 | -0.128 | -0.011 | -0.011 |
| 3 | | | | No Data | | | | | | | No Data | | | |
| RC- 10- 1 | -0.060 | -0.016 | -0.076 | 28.1 | -0.076 | -0.010 | -0.010 | -0.060 | -0.042 | -0.102 | 28.1 | -0.102 | 0.000 | 0.000 |
| 2 | | | | No Data | | | | -0.060 | -0.050 | -0.110 | 29.8 | -0.110 | 0.000 | 0.000 |
| 3 | | | | No Data | | | | | | | No Data | | | |
| RC- 11- 1 | -0.060 | -0.044 | -0.104 | 33.7 | -0.104 | -0.028 | -0.028 | -0.060 | -0.040 | -0.100 | 32.3 | -0.100 | 0.004 | 0.004 |
| 2 | -0.060 | -0.018 | -0.079 | 51.1 | -0.107 | -0.006 | -0.034 | -0.060 | -0.037 | -0.097 | 51.5 | -0.093 | -0.035 | -0.031 |
| RC- 12- 1 | -0.060 | -0.063 | -0.123 | 36.2 | -0.123 | -0.035 | -0.035 | -0.060 | -0.048 | -0.108 | 34.0 | -0.108 | -0.013 | -0.013 |
| 2 | | | | No Data | | | | | | | No Data | | | |
| RC- 13- 1 | -0.048 | -0.092 | -0.140 | 20.7 | -0.140 | -0.035 | -0.035 | -0.048 | -0.023 | -0.071 | 20.7 | -0.071 | 0.000 | 0.000 |
| 2 | -0.048 | -0.137 | -0.185 | 20.1 | -0.220 | -0.062 | -0.097 | -0.048 | -0.039 | -0.087 | 20.1 | -0.087 | 0.000 | 0.000 |
| 3 | | | | No Data | | | | | | | No Data | | | |
| 4 | | | | No Data | | | | | | | No Data | | | |
| RC- 14- 1 | -0.048 | -0.043 | -0.090 | 20.0 | -0.090 | -0.013 | -0.013 | -0.048 | -0.032 | -0.080 | 20.0 | -0.080 | 0.000 | 0.000 |
| 2 | -0.048 | -0.064 | -0.111 | 20.2 | -0.124 | -0.017 | -0.030 | -0.048 | -0.052 | -0.100 | 20.2 | -0.100 | 0.000 | 0.000 |
| 3 | -0.048 | -0.220 | -0.268 | 26.6 | -0.298 | -0.129 | -0.159 | -0.048 | -0.092 | -0.140 | 26.6 | -0.140 | 0.010 | 0.010 |
| 4 | | | | No Data | | | | -0.048 | -0.153 | -0.200 | 26.6 | -0.190 | 0.034 | 0.044 |

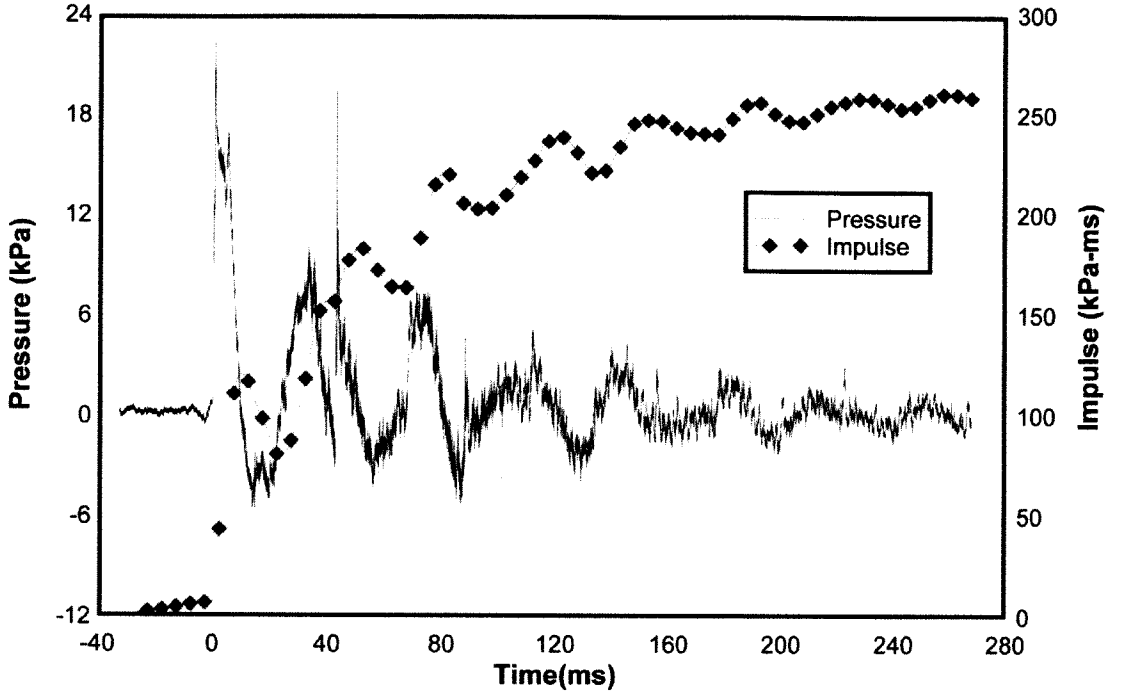


*Figure 4-1: Reflected Pressure and Impulse Time History for Test RC-1-1*

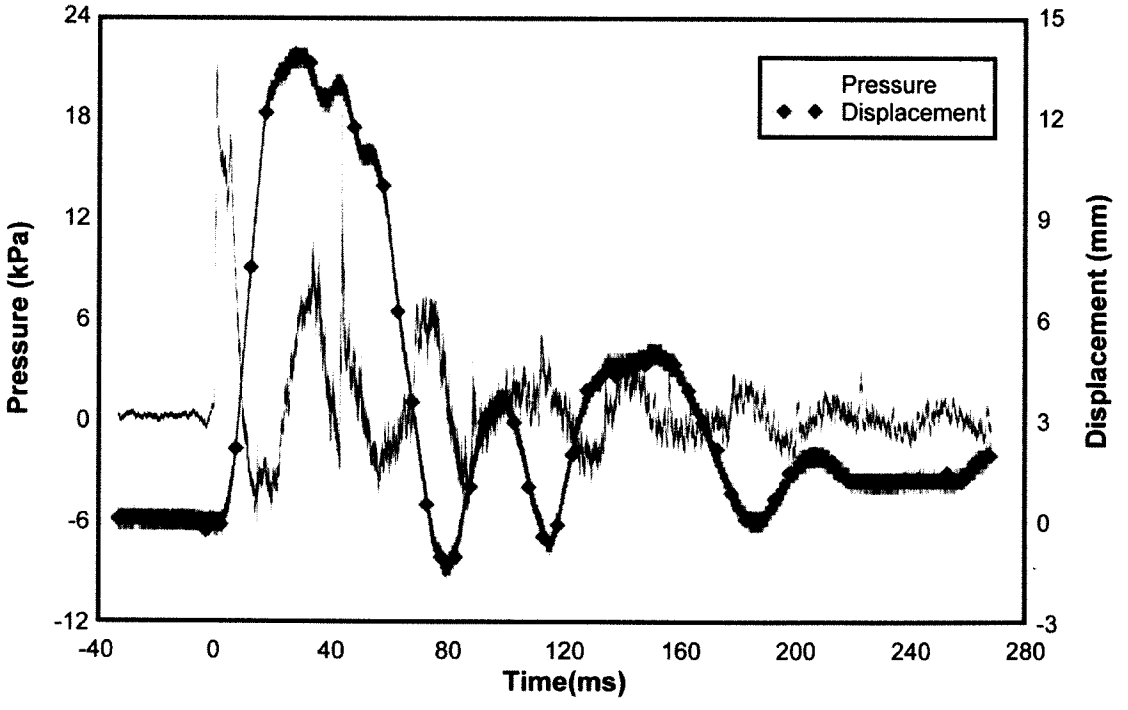


*Figure 4-2: Reflected Pressure and Mid-Height Displacement Time History for Test RC-1-1*

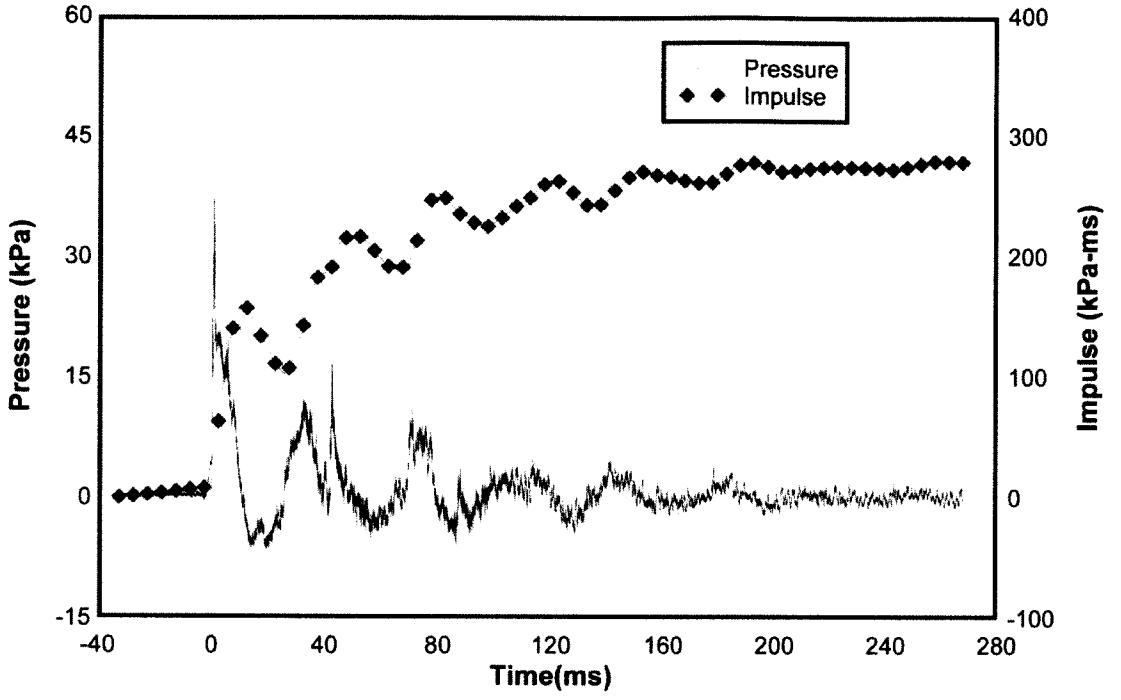


*Figure 4-3: Reflected Pressure and Impulse Time History for Test RC-1-2*

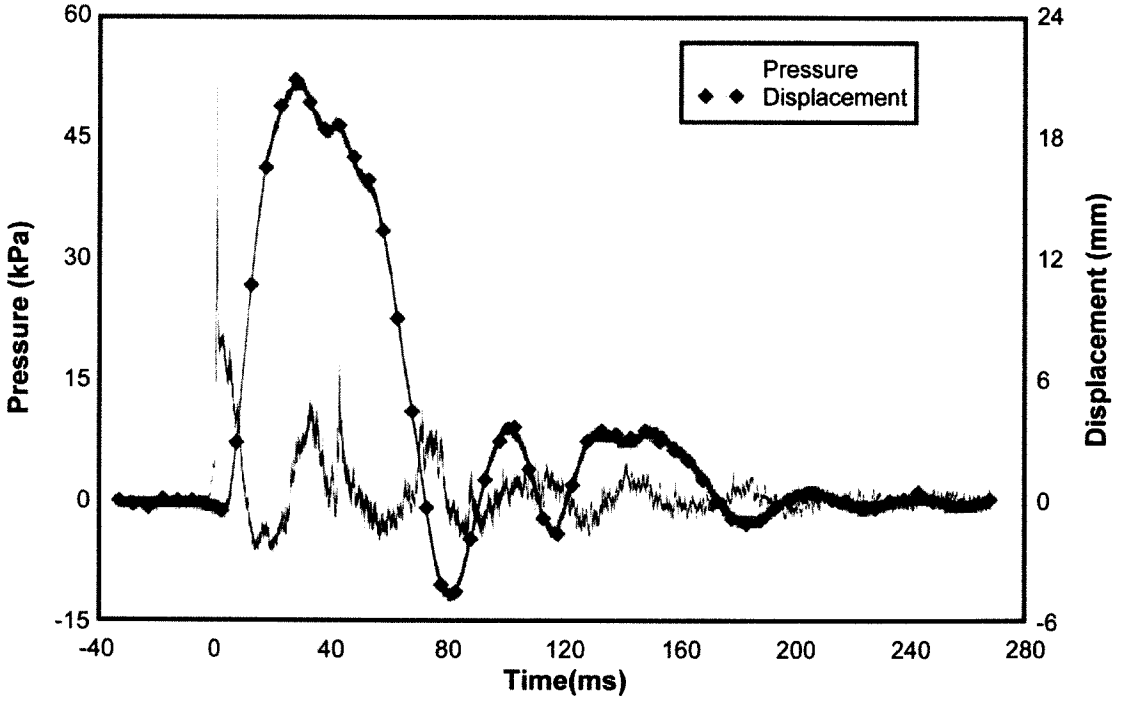


*Figure 4-4: Reflected Pressure and Mid-Height Displacement Time History for Test RC-1-2*

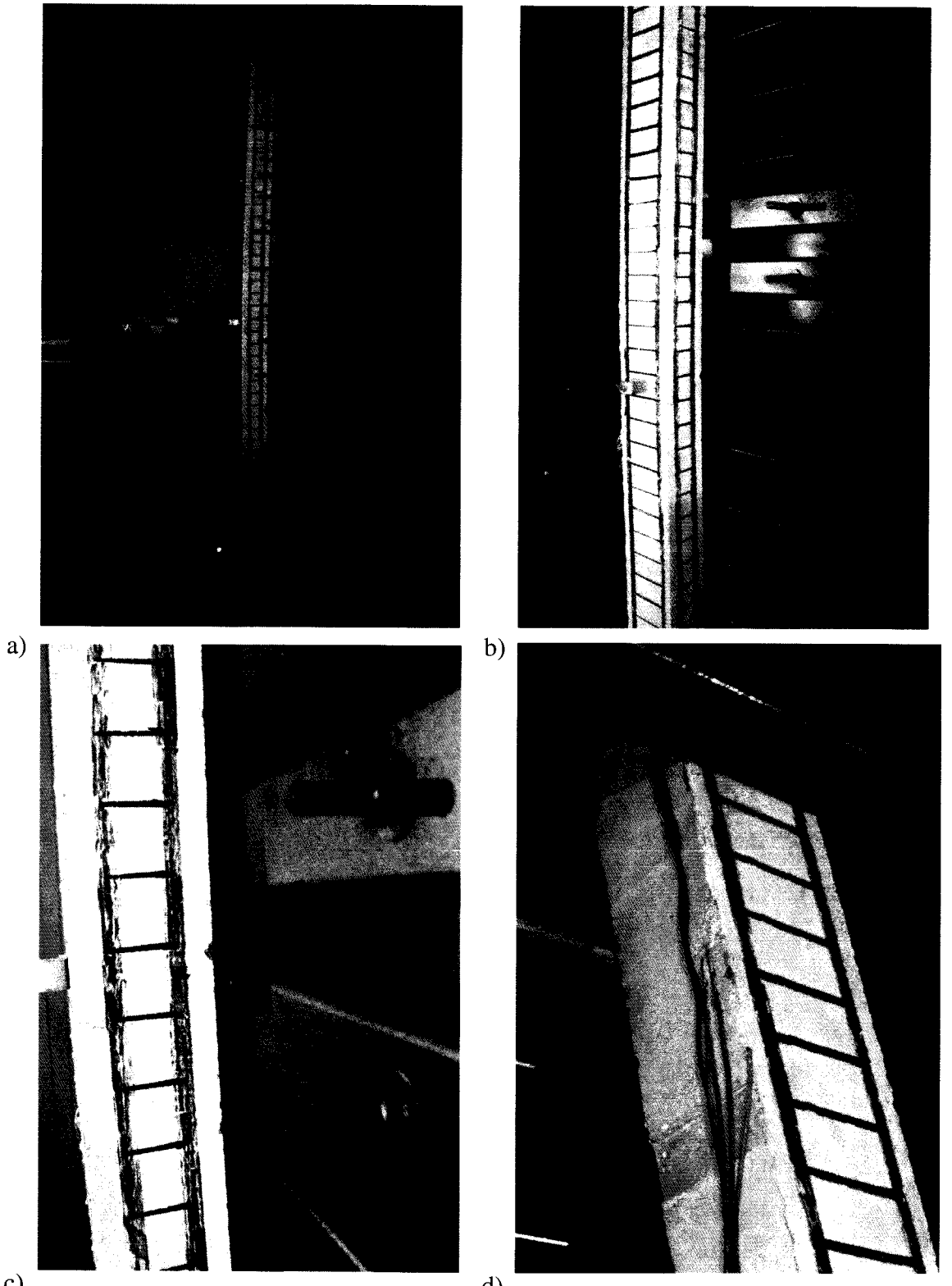


*Figure 4-5: RC-1: a) After Shot 2; b) After Shot 3; c) Mid-Height After Shot 3; d) Support After Shot 3*

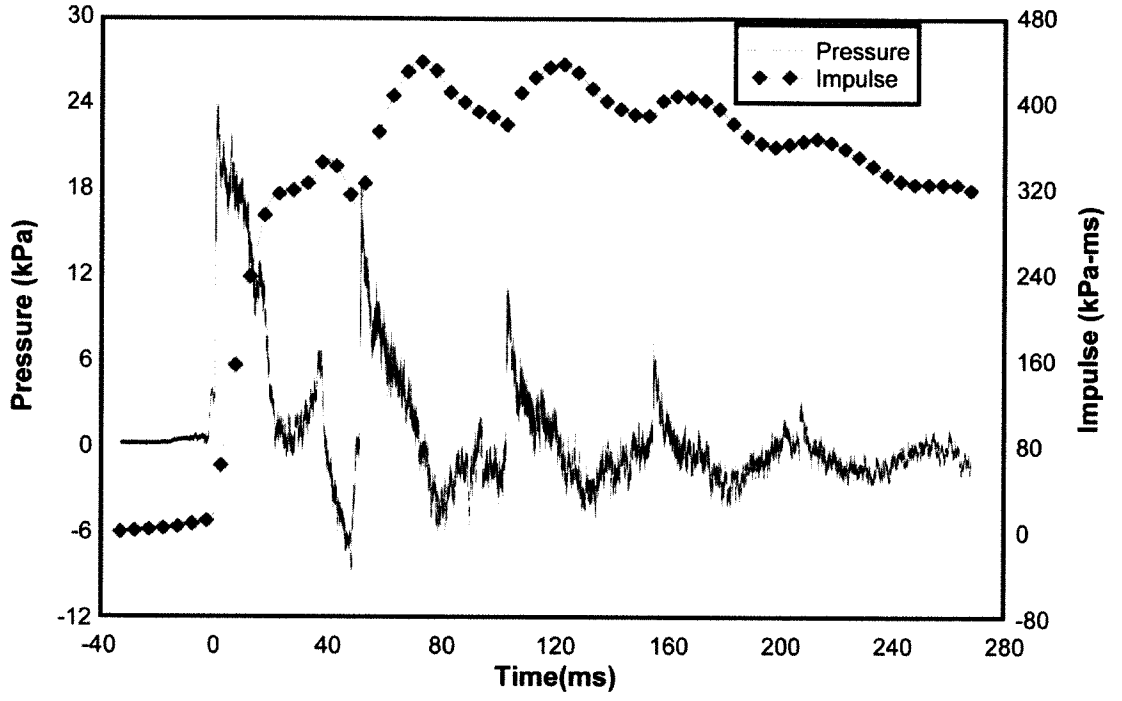


*Figure 4-6: Reflected Pressure and Impulse Time History for Test RC-2-1*

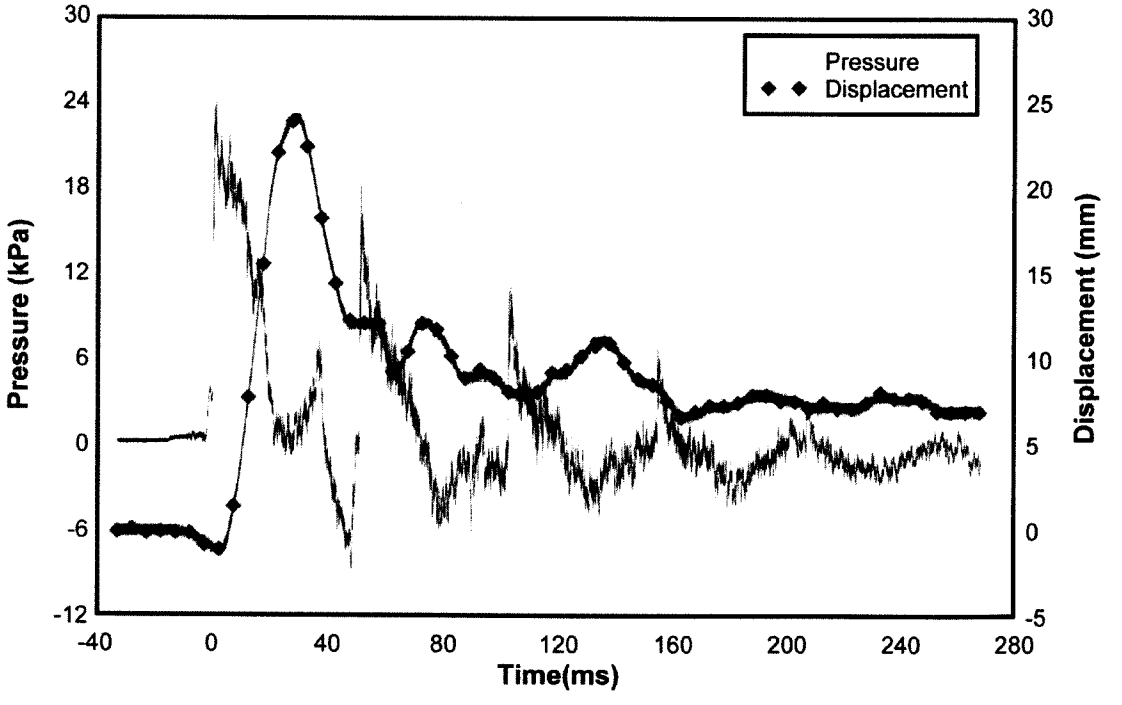


*Figure 4-7: Reflected Pressure and Mid-Height Displacement Time History for Test RC-2-1*

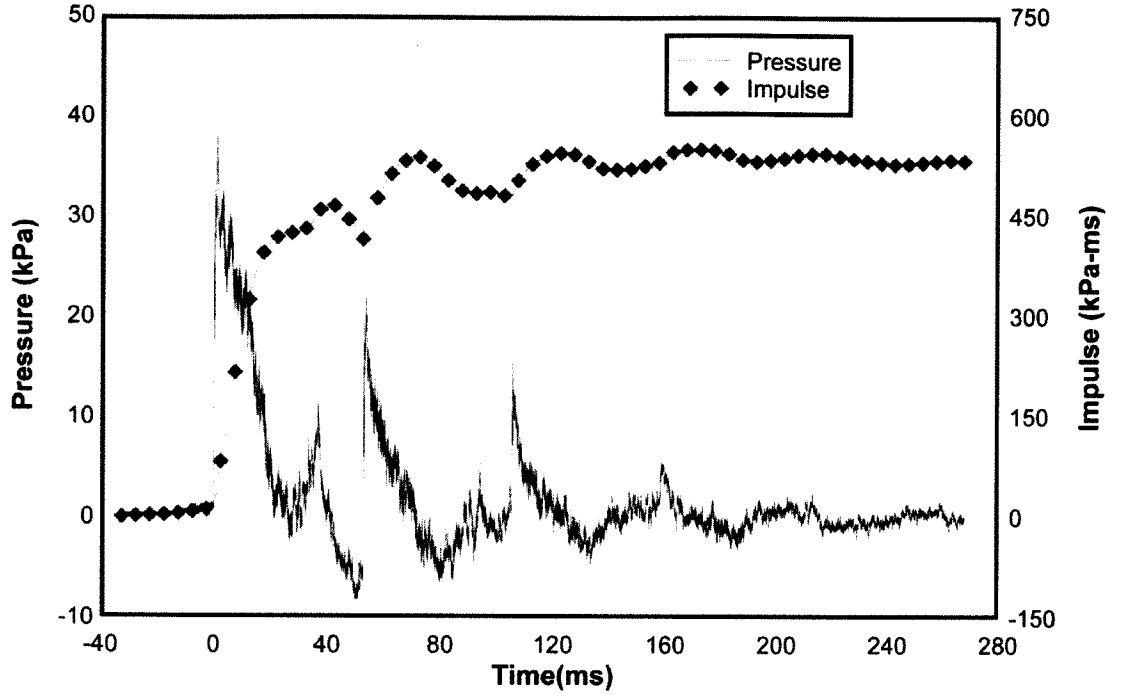


*Figure 4-8: Reflected Pressure and Impulse Time History for Test RC-2-2*

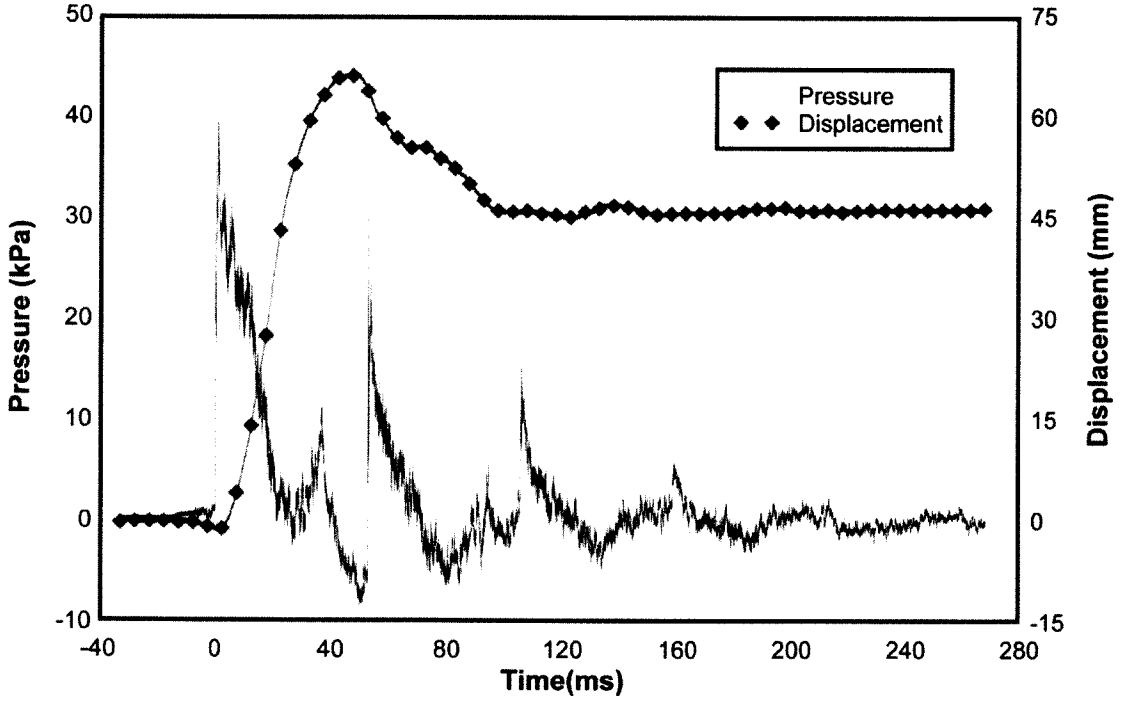


*Figure 4-9: Reflected Pressure and Mid-Height Displacement Time History for Test RC-2-2*

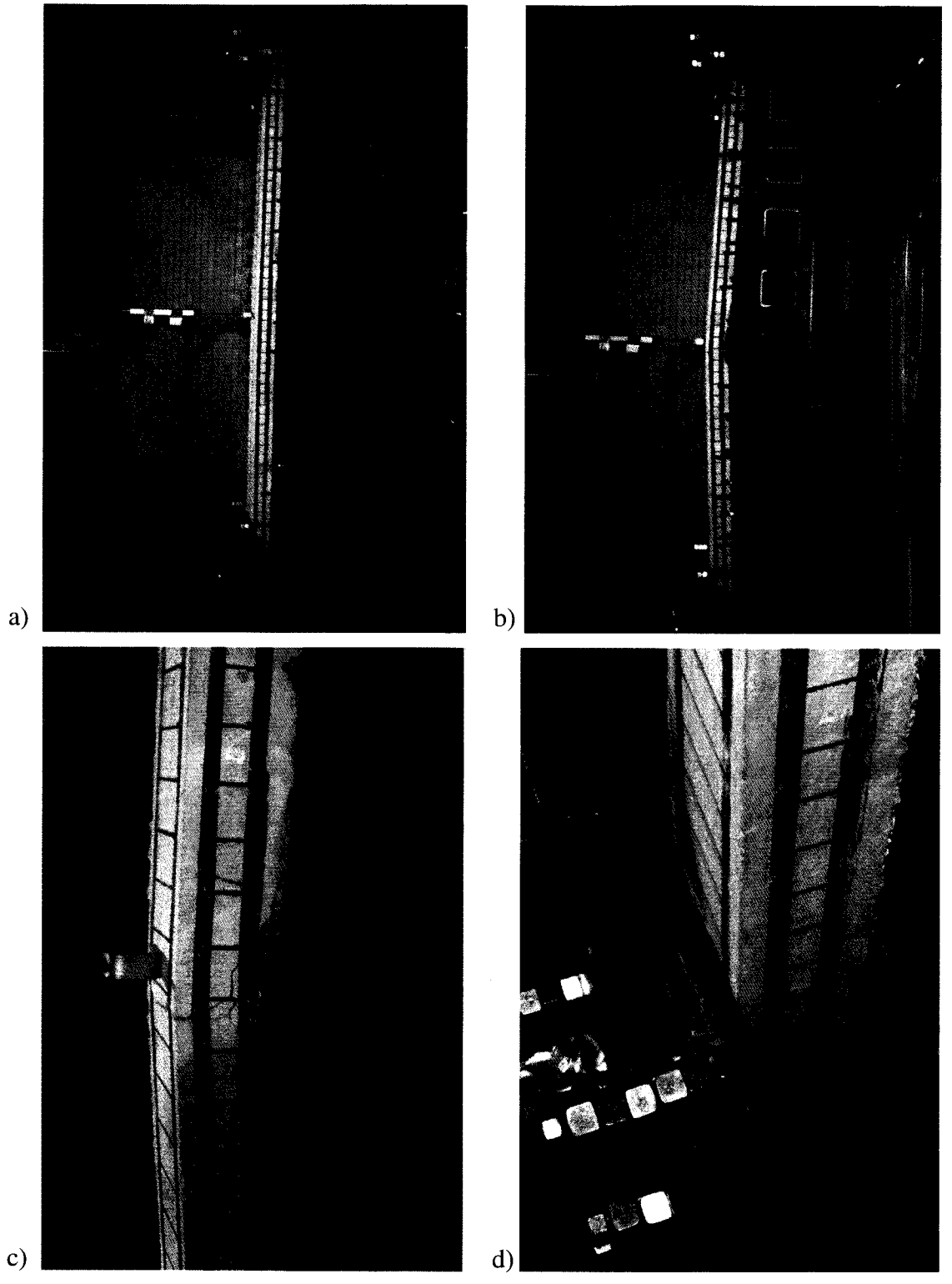


*Figure 4-10: Figure 4.10: RC-2: a) After Shot 1; b) After Shot 2; c) Mid-Height Plastic Hinge After Shot 2; d) Support After Shot 2*

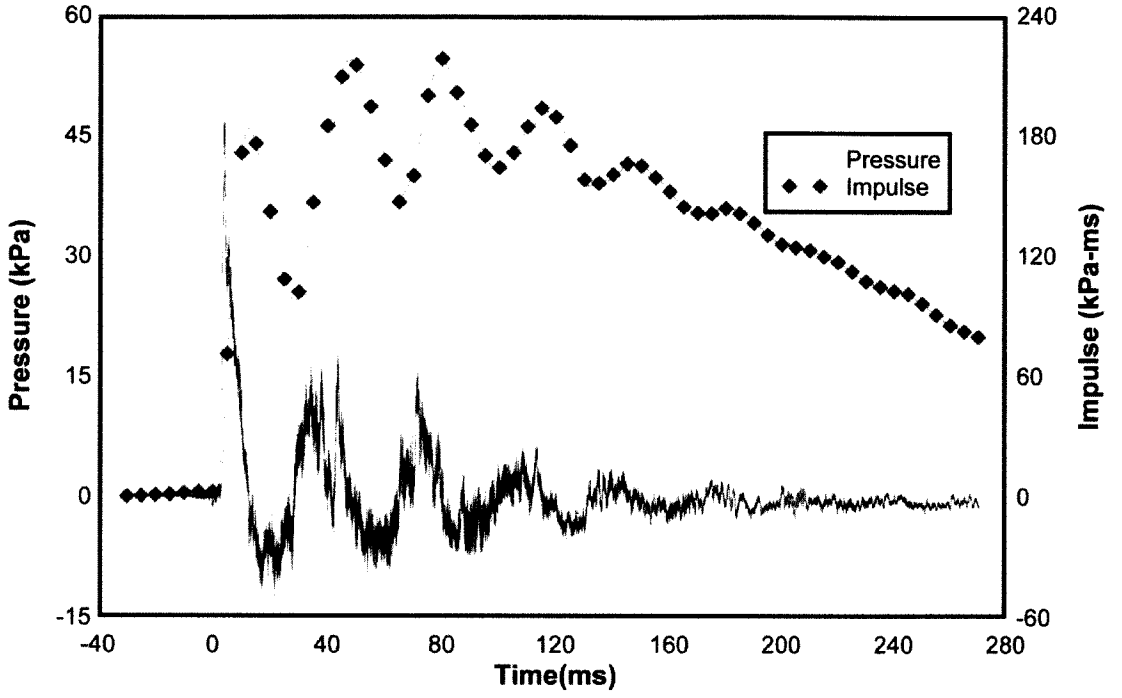


*Figure 4-11: Reflected Pressure and Impulse Time History for Test RC-3-1*

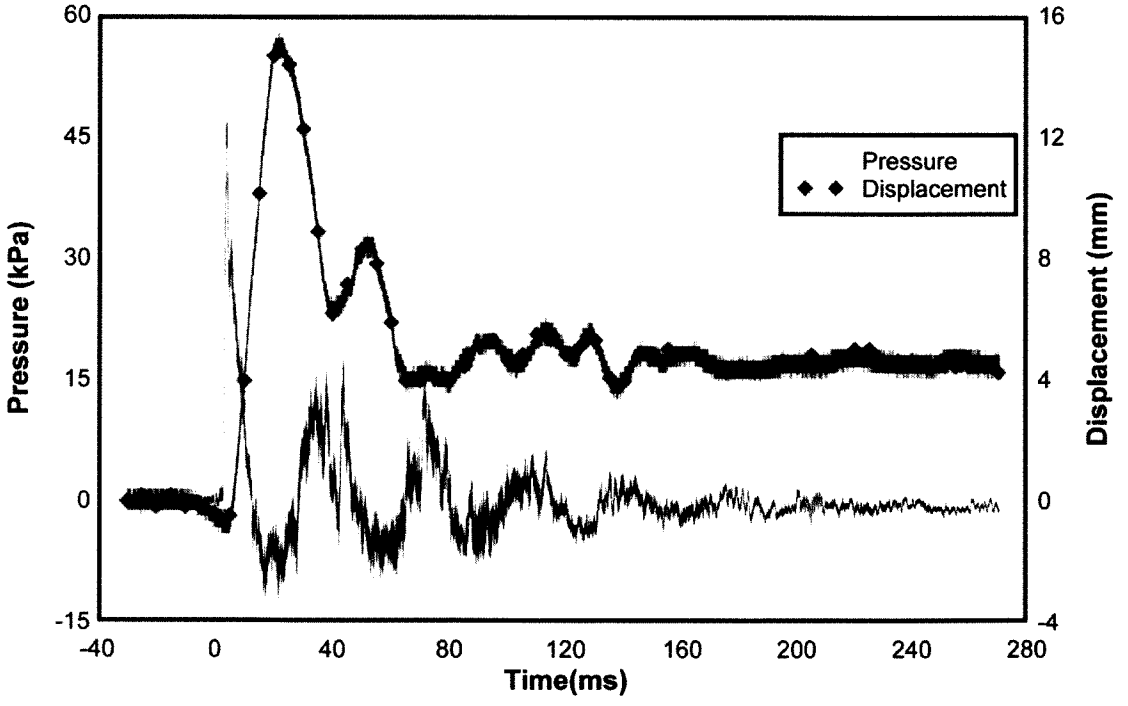


*Figure 4-12: Reflected Pressure and Mid-Height Displacement Time History for Test RC-3-1*

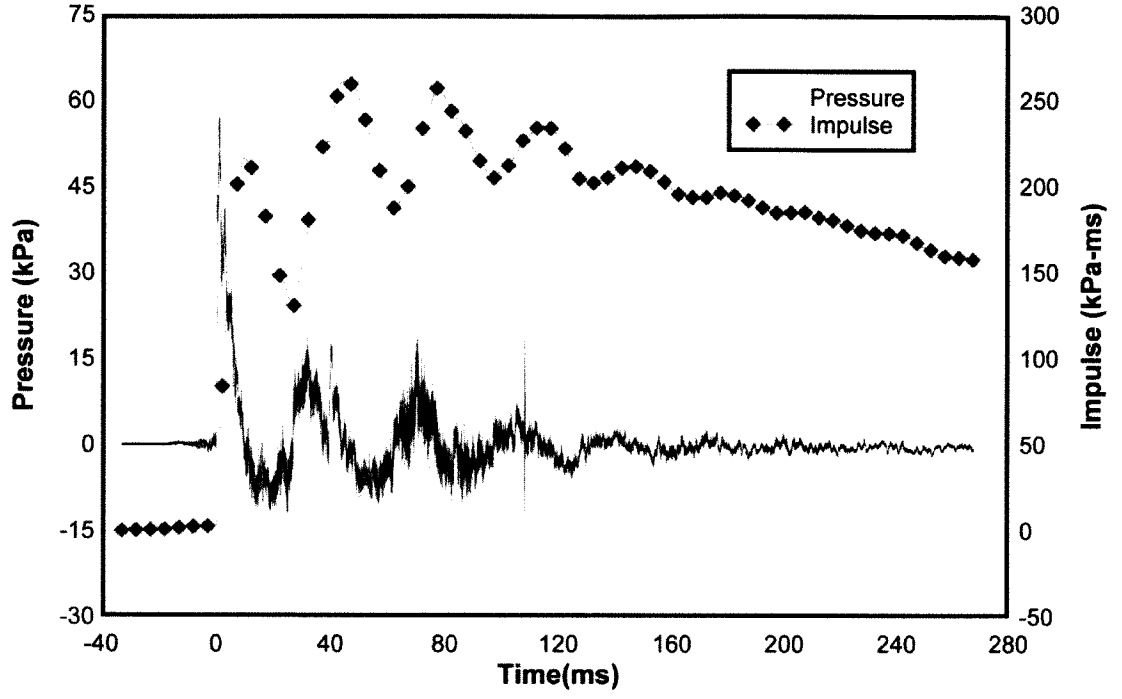


*Figure 4-13: Reflected Pressure and Impulse Time History for Test RC-3-2*

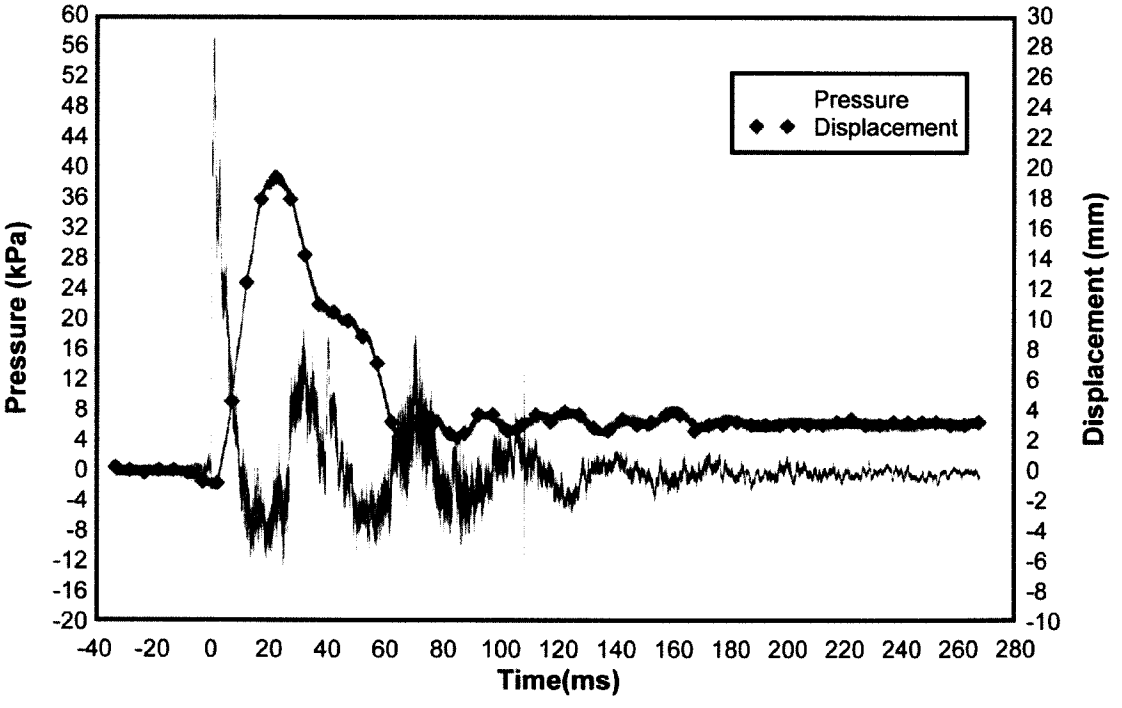


*Figure 4-14: Reflected Pressure and Mid-Height Displacement Time History for Test RC-3-2*

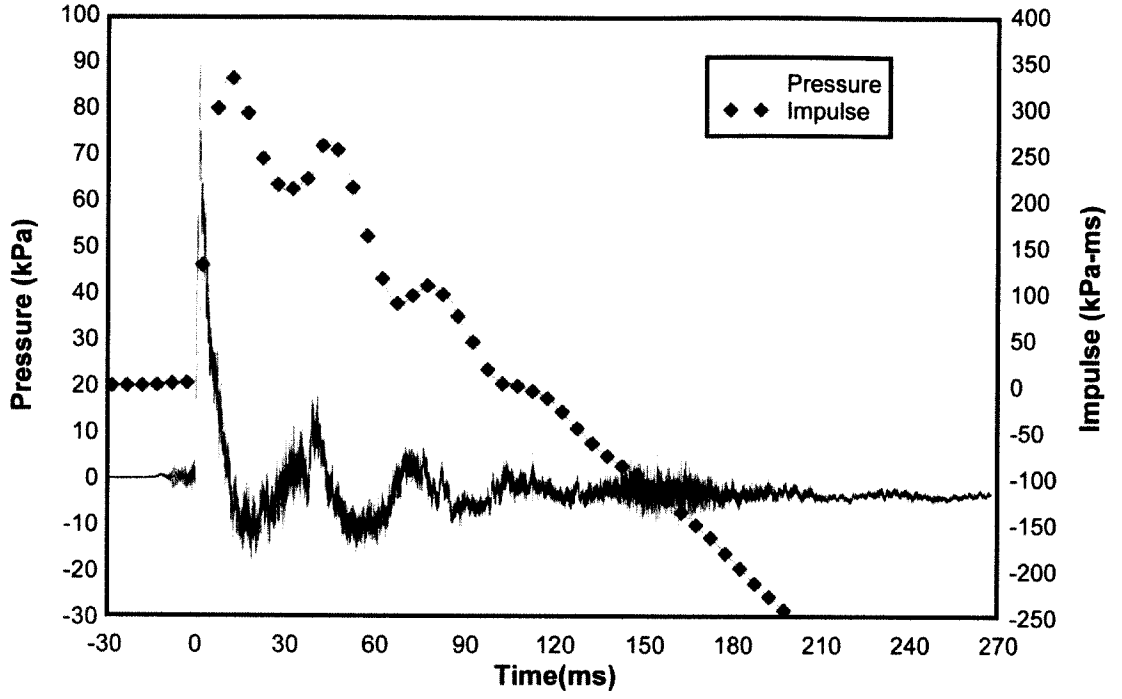


*Figure 4-15: Reflected Pressure and Impulse Time History for Test RC-3-3*

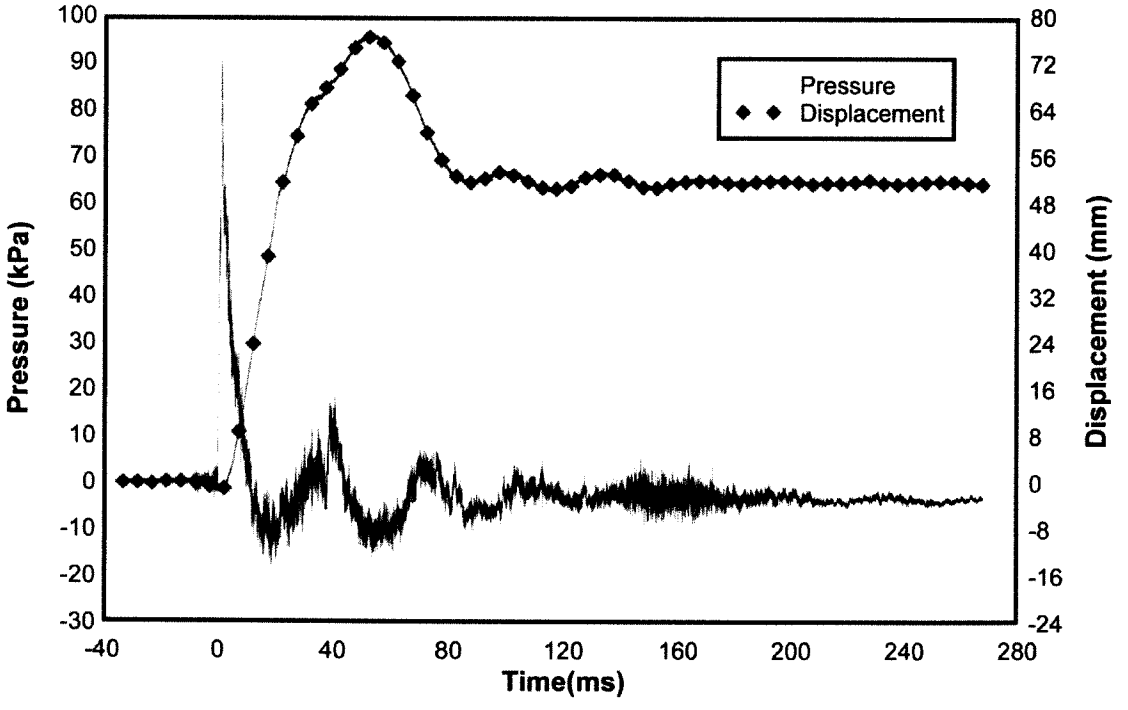


*Figure 4-16: Reflected Pressure and Mid-Height Displacement Time History for Test RC-3-3*

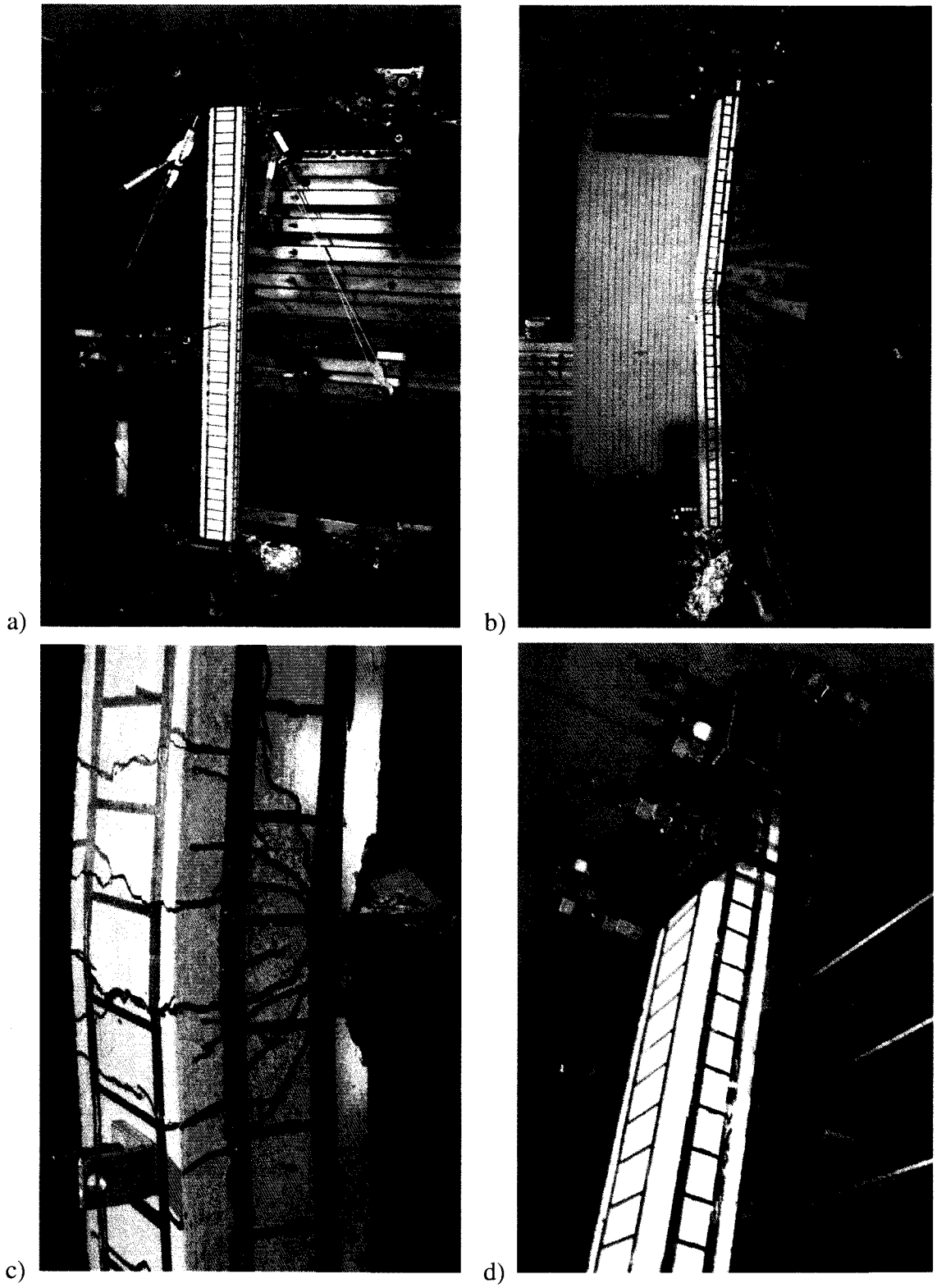


*Figure 4-17: RC-3: a) After Shot 2; b) After Shot 3; c) Mid-Height Plastic Hinge After Shot 3; d) Support Plastic Hinge After Shot 3*

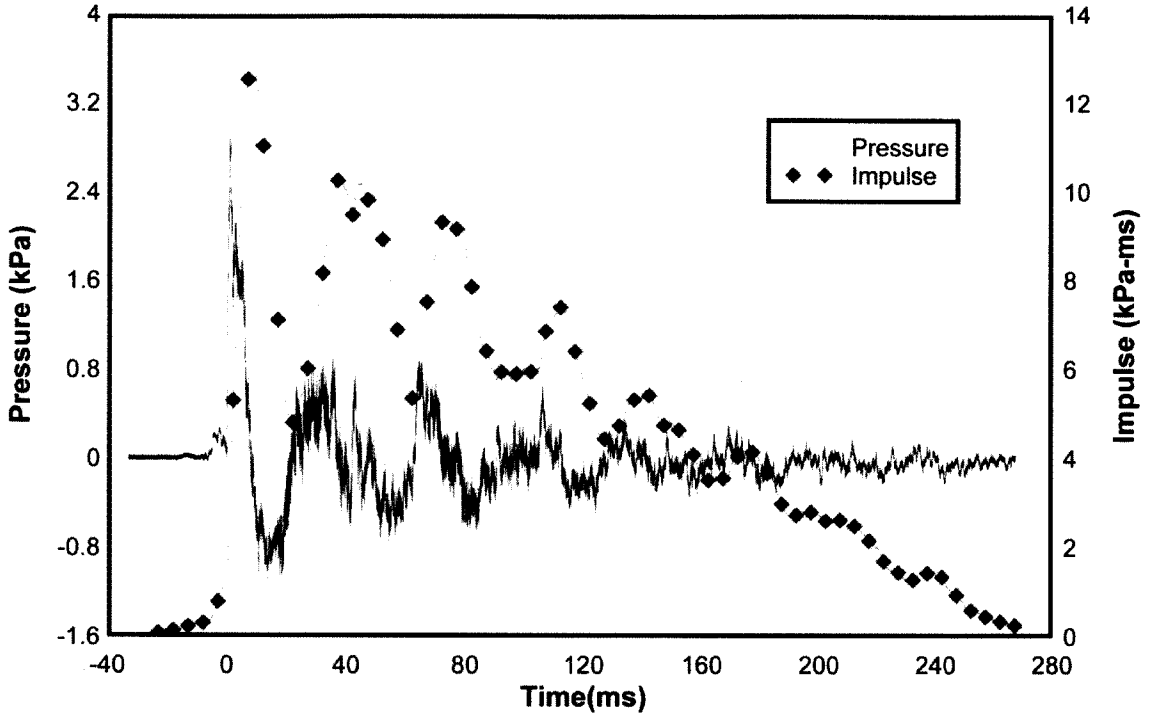


*Figure 4-18: Reflected Pressure and Impulse Time History for Test RC-4-1*

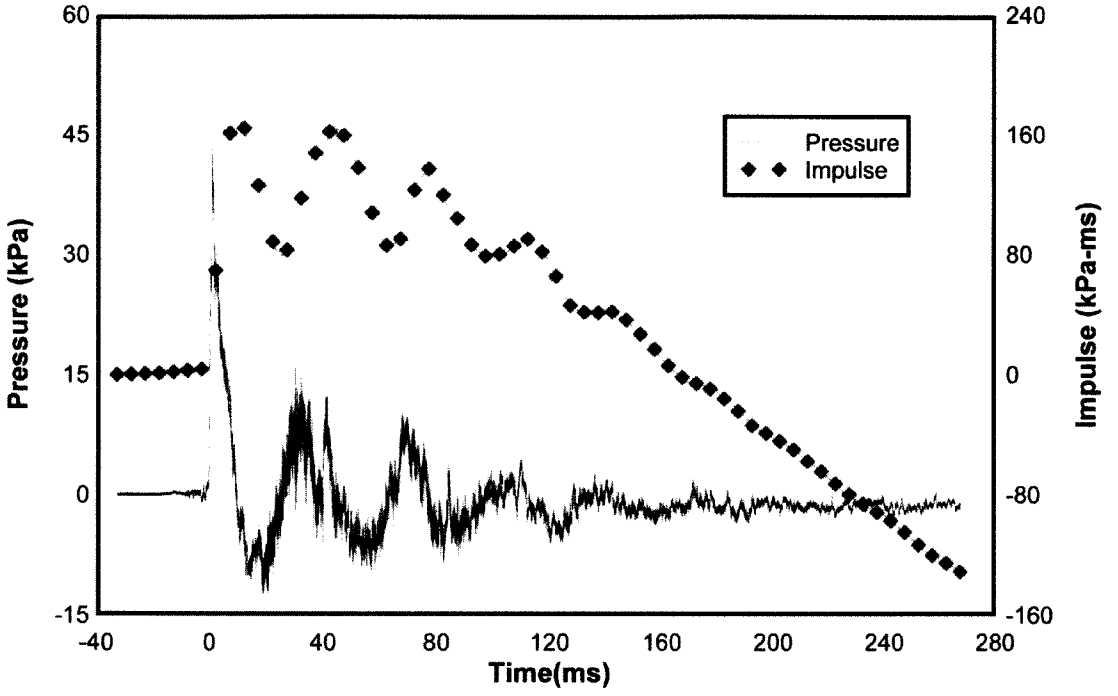


*Figure 4-19: Reflected Pressure and Impulse Time History for Test RC-4-2*

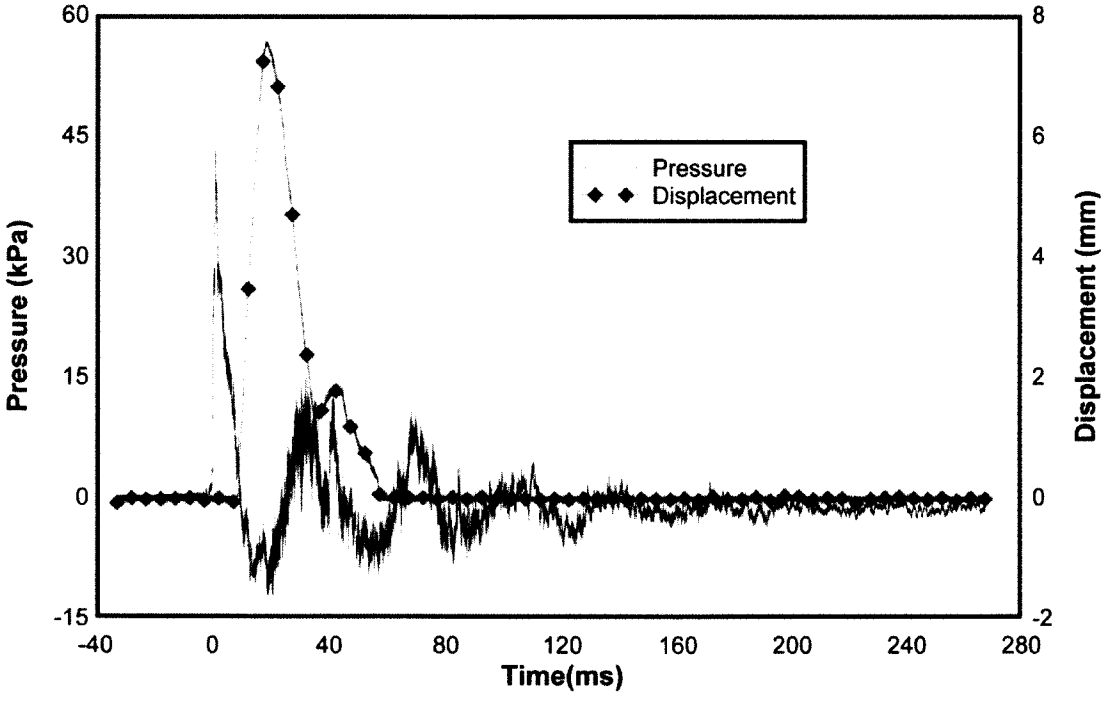


*Figure 4-20: Reflected Pressure and Mid-Height Displacement Time History for Test RC-4-2*

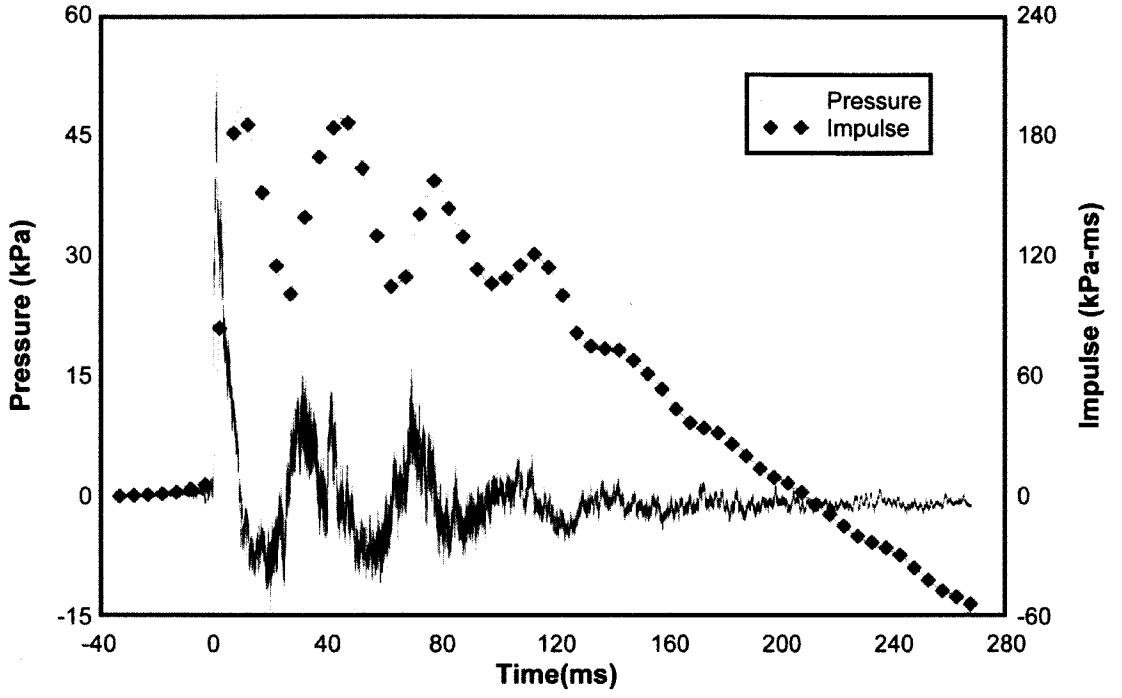


*Figure 4-21: Reflected Pressure and Impulse Time History for Test RC-4-3*

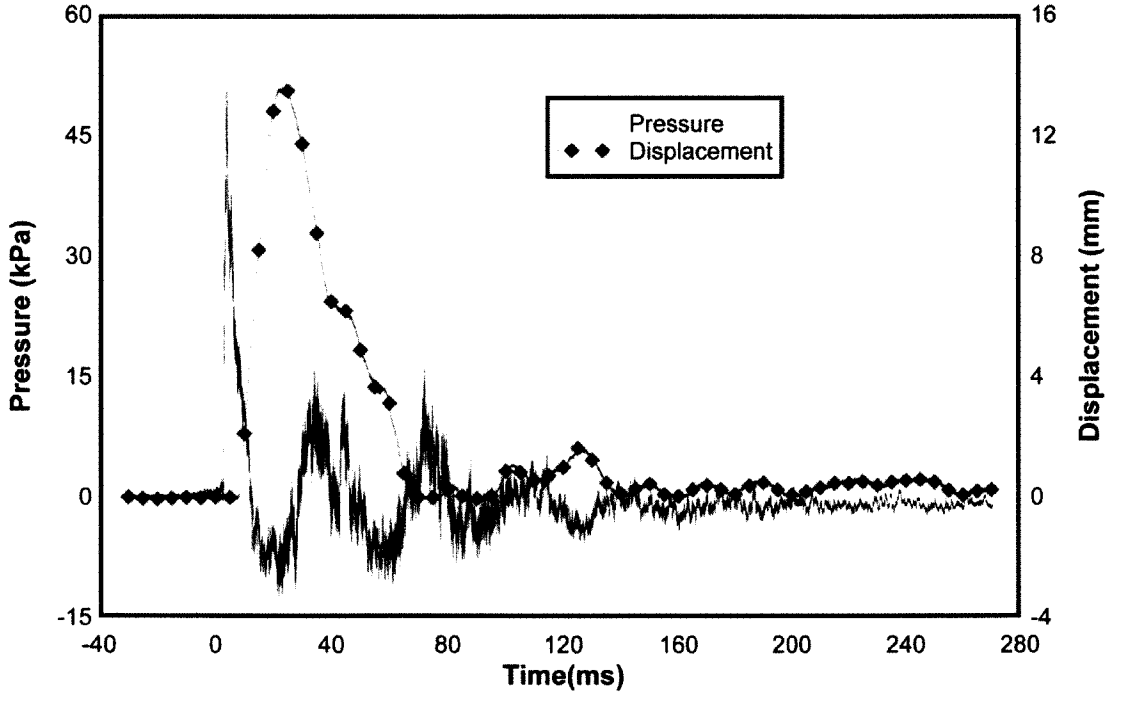


*Figure 4-22: Reflected Pressure and Mid-Height Displacement Time History for Test RC-4-3*

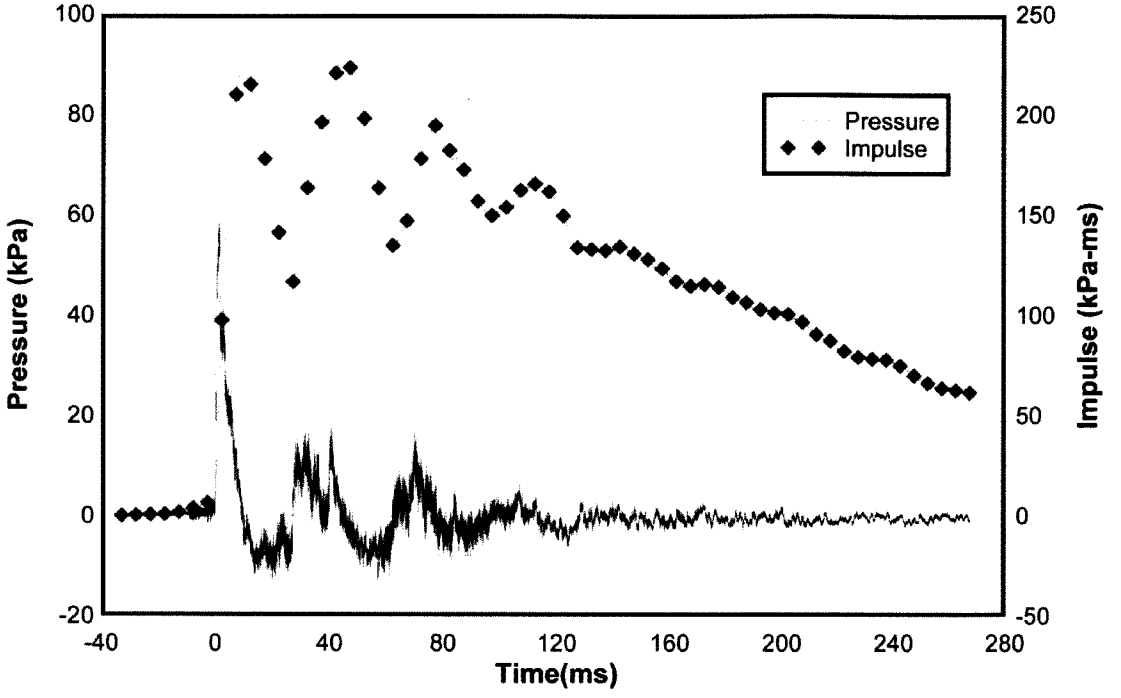


*Figure 4-23: Reflected Pressure and Impulse Time History for Test RC-4-4*

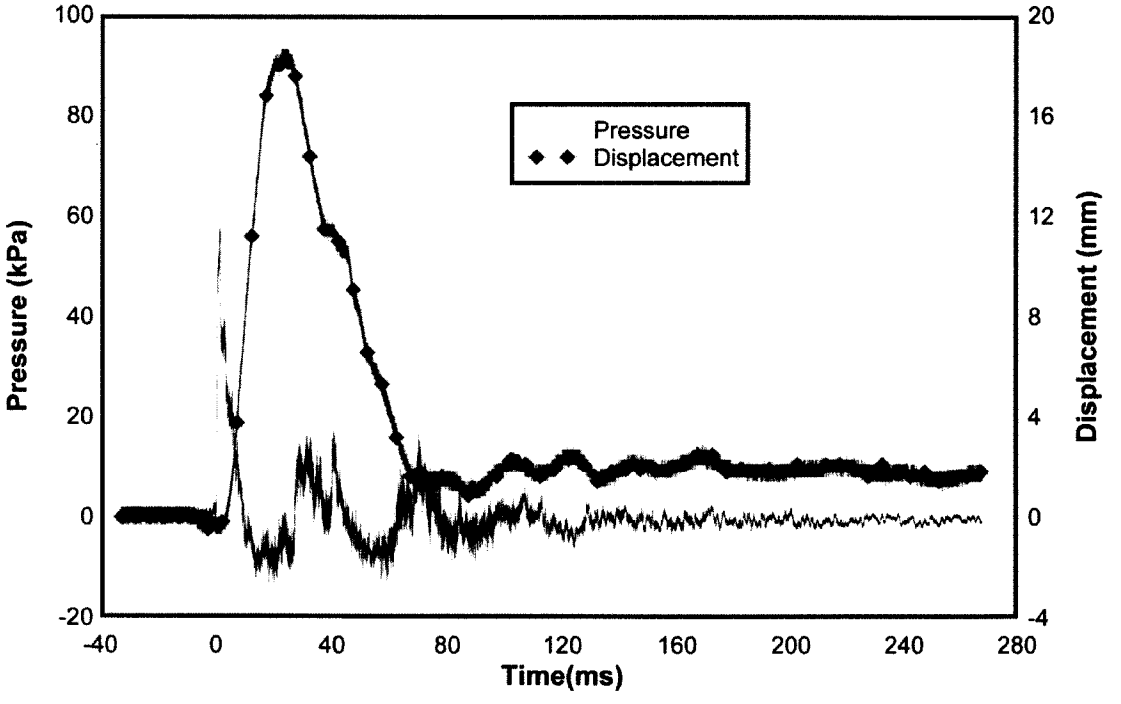


*Figure 4-24: Reflected Pressure and Mid-Height Displacement Time History for Test RC-4-4*

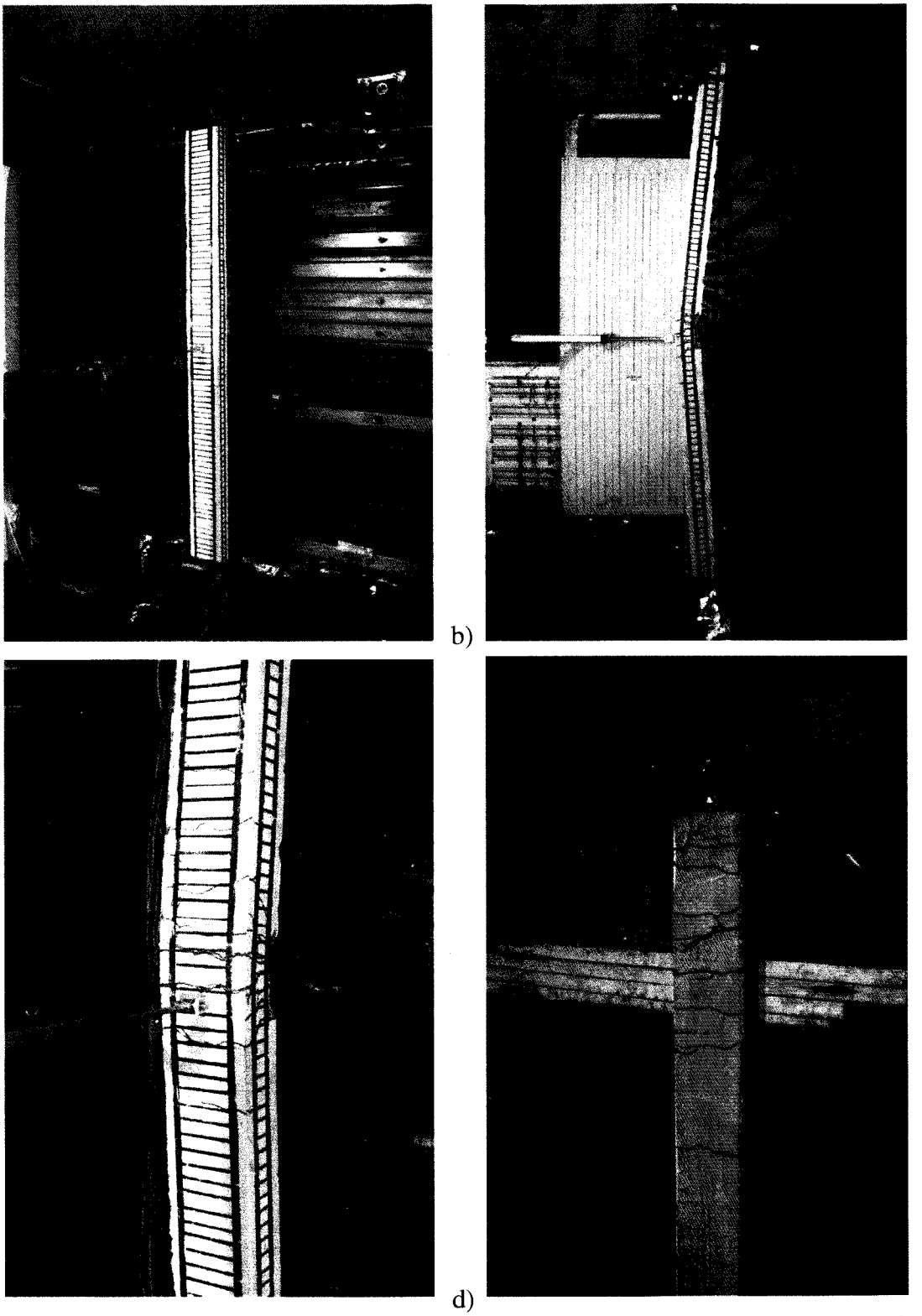

*Figure 4-25: RC-4: a) After Shot 4; b) After Shot 5; c) Mid-Height Plastic Hinge After Shot 5; d) Support Tension Cracks After Shot 5*

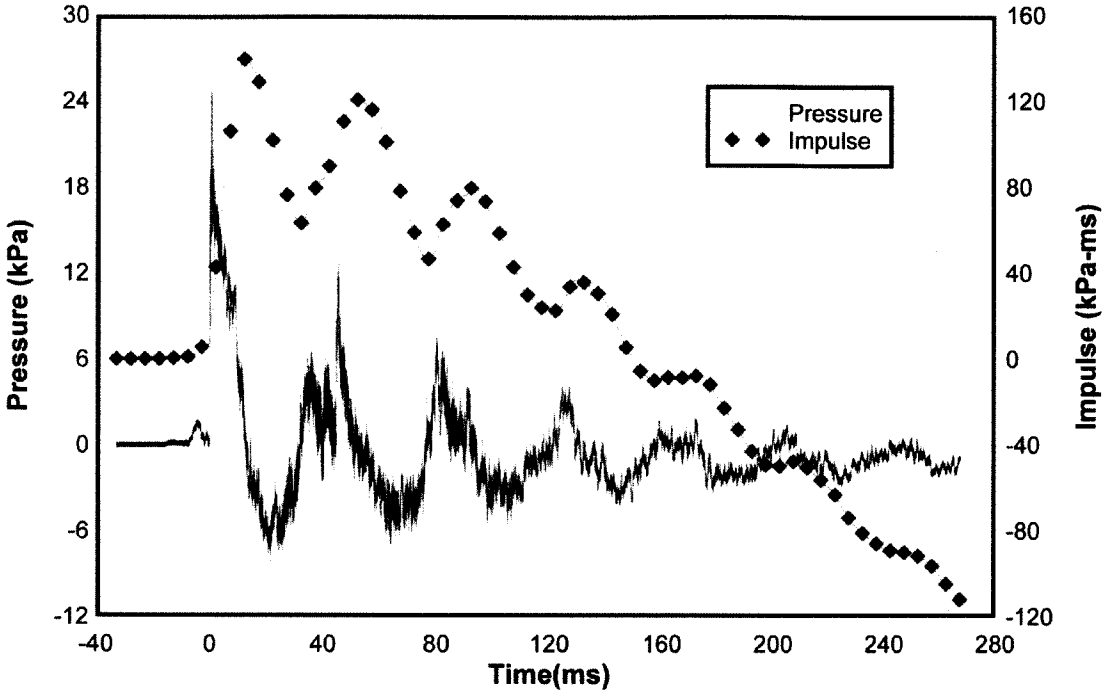


*Figure 4-26: Reflected Pressure and Impulse Time History for Test RC-5-1*

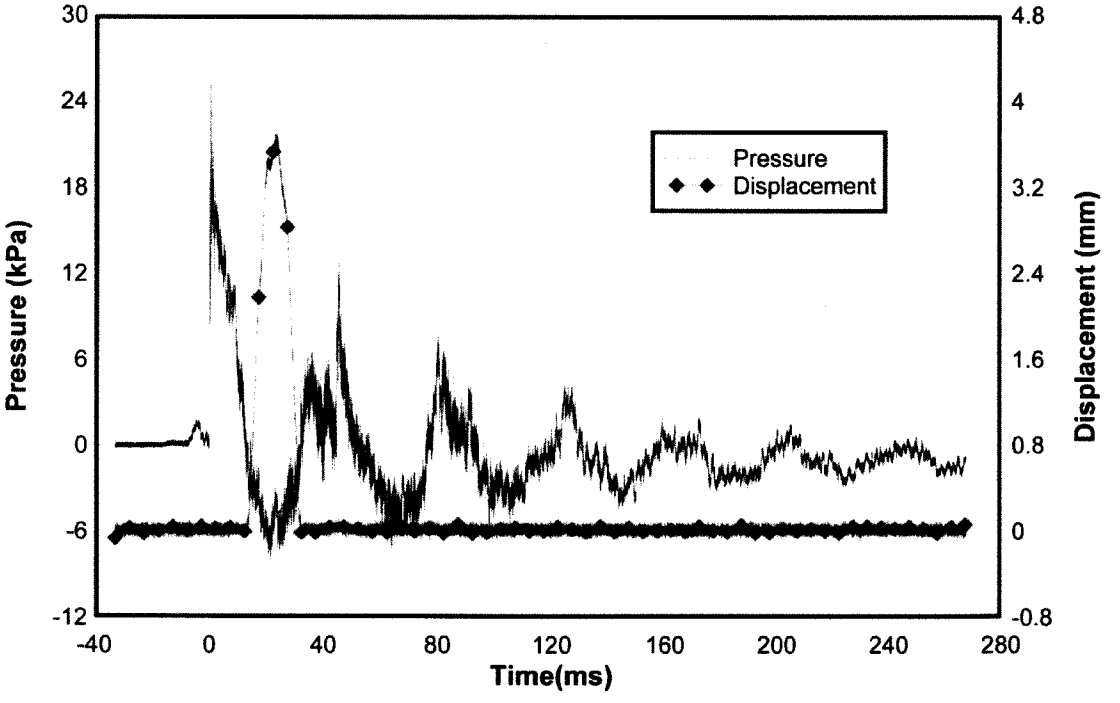


*Figure 4-27: Reflected Pressure and Mid-Height Displacement Time History for Test RC-5-1*

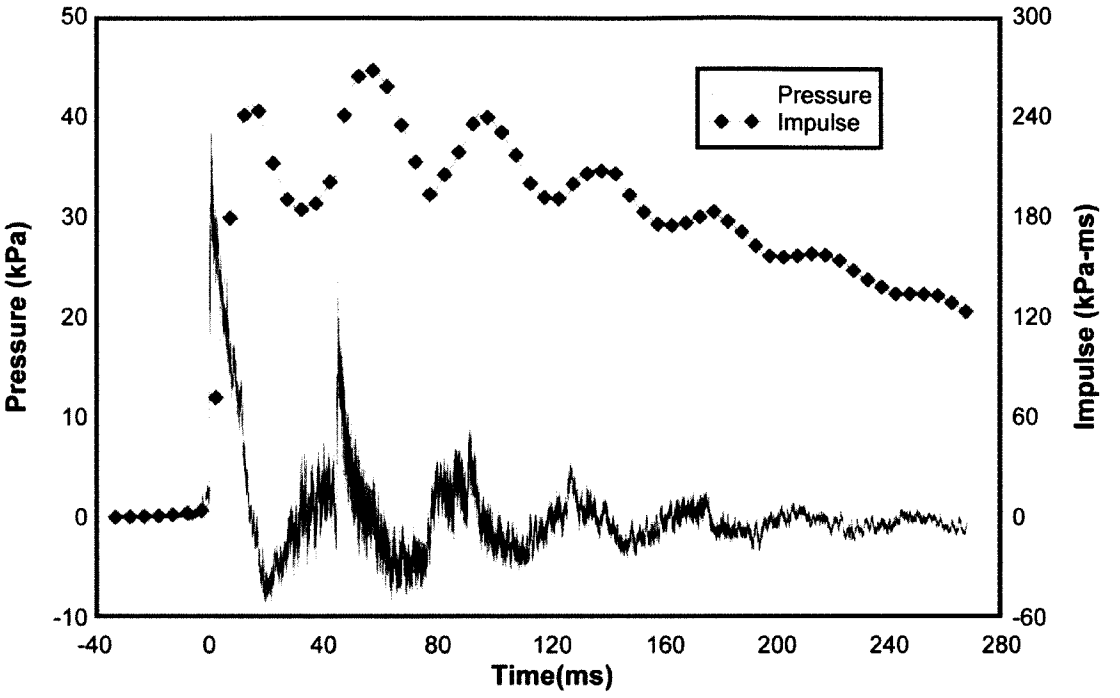


*Figure 4-28: Reflected Pressure and Impulse Time History for Test RC-5-2*

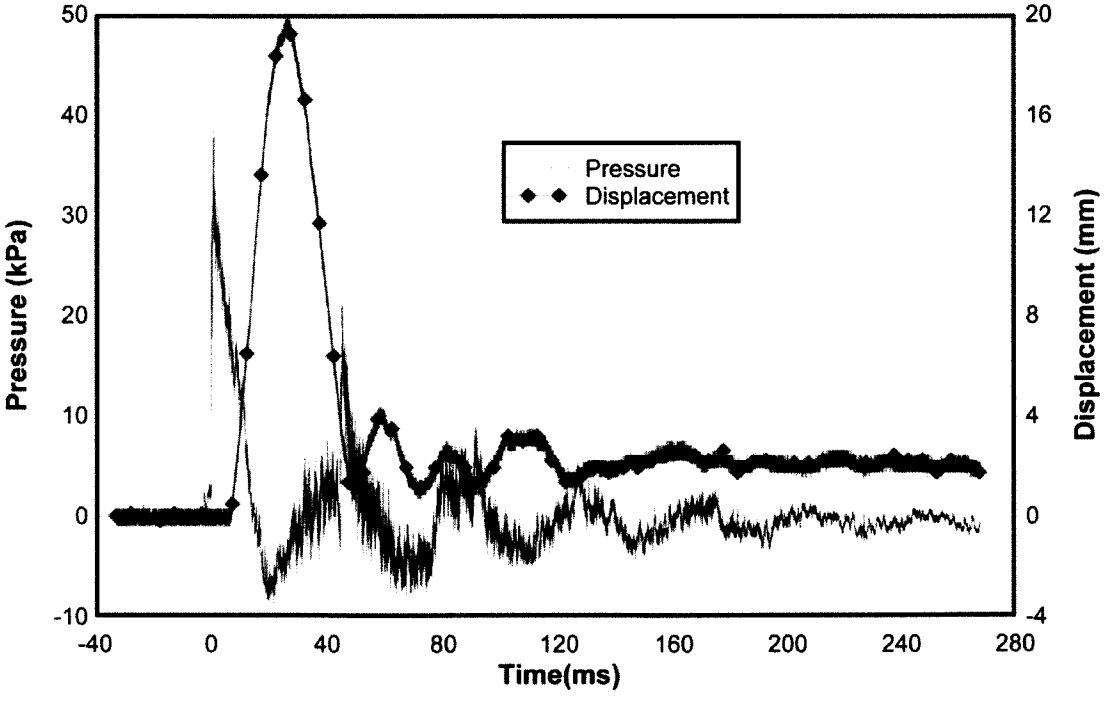


*Figure 4-29: Reflected Pressure and Mid-Height Displacement Time History for Test RC-5-2*

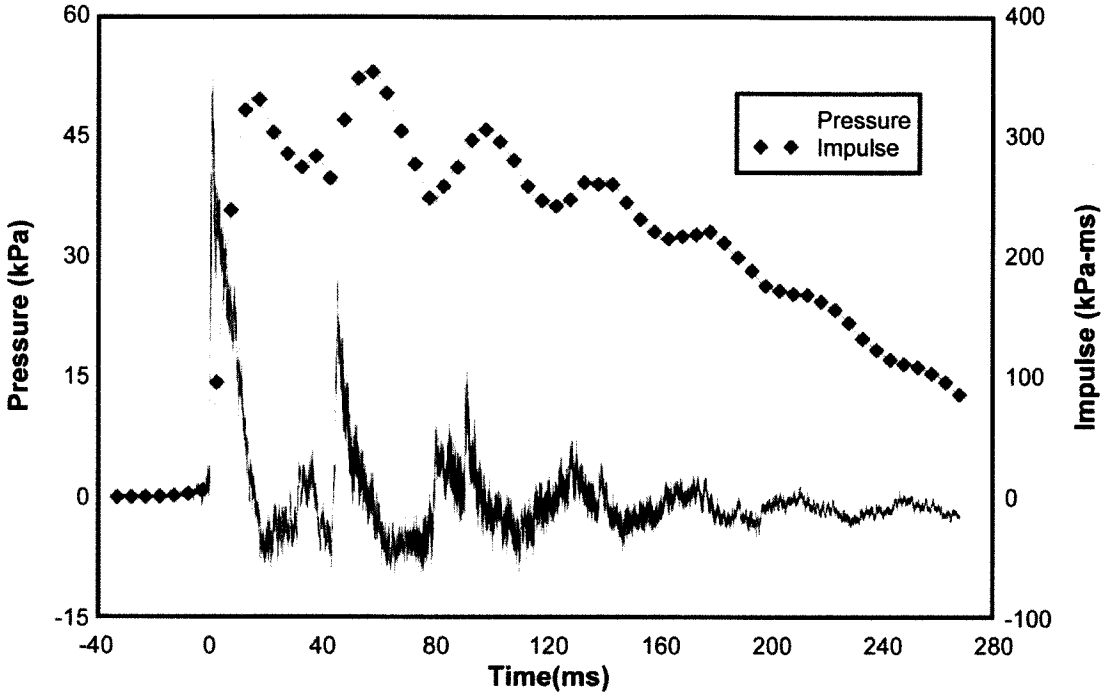


*Figure 4-30: Reflected Pressure and Impulse Time History for Test RC-5-3*

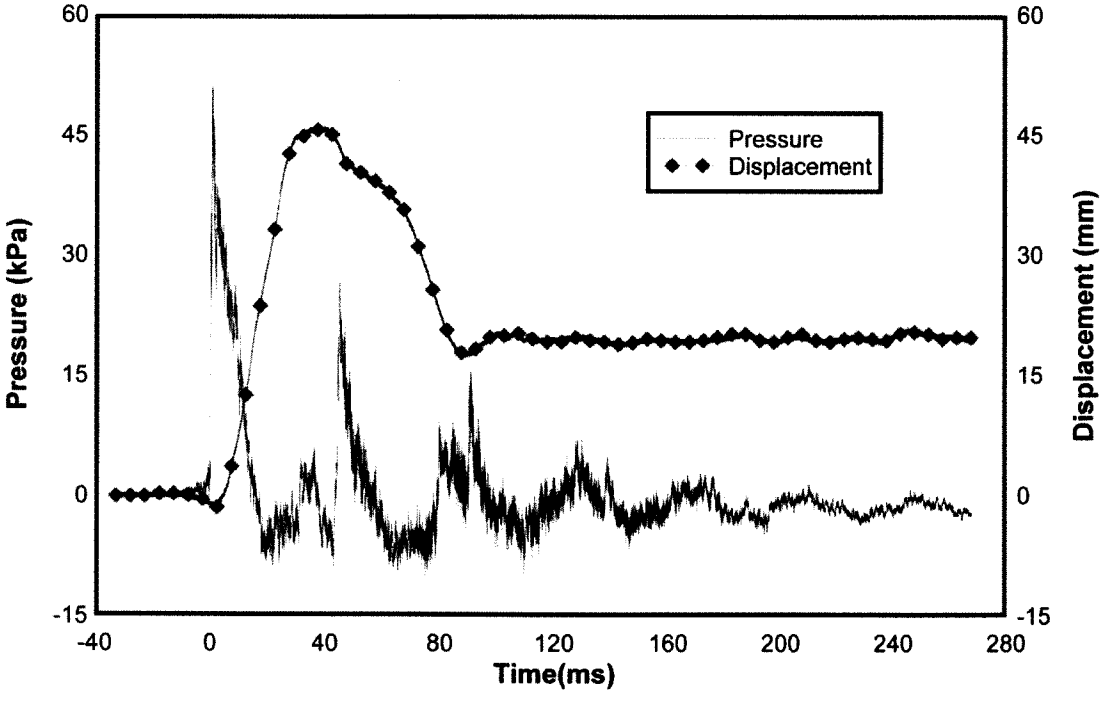


*Figure 4-31: Reflected Pressure and Mid-Height Displacement Time History for Test RC-5-3*

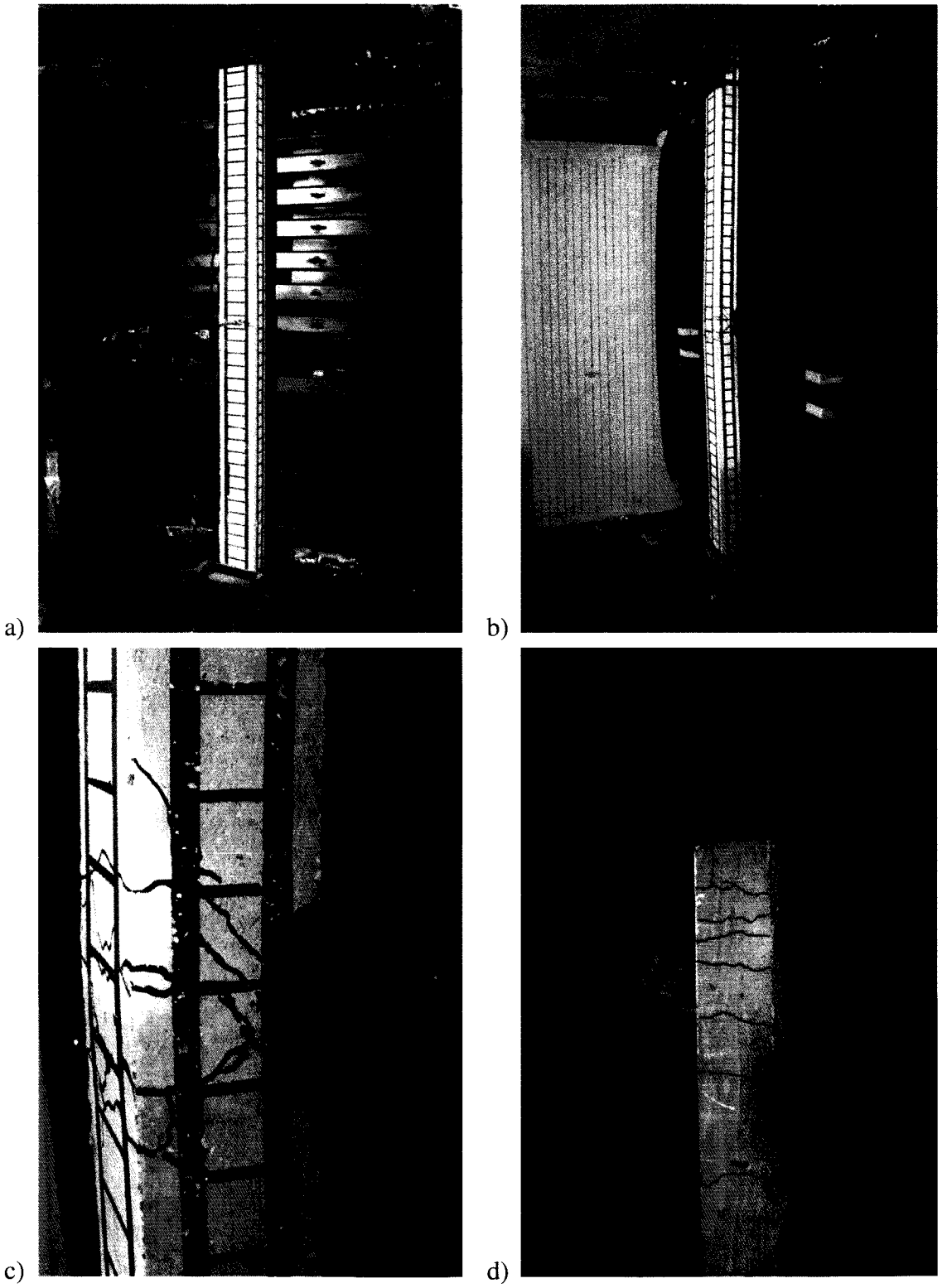

*Figure 4-32: RC-5: a) After Shot 2; b) After Shot 3; c) Mid-Height Plastic Hinge After Shot 3; d) Support Tension Cracks After Shot 3*

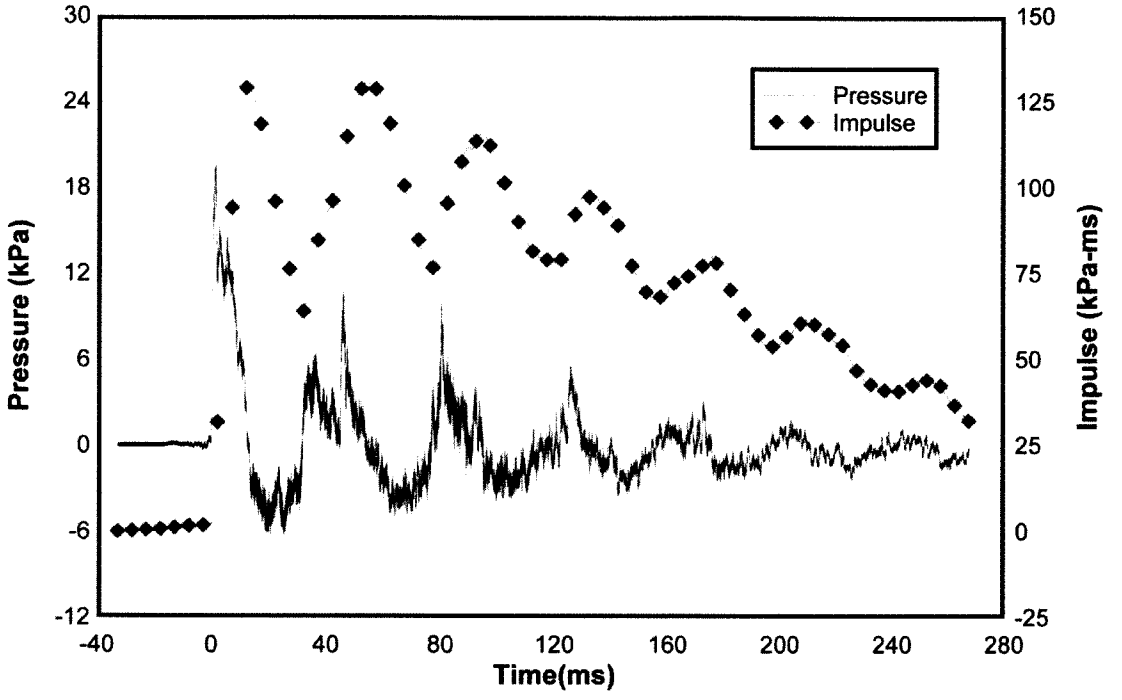


*Figure 4-33: Reflected Pressure and Impulse Time History for Test RC-6-1*

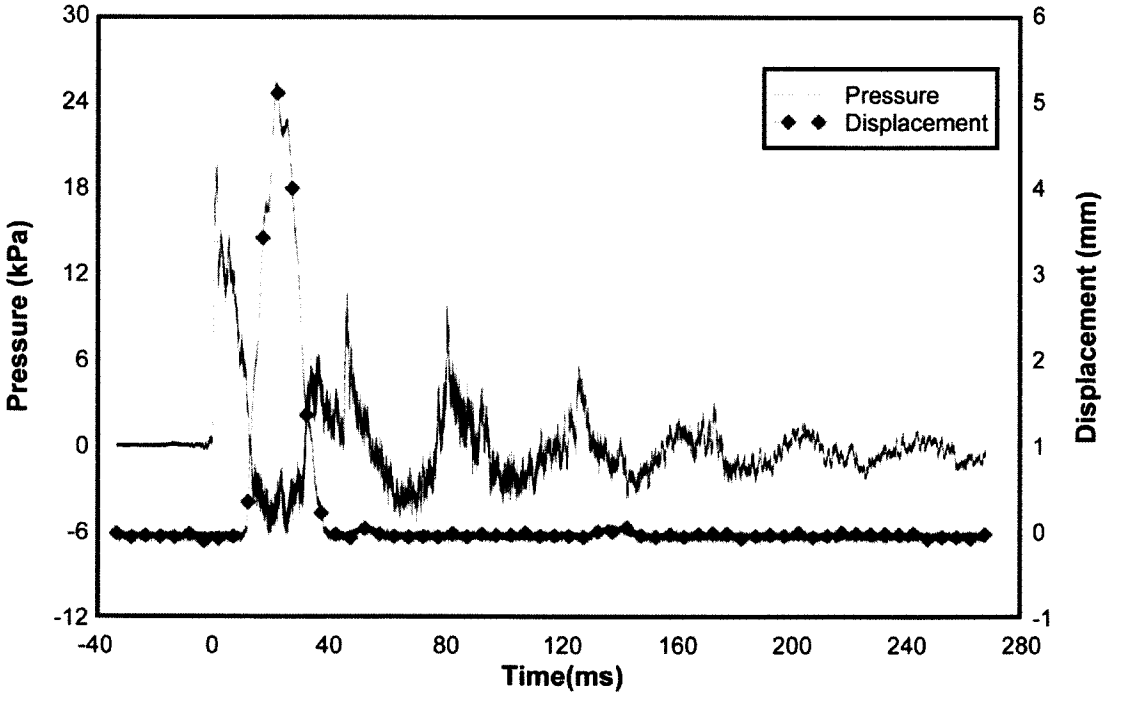


*Figure 4-34: Reflected Pressure and Mid-Height Displacement Time History for Test RC-6-1*

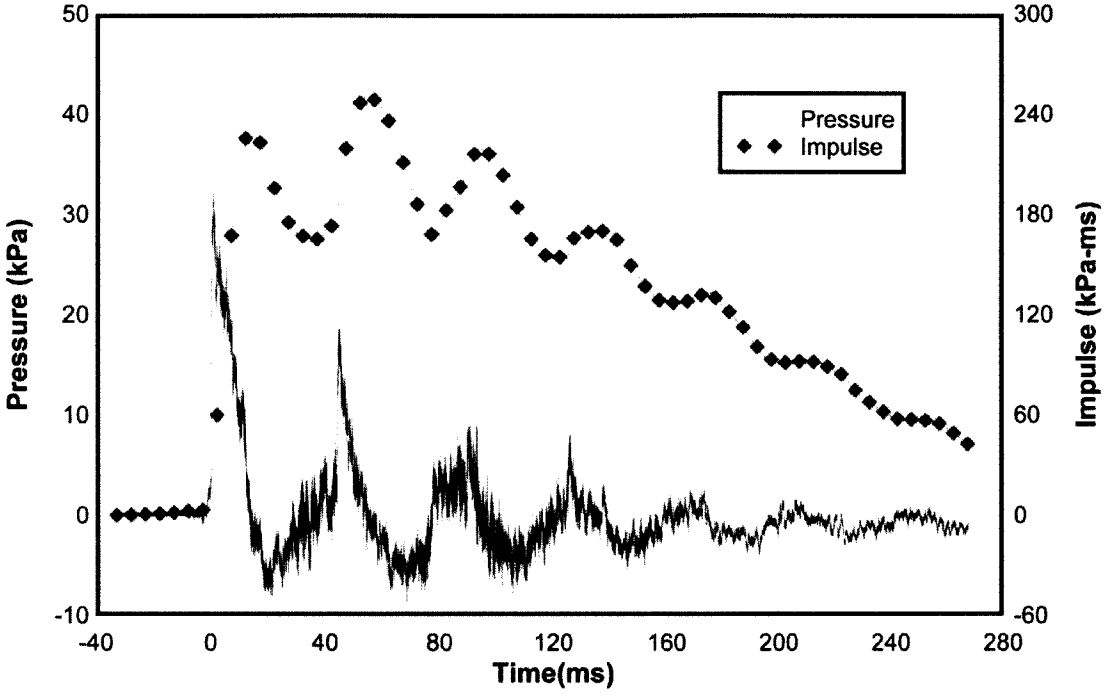


*Figure 4-35: Reflected Pressure and Impulse Time History for Test RC-6-2*

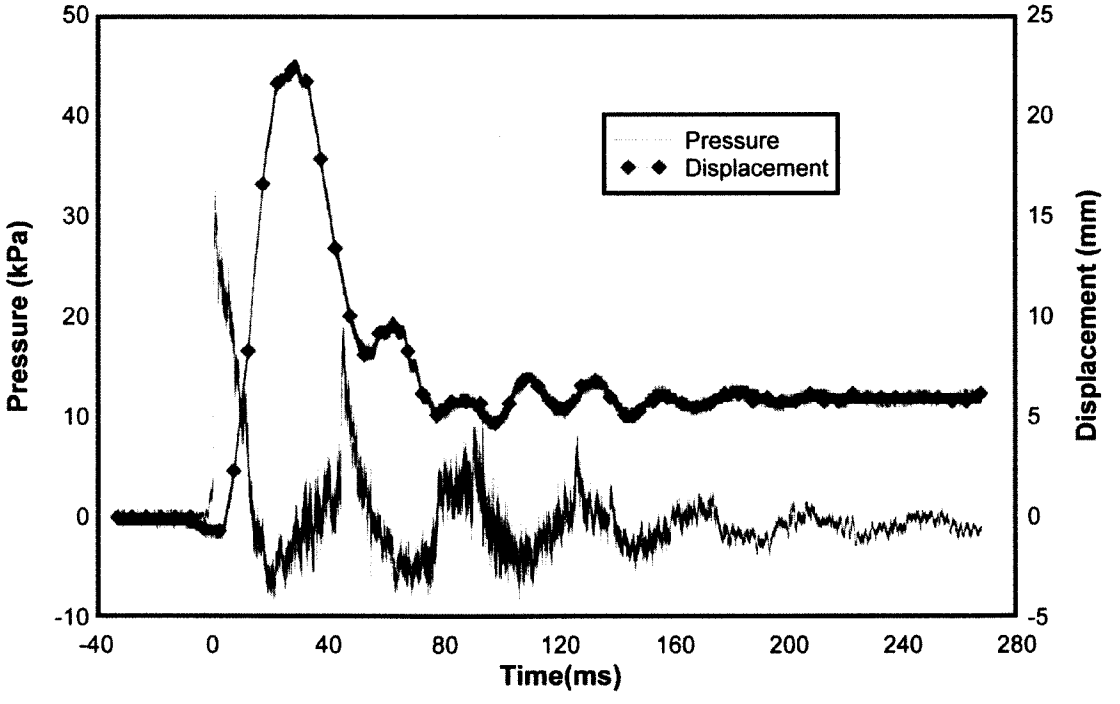


*Figure 4-36: Reflected Pressure and Mid-Height Displacement Time History for Test RC-6-2*

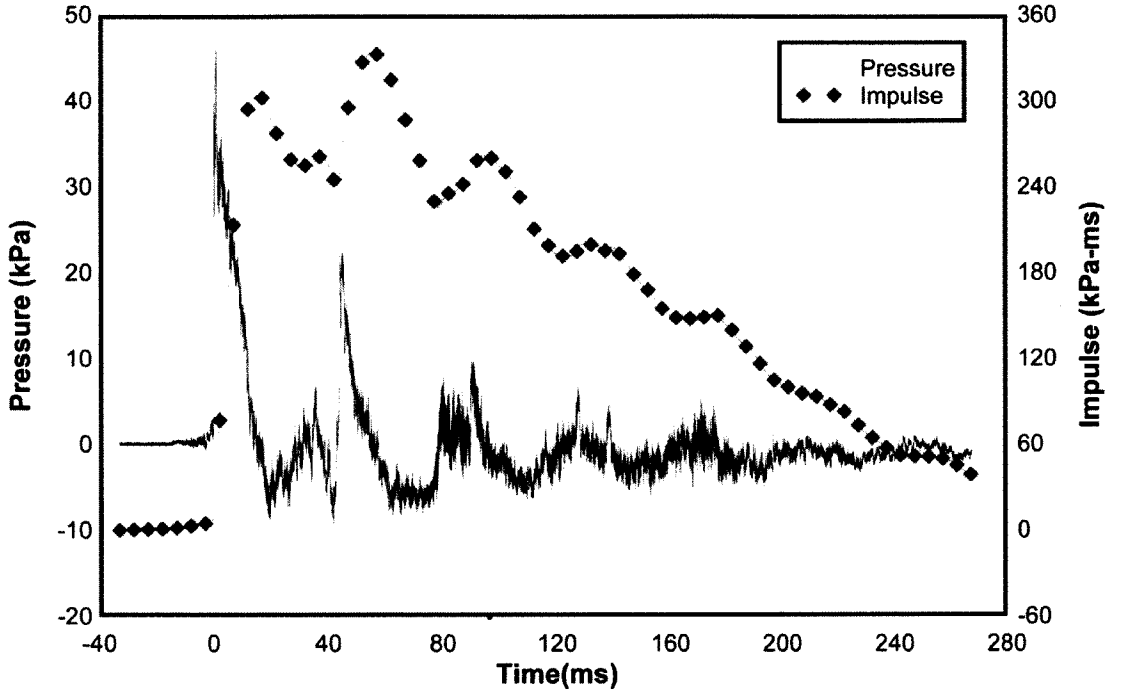


*Figure 4-37: Reflected Pressure and Impulse Time History for Test RC-6-3*

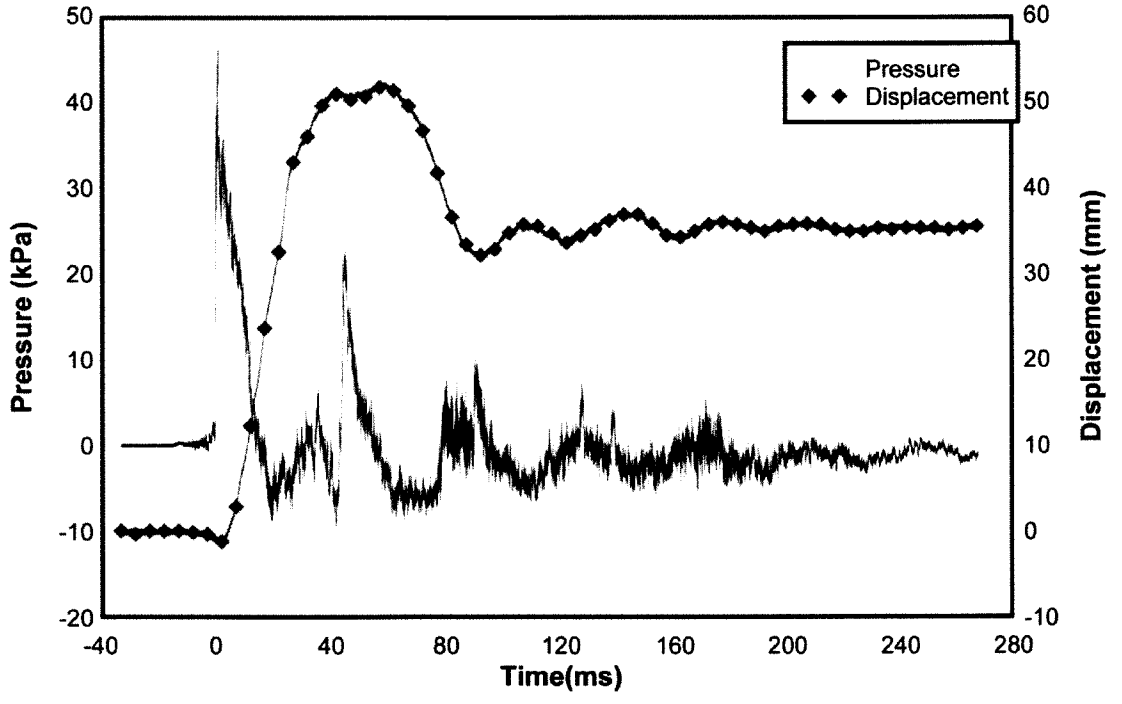


*Figure 4-38: Reflected Pressure and Mid-Height Displacement Time History for Test RC-6-3*

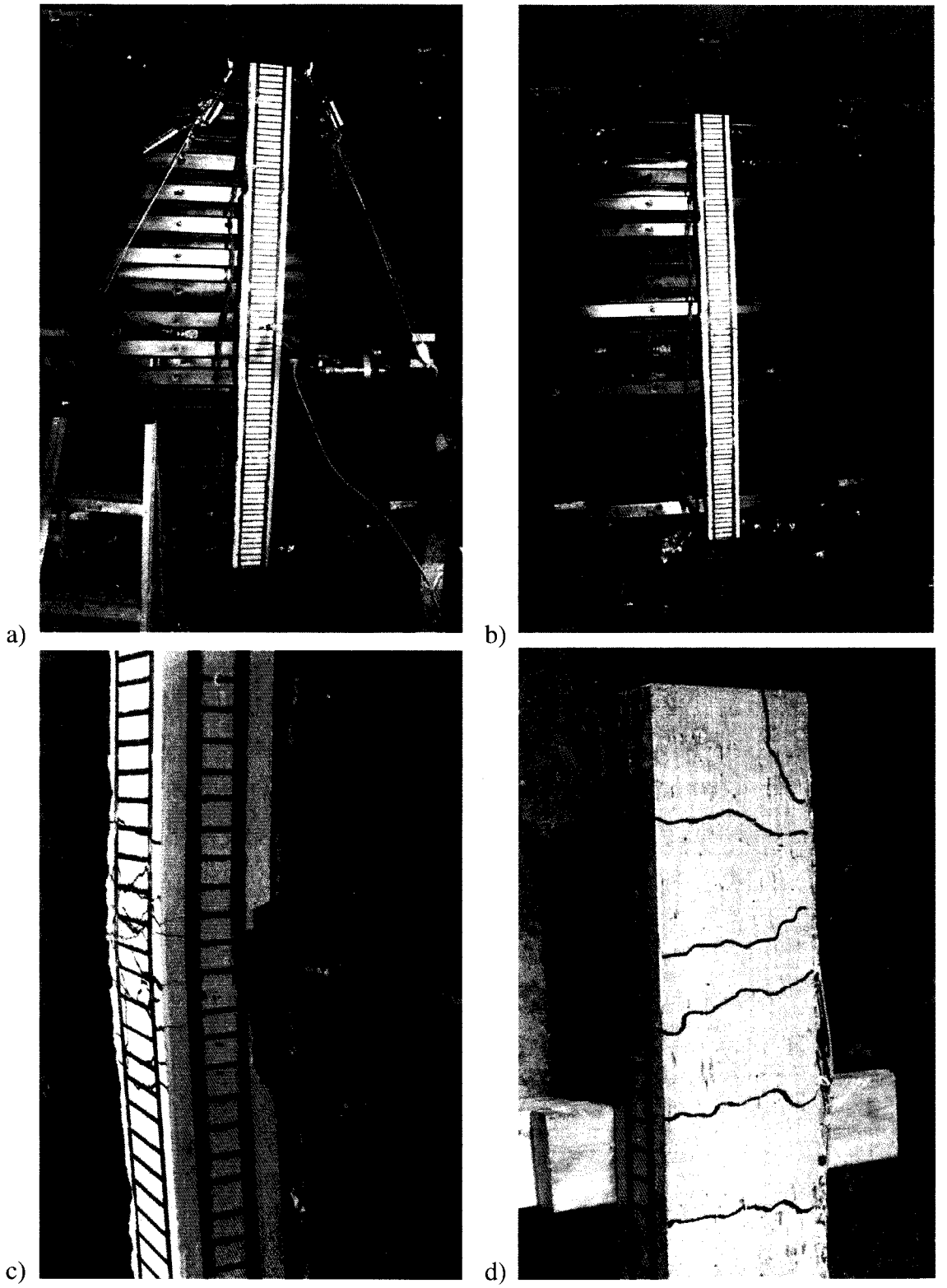


*Figure 4-39: RC-6: a) After Shot 2; b) After Shot 3; c) Mid-Height Plastic Hinge After Shot 3; d) Support Tension Cracks After Shot 3*

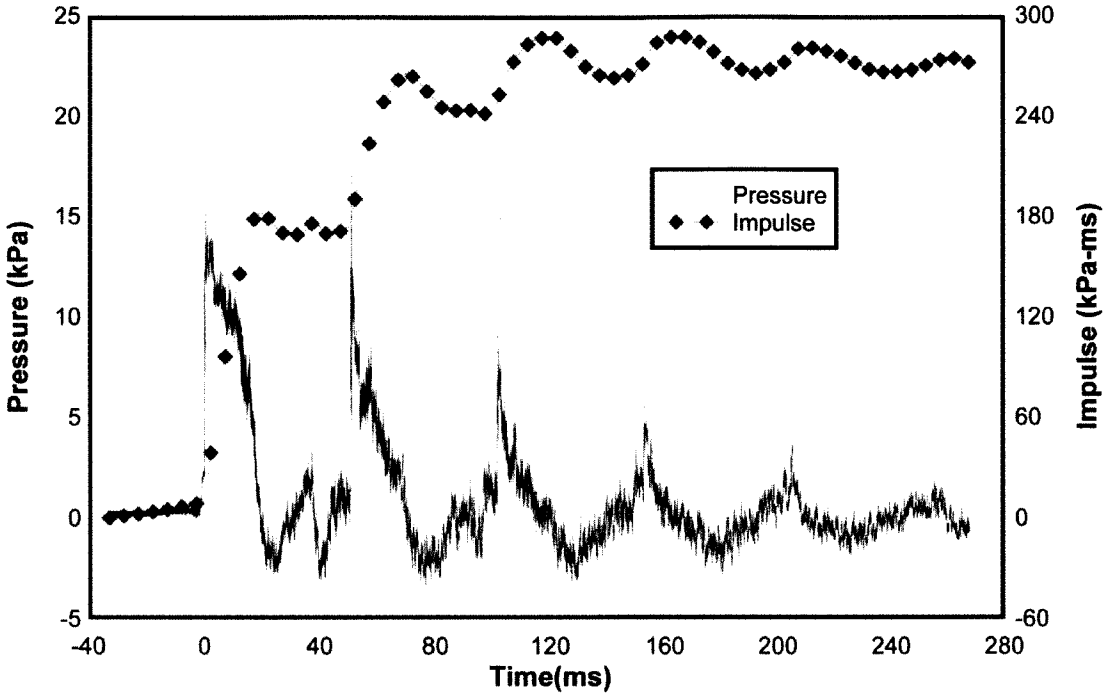


*Figure 4-40: Reflected Pressure and Impulse Time History for Test RC-7-1*

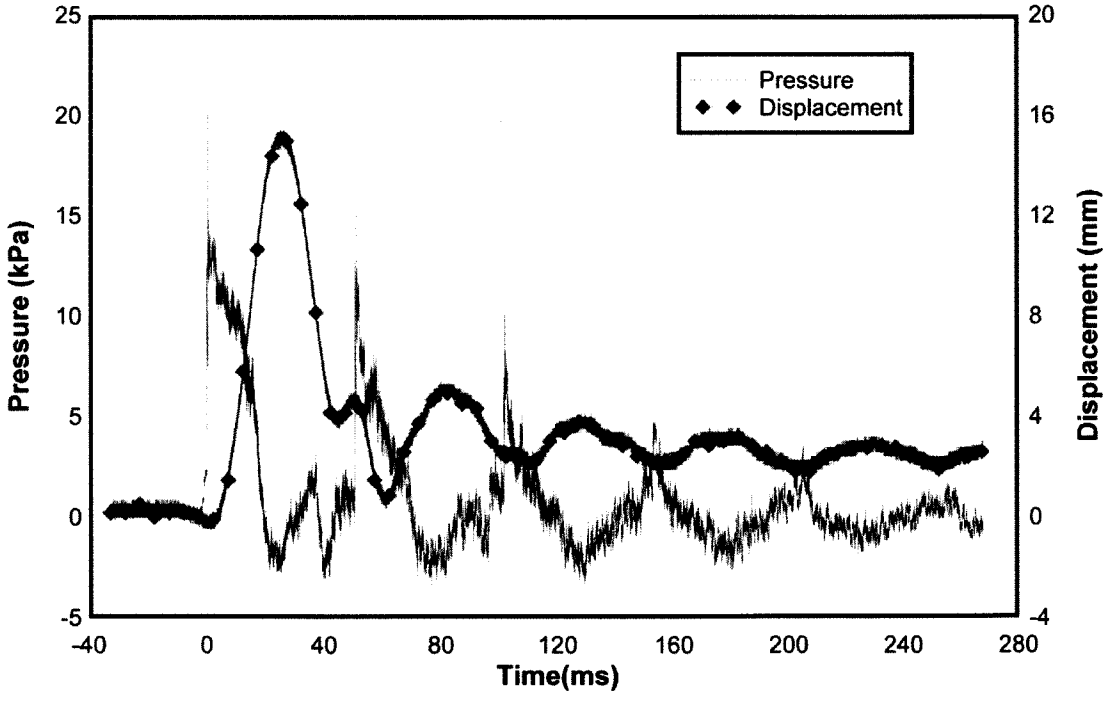


*Figure 4-41: Reflected Pressure and Mid-Height Displacement Time History for Test RC-7-1*

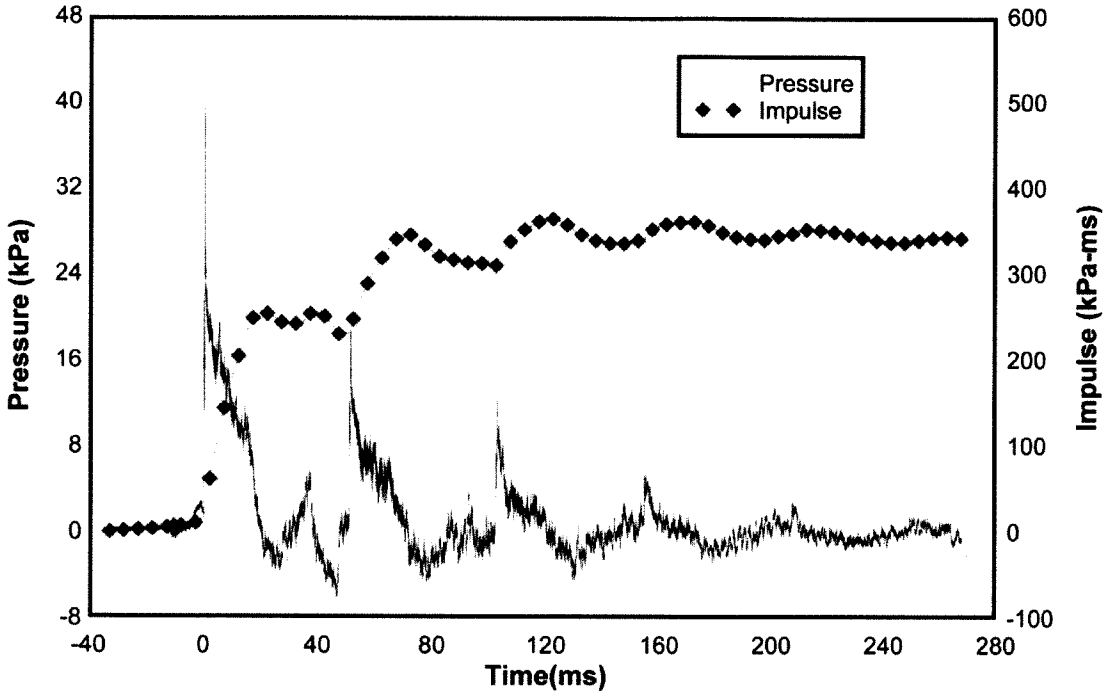


*Figure 4-42: Reflected Pressure and Impulse Time History for Test RC-7-2*

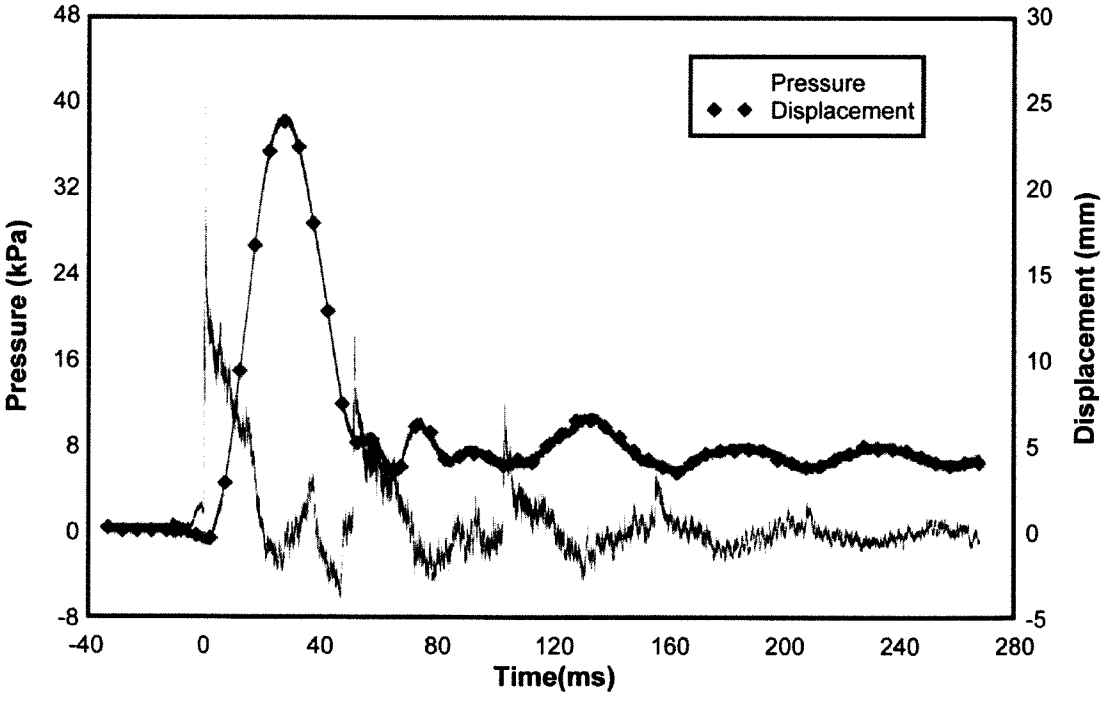


*Figure 4-43: Reflected Pressure and Mid-Height Displacement Time History for Test RC-7-2*

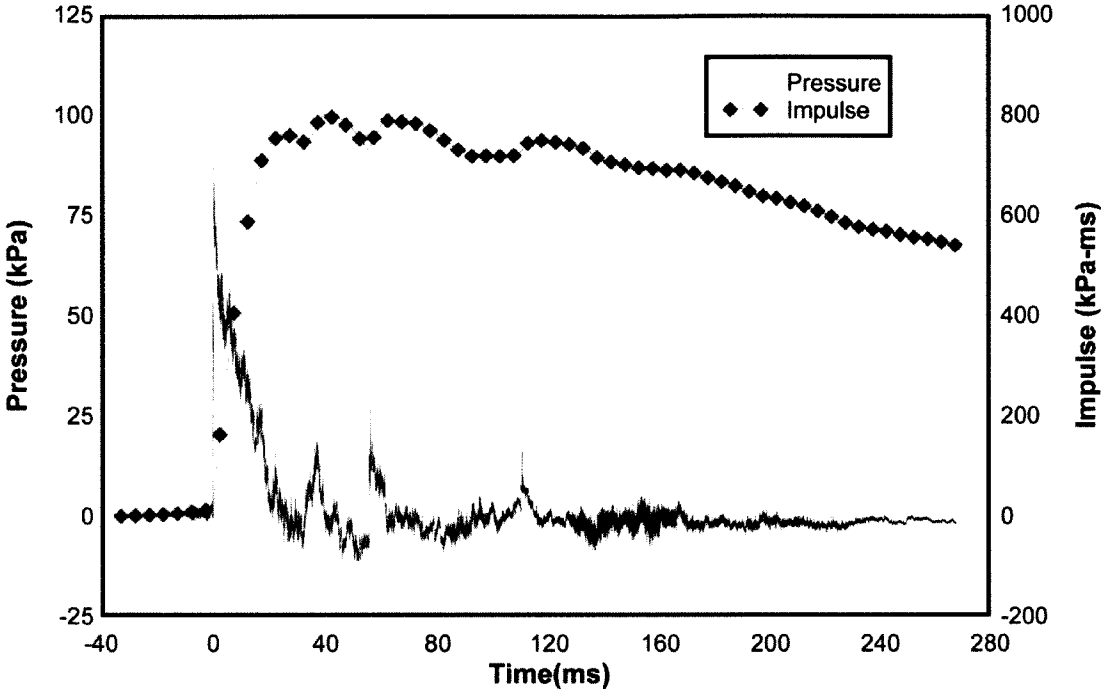


*Figure 4-44: Reflected Pressure and Impulse Time History for Test RC-7-3*

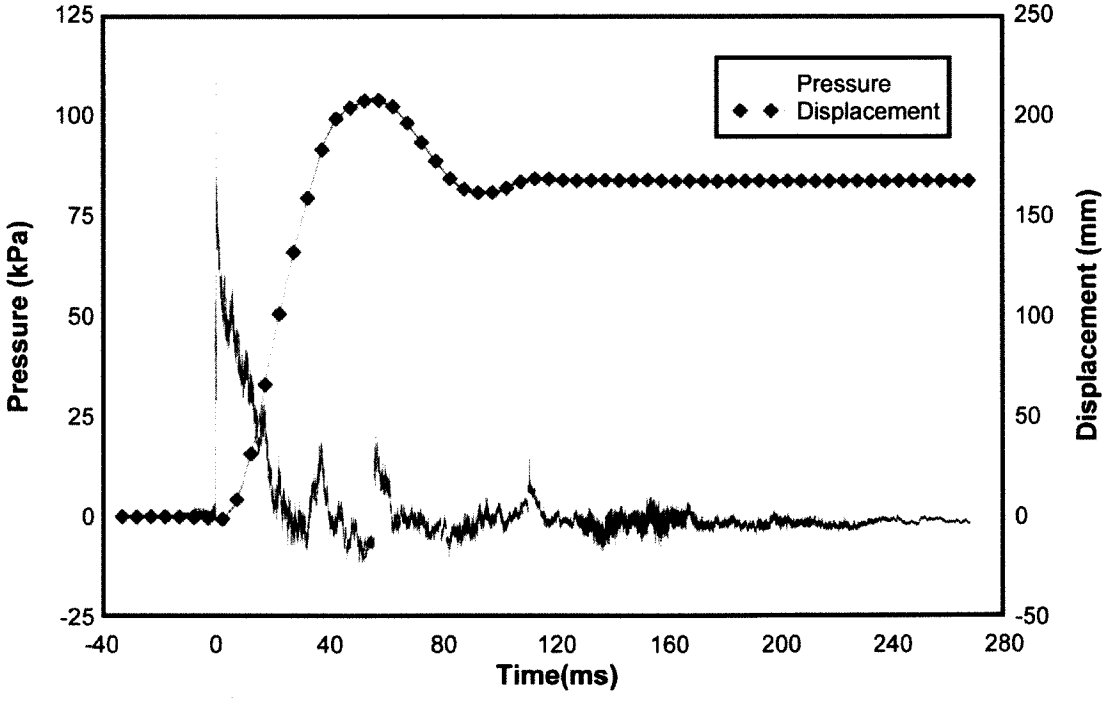


*Figure 4-45: Reflected Pressure and Mid-Height Displacement Time History for Test RC-7-3*

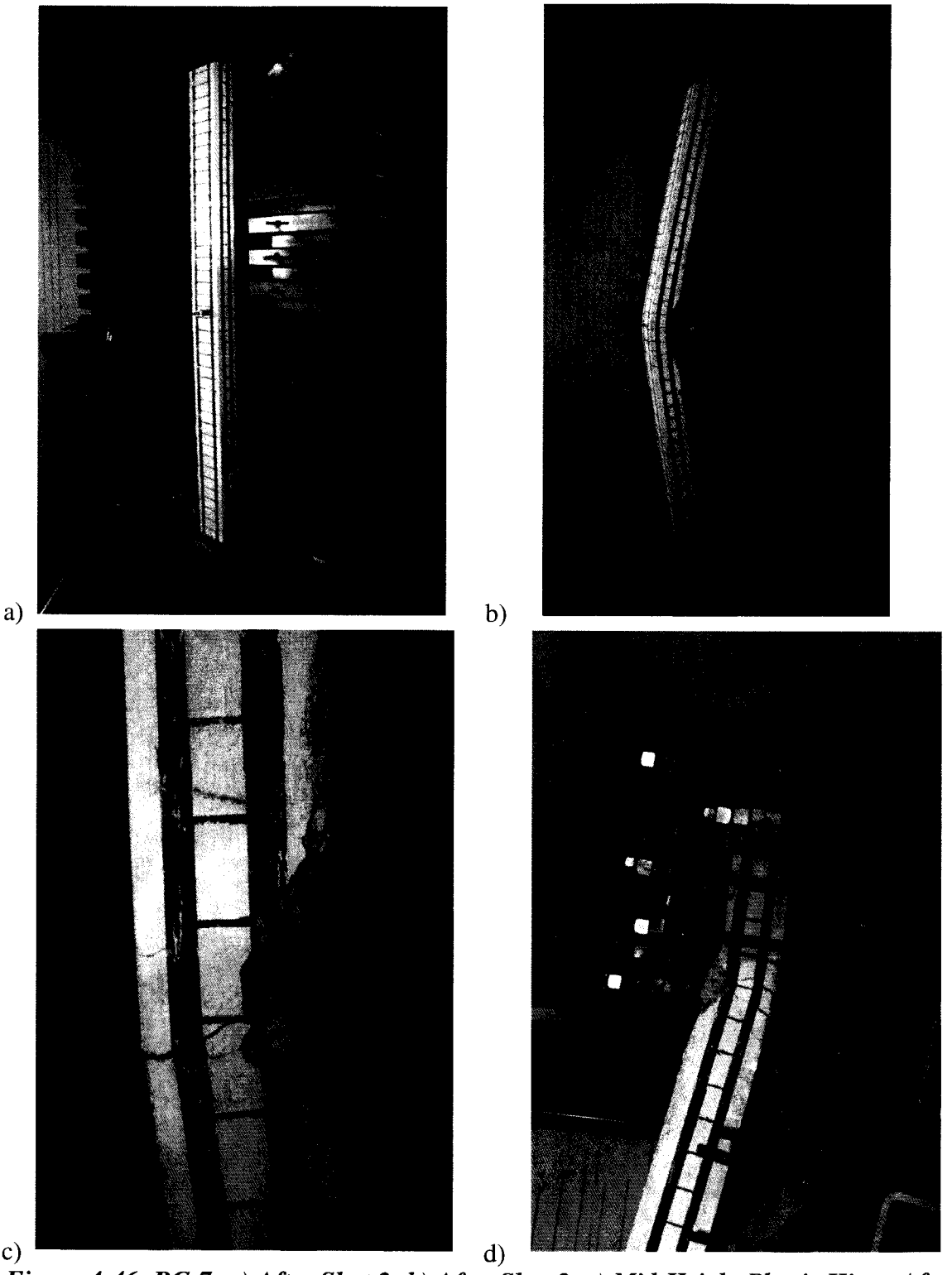


*Figure 4-46: RC-7: a) After Shot 2; b) After Shot 3; c) Mid-Height Plastic Hinge After Shot 3; d) Support Plastic Hinge After Shot 3*

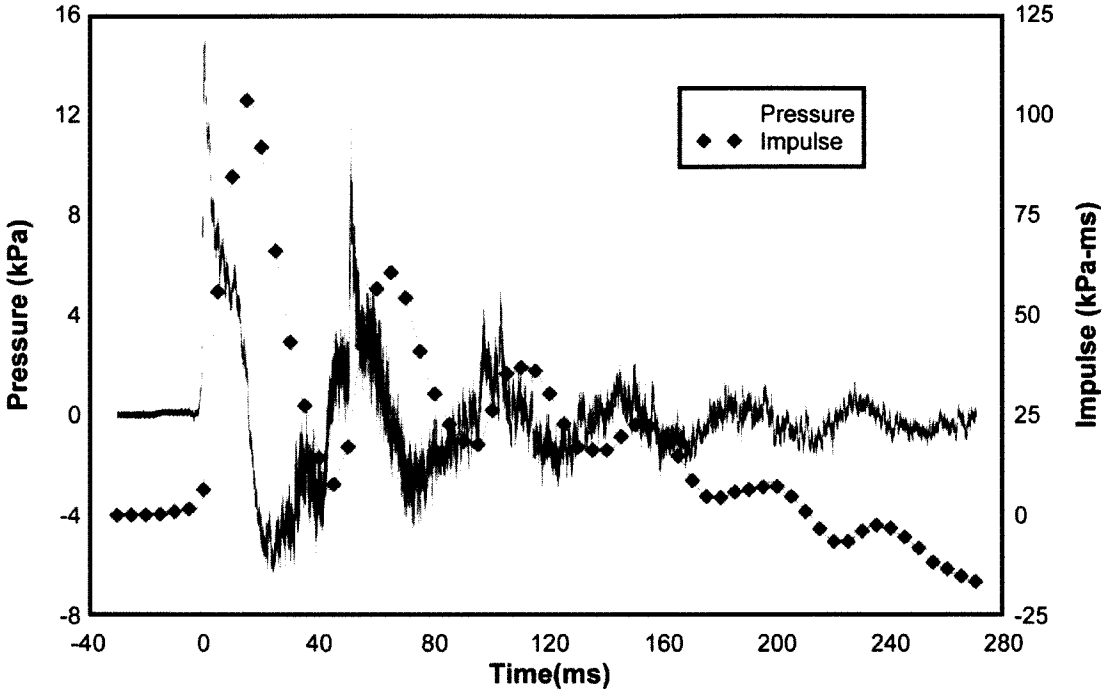


*Figure 4-47: Reflected Pressure and Impulse Time History for Test RC-8-1*

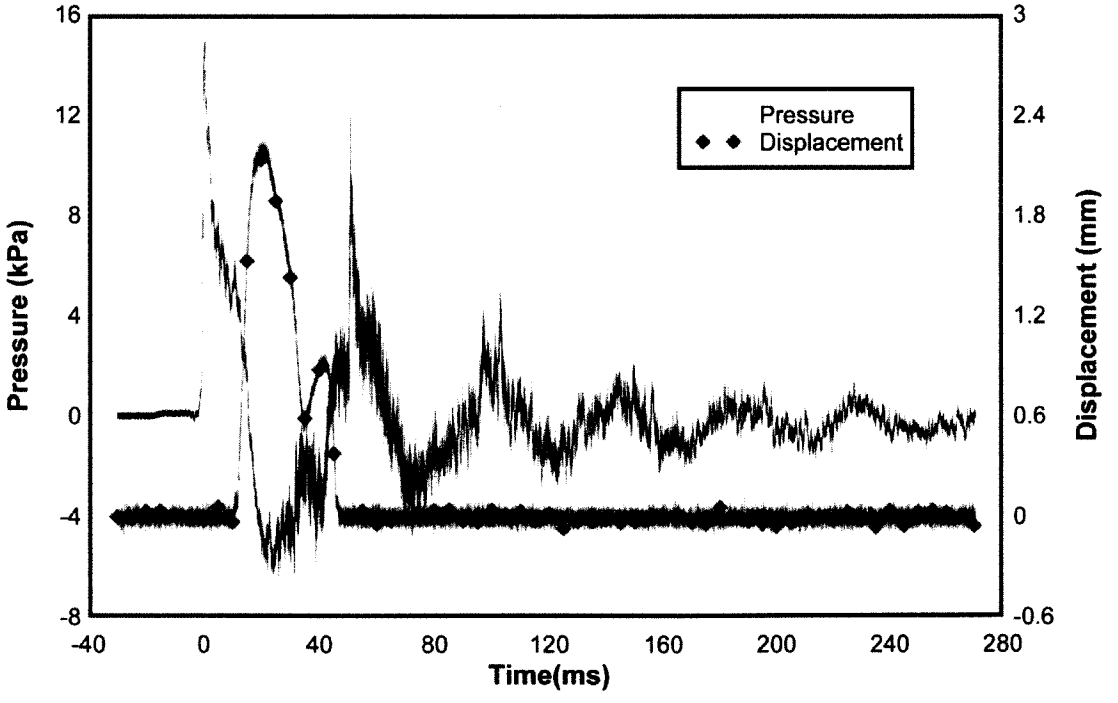


*Figure 4-48: Reflected Pressure and Mid-Height Displacement Time History for Test RC-8-1*

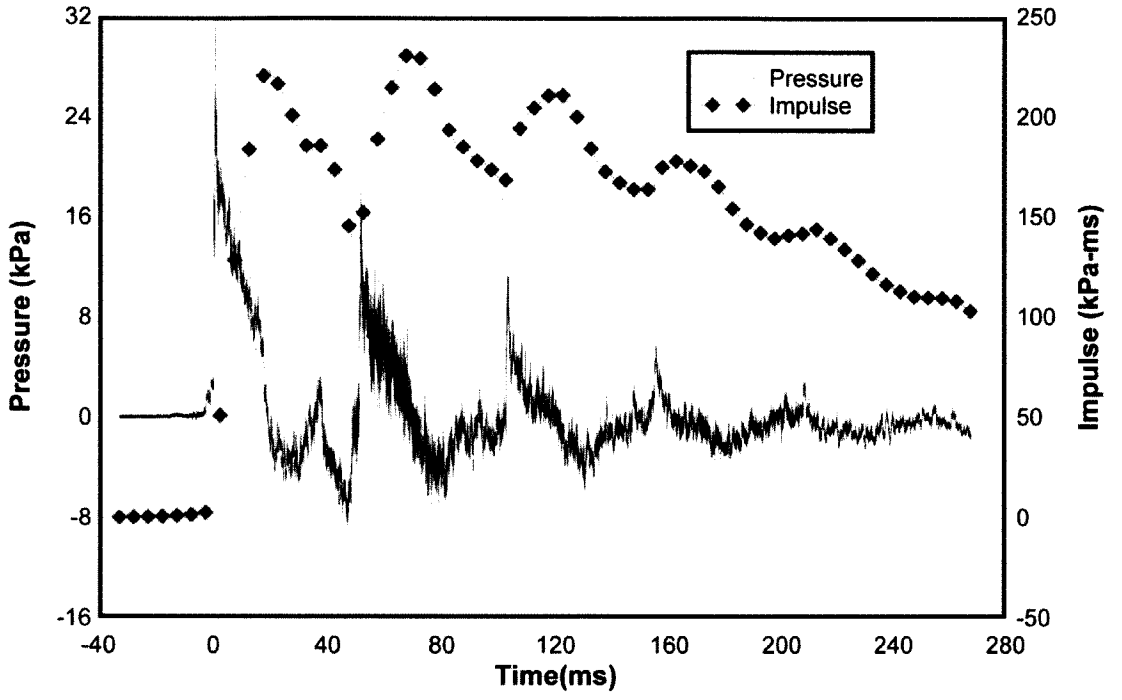


*Figure 4-49: Reflected Pressure and Impulse Time History for Test RC-8-2*

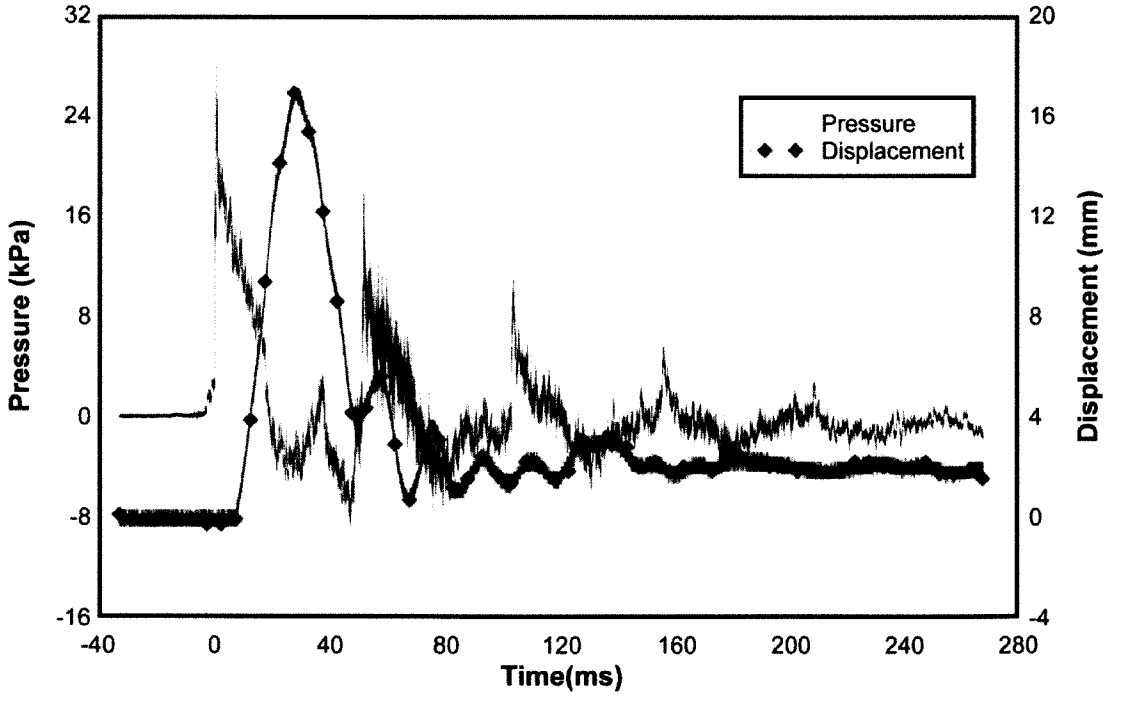


*Figure 4-50: Reflected Pressure and Mid-Height Displacement Time History for Test RC-8-2*

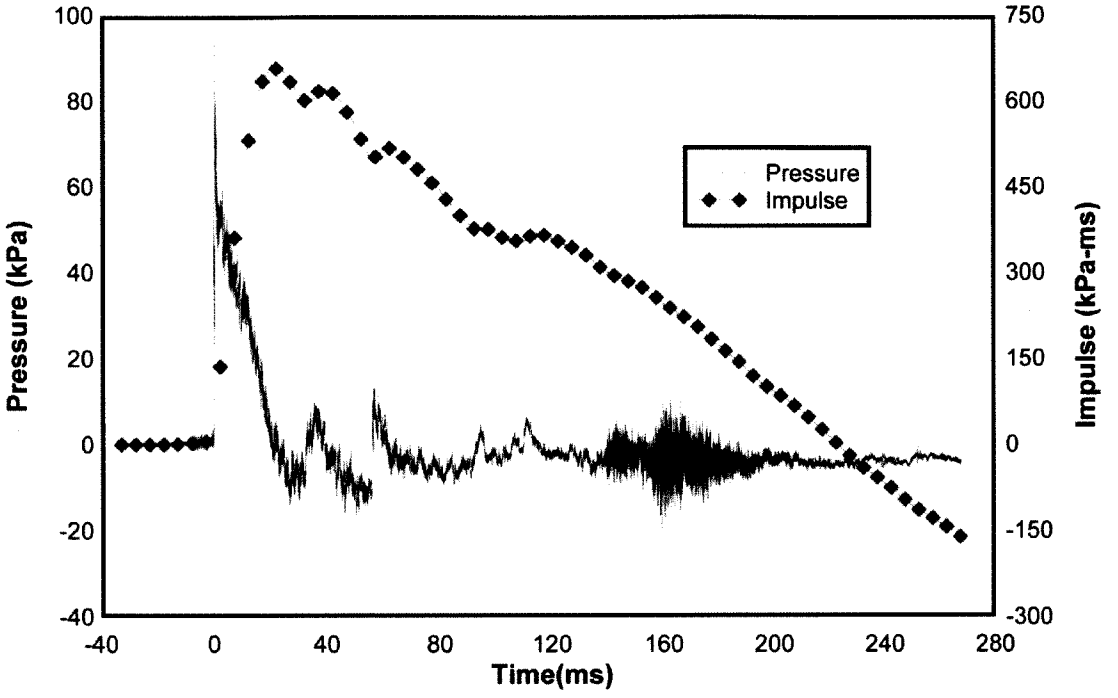


*Figure 4-51: Reflected Pressure and Impulse Time History for Test RC-8-3*

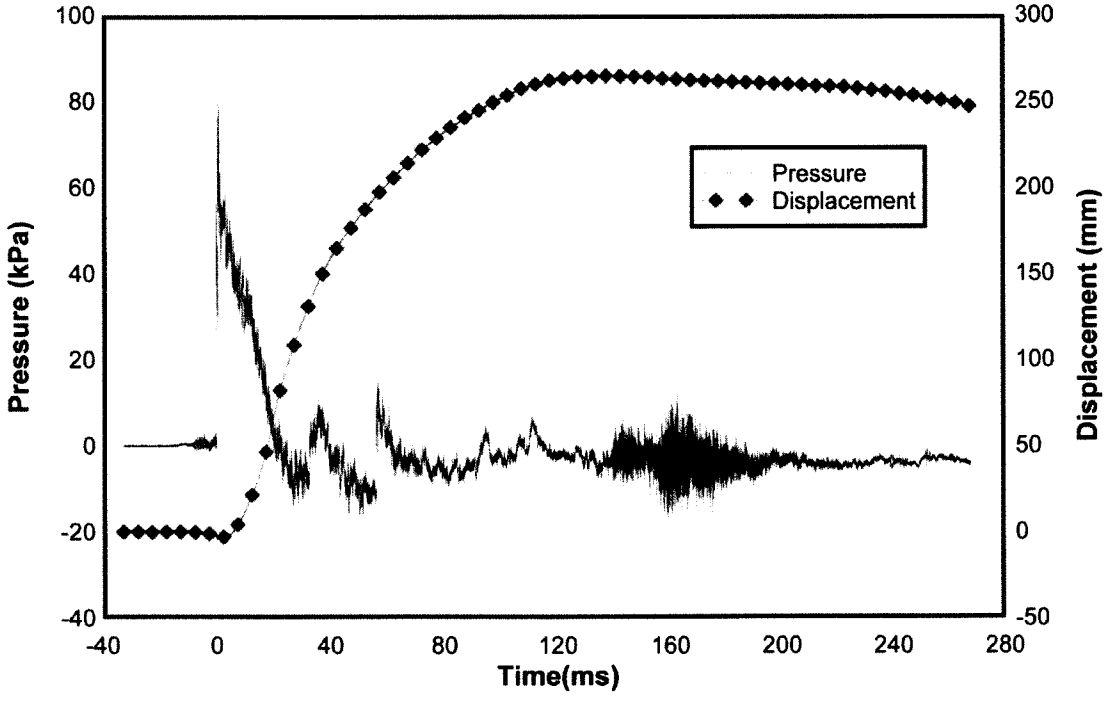


*Figure 4-52: Reflected Pressure and Mid-Height Displacement Time History for Test RC-8-3*

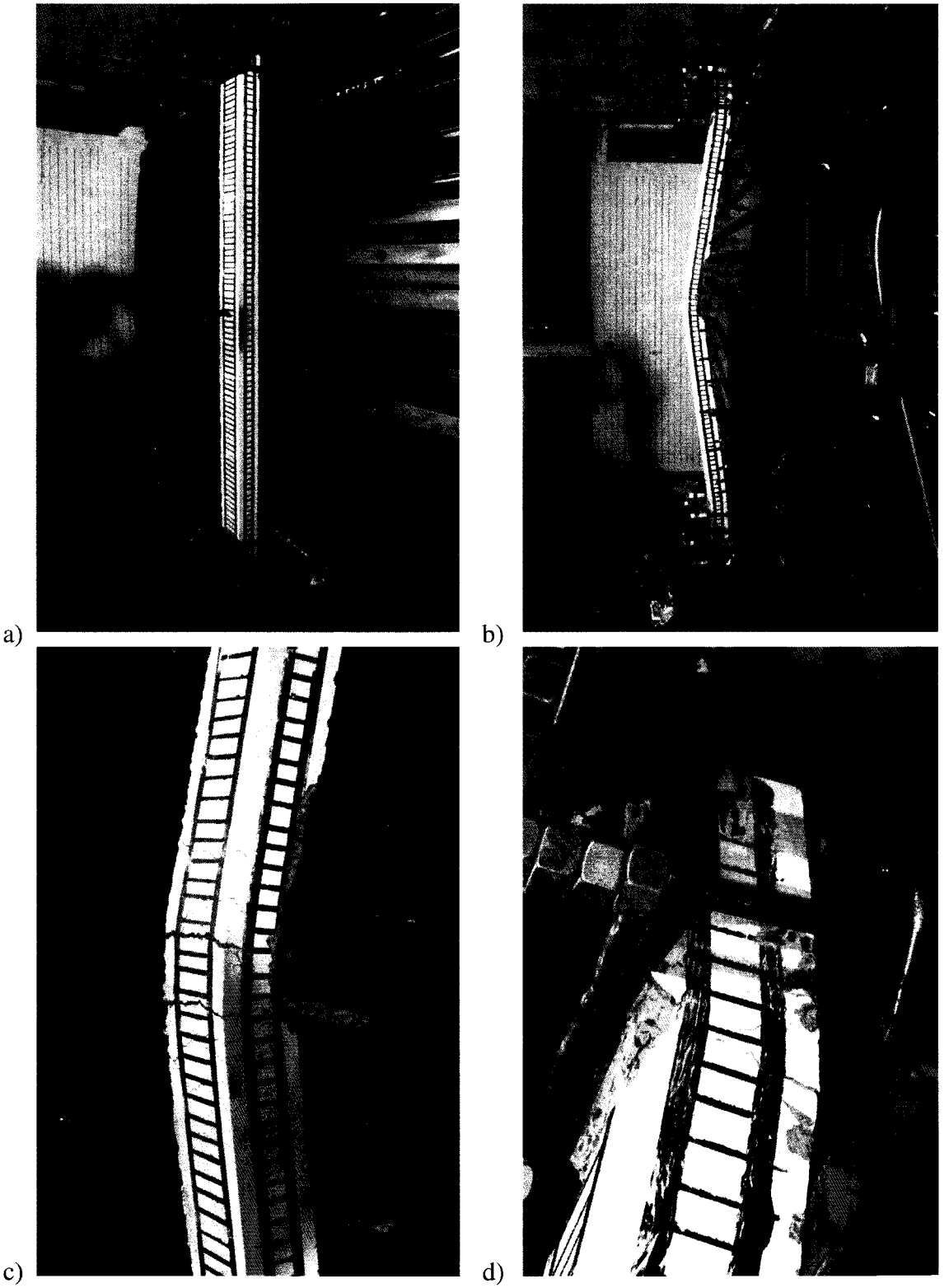


*Figure 4-53: RC-8: a) After Shot 2; b) After Shot 3; c) Mid-Height Plastic Hinge After Shot 3; d) Support Plastic Hinge After Shot 3*

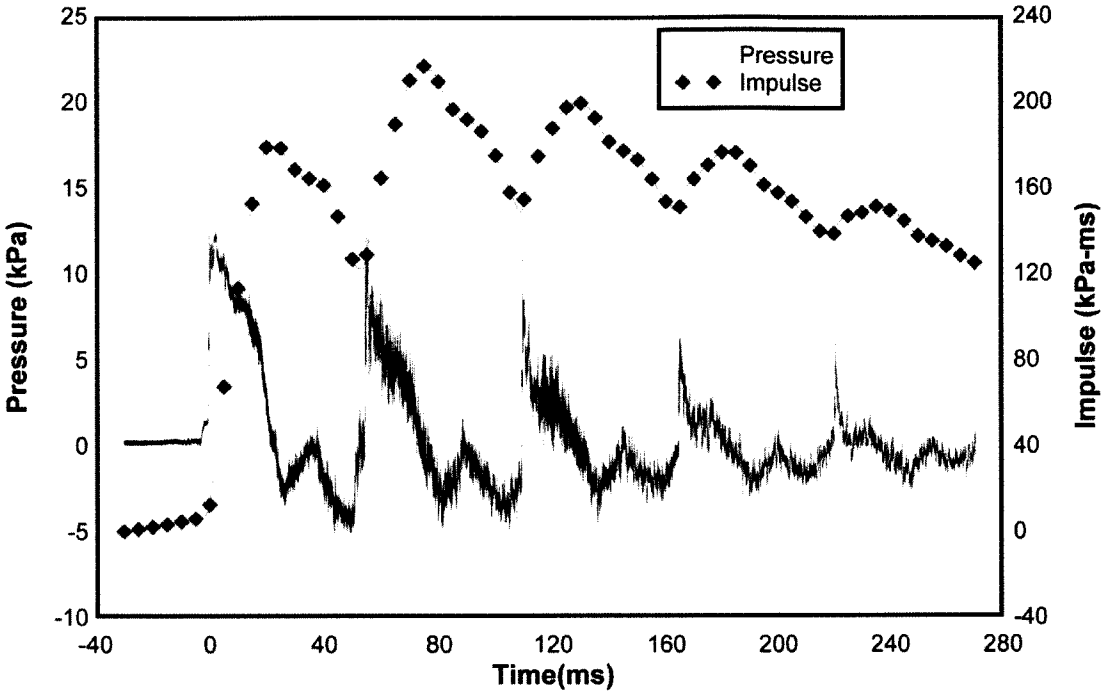


*Figure 4-54: Reflected Pressure and Impulse Time History for Test RC-9-1*

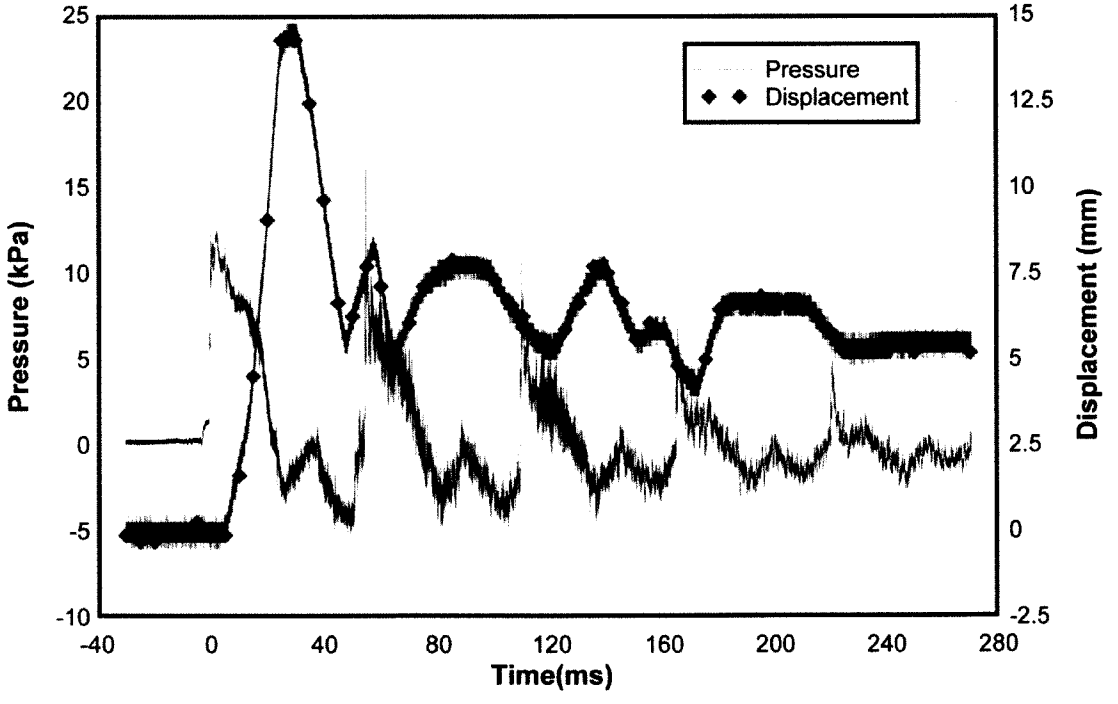


*Figure 4-55: Reflected Pressure and Mid-Height Displacement Time History for Test RC-9-1*

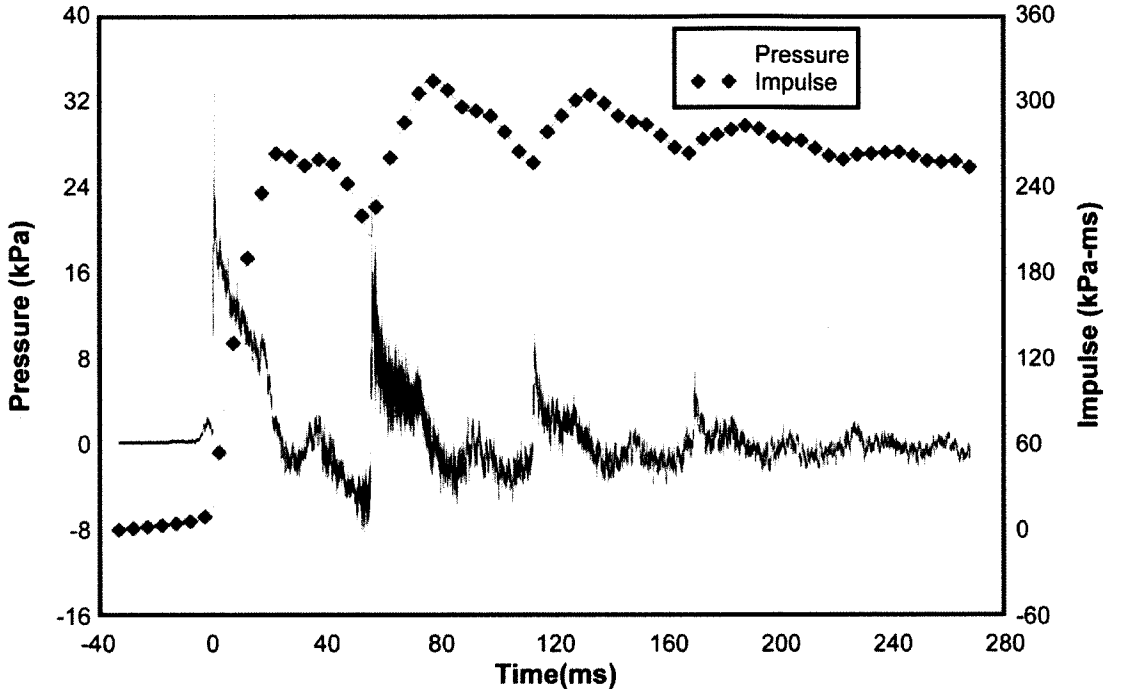


*Figure 4-56: Reflected Pressure and Impulse Time History for Test RC-9-2*

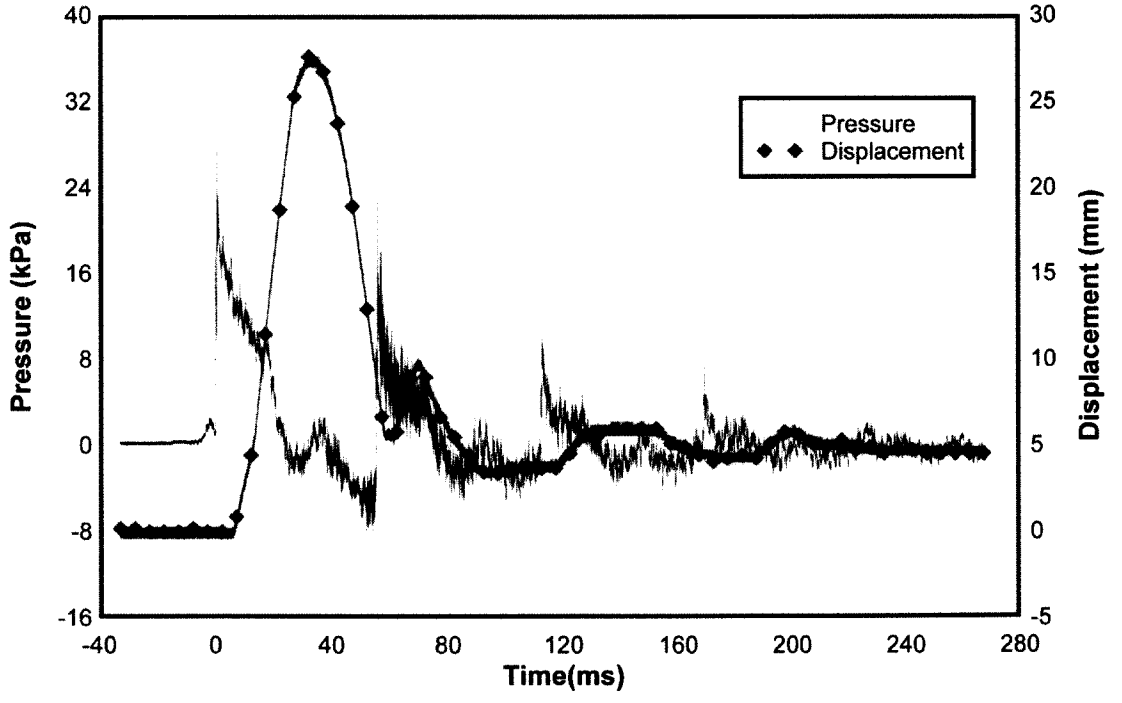


*Figure 4-57: Reflected Pressure and Mid-Height Displacement Time History for Test RC-9-2*

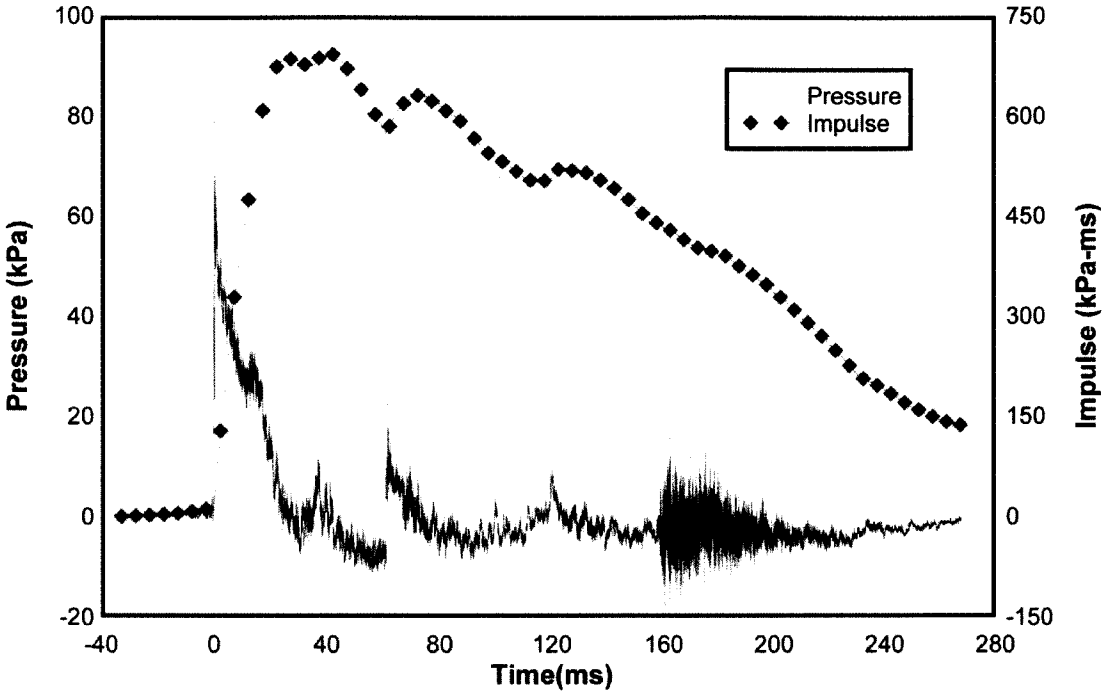


*Figure 4-58: Reflected Pressure and Impulse Time History for Test RC-9-3*

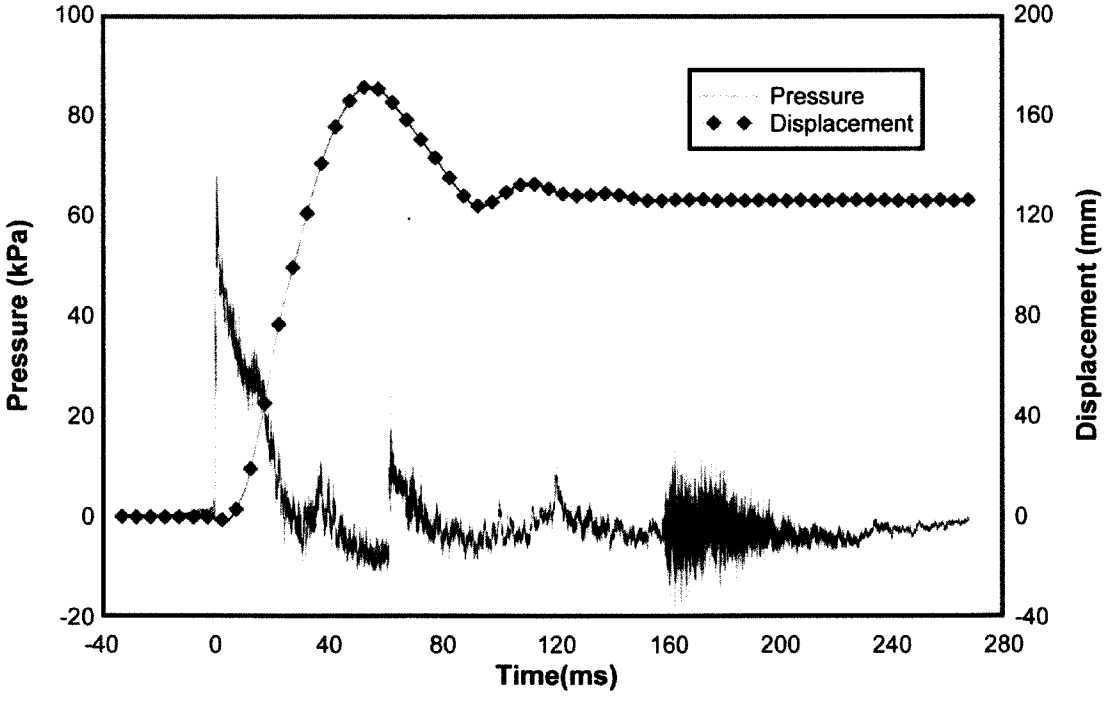


*Figure 4-59: Reflected Pressure and Mid-Height Displacement Time History for Test RC-9-3*

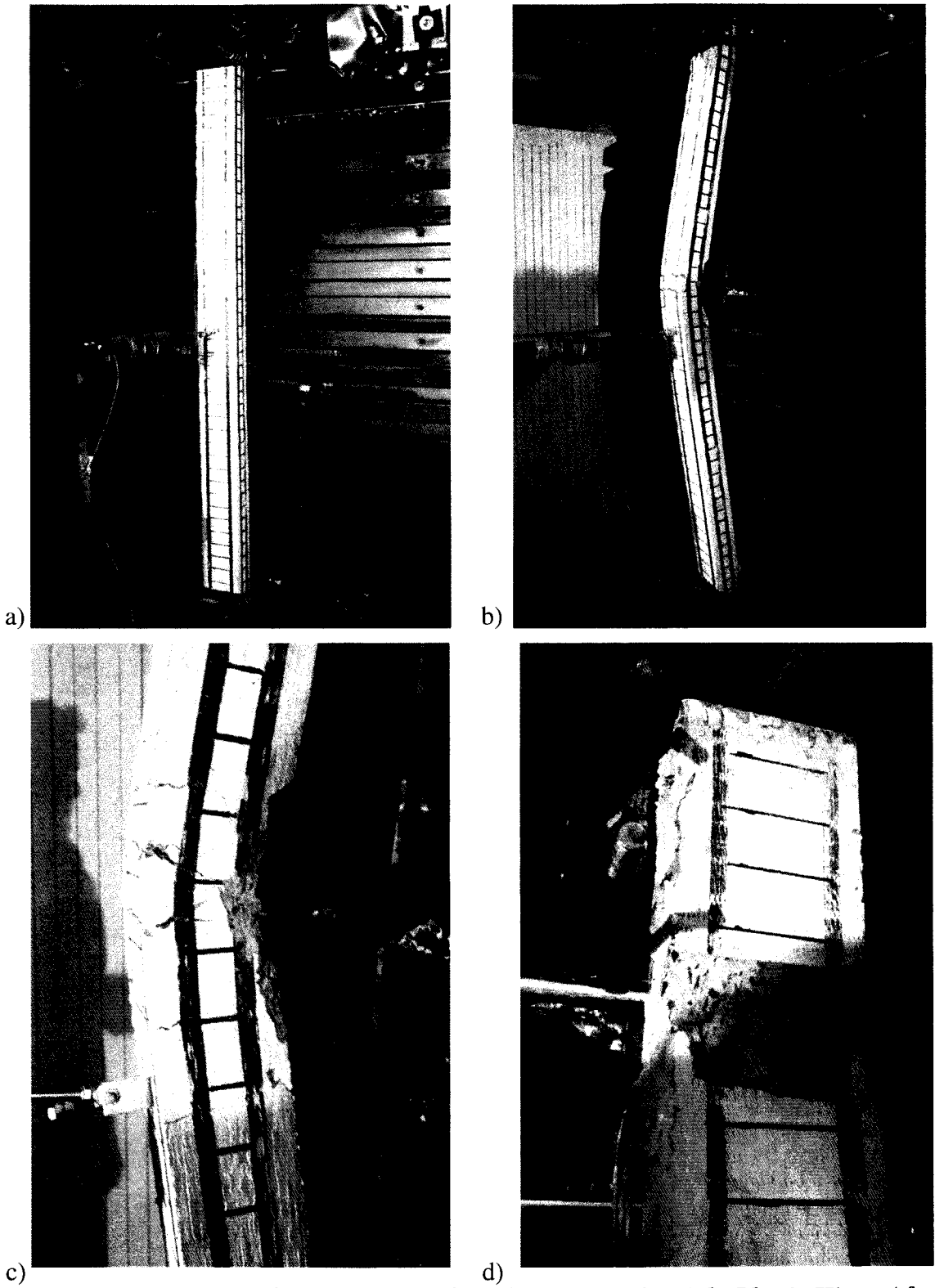


*Figure 4-60: RC-9: a) After Shot 2; b) After Shot 3; c) Mid-Height Plastic Hinge After Shot 3; d) Support Plastic Hinge After Shot 3*

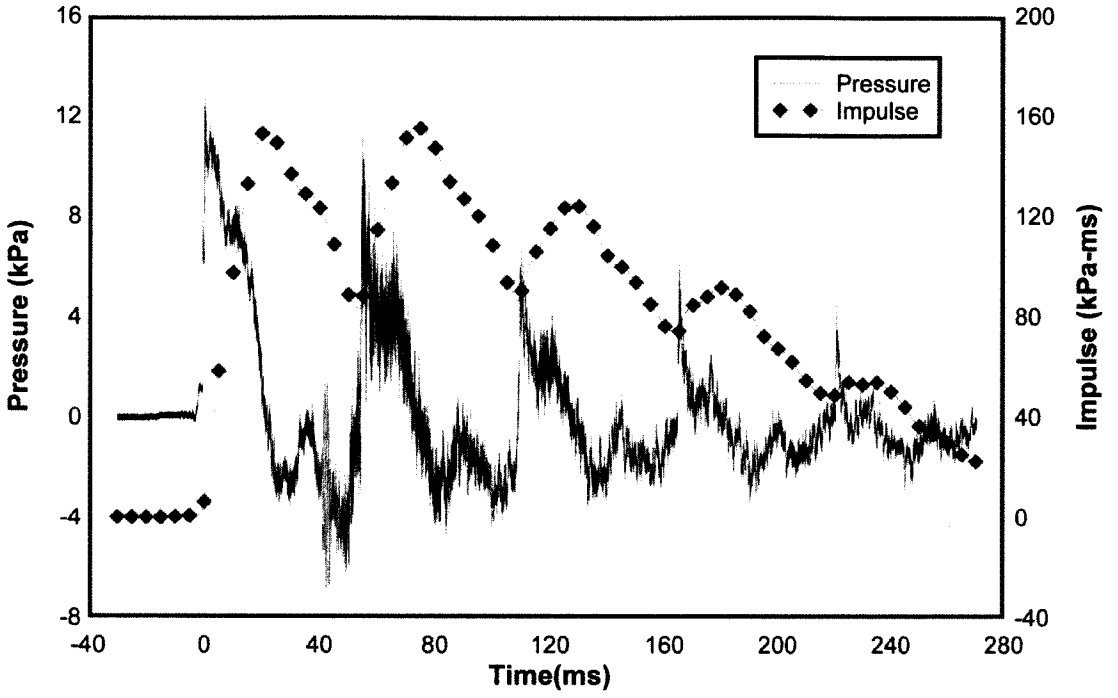


*Figure 4-61: Reflected Pressure and Impulse Time History for Test RC-10-1*

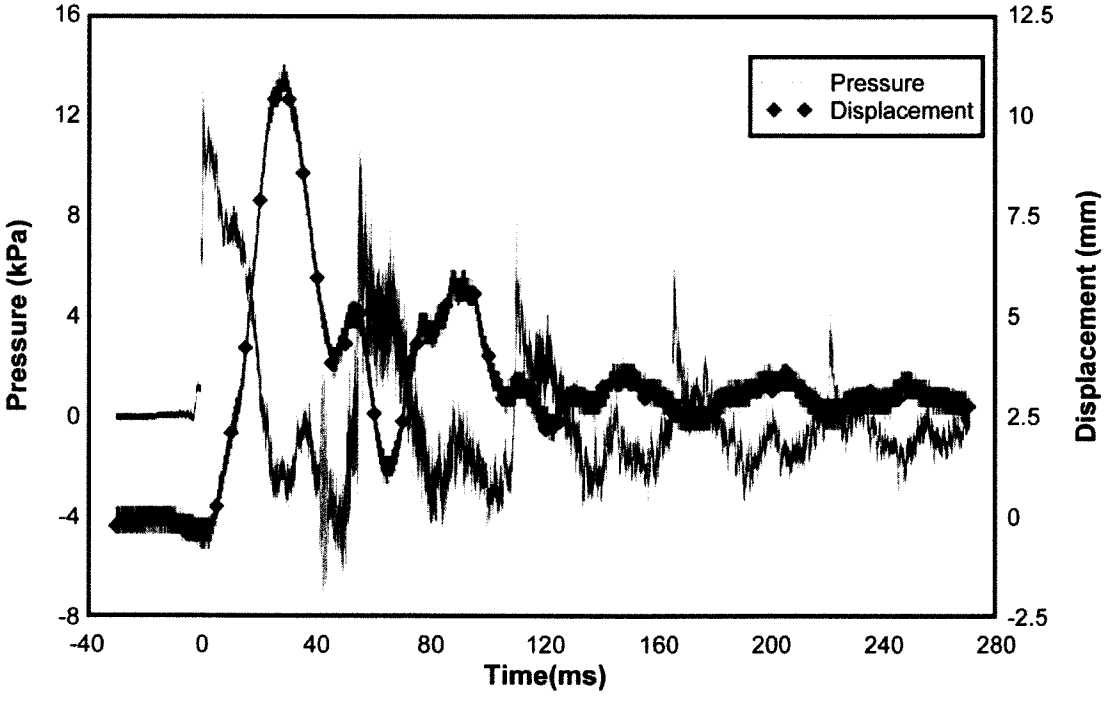


*Figure 4-62: Reflected Pressure and Mid-Height Displacement Time History for Test RC-10-1*

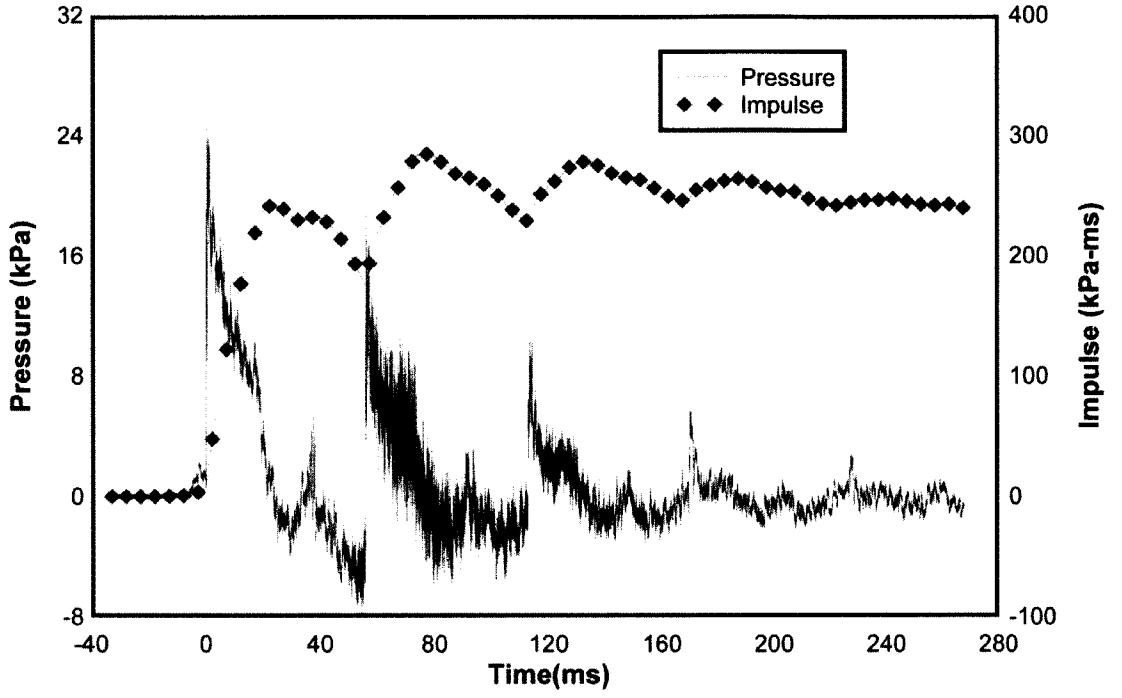


*Figure 4-63: Reflected Pressure and Impulse Time History for Test RC-10-2*

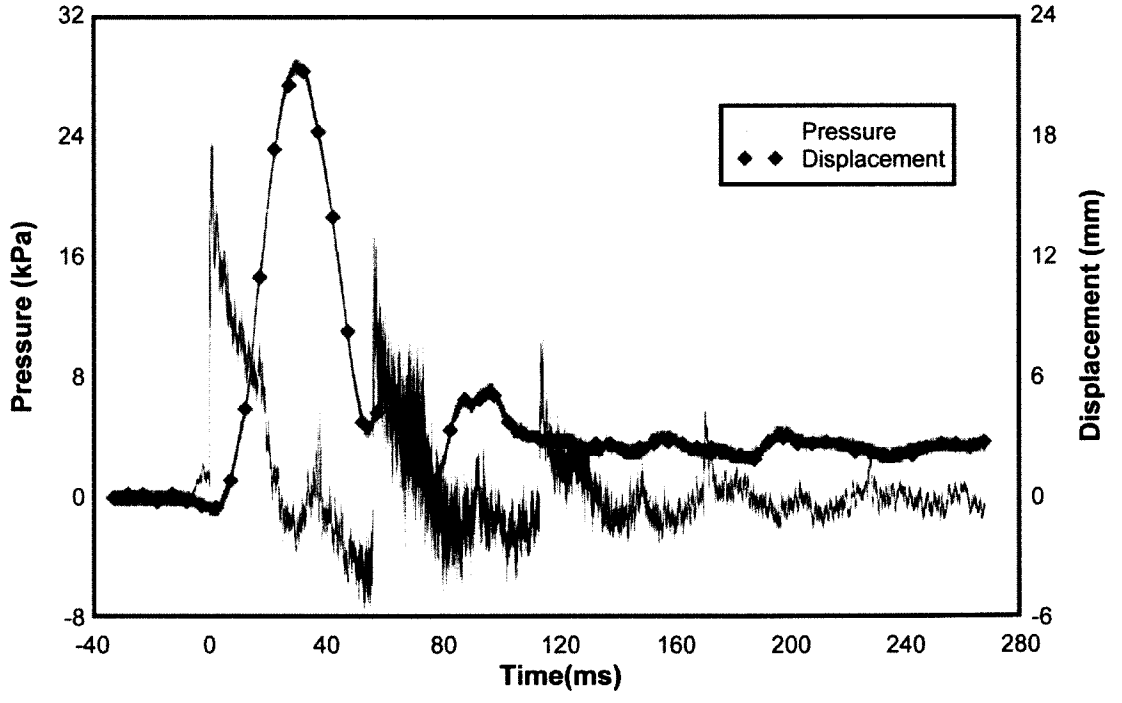


*Figure 4-64: Reflected Pressure and Mid-Height Displacement Time History for Test RC-10-2*

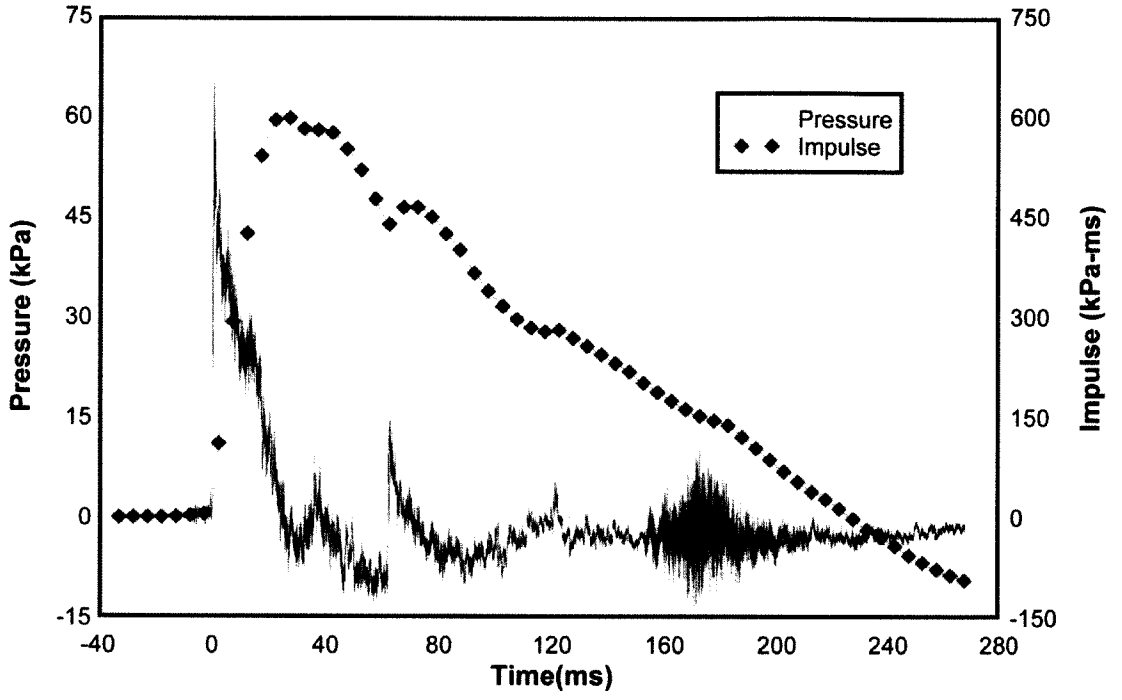


*Figure 4-65: Reflected Pressure and Impulse Time History for Test RC-10-3*

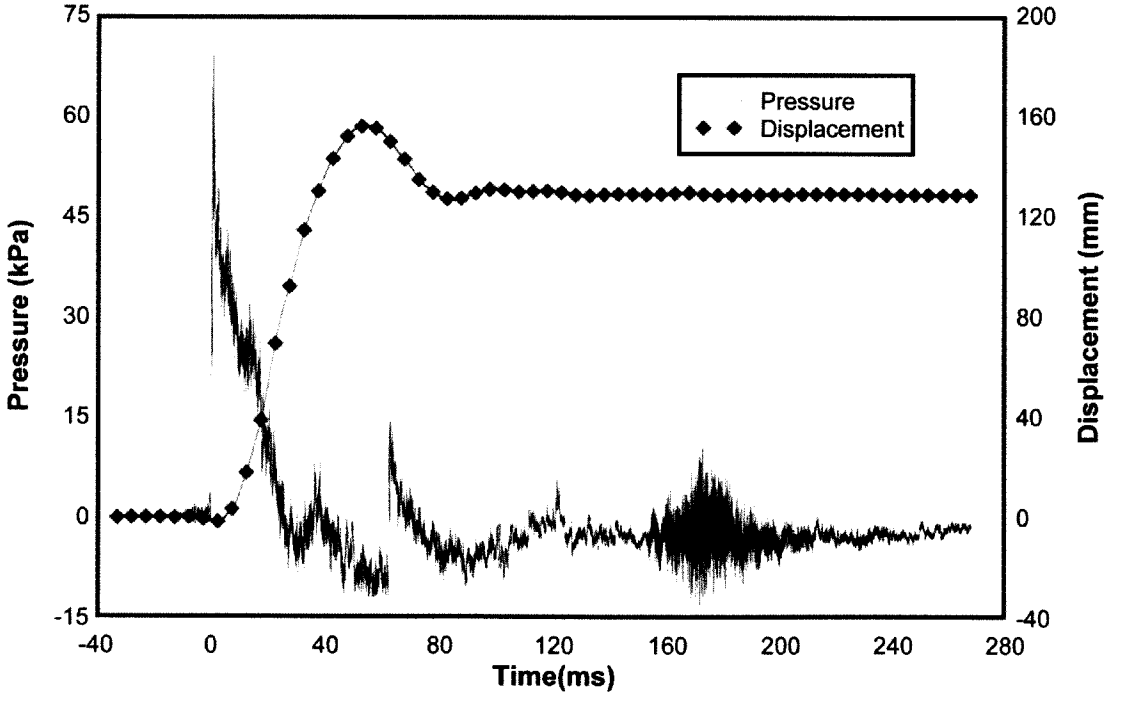


*Figure 4-66: Reflected Pressure and Mid-Height Displacement Time History for Test RC-10-3*

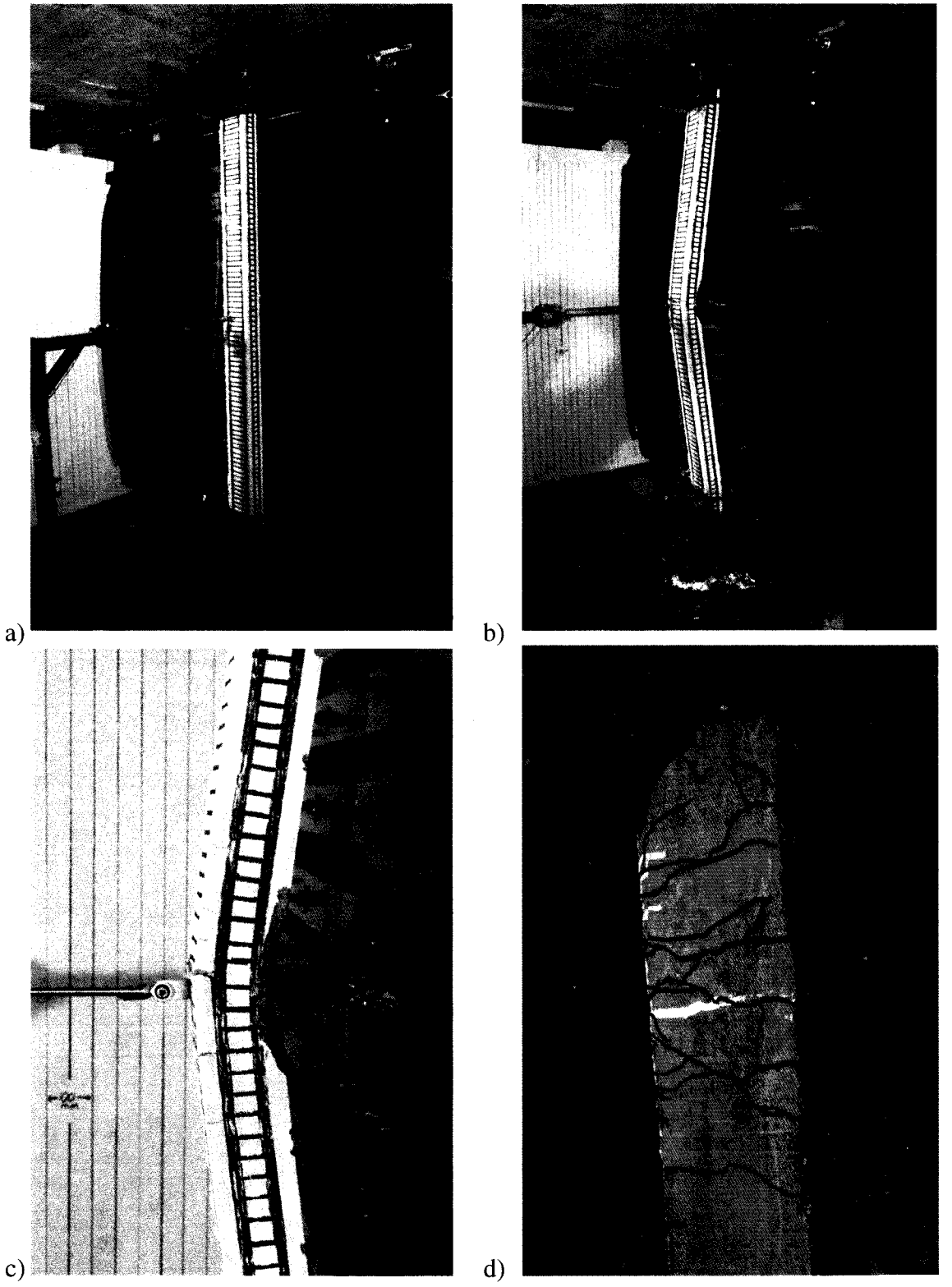


*Figure 4-67: RC-10: a) After Shot 2; b) After Shot 3; c) Mid-Height Plastic Hinge After Shot 3; d) Support Tension Cracks After Shot 3*

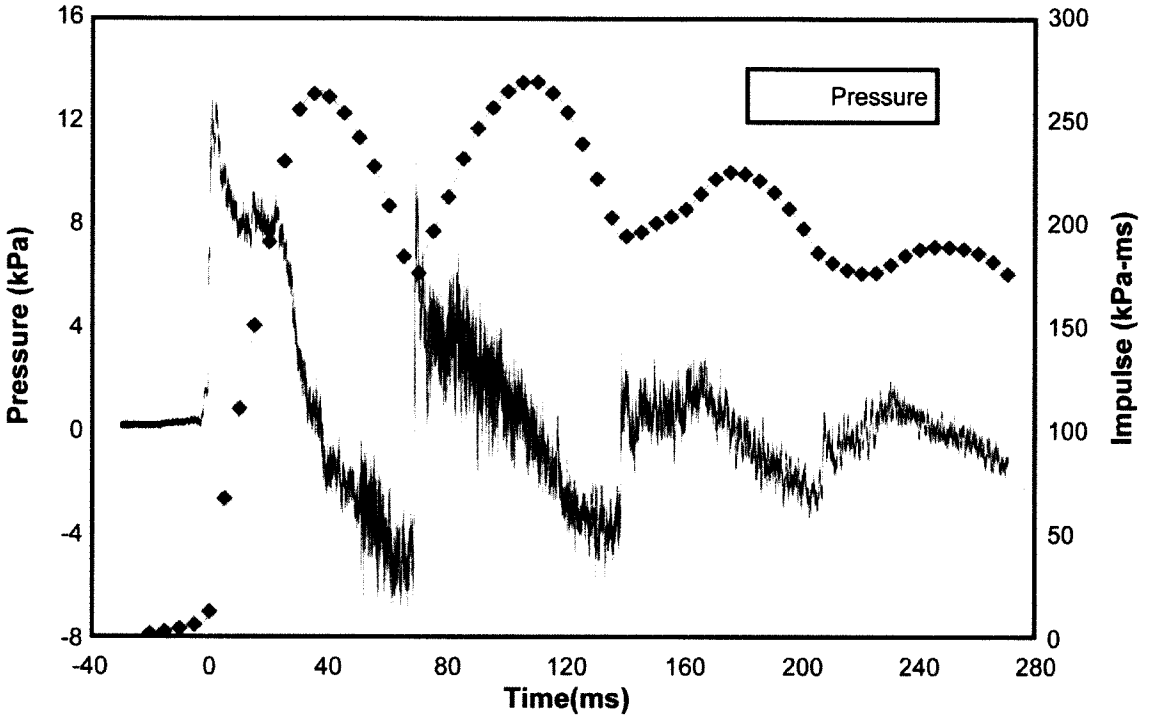


*Figure 4-68: Reflected Pressure and Impulse Time History for Test RC-11-1*

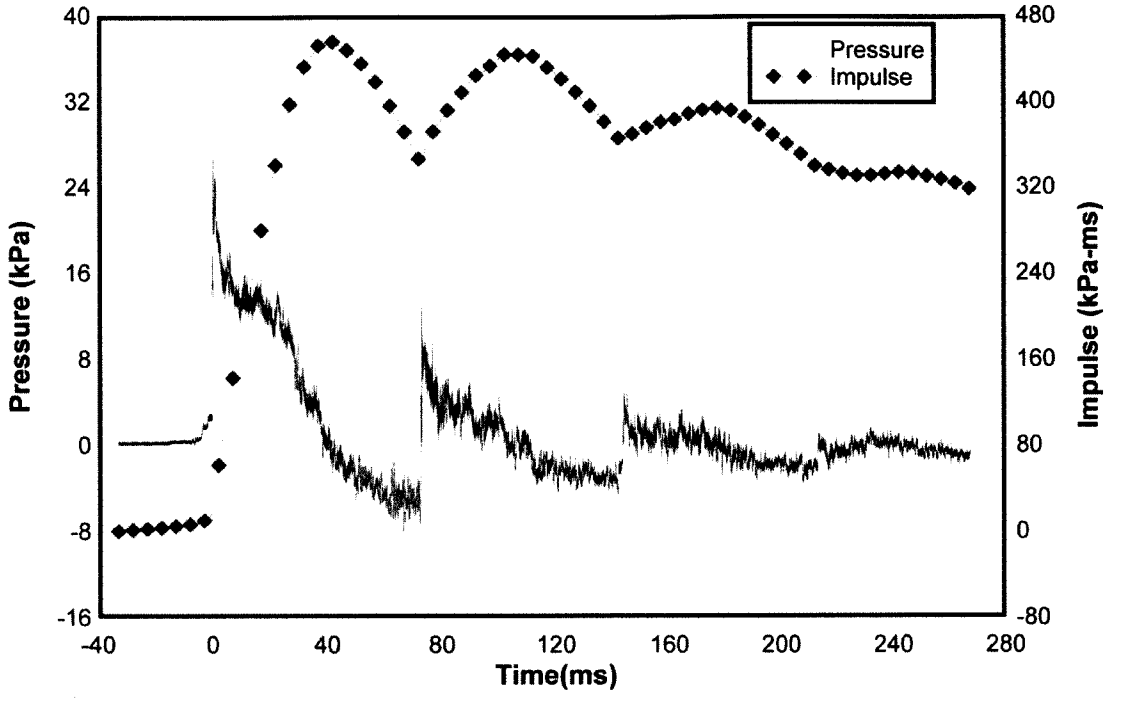


*Figure 4-69: Reflected Pressure and Impulse Time History for Test RC-11-2*

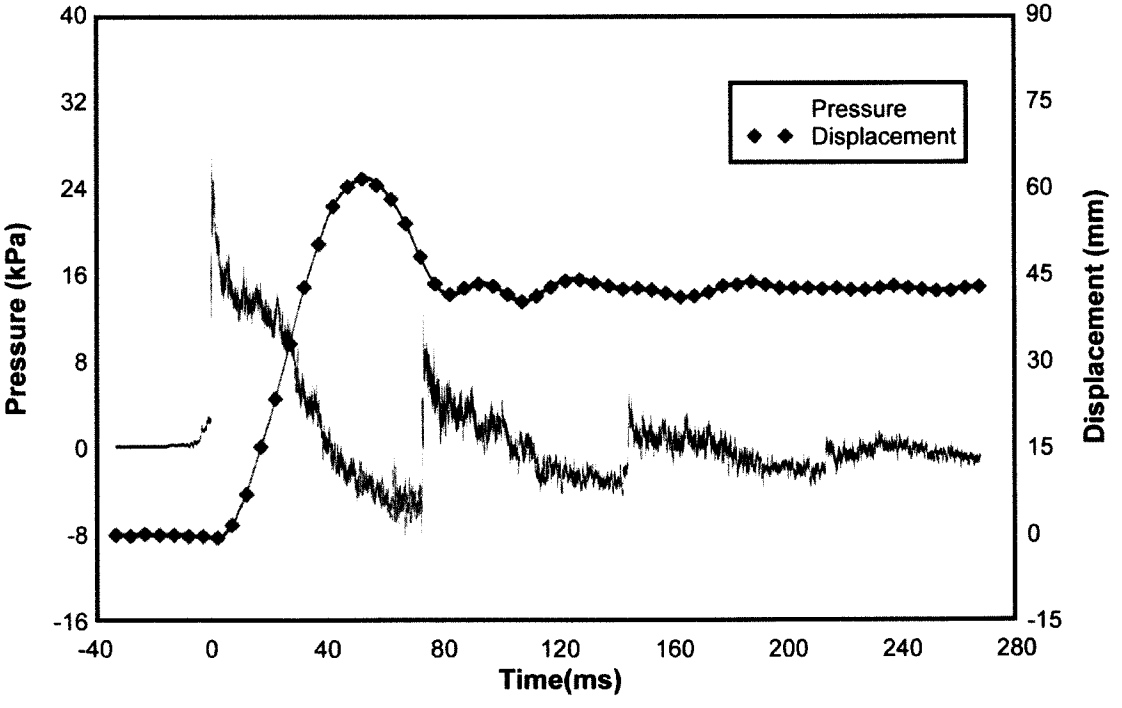


*Figure 4-70: Reflected Pressure and Mid-Height Displacement Time History for Test RC-11-2*

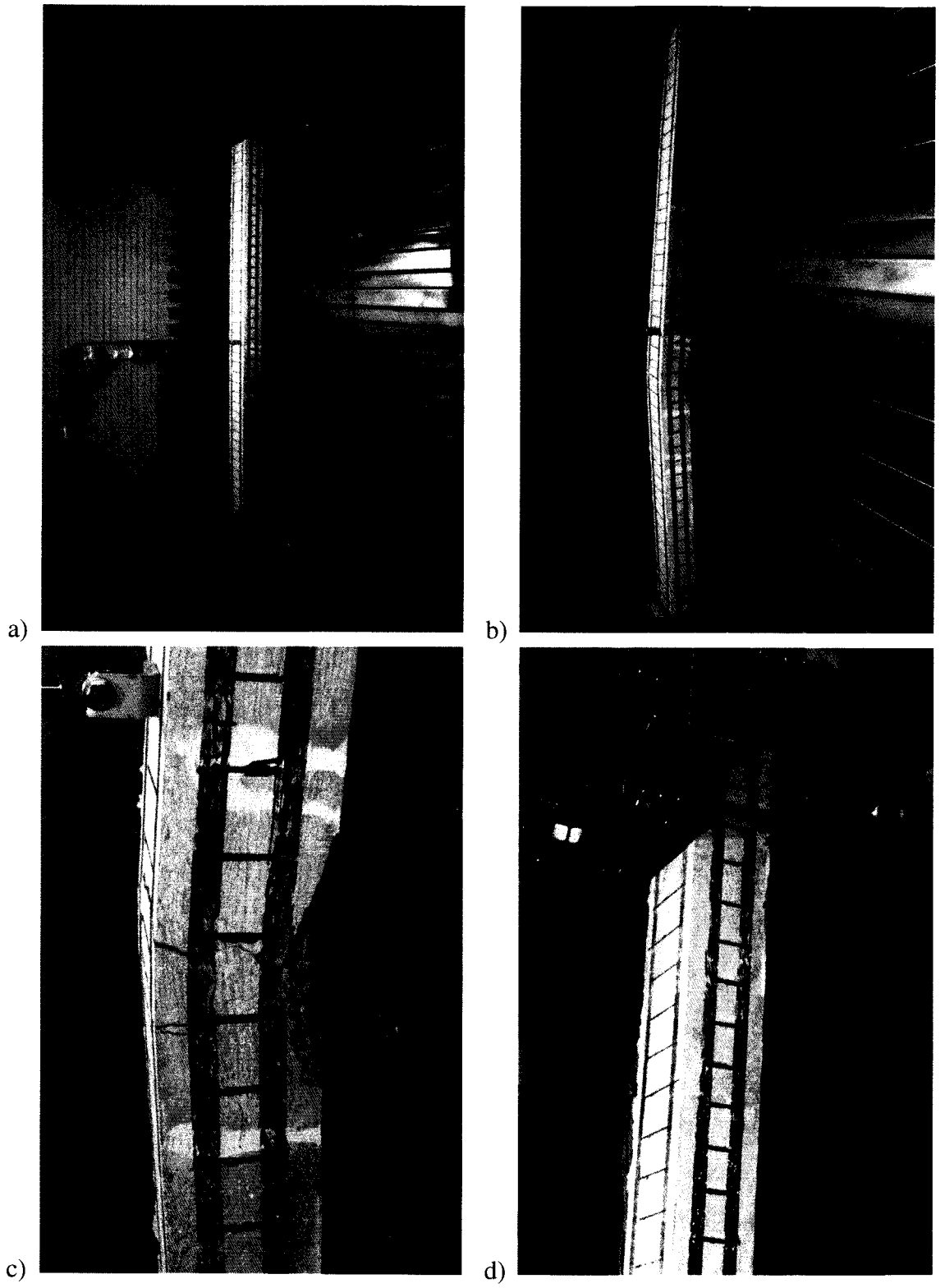


*Figure 4-71: RC-11: a) After Shot 1; b) After Shot 2; c) Mid-Height Plastic Hinge After Shot 2; d) Support Plastic After Shot 2*

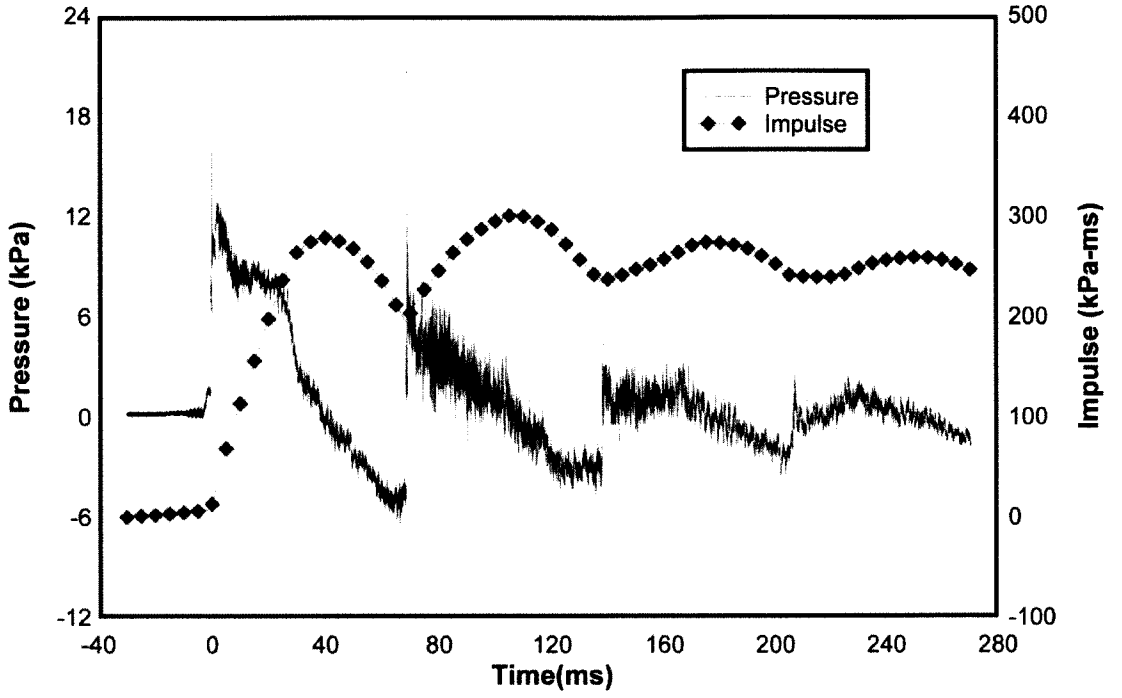


*Figure 4-72: Reflected Pressure and Impulse Time History for Test RC-12-1*

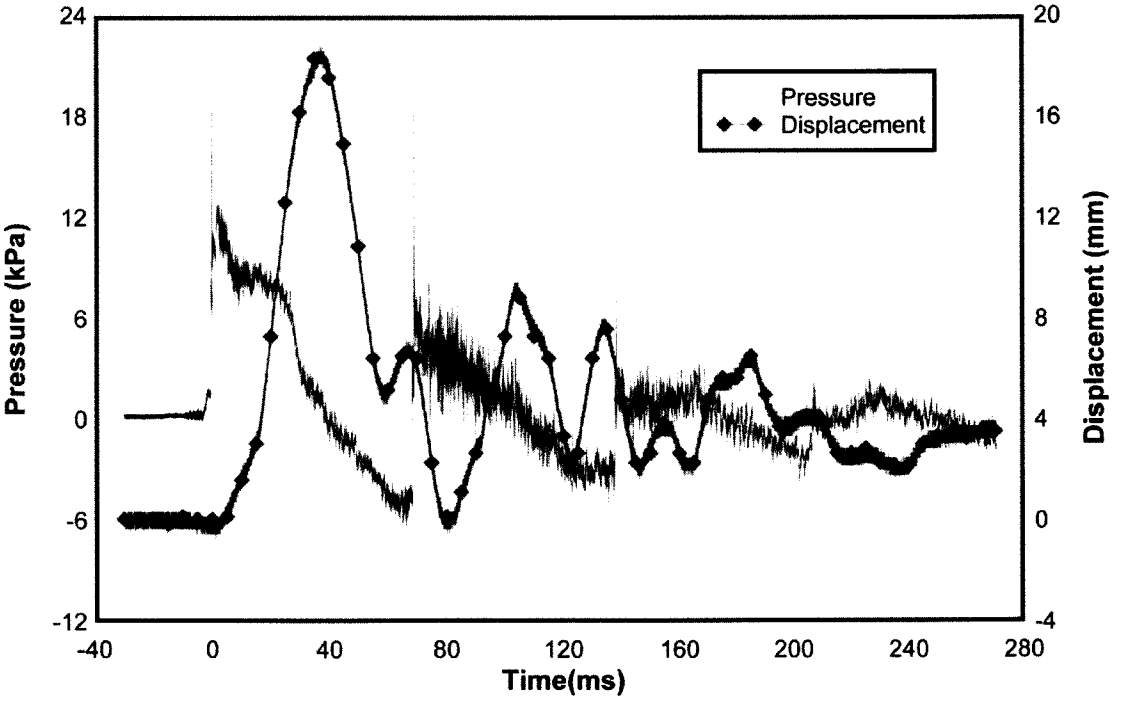


*Figure 4-73: Reflected Pressure and Mid-Height Displacement Time History for Test RC-12-1*

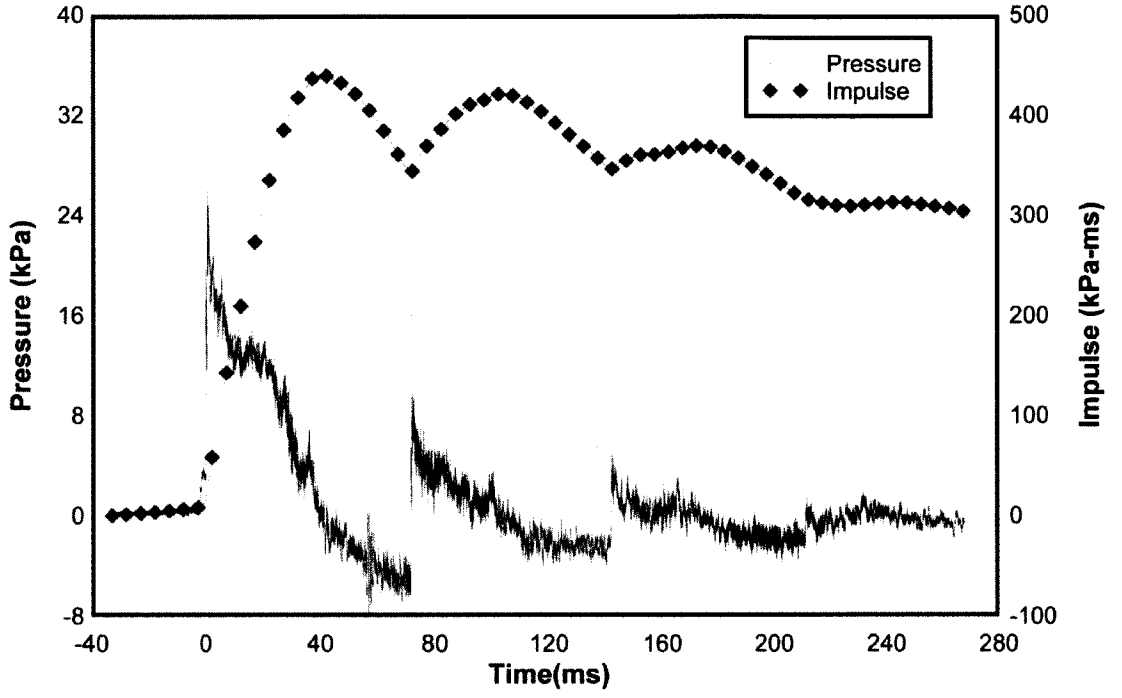


*Figure 4-74: Reflected Pressure and Impulse Time History for Test RC-12-2*

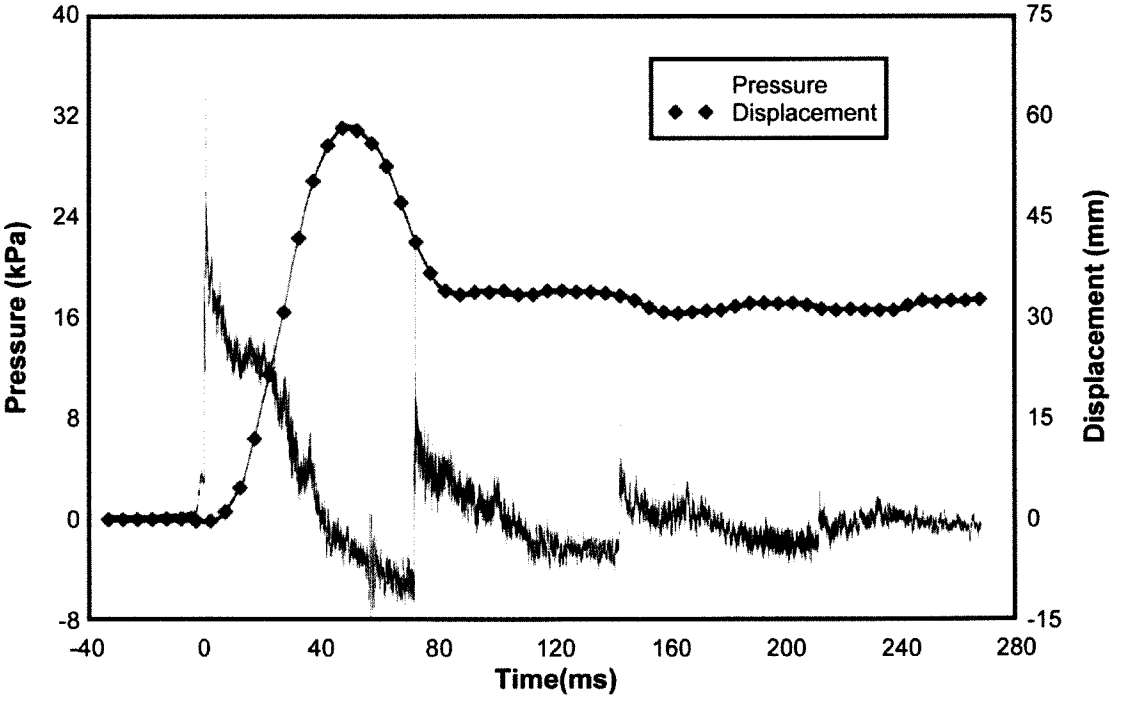


*Figure 4-75: Reflected Pressure and Mid-Height Displacement Time History for Test RC-12-2*

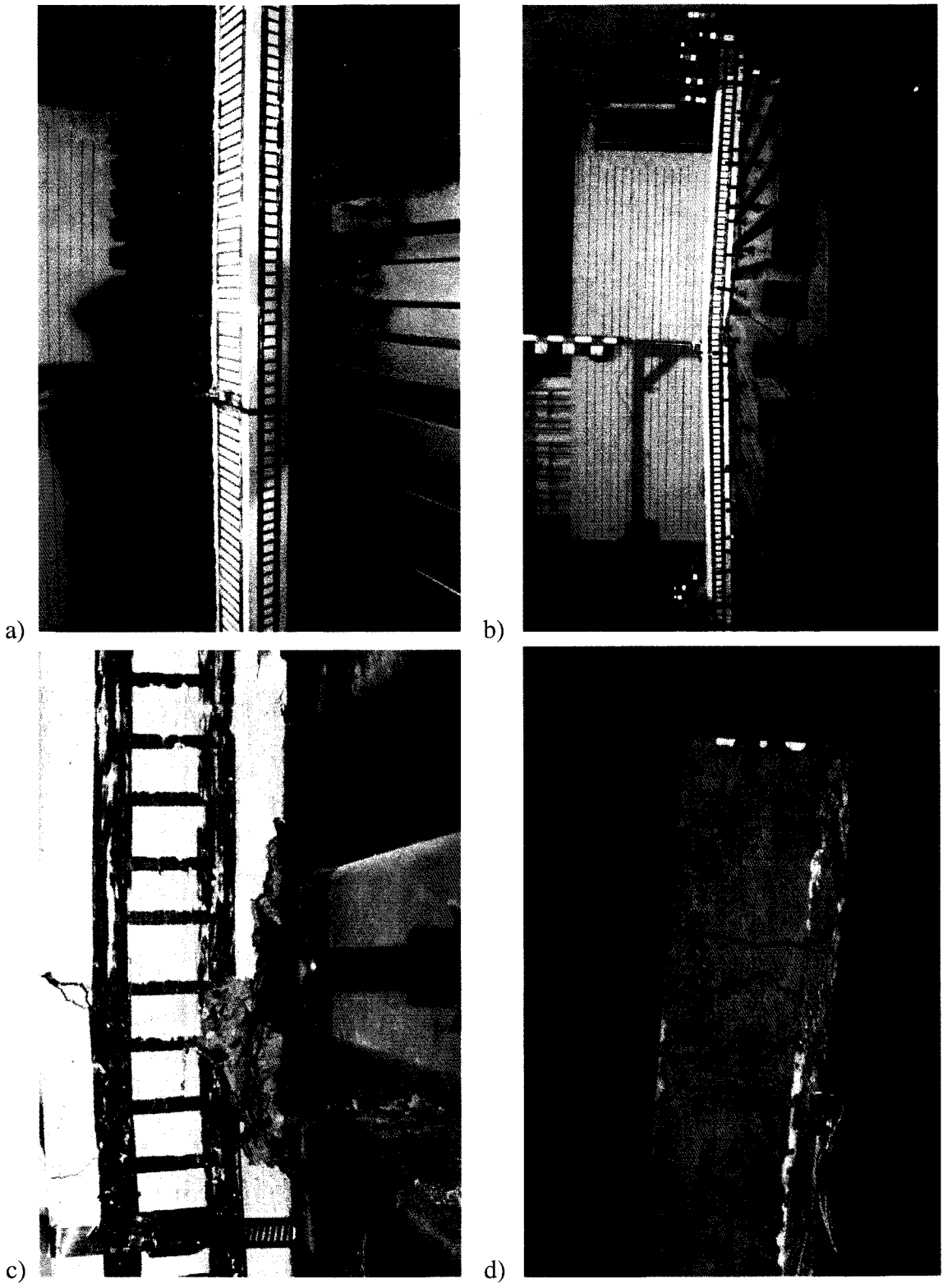


*Figure 4-76: RC-12: a) After Shot 1; b) After Shot 2; c) Mid-Height Plastic Hinge After Shot 2; d) Support Tension Cracks After Shot 2*

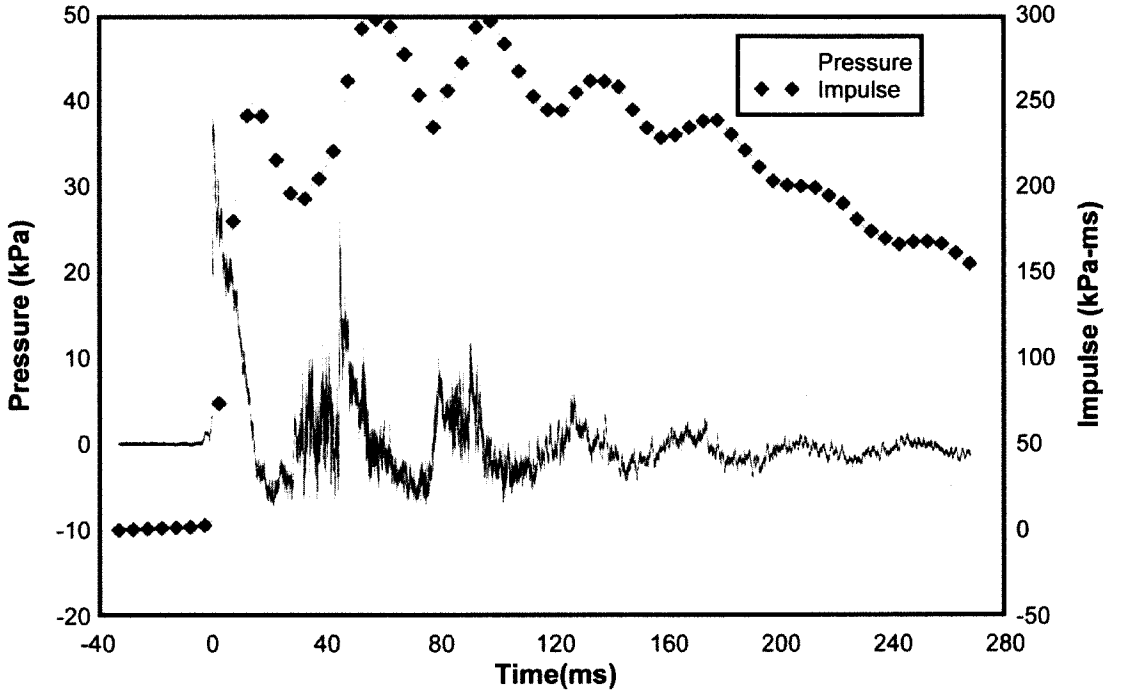


*Figure 4-77: Reflected Pressure and Impulse Time History for Test RC-13-1*

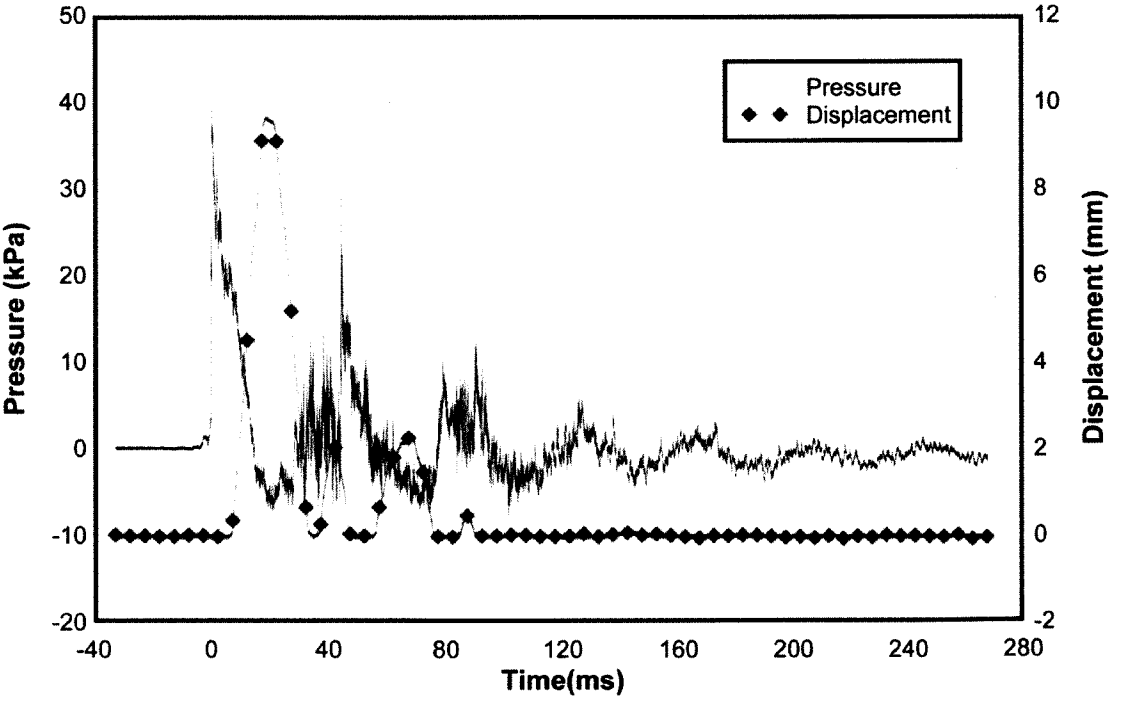


*Figure 4-78: Reflected Pressure and Mid-Height Displacement Time History for Test RC-13-1*

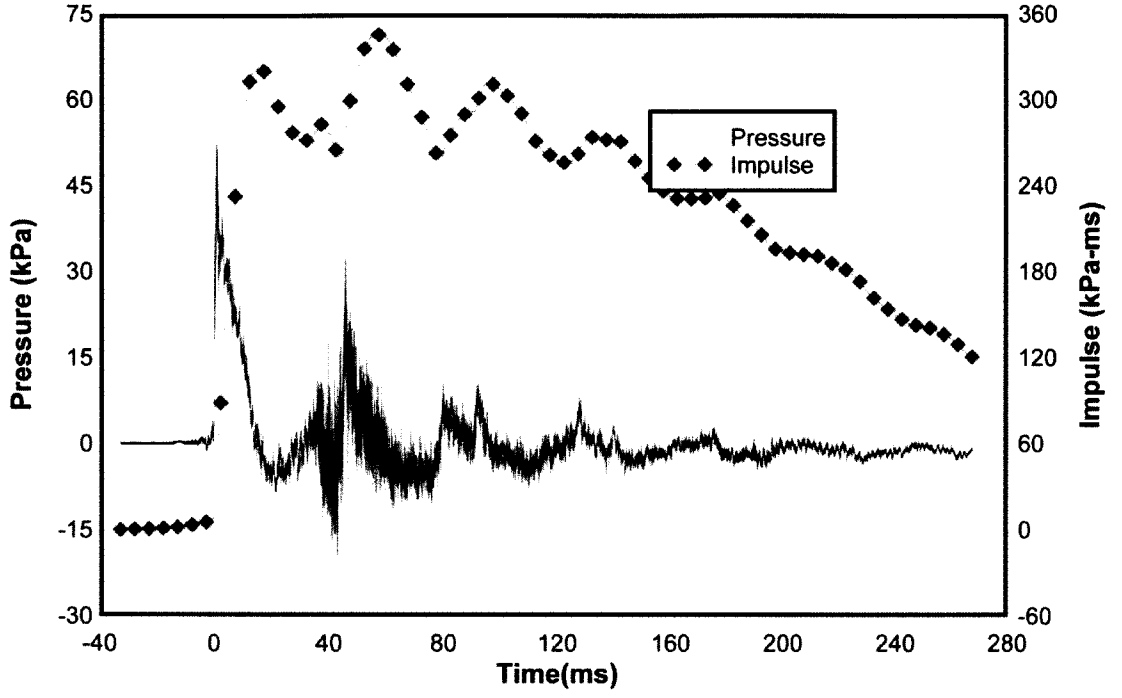


*Figure 4-79: Reflected Pressure and Impulse Time History for Test RC-13-2*

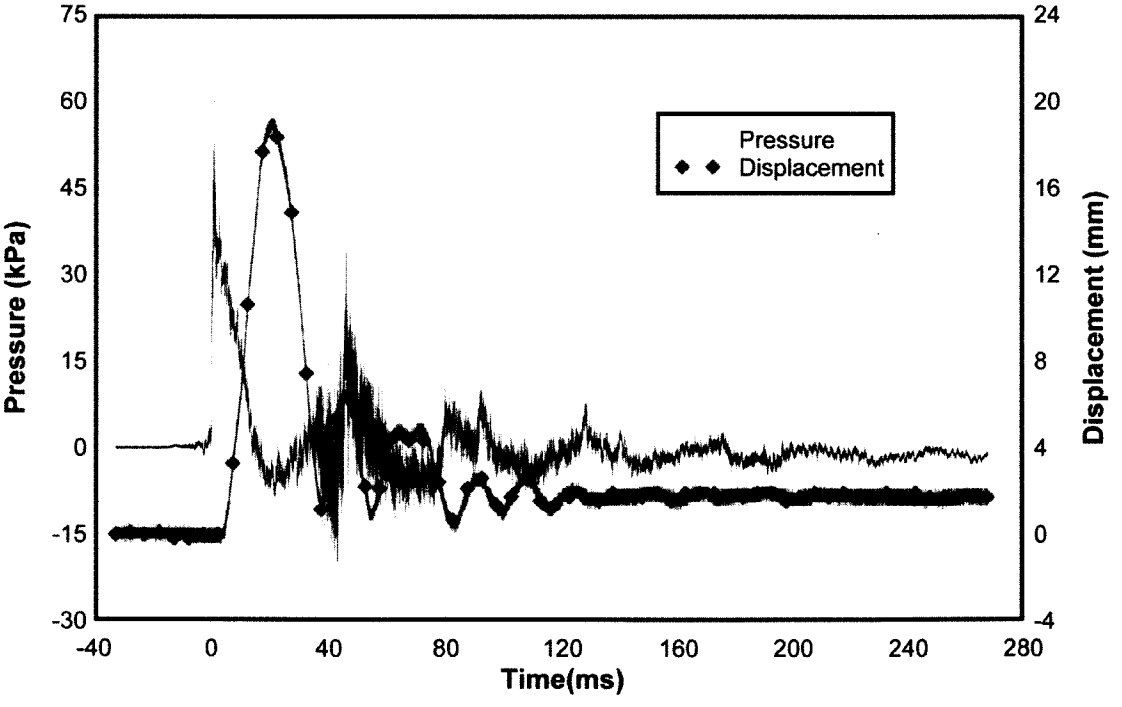


*Figure 4-80: Reflected Pressure and Mid-Height Displacement Time History for Test RC-13-2*

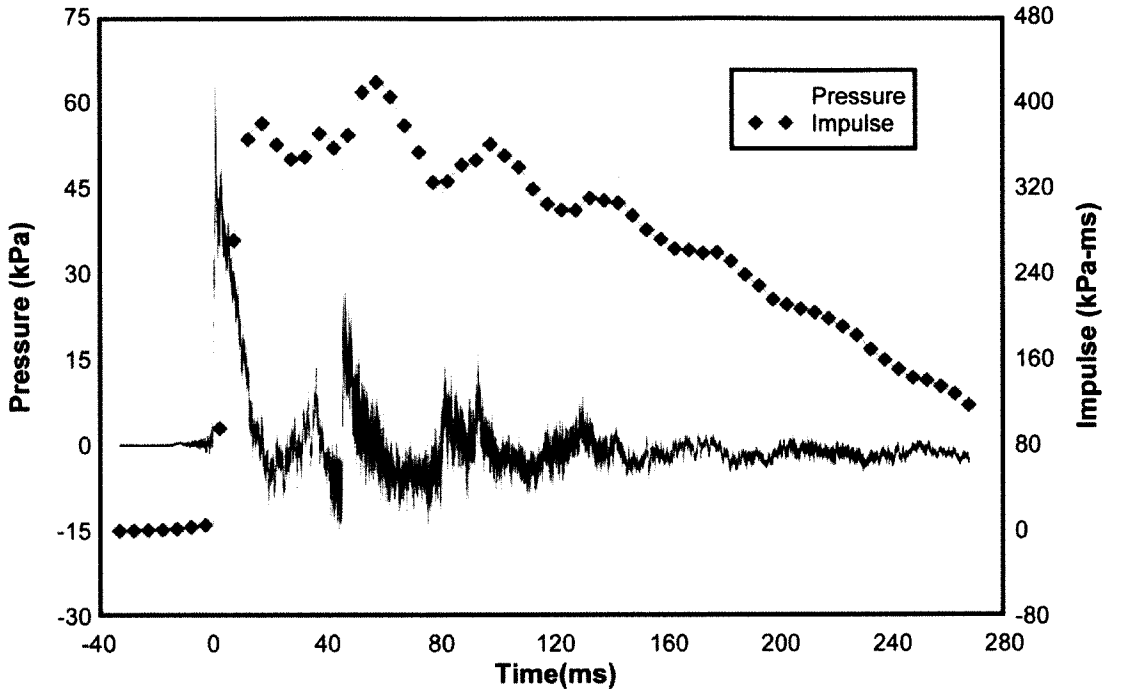


*Figure 4-81: Reflected Pressure and Impulse Time History for Test RC-13-3*

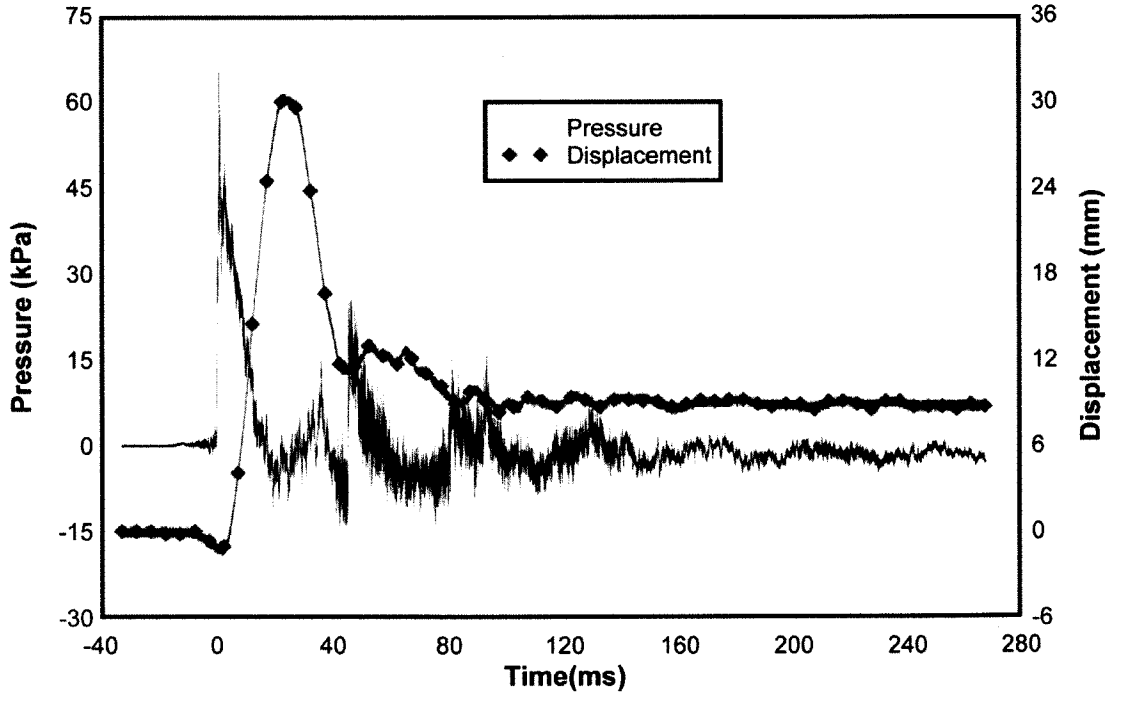


*Figure 4-82: Reflected Pressure and Mid-Height Displacement Time History for Test RC-13-3*

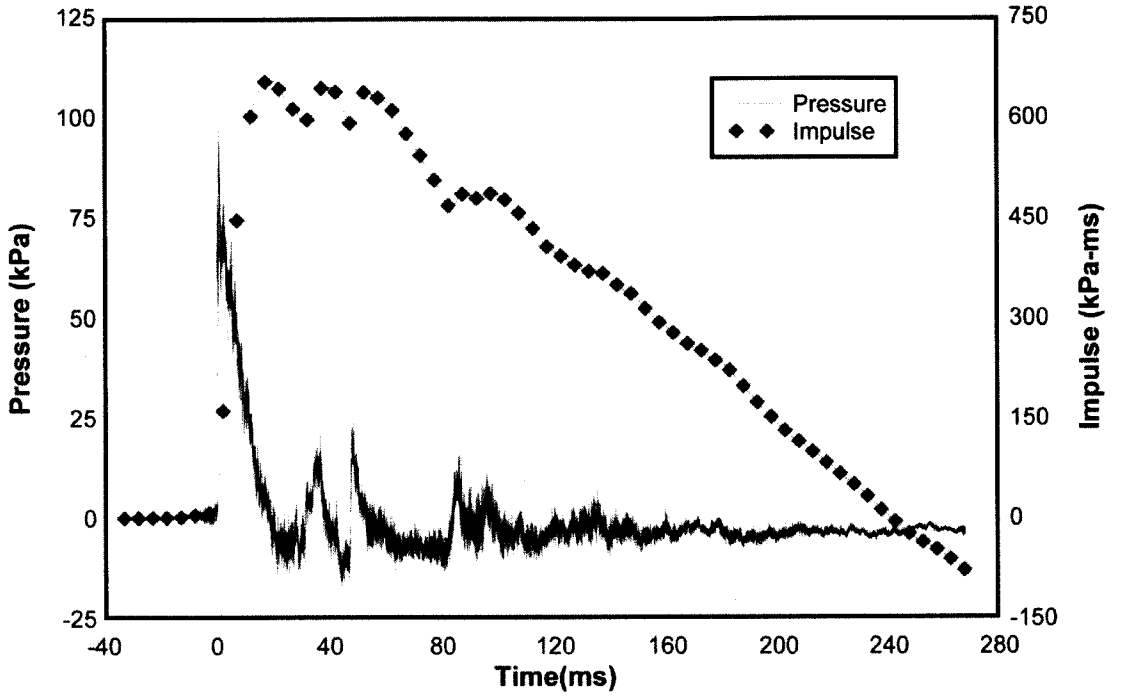


*Figure 4-83: Reflected Pressure and Impulse Time History for Test RC-13-4*

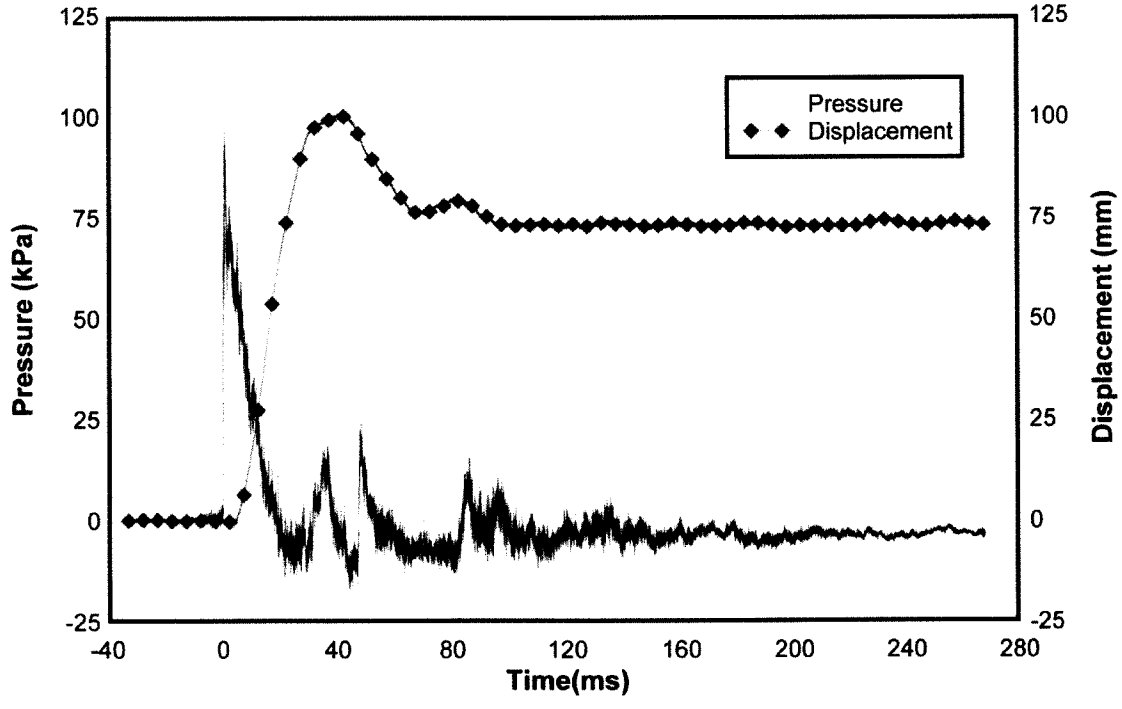


*Figure 4-84: Reflected Pressure and Mid-Height Displacement Time History for Test RC-13-4*

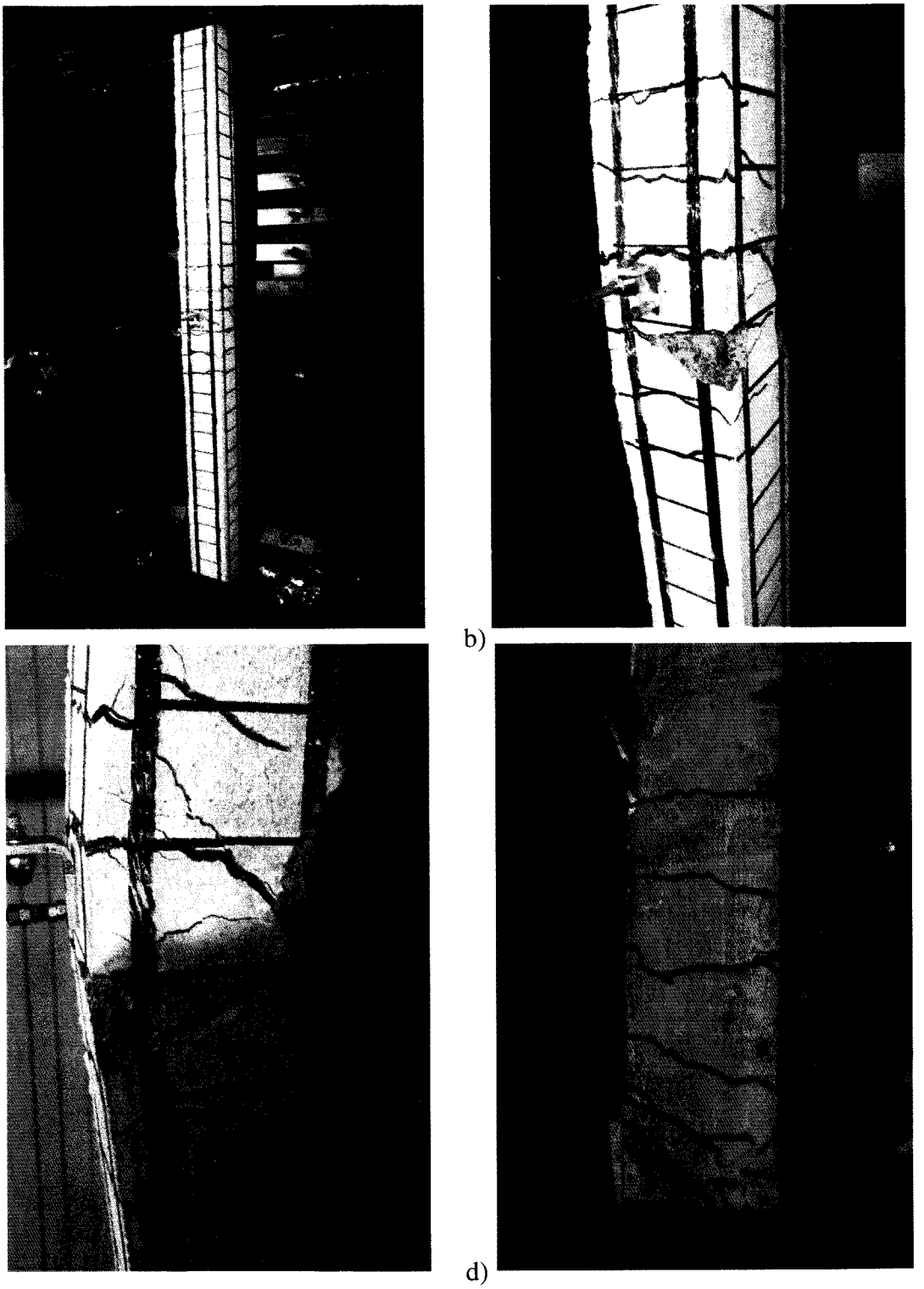

*Figure 4-85: RC-13: a) After Shot 2; b) After Shot 3; c) Mid-Height Plastic Hinge After Shot 3; d) Support Tension Cracks After Shot 3*

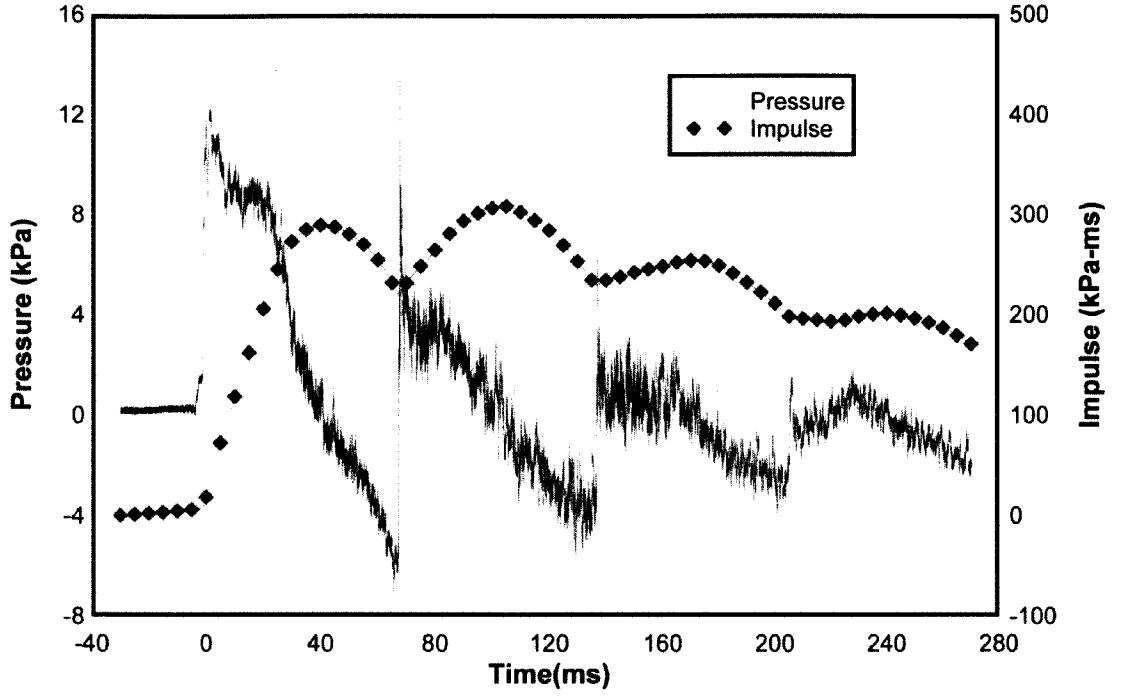


*Figure 4-86: Reflected Pressure and Impulse Time History for Test RC-14-1*

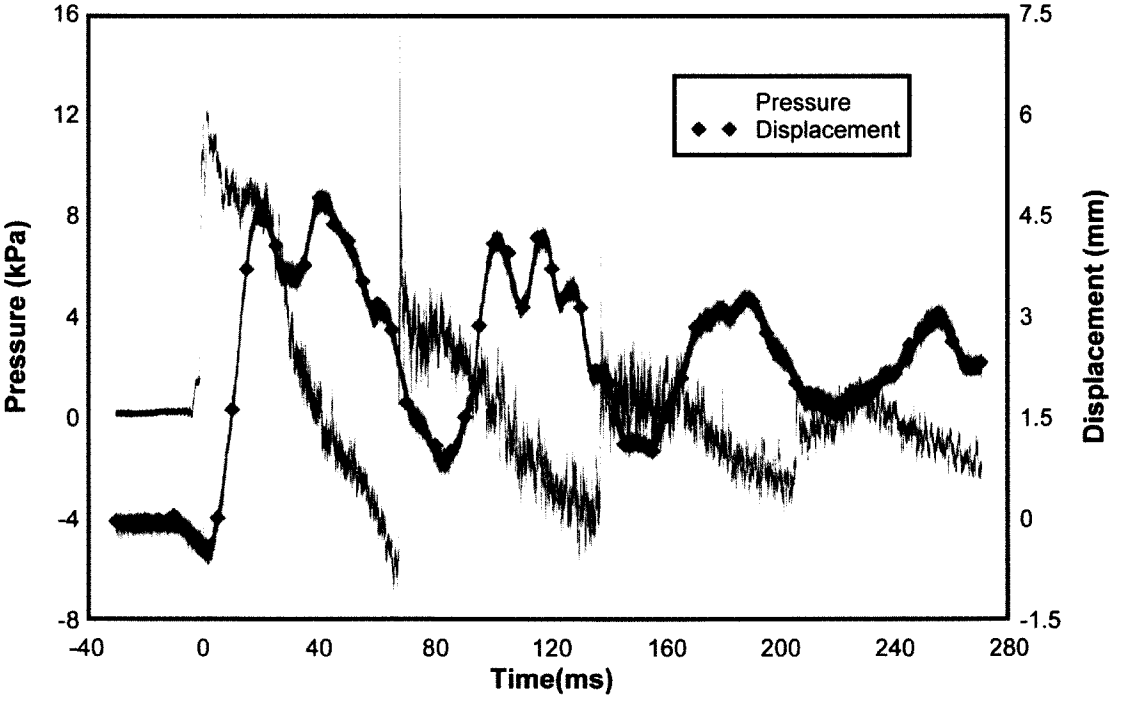


*Figure 4-87: Reflected Pressure and Mid-Height Displacement Time History for Test RC-14-1*

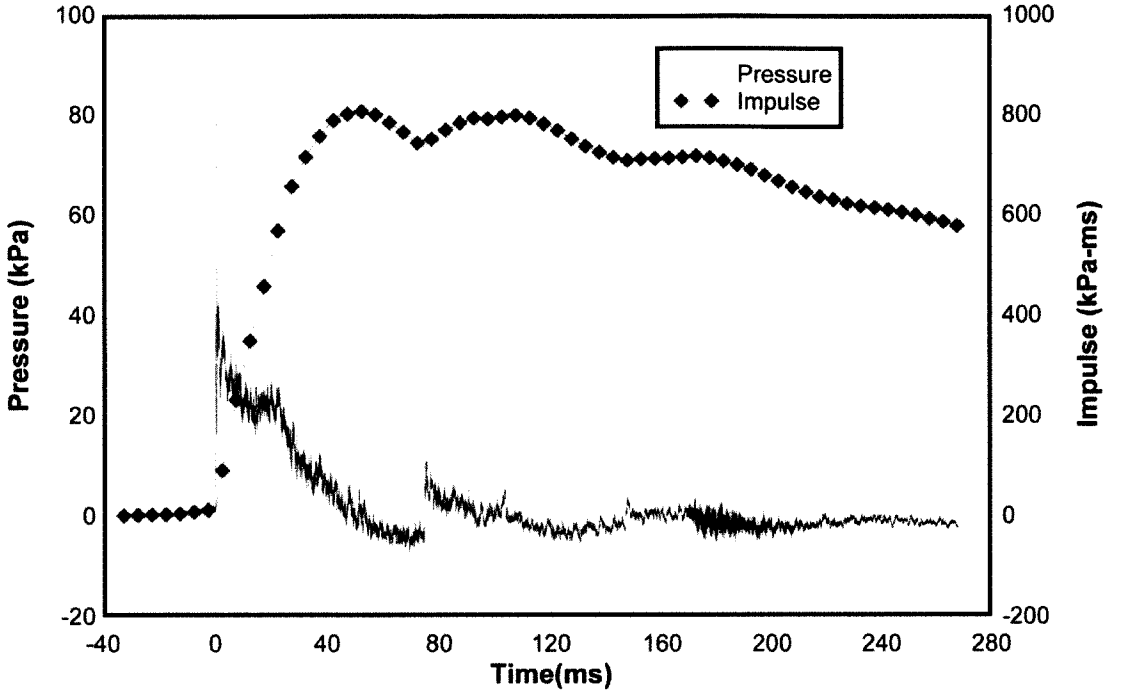


*Figure 4-88: Reflected Pressure and Impulse Time History for Test RC-14-3*

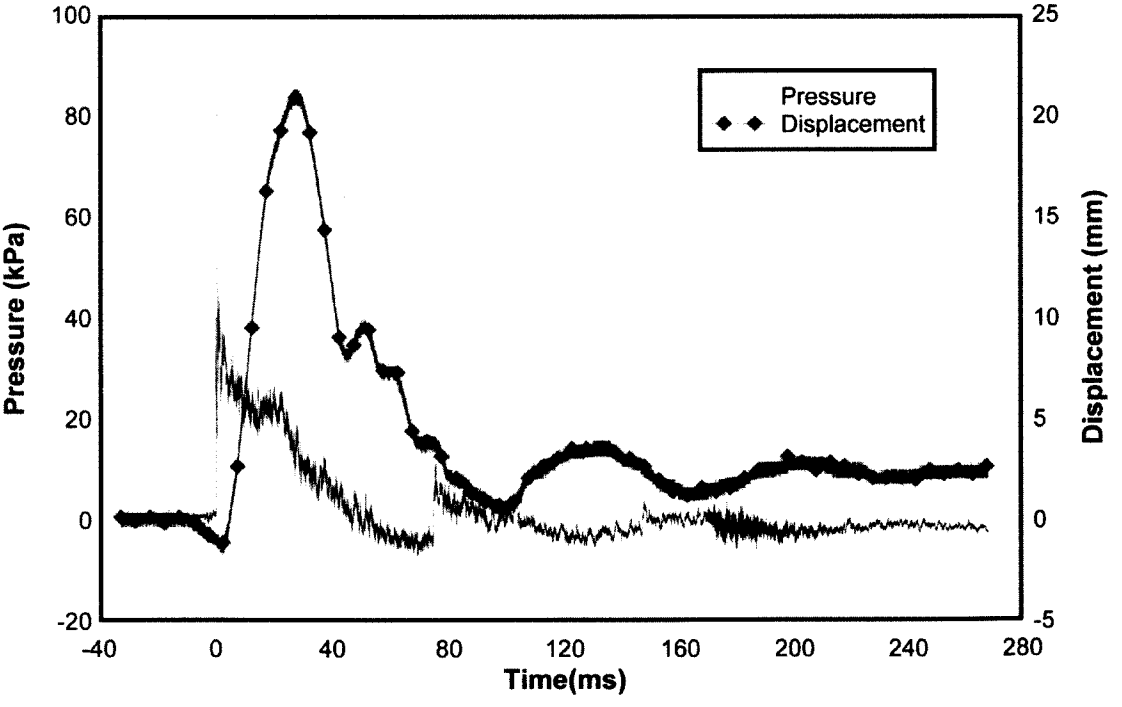


*Figure 4-89: Reflected Pressure and Mid-Height Displacement Time History for Test RC-14-3*

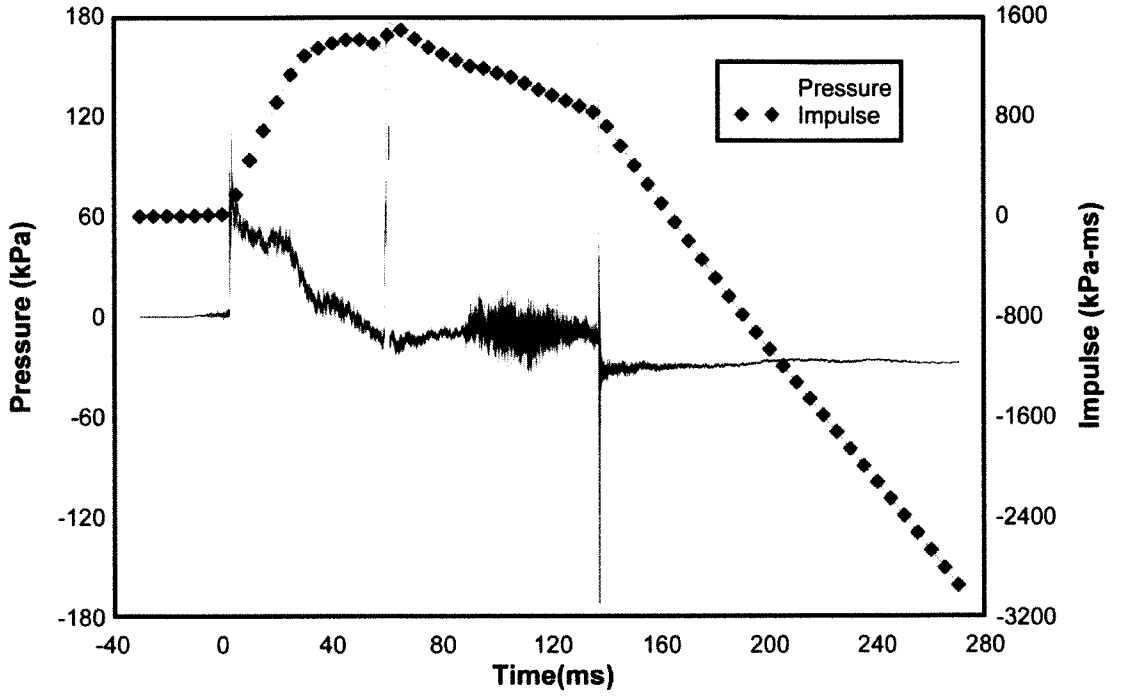


*Figure 4-90: Reflected Pressure and Impulse Time History for Test RC-14-4*

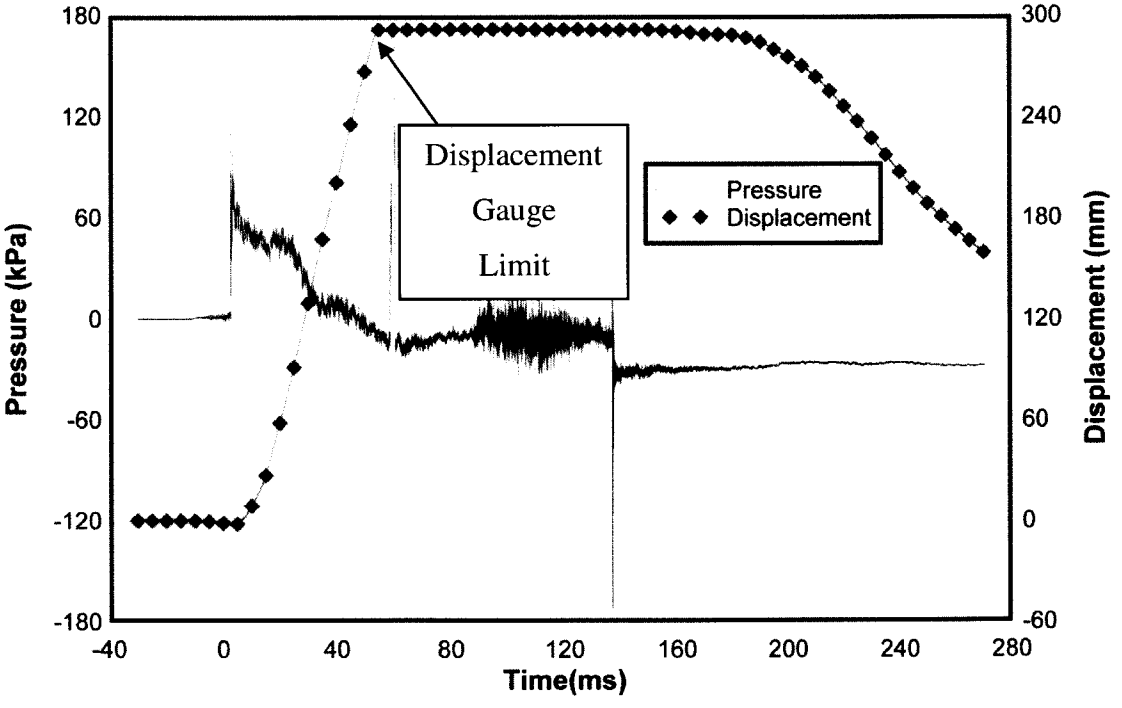


*Figure 4-91: Reflected Pressure and Mid-Height Displacement Time History for Test RC-14-4*

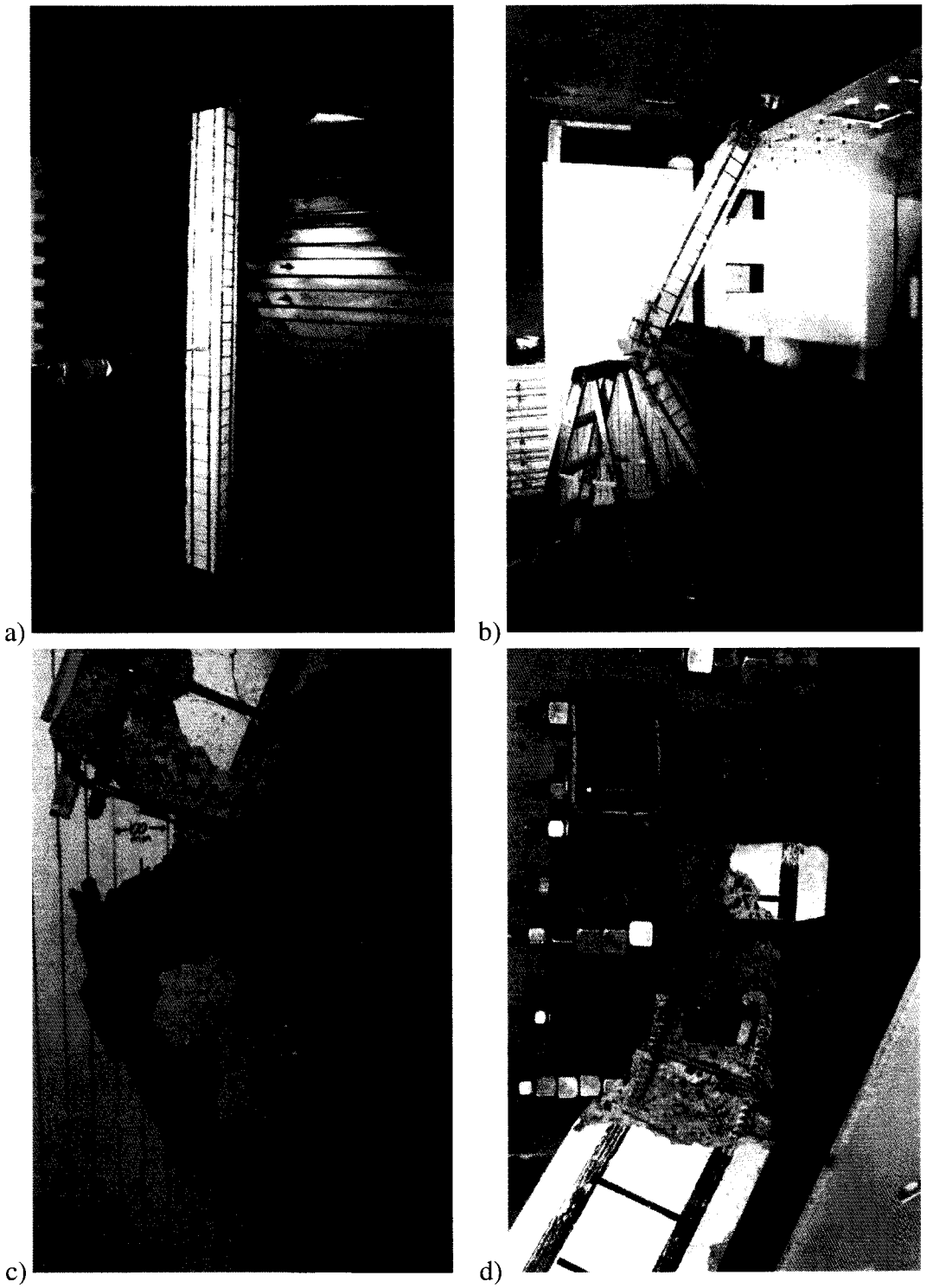


*Figure 4-92: RC-14: a) After Shot 3; b) After Shot 4; c) Mid-Height Plastic Hinge After Shot 4; d) Support Plastic Hinge After Shot 4*

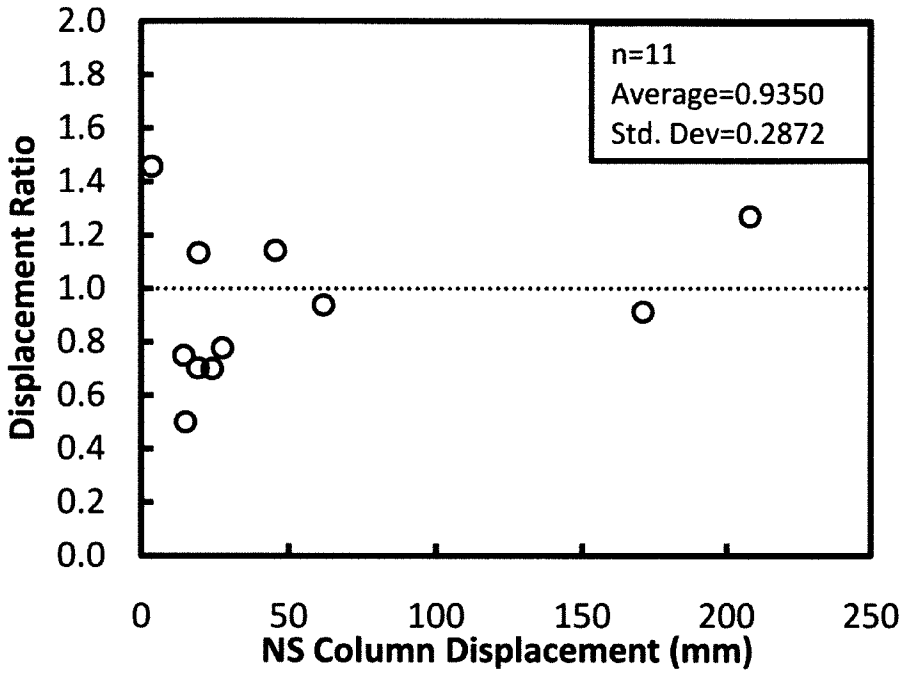


*Figure 4-93: Displacement Ratios for Seismic and Non-Seismic Columns*

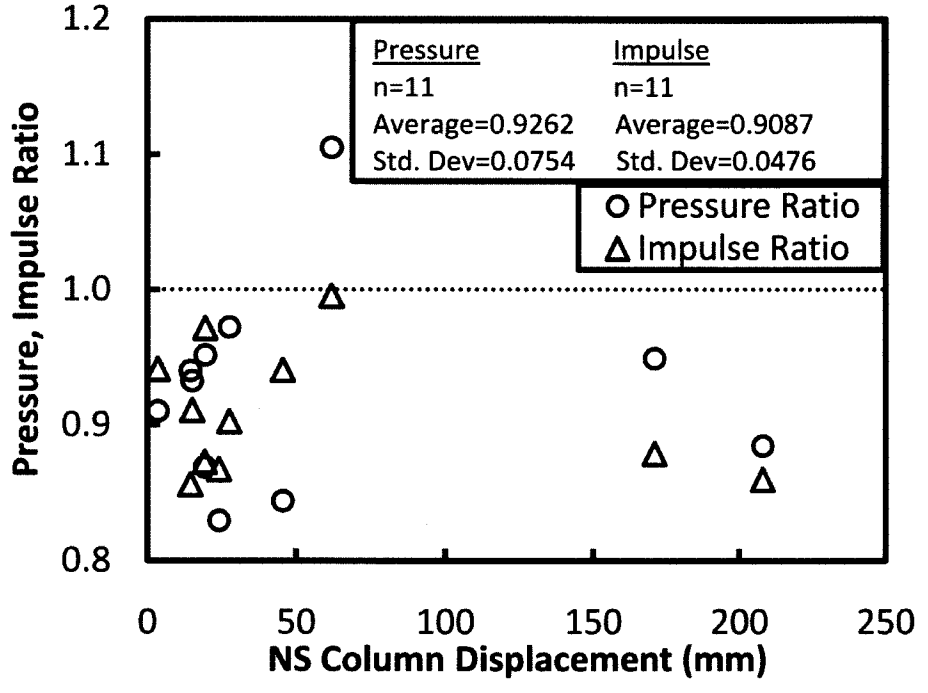


*Figure 4-94: Pressure and Impulse Ratios for Seismic and Non-Seismic Columns*

# 5 CHAPTER 5

# Analytical Results

## *5.1 General*

The experimentally recorded displacement histories for each column tested (presented in Chapter 4) were used to validate an analytical model for predicting mid-height displacement of the columns. The analytical model was developed to allow for generalizations of column behaviour under blast induced shock wave loading without the need for experimental tests. With this relatively simple analytical tool, reinforced concrete columns of different sizes and material properties may be quickly analyzed and conclusions may be drawn as to the structural integrity under shock wave loading.

### 5.1.1 Assumed Tributary Width

It is important to note that all calculations were done using an assumed tributary with of *2032 mm* acting on the *150 mm* width of the column. This tributary width was selected to be equal to that of the experimental test setup. For all calculations, the mass of the load transferring device was added to the mass of the column. Note that in all figures the pressures and impulses given are acting on a large surface area which is approximately *13.55* times wider than the actual column.

## *5.2 Analytical Calculations of Mid-Height Displacement*

Theoretical displacement time histories were generated using an equivalent single degree of freedom model iterated from zero displacement to the point of maximum displacement. Due to the impulsive nature of blast loading, where the load is suddenly applied and rapidly reduced to zero, the maximum displacement of the member will occur as a result of the first peak of the

displacement time history. Depending on the duration of the applied loading, this peak may occur during the transient response phase, when the external applied loading is still present, or more commonly during the post-transient response, or free vibration phase. Since the analytical model was only conducted until this first peak in the displacement response, there was only need to describe the resistance (load)-displacement relationship for increasing displacements. In other words, the unloading response of the member was not described in the analytical model. The change in column stiffness due to the cracking of concrete and yielding and subsequent hinging of columns was computed from the resistance-displacement relationships that were established. These stiffness values were then used in conducting the dynamic inelastic analyses of the member.

### 5.2.1 Resistance-Displacement Curve Generation

Both the mode shape and resistance-displacement curves with respect to lateral load were determined using a non-linear force-equilibrium and strain compatibility procedure developed by Tikka (2005) for the second order analysis of concrete columns and frames. A static force-displacement relationship was computed for columns under combined axial and lateral loading where the lateral force was incremented as a uniformly distributed load over the length of the column until ultimate column capacity was achieved. The analysis method accounted for confinement of core concrete and unconfined concrete outside of the core using the modified Kent-and-Park stress-strain relationship for concrete (Park, Priestly and Gill, 1982) shown in Figure 5.1, second order effects due to the combination of axial load and lateral deflection, strength reduction due to reinforcing steel buckling and strain hardening of reinforcing steel.

#### *5.2.1.1 Element and Section Discritization*

The column cross-section was defined as three materials: Reinforcing steel, unconfined concrete outside of the transverse hoops, and confined concrete within the core region of the cross-section. The cross-section was divided into a series of strips parallel to the neutral axis. Each strip was assigned a material property based on material contained within the discritized area.

The column was divided into a series of elements along the length. Element lengths were specified as being approximately equal to the thickness of the cross-section in the direction of bending.

#### *5.2.1.2 Strain Compatibility and Moment-Curvature*

Using the cross-section discritization and material properties, a strain compatibility solution was found for a given level of loading and a corresponding displacement. The moment-curvature relationship was found for each element using the neutral axis depth and strains found with strain compatibility. Theses section and element properties were used in the displacement calculations described in the following sections.

#### *5.2.1.3 Static Displacement Calculations*

The total transverse load-displacement history for the columns was found using an incremental procedure. This procedure involved calculating the displacements of the column over a series of increasing transverse loads beginning with an initial load of around *10* % of the ultimate transverse load.

Displacements were determined using Newmark`s (1943) method to find the equilibrium state in each element along the length of the column. An initial displacement was provided to the column based on the initial applied end moments and the first and second order moments at the ends of each element were calculated based on the initial displacement. The curvature was found in each element and used to describe the curvature along the length of the column. Using the conjugate beam method, new displacements were calculated at the end of each element. These displacements were compared with the initial assumed displacement and if the agreement was not within *0.05* %, the procedure was repeated until convergence under the given load. Once the displacement converged for a given transverse load, the load was increased by an incremental value and the procedure was repeated (Tikka and Mirza, 2004).

#### *5.2.1.4 Plastic Hinge Formation*

Plastic hinge formation occurs in the model based on the moment-curvature relationship and the stress-strain state in each element. Once an element can no longer satisfy equilibrium conditions due to a high stress state, a plastic hinge will form and stresses will redistribute to the other elements in the model. The plastic hinge occurs over the entire element length which is defined as approximately equal to the width of the cross-section in the direction of bending.

#### *5.2.1.5 Reinforcing Steel Buckling*

The reinforcing steel buckling material model originally presented by Yalcin and Saatcioglu (2000) was incorporated into the static force-displacement calculation procedure (Tikka, 2005). This model assumes that the stress-strain relationship is the same for reinforcing steel in compression and tension as long as buckling is prevented. The spacing of the transverse hoop reinforcement divided the longitudinal reinforcing steel bar diameter give an aspect ratio describing the slenderness of the reinforcement. The model describes different failure paths for reinforcement based on this aspect ratio. It should be noted that the aspect ratio of the columns in question was *2.5* and *5* for columns RC-1 through RC-12 with the seismic columns having the smaller aspect ratio and *7.5* for columns RC-13 and RC-14. In the buckling model, all of these aspect ratios allow for the development of plastic behaviour and at least some strain-hardening.

#### *5.2.1.6 Material Increase Factors for Strain Rate*

For each column type, a series of resistance-displacement curves were generated using varying dynamic increase factors for material strength. The dynamic increase factors, described in Chapter 1, are multiplied with the yield stress ($f_y$) of steel and the concrete strength ($f'_c$) increasing the strength of both materials to reflect the strength increase that has been observed in these materials under high strain rates. For steel, the elastic modulus ($E_s$=*200,000 MPa*) does not change. For concrete, the strength found using the dynamic increase factor is used with the modified Kent-and-Park model to develop a stress-strain relationship for the unconfined and

partially confined concrete. During the dynamic analysis procedure, the appropriate resistance-displacement curve corresponding to the material strain rate was used.

#### *5.2.1.7 Change in Axial Load*

During the physical testing the axial load was applied using a hydraulic jack to apply compression stress to the ends of the column as described in Chapter 3. As the column deflects horizontally, the average projected vertical length decreases. This change in length causes an equivalent reduction in axial load as the horizontal displacement increases and the end of the column moves away from the vertical support (hydraulic jack) which is fixed in place. This change in axial load was included in the development of the resistance-displacement curve by using resistance values from curves developed with various axial loads to form a composite resistance-displacement curve with a variable axial load. The magnitude of the axial load at any given displacement was determined as a function of the initial strain due to the initial axial load and the vertical displacement at the top of the column at a specified horizontal displacement. Resistance-displacement curves developed using dynamic increase factors (*DIF*) for material strength of *1.17* for reinforcing steel yield stress and *1.19* for concrete strength for the five different types of columns are shown in Figures 5.2 to 5.6. In these figures, the idealized curve accounting for varying axial load is plotted along with the resistance-displacement curves for constant axial loads of varying magnitude.

#### *5.2.1.8 Rotational Stiffness*

An analysis of the experimental results indicates that the supports behaved as partially fixed to rotation, rather than fully fixed as intended. Using the experimentally recorded strains in the reinforcing steel measured at mid-height and at the support locations, it was determined that the supports provided between *33* and*46* % of the moment/rotational resistance of a support fully fixed against rotation for columns RC-2 through RC-14. The supports were found to provide approximately *17* % of the moment/rotational resistance of a support fully fixed against rotation for column RC-1. This lower rotational support stiffness was incorporated into the static model used to develop the resistance-displacement curves. Figure 5.7 shows that the rotational stiffness was incorporated into the column model by providing additional pin ended elements extending

perpendicular to the column ends, where the column ends are not restrained rotationally. The length and rigidity of these elements was selected to provide the required rotational stiffness at the column supports.

Since the supports did have rotation, there was the possibility of a compression membrane forming along the length of the member if the rotating ends of the member bear against the vertical supports and therefore cause an increase in the stiffness of the member. In this case, the vertical supports (the hydraulic jack and a steel block and steel plate system bearing against the strong floor) allowed sufficient rotation of the cross-section to prevent the formation of a compression membrane.

#### *5.2.1.9 Constant Resistance for Large Deformations*

A constant resistance of *5* % of the maximum resistance value was given for large (post collapse mechanism) displacements (Figures 5.2 through 5.6). This resistance value was provided to ensure that the single degree of freedom model would eventually achieve a maximum displacement for very large displacement models. If a column displaces into this range, it is experiencing post collapse behaviour and is completely destroyed.

#### *5.2.1.10 Resistance – Displacement Curve Library*

Using the known geometry of the columns along with support rotational stiffness and material stress-strain curves, a library of resistance-displacement curves was developed for each column using dynamic increase factors selected from a range of strain rates. These resistance-displacement curves were used in the single degree of freedom numerical model described below.

### 5.2.2 Single Degree of Freedom Model

Once the resistance-displacement model was developed, conversion factors to equate the continuous system of stiffness and mass into equivalent values describing a single degree of freedom (mid-height displacement) were developed using the constant acceleration method

described in Chapter 1. These equivalent stiffness and mass factors were developed for the member response in three mode shapes: 1) prior to the development of any plastic hinge mechanisms; 2) after the development of the first plastic hinge and prior to the development of the collapse mechanism; 3) and post collapse. Using the resistance-displacement relationship and the conversion to an equivalent single degree of freedom model, the dynamic response of the columns was predicted using the experimentally recorded pressure-time histories multiplied by the total area of the load transfer mechanism as the applied load function and the constant acceleration numerical integration procedure described in Chapter 1.

#### *5.2.2.1 Numerical Integration Time Step*

The time step used for the numerical integration was selected as $10^{-7}$ *seconds*. The constant acceleration method is unconditionally stable for any time step, however, accuracy of the solution improves with a smaller time step. As the ratio between the time step and the natural period of vibration decreases, the accuracy of the solution increases to convergence (Chang, 2009). Using the initial stiffness of the columns, where the natural period is smallest, it was determined that a minimum time step of approximately $10^{-4}$ seconds was required for an accurate solution without significant incremental errors accumulating throughout the analysis. Since the numerical analysis was performed using a computer program, a significantly smaller time step ($10^{-7}$ *seconds*) was used with minimal extra computational time. Several trials were conducted using time steps that ranged between $10^{-4}$ and $10^{-7}$ *seconds* to ensure that no incremental errors were accumulated throughout the numerical integration due to time step size. In all cases it was found that a $10^{-7}$ *second* time step guaranteed convergence in the solution.

#### *5.2.2.2 Iteration for Dynamic Increase Factor*

For the first iteration of the single degree of freedom numerical model, assumed initial strain rate material increase factors of *1.17* for reinforcing steel yield stress and *1.19* for concrete strength were used as recommended by the US Departments of the Army, the Navy, and the Air Force Structures to Resist the Effects of Accidental Explosions (TM 5-1300 1990) design manual were used to compute the maximum displacement. The time to yield, computed from the first iteration for the maximum displacement, was used to determine the approximate material strain

rate and new material increase factors were selected as described in Chapter 1. The new material increase factors were used to develop a refined resistance-displacement curve and the single degree of freedom model was reanalysed. This procedure was repeated until convergence of the strain rate between previous and current solution was achieved. If the material did not yield during the response, the strain rate was approximated using the time to maximum displacement.

#### *5.2.2.3 Single Degree of Freedom Mass*

In the experimental tests, the lateral load-transferring mechanism contributed significant mass to the system, *545 kg*. Although this mass was not physically connected to the column it was assumed to act on the column throughout the entire analysis until maximum displacement was attained. This assumption was verified by observing the interaction between the load distribution system and the column which was reviewed from the high-speed video recorded in each test. The sum of the lateral load-transferring mechanism mass and the mass of the column was multiplied by the equivalent mass factor to form the equivalent single degree of freedom mass used for the numerical analysis.

## *5.3 Analytical Results*

The results of the numerical analysis are shown in terms of pressure-impulse diagrams for iso-displacement values, and individual time histories. Table 5.1 provides summaries of the maximum displacements and time to reach maximum displacements for the single degree of freedom model and the experimentally recorded results.

### 5.3.1 Pressure – Impulse Iso-Damage Curves

Iso-displacement (based on maximum displacement) pressure-impulse diagrams were developed for each type of column tested and are shown in Figures 5.8 through 5.12. These curves were developed using the single degree of freedom model and changing the pressure and impulse values until the predicted maximum displacement was equal to a pre-selected value. The shock wave pressure-time history was approximated as a triangular distribution. The iso-displacement

curves are shown over the range of the approximate pressure and impulse range that can be produced with the shock tube. Displacement levels were chosen as *10 mm, 20 mm, 30 mm, 40 mm, 50 mm, 60 mm, 80 mm, and 150 mm*. These values were selected to reflect a range of response that includes elastic and inelastic behaviour.

### 5.3.2 Experimental vs. Predicted Displacements

Figures 5.13 through 5.52 show the predicted mid-height displacement overlaid upon the plot of the experimental displacement time history and the applied pressure time history for all of the columns tested. The maximum predicted and experimental displacements along with the predicted and experimental time to maximum displacements are reported in Table 5.1. The figures indicate that, in general, the single degree of freedom model accurately predicts the slope of the displacement-time history and predicts maximum displacement values for all column types with reasonable accuracy.

#### *5.3.2.1 Predicted Displacements*

The predicted maximum displacements are plotted against the experimentally recorded maximum displacements in Figures 5.53 and 5.54. Table 5.2 lists the ratios of predicted to experimentally ($d_{SDOF} / d_{EXP}$) recorded maximum displacements for different ranges of experimental maximum displacement. The displacement ratio average for all of the *37* available tests was *1.052* with a standard deviation of *0.613*, and coefficient of variation of *0.583*. The average ratio greater than *1.0* indicates that the predicted displacements are on average about *5 %* larger than those recorded experimentally. The high standard deviation and coefficient of variation can be attributed to the sensitivity of the displacement ratio for small displacements and difficulties predicting very large displacements when plastic hinges form at the mid-span and ends of the column.

For small displacement values, taken as less than *10 mm* recorded experimentally, the average of the displacement ratio was computed as *2.103* with a standard deviation of *0.805* and a coefficient of variation of 0.382 for *6* tests. For this range, the apparent inaccuracy may be

attributed to the sensitivity of the ratio for small displacements where even one millimetre in difference between predicted and recorded displacements will result in a displacement ratio that is *10 %* or more away from unity. There are several sources of error that likely contribute to the over prediction of displacements for small displacement levels including: the small gap between the load transfer mechanism and the column in experimental testing; sensitivity of the displacement measuring sensors; settling of the supports; and settling of the displacement sensor connection to the column.

There is considerably more accuracy in predicting displacements for moderate levels of experimentally recorded displacement, taken as between *10 mm* and *75 mm*. The average displacement ratio was calculated as *0.913* with corresponding standard deviation of *0.261* and coefficient of variation of 0.286. Accuracy over this range improves as many of the sources of errors mentioned above become negligible and the displacement ratio becomes less sensitive to small relative differences between predicted and experimental maximum displacements.

Predictions of displacements for tests resulting in experimental displacements over *75 mm* were under predicted with a displacement ratio average of *0.578*, a standard deviation of *0.208*, and coefficient of variation of *0.360*. This average under prediction can be attributed to the difficulties in predicting very large displacements for damaged members using single degree of freedom models where the actual displacement at the formation of the collapse mechanism is difficult to predict and the post collapse resistance is unknown.

#### *5.3.2.2 Predicted Time to Maximum Displacements*

Figures 5.55 and 5.56 show the ratio of predicted time to maximum displacement ($t_{SDOF} / t_{EXP}$) plotted against the experimentally recorded time to maximum displacement for all tests. Table 5.2 lists the ratios of predicted to experimentally recorded time to maximum displacement for the same displacement level groups described above. There is a general trend of under predicting the time to maximum displacement where the average ratio for all *37* tests is *0.899* with a standard deviation of *0.248* and a coefficient of variation of *0.276*. This under prediction can be largely attributed to a delay in the response of the column in the experimentally recorded time-

histories shown in Figures 5.13 through 5.52. This delay is due to the small gap between the load transfer mechanism and the column as well as possible limitations of the displacement measuring sensors that resulting in small lag times. For low levels of experimentally recorded displacements, the time ratio has an average of *0.939*, a standard deviation of *0.105*, and a coefficient of variation of *0.112*. For mid-range levels of experimentally recorded displacements, the time ratio has an average of *0.904*, a standard deviation of *0.159*, and a coefficient of variation of *0.176*. For high experimentally recorded displacements, the time ratio has an average of *0.839*, a standard deviation of *0.553*, and a coefficient of variation of *0.659*.

The time to maximum displacement and maximum displacement are dependent variables where large maximum displacement will result in a large time to maximum displacement. Since these variables are dependent, the same inaccuracies in predicting small and large displacements apply to predicting the time to maximum displacement.

## *5.4 Summary*

A simple analytical technique for determining the displacement response of reinforced concrete columns under blast induced shock wave loading has been validated using experimental results. It was found that the model, a single degree of freedom numerical integration with statically defined resistance-displacement relationships and material increase factors for high strain rate effects, can accurately predict displacements of a reinforced concrete column under shock wave loading. The model is most accurate for moderate displacements, up to the formation of a collapse mechanism. Accuracy of the model is low for displacements after the formation of the collapse mechanism, however, at this stage in member response, the exact displacement value is of little importance as the member has already failed.

*TABLE 5.1 - Pressure, Impulse, Maximum Displacement, and Time Maximum Displacement Values for Experimental Results and SDOF Predictions.*

| | | Shock Wave Properties | | | Experimental | | SDOF | | | |
|---|---|---|---|---|---|---|---|---|---|---|
| | | $P_r$ (kPa) | $I_r$ (kPa-ms) | $t_d$ (ms) | $d_{max}$ (mm) | $t_{max}$ (ms) | $d_{max}$ (mm) | $t_{max}$ (ms) | $d_{SDOF}/d_{EXP}$ (mm/mm) | $t_{SDOF}/t_{EXP}$ (ms/ms) |
| RC- 1- | 1 | 22.0 | 120.1 | 10.0 | 13.9 | 28.4 | 14.2 | 27.0 | 1.03 | 0.95 |
| No Axial | 2 | 38.0 | 157.7 | 10.4 | 20.8 | 28.9 | 18.7 | 29.2 | 0.90 | 1.01 |
| | 3 | No Data | | | No Data | | No Data | | No Data | |
| RC- 2- | 1 | 23.1 | 193.2 | 24.9 | 24.2 | 28.8 | 28.5 | 37.3 | 1.18 | 1.29 |
| 350 kN Axial | 2 | 39.9 | 425.7 | 26.3 | 66.4 | 46.3 | 59.9 | 48.5 | 0.90 | 1.05 |
| RC- 3- | 1 | 51.1 | 193.2 | 9.9 | 15.0 | 18.3 | 15.6 | 20.5 | 1.04 | 1.12 |
| 350 kN Axial | 2 | 58.0 | 222.2 | 10.0 | 19.2 | 22.6 | 20.9 | 22.9 | 1.09 | 1.01 |
| | 3 | 89.7 | 362.3 | 11.5 | 76.4 | 52.0 | 38.8 | 27.6 | 0.51 | 0.53 |
| RC- 4- | 1 | 2.9 | 12.8 | 8.3 | No Data | | 0.95 | 17.2 | No Data | |
| 350 kN Axial | 2 | 47.6 | 176.0 | 9.5 | 7.5 | 21.3 | 13.4 | 18.4 | 1.79 | 0.86 |
| | 3 | 50.4 | 193.9 | 9.8 | 13.5 | 20.6 | 15.1 | 18.9 | 1.12 | 0.92 |
| | 4 | 58.0 | 227.7 | 9.5 | 18.2 | 24.0 | 19.8 | 21.7 | 1.09 | 0.90 |
| | 5 | No Data | | | No Data | | No Data | | No Data | |
| RC- 5- | 1 | 23.8 | 140.8 | 13.0 | 3.5 | 23.0 | 11.3 | 20.3 | 3.22 | 0.88 |
| 350 kN Axial | 2 | 39.9 | 241.5 | 14.8 | 19.4 | 26.0 | 25.4 | 26.3 | 1.31 | 1.01 |
| | 3 | 53.1 | 324.3 | 15.8 | 45.5 | 37.0 | 37.6 | 30.4 | 0.83 | 0.82 |
| RC- 6- | 1 | 21.7 | 132.5 | 13.0 | 5.1 | 22.0 | 8.4 | 19.0 | 1.64 | 0.86 |
| 350 kN Axial | 2 | 38.0 | 234.6 | 14.2 | 22.0 | 28.0 | 18.2 | 22.3 | 0.83 | 0.80 |
| | 3 | 44.9 | 305.0 | 15.7 | 52.0 | 49.0 | 28.2 | 26.8 | 0.54 | 0.55 |
| RC- 7- | 1 | 15.2 | 182.9 | 19.2 | 15.0 | 25.0 | 13.3 | 24.3 | 0.89 | 0.97 |
| 350 kN Axial | 2 | 30.4 | 254.6 | 20.5 | 24.0 | 27.0 | 21.0 | 27.4 | 0.87 | 1.01 |
| | 3 | 89.7 | 762.5 | 26.2 | 208.0 | 55.0 | 204.5 | 104.6 | 0.98 | 1.90 |

| | | Shock Wave Properties | | | Experimental | | SDOF | | | |
|---|---|---|---|---|---|---|---|---|---|---|
| | | $P_r$ (kPa) | $I_r$ (kPa-ms) | $t_d$ (ms) | $d_{max}$ (mm) | $t_{max}$ (ms) | $d_{max}$ (mm) | $t_{max}$ (ms) | $d_{SDOF}/d_{EXP}$ (mm/mm) | $t_{SDOF}/t_{EXP}$ (ms/ms) |
| RC1- 8- | 1 | 15.0 | 107.0 | 16.3 | 2.2 | 20.0 | 6.7 | 20.1 | 3.03 | 1.01 |
| 350 kN Axial | 2 | 25.2 | 220.8 | 19.0 | 16.8 | 28.0 | 18.0 | 26.3 | 1.07 | 0.94 |
| | 3 | 79.4 | 655.5 | 23.2 | 264.0 | 127.0 | 100.0 | 41.3 | 0.38 | 0.33 |
| RC1- 9- | 1 | 13.8 | 182.2 | 27.8 | 14.4 | 29.0 | 10.7 | 24.1 | 0.74 | 0.83 |
| 350 kN Axial | 2 | 24.8 | 269.1 | 24.0 | 27.5 | 32.0 | 21.3 | 29.5 | 0.77 | 0.92 |
| | 3 | 67.6 | 683.1 | 32.0 | 171.0 | 54.0 | 97.9 | 45.3 | 0.57 | 0.84 |
| RC1- 10- | 1 | 13.0 | 155.9 | 30.2 | 10.8 | 28.3 | 8.5 | 22.6 | 0.78 | 0.80 |
| 350 kN Axial | 2 | 24.2 | 242.9 | 23.3 | 21.4 | 30.0 | 17.3 | 26.8 | 0.81 | 0.89 |
| | 3 | 64.2 | 600.3 | 27.0 | 156.0 | 53.0 | 79.9 | 41.5 | 0.51 | 0.78 |
| RC1- 11- | 1 | 12.8 | 252.5 | 37.5 | No Data | | 13.2 | 27.0 | No Data | |
| 350 kN Axial | 2 | 26.2 | 440.2 | 41.7 | 61.8 | 53.0 | 30.9 | 37.2 | 0.50 | 0.70 |
| RC1- 12- | 1 | 13.5 | 280.1 | 41.2 | 18.4 | 37.0 | 11.5 | 25.9 | 0.63 | 0.70 |
| 350 kN Axial | 2 | 29.0 | 438.2 | 43.0 | 58.0 | 50.0 | 26.4 | 31.9 | 0.45 | 0.64 |
| RC1- 13- | 1 | 39.7 | 241.5 | 14.7 | 9.6 | 19.4 | 13.1 | 17.3 | 1.36 | 0.89 |
| 400 kN Axial | 2 | 56.6 | 324.3 | 15.6 | 18.8 | 20.8 | 18.7 | 18.6 | 1.00 | 0.89 |
| | 3 | 61.4 | 386.4 | 17.1 | 30.2 | 23.6 | 24.4 | 20.0 | 0.81 | 0.85 |
| | 4 | 89.7 | 669.3 | 19.4 | 100.4 | 42.0 | 51.7 | 27.4 | 0.52 | 0.65 |
| RC1- 14- | 1 | 12.3 | 289.8 | 41.0 | 5.5 | 20.0 | 8.7 | 22.5 | 1.58 | 1.12 |
| 400 kN Axial | 2 | | No Data | | No Data | | No Data | | No Data | |
| | 3 | 47.6 | 800.4 | 55.4 | 20.8 | 27.0 | 34.3 | 27.6 | 1.65 | 1.02 |
| | 4 | 89.7 | 1421.4 | 46.2 | 300+ | 300+ | 1351.9 | 200.0 | No Data | |

*TABLE 5.2 - Summary of SDOF Predicted and Experimentally Recorded Maximum Displacements and Time to Maximum Displacements*

| | $d_{EXP} / d_{SDOF}$ | | | | $t_{EXP} / t_{SDOF}$ | | | |
|---|---|---|---|---|---|---|---|---|
| $d_{EXP}$ | <10 | 10-75 | >75 | All | <10 | 10-75 | >75 | All |
| Number | 6 | 25 | 6 | 37 | 6 | 25 | 6 | 37 |
| Maximum | 3.216 | 1.648 | 0.983 | 3.216 | 1.124 | 1.294 | 1.902 | 1.902 |
| Minimum | 1.361 | 0.455 | 0.379 | 0.379 | 0.864 | 0.547 | 0.325 | 0.325 |
| Mean | 2.103 | 0.913 | 0.578 | 1.052 | 0.939 | 0.904 | 0.839 | 0.899 |
| Std. Dev. | 0.805 | 0.261 | 0.208 | 0.613 | 0.105 | 0.159 | 0.553 | 0.248 |
| Coef. of Var. | 0.383 | 0.286 | 0.360 | 0.583 | 0.112 | 0.176 | 0.659 | 0.276 |

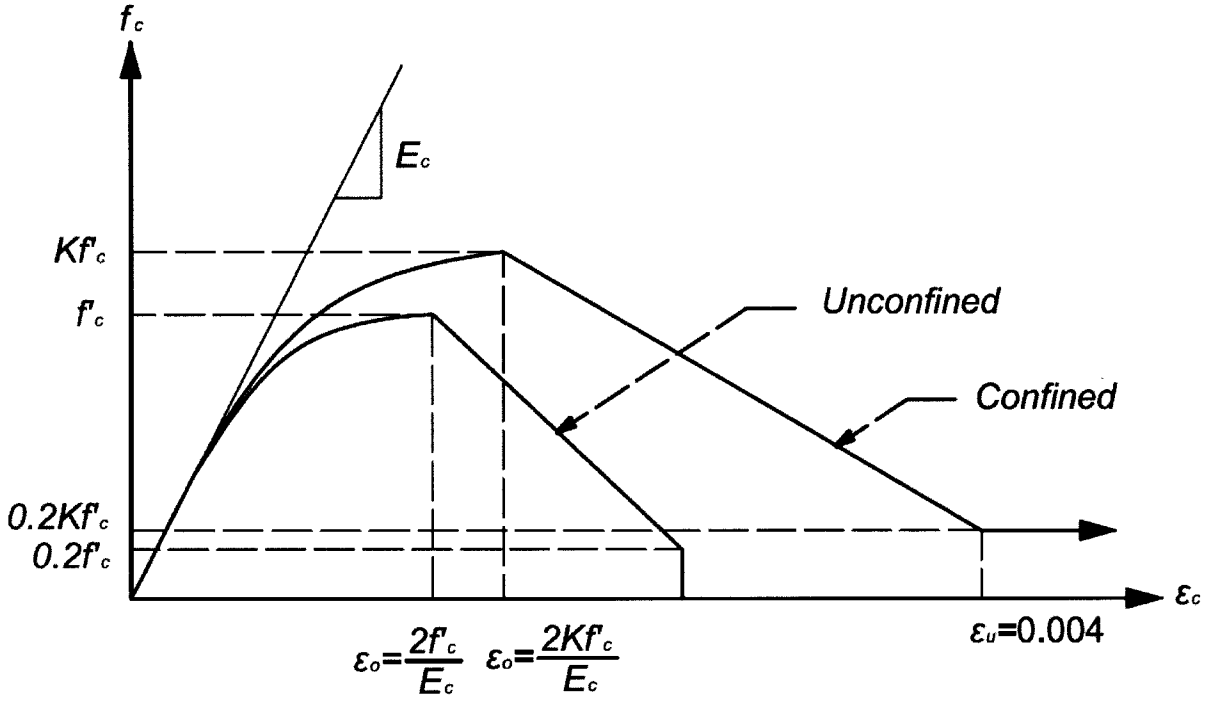


*Figure 5-1: Model Stress-Strain Relationship for Unconfined and Partially Confined Concrete (Park, Priestly and Gill 1982)*

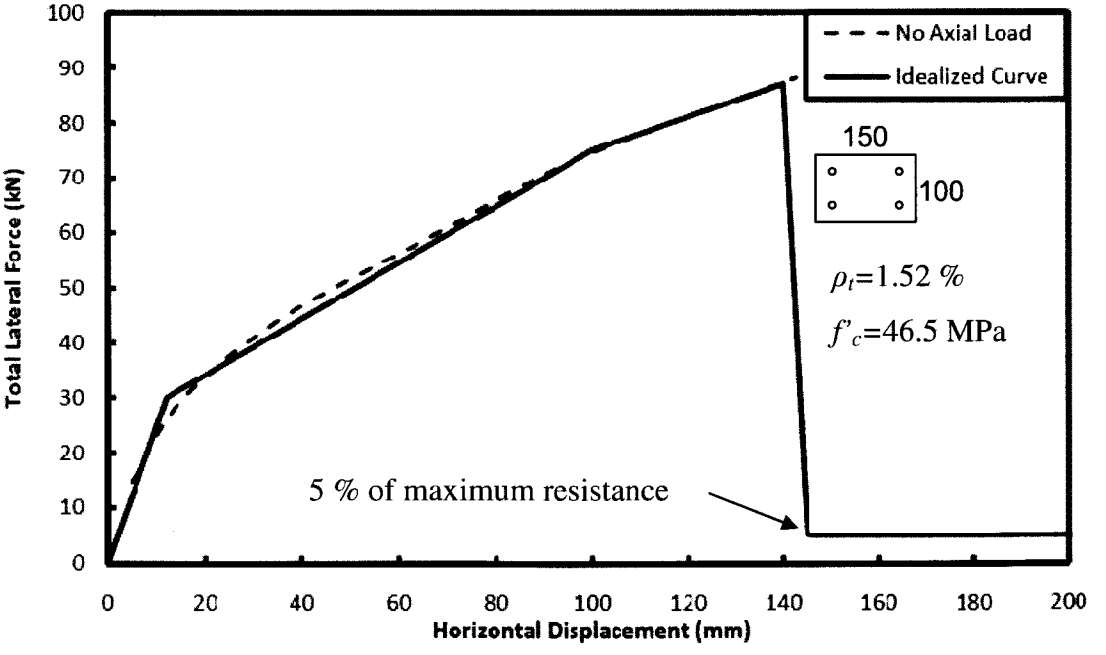


*Figure 5-2: Idealized Resistance-Displacement Curve for Column RC-1*

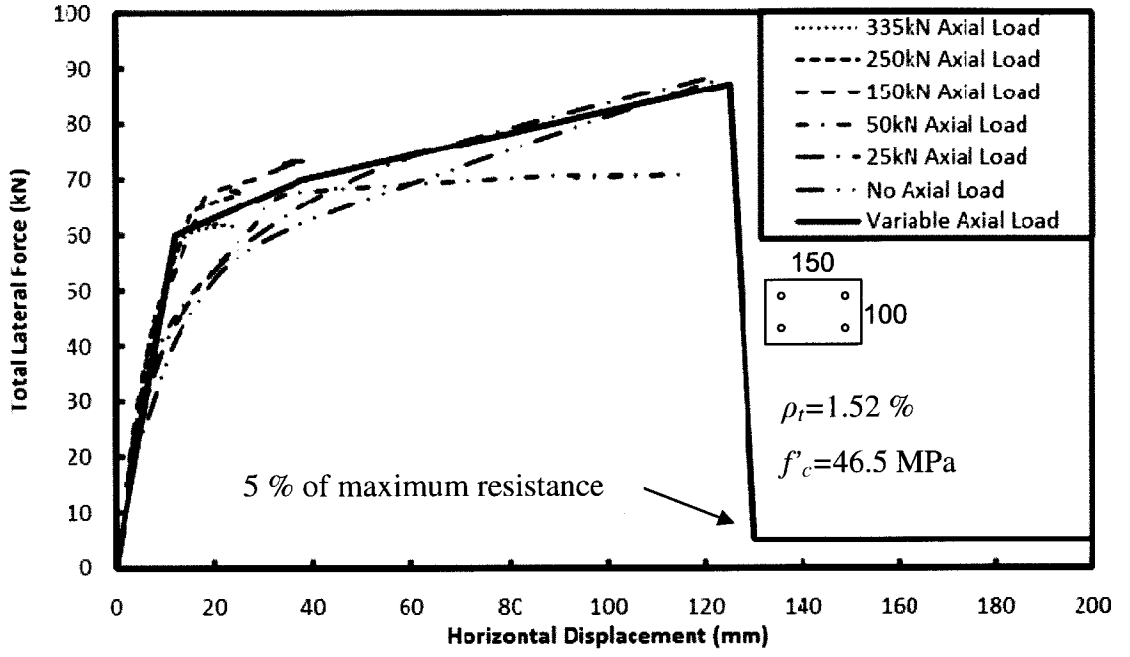


*Figure 5-3: Idealized Resistance-Displacement Curve for Column RC-2*

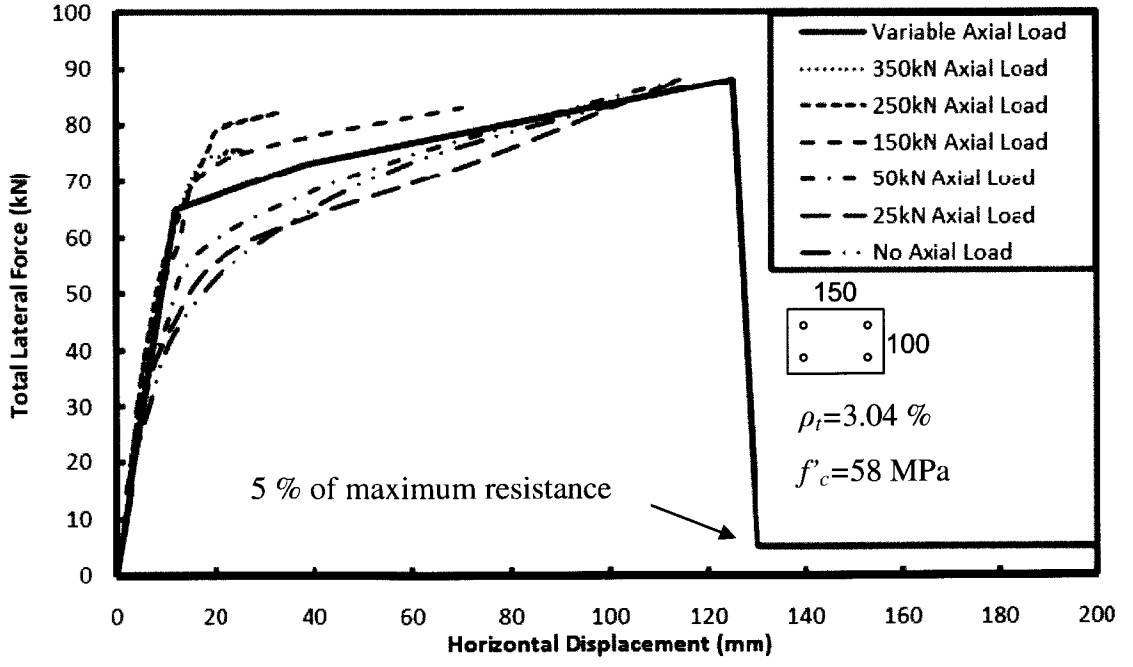


*Figure 5-4: Idealized Resistance-Displacement Curve for Columns RC-4, 6, 8, 10 and 12*

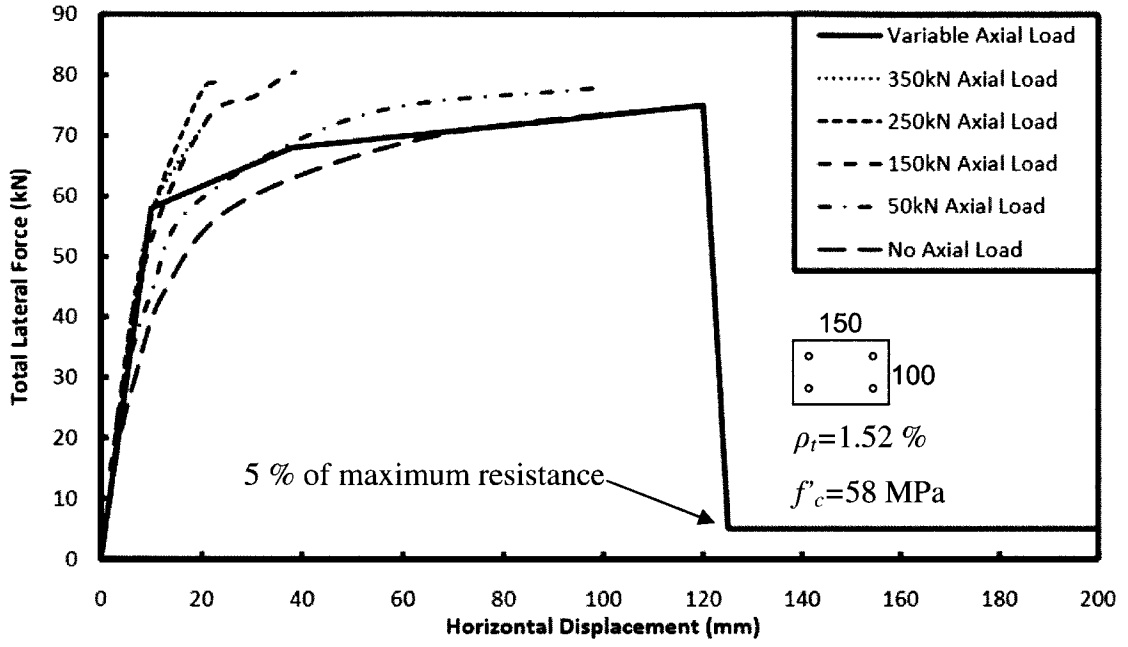


*Figure 5-5: Idealized Resistance-Displacement Curve for Columns RC-3, 5, 7, 9, and 11*

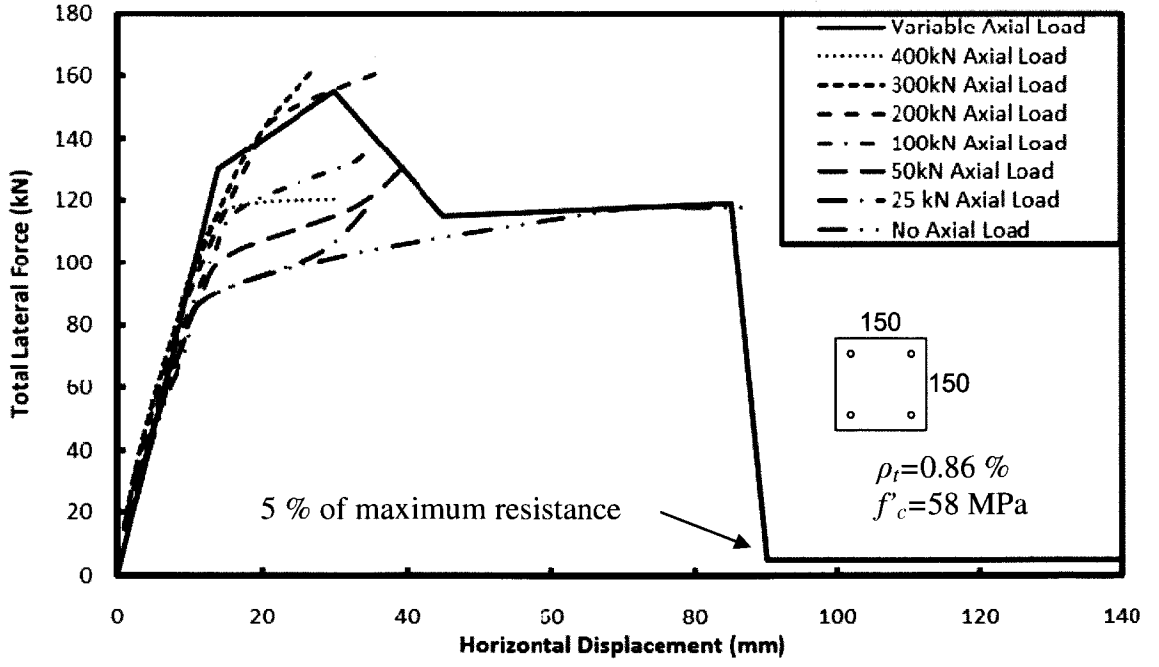


*Figure 5-6: Idealized Resistance-Displacement Curve for Columns RC-13 and 14*

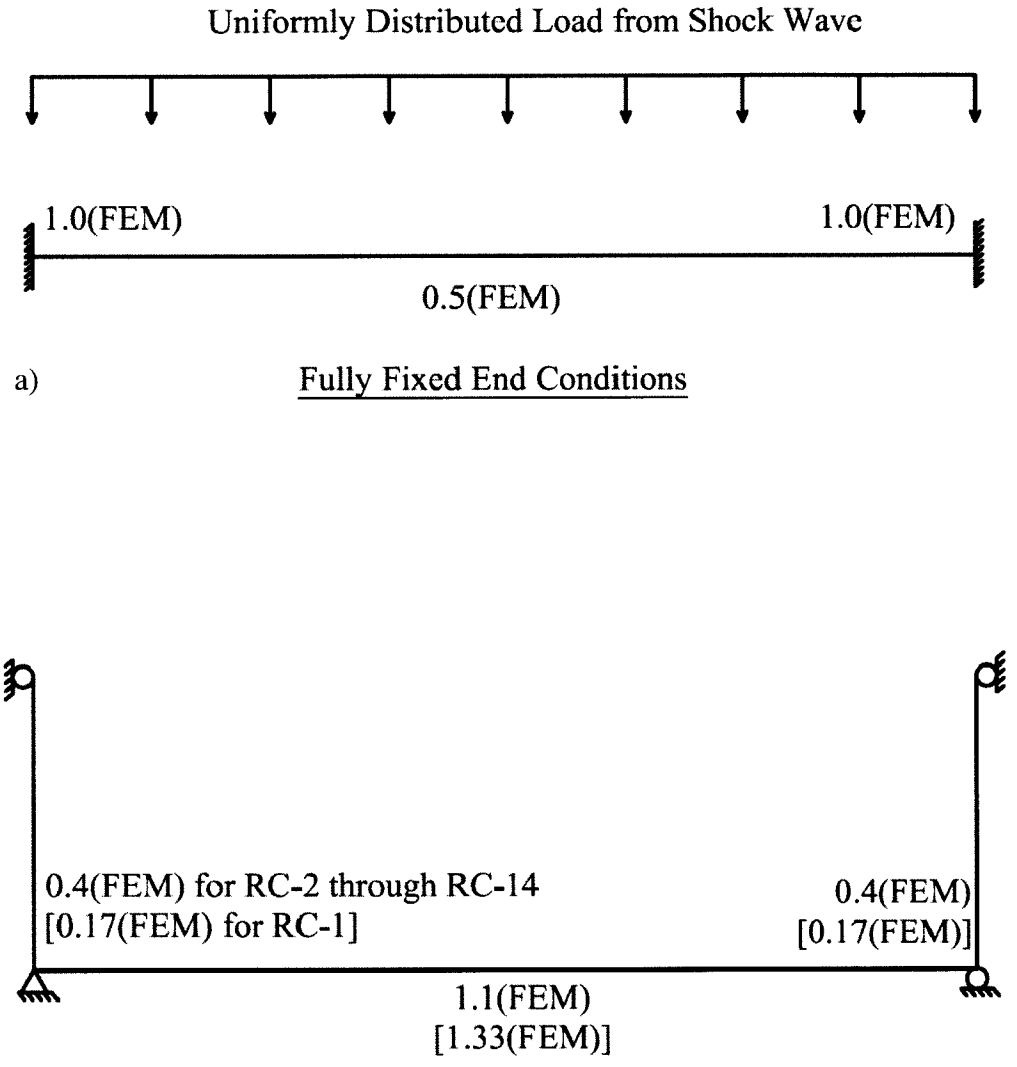


***Figure 5-7: End and Mid-Span Moments for: a) Fully Fixed End Conditions; b) Partially Fixed to Rotation End Conditions***

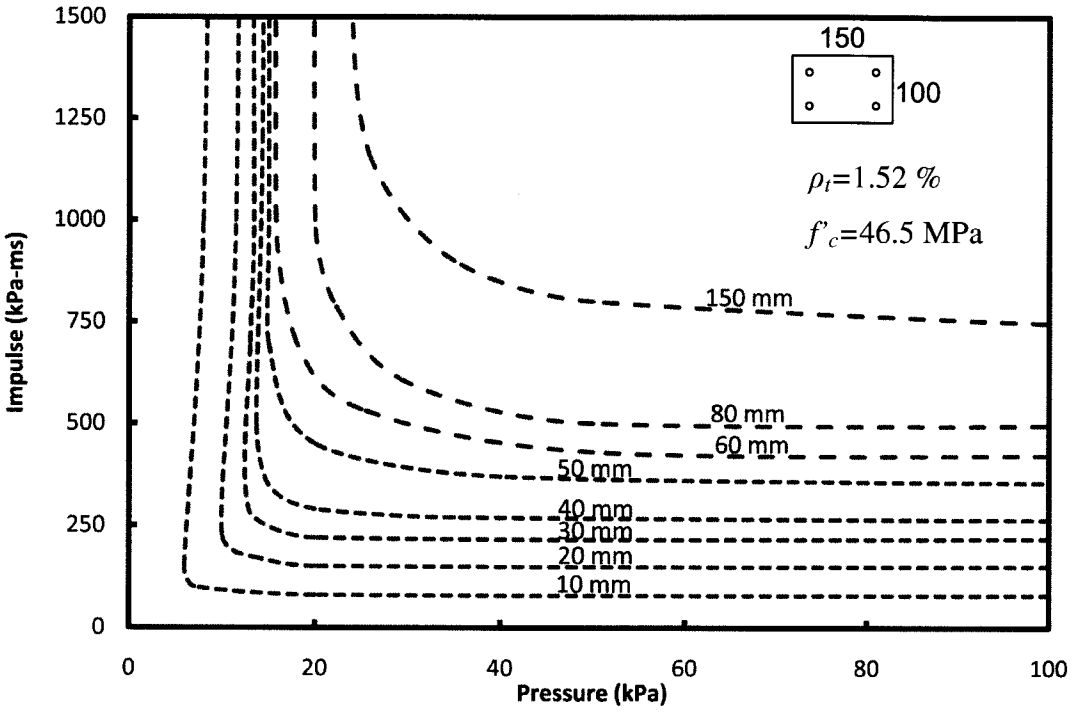


*Figure 5-8: Constant Displacement Pressure-Impulse Diagram for Column RC1*

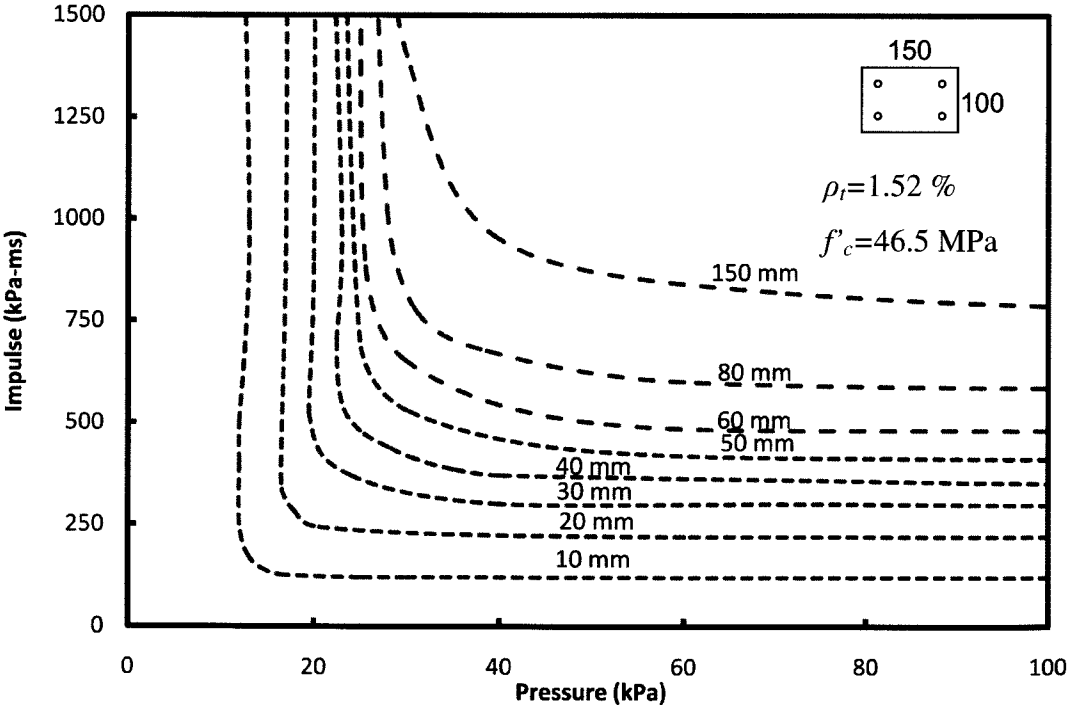


*Figure 5-9: Constant Displacement Pressure-Impulse Diagram for Column RC2*

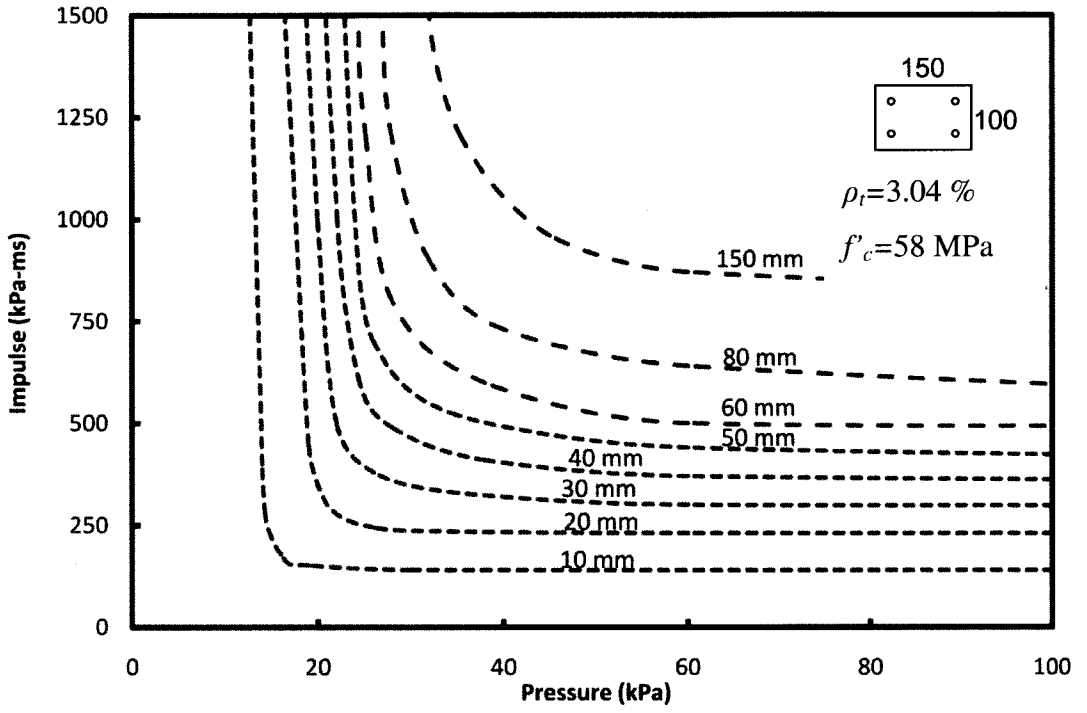


*Figure 5-10: Constant Displacement Pressure-Impulse Diagram for Columns RC-4, 6, 8, 10 and 12*

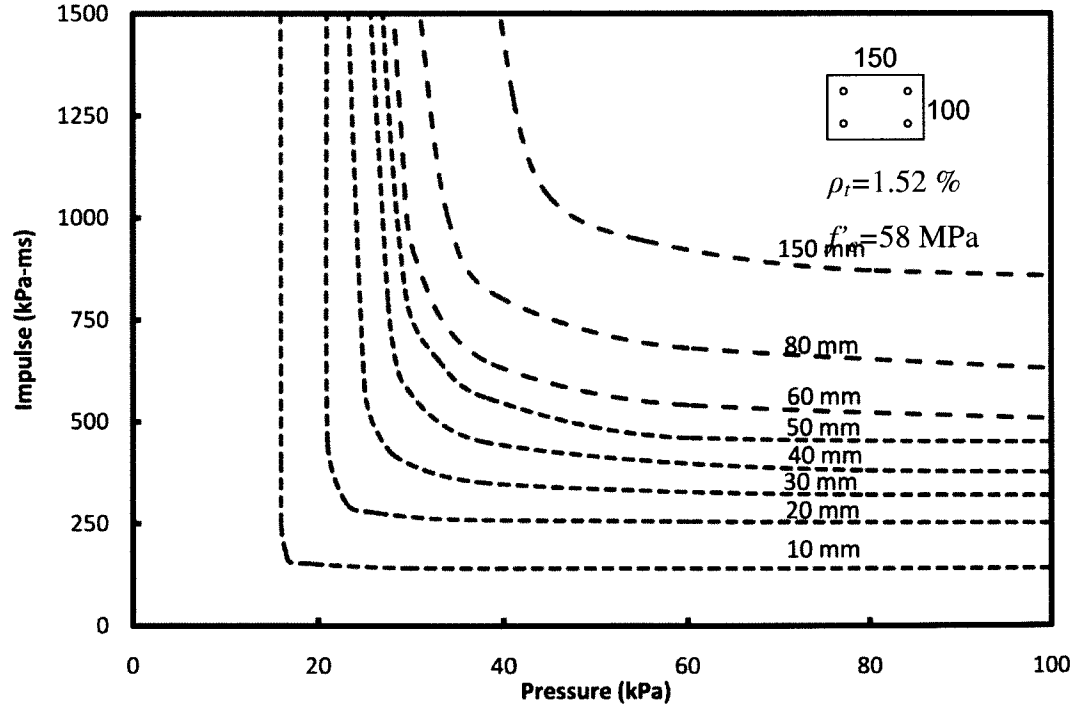


*Figure 5-11: Constant Displacement Pressure-Impulse Diagram for Columns RC-3, 5, 7, 9 and 11*

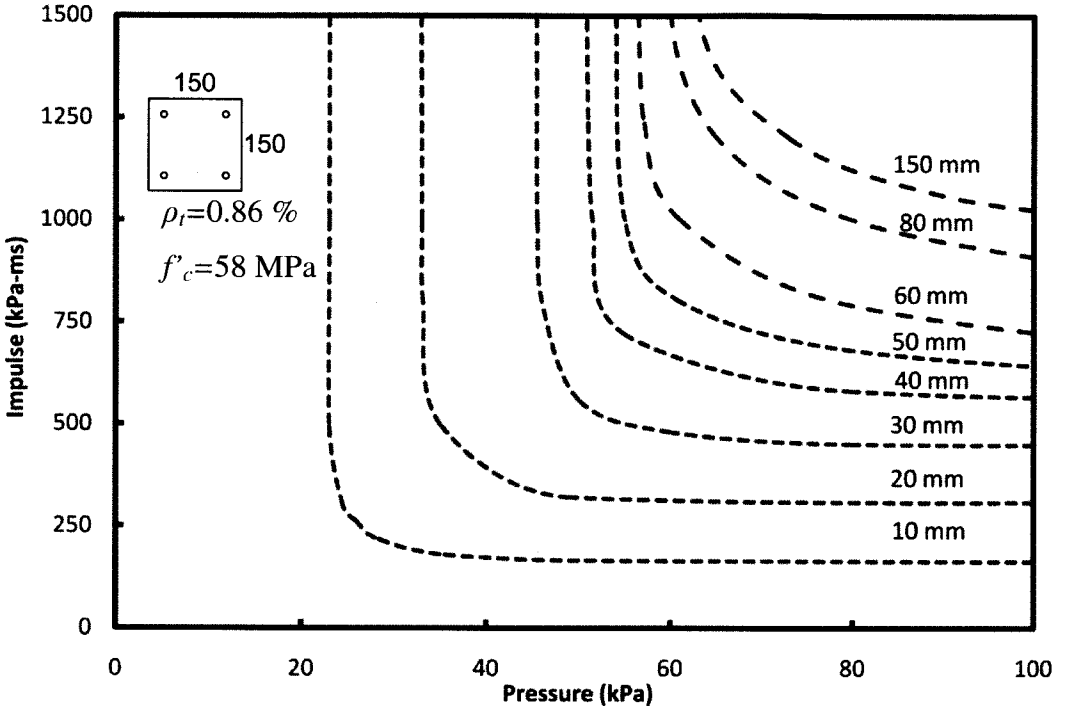


*Figure 5-12: Constant Displacement Pressure-Impulse Diagram for Columns RC-13 and 14*

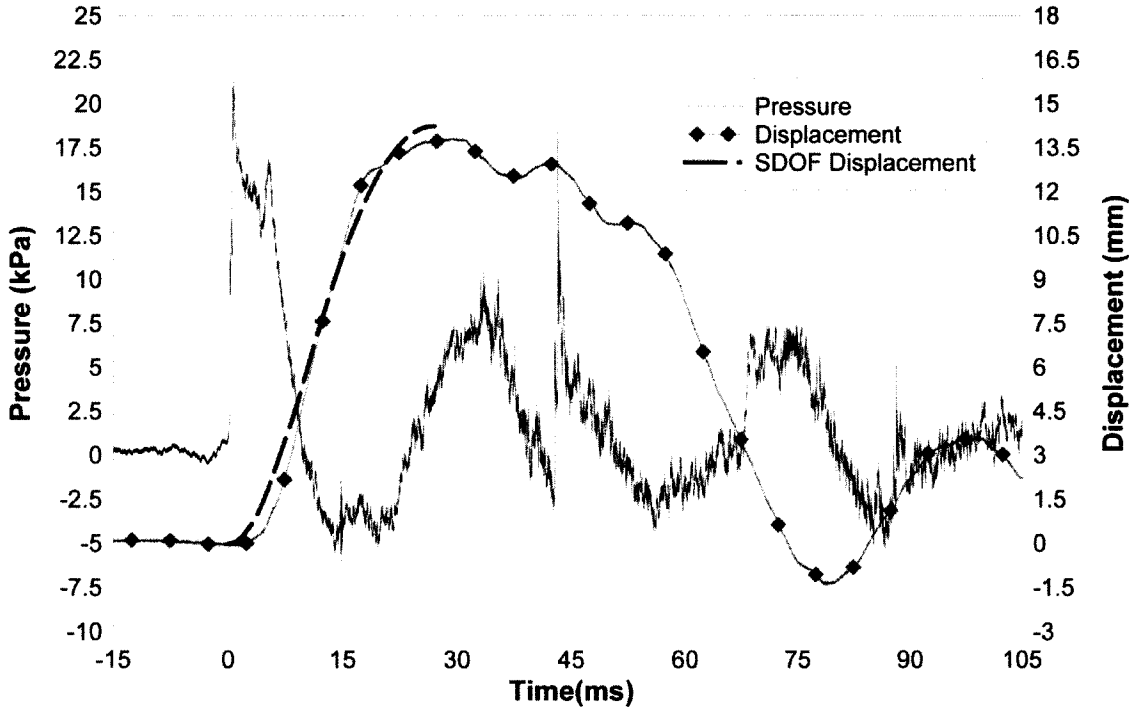


*Figure 5-13: Experimentally Recorded and SDOF Predicted Mid-Height Displacement Time History for Test RC-1-1*

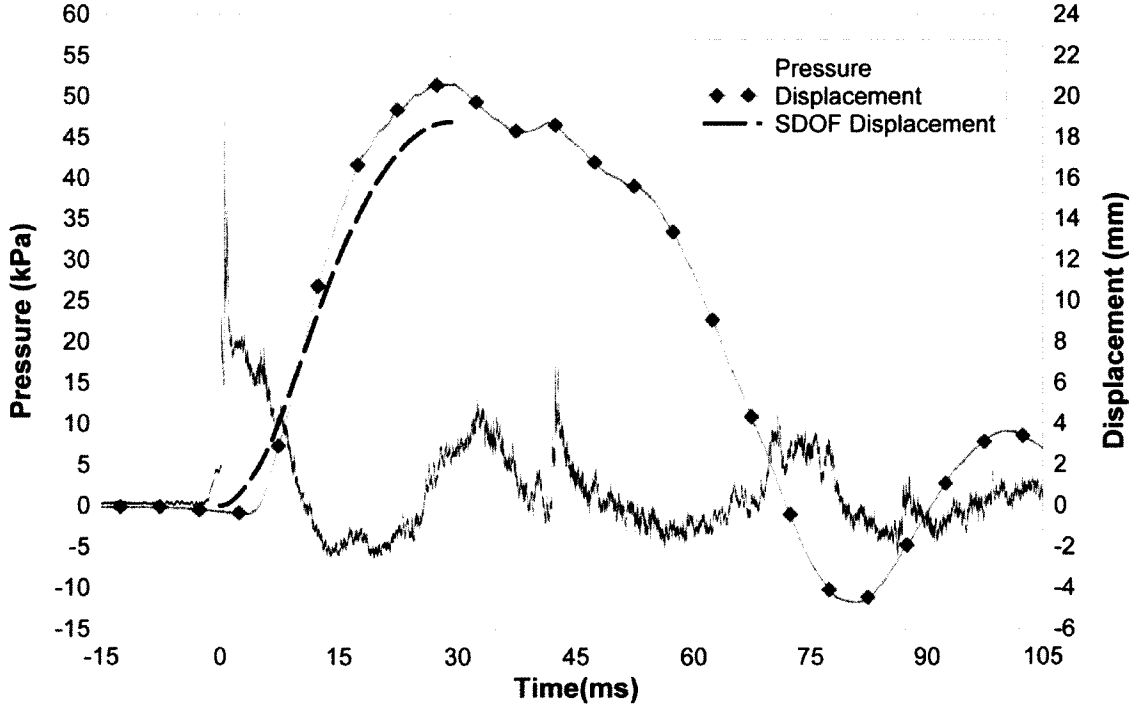


*Figure 5-14: Experimentally Recorded and SDOF Predicted Mid-Height Displacement Time History for Test RC-1-2*

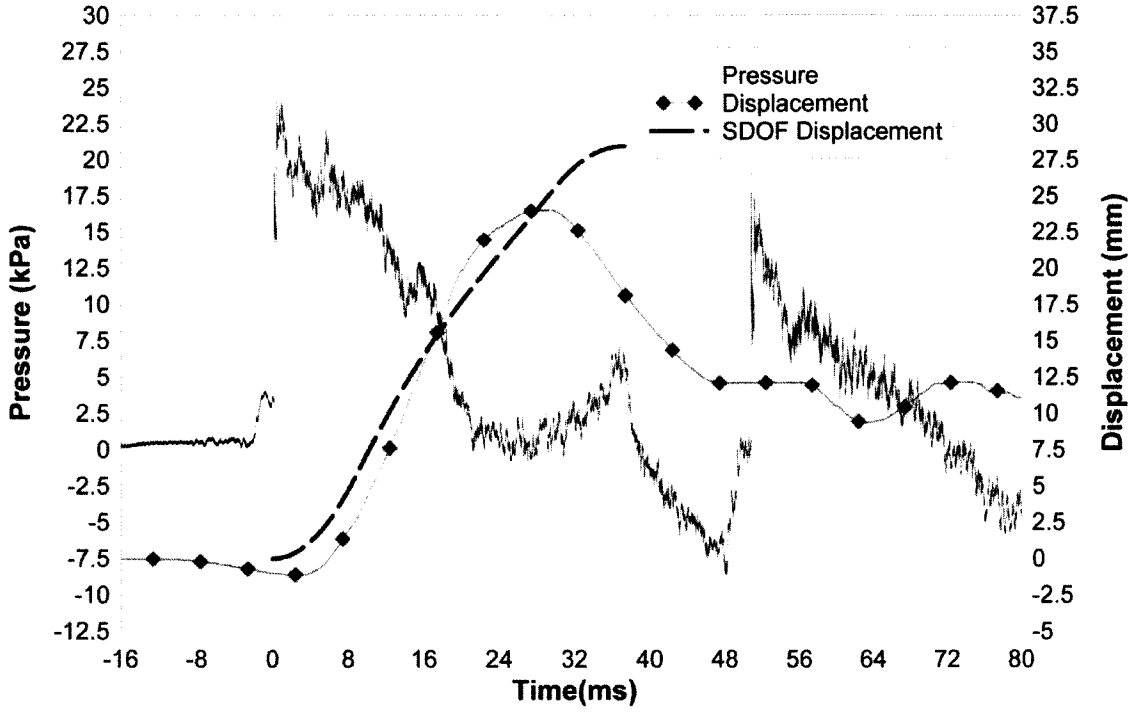


*Figure 5-15: Experimentally Recorded and SDOF Predicted Mid-Height Displacement Time History for Test RC-2-1*

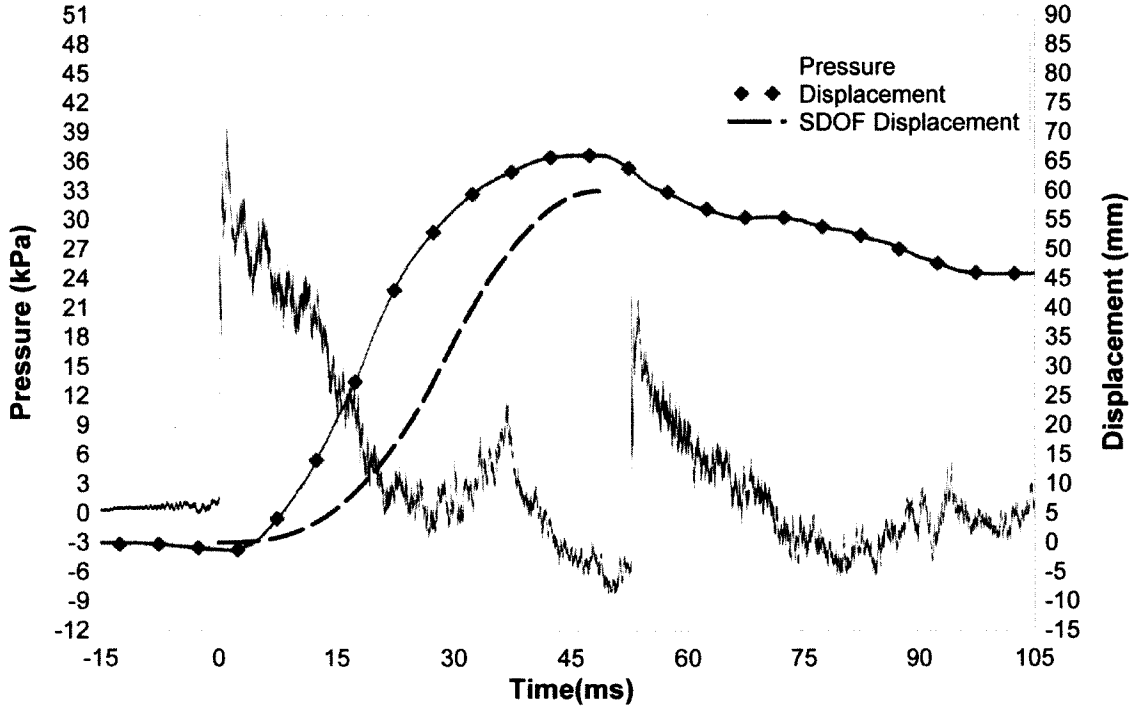


*Figure 5-16: Experimentally Recorded and SDOF Predicted Mid-Height Displacement Time History for Test RC-2-2*

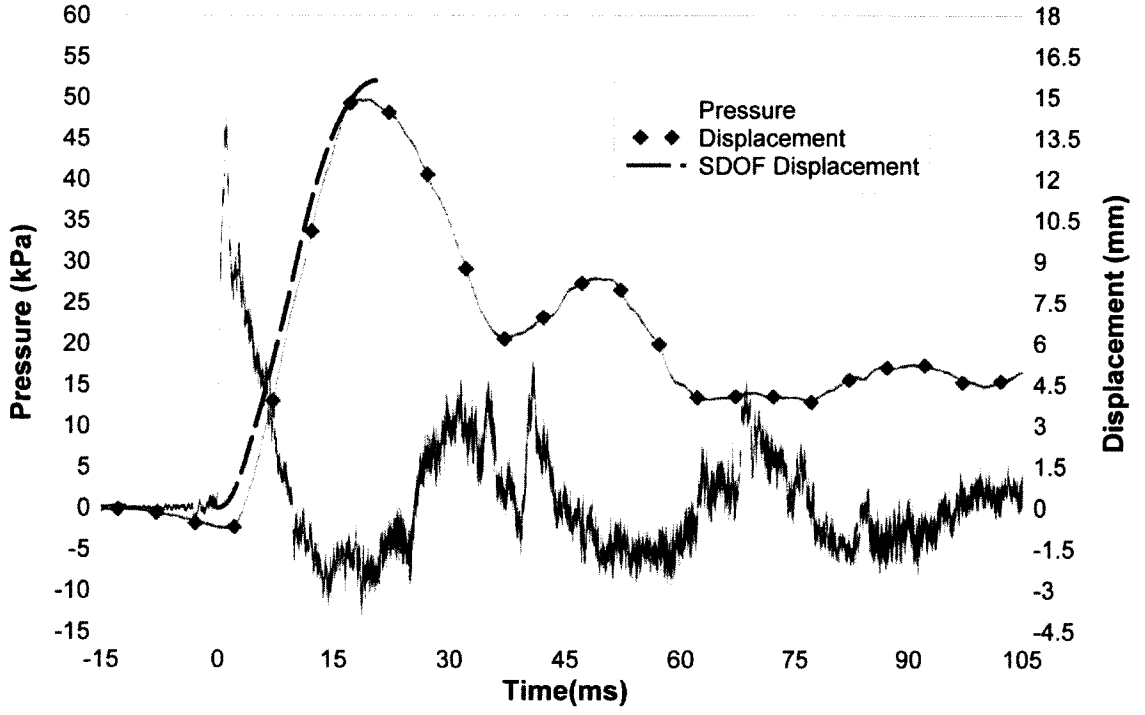


*Figure 5-17: Experimentally Recorded and SDOF Predicted Mid-Height Displacement Time History for Test RC-3-1*

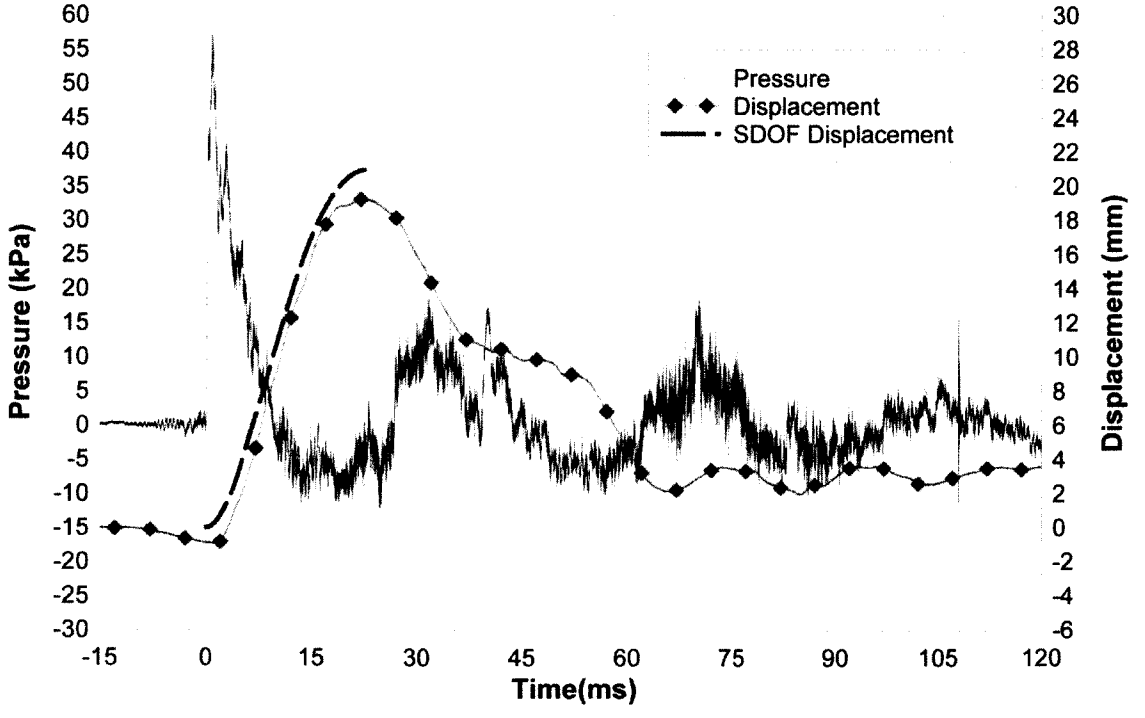


*Figure 5-18: Experimentally Recorded and SDOF Predicted Mid-Height Displacement Time History for Test RC-3-2*

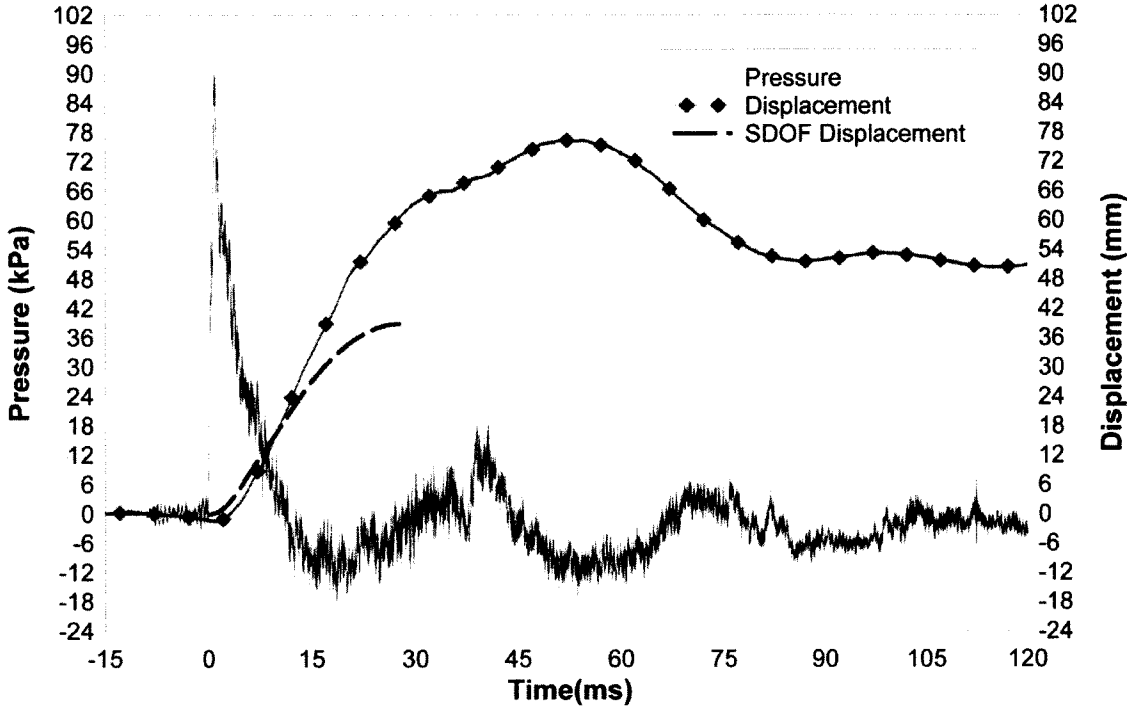


*Figure 5-19: Experimentally Recorded and SDOF Predicted Mid-Height Displacement Time History for Test RC-3-3*

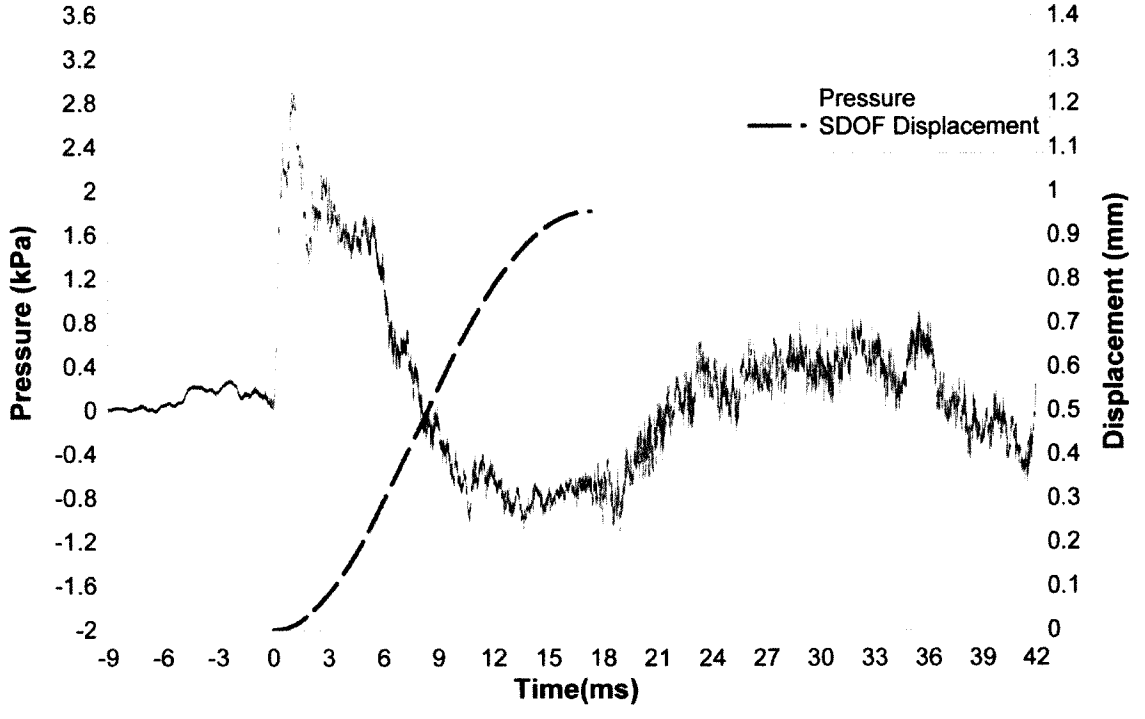


*Figure 5-20: SDOF Predicted Mid-Height Displacement Time History for Test RC-4-1*

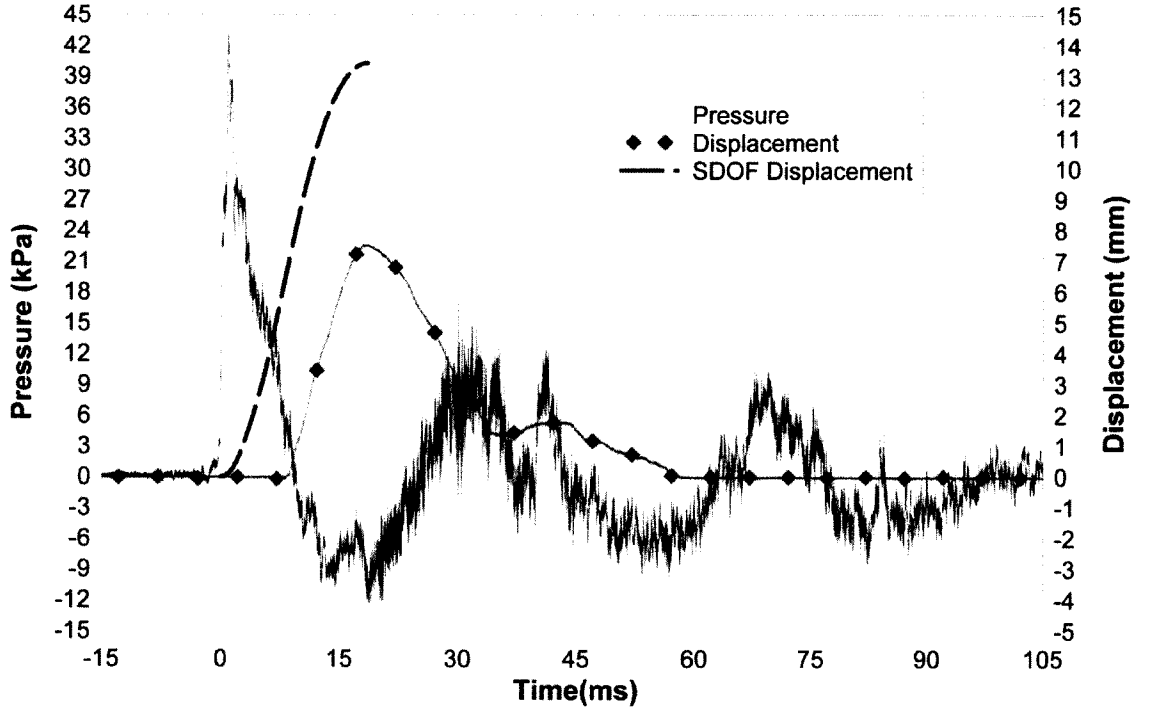


*Figure 5-21: Experimentally Recorded and SDOF Predicted Mid-Height Displacement Time History for Test RC-4-2*

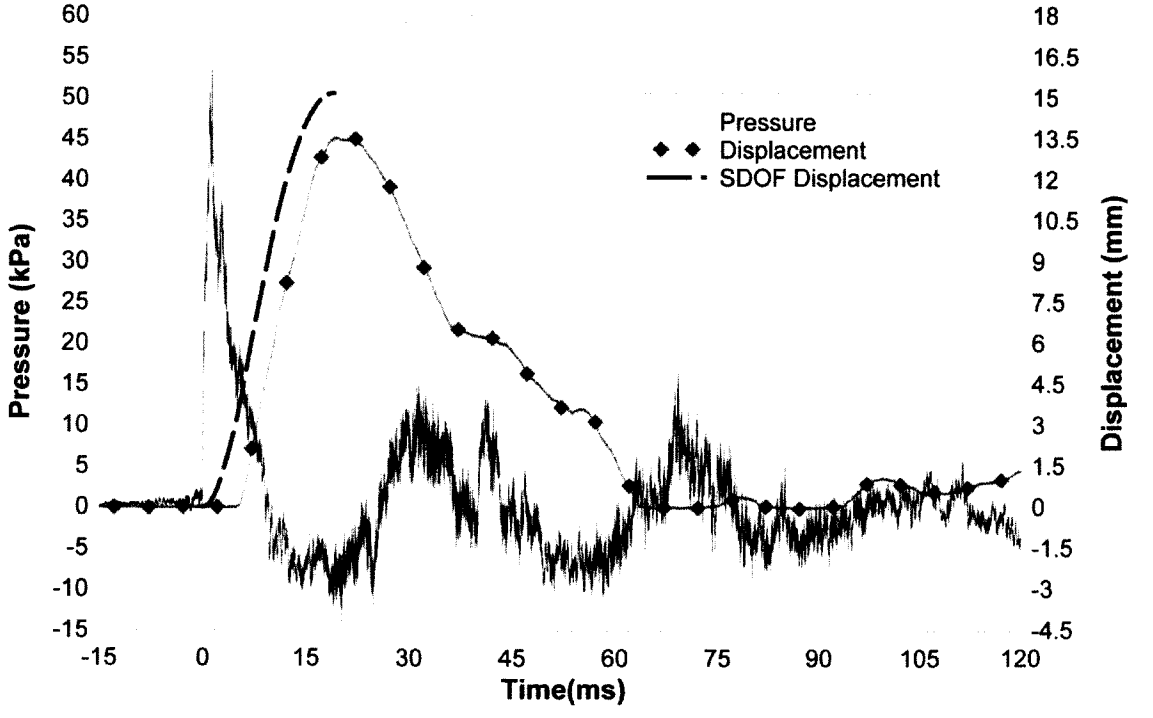


*Figure 5-22: Experimentally Recorded and SDOF Predicted Mid-Height Displacement Time History for Test RC-4-3*

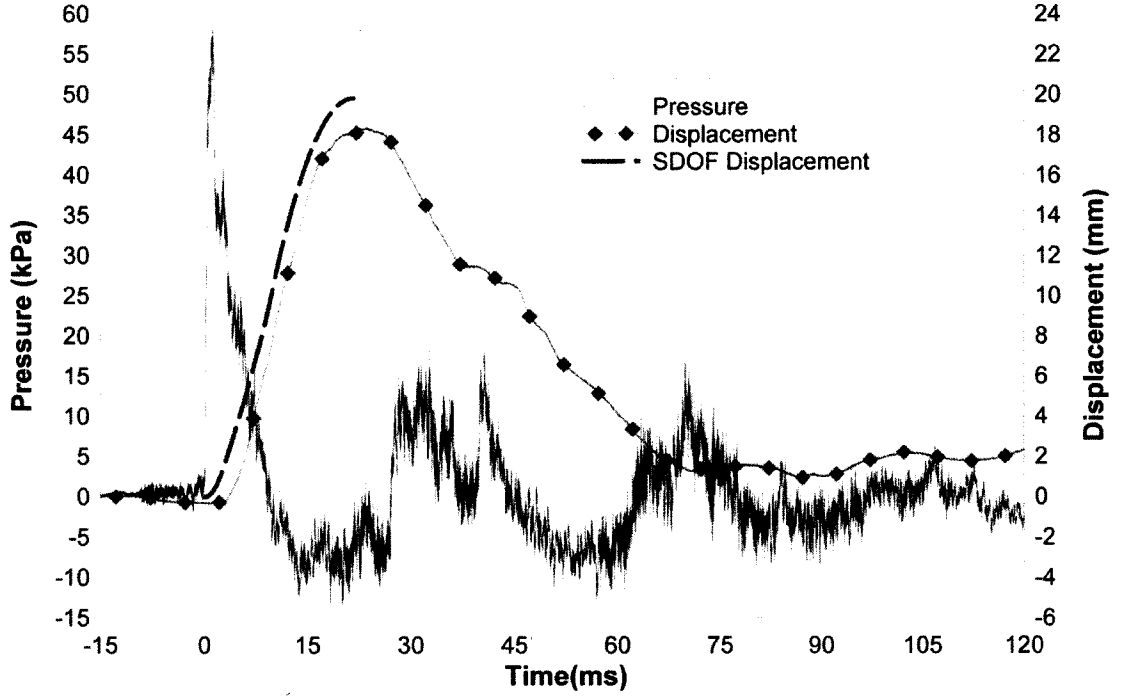


*Figure 5-23: Experimentally Recorded and SDOF Predicted Mid-Height Displacement Time History for Test RC-4-4*

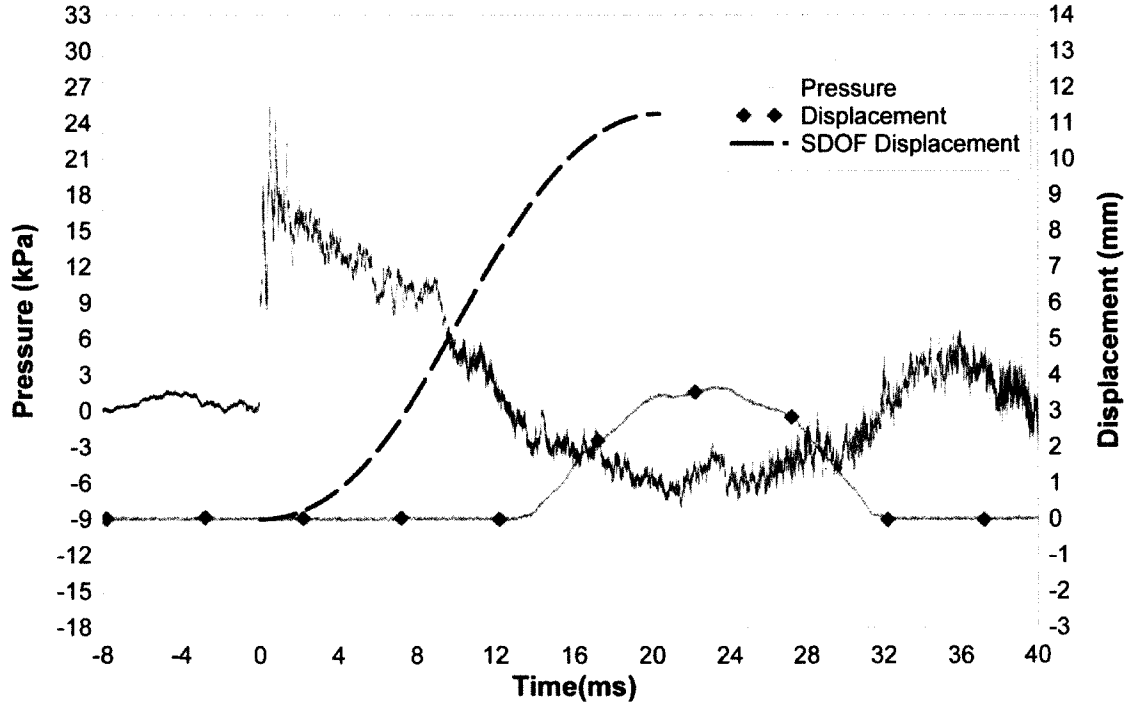


*Figure 5-24: Experimentally Recorded and SDOF Predicted Mid-Height Displacement Time History for Test RC-5-1*

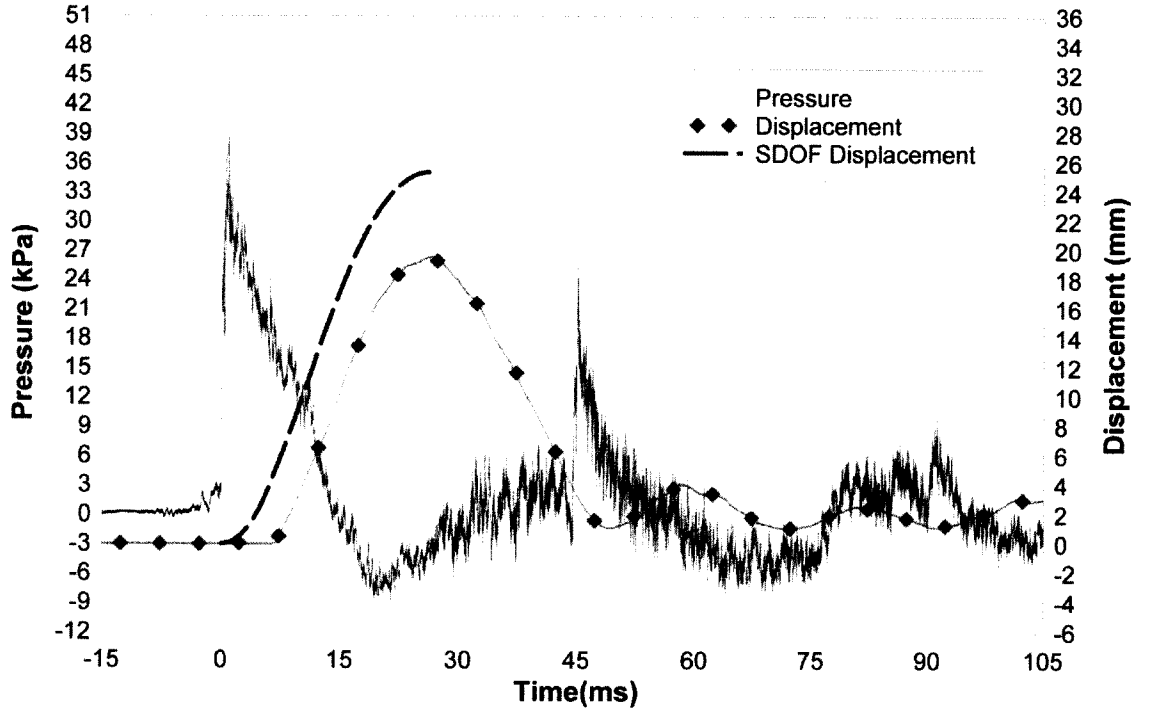


*Figure 5-25: Experimentally Recorded and SDOF Predicted Mid-Height Displacement Time History for Test RC-5-2*

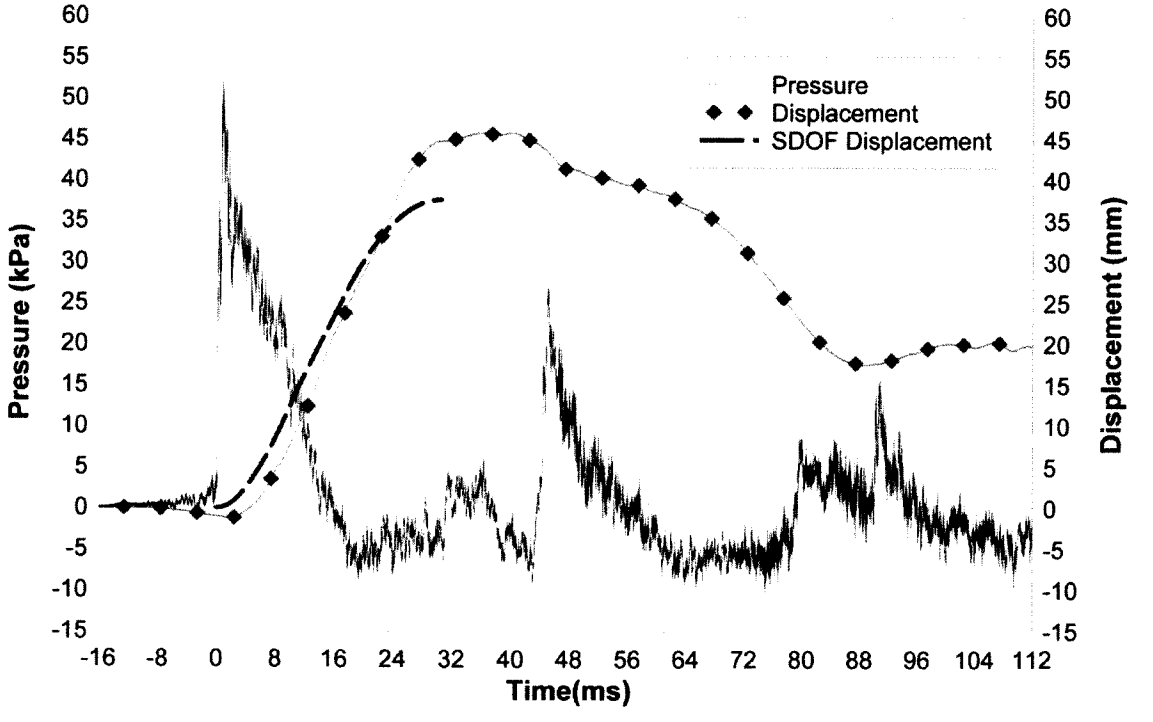


*Figure 5-26: Experimentally Recorded and SDOF Predicted Mid-Height Displacement Time History for Test RC-5-3*

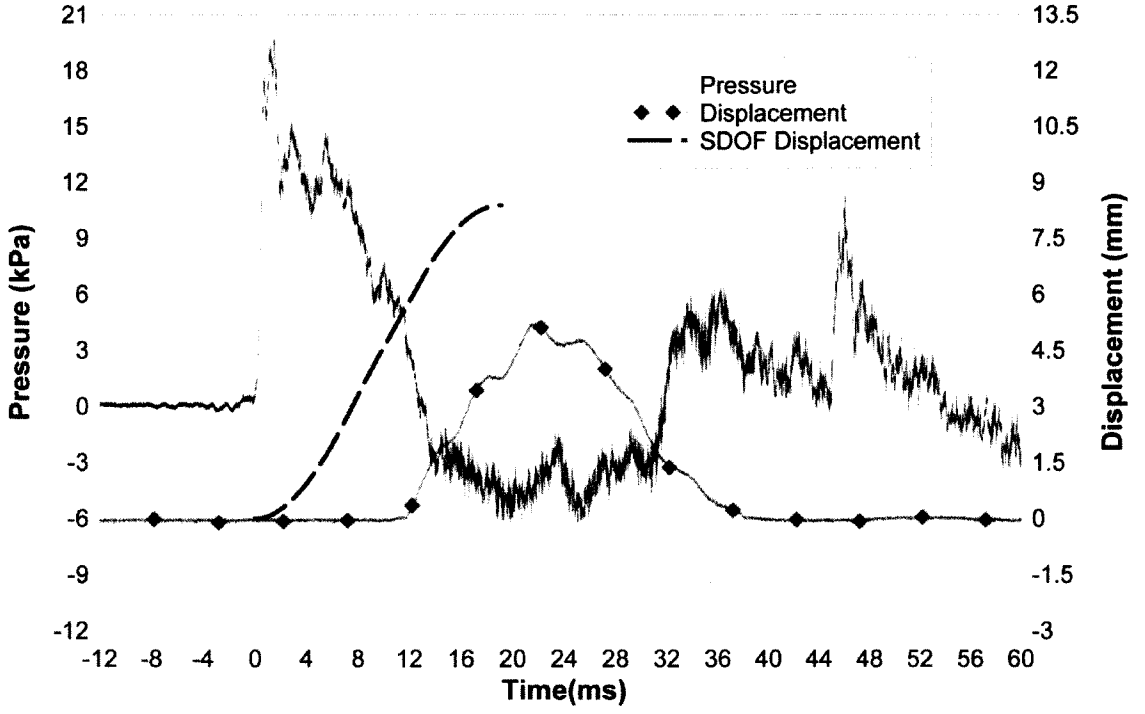


*Figure 5-27: Experimentally Recorded and SDOF Predicted Mid-Height Displacement Time History for Test RC-6-1*

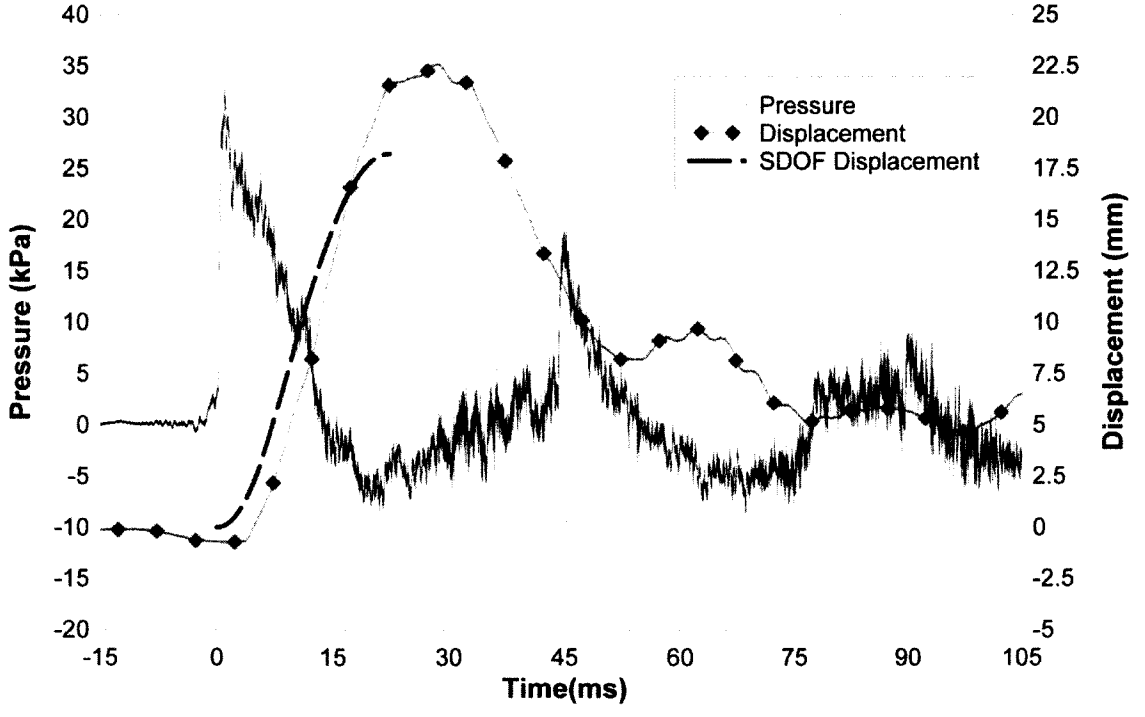


*Figure 5-28: Experimentally Recorded and SDOF Predicted Mid-Height Displacement Time History for Test RC-6-2*

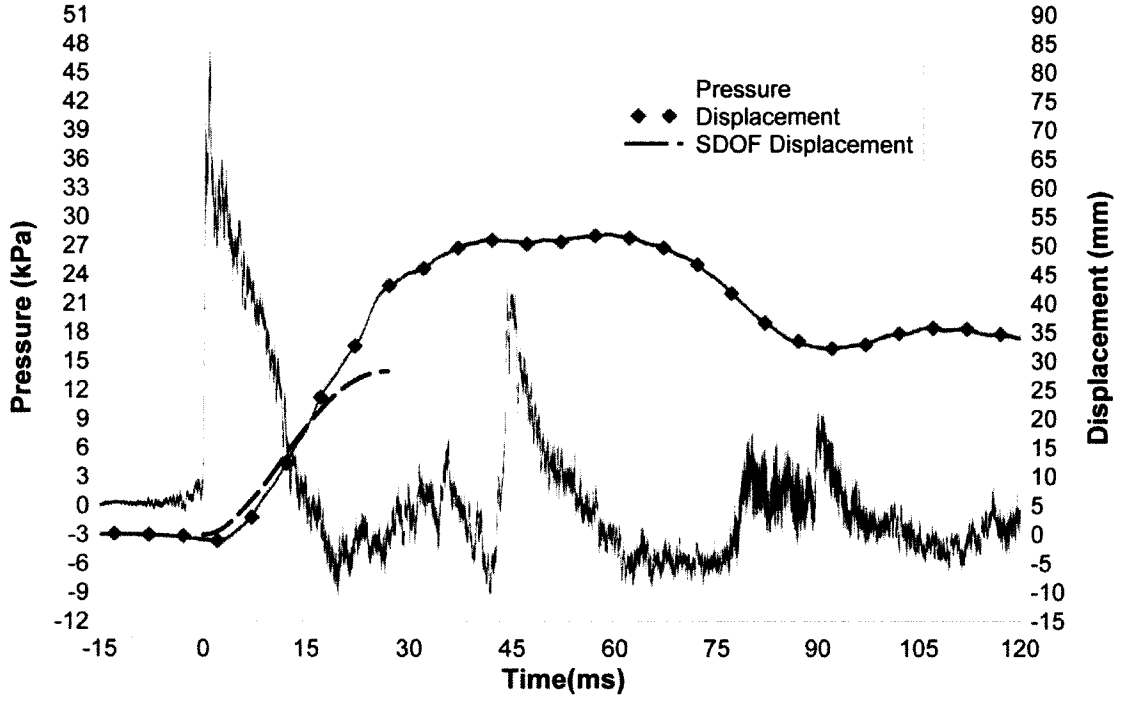


*Figure 5-29: Experimentally Recorded and SDOF Predicted Mid-Height Displacement Time History for Test RC-6-3*

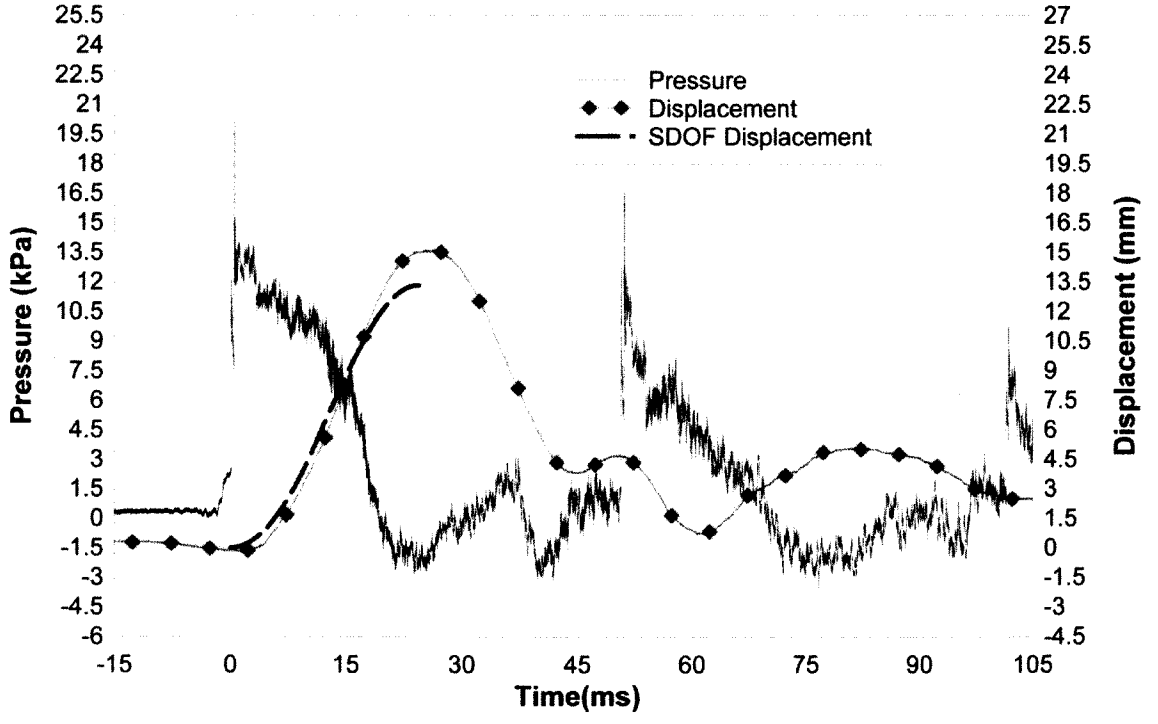


*Figure 5-30: Experimentally Recorded and SDOF Predicted Mid-Height Displacement Time History for Test RC-7-1*

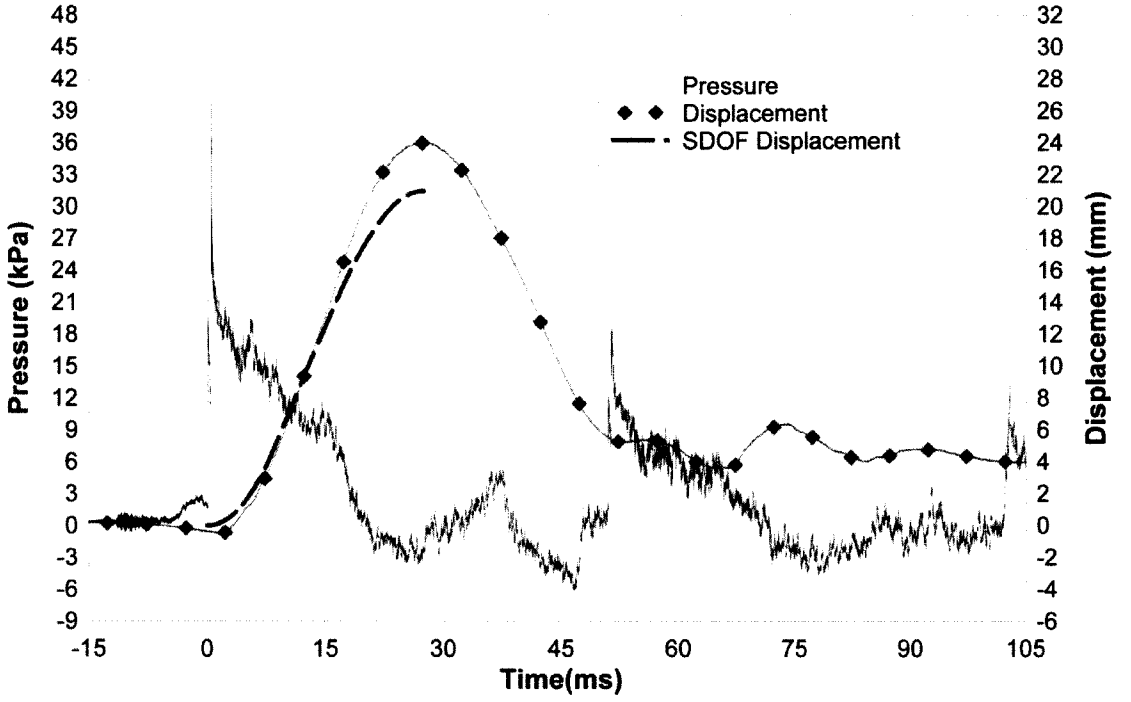


*Figure 5-31: Experimentally Recorded and SDOF Predicted Mid-Height Displacement Time History for Test RC-7-2*

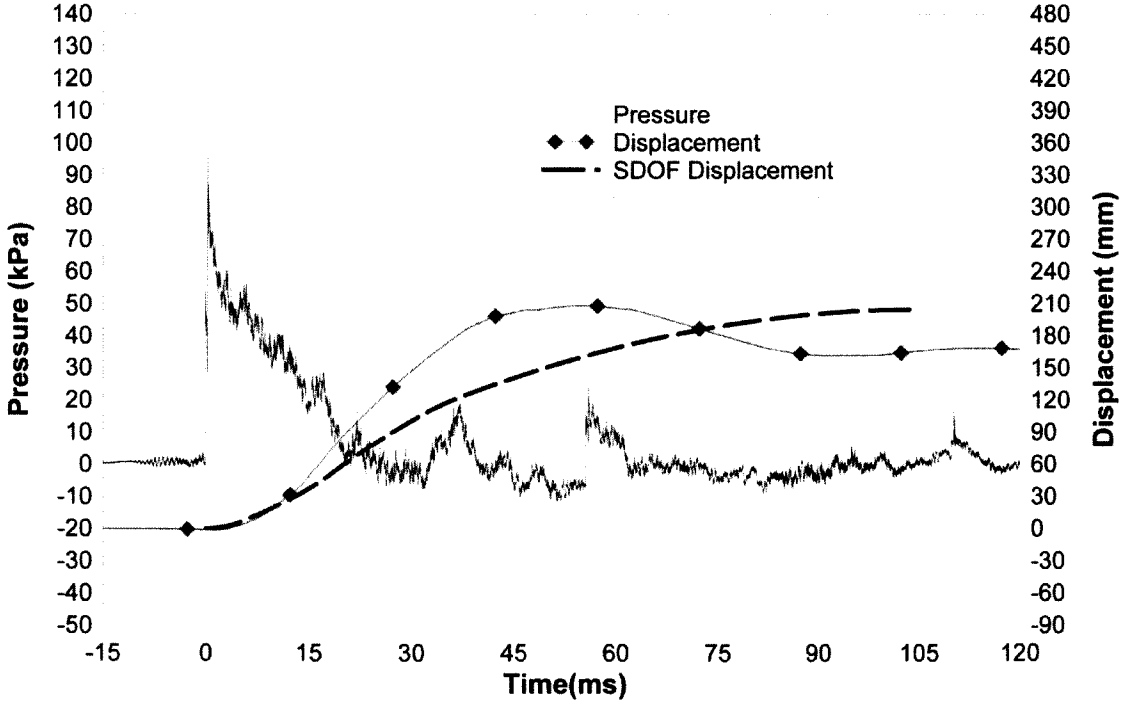


*Figure 5-32: Experimentally Recorded and SDOF Predicted Mid-Height Displacement Time History for Test RC-7-3*

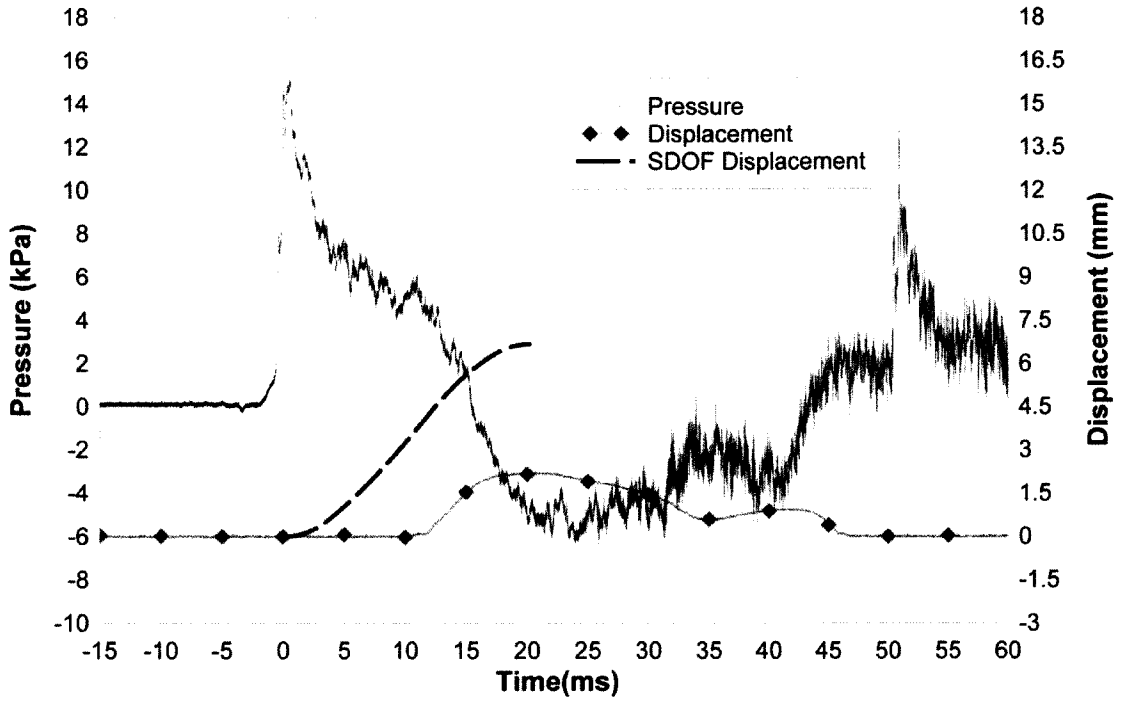


*Figure 5-33: Experimentally Recorded and SDOF Predicted Mid-Height Displacement Time History for Test RC-8-1*

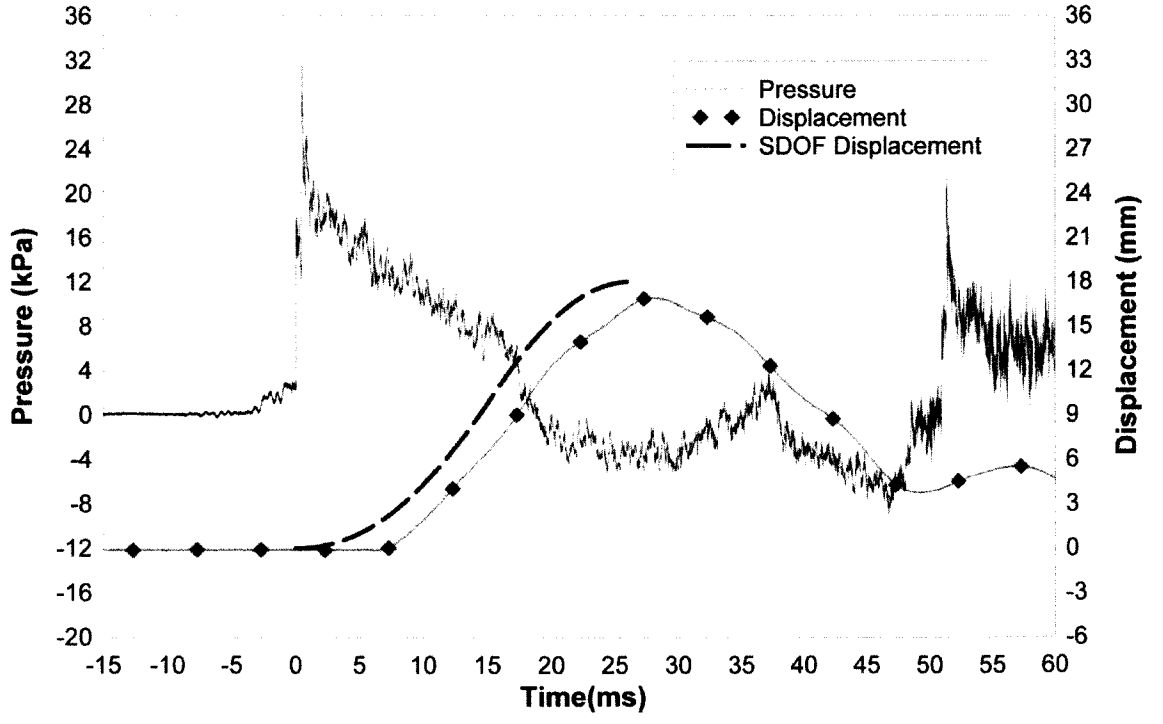


*Figure 5-34: Experimentally Recorded and SDOF Predicted Mid-Height Displacement Time History for Test RC-8-2*

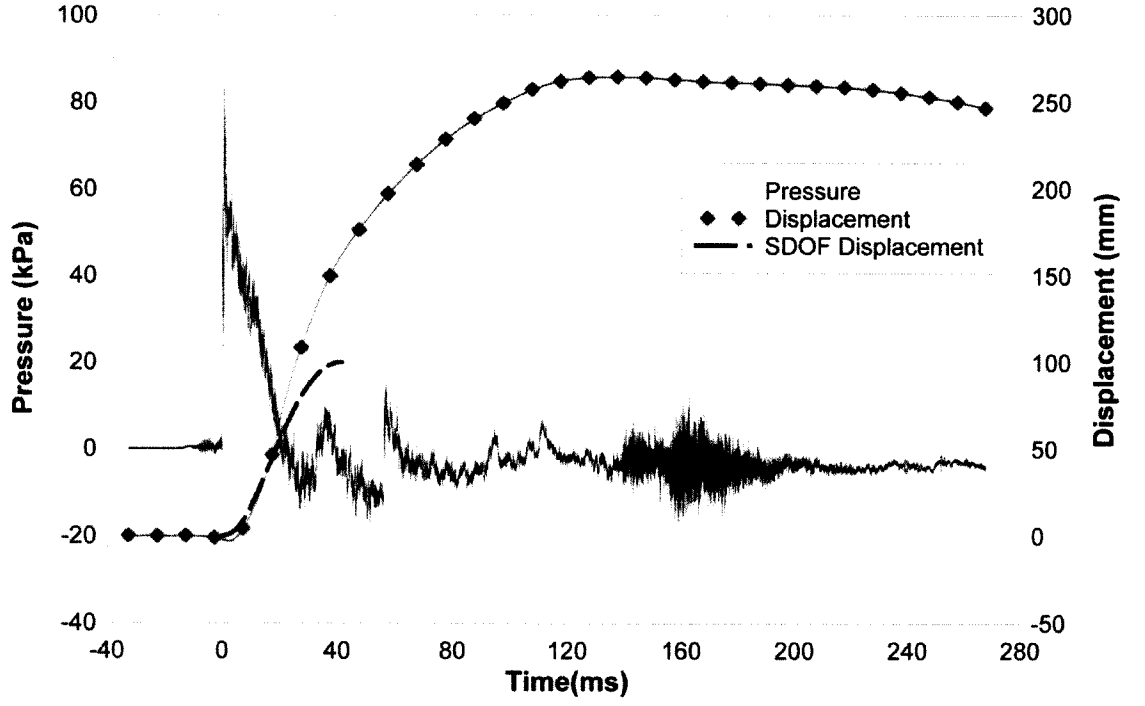


*Figure 5-35: Experimentally Recorded and SDOF Predicted Mid-Height Displacement Time History for Test RC-8-3*

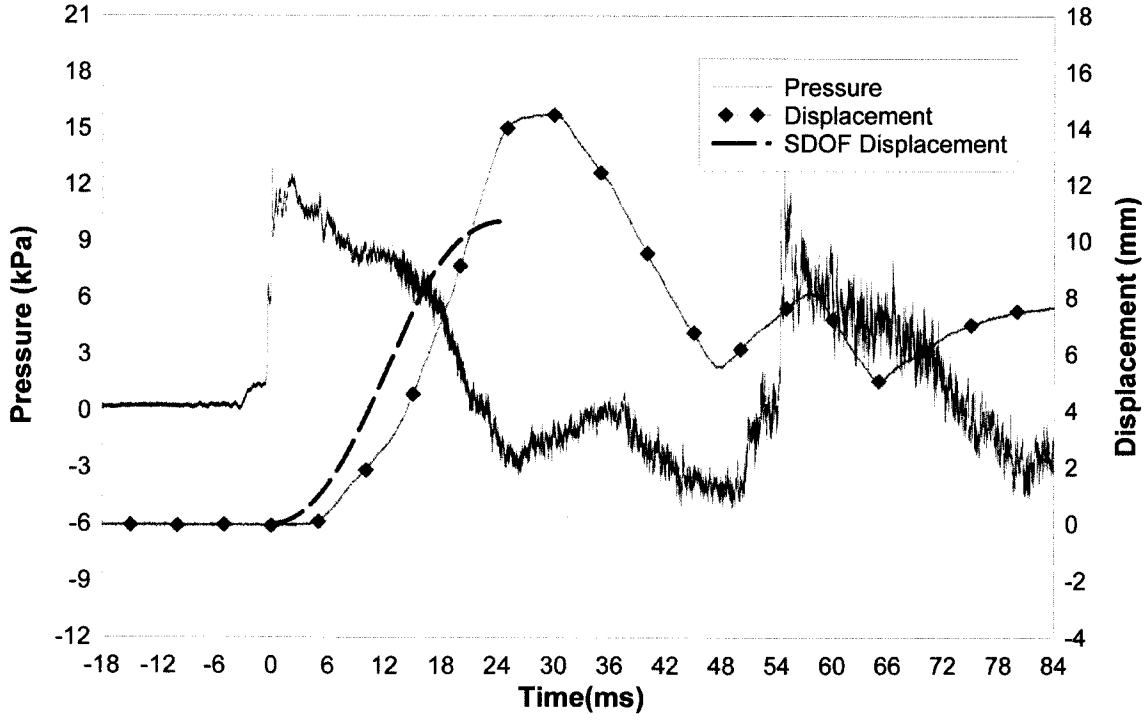


*Figure 5-36: Experimentally Recorded and SDOF Predicted Mid-Height Displacement Time History for Test RC-9-1*

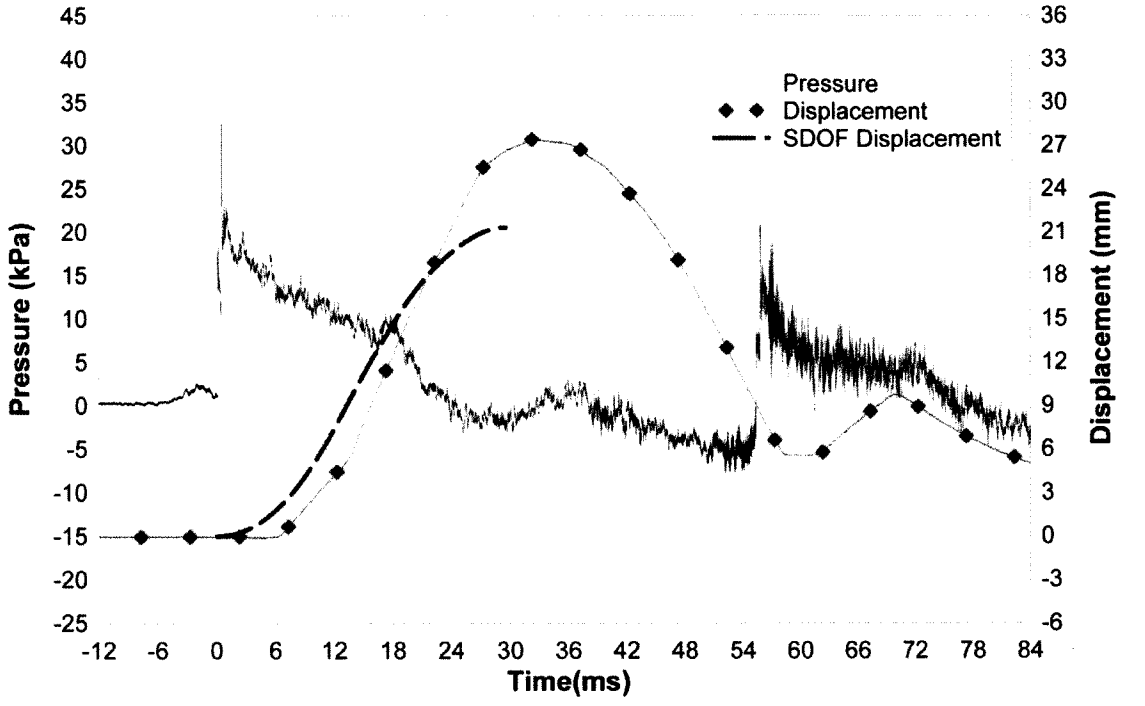


*Figure 5-37: Experimentally Recorded and SDOF Predicted Mid-Height Displacement Time History for Test RC-9-2*

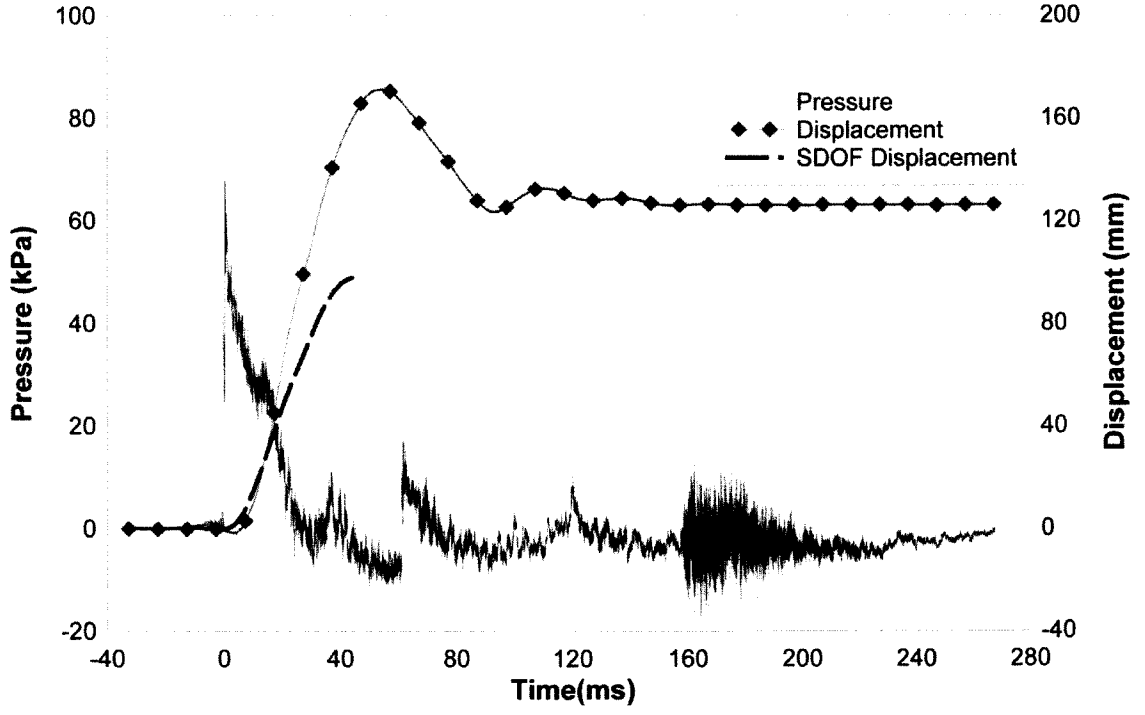


*Figure 5-38: Experimentally Recorded and SDOF Predicted Mid-Height Displacement Time History for Test RC-9-3*

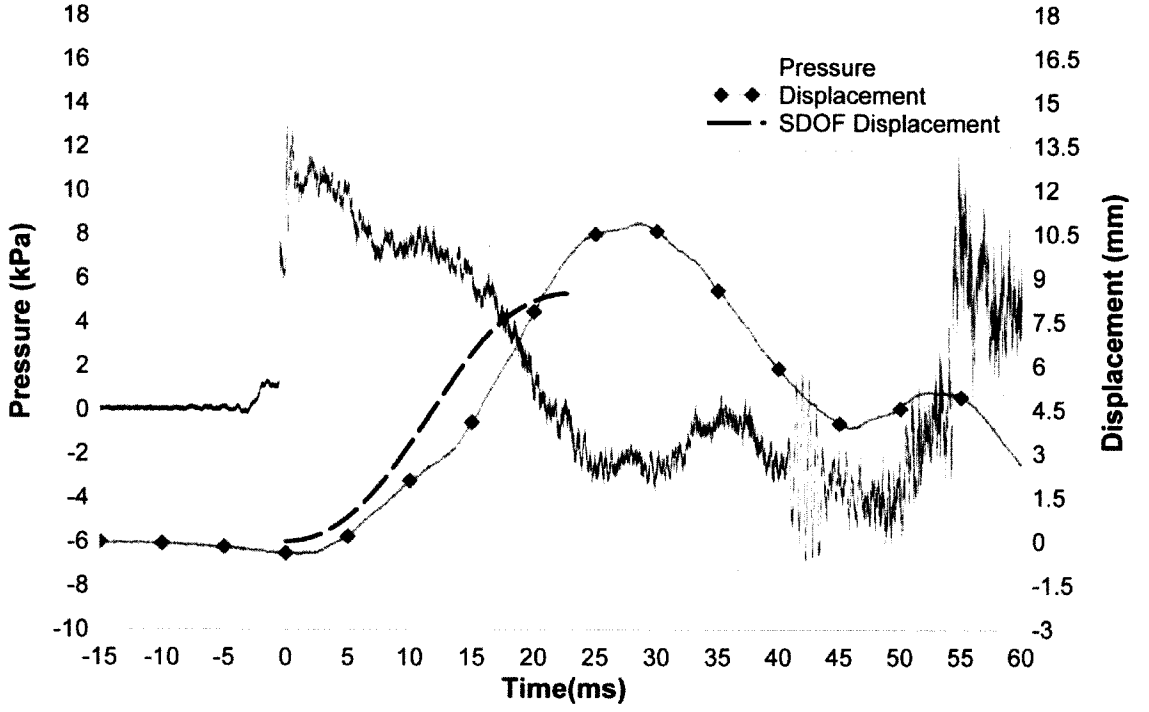


*Figure 5-39: Experimentally Recorded and SDOF Predicted Mid-Height Displacement Time History for Test RC-10-1*

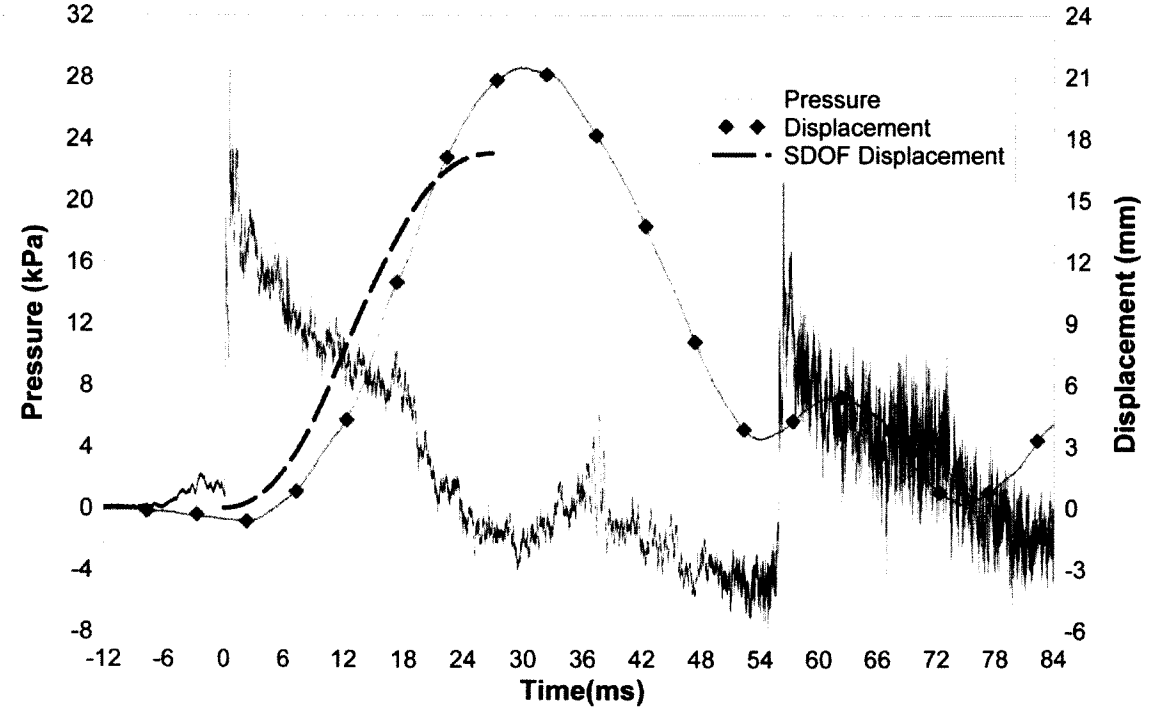


*Figure 5-40: Experimentally Recorded and SDOF Predicted Mid-Height Displacement Time History for Test RC-10-2*

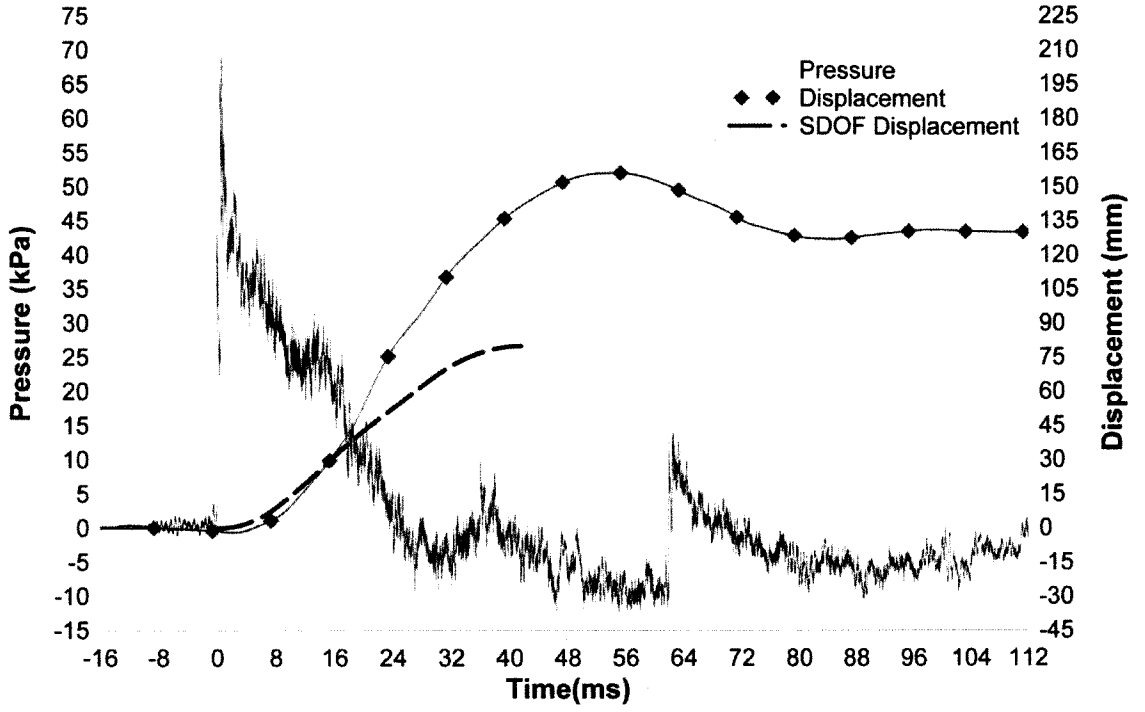


*Figure 5-41: Experimentally Recorded and SDOF Predicted Mid-Height Displacement Time History for Test RC-10-3*

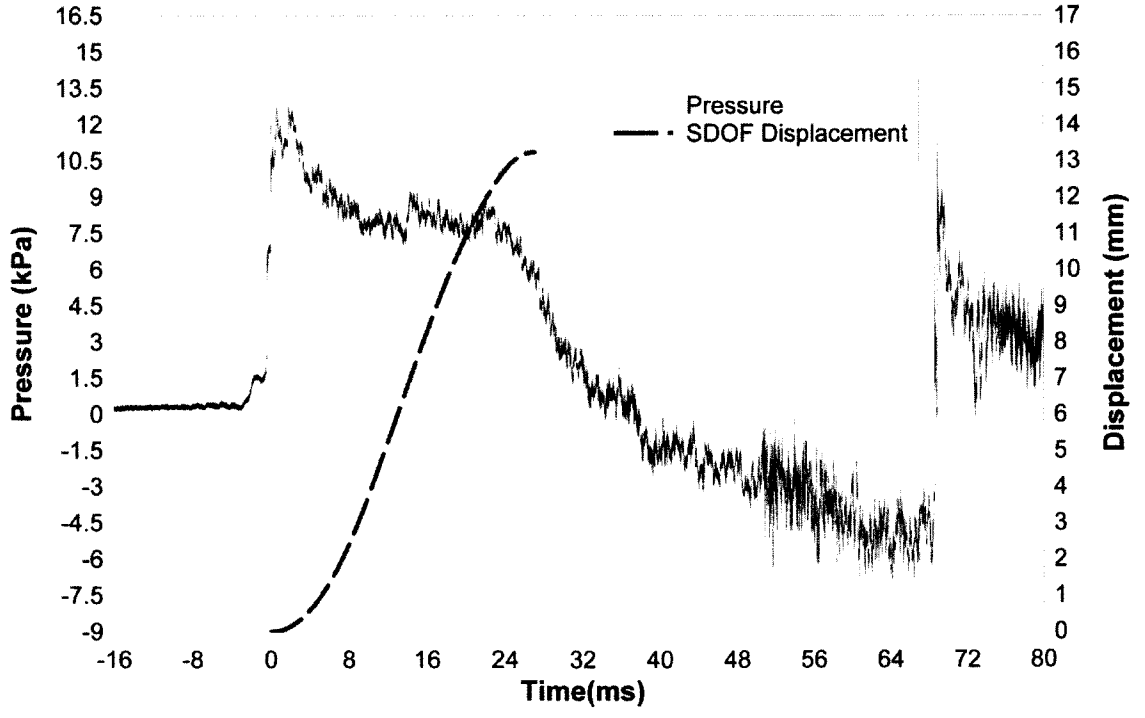


*Figure 5-42: SDOF Predicted Mid-Height Displacement Time History for Test RC-11-1*

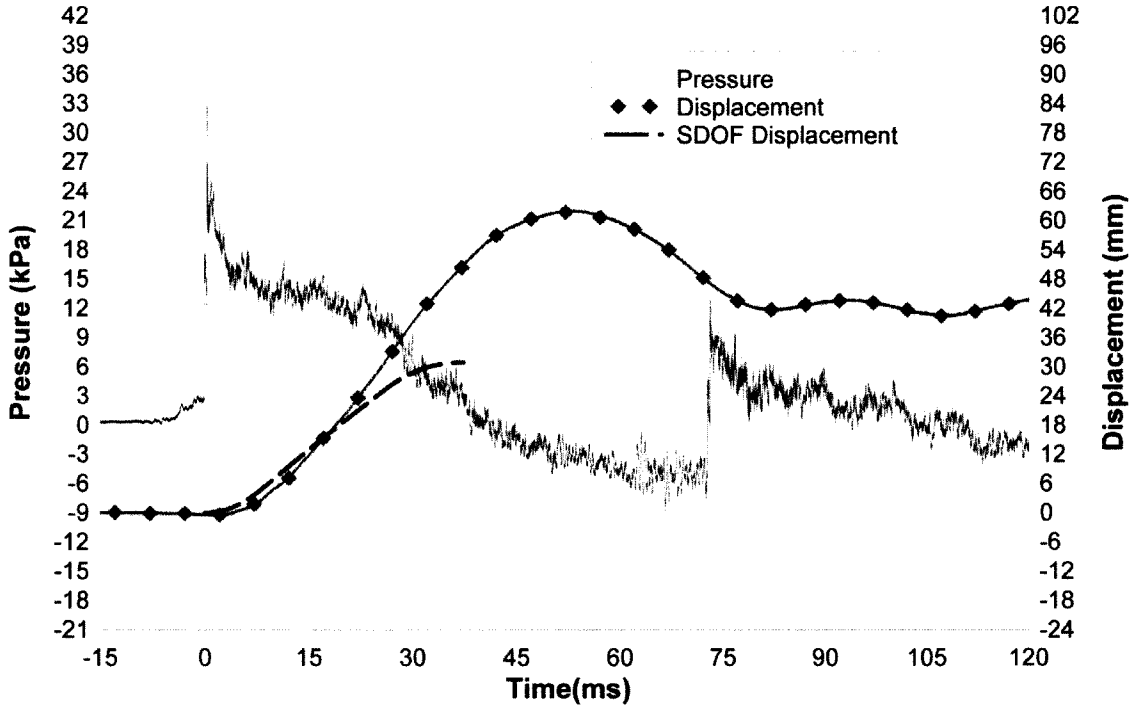


*Figure 5-43: Experimentally Recorded and SDOF Predicted Mid-Height Displacement Time History for Test RC-11-2*

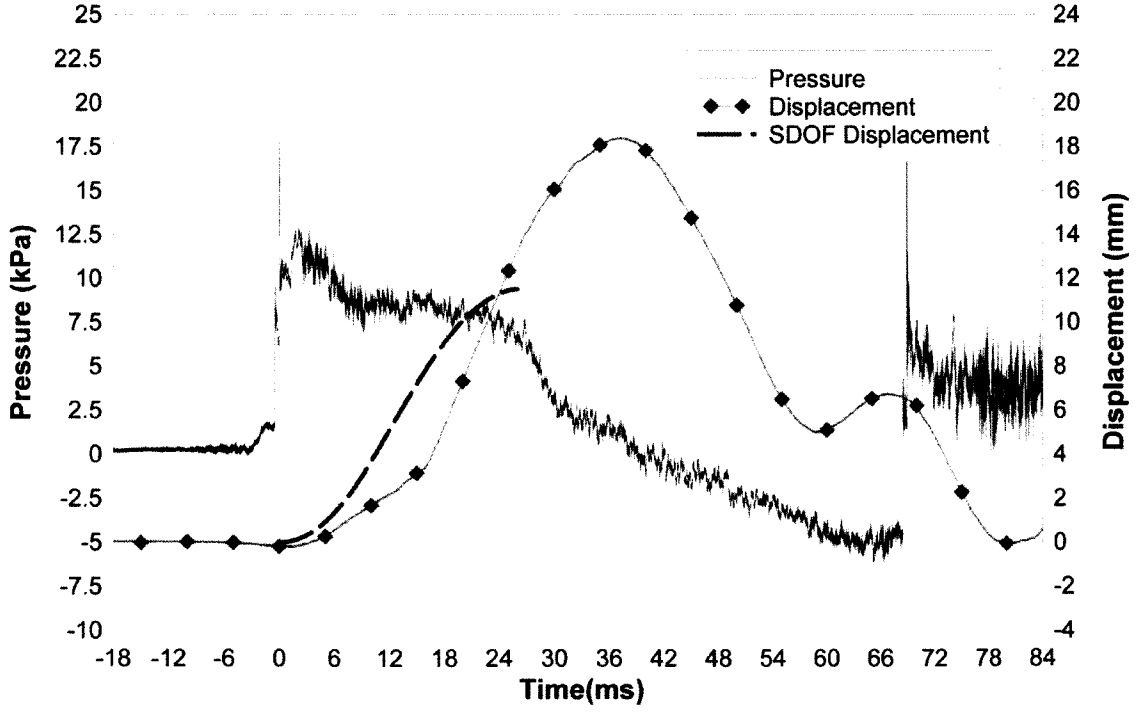


*Figure 5-44: Experimentally Recorded and SDOF Predicted Mid-Height Displacement Time History for Test RC-12-1*

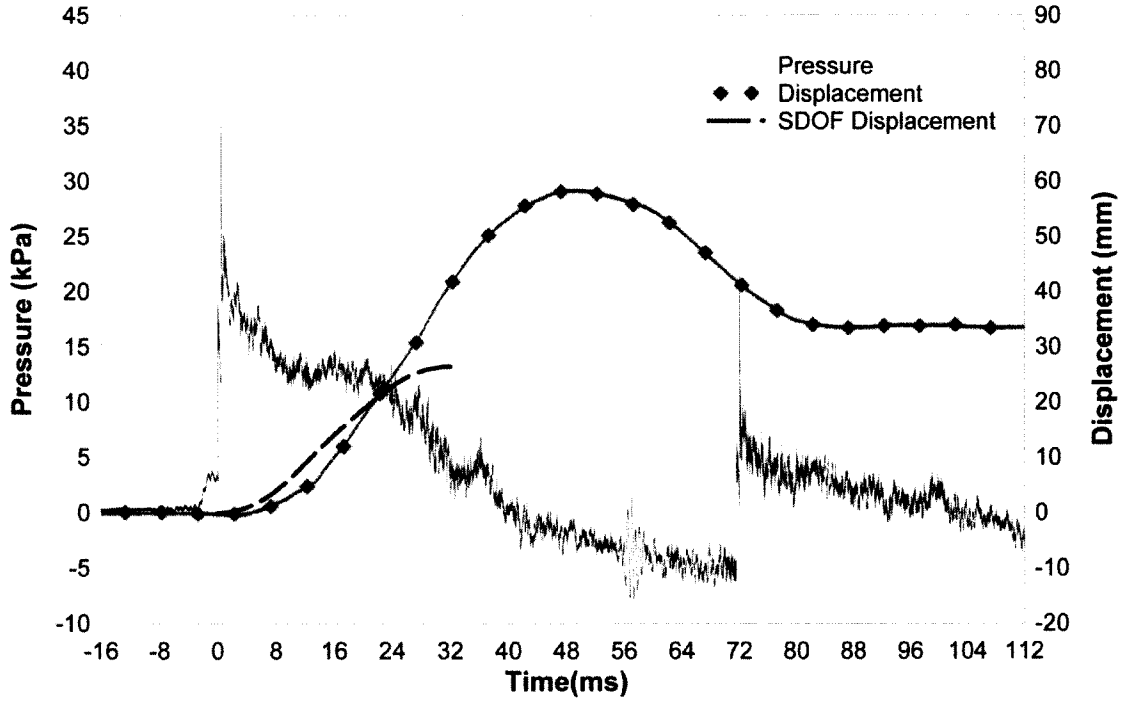


*Figure 5-45: Experimentally Recorded and SDOF Predicted Mid-Height Displacement Time History for Test RC-12-2*

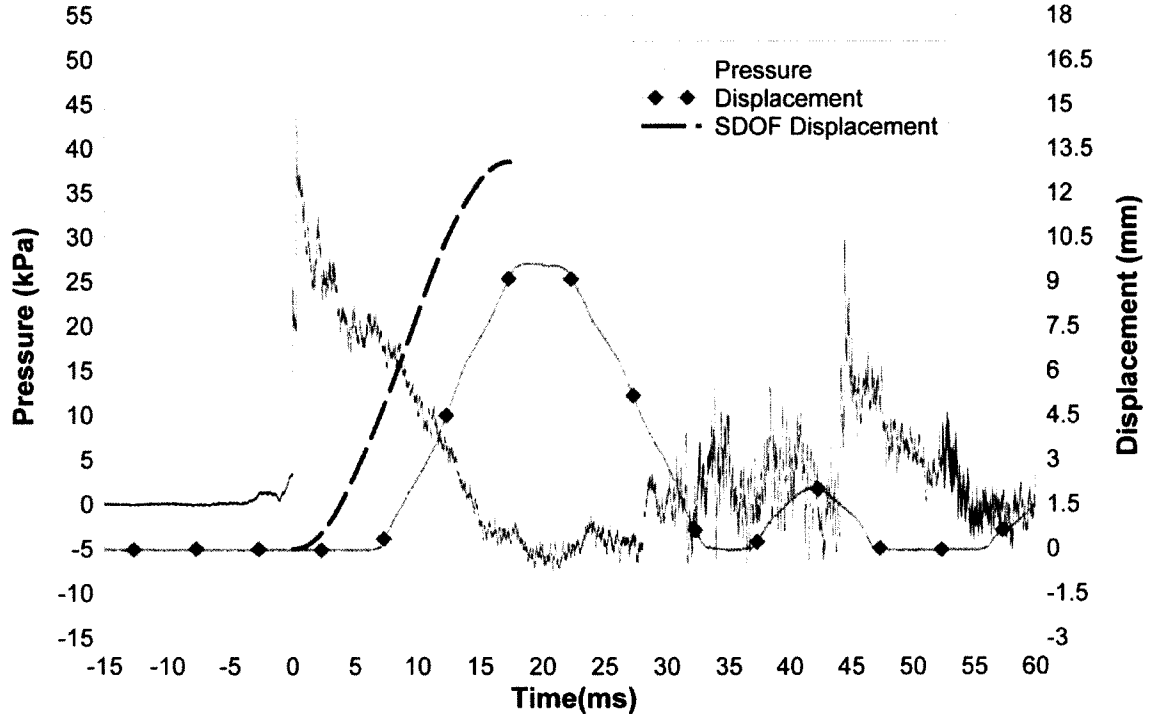


*Figure 5-46: Experimentally Recorded and SDOF Predicted Mid-Height Displacement Time History for Test RC-13-1*

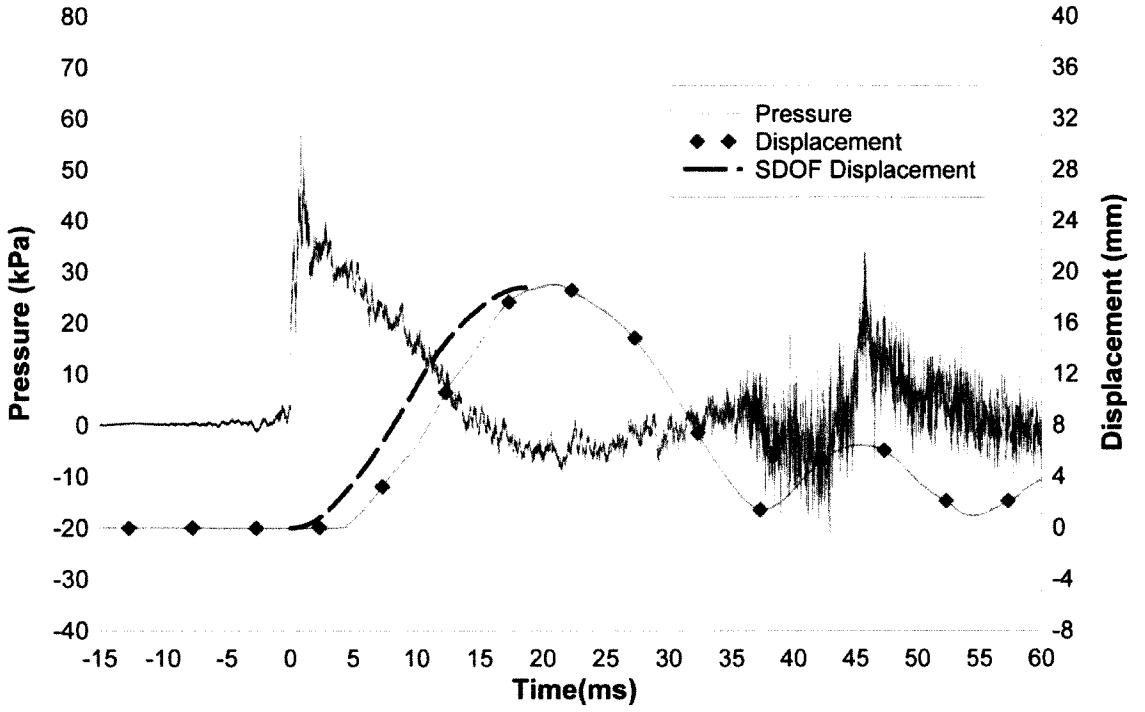


*Figure 5-47: Experimentally Recorded and SDOF Predicted Mid-Height Displacement Time History for Test RC-13-2*

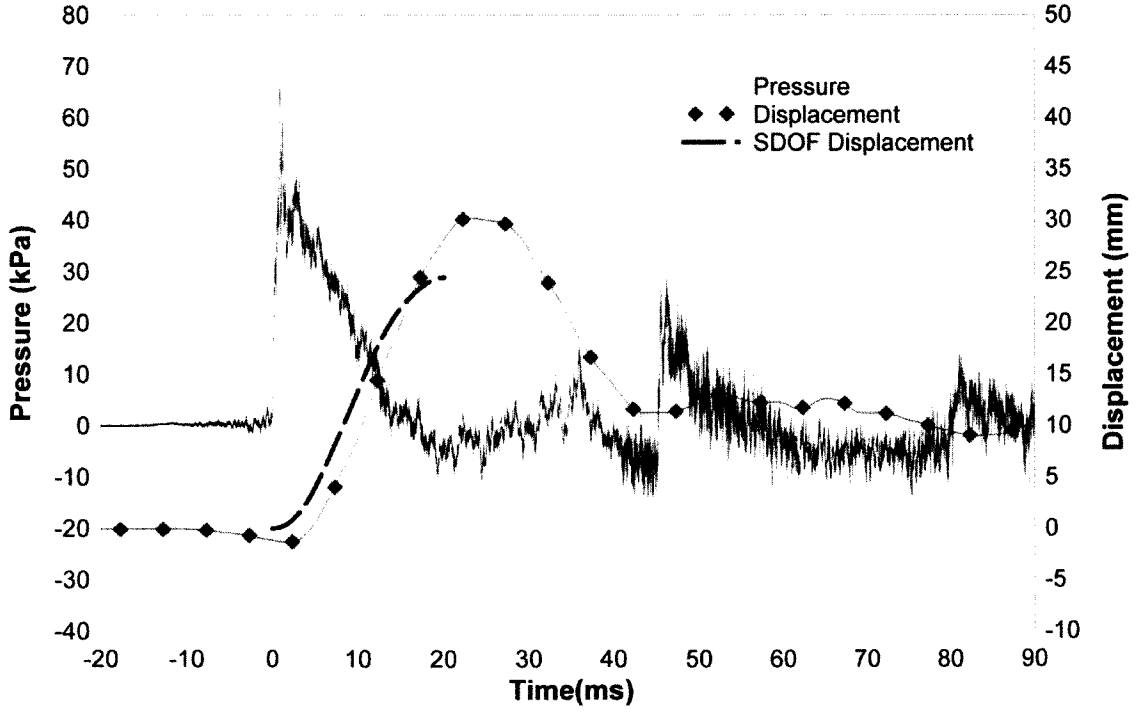


*Figure 5-48: Experimentally Recorded and SDOF Predicted Mid-Height Displacement Time History for Test RC-13-3*

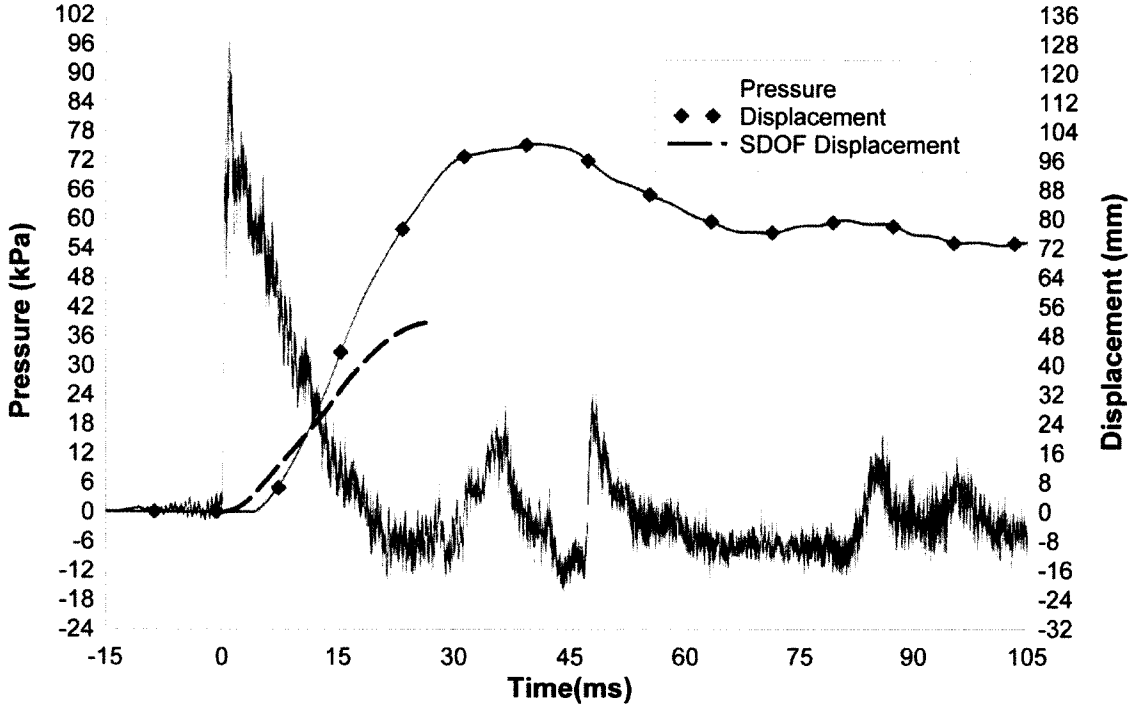


*Figure 5-49: Experimentally Recorded and SDOF Predicted Mid-Height Displacement Time History for Test RC-13-4*

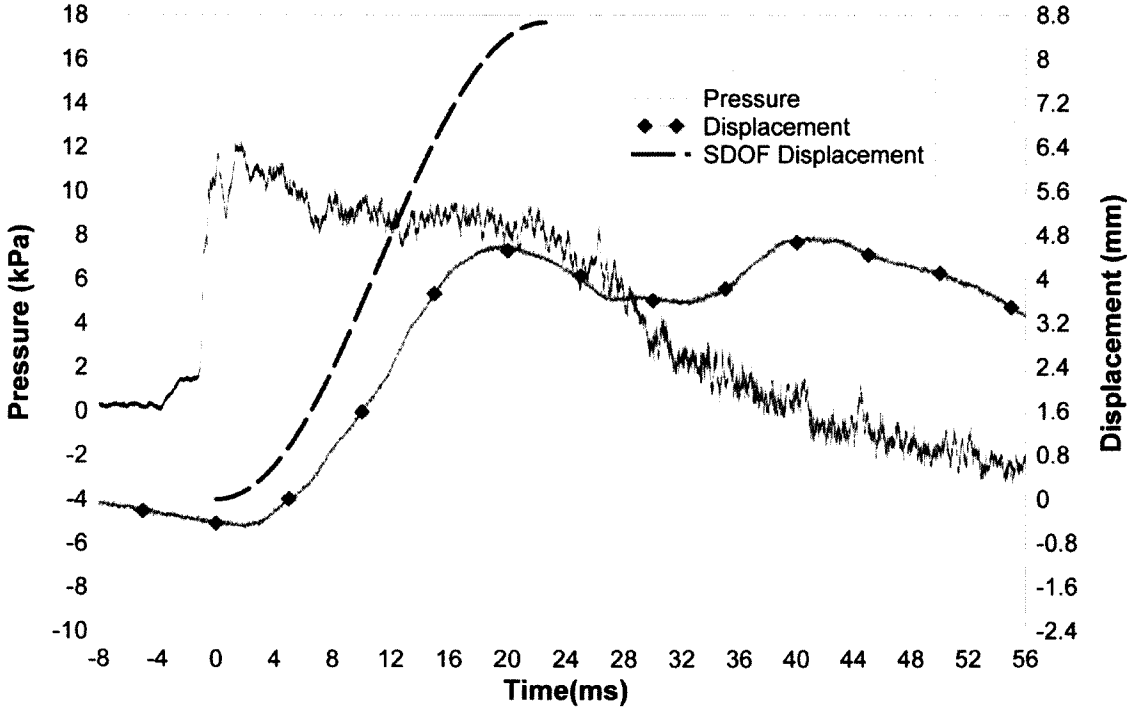


*Figure 5-50: Experimentally Recorded and SDOF Predicted Mid-Height Displacement Time History for Test RC-14-1*

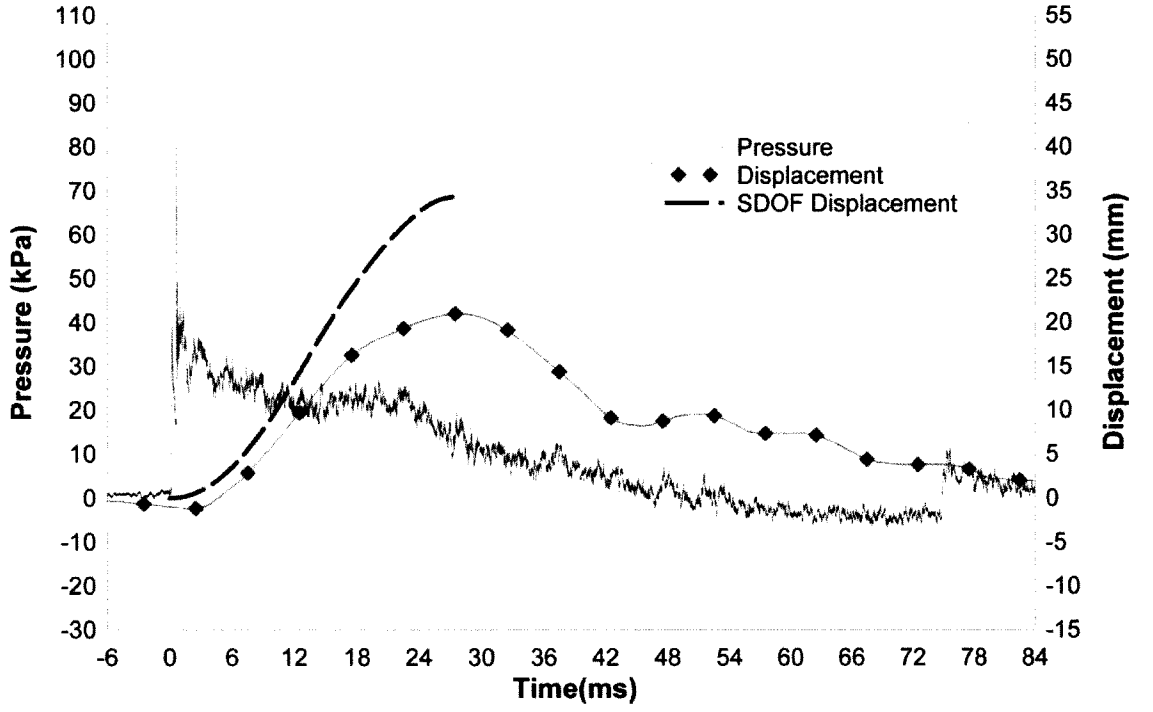


*Figure 5-51: Experimentally Recorded and SDOF Predicted Mid-Height Displacement Time History for Test RC-14-3*

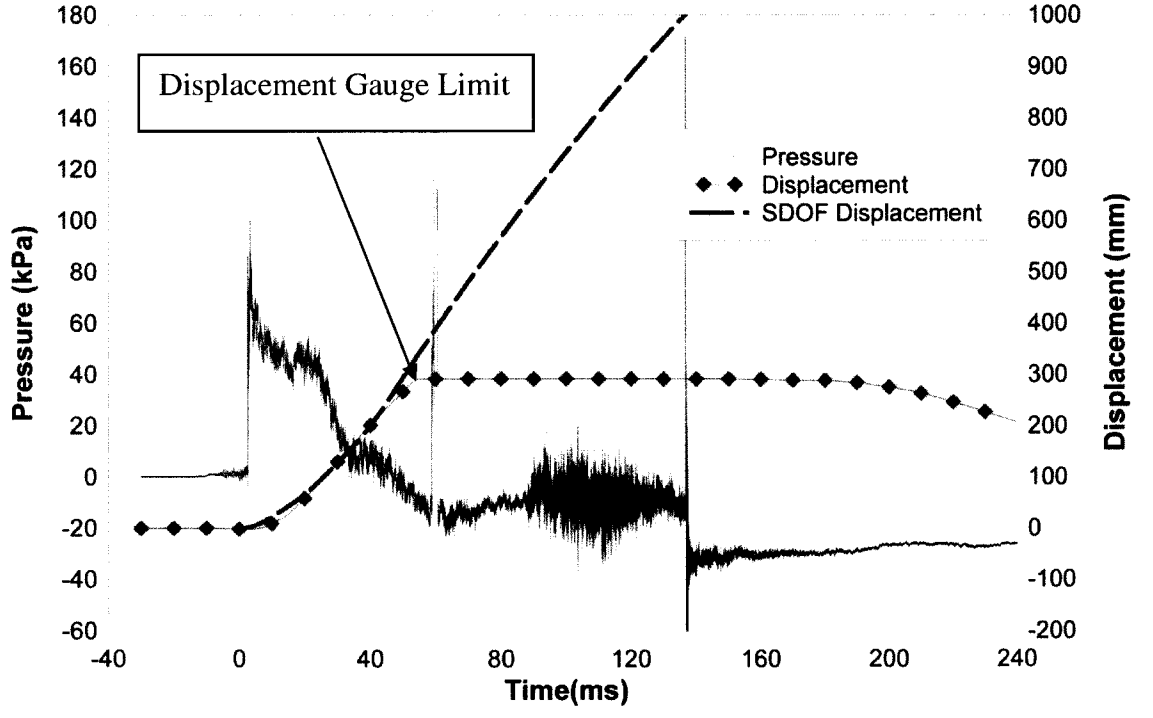


*Figure 5-52: Experimentally Recorded and SDOF Predicted Mid-Height Displacement Time History for Test RC-14-4*

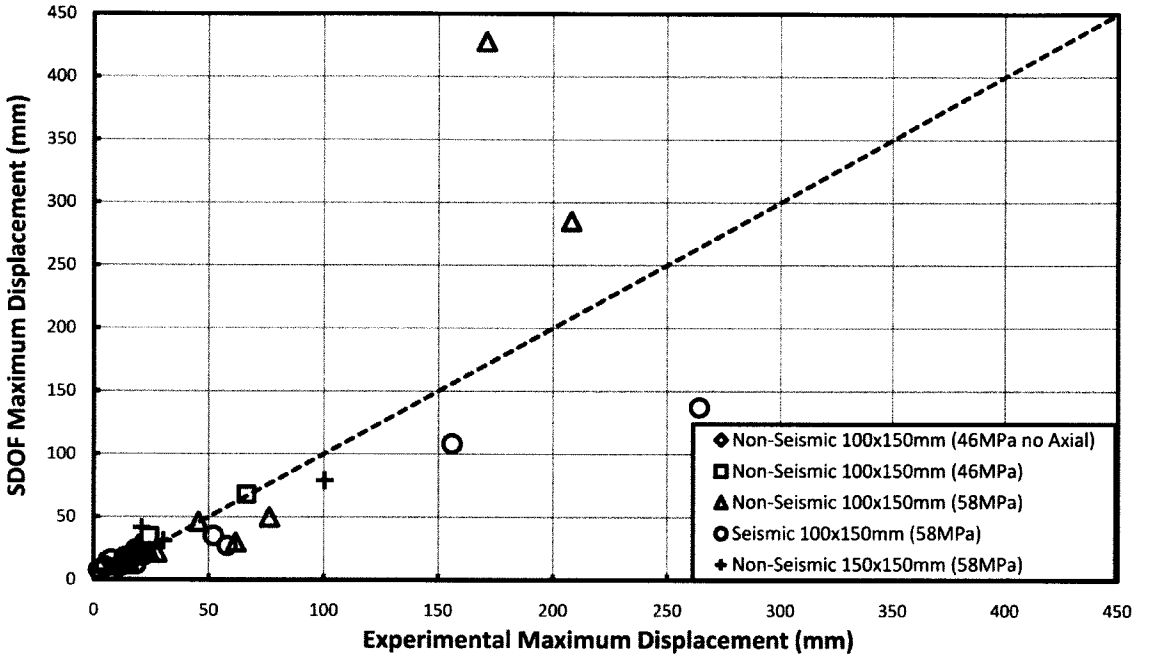


*Figure 5-53: Maximum Displacements Recorded Experimentally Plotted Against those Predicted by SDOF Model*

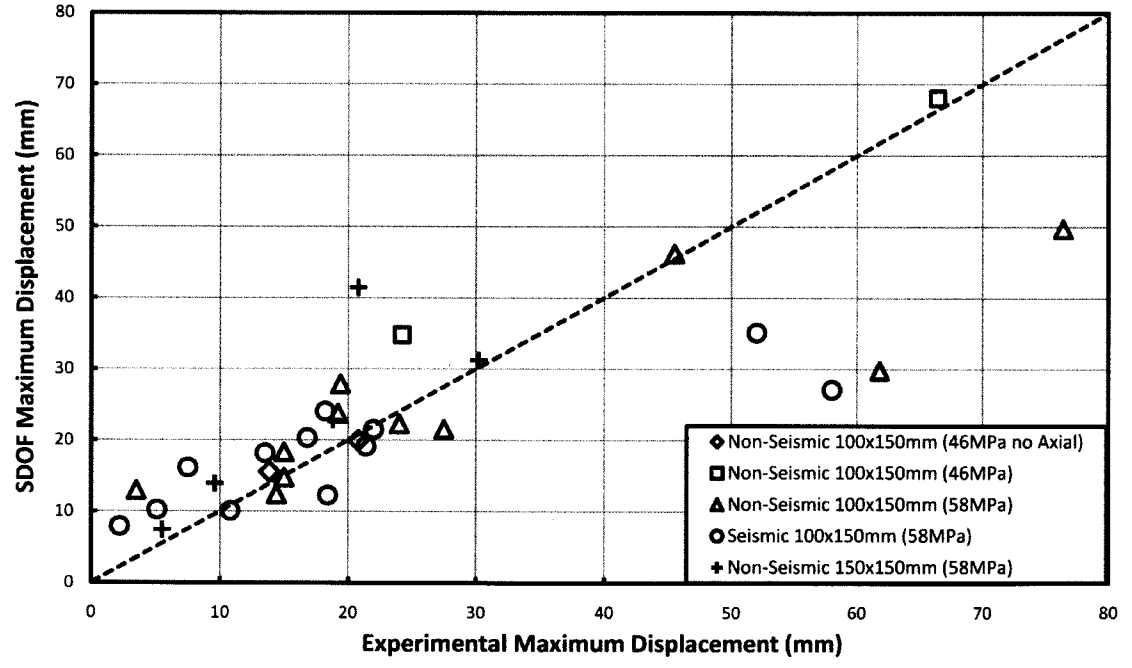


*Figure 5-54: Maximum Displacements Recorded Experimentally Plotted Against those Predicted by SDOF Model for Displacements Less than 80mm*

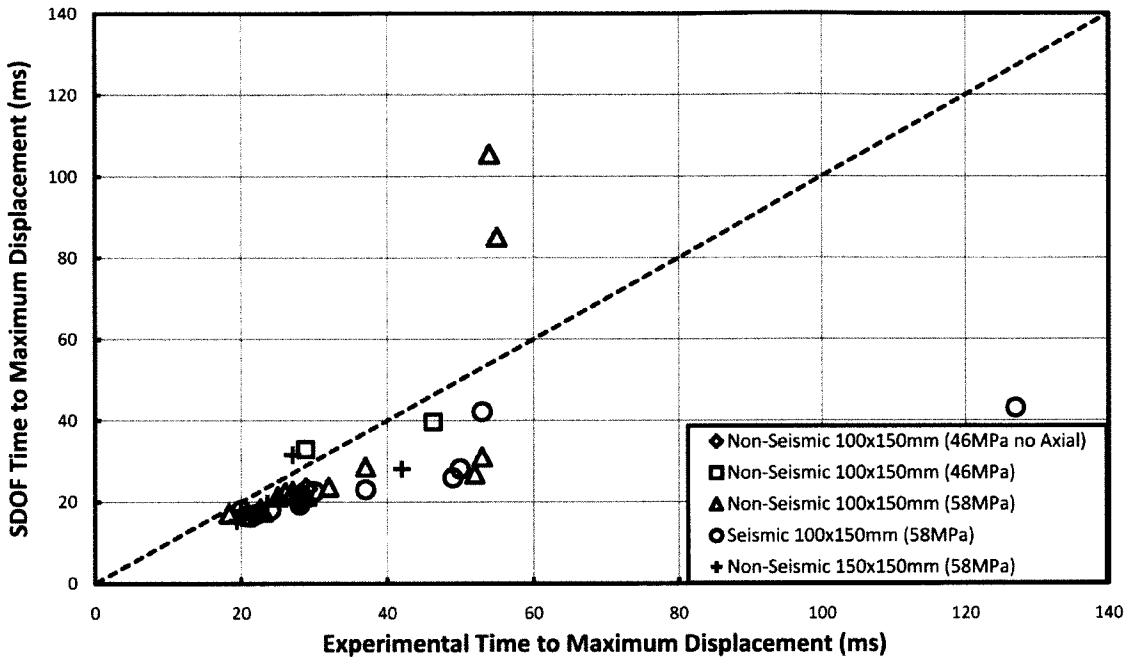


*Figure 5-55: Time to Maximum Displacement Recorded Experimentally Plotted Against those Predicted by SDOF Model*

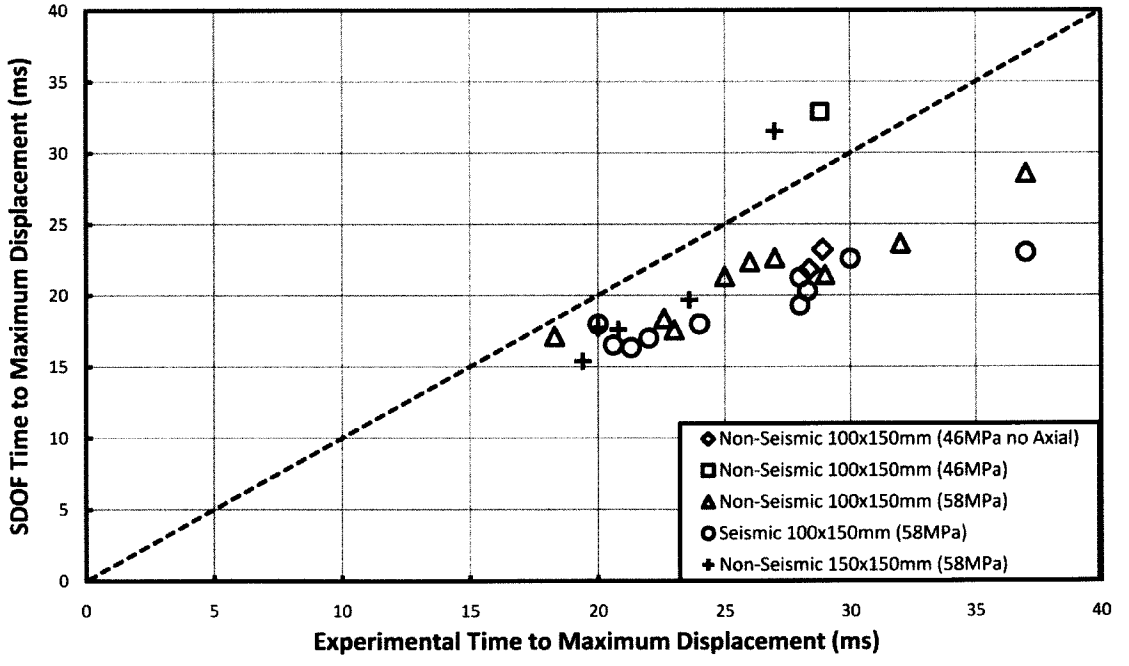


*Figure 5-56: Time to Maximum Displacement Recorded Experimentally Plotted Against those Predicted by SDOF Model for Times Less than 40ms*

# 6 CHAPTER 6

# Conclusions

## *6.1 Summary*

An experimental and analytical investigation was conducted to study the response of reinforced concrete columns under air blast induced shock wave loading. The experimental program was conducted using a shock tube to simulate air blast induced shock waves. A total of *14* reinforced concrete columns were tested under a regimen of shock wave loading. Columns were built to represent columns designed for seismic and non-seismic regions. Pressure-time histories and displacement-time histories were recorded and presented. Strain in reinforcement was also recorded and summarized. The effects of transverse reinforcement spacing in columns were analyzed by comparing the displacement response of seismic and non-seismic columns tested under similar shock wave loading.

An equivalent single degree of freedom numerical analysis was carried out to obtain the dynamic response of columns under shock wave loading. Static resistance-displacement curves were developed using strain rate increase factors for material strength and applied. The static resistance-displacement curves were used along with the constant acceleration numerical integration method to solve the dynamic equation of motion until maximum displacement was predicted. Comparisons of the maximum predicted displacement and those recorded experimentally were made. Finally, constant displacement pressure-impulse curves were developed for all column types using the equivalent single degree of freedom model.

## *6.2 Conclusions*

The following conclusions can be reached from the experimental and analytical research presented in this thesis:

- There was no significant difference in response between the columns designed for seismic regions and those designed for non-seismic regions. It is likely that the slenderness of the columns and the small area of core concrete as well as the loss of axial load with horizontal displacement negated any beneficial effects of core concrete confinement in column response. The combination of these three factors causes the compression zone within the cross-section to move outside of the core confined concrete. This was shown through the comparison of experimental displacement-time histories of seismic and non-seismic columns loaded with similar shock waves.
- The single degree of freedom numerical analysis model accurately predicts the maximum displacement of the columns and the time to maximum displacement for moderate levels of column response. The model under predicts the displacements for large displacement response, however, it still predicts displacements that would cause severe damage to the column causing a collapse mechanism.
- The drop in axial load of the columns that occurred due to the vertical displacement with horizontal deformation is significant and cannot be ignored in calculating response.
- The shock tube was found to have a planar shock wave front with predictable and repeatable pressure-time histories.
- The velocity of the shock wave front is only slightly above the speed of sound in ambient conditions, therefore, diffraction forces on test specimen would be insignificant and the shock tube is not suited for these types of tests.

## *6.3 Recommendations for Future Research*

The following recommendations are made for future research:

- Provide load and displacement sensors to record the change in axial load and the vertical displacement of columns at the support level to better understand the reduction in load with horizontal displacement
- Investigate the redistribution of gravity loads within actual structures due to the horizontal displacement of individual columns. This research would require testing of full structures or components several members of structures loaded with actual mass and would necessitate field testing with live high explosives. Study of the force redistribution would allow for better understanding of the importance second order effects on columns under shock wave loading.
- The load transfer mechanism used in this research was provided as a means to amplify the force on the column due to the shock wave loading. Further research could be conducted into how actual external cladding on structures transfer loads to structural members.
- Tests on columns designed for seismic and non-seismic regions that are less slender is necessary to better understand how partially confined core concrete changes the response of columns under shock wave loading.
- Investigation into reinforcement bond and development length in support regions under high strain rate is recommended.

# Bibliography

Baker, W. E., Cox, P. A., Westine, P. S., Kulesz, J. J., and Strehlow, R. A., "Explosive Hazards and evaluation," *Elsevier Scientific Publishing Company*, New York, USA, 1983.

Bangash, M. Y. H., Bangash, T., "Explosion - Resistant Buildings," *Springer Berlin Heidelber*, New York, New York, USA, 2006.

Biggs, J.M. "Introduction to Structural Dynamics," *McGraw-Hill*, New York, USA, 1964.

Brode, H. L., "Numerical Solution of Spherical Blast Waves," *Journal of Applied Physics*, No. 6, June 1955.

Bulson, P., "Explosive Loading on Engineering Structures," *E&FN Spon*, London, UK, 1997.

Chang, S. Y., "Numerical characteristics of constant average acceleration method in solutions of nonlinear systems," *Journal of the Chinese Institute of Engineers*, Vol. 32, No. 4, 2009, pp. 519-529.

CSA A23.3-04, "Design of Reinforced Concrete Structures," *Canadian Standards Association*, Mississauga, Ontario, Canada, 2004.

Fike Corportation, "Conventional Bolted Type Rupture Disc Holder Data Sheet", July 2005.

Henrych, J., "The Dynamics of Explosion and Its Use," *Elsevier*, Amsterdam, 1979.

Hyde , D., "conWep – Application of TM 5-1300," *U.S. Army Engineer Waterways Experiment Station*, Vicksburg, MA, USA, 1992.

Li, Q. M., Meng, H., "Pressure-Impulse Diagram for Blast Loads based on Dimensional Analysis and Single-Degree-of-Freedom Model," *ASCE Journal of Engineering Mechanics*, Vol. 128, No. 1, 2002, pp. 87-92.

Lipmann, H. W., Roshko, A., "Elements of Gas Dynamics," *Wiley*, New York, USA, 1957.

Lu, Y., Xu, K., "Modelling of Dynamic Behaviour of Concrete Materials under Blast Loading," *International Journal of Solids and Structures*, Vol. 41, 2004, pp. 131-143.

Magnusson,J., "Structural Concrete Elements Subjected to Air Blast Loading," *Licentiate Thesis, Division of Concrete Structures, Royal Institute of Technology*, Stockholm, Sweden, 2007.

Muszynski, L. C., Purcell, M. R., "Composite Reinforcement to Strengthen Existing Concrete Structures Against Air Blast," *Journal of Composites for Construction*, Vol. 7, No. 2, 2003, pp. 93-97.

Newmark, N. M., "Numerical Procedure for Computing Deflections, Moments, and Buckling Loads," *ASCE Transactions*, Vol. 108, 1943, pp. 1161-1234.

Park, R., Priestly, M.J.N., and Gill, W.D., "Ductility of Square-Confined Concrete Columns," *Journal of the Structural Division, ASCE*, 108(ST4), 1982, 929-950.

Razaqpur, A. G., Tolba, A., Contestabile, E., "Blast Loading of Reinforced Concrete Panels Reinforced with Externally Bonded GFRP Laminates," *Journal of Composites: Part B*, No. 38, 2007, pp. 535-546.

Schenker, A., Anteby, I., Nizri, E., Ostraich, B., Kivity, Y., Sadot, O., Haham, O., Michaelis, R., Gal, E., Ben-Dor, G., "Foam-protected reinforced concrete structures under impact: Experimental and numerical studies," *ASCE Journal of Structural Engineering*, Vol. 131, No. 8, 2007, pp. 1233-1242.

Smith, P. D., Hetherington, J. G., "Blast and Ballistic Loading of Structures," *Butterworth – Heinemann*, Oxford, UK, 1994.

Tikka, T. K., "Nonlinear Analysis of Reinforced Concrete Sway Frames," *Annual Conference Proceedings, Canadian Society of Civil Engineering*, 2005, GC-131.

Tikka, T. K., Mirza, S.A. "Nonlinear EI Equation for Slender Reinforced Concrete Columns," *ACI Structural Journal,* Vol. 102, No. 6, November-December 2005, pp. 839-848.

Tikka, T. K., "Nonlinear Analysis of Reinforced Concrete Braced Frames," *Australian Structural Engineering Conference (ASEC)*, Newcastle, Australia, September 11-15 2005.

TM 5-1300, "Structures to Resist Effects of Accidental Explosions," *Technical Manual 5-1300, Department of the Army, Navy and Air Force*, Washington DC, 1990.

Toutlemonde, F., Rossi, P., Boulay, C., Gourraud, C., Guedon, D., "Dynamic Behaviour of Concrete: Tests of Slabs with a Shock Tube," *Materials and Structures*, No. 28, 1995, pp. 293-298.

Woodson, S. C., Baylot, J. T., "Structural Collapse: Quarter-Scale Model Experiments," *US Army Corps of Engineers* Technical Report SL-99-8, Vicksburg, MS, USA, 1999.

Yalcin, C., Saatcioglu, M., "Inelastic Analysis of Reinforced Concrete Columns," *Computers and Structures*, Vol. 77, No. 5, pp. 539-555.

# 7 APPENDIX A

## Strain Data

Strain gauges were placed on the longitudinal steel and on select transverse hoops for each column. The locations of these strain gauges and the strain gauge numbering convention is shown in Figure 7-1. This appendix presents the time history of the strain that was recorded during the column tests. Note that not all strain channels were monitored during testing so only a limited number are presented for each test. The strain time history plots for all tests are found in Figures 7-2 through 7-43.

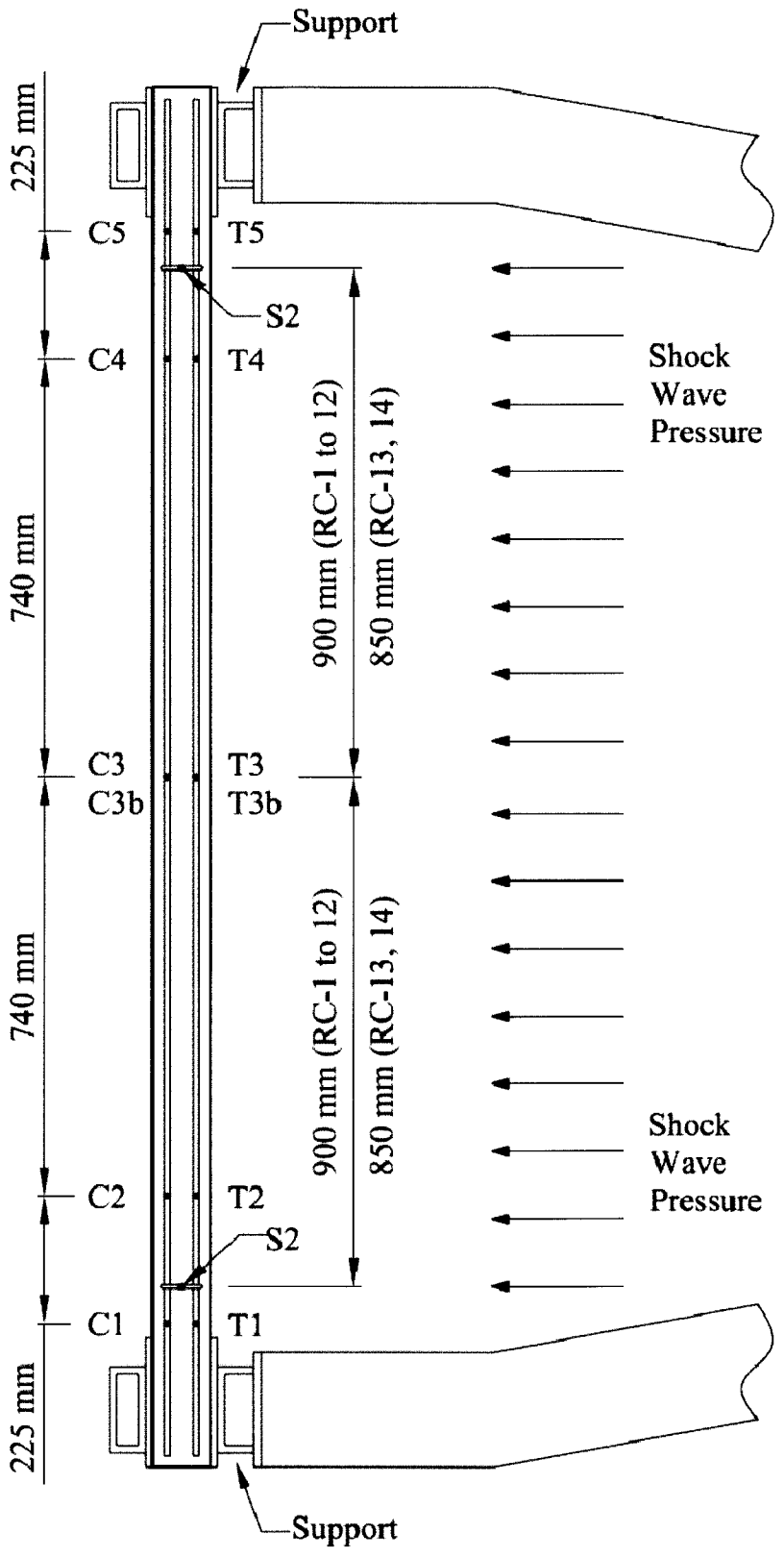


*Figure 7-1: Locations of Strain Gauges*

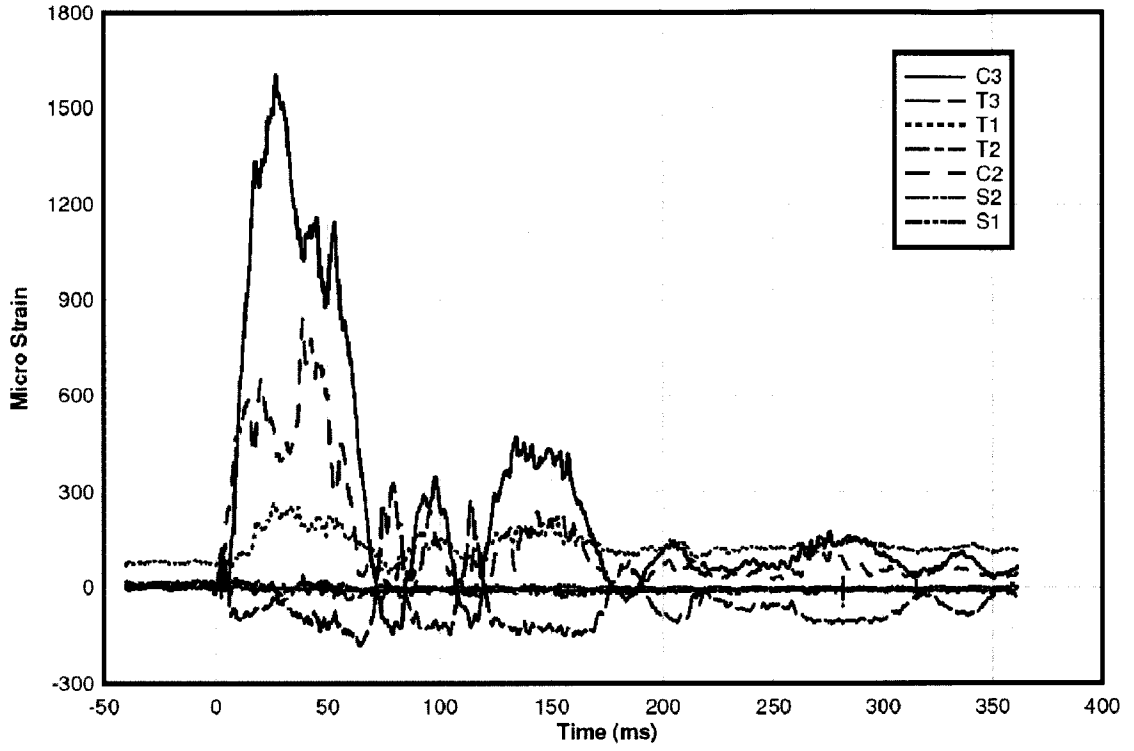


*Figure 7-2: Strain Time History for Test RC-1-1*

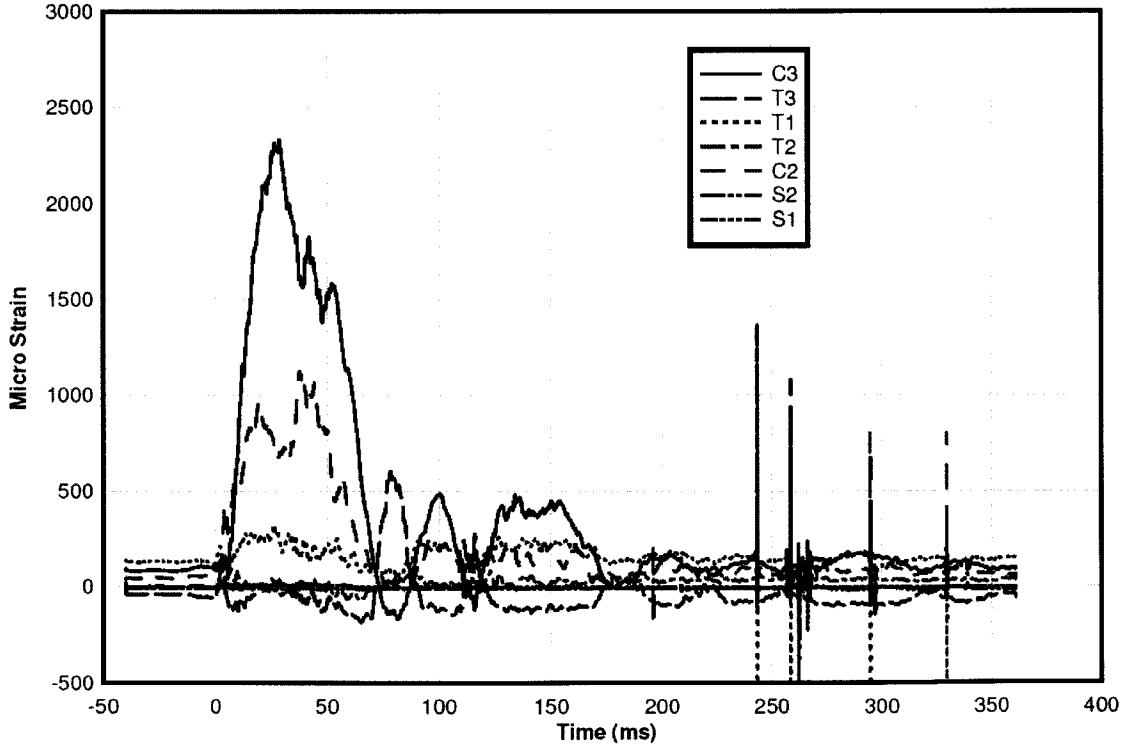


*Figure 7-3: Strain Time History for Test RC-1-2*

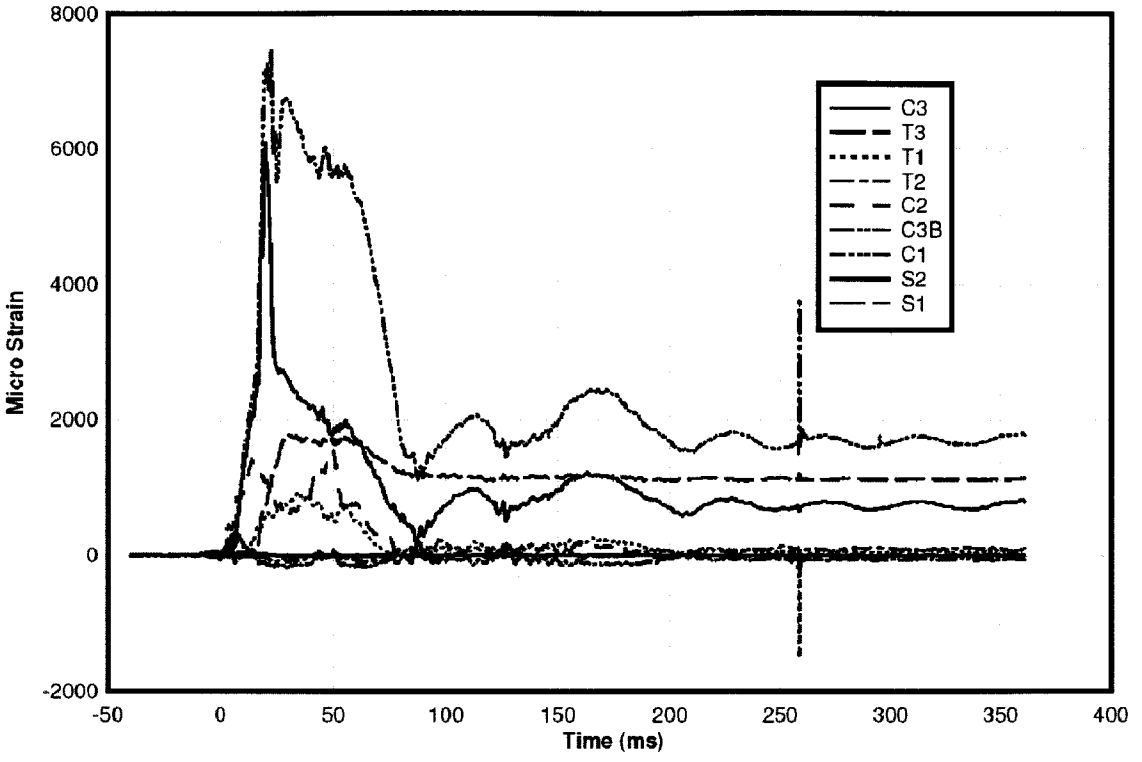


*Figure 7-4: Strain Time History for Test RC-1-3*

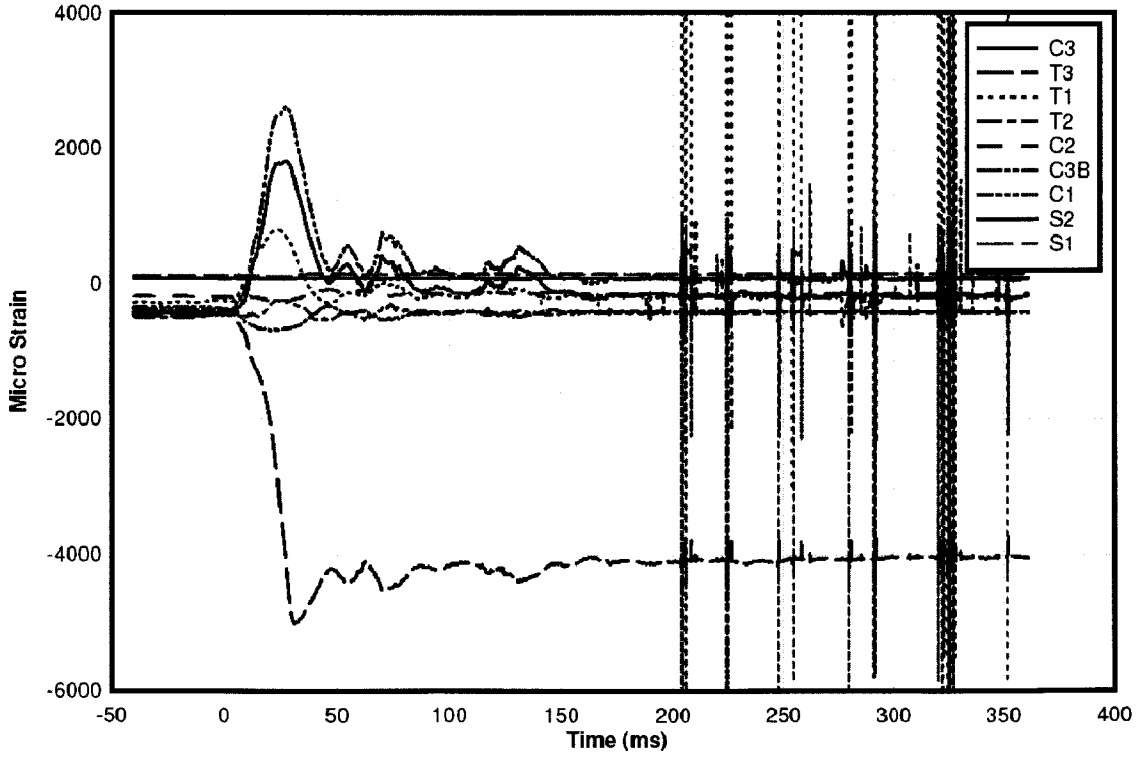


*Figure 7-5: Strain Time History for Test RC-2-1*

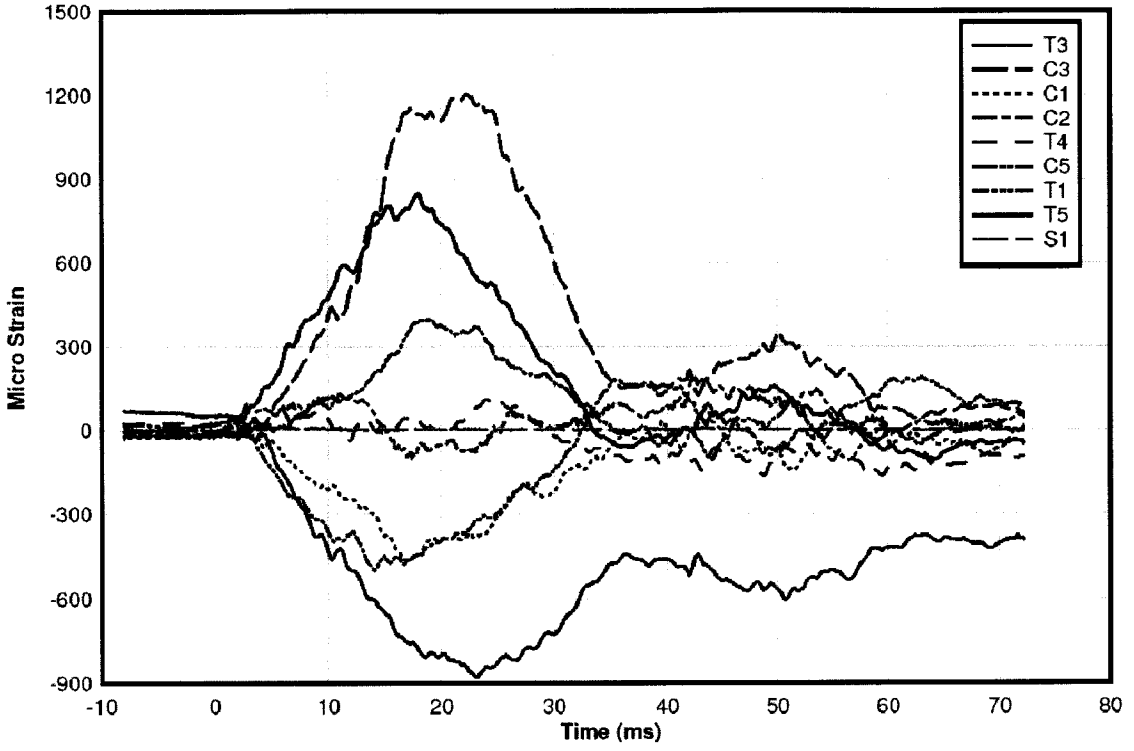


*Figure 7-6: Strain Time History for Test RC-3-1*

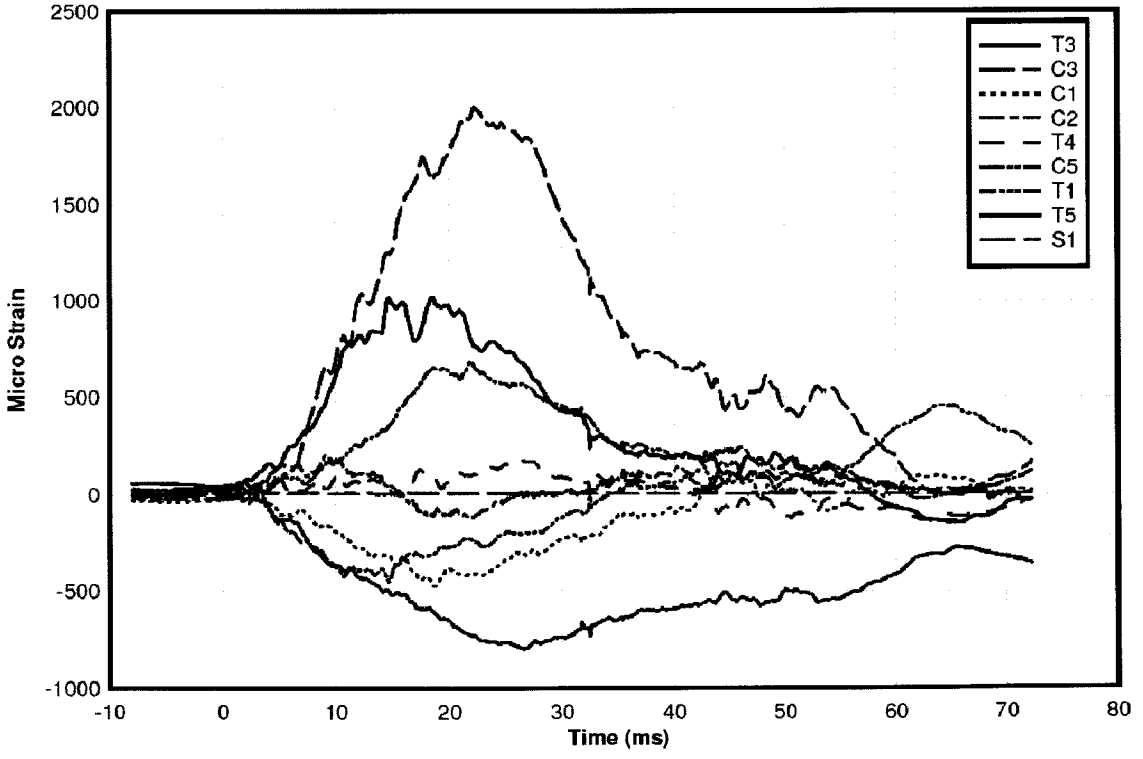


*Figure 7-7: Strain Time History for Test RC-3-2*

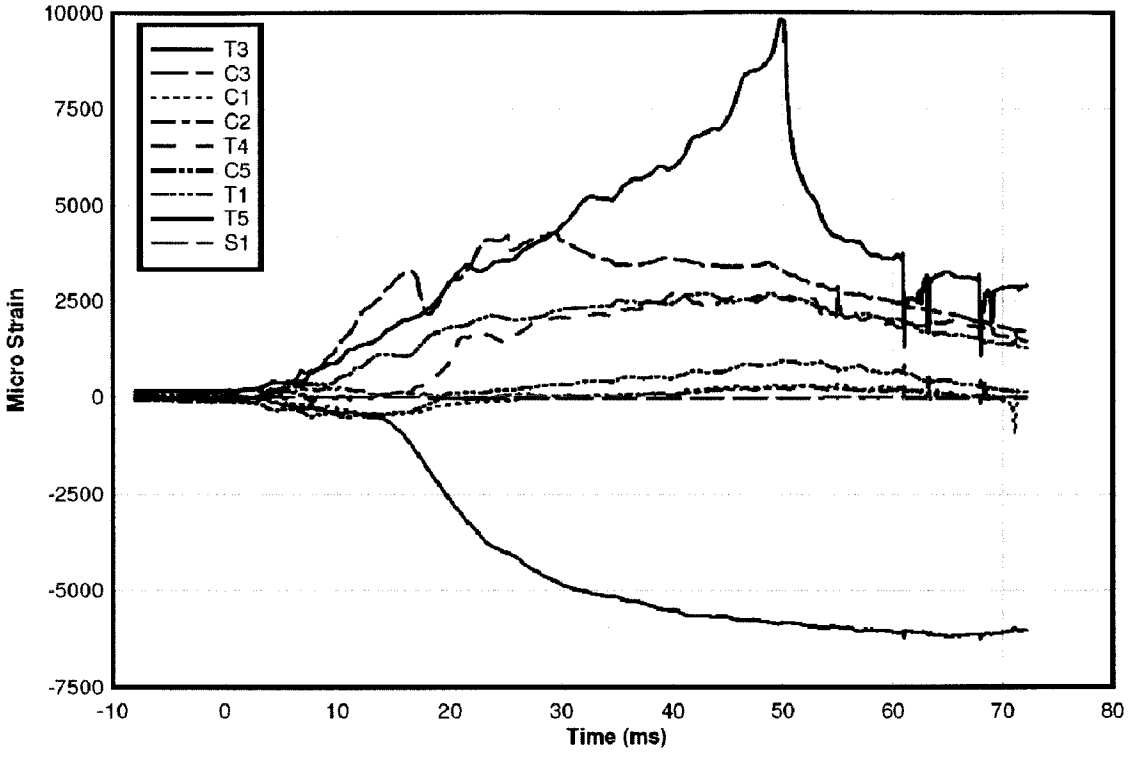


*Figure 7-8: Strain Time History for Test RC-3-3*

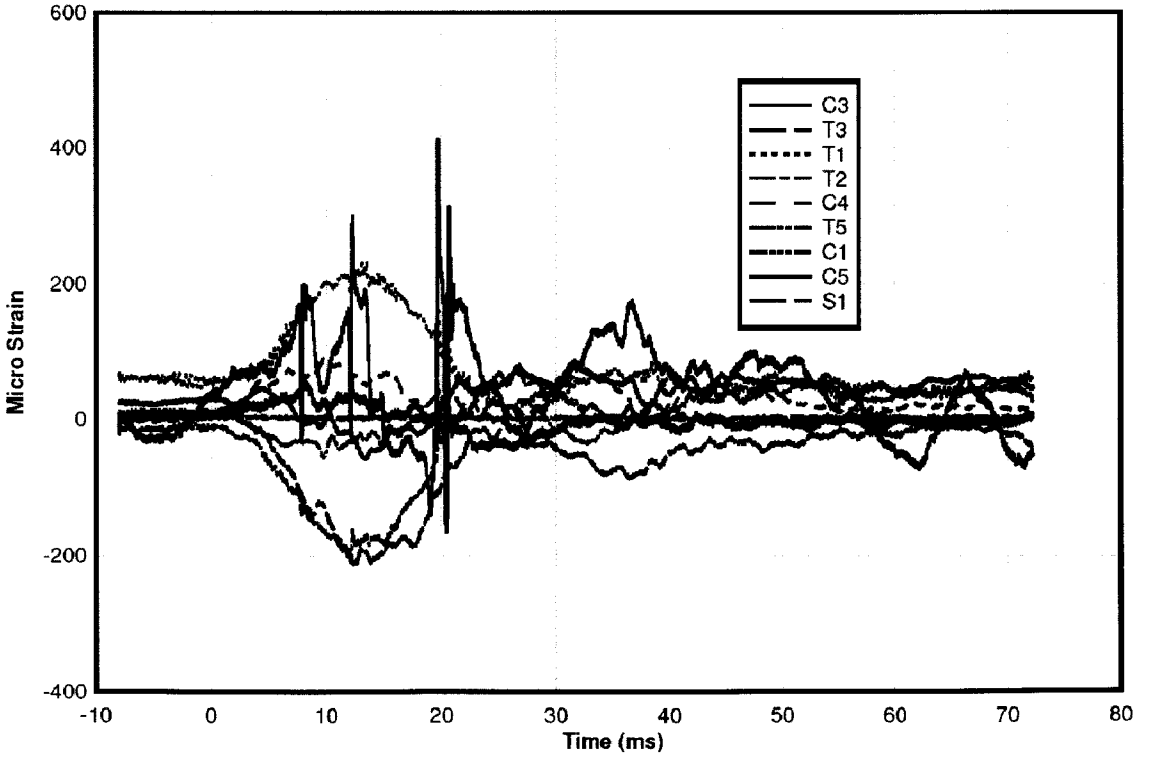


*Figure 7-9: Strain Time History for Test RC-4-1*

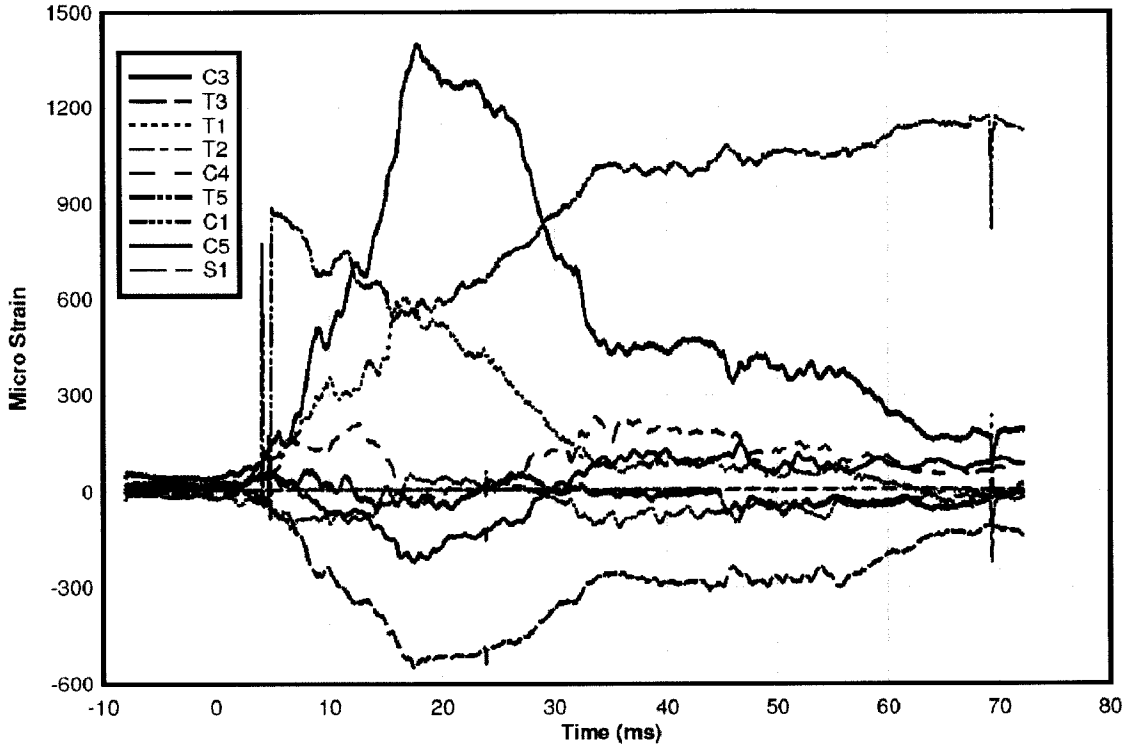


*Figure 7-10: Strain Time History for Test RC-4-2*

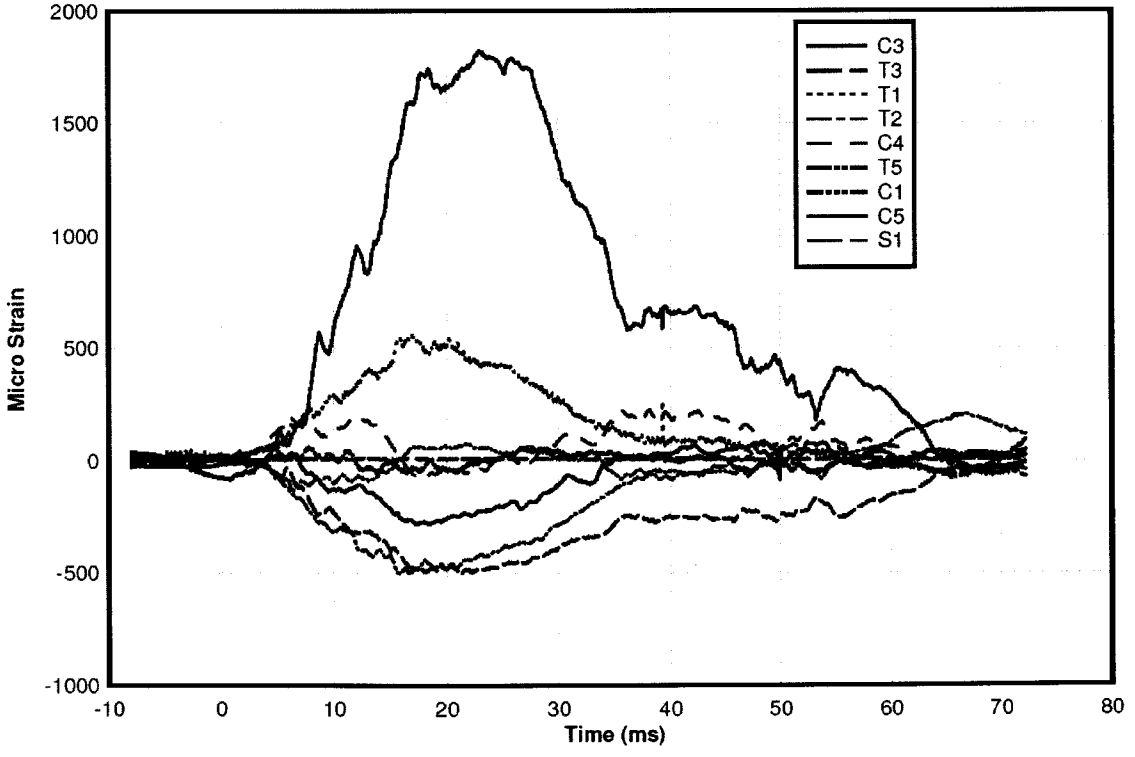


*Figure 7-11: Strain Time History for Test RC-4-3*

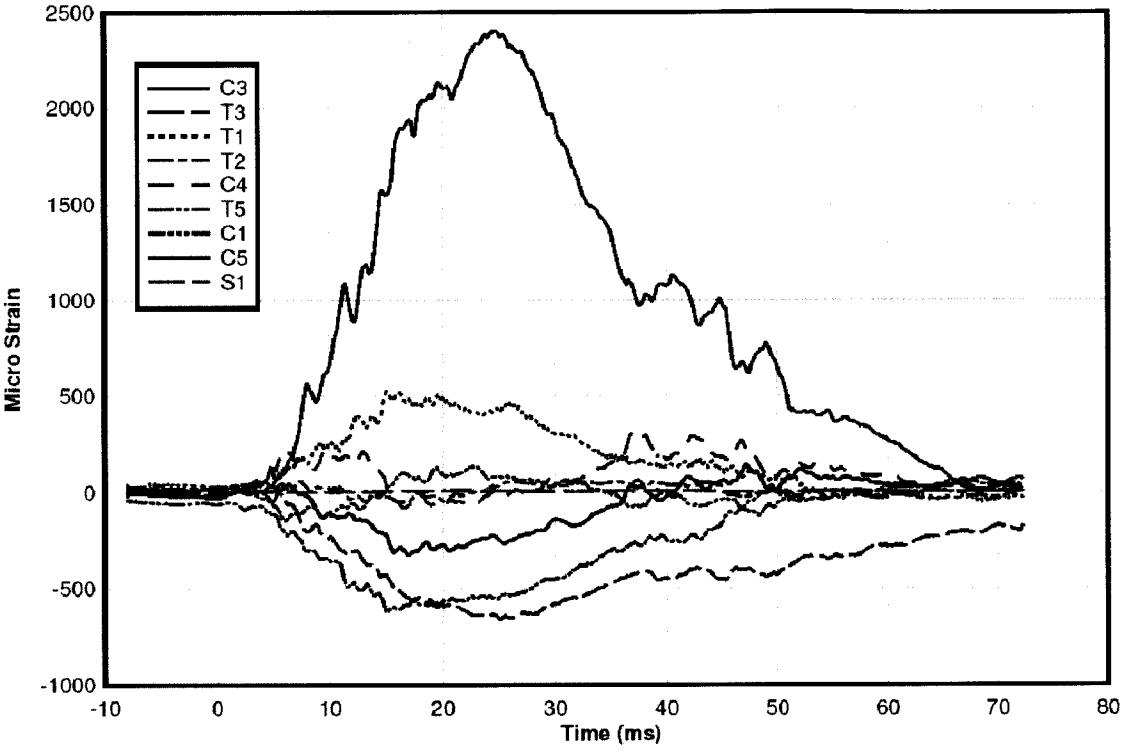


*Figure 7-12: Strain Time History for Test RC-4-4*

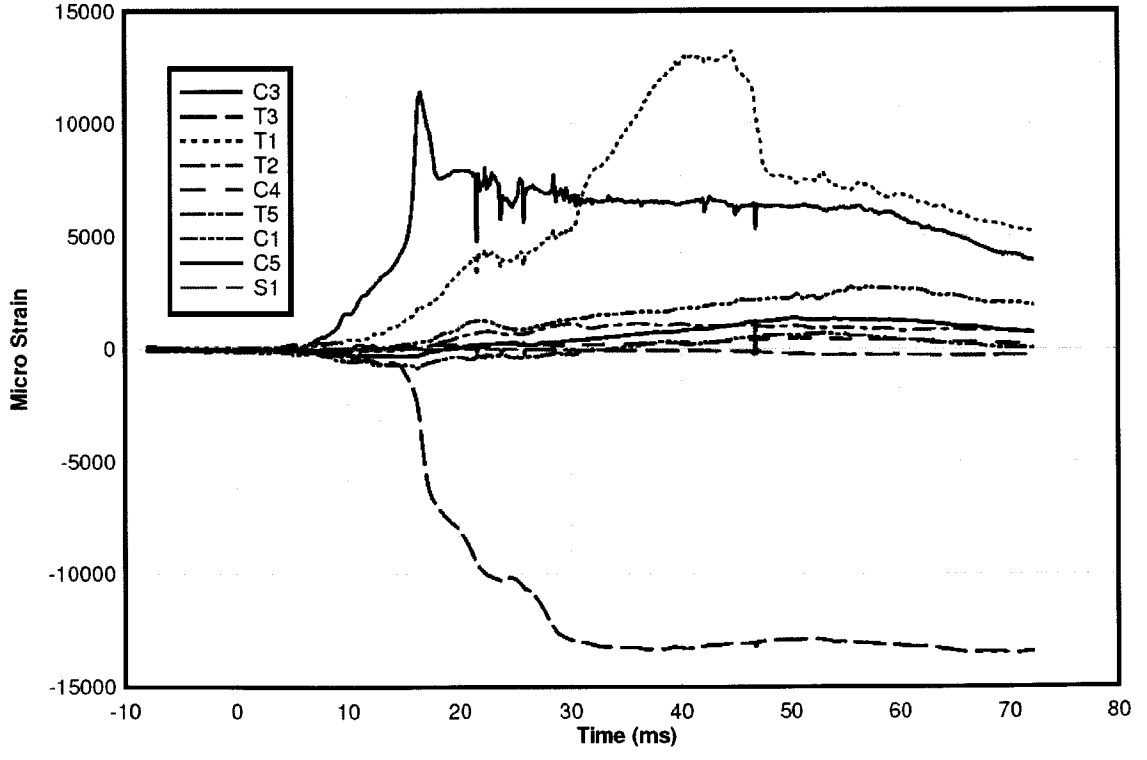


*Figure 7-13: Strain Time History for Test RC-4-5*

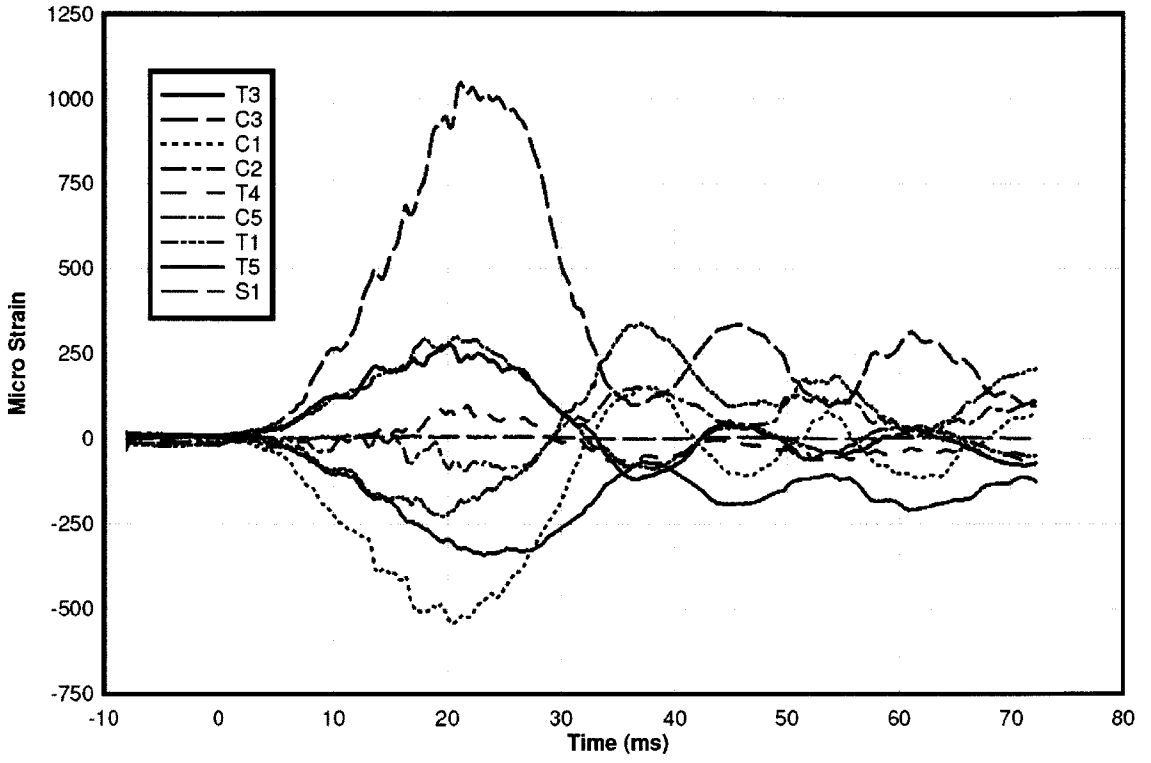


*Figure 7-14: Strain Time History for Test RC-5-1*

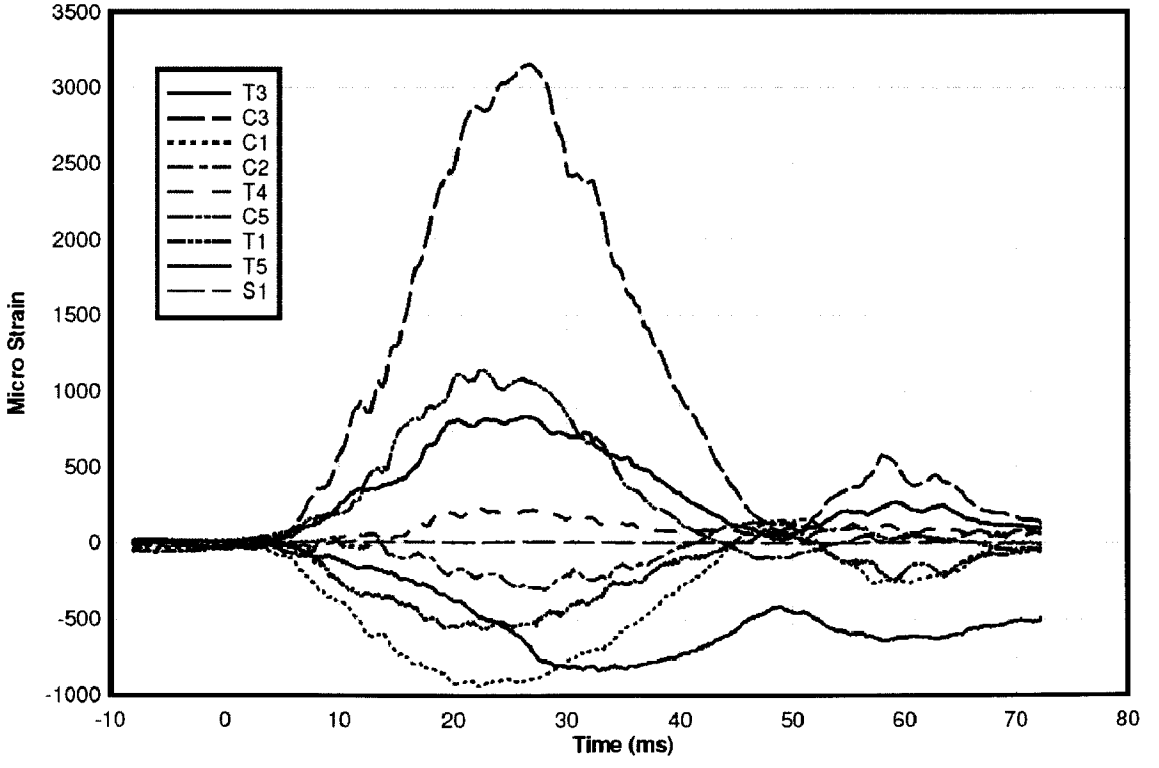


*Figure 7-15: Strain Time History for Test RC-5-2*

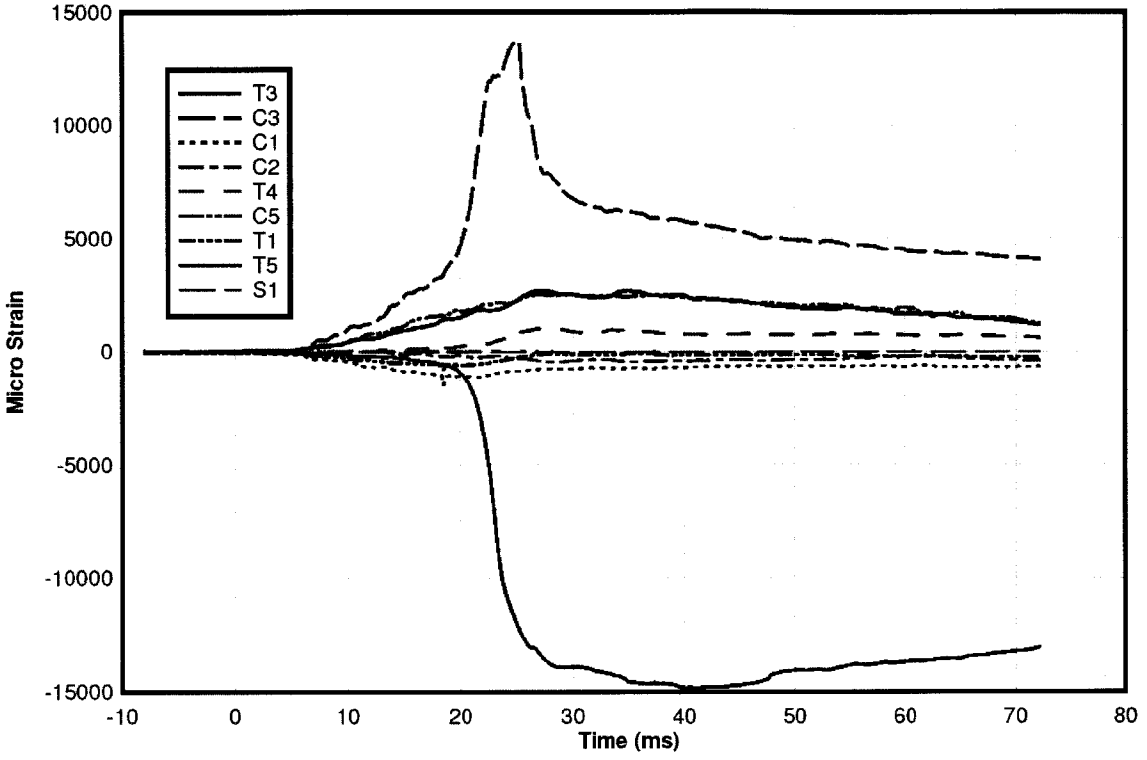


*Figure 7-16: Strain Time History for Test RC-5-3*

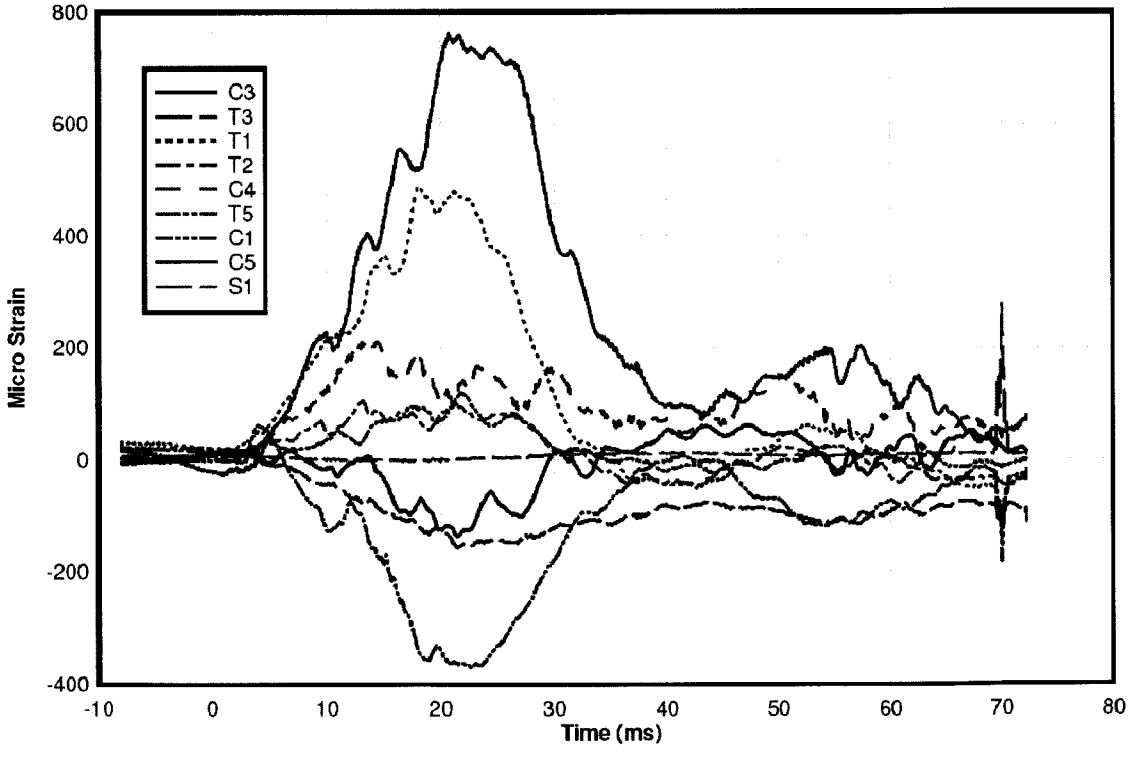


*Figure 7-17: Strain Time History for Test RC-6-1*

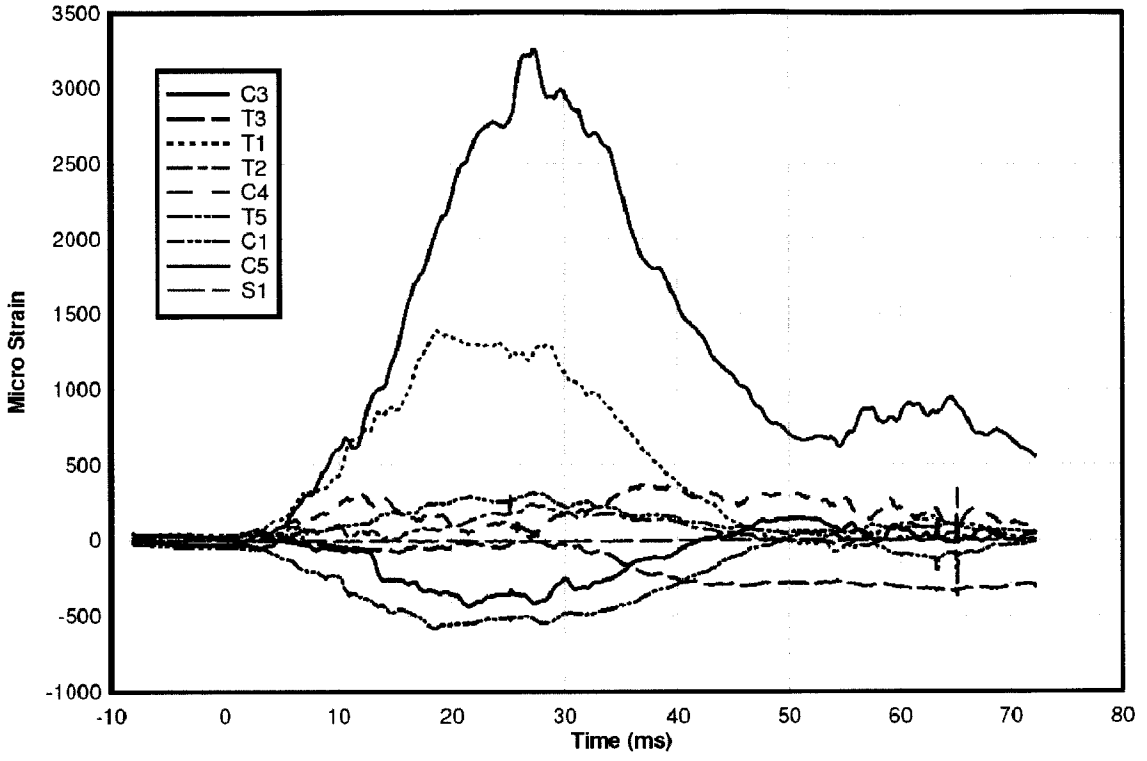


*Figure 7-18: Strain Time History for Test RC-6-2*

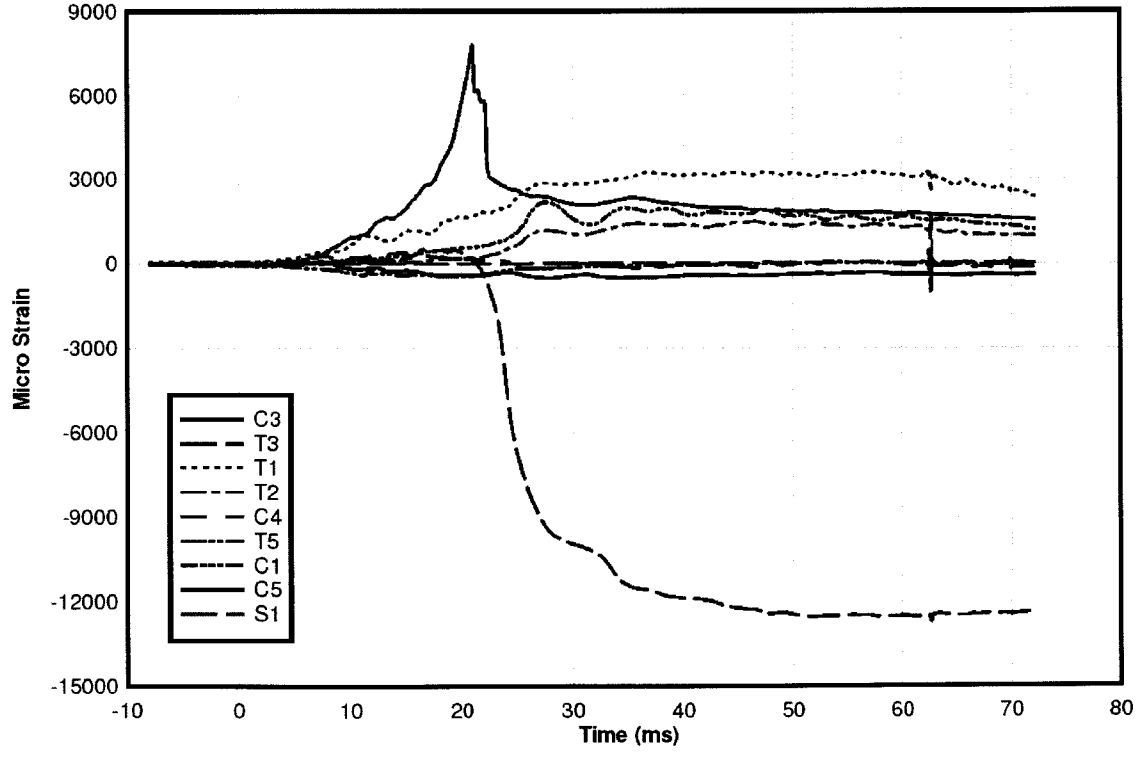


*Figure 7-19: Strain Time History for Test RC-6-3*

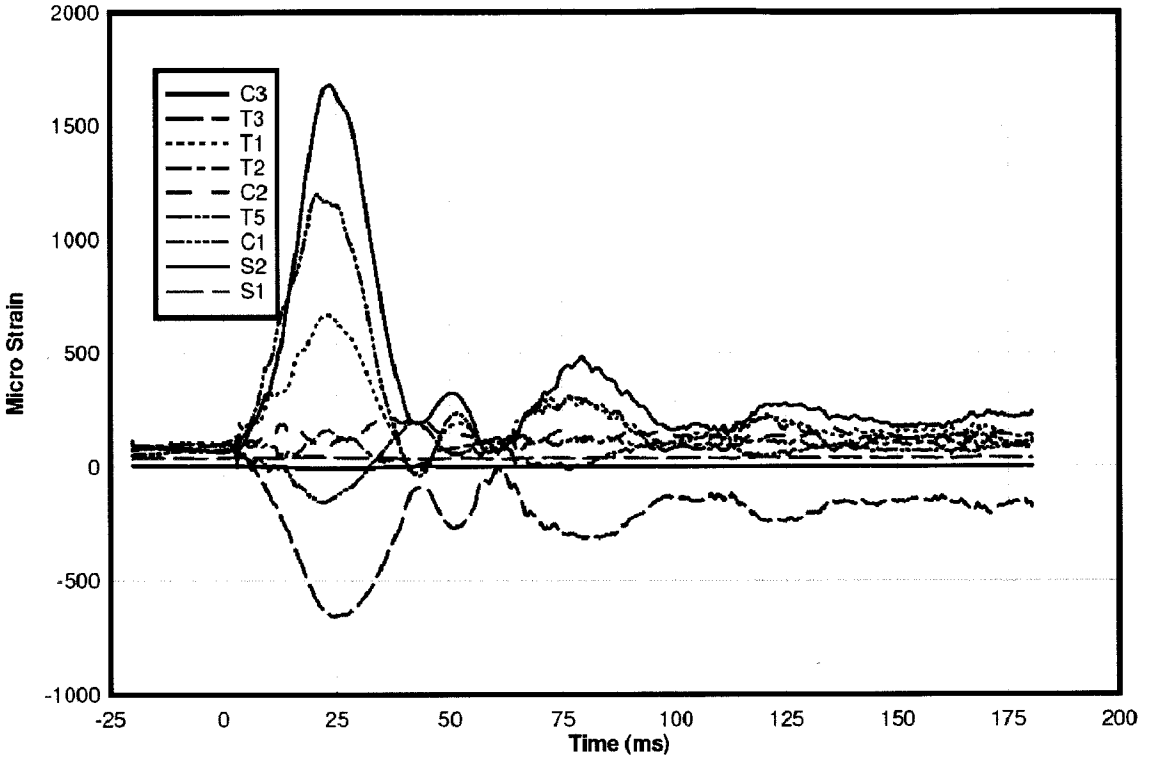


*Figure 7-20: Strain Time History for Test RC-7-1*

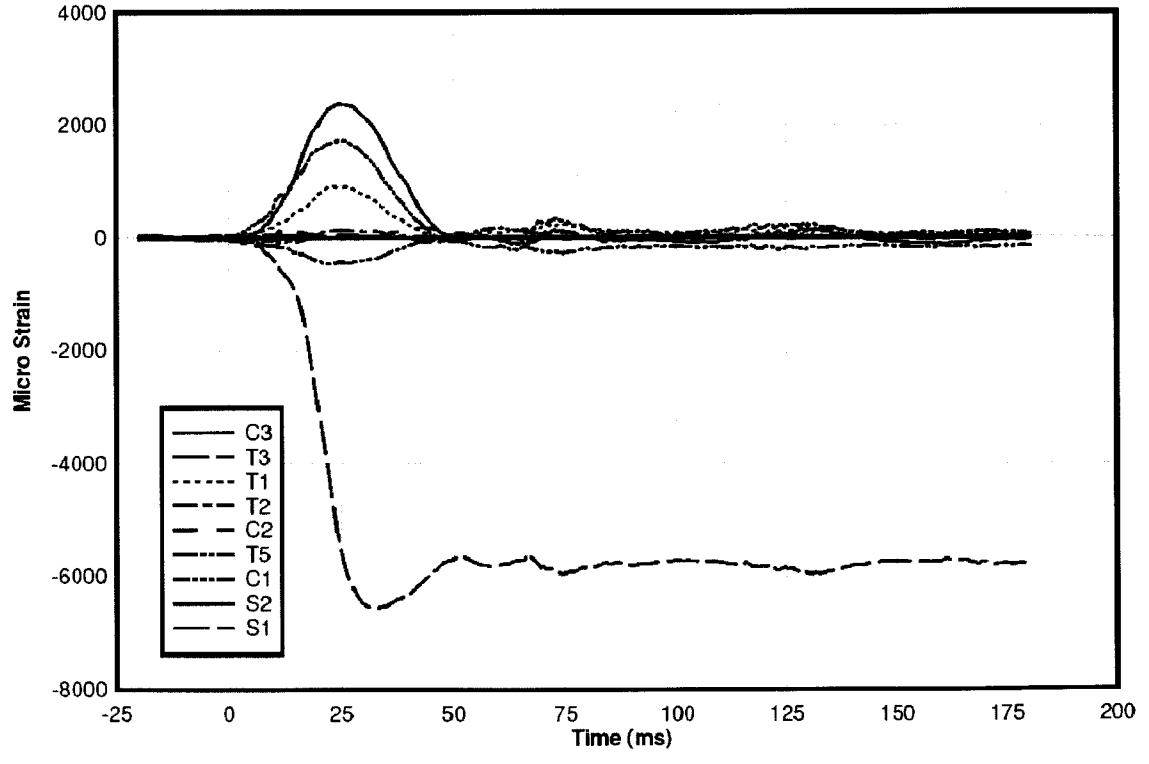


*Figure 7-21: Strain Time History for Test RC-7-2*

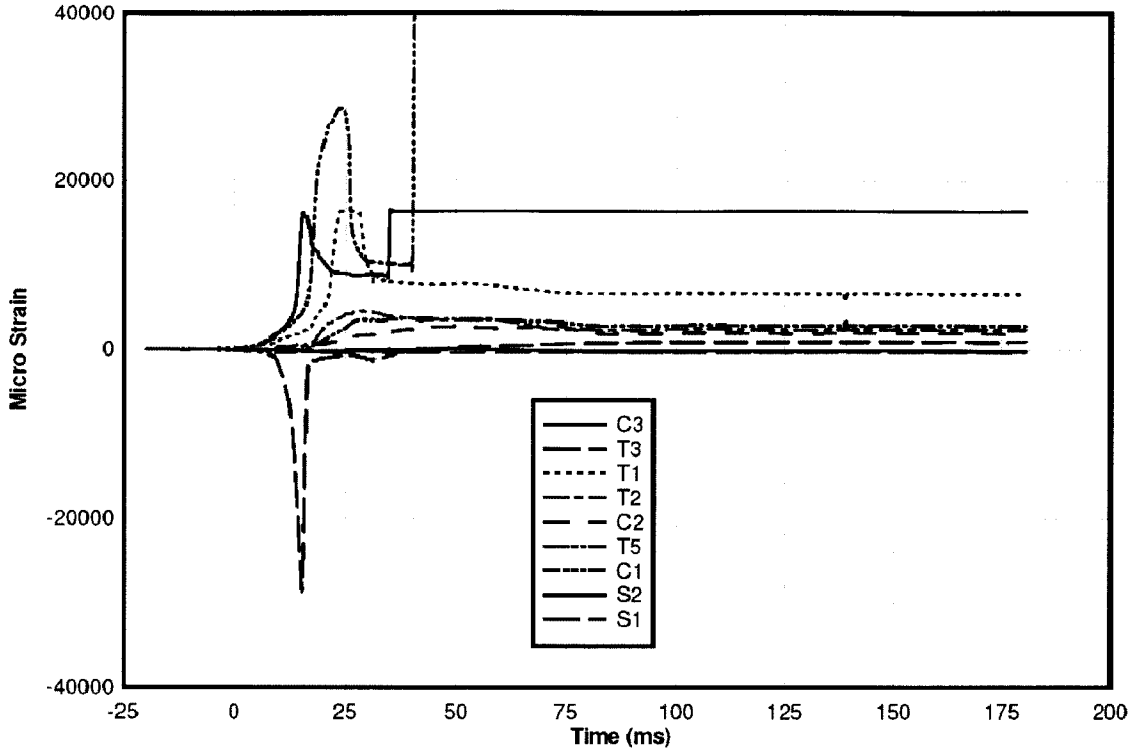


*Figure 7-22: Strain Time History for Test RC-7-3*

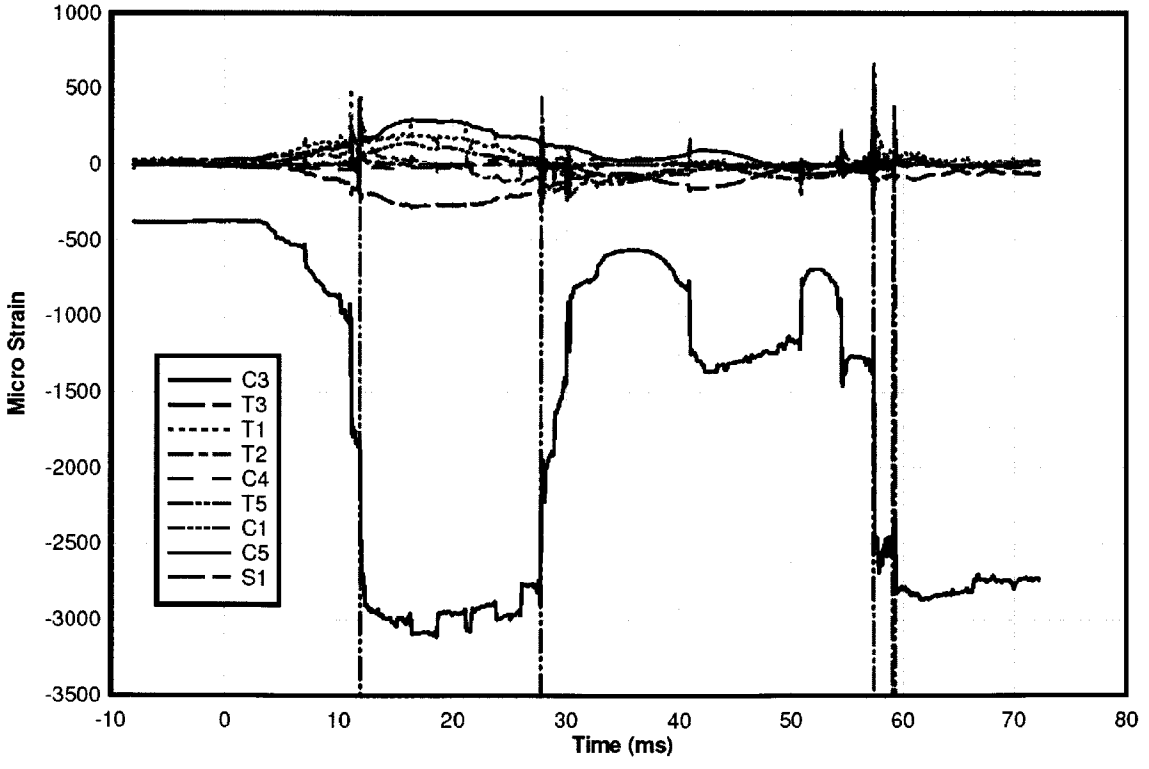


*Figure 7-23: Strain Time History for Test RC-8-1*

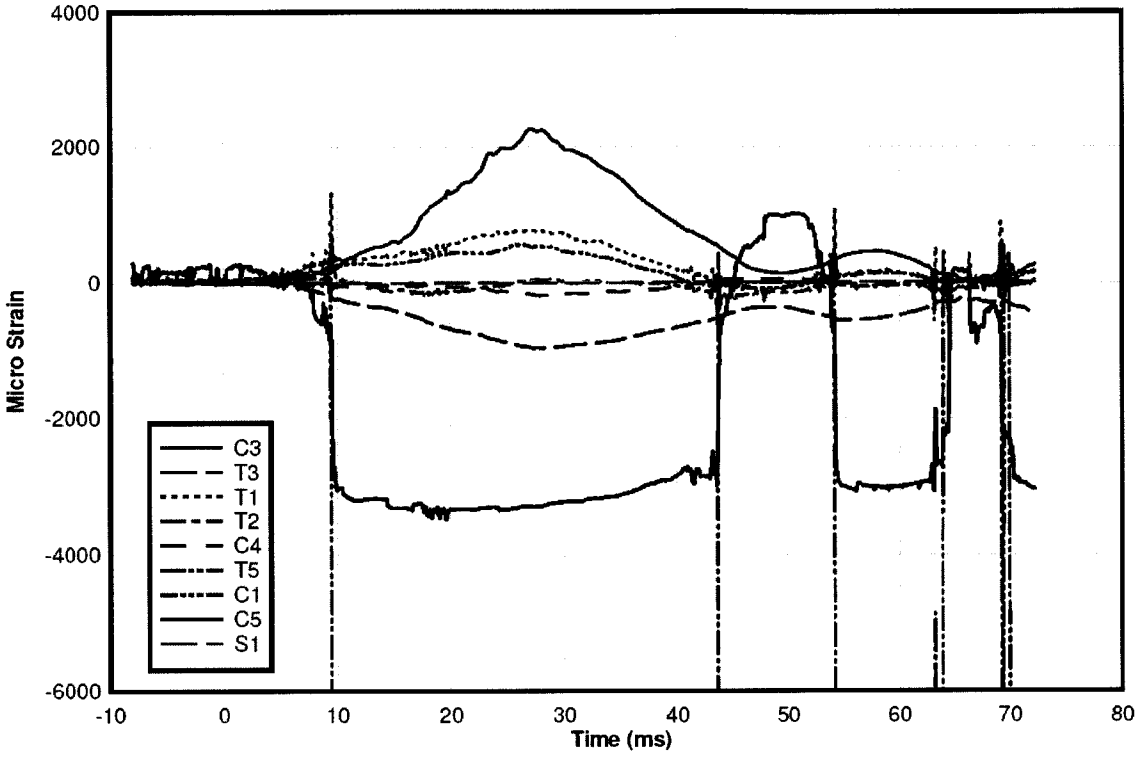


*Figure 7-24: Strain Time History for Test RC-8-2*

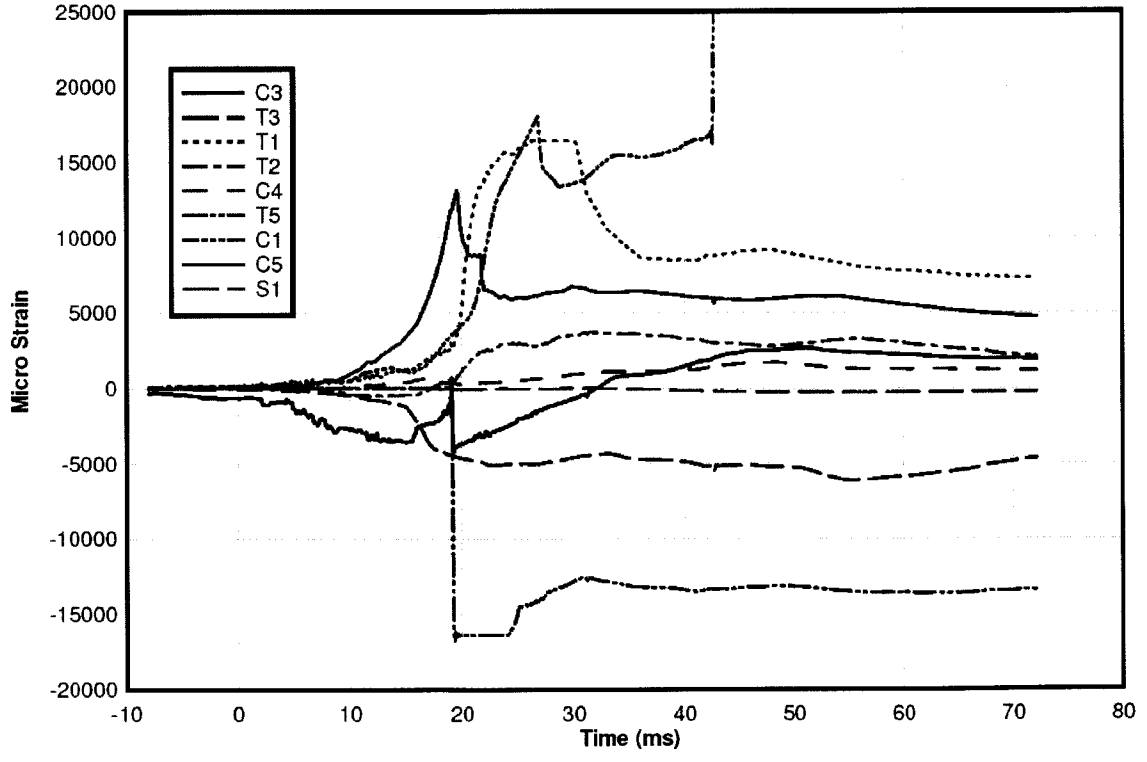


*Figure 7-25: Strain Time History for Test RC-8-3*

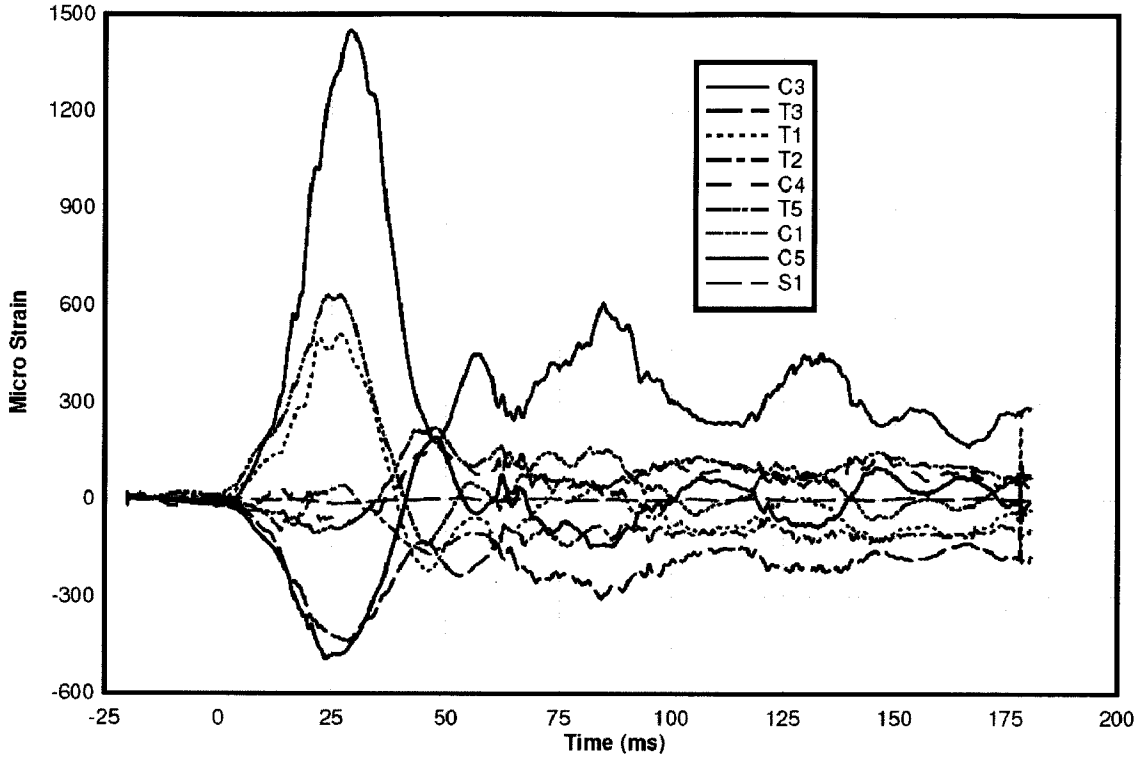


*Figure 7-26: Strain Time History for Test RC-9-1*

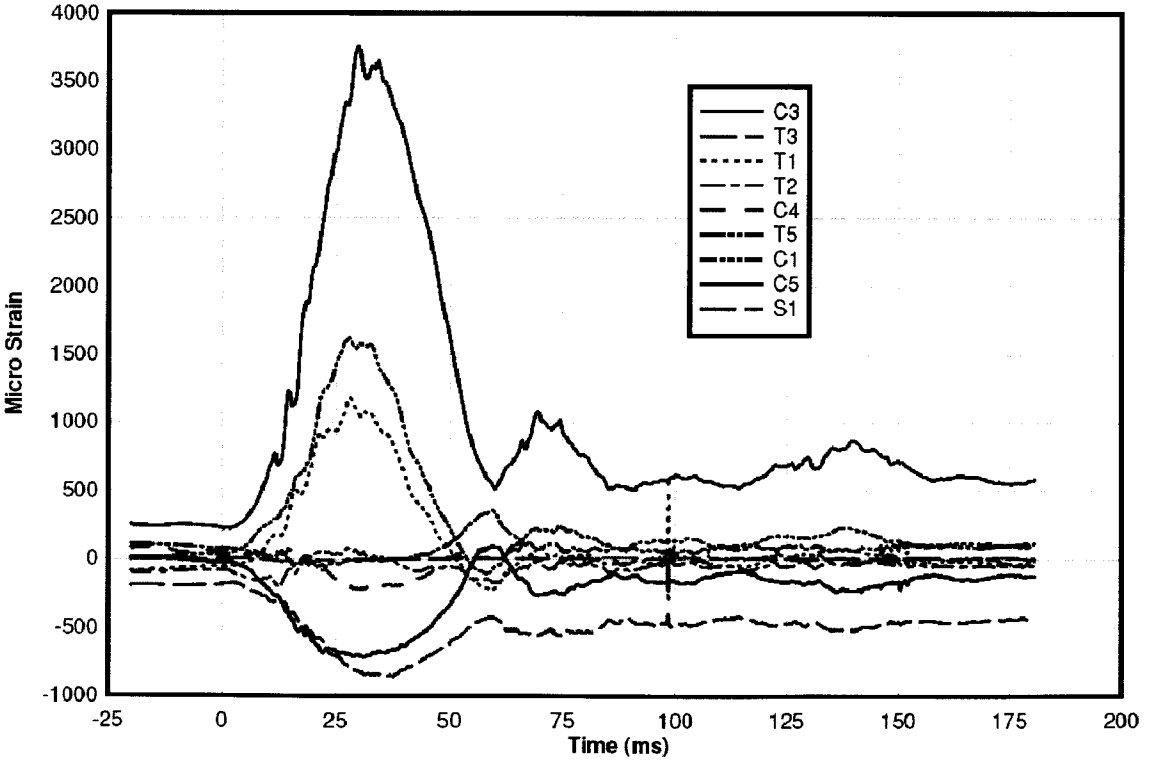


*Figure 7-27: Strain Time History for Test RC-9-2*

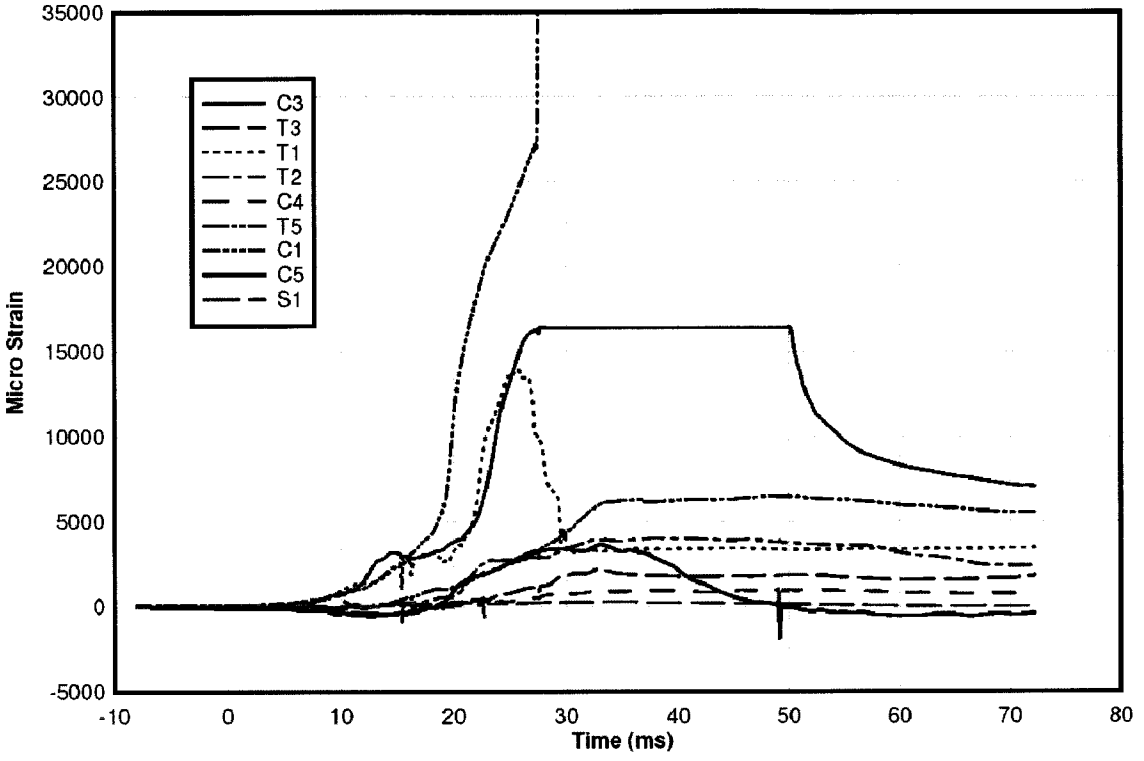


*Figure 7-28: Strain Time History for Test RC-9-3*

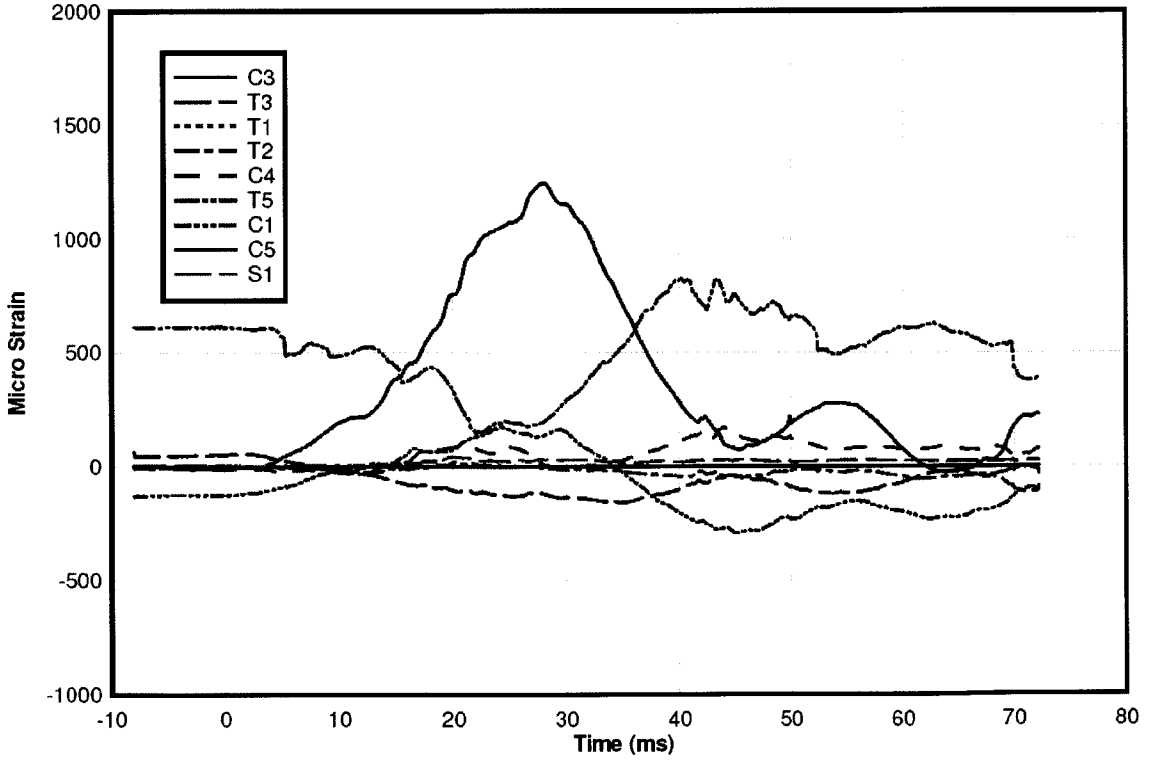


*Figure 7-29: Strain Time History for Test RC-10-1*

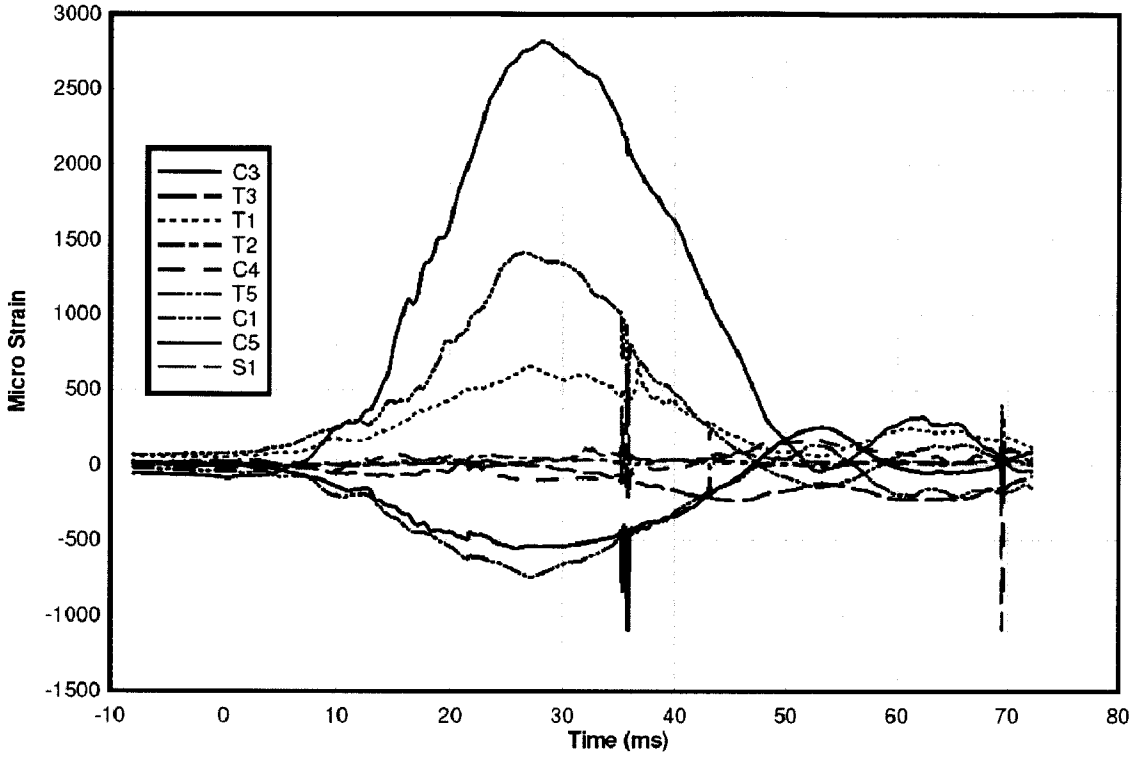


*Figure 7-30: Strain Time History for Test RC-10-2*

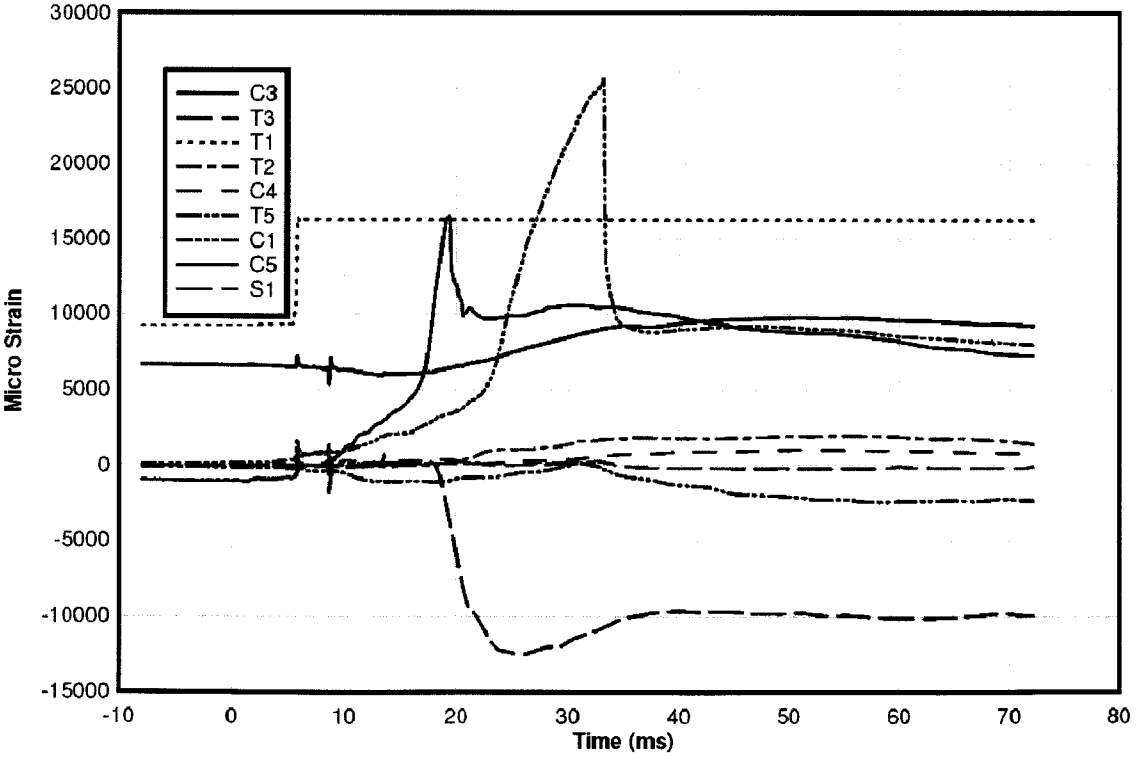


*Figure 7-31: Strain Time History for Test RC-10-3*

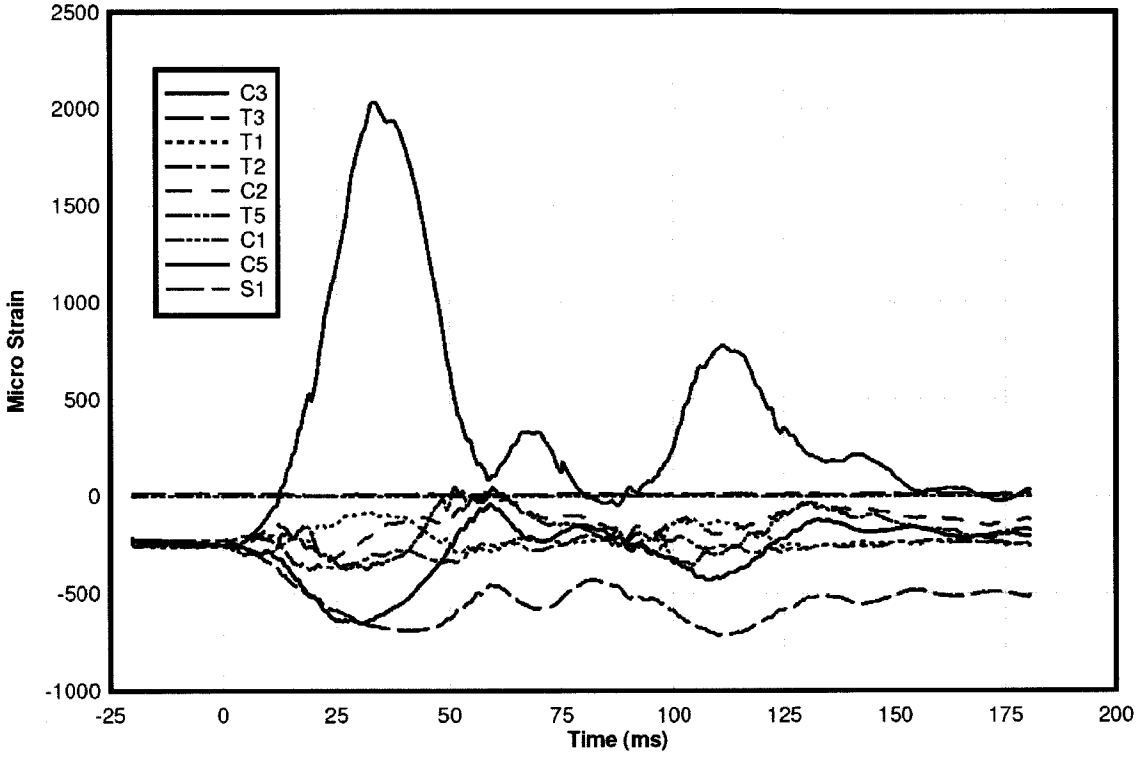


*Figure 7-32: Strain Time History for Test RC-11-1*

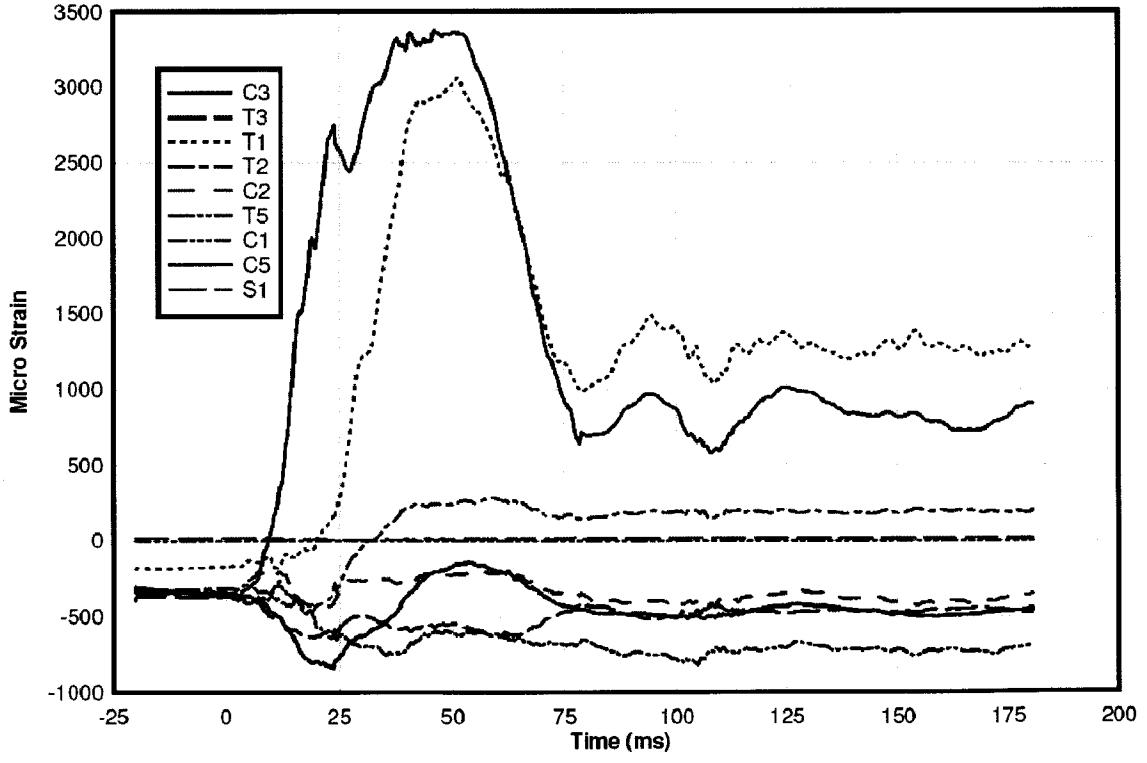


*Figure 7-33: Strain Time History for Test RC-11-2*

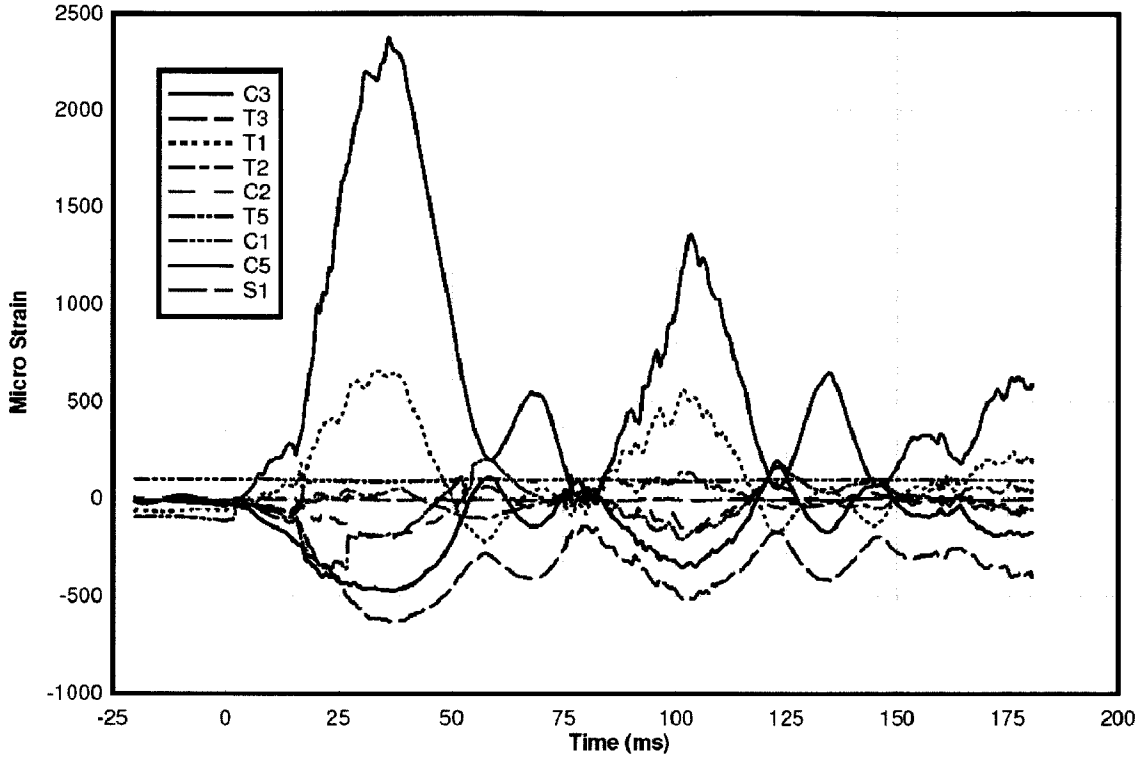


*Figure 7-34: Strain Time History for Test RC-12-1*

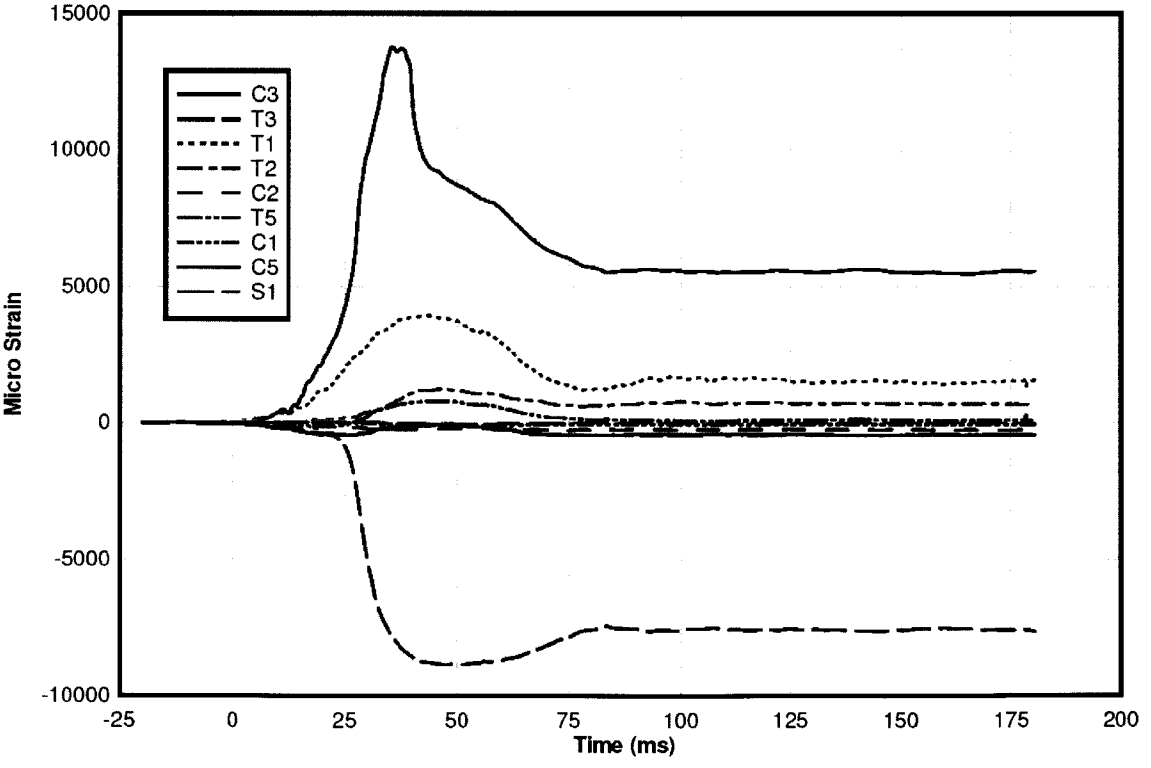


*Figure 7-35: Strain Time History for Test RC-12-2*

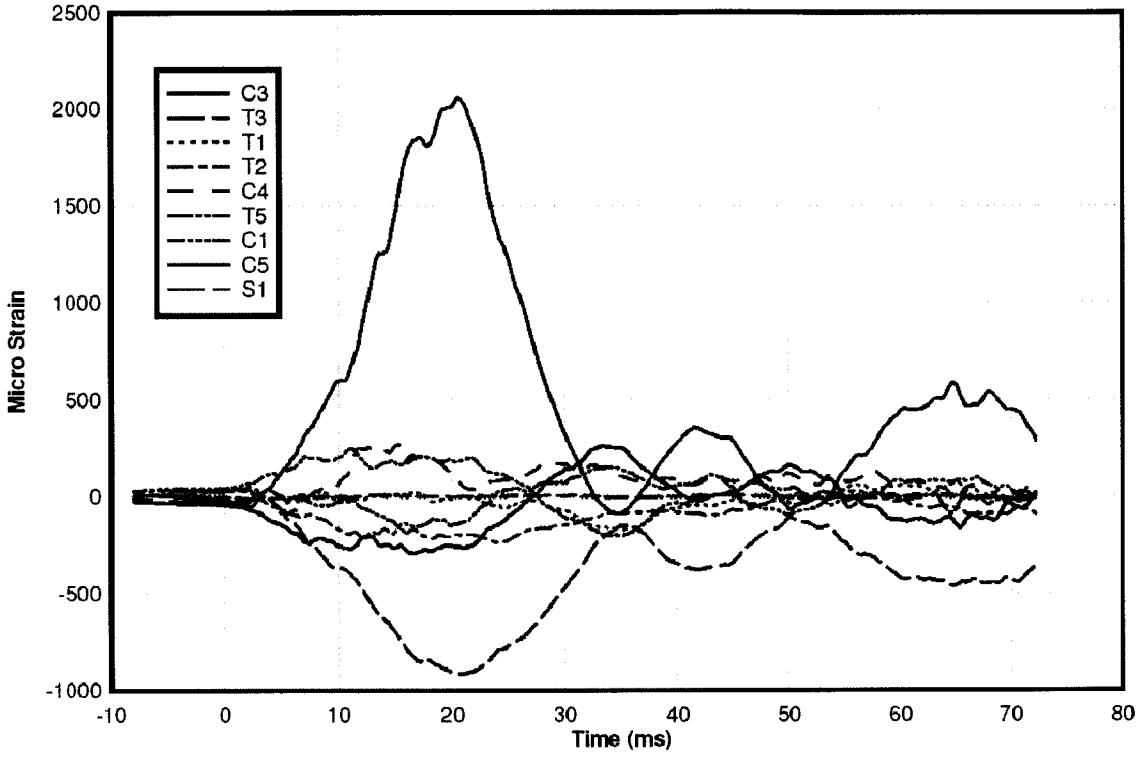


*Figure 7-36: Strain Time History for Test RC-13-1*

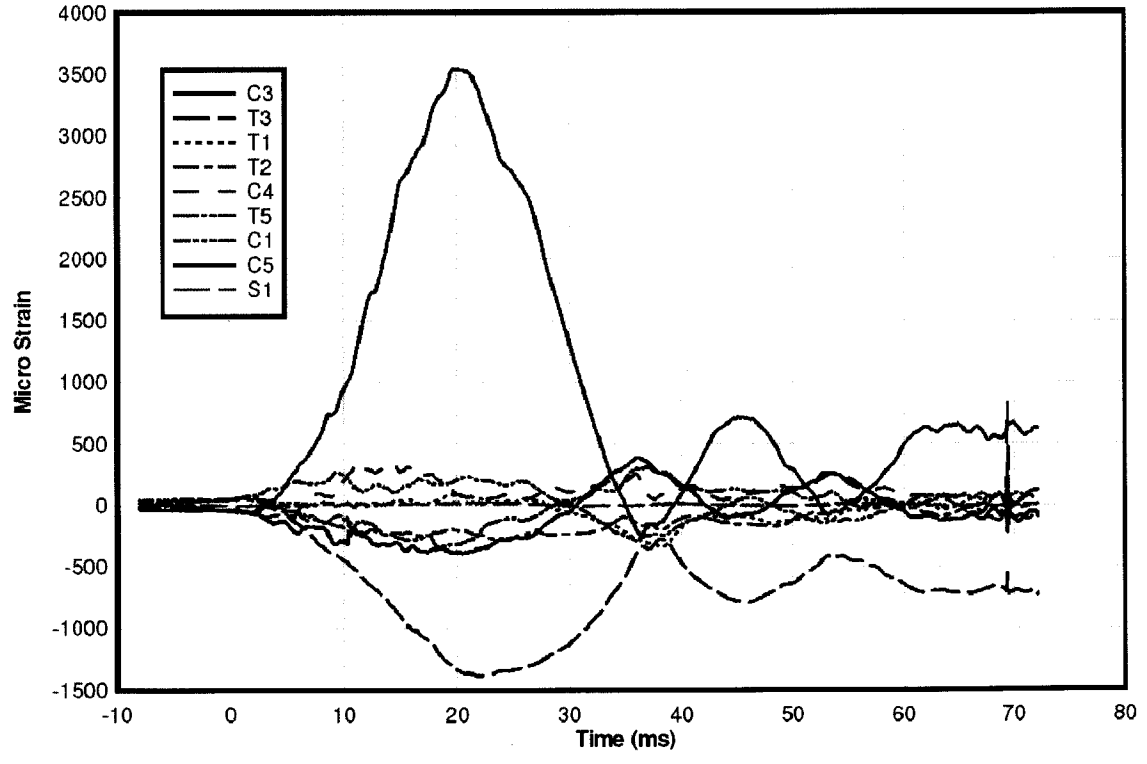


*Figure 7-37: Strain Time History for Test RC-13-2*

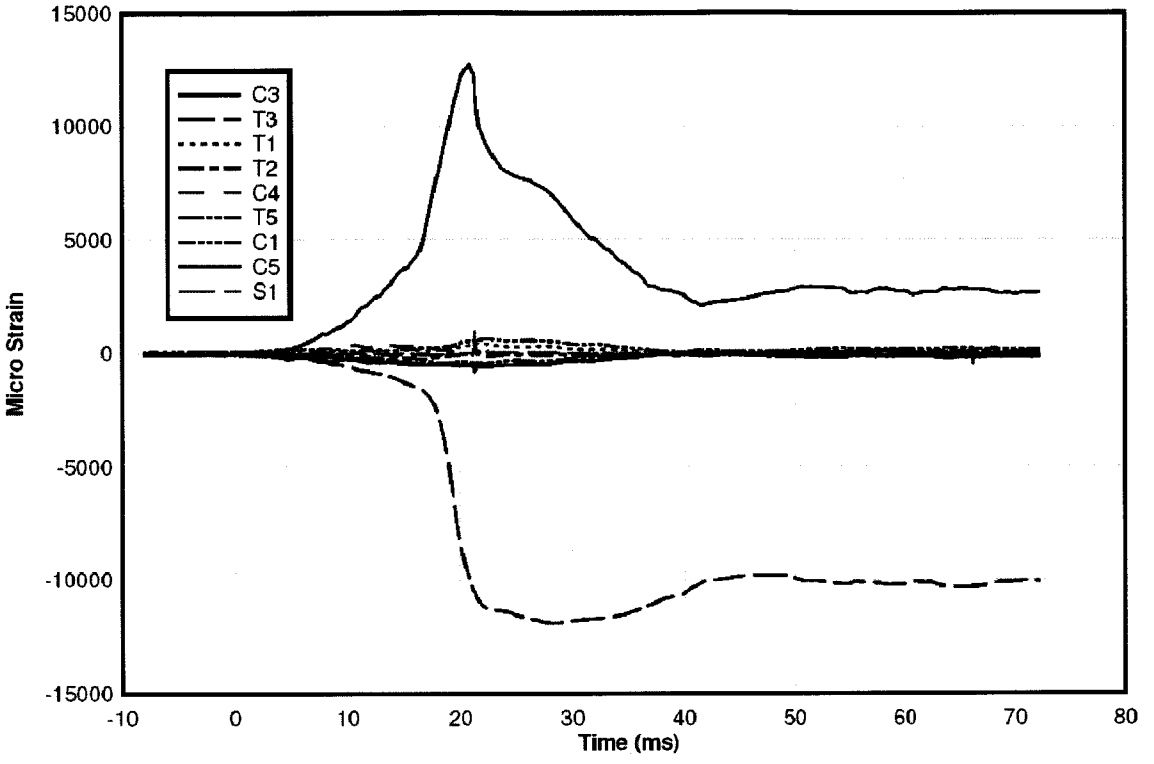


*Figure 7-38: Strain Time History for Test RC-13-3*

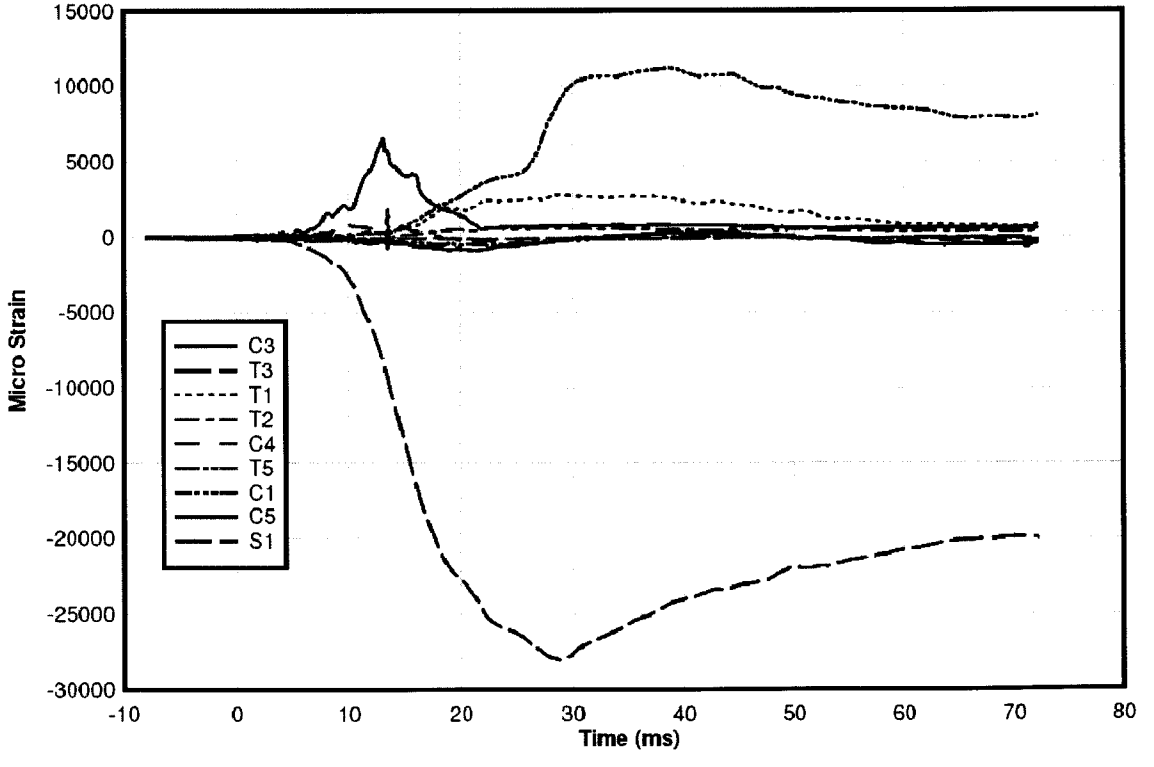


*Figure 7-39: Strain Time History for Test RC-13-4*

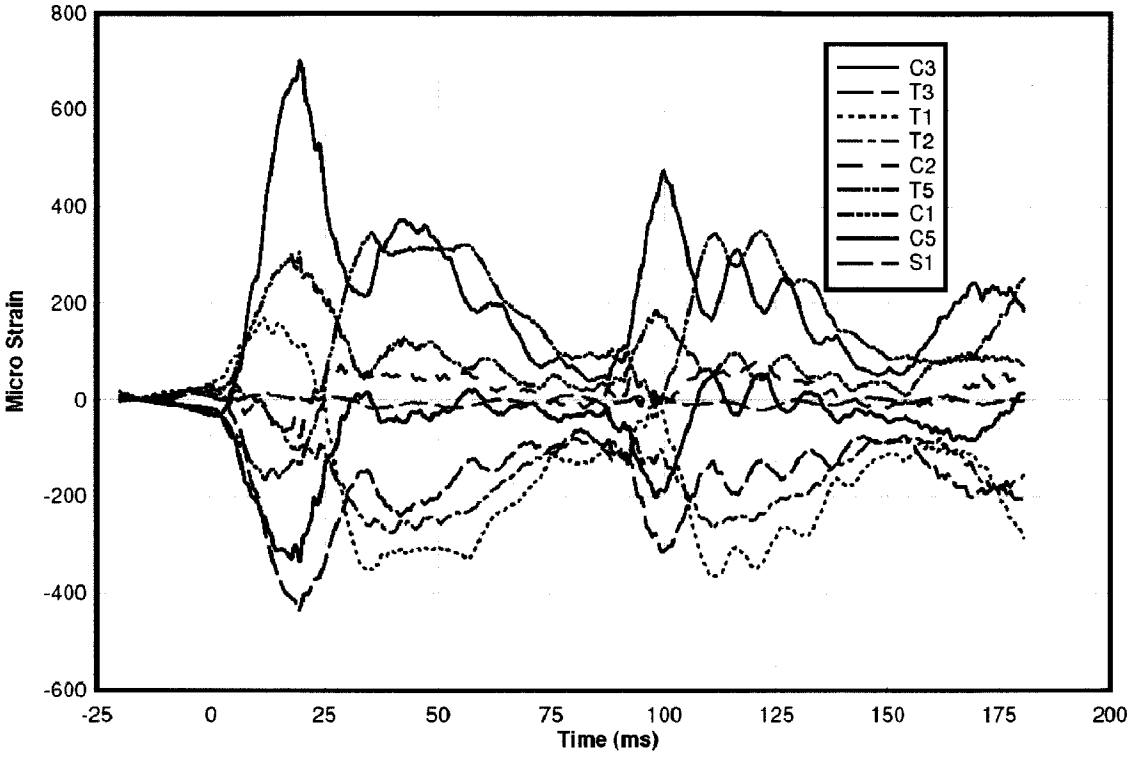


*Figure 7-40: Strain Time History for Test RC-14-1*

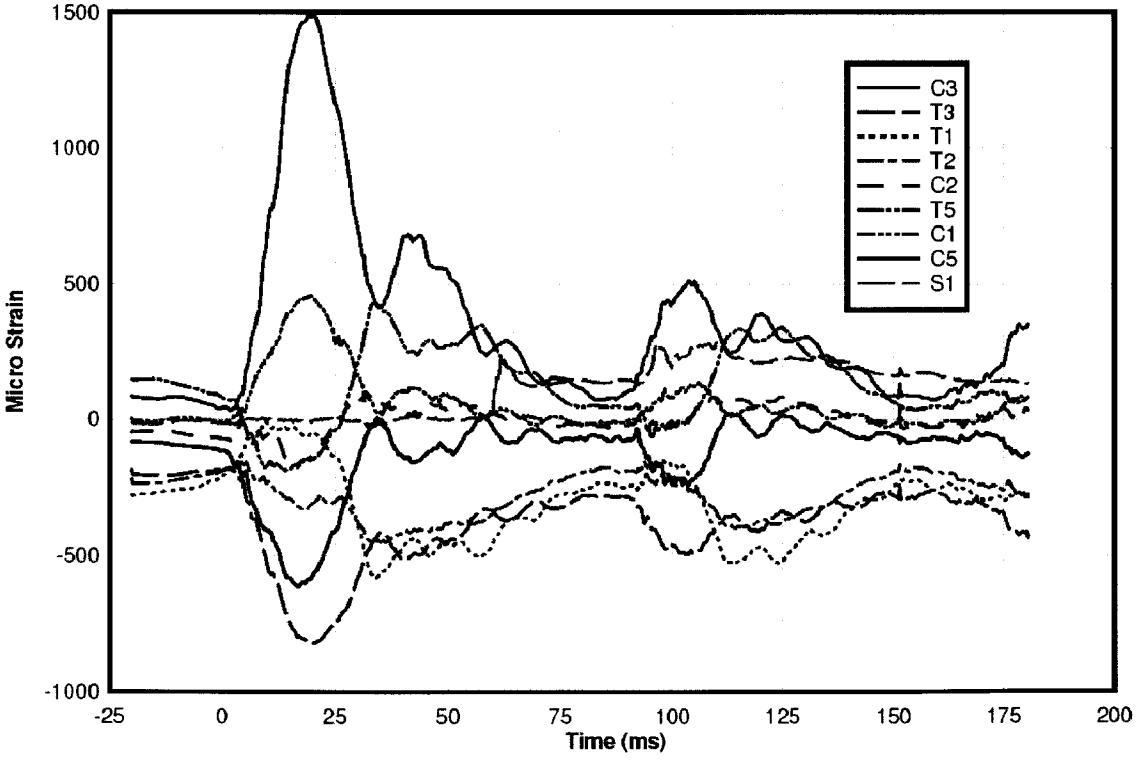


*Figure 7-41: Strain Time History for Test RC-14-2*

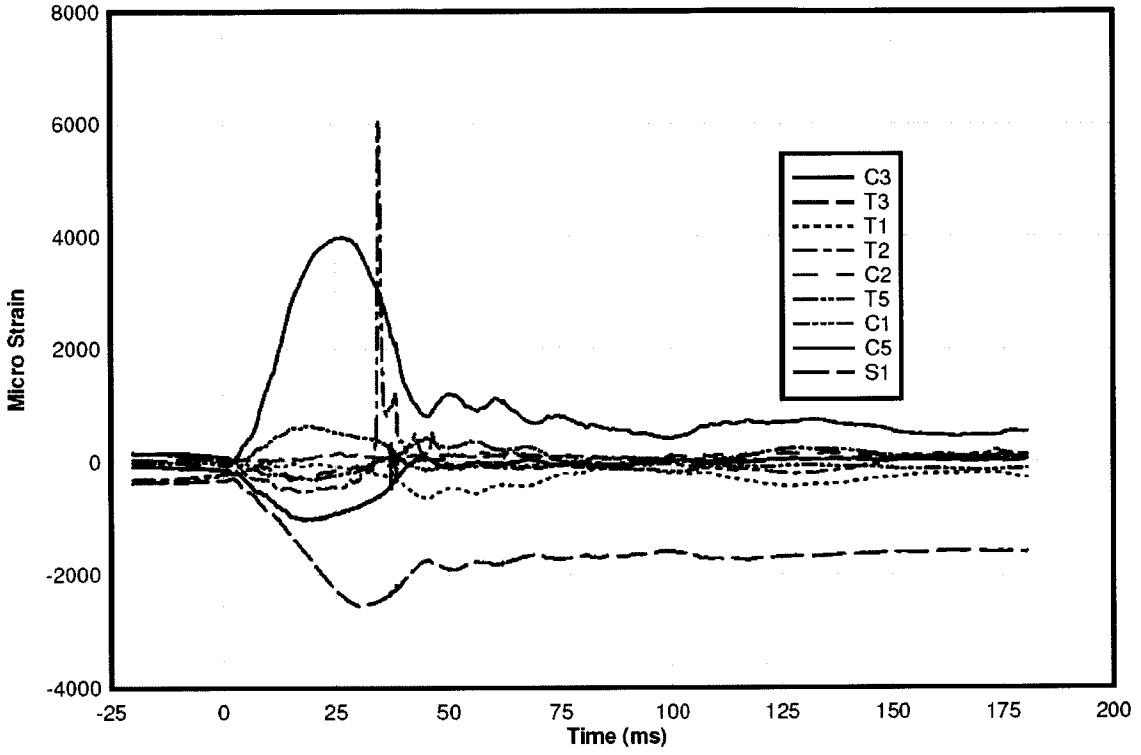


*Figure 7-42: Strain Time History for Test RC-14-3*

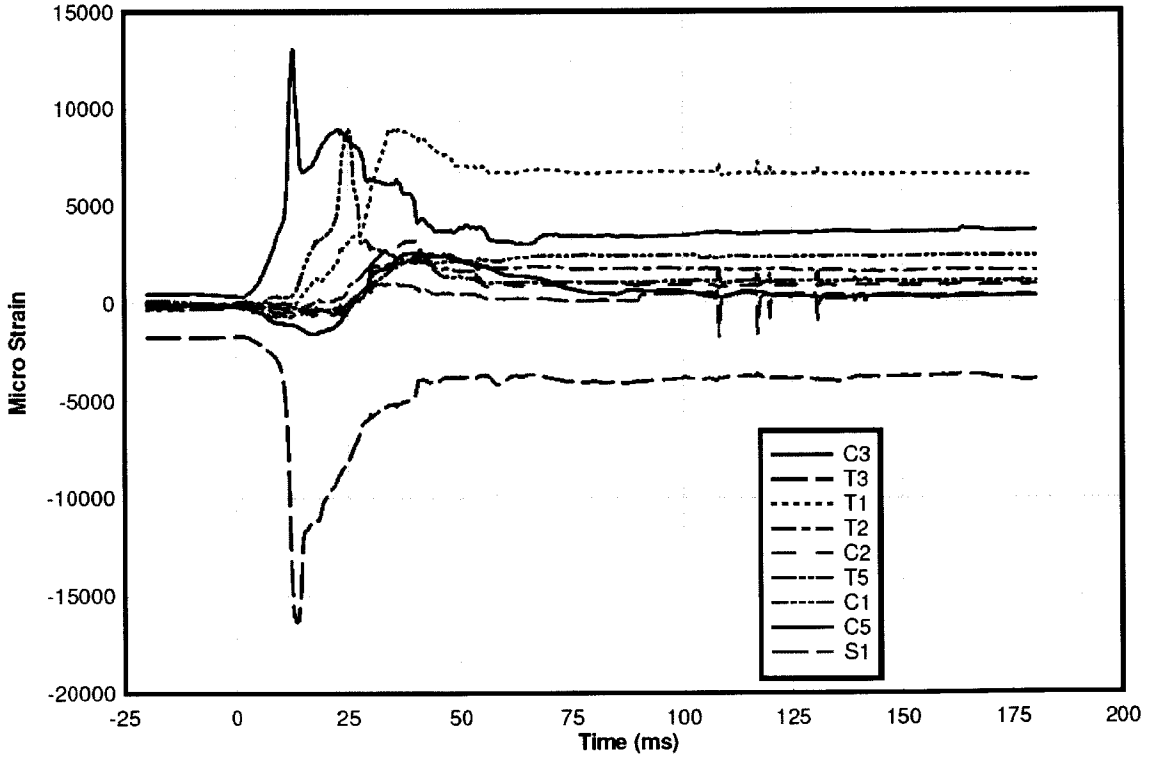


*Figure 7-43: Strain Time History for Test RC-14-4*